UC San Diego
UC San Diego Electronic Theses and Dissertations

Title
Frequency Response Function Based Damage Identification for Aerospace Structures

Permalink
https://escholarship.org/uc/item/5ff370hm

Author
Oliver, Joseph Acton

Publication Date
2015

Peer reviewed|Thesis/dissertation

UNIVERSITY OF CALIFORNIA, SAN DIEGO

Frequency Response Function Based Damage Identification for Aerospace Structures

A dissertation submitted in partial satisfaction of the requirements for the degree of
Doctor of Philosophy

in

Structural Engineering

by

Joseph Acton Oliver

Committee in charge:

 Professor John B. Kosmatka, Chair
 Professor Joel Conte
 Professor Raymond De Callafon
 Professor Charles Farrar
 Professor William Hodgkiss

2015

SIGNATURE PAGE

The dissertation of Joseph Acton Oliver is approved, and it is acceptable

in quality and form for publication on microfilm and electronically:

_____

_____

_____

_____

Chair

University of California, San Diego

2015

DEDICATION

To my parents, for everything.

And to my beautiful Sandra.

EPIGRAPH

It is not the mountain we conquer, but ourselves.

Sir Edmund Hillary

TABLE OF CONTENTS

LIST OF FIGURES

xiv

LIST OF TABLES

ACKNOWLEDGEMENTS

Finally, endless gratitude is owed to my parents Mimi and Peter Oliver, my siblings Dr. John Oliver, Jenny Oliver, and Madeleine Oliver, and my wife Sandra Ward for their unwavering support, encouragement, and love through the years of my graduate study, research, and writing. This dissertation belongs to them.

The material contained in Chapter 7 was developed in collaboration with Prof. John B. Kosmatka, Prof. Charles Farrar, Prof. Joel Conte, and Prof. Francesco Lanza di Scalea. The dissertation author was the primary investigator and author of this work.

The material contained in Appendix E was developed in collaboration with Prof. John B. Kosmatka, Prof. Charles Farrar, and Dr. Francois Hemez. The dissertation author was the primary investigator and author of this work.

VITA

2002   Bachelor of Science, University of California, Santa Barbara

2006   Master of Science, University of California, San Diego

2008   Candidate of Philosophy, University of California, San Diego

2010 – 2015   Environments Engineer, Space Exploration Technologies Corp.

2015   Doctor of Philosophy, University of California, San Diego

PUBLICATIONS

Oliver, J. A., Kosmatka, J. B., "Frequency Response Function Based Statistical Damage Identification Applied to Composite Sandwich Plates," *51st AIAA/ASME/ASCE/AHS/ASC Structures, Structural Dynamics, and Materials Conference*, Orlando, FL, 2010

Oliver, J. A., Kosmatka, J. B., "Statistical Damage Identification by Frequency Response Function Based Residual Force Minimization," *50th AIAA/ASME/ASCE/AHS/ASC Structures, Structural Dynamics, and Materials Conference*, Palm Springs, CA, 2009

Gobbato, M., Conte, J.P., Kosmatka, J.B., Oliver, J.A., Farrar, C.R., "Reliability-Based Framework for Damage Prognosis of Composite Unmanned Aerial Vehicles Structural Components," *Inaugural International Conference of the Engineering Mechanics Institute*, Minneapolis, MN. May 18-21, 2008

Oliver, J. A., Kosmatka, J. B., Hemez, F. M., Farrar, C. R., "Finite element model correlation of a composite UAV wing using modal frequencies", *Health Monitoring of Structural and Biological Systems,* Proc. SPIE, **6532**, 2007

Oliver, J. A., Kosmatka, J. B., Farrar, C. R., Park, G., "Development of a composite UAV wing test-bed for structural health monitoring research", *Health Monitoring of Structural and Biological Systems,* Proc. SPIE, **6532**, 2007

Oliver, J. A., Kosmatka, J. B., Hemez, F. M., Farrar, C. R., "Validating finite element models of composite aerospace structures for damage detection applications", *Nondestructive Evaluation and Health Monitoring of Aerospace Materials, Composites, and Civil Infrastructure V*, Proc. SPIE, **6176**, 2006

Kosmatka, J.B., Oliver, J.A., "Development of an In-Flight Structural Health Monitoring System for Composite Unmanned Aircraft," *47th AIAA/ASME/ASCE/AHS/ASC Structures, Structural Dynamics, and Materials Conference*, Newport, Rhode Island (paper AIAA-1881), 1 - 4 May (2006)

Matt, H., Bartoli, I., Coccia, S., Lanza di Scalea, F., Oliver, J. A., Kosmatka, J. B., Park, G., Farrar, C. R., "Ultrasonic guided wave monitoring of composite bonded joints using macro fiber composite transducers", *Smart Structures and Materials 2006: Sensors and Smart Structures Technologies for Civil, Mechanical, and Aerospace Systems*, Proc. SPIE, **6174**, 2006

Oliver, J. A., Kosmatka, J. B., "Evaluation of the Hilbert-Huang transform for modal-based structural health monitoring applications" *Nondestructive Evaluation and Health Monitoring of Aerospace Materials, Composites, and Civil Infrastructure IV*, Proc. SPIE, **5767**, 274-285, 2005

Oliver, J. A., Kosmatka, J. B., "Evaluation of modal-based damage detection techniques for composite aircraft sandwich structures", *Nondestructive Evaluation and Health Monitoring of Aerospace Materials, Composites, and Civil Infrastructure IV,* Proc. SPIE , **5767**, 264-273, 2005

Matt, H. M., Lanza di Scalea, F., Marzani, A., Coccia, S., Oliver, J. A., Kosmatka, J. B., Rizzo, P., Restivo, G., "A guided-wave system for monitoring the wing skin-to-spar bond in unmanned aerial vehicles", *Sensors and Smart Structures Technologies for Civil, Mechanical, and Aerospace Systems*, Proc. SPIE, **5765**, 758 – 768, 2005

Matt, H. M., Marzani, A., Oliver, J. A., Lanza di Scalea, F., Kosmatka, J. B., Sohn, H., Park, G., Farrar, C. R., "A Guide-wave Monitoring System for the Wing Skin-to-Spar Bond in Unmanned Aerial Vehicles," *Proceedings of the 23rd International Modal Analysis Conference, Orlando, FL, January 31- February 3, 2005.*

ABSTRACT OF THE DISSERTATION

Frequency Response Function Based Damage Identification for Aerospace Structures

by

Joseph Acton Oliver

Doctor of Philosophy

University of California, San Diego, 2015

Professor John B. Kosmatka, Chair

Structural health monitoring technologies continue to be pursued for aerospace structures in the interests of increased safety and, when combined with health prognosis, efficiency in life-cycle management. The current dissertation develops and validates damage identification technology as a critical component for structural health monitoring of aerospace structures and, in particular, composite unmanned aerial vehicles. The primary innovation is a statistical least-squares damage identification algorithm based in concepts of parameter estimation and model update. The algorithm uses frequency response function based residual force vectors derived from distributed vibration measurements to update a structural finite element model through statistically weighted least-squares minimization producing location and quantification of the damage, estimation uncertainty, and an updated model. Advantages compared to other approaches

include robust applicability to systems which are heavily damped, large, and noisy, with a relatively low number of distributed measurement points compared to the number of analytical degrees-of-freedom of an associated analytical structural model (e.g., modal finite element model).

Motivation, research objectives, and a dissertation summary are discussed in Chapter 1 followed by a literature review in Chapter 2. Chapter 3 gives background theory and the damage identification algorithm derivation followed by a study of fundamental algorithm behavior on a two degree-of-freedom mass-spring system with generalized damping. Chapter 4 investigates the impact of noise then successfully proves the algorithm against competing methods using an analytical eight degree-of-freedom mass-spring system with non-proportional structural damping. Chapter 5 extends use of the algorithm to finite element models, including solutions for numerical issues, approaches for modeling damping approximately in reduced coordinates, and analytical validation using a composite sandwich plate model. Chapter 6 presents the final extension to experimental systems—including methods for initial baseline correlation and data reduction—and validates the algorithm on an experimental composite plate with impact damage. The final chapter deviates from development and validation of the primary algorithm to discuss development of an experimental scaled-wing test bed as part of a collaborative effort for developing structural health monitoring and prognosis technology. The dissertation concludes with an overview of technical conclusions and recommendations for future work.

1 INTRODUCTION

Fiber-reinforced polymer composites are used with increasing frequency in aerospace primary structures because of excellent and tailorable specific strength and stiffness characteristics. Full acceptance of their use in primary structures is hampered, however, by internal damage modes with little-to-no yield before failure. Aircraft structures in particular suffer from impact, overload, and fatigue damage, which can then grow internally under cyclic operational loads and overloads to the point of catastrophic failure either by strength exceedance or stiffness degradation leading to dynamic instability (aeroelastic flutter). The standard practice for preventing structural failure in manned aircraft throughout history has been to perform regular break-down inspections, a practice which has led to an exceptional safety record for traditional metallic airframes but at the expense of non-critical labor and time out-of-service. Newly designed aircraft include conservative safety factors to account for future growth and also unexpected damage events which might be missed during regular inspections or might propagate to failure before the next inspection, cutting into potential structural efficiency. In the case of future composite airframes and the associated uncertainty associated with invisible damage modes, however, these current safe-guards may prove inadequate or will cut into structural potential and increase costs in any case. In addition to aircraft, next generation space craft and orbital structures will be reliant on composites because of the potential for weight savings, thermal neutrality, and innovative design. In these cases, even the

smallest structural failure can lead to catastrophic loss of the system, and potentially the lives depending on it, and must be avoided at all costs. In this case, knowledge of potential defects before they reach critical levels is of paramount importance.

Systems for structural health monitoring and prognosis have the potential to mitigate structural damage issues by acting like a biological nervous system. Such systems will analyze measured data along with other information, measured and estimated, to infer current and future damage states and operational capacities of the structure. The structural health monitoring components, which provide regular quantification of current structural health, will help with system safety and provide information for required maintenance. Prognosis systems, which when coupled with concepts of damage-tolerant design and life-cycle management provide a current estimate of life remaining, will lead to optimized and cost-efficient operating-cycles by allowing the structure to be taken out of service only when necessary.

Although structural health monitoring will be useful and enabling in itself, the extension to structural health prognosis represents a true paradigm shift in aerospace structure design and operation. The key change is from traditional deterministic analysis to the fully probabilistic design and life-cycle management approaches which will define the future of the industry. Since prognosis must be based on probabilistic principles, with respect to current structural health and estimates of future operating conditions, damage occurrence, and damage evolution, fully developed prognosis capability will both demand and support this general evolution. One promising path to meaningful prognosis

capability is through a structural reliability based framework, such as the Pacific

Earthquake Engineering Research Center (PEER) reliability system for earthquake and

civil structure prognosis and management [1-1] and its adaptation to composite

unmanned aerial vehicle (UAV) structures [1-2][1-3]. No matter how prognosis is

formulated, however, the starting point should be regular probabilistic estimations of the

current damage state. Furthermore, the damage should be accurately describable in a

correlated analytical structural model so that the system can analyze the effects of

potential damage evolution cases and build statistical databases. In other words, even

viewed separately, the future prognosis-based industry standard will likely demand that

structural health monitoring and model correlation be statistically formulated.

Fully matured systems for structural health monitoring and prognosis, including

constant real-time monitoring and consistently updated structural models and life-

remaining estimates unique to each structure, will certainly exist as a fundamental

component of future aerospace structures. In the nearer term, however, even the most

basic systems must be designed and implemented in order to begin realizing the potential

of composite materials and the next-generation designs they will allow. Modern UAVs,

for instance the General Atomics Predator shown in Figure 1-1, are well-suited platforms

for development of structural health monitoring and prognosis, as well as candidates for

the technology themselves. These increasingly popular aircraft make heavy use of

composites in their primary structures, are designed using lower safety factors than

Figure 1-1: The all-composite Predator UAV by General Atomics.

traditional manned vehicles, and are operated under harsh conditions with a minimum of

between-flight inspection and no in-flight inspection. Being unmanned they are routinely

operated to performance limits, and the common practice is to replace key structural

components, such as wings, after a certain number of flight hours, regardless of the

structure's integrity, to avoid the prohibitive costs and uncertainty associated with regular

inspection and damage tolerant structural analysis. Because unmanned vehicles are

cheaper, more accessible, and less regulated than their manned counterparts,

developmental on-board systems for structural health monitoring and prognosis can be

flight tested with relative ease. Much of the work accomplished towards this dissertation

has been developed with application to all-composite UAVs in mind.

1.1 Aerospace Structural Health Monitoring Systems Overview

A complete system for structural health monitoring and prognosis for aerospace structures will ideally provide four levels of information: (1) damage existence; (2) damage location; (3) damage severity quantification, or *damage identification*, including possible information on size, severity, and damage type; and (4) estimate of remaining life. The first three levels are the goal of structural health monitoring; the fourth is the goal of prognosis. A high-level overview of a combined system is given in Figure 1-2, showing the major information components required from a structural health monitoring system which will support prognosis: damage information, estimation uncertainty, and an analytical structural model correlated to the current damage state.

It can be assumed that structural health monitoring systems will include structural dynamic response from a distributed sensor network. High frequency dynamic response methods based on ultrasonic waves have been vigorously pursued because of their potential to detect and localize small damage cases. Although potentially successful in localizing damage close to sensors, the response can't be easily and generally tied back to analytical models of the sort required for global structural analysis. It is possible to use the location ability with an assumed damage type (for instance, delamination of a certain size), but global prognosis will require the damage model to be as accurate as possible. High frequency methods are promising for damage location in specific areas but full-vehicle damage identification will require more information related to the global system.
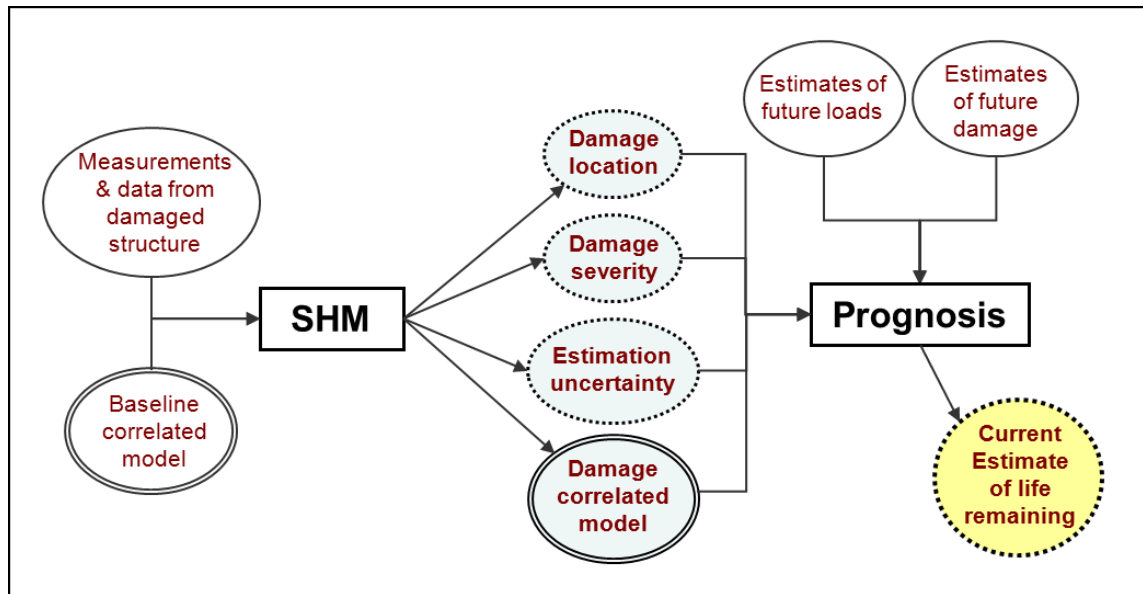
Figure 1-2: Overview of structural health monitoring (SHM) and prognosis for aerospace structures.

Low frequency vibrations on the other hand are sensitive to changes in the

structure (damage), are measurable in a global sense from a relatively small number of

sensors, and exist in the same wavelength range as the operating structure meaning that

changes in vibration are directly linked to structural performance in the operational

domain. Additionally, low-frequency vibrations can be easily and accurately related to

the response of analytical structural models, as required by prognosis. It can thus be

assumed that low-frequency analysis is required in some form in a structural health

monitoring system that supports prognosis. Additionally, the system must identify very

small levels of damage relative to the size of the structure and resolution of a reasonably

distributed sensor grid, and coupling a finite element model with the system provides more information for this analysis.

The disparity between vibration wavelength and damage size, however, means that structural health monitoring by low-frequency methods alone is challenging. One potential solution is to combine a low-frequency damage identification system with high-frequency systems for damage location (see Section 1.2). A second is to use measured frequency response functions instead of the derived modal parameters—natural frequencies, mode shapes, and modal damping ratios—which have historically dominated low-frequency structural health monitoring research. Frequency response functions are attractive because they capture a wide array of vibration information, including complex and coupled modes and full damping characteristics. They additionally allow the use of almost unlimited amounts of data—generally thousands of complex measurements at every sensor location—and can provide information on nonlinear behavior which can be indicative of damage in nominally linear structures, as most aerospace structures are assumed to be.

To summarize, it is proposed that a structural health monitoring system to support prognosis for composite aerospace structures has the following requirements:

(1)   Automatically detect, localize, and quantify unknown damage cases in a complex structure

(2)   Quantify the estimation uncertainty

(3)   Update an analytical structural model (assumed to be a finite element model

hereafter).

For accurate and complete damage identification, the system must also be able to

differentiate between changes in mass, stiffness, damping, and other system changes. To

accomplish these goals, especially those of automation, describing damping adequately,

and accuracy of estimation, such a system should include statistical finite element model

correlation based on measured frequency response functions taken from a distributed

sensor grid.

The proposed structural health monitoring system solution, summarized in Figure

1-3, operates in two independent stages: (a) damage location, and (b) damage

identification. In the first step, damage is detected and localized using a range of

information, as available. In the second step, the damage location information is used to

select a set of parameters which are then updated to statistically identify the damage and

update a finite element model. Options for damage location are discussed in more detail

next; development and validation of a new method for statistical damage identification,

including additional tools for model correlation and prognosis, are the main focus of the

remainder of this dissertation.
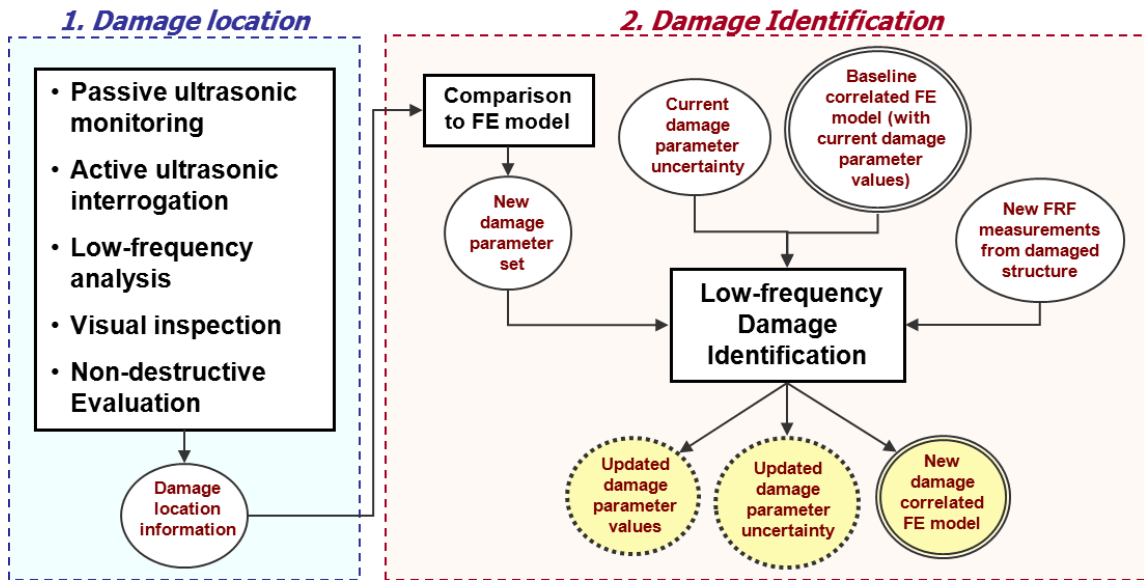
Figure 1-3: Overview of the proposed system for structural health monitoring in two steps: 1) damage location, 2) damage identification (FRF=Frequency response function, FE=finite element).

1.2   Damage Location

Methods specifically for damage location by dynamic response analysis fall

generally into two categories: those relying on lower-frequency structural vibrations, and

those relying on high-frequency guided waves. The first category—including such

methods as the residual force vector based method of Ricles and Kosmatka [1-4]—offers

the possibility for structure-wide coverage—anywhere with stored modal strain energy;

however, this comes at the expense of low sensitivity and fidelity, and is essentially

confined to the spatial measurement resolution. Localization to a finer resolution, such as

the finite element mesh, invites a lack of uniqueness. The method of element signature

recognition by Zimmerman [1-5] is shows promise in bridging this gap; however, as mentioned above, the fundamental difference in size between vibration shape wavelength and damage size will always prove challenging.

Active high-frequency analysis techniques on the other hand, such as the methods presented in references [1-6] and [1-7], can lead to extremely accurate damage localization because of the direct sensitivity of low-wavelength (high-frequency) waves to small damage features and the necessity of these methods to interrogate locally. These methods generally require limiting assumptions, such as assuming damage type (e.g., delamination), and are usually only sensitive to symptoms of damage (e.g., changing damage boundaries and decrease in transmissibility) which are not connected to the operational structural response. Passive techniques, for example the methods presented in references [1-8] through [1-12], essentially 'listen' for events that could signal either damage occurrence or damage propagation and then use methods based in triangulation and optimization to locate the source. This can be a powerful approach, also providing highly accurate damage location. Limitations include that data acquisition must be operating at the instant of damage to capture the event and the damage event must create a measurable wave. For composite structures the first damage event may create a large wave but subsequent damage propagation may fall below the measureable threshold, limiting the ability of passive techniques alone to characterize a worsening structural state. An additional point pertaining to all high-frequency methods is that they are by nature local and only sensitive to damage occurring close to operating sensors. Global

structural health monitoring for general unknown damage cases on a realistically sized structure would therefore require a large number of sensors. These limitations aside, high-frequency methods—passive and active—will certainly be useful, even critical, in a functional global structural health monitoring system.

In order to bridge this gap between sensor and hardware requirements and available technology in the short term, and to increase fidelity in the longer term, non-destructive evaluation techniques (which are currently used as part of regular inspection routines in some commercial aerospace structures) could potentially be used to provide accurate localization. However, in addition to the requirement that non-destructive evaluation requires the structure to be temporarily removed from service and be available to technicians (impossible for on-orbit space structures, for instance), these methods have their own limitations, such as expense, operator variability, and the fact that they usually cannot be applied to internal structures without returning to full-scale break-down inspections.

As indicated in Figure 1-3, it is therefore assumed that a realistic functional system would need to use a combination of techniques, and in particular, as many available techniques as possible in order to gain their benefits and reduce the impact of their deficiencies. This could include passive high-frequency monitoring (indicative of impact events and/or damage propagation) and localization, event logging by structural operators (similar to the current practice of pilots logging heavy landings in commercial aircraft), load event monitoring by force transducers and accelerometers, active high-

frequency inspection of selected regions considered high-risk or high-criticality (leading edges, structural joints, main load paths), visual inspection information between operational cycles by technicians or during operation via camera, any non-destructive testing which is carried out because of events or as regularly required, and results of low-frequency analysis based on specifically measured vibration data. In the proposed system, all of this information can be fused into a selection of parameters which *may* represent damage, and which are then updated to describe the damage state by the damage identification algorithm. So long as all potential damage cases are considered, the damage identification should then determine the current damage state within the limits of the provided parameters, updating the structural model in the process.

1.3 Damage Identification Algorithm Overview

The primary innovation of the dissertation is a statistical model-update method for structural damage identification. Required algorithmic inputs are a structural model, a set of reference data from the baseline structure if the model is not sufficiently correlated to the baseline state, and a set of reference data from the damaged system. Any information on damage location and form can be included as an input, if available. If the analytical model does not have high enough fidelity to the baseline data it can be correlated using optimization-based techniques, including a modified version of the damage identification algorithm. Once the analytical model is correlated to the baseline state, the damage

identification algorithm uses a statistically weighted least-squares minimization of

frequency response function based residual force vectors to update the structural model,

thereby producing refined location information, quantification of the damage, estimation

uncertainty, and an updated structural model.

The dissertation's algorithm requires the following limiting assumptions to be

true:

1. The target physical system must be analytically modeled as a multiple degree-
    of-freedom system in the linear frequency domain.

2. Frequency response function reference data must be available across multiple
    frequency lines and degrees-of-freedom in a way that can be replicated by the
    analytical model with acceptably low error. Environmental factors affecting
    structural and model response, for example temperature, must be normalized
    between the structural test configuration and model. For practical
    implementation, for instance on an aircraft, this likely requires testing the
    structure in a controlled environment where boundary conditions and
    environmental factors can be controlled and measured with sufficient
    accuracy to be replicated precisely in the analytical model.

3. System properties and potential damage parameters must be modeled as
    implicit, smoothly varying parameters which are tied to dynamic system
    response in the same regime as the reference data.

4. The system damping must be able to be captured using a linear combination of structural and viscous damping matrices (albeit with no restrictions on proportionality).

5. The model must be capable of producing the global frequency domain dynamic response of the physical structure in the baseline and damaged states with a lower level of error than is caused by the target damage cases being identified.

When properly implemented, the current algorithm demonstrates the following notable advantages:

- The algorithm can identify damage in the form of changes in stiffness, mass, damping, and any parameter that can be structurally modeled and impacts vibration response.

- The algorithm does not require modal parameters, although they can be incorporated to increase fidelity through damping model identification and frequency line selection.

- The algorithm can be applied to systems with non-proportional generalized and/or heavy damping provided only that it can be modeled via complex stiffness and/or viscous damping matrices in the linear frequency response function formulation.

- Because of the basis in frequency response functions, large amounts of reference data can be incorporated into the damage identification process, producing a resilience to incoherent noise.

- In combination with the integrated method for degree-of-freedom reduction, the algorithm also supports successful implementation in cases where the number of degrees-of-freedom in the model is far greater than in the reference data—a situation which is unavoidable for realistically sized aerospace structures.

- Because of the connection to full-system structural models—e.g., dynamic finite element models—the only limitation in terms of structural applicability is related to computational processing power (which scales as a function of number of degrees-of-freedom). It should be noted that increasing the size of the update parameter set increases the potential for non-uniqueness—the curse of dimensionality—requiring additional down-selection from upstream damage location activities and care in implementation.

- The statistical framework produces a posterior uncertainty values along with updated damage parameters, providing a relative estimate of confidence in updated parameters in addition to a basis for downstream prognosis.

1.4   **Summary of Dissertation**

     This dissertation is primarily concerned with development and validation of an algorithm for statistical damage identification and model correlation, in the context of supporting full-vehicle structural health monitoring and prognosis. Chapters 2 through 6 are devoted to this work. In addition, Chapter 7 discusses development of a scaled-wing test-bed as part of a multi-disciplinary collaborative project on structural health monitoring and prognosis.

     The remaining chapters are organized as follows:

- Chapter 2: Review of literature on structural health monitoring and statistical damage identification.

- Chapter 3: Theoretical development of the damage identification algorithm and related aspects of structural dynamics followed by a detailed study of fundamental algorithm behavior on a two degree-of-freedom mass-spring system with generalized damping.

- Chapter 4: Implementation of the algorithm on systems with noise followed by validation on a noisy eight degree-of-freedom mass-spring system with nonproportional structural damping and comparison to several competing damage identification algorithms.

- Chapter 5: Implementation of the statistical damage identification algorithm on realistically sized structures, including development of a code coupling the

algorithm to a commercial finite element code with reduced coordinate reference

data, and analytical validation and parametric studies on damped composite

sandwich plate structures with additive noise and proportional damping.

- Chapter 6: Experimental implementation of the statistical damage identification

  algorithm, including treatment of initial model correlation and exact measured

  damping modeling, and experimental validation of the method on a composite

  plates with impact damage.

- Chapter 7: Development of an all-composite scaled-wing test-bed as part of a

  collaborative effort towards furthering technology for integrated structural health

  monitoring and prognosis.

- Chapter 8: Conclusions and recommendations for future work.

1.5   Chapter 1 References

[1-1]   Zhang, Y., Acero, G., Conte, J., Yang, Z., Elgamal, A., "Seismic Reliability Assessment of a Bridge Ground System," *13th World Conference on Earthquake Engineering*, Vancouver, B.C., Canada, August 1-6, 2004, Paper No. 2978, (2004)

[1-2]   Gobbato, M., Conte, J.P., Kosmatka, J.B., Oliver, J.A., Farrar, C.R., "Reliability-Based Framework for Damage Prognosis of Composite Unmanned Aerial Vehicles Structural Components," *Inaugural International Conference of the Engineering Mechanics Institute*, Minneapolis, MN. May 18-21, (2008)

[1-3]   Gobbato, M., Kosmatka, J.B., Conte, J.P., "Developing an Integrated Structural Health Monitoring and Damage Prognosis (SHM-DP) Framework for Predicting the Fatigue Life of Adhesively-Bonded Composite Joints," Chapter 17 in *Fatigue and Fracture of Adhesively Bonded Composite Joints: Behaviour, Simulation and Modelling*, A.P. Vassilopoulos Ed., Cambridge, UK: Woodhead publishing Limited, pp. 493-526, (2014)

[1-4]   Ricles, J.M., Kosmatka, J.B., "Damage Detection in Elastic Structures Using Vibratory Residual Forces and Weighted Sensitivity," *AIAA Journal*, **30**(9), pp. 2310-2316, (1992)

[1-5]   Zimmerman, D.C., Lopez, F.P., "Structural damage localization using element signature recognition," *AIAA Journal*, **45**(1), pp.71-78, (2007)

[1-6]   Matt, H.M., "Structural Diagnostics of CFRP Composite Aircraft Components by Ultrasonic Guided Waves and Built-In Piezoelectric Transducers," *Ph.D. Dissertation, University of California, San Diego*, (2006)

[1-7]   Yuan S., Lei W. and L. Shi, "Active monitoring for on-line damage detection in composite structures," *Journal of Sound and Vibration*, **125**, pp. 178-186, (2003)

[1-8]   Prosser W.H., Jackson K.E., Kellas S., Smith B.T. McKeon J. and A. Friedman., "Advanced waveform based acoustic emission detection of matrix cracking in composites," *Materials Evaluation*, **53**(9), pp. 1052-1058, (1995)

[1-9]   Seydel R. and F-K. Chang., "Impact identification of stiffened composite panels: I. System development," *Smart Materials and Structures*, **10**, pp. 354-369, (2001)

[1-10]   Coverly P.T. and W.J. Staszewski., "Impact damage location in composite structures using optimized sensor triangulation procedure," *Smart Materials and Structures*, **12**, pp. 795-80, (2003)

[1-11]   Ip K.-H. and Mai., Y.-W., "Delamination detection in smart composite beams using Lamb waves," *Smart Materials and Structures*, **13,** pp. 544-551, (2004)

[1-12]   Velazquez, E., Kosmatka, J.B., "Detecting Impending Bond Joint Failures in Unmanned Aircraft Composite Wing Structures," SAMPE 2010 - Seattle, WA May 17-20, (2010)

2   LITERATURE REVIEW

The problem of structural health monitoring has been driven since 1975 by the needs of a wide range of industries including those related to civil infrastructure, commercial and military aircraft, space structures, industrial machinery, and mass energy production. Work conducted on the subject by government laboratories, commercial entities, and universities around the globe has resulted in a large pool of published literature. Significant progress has been made towards solving the issues of meaningful data acquisition, data mining, feature discrimination, damage identification, and implementation of functional systems. Still, with the exception of a small number of focused applications, such as the condition monitoring of rotating industrial machinery, practical solutions to the many structural health monitoring problems have proven elusive and structural health monitoring remains an active research field.

The specific problem of statistical vibration- and model-based damage identification as defined in Chapter 1 is directly treated in a relatively narrow subset of the related literature; however, the works most directly foundational to this dissertation have their roots in research across the field of damage detection and structural health monitoring. The current chapter therefore discusses early work and applications of structural health monitoring and provides an overview of vibration based damage detection methods before focusing on the damage identification specific literature which forms the primary theoretical basis of the dissertation's main algorithm.

2.1 Foundations and Applications of Structural Health Monitoring

One of the earliest structural health monitoring technology research efforts was related to the gradual deterioration of off-shore oil drilling platforms with studies seeking to determine if changes in global modal parameters could be used to identify the existence of damage in the primary platform structures. Examples include works by Vandiver ([2-1] and [2-2]), Wojnarowski et al. [2-3], Kenley and Dodds [2-4], Coppolino and Rubin [2-5], Shahriver and Bouwkamp [2-6], and Brederode et al. [2-7]. These works were largely restricted to identifying and monitoring the fundamental natural frequencies of the platforms and major structural members. Many concluded that environmental factors, such as changing mass on the platform and the effects of water motion, make the existence and structural impact of structural damage difficult to ascertain.

The development of structural health monitoring capability for bridges also started early and has continued to be an active research field for several decades because of the scale of financial investment in these structures, a requirement for long functional lifespans, their susceptibility to damage from earthquakes and other environmentally induced deterioration, and cost of structural failures. A considerable portion of the approaches, for example the works of Savage and Hewlett [2-8][2-1], Salane et al. [2-9], Kato [2-10], Price [2-11], Brownjohn [2-12], and Mizra [2-13] focus on using vibration based quantities—especially natural frequencies, mode shapes, and/or frequency response functions—to detect the structural deterioration either on a global scale or in specific

components (e.g., reinforced concrete columns, pre-tensioned concrete beams, steel structures, or tensioned cables). Most researchers have achieved promising results while concluding that although changes in modal properties correlate with damage on the component level there remain significant challenges because of the low sensitivity of global dynamics to local damage and the corrupting influence of environmental effects and mass changes during use. The work of Farrar et al. [2-14] involved a multi-year effort collecting vibration data and testing various damage identification methods on two relatively small bridges, including imparting various levels of known damage on primary structural components. The authors found that simulated damage on one bridge had a negligible effect on global dynamics while real damage on the other bridge had to be severe before it could be identified with statistical significance above the test and environmental variability. Despite the challenges, modern research efforts, for example as detailed in Ahlborn et al. [2-15], continue with increasing promise as approaches mature and improving data acquisition technologies allow increasing measurement resolution. As summarized in Gastineau et al. [2-16], there were at least 72 companies around the world offering services in the general field of bridge structural health monitoring at the time of their survey.

Commercial and military aircraft present another structural health monitoring interest that has led to a wide range of research efforts from government, commercial, and academic entities over several decades. Generally speaking, the methods fall into two primary categories: those concerned with monitoring specific high-strain locations in

order to assess fatigue and remaining life (e.g., the works of Berens et al. [2-17], Hunt

and Hebden [2-18][2-19], and Boller [2-20]) and those seeking to identify unknown

damage cases to prevent sudden catastrophic failure (e.g., the works of Worden et al. [2-

21], Manson et al. [2-22][2-23], Diamanti and Soutis [2-24], and Panopoulou [2-25]).

Even more so than with civil infrastructure, aircraft require regular and costly inspection

through-out their life-cycles which could be reduced through automated health

monitoring. Additionally, since airframes already require distributed onboard power and

data systems for operation and are relatively small, they naturally lend themselves to

integrated health monitoring systems such as those discussed by Boller [2-26] and Ye et

al. [2-27]. More recently, structural health monitoring for unmanned aerial vehicles,

where low-cost life cycles preclude regular detailed inspection, has grown into a discrete

field of research with works such as those of Matt et al. [2-28], Nichols et al. [2-29], and

Lanza di Scalea et al. [2-30].

A large quantity of research has also been performed towards damage inspection

and health monitoring for space structures, including launch vehicles, satellites, and

reusable vehicles like the recently retired Space Shuttle. Examples include the works of

Hunt et al. [2-31], Kim and Bartkowicz [2-32], and Renson [2-33]. Global vibration

based damage identification methods are particularly attractive for mass-sensitive

satellite structures which feature well defined load paths, low-structural redundancy,

relatively simple loading conditions, and global vibrations that are likely to be sensitive

to damage. The motivation for structural health monitoring of reusable launch and reentry

vehicles is typified by the Shuttle Columbia which disintegrated during reentry after sustaining impact damage from a falling piece of foam during ascent. Systems for health monitoring and management of future launch and orbital systems are discussed further in references [2-34] through [2-38].

One notably successful health monitoring application is the case of rotating machinery diagnostics, usually referred to as condition monitoring. Rotating machinery offers advantages for fault detection and monitoring when compared to other structural health monitoring applications. Usually the systems exhibit a high consistency in health operating behavior which can be accurately characterized using vibratory signatures, allowing well characterized baselines. The machines are also stationary, accessible, and self-generating in their vibrations, meaning that they can be instrumented relatively easily and monitored during normal operation. Machine malfunctions are potentially expensive to large industries and so there has been a lot of motivation and financial support for solutions. Additional information can be found in references [2-39] through [2-41].

2.2 **Vibration Based Damage Detection Methods**

The majority of damage identification methods investigated in the literature have been based on measured dynamic data and comparison to some kind of analytical model, from simple beams and plates to complex finite element models. The general idea in each case is to find an adjustment of model parameters—usually related to stiffness and/or

mass—which produces normal modes matching the measured response. The change in model parameters then is assumed to represent damage. Damage identification algorithms usually have two major components: (1) a metric derived from the measured data and model (if applicable) indicating the existence and location of damage; and (2) a numerical mechanism for quantifying damage severity.

Change in natural frequencies was one of the earliest damage identification metrics pursued as a basis for detecting and identifying damage. Lifshitz and Rotem [2-42] showed that dynamic moduli can be used to detect damage in simple elastomeric rods. Cawley and Adams in references [2-43] and [2-44] used the ratio of pairs of natural frequencies to determine the existence and location of damage in composite plates. Springer et al [2-45], Liang et al. [2-46], Salawu [2-47], Diaz Valdes and Soutis [2-48], and Williams and Messina [2-49] likewise investigated methods for natural frequency based damage identification in beam structures. Despite some success applying the methods to simple structures, damage metrics derived from natural frequencies alone tend to be too low in sensitivity and produce too few overall data to allow reliable information on damage location or severity.

The addition of mode shapes has the potential to improve damage identification by adding spatial resolution and a higher quantity of relevant data in general. Approaches to damage location and identification using mode shapes include those based on the modal assurance criterion (MAC) or coordinate modal assurance criterion (a.k.a., COMAC) [2-50], mode shape based multiple damage location assurance criterion [2-51],

and system matrix based multiple rank perturbation theory [2-52]. Ricles and Kosmatka performed successful damage location and identification through regularized minimization of an error vector based on both frequencies and mode shapes in references [2-53] and [2-54]. More recently, Titurus and Friswell have demonstrated damage detection using successive parameter subset selections and modal residuals [2-55].

Operational deflection shapes, which are similar to mode shapes but include the superimposed effect of nearby mode shapes and are obtainable without measured input force or modal parameter estimation, have also been studied as a basis for damage identification. Examples are the works of Waldron et al. [2-55] and Maia [2-57]. Similarly, mode shapes based techniques can be evolved to use frequency response functions, methods for which are detailed in Section 2.4.

Yet another extension is to calculate the second spatial derivative of a mode shape vector, producing modal curvature. Related methods for damage location and identification, for example the works of Pandy et al. [2-58] and Ratcliffe and Bagaria [2-60], have been studied with a combination of promising and mixed results. One benefit of using curvature based damage damage metrics is that curvature can be derived from measured strain, opening up additional data acquisition options.

Modal strain energy based methods have also been investigated for damage localization and identification and are different to many alternatives in that the resulting damage metrics are based on element properties rather than responses at the degrees-of-freedom. One approach, with strain energy calculated based on pre- and post-multiplying

stiffness matrices by mode shape vectors, is presented by Shi and Law [2-61] with a

followup work including updates to reduce modal truncation error [2-62]. Kim and

Stubbs pursue a similar approach with two additional improved algorithms in [2-63].

Cornwell et al present a different approach for plate structures where the strain energy is

calculated based on the measured curvature [2-64].

2.3   **Data Acquisition and Model Incompleteness**

A pivotal question with all vibration-based damage identification approaches is

how to acquire the required data on physical structures. In general, the level of damage

identification achievable depends on the density of information available. This is why

non destructive evaluation techniques include visual inspection, thermography, and

manual ultrasonic inspection—all methods that provide near continuum coverage of the

structure, including the potential of secondary inspections to zoom in on suspect regions.

Most structural health monitoring applications, however, do not allow spatially

continuous information because the structures are remote, inaccessible, or cannot be

brought out of service long enough for detailed inspection. Damage identification

approaches therefore generally rely on data measured at discrete locations on a

structure—for instance using temporarily or permanently installed single-point dynamic

sensors. The most common vibration data acquisition technique is hammer-impact or

shaker excited dynamic testing with accelerometers mounted at the desired measurement

locations and dynamic force measured at the input. The acceleration and force-based time series can then be transformed by Fourier analysis into the frequency domain and combined into transfer functions; these can subsequently then be decomposed through modal parameter estimation into natural frequencies and mode shapes. The acceleration data can also be transformed into the velocity or displacement domain and derivatives calculated if desired. However, there are practical limitations to how many point measurement sensors (e.g., accelerometers) can be installed on a structure because of cost, wiring bulk and mass, sensor power requirements, data acquisition capability, and related issues.

The first major question is therefore how to acquire enough data compared to critical damage size. Microelectromechanical system (MEMS) based dynamic sensors with wireless connectivity and mass-multiplexing capability are one potential future solution being pursued for structural health monitoring [2-66]. However, hurdles related to sensor sensitivity, power source, and telemetry remain to be overcome before MEMS sensors can be widely implemented for structural health monitoring. Scanning laser Doppler vibrometers (SLDVs) have also been pursued for use with damage identification since they allow rapid acquisition of large numbers of dynamic point measurements over densely spaced measurement grids, can be operated over moderate distances and do not require contact or mass-loading of the structure. Examples of related works are Tung et al., [2-67] and Waldron et al. [2-68]. On the negative side, SLDVs require line-of-sight access to the measurement locations and therefore cannot be used on internal structures

or when certain structures, such as aircraft and spacecraft, are in operation. For damage

identification methods based on curvature, such as some strain energy and curvature

mode shape methods, the required data can be derived from fiber optic based fiber bragg

grating strain sensors [2-69], which can be highly accurate, multiplexible, and

environmentally robust.

The second major question is how to relate a small number of available data

locations to an analytical model with many more degrees-of-freedom. An aircraft wing,

for example, may require at least 10,000 nodes to be modeled accurately using finite

element analysis but measured data from the physical structure may only be available

from 100 discrete locations. Additionally, a finite element model will often have three

translational and three rotational degrees-of-freedom at each node while measurements

will likely only be available at one to three of the translational degrees-of-freedom.

Approaches to bridging this gap include using the analytical degrees-of-freedom in place

of unknown measured degrees-of-freedom [2-70] or including algorithms to either

condense the analytical degree-of-freedom set to the measurement degree-of-freedom set

[2-71], expand the measurement set to the analytical set [2-72], or a combination of both

[2-73]. Methods for performing the algorithmic condensation and/or expansion are a field

of research in of themselves, with applications other than damage identification.

Examples of available methods are given in references [2-74] through [2-77].

2.4   **Deterministic Frequency Domain Damage Identification**

Many algorithms for statistical damage identification, and the related field of

parameter estimation, are essentially evolved versions of simpler deterministic methods.

Although the focus of this dissertation is a statistical method, deterministic algorithms

with similar damage metrics—those based on measured frequency response functions

instead of modal parameters—are especially relevant.

The work of Lin and Ewins [2-78] presents a deterministic method for model

correlation based on the difference between measured and analytical frequency response

functions. Changes to system mass, stiffness, and damping matrices are solved from the

resulting linear equation using the singular value decomposition. Special attention is

given to the case of incomplete measurement degrees-of-freedom compared to the

analytical system, and analytical validation is performed on mass-spring and truss

structures. Follow-up works by Imgerun, Visser, and Ewins in references [2-79] and [2-

80] further explore the method and attempt experimental implementation. Results are

mixed because of challenges related to modeling damping accurately. A related work by

Wang, Lin, and Lim [2-81] applies the method to analytical and experimental damage

detection on a mild steel frame structure, adding algorithmic refinements including using

a pseudo-inverse to solve the over-determined set of linear equations by least-squares.

Although the analytical validations are very accurate, relative inaccuracy in the

experimental results is attributed to modeling error in the frame joints and damage parameters.

The work of Araujo dos Santos et al. [2-82] develops a similar frequency response function difference method for damage identification, including a Taylor series expansion of damage based system matrix changes in order to generate sensitivities and allow a least-squares solution by pseudo-inverse. Through analytical validation studies the authors determine that dynamic expansion of the reduced measured degree-of-freedom set to the full analytical degree-of-freedom space is preferable to static expansion, and that the frequency response function method performs better than a previous similar technique using modal parameters.

A similar approach can be developed using frequency response residual forces instead of the frequency response function data directly, a path also pursued in the current work. The paper of Napolitano and Kosmatka [2-83] presents development of such an algorithm based on deterministic least-squares minimization of frequency response residual forces, including first order Taylor series based sensitivity and dynamic reduction of analytical degrees-of-freedom to the reduced measurement set. Analytical validation on a highly damped truss structure produced favorable results, although experimental validation was not attempted. The work of Huynh et al. [2-84] develops a so-called *damage location vector*, which appears to be equivalent to a residual force vector, and, after applying dynamic expansion to the analytical degree-of-freedom set, uses the quantity to locate and qualitatively estimate the severity of damage in an

aluminum plate. The authors do not, however, solve for quantitative parametric damage estimation.

Yet another least-squares sensitivity based approach to parametric damage identification is presented in the work of Zang and Imregun [2-85]. Based on previous model correlation work ([2-86] and [2-87]), this method uses minimization of two frequency response correlation functions to generate parametric model changes describing damage. The method is further extended using neural networks in the work of Zang et al. [2-88].

Minimum rank perturbation theory takes a different approach by attempting to determine matrix perturbations which can be attributed to damage—a process known generally as optimal matrix update. Originally developed to use modal parameters, minimum rank perturbation theory is updated to use frequency response functions for structural health monitoring in the work of Zimmerman et al. [2-89]. Analytical and experimental validations give promising results, in some cases similar to a comparison with the modal version but requiring substantially less computational effort.

Additional works using more varied approaches to parametric damage identification based on frequency response functions can also be found in works by Furukawa and Otsuka [2-90], Lee and Shin [2-91], Kouchmeshky et al. [2-92], Dackermann et al. [2-93], Bandara et al. [2-94], and Mohan et al. [2-95].

2.5   **Statistical Model-Based Damage Identification**

Statistical damage identification forms a much smaller group of research than the previously mentioned deterministic methods. The distinction between the two is that statistical methods quantify measurement errors and initial parameter uncertainty when solving the damage identification problem, and then additionally use that extra information to describe the updated damage state probabilistically. Quantifying the damage estimation uncertainty means that the damage estimate can be interpreted either as a range of possible values for a desired confidence level, or as a particular value (usually the mean) with an associated confidence factor. Consequences of the damage can then be bounded for a given confidence level. Alternatively, updated damage parameter uncertainty levels can be inspected relative to each other and parameters with high posterior uncertainty, possibly indicating a breakdown in the model or data, flagged for further inspection.

Statistical methods reviewed in this section can be loosely split into two groups depending on their primary origin: (1) methods derived from statistics, and (2) methods derived from structural mechanics. Statistics-derived methods are discussed first; the second group, which forms the basis for the current algorithm, is the focus for the remainder of the current chapter. It should be noted that many of these works were developed for application to general parameter estimation and/or model correlation as opposed to damage identification or health monitoring.

Methods from the statistics-derived group generally try to minimize statistical assumptions—not assuming a distribution type for example—and then use numerical optimization to determine full distributions of the input parameters based on a statistical cost function. Often some form of sampling is used to help propagate, or back propagate, the uncertainty. The Markov Chain Monte Carlo algorithm presented by Higdon et al. [2-96] is an example of a statistical sampling and optimization based methodology for solving inverse problems. In this approach, the uncertainty is forward sampled using Monte Carlo from trial parameter values and a directed search is then employed to find regions of parameter values which are statistically responsible for the output distribution based on a specified criteria (such as maximum likelihood). The statistical criteria level is generated and saved for each parameter value and the resulting histograms can be interpreted as the parameter value distributions. Additional examples of this general approach can be found in references [2-97] through [2-102].

Such 'statistics' methods usually require the use of statistical sampling and have been validated on small models only because of computational limitations. Fast-running meta-models, which reproduce the input-output relationship of the physical analytical model, can be used to make the methods more practical. Meta-models, discussed by Shultz et al. [2-103] and Hemez and Tippetts [2-104], can be as simple as low order polynomials, or more complex. The meta-models are fit to training data generated by running the finite element model at specific known combinations of parameter values in order to establish the input-output relationship over a certain parameter space. Once

trained, the meta-model can be used to propagate uncertainty approximately at a fraction of the computational cost as using the physical model directly, meaning that sampling is possible but at the cost of another layer of approximation.

Methods from the 'structural mechanics' group seek to solve near-closed form engineering equations derived from knowledge of underlying system physics, usually incarnated as a finite element model of the structure. Many of the works include some incarnation of the Bayesian interpretation of linear least-squares minimization, and treatment of parametrically nonlinear problems then involves the iterative application of the linear solution. In this case, assumptions need to be made on the parameters' statistics to allow problem formulations and solutions. The standard assumption is to make all distributions Gaussian normal, so random variables can be completely described by the mean and variance. In addition, randomness from different sources, such as material uncertainty and measurement noise, is assumed to be statistically independent. The solution then proceeds by iterative linearization, where the linearized system problem can be solved in a closed form at each step. Finally, despite the requirement to run the analytical model multiple times per iteration for these methods in order to compute sensitivities, the level of computation required can be assumed to be orders of magnitude less than that required for the numerical optimization and sampling required by the first group of methods, which is important for near real-time structural health monitoring.

An early paper by Gura [2-105] describes algorithms for linear and nonlinear statistical parameter estimation using a generic response quantity. The mathematically

consistent extension to parametrically nonlinear systems is reached algebraically by

careful successive applications of the known linear solution. The algorithm is not

validated analytically or experimentally. In a doctoral dissertation [2-106] and summary

report [2-107] Martinez applies the non-application-specific algorithm of Gura, using

frequency response function difference implemented in a Kalman filter framework for

finite element model update. In addition, the equivalence of inverse-covariance-weighted

regularized linear least-squares minimization to several Bayesian optimal estimators is

explained, and the method is successfully validated analytically on truss structures. The

method is further validated experimentally on a polycarbonate truss structure and then an

electronics component box in a follow-up work with Allen [2-108], demonstrating

significant model improvement in relation to the measured test data. The widely

referenced work of Collins et al. [2-109] presents a minimum variance approach to

finding the best linear unbiased estimator (equivalent to the linear solution referenced by

Gura), then directly applies an iterative version of the linear solution to parametrically

nonlinear finite element model update problems using natural frequencies and mode

shape vectors. The method was validated analytically on a two element beam model and

then experimentally using measured data and a 28 element beam finite element model

from the Saturn V rocket. In both cases, the model accuracy improved significantly in a

low number of iterations. A completely independent work by Tarantola and Valette [2-

110] also derives general parameter estimation equations, equivalent to those of Gura,

from the point of view of maximizing the posterior Gaussian parameter distribution while

minimizing the error in system equations. Validation on a few previously ill-posed geophysics problems demonstrates excellent performance even for difficult parameter estimation problems. Gura, Martinez, and Tarantola and Valette all independently state that direct iterative application of the linear solution to parametrically nonlinear problems (e.g., the method used by Collins et al.) is mathematically inconsistent, being equivalent to the assumption that iteration estimates are statistically independent from each other; however, the favorable analytical results obtained by Collins et al. suggest that the inconsistency may be acceptable.

Ricles and Kosmatka [2-53] give an early application of statistical parameter estimation to the specific task of damage identification. This work applies a two-part process: (1) inspection of the modal residual force vectors to locate damaged members, and (2) application of the Bayesian update form of Collins et al. to find updated stiffness and mass parameters which minimize the difference between analytical and measured natural frequencies and mode shapes. Validation on an analytical space frame with varying levels of mass and stiffness damage gives excellent results, and experimental validation on a space frame, including uncertainty quantification, is achieved in a follow-up work [2-54]. One of the interesting algorithmic additions in this method is a filtering step to ensure that only modes showing a greater change between baseline and damaged data sets than between baseline and correlated analytical data sets are used for damage update. Additionally, the practical case of having fewer measurement than analytical

degrees-of-freedom is treated by Guyan reduction and the approach is successfully validated for removing unknown rotational degrees-of-freedom.

A similar technique based on minimization of the modal residual force vector is developed by Alvin [2-111] from the deterministic method of Hemez and Farhat [2-112] and validated analytically and experimentally on a portal frame. Hemez and Doebling [2-113] subsequently adopt a version of the method for an experimental study on a multi-degree-of-freedom mass-spring system and an engine mount, where incomplete measurement coordinates are treated by expanding mode shapes using dynamic expansion in a staggered 'predictor-corrector' scheme. Experimental validation results are positive, and the additional benefit of being able to inspect posterior parameter variances to assess updated parameter validity is emphasized and discussed.

The work of Xia et al. [2-114] pursues a different approach to damage identification, using mean response values with a basic deterministic least-squares solution to produce mean parameter estimates and then estimating the covariance in a second step using a first order approximation. This approach appears to be statistically inconsistent when viewed from the perspective of statistical least-squares parameter estimation. Infinite parameter variance is implicitly assumed in the deterministic least-squares solution and then a finite variance is assumed when computing the statistics. However, the method is successfully validated on an analytical and experimental cantilever beam with positive results, including verification of derived statistics on the analytical beam by Monte Carlo analysis.

The studies presented in references [2-115] through [2-118] have also attempted solutions to the problem of statistical parameter estimation in similar ways with varying results. It should be noted that of central importance in all these statistical least-squares methods—and the method developed in the following chapters—is recognition that the covariance matrix of the updated parameters can be interpreted as a measure of confidence in the estimation. Another subset of literature which is pertinent to the current development includes algorithms which statistically treat the randomness in measurements and parameters without explicitly quantifying the estimation uncertainty. Two works by Mottershead et al. (references [2-119] and [2-120]) are particularly noteworthy since they develop estimation algorithms based on filtering concepts which minimize the frequency response function based residual force vector. These are similar to algorithms presented in the next chapter, although the filter implementation is different and they do not quantify the estimation uncertainty.

2.6 **Reviews**

The papers reviewed in this chapter are necessarily selective and more thorough treatments can be found in a number of excellent reviews. Salawu et al. [2-121] discuss approaches to damage detection using changes in frequency. Zou et al. [2-122] review analytical model-based damage identification methods for composite structures. The work of Sohn et al. [2-123] covers all vibration-based structural health monitoring and

updates an initial review on structural health monitoring literature through 1996 by

Doebling et al. [2-124], also summarized in a separate article by the same authors [2-125]. Carden and Fanning present a similarly aligned review covering a wide range of

vibration based damage detection literature [2-126], as do Yan et al. [2-127] and Friswell

2007 [2-128]. Mode shape methods are reviewed by Gandomi et al. [2-129] and a review

on vibration-based structural health monitoring with a specific emphasis on composite

materials is additionally presented by Montalvão et al. [2-130].

The 2014 text Structural Health Monitoring: A Machine Learning Perspective by

Farrar and Worden gives a comprehensive overview of the field of structural health

monitoring, touching on every facet of the field and its numerous challenges and

solutions, and providing a particular focus on approaches based on machine learning

techniques.

The material contained in Chapter 2 was developed in collaboration with Prof.

John B. Kosmatka. The dissertation author was the primary investigator and author of

this work.

2.7 Chapter 2 References

[2-1]   Vandiver, J.K., "Detection of Structural Failure on Fixed Platforms by Measurement of Dynamic Response," *Proceedings of the 7th Annual Offshore Technology Conference*, pp. 243–252, (1975)

[2-2]   Vandiver, J.K., "Detection of Structural Failure on Fixed Platforms by Measurement of Dynamic Response," *Journal of Petroleum Technology*, pp. 305–310, (1977)

[2-3]   Wojnarowski, M.E., Stiansen, S.G., Reddy, N.E., "Structural Integrity Evaluation of a Fixed Platform Using Vibration Criteria," *Proceedings of the 9th Annual Offshore Technology Conference*, Houston, Texas, pp. 247–256, (1977)

[2-4]   Kenley, R.M., Dodds, C.J., "West Sole WE Platform: Detection of Damage by Structural Response Measurements," *Proceedings of the 12th Offshore Technology Conference*, Houston, Texas, **4**, pp. 111-118, (1980)

[2-5]   Coppolino, R. N., Rubin, S., "Detectability of Structural Failure in Offshore Platforms by Ambient Vibration Monitoring," *Proceedings of the 12th Offshore Technology Conference*, Houston, Texas, **4**, pp. 101-110, (1980)

[2-6]   Shahrivar, F & Bouwkamp, J. G., "Damage Detection in Offshore Platforms using Vibration Information," *Journal of Energy Resources Technology*, **108**(2), (1986)

[2-7]   Brederode, P., De Winter, P., Van Staalduinen, P., Segers, W., "Dynamic Offshore Structure Test (DOST) Project—A New Approach to Quality Assessment of Offshore Structures," *Proc. Inspection, Repair and Maintenance IRM/AODC*, Aberdeen, (1986)

[2-8]   Savage, R, J. and Hewlett, P. C., "A New NDT Method for Structural Integrity Assessment," *NDT International*, **11**, pp. 61-66, (1978)

[2-9]   Salane, H. J., Baldwin, J. W. and Duffield, R. C., "Dynamics Approach for Monitoring Bridge Deterioration," *Transportation Research Record*, **832**, pp. 21-28, (1987)

[2-10]   Kato, M., Shimada, S., "Vibration of PC Bridge During Failure Process," *Journal of Structural Engineering, ASCE*, **112**(7), pp. 1692-1703, (1986)

[2-11]   Price, W.I.J., Aguila, L.A., "Assessment of deteriorating Prestressed Concrete Bridges," In *Assessment of Reinforced and Pre-stressed Concrete Bridges*, The Institution of Structural Engineers, London, pp. 21-26, (1988)

[2-12]   Brownjohn, J.M.W., "Assessment of Structural Integrity by Dynamic Measurements', *Ph.D. Thesis, Department of Civil Engineering, University of Bristol*, Bristol, (1988)

[2-13]   Mirza, M. S., Ferdjani, O., Hadj-Arab, A., Joucdar, K., Khaled, A., Razaqpur, A.G., "An experimental Study of Static and Dynamic Responses of Prestressed Concrete Box Girder Bridges," *Canadian Journal of Civil Engineering*, **17**(3), pp. 481-493, (1990)

[2-14]   Farrar, C.R., Cornwell, P.J., Doebling, S.W., Prime, M.B., "Structural Health Monitoring Studies of the Alamosa Canyon and I-40 Bridges," *Los Alamos National Laboratory Report LA-13635-MS*, July 2000

[2-15]   Ahlborn, T.M., Shuchman, R., Sutter, L.L., Brooks, C.N., Harris, D.K., Burns, J.W., Endsley, K.A., Evans, D.C., Vaghefi, K., Oats, R.C., "The State-of-the-Practice of Modern Structural Health Monitoring for Bridges: A Comprehensive Review," *US Department of Transportation Task 2 Report, DTOS59-10-H-00001*, July 2010

[2-16]   Gastineau, A., Johnson, T., Schultz, A., "Bridge Health Monitoring and Inspections – A Survey of Methods," *US Department of Transportation Technical Report MN/RC 2009-29*, September 2009

[2-17]   Berens, A.P., Hovey, P.W., Skinn, D.A., "Risk Analysis for Aging Aircraft Fleets-Vol 1 Analysis," *Air Force Systems Command Report WL-TR-91-3066*, (1991)

[2-18]   Hunt, S.R., Hebden, I.G., "Eurofighter 2000: An Integrated Approach to SHM and Usage Monitoring," *RTO AVT Specialists' Meeting on Exploitation of Structural Loads/Health Data for Reduced Life Cycle Costs*, 11-12 May, (1998)

[2-19]   Hunt, S.R., Hebden, I.G., "Validation of the Eurofighter Typhoon Structural Health and Usage Monitoring System," *Smart Materials and Structures*, **10**, pp. 497–503, (2001)

[2-20]   Boller, C., Buderath, M., "Fatigue in Aerostructures—Where Structural Health Monitoring Can Contribute to a Complex Subject," *Philosophical Transactions of the Royal Society A*, **365**, pp. 561–587, (2007)

[2-21]   Worden, K., Manson, G., Allman, D.J., "Experimental Validation of a Structural Health Monitoring Methodology: Part I. Novelty Detection on a Laboratory Structure," *Journal of Sound and Vibration*, **259**, pp. 323-343, (2003)

[2-22]   Manson, G., Worden, K., Allman, D.J., "Experimental Validation of a Structural Health Monitoring Methodology: Part II. Novelty Detection on an Aircraft Wing," *Journal of Sound and Vibration*, **259**, pp. 345-363, (2003)

[2-23]   Manson, G., Worden, K., Allman, D.J., "Experimental Validation of a Structural Health Monitoring Methodology: Part II. Damage Location on an Aircraft Wing," *Journal of Sound and Vibration*, **259**, pp. 365–385, (2003)

[2-24]   K. Diamanti, C. Soutis, "Structural Health Monitoring Techniques for Aircraft Composite Structures," *Progress in Aerospace Sciences*, **46**(8), pp. 342-352, (2010)

[2-25]   Panopoulou, A., Roulias, D., Loutas, T.H., Kostopoulous, V., "Health Monitoring of Aerospace Structures Using Fibre Bragg Gratings Combined with Advanced Signal Processing and Pattern Recognition Techniques," *Strain*, **48**(3), pp. 267-277, (2011)

[2-26]   Boller, C., "Ways and Options for Aircraft Structural Health Management," *Smart Materials and Structures*, **10**, pp.432-440, (2001)

[2-27]   Ye, L., Lu, Y., Su, Z., Meng, G., "Functionalized Composite Structures for New Generation Airframes: A Review," *Composites Science and Technology*, **65**(9), pp. 1436-1446, (2005)

[2-28]   Matt, H., Bartoli, I., Lanza di Scalea, F., "Ultrasonic Guided Wave Monitoring of Composite Wing Skin-to-Spar Bonded Joints in Aerospace Structures," *Acoustical Society of America Journal*, **118**(4), pp. 2240-2252, (2005)

[2-29]   Nichols, J.M., Seaver, M., Trickey, S.T., Salvino, L.W., Pecora, D.L., "Detecting Impact Damage in Experimental Composite Structures: An Information-Theoretic Approach," *Smart Materials and Structures*, **15**(2), pp. 424-434, (2006)

[2-30]   Lanza di Scalea, F., Matt, H., Bartoli, I., Coccia, S., Park, G., Farrar, C., "Health Monitoring of UAV Wing Skin-to-spar Joints using Guided Waves and Macro Fiber Composite Transducers," *Journal of Intelligent Material Systems and Structures*, **18**, (2007)

[2-31]   Hunt, D.L., Weiss, S.P., West, W.M., Dunlap, T.A., Freesmeyer, S.R., "Development and Implementation of a Shuttle Modal Inspection System," Sound and Vibration, **24**(9), pp. 34–42, (1990)

[2-32]   Kim, H.M., Bartkowicz, T.J., "An experimental study for damage detection using a hexagonal truss," *Computers & Structures*, **79**(2), pp. 173-182, (2001)

[2-33]   Renson, L., "Risk Management of Future Reusable Launcher Mission Using Active Health Monitoring Systems (HMS)," *Joint ESA-NASA Space-Flight Safety Conference*. Edited by B. Battrick and C. Preyssi. European Space Agency, ESA SP-486, (2002)

[2-34]   Prosser, W.H., Allison, S.G., Woodard, S. E., Wincheski, R.A., Cooper, E.G., Price, D. C., Hedley, M., Prokopenko, M., Scott, D. A., Tessler, A. and Spangler, J. L., 2004, "Structural Health Management for Future Aerospace Vehicles," *Proceedings of the 2nd Australian Workshop on Structural Health Management*, December, (2004)

[2-35]   Mancini, S., Tumino, G., Gaudenzi, P., "Structural Health Monitoring for Future Space Vehicles," *Journal of Intelligent Material Systems and Structures*, **17** (2006)

[2-36]   Tessler, A., "Structural Analysis Methods for Structural Health Management of Future Aerospace Vehicles," *Key Engineering Materials*, **347**, pp. 57-66, (2007)

[2-37]   Zagrai, A., Doyle, D., Gigineishvili, V., Brown, J., Gardenier, H., Arritt, B., "Piezoelectric Wafer Active Sensor Structural Health Monitoring of Space Structures," *Journal of Intelligent Material Systems and Structures*, **21**, pp. 921-940, (2010)

[2-38]   *System Health Management: With Aerospace Applications*, Stephen B. Johnson, Thomas J. Gormley, Seth S. Kessler, Charles D. Mott, Ann Patterson-Hine, Karl M. Reichard, Philip A. Scandura (Editors), John Wiley & Sons, Ltd, 2011

[2-39]   *Vibroacoustic Condition Monitoring*, Cempel, C., and Haddad, S.D. (Editors), Ellis Horwood Series in Mechanical Engineering, Ellis Horwood, New York, 1991

[2-40]   *Vibratory Condition Monitoring of Machines*, Rao, J.S., CRC Press/Narosa Publishing House, Boca Raton, Florida, 2000

[2-41]   Jardine, A.K.S., Lin, D., Banjevic, D., "A Review on Machinery Diagnostics and Prognostics Implementing Condition-Based Maintenance," *Mechanical Systems and Signal Processing*, **20**(7), pp. 1483-1510, (2006)

[2-42]   Lifshitz, J.M., Rotem, A., "Determination of Reinforcement Unbonding of Composites by a Vibration Technique," *Journal of Composite Materials*, **3**, pp. 412–423, (1969)

[2-43]   Cawley, P., Adams, R.D., "The Locations of Defects in Structures from Measurements of Natural Frequencies," *Journal of Strain Analysis for Engineering Design*, **14**(2), pp. 49–57, (1979)

[2-44]   Cawley, P. and R.D. Adams, "A Vibration Technique for Non-Destructive Testing of Fibre Composite Structures," *Journal of Composite Materials*, **13**, pp. 161–175, (1979)

[2-45]   Springer, W.T., Lawrence, K.L., Lawley, T.J., "Damage Assessment Based on the Structural Frequency Response Function', *Experimental Mechanics*, **28**(1), pp. 34-37, (1988)

[2-46]   Liang, R.Y., Choy, F.K., Hu, J., "Detection of Cracks in Beam Structures Using Measurements of Natural Frequencies," *Franklin Institute, Journal* (ISSN 0016-0032), **328**(4), pp. 505-518, (1991)

[2-47]   Salawu, O.S., "An Integrity Index Method for Structural Assessment of Engineering Structures Using Modal Testing," *Insight: The Journal of the British Institute of Non-Destructive Testing*, **39**(1), (1997)

[2-48]   Diaz Valdes, S.H., Soutis, C., "Delamination Detection In Composite Laminates From Variations Of Their Modal Characteristics," *Journal of Sound and Vibration*, **228**(1), pp. 1-9, (1999)

[2-49]   Williams, E.J., Messina, A., "Applications of the Multiple Damage Location Assurance Criterion," *Key Engineering Materials*, **167-168**, pp. 256-264, (1999)

[2-50]   Ndambi, J.-M., Vantomme, J., Harri, K., "Damage Assessment In Reinforced Concrete Beams Using Eigenfrequencies and Mode Shape Derivatives," *Engineering Structures*, **24**, pp. 501–515, (2002)

[2-51]   Shi, Z.Y., Law, S.S., Zhang, L.M., "Damage Localization by Directly Using Incomplete Mode Shapes," *Journal of Engineering Mechanics*, **126**(6), pp. 656–660, (2000)

[2-52]   Kaouk, M., Zimmerman, D.C., Simmermacher, T.W., "Assessment of Damage Affecting All Structural Properties Using Experimental Modal Parameters," *Transactions of the ASME*, **122**, pp. 456, (2000)

[2-53]   Ricles, J.M., Kosmatka, J.B., "Damage Detection in Elastic Structures Using Vibratory Residual Forces and Weighted Sensitivity," *AIAA Journal*, **30**(9), pp.2310-2316, (1992)

[2-54]   Kosmatka, J.B., Ricles, J.M., "Damage Detection in Structures By Modal Vibration Characterization," *Journal of Structural Engineering*, **125**(12), pp.1384-1392, (1999)

[2-55]   Titurus, B., Friswell, M.I., "Damage Detection using Successive Parameter Subset Selections and Multiple Modal Residuals," *Mechanical Systems and Signal Processing*, **45**, pp. 193-206, (2014)

[2-56]   Waldron, K., Ghoshal, A., Schulz, M.J., Sundaresan, M.J., Ferguson, F., Pai, P.F. and Chung, J.H., "Damage Detection Using Finite Element and Laser Operational Deflection Shapes," *Finite Elements in Analysis and Design*, **38**, pp. 193-226, (2002)

[2-57]   Maia, N.M.M., Silva, J.M.M., Almas, E.A.M., "Damage Detection in Structures- from Mode Shape to Frequency Response Function Methods" *Mechanical Systems and Signal Processing*, **17**(3), pp. 489-498, (2003)

[2-58]   Pandey, A.K., Biswas, M., Samman, M.M., "Damage Detection Form Changes in Curvature Mode Shapes," *Journal of Sound and Vibration*, **145**, pp. 321-332, (1991)

[2-59]   Ratcliffe, C.P., Bagaria, W.J., "Vibration Technique for Locating Delamination in a Composite Plates," *AIAA Journal*, **36**, pp. 1074-1077, (1998)

[2-60]   Wahab, M.M.A., "Effect of Modal Curvatures on Damage Detection using Model Updating," *Mechanical Systems and Signal Processing*, **15**(2), pp. 439–445, (2001)

[2-61]   Shi, Z.Y., Law, S.S., and Zhang, L.M., ''Structural Damage Detection from Elemental Modal Strain Energy Change,'' *Journal of Engineering Mechanics*, **126**(12), pp. 1216–1223, (2000)

[2-62]   Shi, Z.Y., Law, S.S, Zhang, L.M., "Improved Damage Quantification from Elemental Modal Strain Energy Change ," *Journal of Engineering Mechanics*, **128** (5), pp. 521-529, (2002)

[2-63]   Kim, J.-T., Stubbs, N., "Improved Damage Identification Method Based On Modal Information," *Journal of Sound and Vibration*, **252**(2), pp.223-238, (2002)

[2-64]   Cornwell, P., Doebling, S.W., Farrar, C.R., "Application of the Strain Energy Damage Detection Method to Plate-Like Structures," *Journal of Sound and Vibration*, **224**(2), pp. 359-374, (1999)

[2-65]   A.W. Otieno, P. Liu, V.S. Rao and L.R. Kova, "Damage Detection Using Modal Strain Energy and Laser Vibrometer Measurements," *In Smart Structures and Materials 2000: Smart Structures and Integrated Systems*, Norman M. Wereley, Editor, Proceedings of SPIE, **3985**, (2000)

[2-66]   Tung, S., Witherspoon, S.R., Roe, L.A., Silano, A., Maynard, D.P., Ferraro, N., "A MEMS-Based Flexible Sensor and Actuator System for space Inflatable Structures," *Smart Materials and Structures*, **10**, pp. 1230-1239, (2001)

[2-67]   Khan, A.Z., Stanbridge, A.B. and Ewins, D.J. (2000). Detecting damage in vibrating structures with a scanning LDV. Optics and Lasers in Engineering, 32, 583–592.

[2-68]   Waldron, K., Ghoshal, A., Schulz, M.J., Sundaresan, M.J., Ferguson, F., Pai, P.F. and Chung, J.H. (2002). Damage detection using finite element and laser operational deflection shapes. Finite Elements in Analysis and Design, 38, 193–226.

[2-69]   Todd, M. D. Nichols, J. M. Trickey, S. T. Seaver, M. Nichols, C. J. Virgin, L. N., "Bragg grating-based fibre optic sensors in structural health monitoring," *Philosophical Transactions of the Royal Society of London A: Mathematical Physical And Engineering Sciences*, **365**(1851), pp. 317-344, (2007)

[2-70]   Law, S.S., Shi, Z.Y., Zhang, L.M., "Structural Damage Detection from Incomplete and Noisy Modal Test Data," *Journal of Engineering Mechanics*, pp.1280-1288, (1998)

[2-71]   Gupta, P., Giridhara, G., Gopalakrishnan, S., "Damage Detection Based on Damage Force Indicator Using Reduced-Order FE Models," *International Journal for Computational Methods in Engineering Science and Mechanics*, **9**, pp. 154–170, (2008)

[2-72]   Abdalla, M., Grigoriadis, K. M., Zimmerman, D., ''Experimental validation of the LMI methods for structural damage detection,'' *Proceedings of the 17th IMAC Conference*, Orlando, Florida, pp. 1373-1379, (1999)

[2-73]   Kim, H.K., Bartkowicz, T.J., "An Experimental Study for Damage Detection Using a Hexagonal Truss," *Computers and Structures*, **79**, pp. 173-182, (2001)

[2-74]   Guyan, R.J., "Reduction of stiffness and mass matrices," *AIAA Journal*, **3**, pp. 380, (1965)

[2-75]   Kidder, R., "Reduction of Structural Frequency Equations," *AIAA Journal*, **11**(6), (1973)

[2-76]   Xia, Y., Lin, R., "Improvement on the iterated IRS method for structural eigensolutions," *Journal of Sound and Vibration*, **270**, pp.713–727, (2004)

[2-77]   Kim,K.-O., Choi, D.-W., "System condensations for inverse problems of linear dynamic systems," *Inverse Problems in Science and Engineering*, **14**(3), pp. 267-285, (2006)

[2-78]   Lin, R.M., Ewins, D.J., "Analytical model improvement using frequency response functions," *Mechanical Systems and Signal Processing*, **8**(4), pp. 437-458, (1994)

[2-79]   Imgerun, M., Visser, W.J., Ewins, D.J., "Finite Element Model Updating Using Frequency Response Function Data—I. Theory and Initial Investigation," *Mechanical Systems and Signal Processing*, **9**(2), pp.187-202, (1995)

[2-80]   Imgerun, M., Sanliturk, K.Y., Ewins, D.J., "Finite Element Model Updating Using Frequency Response Function Data—II. Case Study on a Medium Sized Finite Element Model," *Mechanical Systems and Signal Processing*, **9**(2), pp.203-213, (1995)

[2-81]   Wang, Z., Lin, R.M., Lim, M.K., "Structural damage detection using measured frequency response function data," *Computational Methods in Applied Mechanics and Engineering*, **147**, pp.187-197, (1997)

[2-82]   Araujo dos Santos, J.V., Mota Soares, C.M., Mota Soares, C.A., Maia, N.M.M., "Structural damage identification in laminated structures using frequency response function data," *Composite Structures*, **67**, pp.239-249, (2005)

[2-83]   Napolitano, K., Kosmatka, J.B., "Damage detection of highly damped structures using direct frequency response measurements and residual force vectors," *Proceedings of SPIE*, **2720**, pp. 110-121, (1996)

[2-84]   Huynh, D., He, J., Tran, D., "Damage location vector: A non-destructive structural damage detection technique," *Computers and Structures*, **83**, (2005)

[2-85]   Zang, C., Imregun, M., "Structural Damage Detection and Localization Using FRF-Based Model Updating Approach," *Key Engineering Materials*, **245-246**, pp. 191-200, (2003)

[2-86]   Grafe, H., "Model Updating of Large Structural Dynamics Models Using measured Response Functions,' *Ph.D. Dissertation, Imperial College of Science, Technology and Medicine, University of London*, (1998)

[2-87]   Zang, C., Grafe, H., Imregun, M., "Frequency-domain criteria for correlating and updating dynamic finite element models," *Mechanical Systems and Signal Processing*, **15**(1), pp.139-155, (2001).

[2-88]   Zang, C., Friswell, M.I.,Imregun, M., "Structural Health Monitoring and Damage Assessment Using Frequency Response Correlation Criteria," *Journal of Engineering Mechanics*, **133**(9), pp. 981-993, (2007)

[2-89]   Zimmerman, D.C., Simmermacher, T., Kaouk, M., "Model correlation and system health monitoring using frequency domain measurements," *Structural Health Monitoring*, **4**(3), pp.213- 227, (2005)

[2-90]   Furukawa, A., Otsuka, H., "Structural Damage Detection Method Using Uncertain Frequency Response Functions," *Computer-Aided Civil and Infrastructure Engineering*, **21** pp.292–305, (2006)

[2-91]   Lee, U., SHIN, J., "A Frequency-Domain Method of Structural Damage Identification Formulated from the Dynamic Stiffness Equation of Motion," *Journal of Sound and Vibration*, **257**(4), pp.615-634, (2002)

[2-92]   Kouchmeshky, B., Aquino, W., Billek, A.E., "Structural damage identification using co-evolution and frequency response functions," *Structural Control and Health Monitoring*, **15**, pp.162–182, (2008)

[2-93]   Dackermann, U., Li, J., Samali, B., "Identification of member connectivity and mass changes on a two-storey framed structure using frequency response functions and artificial neural networks," *Journal of Sound and Vibration*, **332**(16), (2013)

[2-94]   Bandara, R.P., Chan, T.H.T., Thambiratnam, D.P., "Structural damage detection method using frequency response functions," *Structural Health Monitoring*, **13**(4), pp. 418-429, (2014)

[2-95]   Mohan, S.C., Maiti, D.K., Maity, D., "Structural damage assessment using FRF employing particle swarm optimization," *Applied Mathematics and Computation*, **219**, pp. 10387-10400, (2013)

[2-96]   Higdon, D., Gattiker, J., Williams, B., "Computer Model Calibration Using High Dimensional Output," *Journal of the American Statistical Association*, **103**(482), pp. 570-583, (2008)

[2-97]   Beck, J.L., Au, S.-K., "Monitoring Structural Health Using a Probabilistic Measure," *Computer-Aided Design and Infrastructure Engineering*, **16**, pp. 1-11, (2001)

[2-98]   Lam, H.F., Katafygiotis, L.S., Mickleborough, N.C., "Application of a Statistical Model Updating Approach on Phase 1 of the IASC-ASCE Structural Health Monitoring Benchmark Study," *Journal of Engineering Mechanics*, **130**(1), pp. 34-48, (2004)

[2-99]   Ching, J., Muto, M., Beck, J.L., "Structural Model Updating and Health Monitoring with Incomplete Modal Data Using Gibbs Sampler," *Computer-Aided Design and Infrastructure Engineering*, **21**, pp. 242-257, (2006)

[2-100] Yuen, K.-V., Katafygiotis, L.S., "Substructure Identification and Health Monitoring Using Noisy Response Measurements Only," *Computer-Aided Design and Infrastructure Engineering*, **21**, pp. 280-291, (2006)

[2-101] Sohn, H., Law, K.H., "A Bayesian Probabilistic Approach for Structure Damage Detection," *Earthquake Engineering and Structural Dynamics*, **26**, pp. 1259-1281, (1997)

[2-102] Sohn, H., "A Bayesian Probabilistic Approach to Damage Detection for Civil Structures," *Ph.D. Dissertation*, *Stanford University*, (1998)

[2-103] Schultze, J.F., Hemez, F.M., Doebling, S.W., Hoon, S., "Statistical Based Non-linear Model Updating Using Feature Extraction," *19th International Modal Analysis Conference (IMAC)*, Kissimmee, Florida, February 5-8, (2001)

[2-104] Hemez, F.M., Tippetts, T.B., "Verification and Validation of a Composite Model," *Internal Report, Los Alamos National Laboratory,* Los Alamos, New Mexico LA-UR-04-8195, December, (2004)

[2-105] Gura, I.A., "Extension of Linear Estimation Techniques to Nonlinear Problems," *Journal of the Astronautical Sciences*, **15**(4) **,** pp. 194-205, (1968)

[2-106] Martinez, D.R., "Parameter Estimation in Structural Dynamics Models," *Ph.D. Dissertation, University of California, Los Angeles*, (1979)

[2-107] Martinez, D.R., "Estimation Theory Applied to Improving Structural Dynamics Models," *Sandia National Laboratory Report* SAND82-0572, (1982)

[2-108] Allen, J.J., Martinez, D.R., "Techniques for Implementing Structural Model Identification Using Test Data," AIAA Journal, **29**(11), pp. 1937-1944, (1991)

[2-109] Collins, J.D., Hart, G.C., Hasselman, T.K., and Kennedy, B., "Statistical Identification of Structures," *AIAA Journal*, 1**2**(2), pp. 185–190, (1974)

[2-110] Tarantola, A., Valette, B., "Generalized Nonlinear Inverse Problems Solved Using the Least Squares Criterion," *Reviews of Geophysics and Space Physics*, **20**(2), (1982)

[2-111] Alvin, K.F., "Finite Element Model Update via Bayesian Estimation and Minimization of Dynamic Residuals," *AIAA Journal*, **35**(5), pp. 879-886, (1997)

[2-112] Farhat, C., Hemez, F.M., "Updating finite element dynamic models using an element-by-element sensitivity methodology," *AIAA Journal*, **31**(9), pp. 1702-1711, (1993)

[2-113] Hemez, F.H., Doebling, S.W., "A Validation of Bayesian Finite Element Model Updating for Linear Dynamics," *17th International Modal Analysis Conference (IMAC)*, Kissimmee, Florida, February 8-11, (1999)

[2-114] Xia, Y., Hao, H., Brownjohn, J.M.W., Xia, P.-Q., "Damage Identification of Structures with Uncertain Frequency and Mode Shape Data," *Earthquake Engineering and Structural Dynamics*, **31**, pp. 1053-1066, (2002)

[2-115] Mares, Mottershead, J.E., Friswell, M.I., "Stochastic Model Updating: Part 1— Theory and Simulated Example," *Mechanical Systems and Signal Processing*, **20**, pp. 1674-1695, (2006)

[2-116] Furukawa, A., Kiyono, J., Iemura, H., Otsuka, H., "Damage identification Method Using Harmonic Excitation Force Considering Both Modelling and Measurement errors," *Earthquake Engineering and Structural Dynamics*, **34**, (2005)

[2-117] Capecchi, D., Vestroni, F., "Identification of Finite Element Models in Structural Dynamics," *Engineering Structures*, **5**(1), pp. 21-30, (1993)

[2-118] Hasselman, T.K., Wathugala, G.W., "A Hierarchical Approach for Modal Validation and Uncertainty Quantification," *WCCM V, Fifth World Congress on Computational Mechanics*, Vienna, Austria, July 7-12, (2002)

[2-119] Mottershead, J.E., Stanway, R., "Identification of Structural Vibration Parameters By Using a Frequency Domain Filter," *Journal of Sound and Vibration*, **109**(3), pp. 495-506, (1986)

[2-120] Mottershead, J.E., Lees, A., Stanway, R., " A linear, Frequency Domain Filter for Parameter Identification of Vibrating Structures, " *Journal of Vibration, Acoustics, Stress, and Reliability in Design*, **109**, pp. 262-269, (1987)

[2-121] Salawu, O.S., "Detection of structural damage through changes in frequency: a review", Eng. Structures, **19**, pp. 718–23, (1997)

[2-122] Zou, Y., Tong, L., Steven, G.P., "Vibration based model dependent damage (delamination) identification and health monitoring for composite structures: a review" J. Sound and Vibration, **230**, pp. 357-78, (2000)

[2-123] Sohn, H., Farrar, C.R., Hemez, F.M., Czarnecki, J.J., Shunk, D.D., Stinemates, D.W., Nadler, B.R., "A Review of Structural Health Monitoring Literature: 1996-2001", *Los Alamos National Laboratory Report*, LA-13976-MS, (2004)

[2-124] Doebling, S.W., Farrar, C.R., Prime, M.B., Shevitz, D.W., "Damage Identification and Health Monitoring of Structural and Mechanical Systems From Changes in their Vibration Characteristics: A Literature Review," *Los Alamos National Laboratory Report* LA-13070-MS, (1996)

[2-125] Doebling, S.W., Farrar, C.R., Prime, M.B., "A Summary Review of Vibration-Based Damage Identification Methods", *The Shock and Vibration Digest*, **30**, pp. 91-105, (1998)

[2-126] Carden, E.P., Fanning, P., "Vibration Based Condition Monitoring: A Review," Structural Health Monitoring, **3**(4), pp. 355–377, (2004)

[2-127] Yan, Y.J., Cheng, L., Wu, Z.Y., Yam, L.H., "Development in vibration-based structural damage detection technique," *Mechanical Systems and Signal Processing*, **21**, pp. 2198–2211, (2007)

[2-128] Friswell, M.I., "Damage Identification Using Inverse Methods," *Philosophical Transactions of the Royal Society of London A*, **365**, pp. 393-410, (2007)

[2-129] Gandomi, A.H., Sahab, M.G., Rahaei, A., Safari Gorji, M., "Development in Mode Shape-Based Structural Fault Identification Technique," *World Applied Sciences Journal*, **5**(1), pp. 29-38, (2008)

[2-130] Montalvão, D., Maia, N.M.M., Ribeiro, A.M.R., "A Review of Vibration-based Structural Health Monitoring with Special Emphasis on Composite Materials," *The Shock and Vibration Digest*, **38**(4), pp. 295-324, (2006)

[2-131]   Farrar, C.R., Worden, K., "Structural Health Monitoring: A Machine Learning Perspective," Wiley, (2014)

3 THEORETICAL ALGORITHM DEVELOPMENT

The theoretical foundations and base equations of the dissertation's primary damage identification algorithm are now developed. The algorithm relies on the target physical system being analytically modeled as a multiple degree-of-freedom system in the linear frequency domain with system properties and potential damage cases represented as implicit parameters. Special considerations are given for including damping and noise. The damage identification algorithm then provides a mechanism for updating the analytical system so that its analytical frequency domain response matches frequency domain reference data from the physical system. When the analytical model accurately represents the undamaged physical system and appropriate parameters are selected for modeling damage, the algorithm will provide an estimate of system damage and a measure of the estimation uncertainty.

The linear frequency-domain dynamic theory on which the algorithm is built is derived first, followed by methods for modal decomposition for the cases of proportional and generalized viscous damping and structural damping. Reduction of the multi degree-of-freedom system to a subset of degrees-of-freedom by dynamic reduction is presented next and the influence of noise is quantified. Derivation of the basic damage identification algorithm equations based on nonlinear Bayesian least-squares minimization is then presented. The chapter concludes with a walk-through demonstration of the algorithm's functionality using a damped 2 degree-of-freedom

mass-spring system, including a study on the effect of using proportional methods to approximately model generalized viscous damping.

3.1 **Dynamical System Description**

All damage identification operations are performed in the frequency domain, where measured reference data derived from frequency response functions are compared to an analytical representation of the physical system based on mass, stiffness, and damping matrices. The analytical system has N_D degrees-of-freedom and is defined in the frequency domain over N_ω frequency lines. Damage identification brings the analytical system into accordance with the reference data by altering a set of N_r structural model parameters, previously selected as being likely to describe the current damage state (e.g., stiffnesses, densities, damping parameters, or essentially any smoothly varying model feature connected to dynamic response and representative of potential damage cases).

To derive the algorithm, the analytical system equations of motion are first presented in the time domain with respect to displacement $\{x(t)\}$, velocity $\{\dot{x}(t)\}$, acceleration $\{\ddot{x}(t)\}$, and forcing vector $\{f(t)\}$, as

$$[M]\{\ddot{x}(t)\} + [C]\{\dot{x}(t)\} + \left[K^*\right]\{x(t)\} = \{f(t)\}, \qquad (3.1)$$

where $[M]$ is the system mass matrix, $[K^*]$ is the complex system stiffness matrix (real valued and represented by $[K]$ if structural damping is not present), and $[C]$ is the system viscous damping matrix. Although potential formulations for both structural and viscous damping will be discussed in detail later in the chapter, at this stage they can both be considered in their most general, unrestricted forms with no impact on the frequency domain system development. A function representing harmonic forcing at one or more degrees-of-freedom is defined as

$$\{f(t)\} = \{F(\omega)\} e^{j\omega t}, \tag{3.2}$$

where $\{F(\omega)\}$ is an $(N_D \times 1)$ spectral representation of the forcing function. A harmonic solution can then be assumed as

$$\{x(t)\} = \{X(\omega)\} e^{j\omega t}. \tag{3.3}$$

where $\{X(\omega)\}$ is the $(N_D \times 1)$ spectral representation of the response. Taking the first and second time derivatives produces

$$\{\dot{x}(t)\} = j\omega \{X(\omega)\} e^{j\omega t}, \tag{3.4}$$

$$\{\ddot{x}(t)\} = -\omega^2 \{X(\omega)\} e^{j\omega t}; \tag{3.5}$$

substituting the derivatives into Eq. (3.1), dividing by $e^{j\omega t}$, and rearranging terms then produces the harmonic dynamic system equations in the frequency domain,

$$\left(\left[K^* \right] + j\omega [C] - \omega^2 [M] \right) \{ X(\omega) \} = \{ F(\omega) \}. \tag{3.6}$$

The parenthesized term on the left containing the system definition is defined as the

dynamic stiffness (or impedance) matrix,

$$\left[Z(r, \omega_k) \right] \triangleq \left[K^* \right] + j\omega_k [C] - \omega_k^2 [M], \tag{3.7}$$

where a discrete-time frequency definition ω_k has been adopted in anticipation of the

need to implement further equations at discrete frequency points, and r refers to damage

identification parameters that are embedded within the system matrices. The parameter

dependency is written explicitly in $\left[Z(r, \omega_k) \right]$ but is also implicitly contained within the

system matrices $\left[K^* \right]$, $[M]$, and $[C]$, depending on which parameters are being used.

The $(N_D \times 1)$ frequency response transfer function vector is defined at each frequency as

$$\{ a(r, \omega_k) \} \triangleq \left\{ \frac{X(r, \omega_k)}{F(\omega_k)} \right\}. \tag{3.8}$$

Finally, the basic frequency response function dynamic system formulation for forcing at

a single degree-of-freedom can be given as

$$\left[Z(r, \omega_k) \right] \{ a(r, \omega_k) \} = \{ i \}, \tag{3.9}$$

where $\{ i \}$ is the nth column of the $(N_D \times N_D)$ sized identity matrix $[I]$, representing a

unit forcing at the nth degree-of-freedom. If the frequency response according to forcing

at each degree-of-freedom in term is considered, the resulting relationships can be

collected as

$$[Z(r,\omega_k)]\Big[\{a(r,\omega_k)\}_1\,\{a(r,\omega_k)\}_2\,...\{a(r,\omega_k)\}_{N_D}\Big]=[I], \qquad (3.10)$$

or

$$[Z(r,\omega_k)][A(r,\omega_k)]=[I], \qquad (3.11)$$

where the full $(N_D \times N_D)$ frequency response function matrix $[A(r,\omega_k)]$ is defined

based on the assembled the single degree-of-freedom response vectors, as

$$[A(r,\omega_k)]\triangleq\Big[\{a(r,\omega_k)\}_1\,\{a(r,\omega_k)\}_2\,...\{a(r,\omega_k)\}_{N_D}\Big]. \qquad (3.12)$$

Finally, taking multiplying both sides of Eq. (3.11) by $[Z(r,\omega_k)]^{-1}$ shows that the full

frequency response matrix and dynamic stiffness matrix are inverses, and thus the

frequency response function matrix can be calculated from $[Z(r,\omega_k)]$ as

$$[A(r,\omega_k)]=[Z(r,\omega_k)]^{-1}. \qquad (3.13)$$

3.2   **Modal Decomposition**

The N_D degree-of-freedom dynamic system can be decomposed into modal

coordinates where all vibrational response is viewed as the scaled superposition of N_m

modal vibration shapes $\{\phi_n\}$, each vibrating at a fixed natural frequency ω_n and

exhibiting a particular modal damping ratio ζ_n, where n refers to the nth mode.

Theoretically, N_m will always equal N_D; however, one of the benefits of modal

coordinates is that accurate results can usually be reached by working with a subset of

modes where $N_m < N_D$. For an idealized undamped system (i.e., $[C]$ equal to zero,

$\left[K^*\right] = [K]$) the modes shapes and natural frequencies are the eigenvectors and

eigenvalues, respectively, of the system, satisfying the equation

$$\left([K] - \omega_n^2 [M]\right)\{\phi_n\} = \{0\}, \tag{3.14}$$

for each mode n. Mode shapes adhering to this relationship, known as *normal modes*, are

real valued and orthogonal to each other and the mass and stiffness matrices.

Decomposition to modal space is achieved by changing from physical coordinates

$\{x(t)\}$ to generalized modal coordinates $\{q(t)\}$, using the transformation

$$\{x(t)\} = [\Phi]\{q(t)\}, \tag{3.15}$$

where $[\Phi]$ is the full mode shape matrix, formed as

$$[\Phi] = \left[\{\phi_1\} \ \{\phi_2\} \ \cdots \ \{\phi_{N_m}\}\right], \tag{3.16}$$

and $\{q(t)\}$ contains a modal coordinate for each mode, as

$$\{q(t)\} = \begin{Bmatrix} q_1(t) \\ q_2(t) \\ \vdots \\ q_{N_m}(t) \end{Bmatrix}, \tag{3.17}$$

Taking time derivatives of Eq. (3.16), substituting into Eq. (3.1), and pre-multiplying by $[\Phi]^T$ produces

$$[\Phi]^T[M][\Phi]\{\ddot{q}(t)\}+[\Phi]^T[K][\Phi]\{q(t)\}=[\Phi]^T\{f(t)\}. \qquad (3.18)$$

Orthogonality between the mode shapes and system matrices gives the relationships

$$\{\phi\}_m^T[M]\{\phi\}_n = \begin{cases} M_n, & \text{if } m=n \\ 0, & \text{if } m \neq n \end{cases}, \qquad (3.19)$$

$$\{\phi\}_m^T[K]\{\phi\}_n = \begin{cases} K_n, & \text{if } m=n \\ 0, & \text{if } m \neq n \end{cases}, \qquad (3.20)$$

where M_n and K_n are the modal mass and modal stiffness, respectively, for mode n. The quantities $[\Phi]^T[M][\Phi]$ and $[\Phi]^T[K][\Phi]$ are therefore diagonal and can be represented by $[M_n]$ and $[K_n]$, respectively. The uncoupled transformed system in generalized coordinates can then be rewritten as

$$[M_n]\{\ddot{q}(t)\}+[K_n]\{q(t)\}=\{P(t)\}. \qquad (3.21)$$

where $\{P(t)\}$ is the vector of modal forces,

$$\{P(t)\} = \begin{Bmatrix} P_1(t) \\ P_2(t) \\ \vdots \\ P_{N_m}(t) \end{Bmatrix} \triangleq [\Phi]^T\{f(t)\}, \qquad (3.22)$$

Premultiplying Eq. (3.14) by $\{\phi\}_n$ and expanding shows that natural frequency is related to the modal mass and modal stiffness by

$$\omega_n^2 = \frac{K_n}{M_n}.$$
(3.23)

Dividing Eq. (3.21) on both sides by $[M_n]$ produces N_m uncoupled single degree-of-freedom harmonic oscillators of the form

$$\ddot{q}_n(t) + \omega_n^2 q_n(t) = \frac{P_n(t)}{M_n}$$
(3.24)

for mode n, each representing a mode shape vibrating at frequency ω_n. Given initial conditions and loading the physical response can be recovered by solving the modal equations and transforming back into physical coordinates using Eq. (3.15).

3.3   Damping Models

For the previously described undamped system the modal decomposition is exact. However, physical structural systems always include some form of vibratory energy dissipation which is modeled as damping. As specified in Section 3.1, the two most common methods for modeling damping in aerospace structures are velocity proportional viscous damping using a matrix $[C]$ and displacement proportional structural damping using an imaginary component to the system stiffness matrix, $[K_{\mathrm{Im}}]$. Viscous damping can be further divided into proportional models or non-proportional generalized damping, where the former is essentially a simplification of the latter. These three mathematical damping models are now discussed.

3.3.1   Proportional Viscous Damping

Proportional viscous damping occurs when $[C]$ is proportional to the global

system mass and/or stiffness matrices. In this case, the system natural frequencies and

mode shapes are equal to their undamped values and can be calculated using the

eigenvalue analysis given in Eq. (3.14). Taking time derivatives of Eq. (3.15),

substituting into Eq. (3.1), and pre-multiplying by $[\Phi]^T$ produces the transformed system

$$[\Phi]^T [M][\Phi]\{\ddot{q}(t)\}+[\Phi]^T [C][\Phi]\{\dot{q}(t)\}+[\Phi]^T [K][\Phi]\{q(t)\}=[\Phi]^T \{f(t)\}. \quad (3.25)$$

The damping matrix $[C]$ is proportional to $[M]$ and/or $[K]$ and thus will also be

orthogonal with respect to the mode shapes through the relationship

$$\{\phi\}_m^T [C]\{\phi\}_n = \begin{cases} C_n, & \text{if } m=n \\ 0, & \text{if } m \neq n \end{cases}, \quad (3.26)$$

with C_n defined in terms of the modal damping ratio ζ_n as

$$C_n = 2\omega_n \zeta_n M_n. \quad (3.27)$$

The damping term in Eq. (3.25), $[\Phi]^T [C][\Phi]$, is therefore diagonal and the transformed

system will be uncoupled. Even if the system damping is not truly proportional, assuming

that the relationship in Eq. (3.26) holds may be a reasonable approximation if the system

is lightly damped (mode shapes and natural frequencies close to the undamped system

eigenvalues and eigenvalues) and the damping matrix is approximately orthogonal to the

mode shapes (similar connectivity and value-ratios to the stiffness matrix).

If the viscous damping matrix is unknown but can be assumed to be proportional

the classic approach known as *Rayleigh damping* can be used to compute an approximate

matrix in terms of the mass and stiffness matrices as

$$[C] = \alpha[K] + \beta[M], \tag{3.28}$$

where α and β are proportionality constants. The transformed damping term then

becomes

$$[\Phi]^T [C][\Phi] = \begin{bmatrix} \ddots & & \\ & (\alpha\omega_n^2 + \beta)M_n & \\ & & \ddots \end{bmatrix}, \tag{3.29}$$

which, when compared to Eqs. (3.26) and (3.27), produces the modal damping

relationship

$$\zeta_n = \frac{1}{2}\left(\alpha\omega_n + \frac{\beta}{\omega_n}\right). \tag{3.30}$$

Given estimated or measured values of ζ_n and ω_n, Eq. (3.30) can be solved for the

proportionality constants α and β. If only damping on one mode is desired, the equation

can be solved exactly for α to give stiffness proportional damping or for β to give mass

proportional damping. If damping on two modes is desired, α and β can be found together

by writing the equation for each mode and solving simultaneously. Examination of Eq.

(3.30) shows that a stiffness proportional damping formulation (i.e., $\alpha \neq 0,\ \beta = 0$) will

result in modal damping that increases with natural frequency; likewise, mass

proportional damping ($\alpha = 0,\ \beta \neq 0$) will result in modal damping that goes to zero with

natural frequency. While neither case is strictly observable in the real world, Rayleigh

damping offers a simple way to match modal damping on a small number of modes and

is thus often used by engineers to produce a convenient damped model with real

eigenvectors and eigenvalues and uncoupled modal equations. However, even for

sympathetic cases the damping prediction over more than two modes (i.e., equal to the

number of proportionality constants) will rapidly loose accuracy unless the modal

damping ratios are very similar over all modes of interest.

It is possible to circumvent this two-mode limitation by using a summation of

scaled mass and stiffness matrices, with proportionality constants calculated to match

measured damping ratios, in a process called the *extended Rayleigh method*, which is

related to the more generally described *Caughey* damping [3-1]. One method for

implementing this concept, presented by Clough and Penzien [3-2] and derived in detail

in Appendix A, produces a viscous damping matrix through the relationship

$$[C] = \left(\frac{2\zeta_c}{\omega_c} \right)[K] + [M]\left[\sum_{n=1}^{c-1} 2\left(\zeta_n - \zeta_c\left(\frac{\omega_n}{\omega_c} \right) \right)\frac{\omega_n}{M_n}\{\phi_n\}\{\phi_n\}^T \right][M], \qquad (3.31)$$

where *c* refers to the highest mode of interest. So long as the basic assumption of proportional viscous damping holds and real natural frequencies and mode shapes can be derived which are approximately orthogonal to the mass and stiffness matrix (i.e., damping light and distributed), this method has the capability to produce a viscous damping matrix which accurately models measured damping across any number of modes. Even if the true damping is not proportional, the method may provide an acceptable approximation for the purposes of recreating modal damping ratios and frequency response functions. The restriction to proportional damping means that the Rayleigh methods are potentially useful candidates for plane structures and homogeneous sub-components of built up systems (e.g., wing skin regions and spars) where damping is distributed with mass and stiffness. However, for global built-up systems, such as aircraft, where global damping behavior is dominated by structural connections and joints and damping is concentrated in regions with negligible stiffness or mass, proportional damping methods may be inadequate.

3.3.2 Generalized Viscous Damping

When the viscous damping matrix is not proportional to the global mass or stiffness matrices the mode shapes and natural frequencies will not be equal to their undamped values. The mode shapes and natural frequencies for a system with generalized damping are found instead by performing an eigenvalue analysis of the system in state-space. This is accomplished by introducing the identity

$$[M]\{\dot{x}(t)\} - [M]\{\dot{x}(t)\} = \{0\} \tag{3.32}$$

and combining with the system equations-of-motion,

$$[M]\{\ddot{x}(t)\} + [C]\{\dot{x}(t)\} + [K]\{x(t)\} = \{f(t)\}, \tag{3.33}$$

to produce the state-space equation

$$\begin{bmatrix} [M] & [0] \\ [0] & [M] \end{bmatrix} \begin{Bmatrix} \{\dot{x}(t)\} \\ \{\ddot{x}(t)\} \end{Bmatrix} + \begin{bmatrix} [0] & -[M] \\ [K] & [C] \end{bmatrix} \begin{Bmatrix} \{x(t)\} \\ \{\dot{x}(t)\} \end{Bmatrix} = \begin{Bmatrix} \{0\} \\ \{f(t)\} \end{Bmatrix}. \tag{3.34}$$

Considering the free-vibration case ($\{f(t)\} = \{0\}$) and multiplying by $[M]^{-1}$ gives the

expression

$$\begin{bmatrix} [I] & [0] \\ [0] & [I] \end{bmatrix} \begin{Bmatrix} \{\dot{x}(t)\} \\ \{\ddot{x}(t)\} \end{Bmatrix} - \begin{bmatrix} [0] & [I] \\ -[M]^{-1}[K] & -[M]^{-1}[C] \end{bmatrix} \begin{Bmatrix} \{x(t)\} \\ \{\dot{x}(t)\} \end{Bmatrix} = \begin{Bmatrix} \{0\} \\ \{0\} \end{Bmatrix}. \tag{3.35}$$

Introducing the solution

$$\begin{Bmatrix} \{x(t)\} \\ \{\dot{x}(t)\} \end{Bmatrix} = \{\psi\} e^{\lambda t} \tag{3.36}$$

and its derivative

$$\begin{Bmatrix} \{\dot{x}(t)\} \\ \{\ddot{x}(t)\} \end{Bmatrix} = \lambda \{\psi\} e^{\lambda t} \tag{3.37}$$

then allows the system to then be written in the standard eigenvalue problem form

$$\left(\begin{bmatrix} [0] & [I] \\ -[M]^{-1}[K] & -[M]^{-1}[C] \end{bmatrix} - \lambda \left(\begin{bmatrix} [I] & [0] \\ [0] & [I] \end{bmatrix} \right)\right)\{\psi\} = \begin{Bmatrix} \{0\} \\ \{0\} \end{Bmatrix}. \tag{3.38}$$

The solution of Eq. (3.38) is $2N_D$ complex eigenvalues λ and $2N_D$ complex

eigenvectors $\{\psi\}$ in complex conjugate pairs.

The standard eigenvalue problem derived using state-space in Eq. (3.38) is

equivalent to the quadratic eigenvalue problem

$$\left(\lambda^2[M] + \lambda[C] + [K]\right)\{\phi\} = \{0\}, \tag{3.39}$$

and the eigenvalues therefore satisfy the equation

$$\lambda_n^2 + 2\zeta_n\omega_n\lambda_n + \omega_n^2 = 0. \tag{3.40}$$

When the system damping is less than critical ($\zeta_n < 1$), the solution to this equation is

$$\lambda_{n,n+1} = -\zeta_n\omega_n \pm j\omega_n\sqrt{1 - \zeta_n^2}, \tag{3.41}$$

for mode n. The undamped natural frequencies can therefore be recovered using

$$\omega_n = \sqrt{\lambda_{\text{Re},n}^2 + \lambda_{\text{Im},n}^2}, \tag{3.42}$$

where $\lambda_{\text{Re},n}$ and $\lambda_{\text{Im},n}$ are defined by the format $\lambda_{n,n+1} = \lambda_{\text{Re},n} \pm j\lambda_{\text{Im},n}$. The modal

damping ratios are likewise found using

$$\zeta_n = \frac{-\lambda_{\text{Re},n}}{\omega_n}. \tag{3.43}$$

The eigenvectors are related to the mode shapes by the relationship

$$\{\psi_{n,n+1}\} = \left\{\begin{array}{c} \{\phi_n\} \\ \lambda_n\{\phi_n\} \end{array}\right\}. \tag{3.44}$$

or equivalently as

$$\{\psi_{n,n+1}\} = \left\{\begin{array}{c} \{\phi_n\}_{\mathrm{Re}} \\ \lambda_{\mathrm{Re},n}\{\phi_n\}_{\mathrm{Re}} - \lambda_{\mathrm{Im},n}\{\phi_n\}_{\mathrm{Im}} \end{array}\right\} \pm j \left\{\begin{array}{c} \{\phi_n\}_{\mathrm{Im}} \\ \lambda_{\mathrm{Re},n}\{\phi_n\}_{\mathrm{Im}} - \lambda_{\mathrm{Im},n}\{\phi_n\}_{\mathrm{Re}} \end{array}\right\} \tag{3.45}$$

where $\{\phi_n\}_{\mathrm{Re}}$ and $\{\phi_n\}_{\mathrm{Im}}$ are defined by the format $\{\phi_{n,n+1}\} = \{\phi_n\}_{\mathrm{Re}} \pm j\{\phi_n\}_{\mathrm{Im}}$.

The system mode shapes are therefore equal to the first n values from the first of each

complex conjugate pair of eigenvectors for $n = 1,2,\ldots,N_{\mathrm{D}}$. The non-proportionally

damped mode shapes are orthogonal to one another (see reference [3-3] for formal

proof) and to the left-most matrix quantity in Eq. (3.38). However, they will not be

orthogonal to the system matrices and thus systems with generalized viscous damping

will have coupled modal equations-of-motion. Furthermore, the elements of complex

mode shapes are not 180° out-of-phase with each other as with undamped and

proportionally damped systems. When complex mode shapes are animated for

visualization the node lines will move and the shapes will appear to be wave-like or

galloping.

It should be noted that in the case of both proportional and generalized viscous

damping the resulting system frequency response function modal peaks will be decreased

from their undamped values. For sub-critical viscous damping ($\zeta_n < 1$), the so-called

damped natural frequencies can be estimated using the relationship

$$\omega_n^{damped} = \omega_n \sqrt{1 - \zeta_n^2} \tag{3.46}$$

for each mode n. From this equation it can be seen that critical damping ($\zeta_n = 1$)

corresponds to a zero value damped natural frequency. For overdamped systems ($\zeta_n > 1$),

the damped natural frequencies can be estimated using

$$\omega_n^{damped} = \omega_n \sqrt{\zeta_n^2 - 1}. \tag{3.47}$$

3.3.3 Structural Damping

Structural damping (also known as complex stiffness or material damping) is

modeled by adding an imaginary component $[K]_{Im}$ to the stiffness matrix to produce the

complex stiffness matrix

$$\left[K^* \right] = \left[K \right] + j \left[K \right]_{Im}. \tag{3.48}$$

The resulting dynamic dissipation is independent of frequency and is often more accurate

for losses caused by friction and other losses on the material level than viscous damping.

When structural damping is present with no viscous damping, the free-vibration

equations-of-motion can be written as

$$[M]\{\ddot{x}(t)\}+\left[K^*\right]\{x(t)\}=\{0\}. \tag{3.49}$$

The modal decomposition is then found by assuming the harmonic solution

$$\{x(t)\}=\{\psi\}e^{j\lambda t}, \tag{3.50}$$

for eigenvalue λ^2 and eigenvector $\{\psi\}$, then taking time derivatives, substituting into Eq. (3.49), and multiplying by $[M]^{-1}$ to produce the complex eigenvalue equation

$$\left([M]^{-1}\left[K^*\right]-\lambda\right)\{\psi\}=\{0\}. \tag{3.51}$$

For the general case of $[K]_{\text{Im}}$ not proportional to $[K]$, solving the eigenvalue equation produces N_D complex eigenvalues and N_D complex eigenvectors. The eigenvalues have the form

$$\lambda_n=\omega_n^2\left(1+j\eta_n\right), \tag{3.52}$$

where ω_n are the natural frequencies and η_n are the modal damping loss factors. The system natural frequencies can therefore be found as

$$\omega_n=\sqrt{\text{Re}\left(\lambda_n\right)}, \tag{3.53}$$

and the modal damping can be found as

$$\zeta_n=\frac{\text{Im}\left(\lambda_n\right)}{\text{Re}\left(\lambda_n\right)}. \tag{3.54}$$

The system complex mode shapes are equal to the eigenvectors [3-4],

$$\{\phi_n\} = \{\psi_n\}. \tag{3.55}$$

As with the case of generalized viscous damping, the elements of the complex mode shapes are not 180° out-of-phase with each other and the complex mode shapes will be coupled.

In the case of global stiffness proportional structural damping, where

$$\left[K^*\right] = \left[K\right](1 + j\eta), \tag{3.56}$$

the modal damping loss factors will all be equal to the global structural damping constant η. The system will have real natural frequencies and modes and the natural frequencies will be equal to the undamped system natural frequencies.

3.4 Dynamic Reduction of Degrees-of-Freedom

The combination of present day analytical structural modeling methods (e.g., finite element method) and dynamic testing methods (e.g., scanning laser vibrometry) almost always produce models with many more analytical degrees-of-freedom than measurement degrees-of-freedom. For the data to be compared to the model either the analytical degrees-of-freedom must be reduced, the measurement degrees-of-freedom expanded, or a combination of the two until the model and reference data share a

common degree-of-freedom set. The method recommended herein is to reduce the

analytical degree-of-freedom set to the test data set using the method of dynamic

reduction [3-5], which is essentially a dynamic version of the classical method of Guyan

reduction [3-6]. Dynamic reduction is performed by reorganizing and partitioned the

dynamic stiffness matrix and associated vectors into the *m*-set of measurement (or

master) degrees-of-freedom and the remaining *s*-set of slave degrees-of-freedom, as

$$
\begin{bmatrix} [Z(r,\omega_k)]_{mm} & [Z(r,\omega_k)]_{ms} \\ [Z(r,\omega_k)]_{sm} & [Z(r,\omega_k)]_{ss} \end{bmatrix} \begin{Bmatrix} \{a(r,\omega_k)\}_m \\ \{a(r,\omega_k)\}_s \end{Bmatrix} = \begin{Bmatrix} \{i\}_m \\ \{i\}_s \end{Bmatrix},
\tag{3.57}
$$

where subscripts *m* and *s* indicate membership in the *m*-set and/or *s*-set. The measured

frequency response functions , $\{a(r,\omega_k)\}_m$, are known while the frequency response

functions at the unmeasured analytical degrees-of-freedom, $\{a(r,\omega_k)\}_s$, are missing.

Since the forcing degree-of-freedom must be in the *m*-set, $\{i\}_s$ is a vector of zeros. The

partitioned dynamic equation second line can therefore be expanded to

$$
[Z(r,\omega_k)]_{sm}\{a(r,\omega_k)\}_m + [Z(r,\omega_k)]_{ss}\{a(r,\omega_k)\}_s = \{0\},
\tag{3.58}
$$

and then solved for $\{a(r,\omega_k)\}_s$, giving

$$
\{a(r,\omega_k)\}_s = -[Z(r,\omega_k)]_{ss}^{-1}[Z(r,\omega_k)]_{sm}\{a(r,\omega_k)\}_m.
\tag{3.59}
$$

Substituting this expression into the expanded first line and collecting terms leads to

$$
\left([Z(r,\omega_k)]_{mm} - [Z(r,\omega_k)]_{ms}[Z(r,\omega_k)]_{ss}^{-1}[Z(r,\omega_k)]_{sm} \right)\{a(r,\omega_k)\}_m = \{i\}_m.
\tag{3.60}
$$

Comparing this expression to the expected dynamic system description in reduced

coordinates,

$$\left[Z(r,\omega_k)\right]_m \left\{a(r,\omega_k)\right\}_m = \left\{i\right\}_m, \tag{3.61}$$

shows the reduced coordinate dynamic stiffness matrix to be

$$\left[Z(r,\omega_k)\right]_m = \left[Z(r,\omega_k)\right]_{mm} - \left[Z(r,\omega_k)\right]_{ms} \left[Z(r,\omega_k)\right]_{ss}^{-1} \left[Z(r,\omega_k)\right]_{sm}. \tag{3.62}$$

For simplicity of implementation, a dynamic transformation matrix for reduction

or expansion can be constructed as

$$\left[T(r,\omega_k)\right] = \begin{bmatrix} \left[I\right]_{mm} \\ -\left[Z(r,\omega_k)\right]_{ss}^{-1}\left[Z(r,\omega_k)\right]_{sm} \end{bmatrix}, \tag{3.63}$$

and the dynamic stiffness matrix, or any of the individual system matrices, are then

reduced to the measurement m-set, for each frequency line, by partitioning and using the

relationships

$$\left[Z(r,\omega_k)\right]_m = \left[T(r,\omega_k)\right]^T \left[Z(r,\omega_k)\right]\left[T(r,\omega_k)\right], \tag{3.64}$$

$$\left[M(r,\omega_k)\right]_m = \left[T(r,\omega_k)\right]^T \left[M\right]\left[T(r,\omega_k)\right], \tag{3.65}$$

$$\left[K^*(r,\omega_k)\right]_m = \left[T(r,\omega_k)\right]^T \left[K^*\right]\left[T(r,\omega_k)\right], \tag{3.66}$$

$$\left[C(r,\omega_k)\right]_m = \left[T(r,\omega_k)\right]^T \left[C\right]\left[T(r,\omega_k)\right]. \tag{3.67}$$

Additionally, the full degree-of-freedom frequency response function matrix can be

recovered by

$$\{a(r,\omega_k)\} = [T(r,\omega_k)]\{a(r,\omega_k)\}_m. \qquad (3.68)$$

The dynamic method for reduction or expansion has the advantage of being exact,

so long as the parameter set used to create the matrices being reduced is known exactly

and the excitation degree of freedom is contained in the m-set. Reduced matrices

therefore produce the exact same frequency response functions at the m-set degrees of

freedom as the full matrices. It should be noted that reduction makes $[Z(r,\omega_k)]_m$

nonlinear with $\{r\}$, even if it was linear in the unreduced system. However, if

measurement points happen to be clustered close to damage parameter locations, the

parameter dependency in $[Z(r,\omega_k)]_{ss}^{-1}$ will be weak and the nonlinearity will be reduced.

Throughout the damage identification algorithm's operation system matrices are

reduced to the measurement degrees-of-freedom set as soon as possible (generally as

soon as damping has been added), after which all matrices and vectors have the same

dimensional basis. The m subscript is therefore generally omitted hereafter, although it is

implied if measurements are not available at every analytical degree of freedom.

Dynamic expansion can also be applied to mode shapes. The undamped

transformation matrix is formed using real normal natural frequencies in place of the

specified update frequency lines, to produce, for mode n,

$$[T_n(r)] = \begin{bmatrix} [I]_{mm} \\ -\left[[K(r)]_{ss} - \omega_n^2 [M(r)]_{ss}\right]^{-1}\left[[K(r)]_{sm} - \omega_n^2 [M(r)]_{sm}\right] \end{bmatrix}. \qquad (3.69)$$

Mode shape expansion is then conducted using the transformation

$$\{\phi_n\} = [T_n(r)]\{\phi_n\}_m, \qquad (3.70)$$

for each mode n.

3.5   Measured Frequency Response and Residual Force Vector

Returning to the initial dynamic system description, it can be seen from Eq. (3.9) that the analytical frequency response function matrix from forcing at a single degree-of-freedom in reduced coordinates can be calculated from the dynamic stiffness matrix (in reduced coordinates if $N_d < N_D$) by

$$\{a(r, \omega_k)\} = [Z(r, \omega_k)]^{-1}\{i\}. \qquad (3.71)$$

The real-life system being modeled by $\{a(r, \omega_k)\}$ includes randomness, both in the true value of parameters and in additive noise, and in irreducible modeling error. It is therefore assumed that the relationship between the measured frequency response functions, $\{\tilde{a}(\omega_k)\}$, and the model can be represented by

$$\{\tilde{a}(\omega_k)\} = \{a(\tilde{r}, \omega_k)\} + \{e(\omega_k)\} + \{v(\omega_k)\}, \qquad (3.72)$$

where $\{e(\omega_k)\}$ is a vector of deterministic error and $\{v(\omega_k)\}$ is a vector of random zero-mean additive noise (Note: if the random noise is known to not be zero mean, the mean can be removed from $\{v(\omega_k)\}$ and added to $\{e(\omega_k)\}$, creating the same affect). The vector $\{\tilde{r}\}$ represents 'true' system parameters best corresponding to $\{\tilde{a}(\omega_k)\}$ — i.e., the desired damaged parameters—and $\{a(\tilde{r},\omega_k)\}$ is the model evaluated at these unknown values. It is further assumed that the two basic random quantities, parameter vector $\{r\}$ and noise vector $\{v(\omega_k)\}$, and all quantities dependent on them are close to Gaussian, and therefore can be described adequately through their mean and covariance matrix.

With the deterministic modeling error separated, the noise is assumed to be zero mean with covariance $[S_{vv}(\omega_k)]$. The parameter vector begins each update with a prior (or baseline correlated) distribution described by mean $\{\hat{r}_0\}$ (where the caret denotes an estimate) and covariance $\left[S_{\hat{r}_0\hat{r}_0}\right]$. After update, the parameter vector will have a posterior (or damage correlated) distribution described by mean $\{\tilde{r}\}$, and covariance $[S_{\tilde{r}\tilde{r}}]$. The frequency response function covariance can be found by first writing its expected value, (denoted by $E(...)$), as

$$E\left(\{\tilde{a}(\omega_k)\}\right) = E\left(\{a(\tilde{r},\omega_k)\} + \{e(\omega_k)\} + \{v(\omega_k)\}\right). \tag{3.73}$$

Bringing the expected value around each term and recognizing

$$E\left(\{a(\tilde{r},\omega_k)\}\right) = \{a(\tilde{r},\omega_k)\}, \tag{3.74}$$

$$E\left(\{e(\omega_k)\}\right) = \{e(\omega_k)\}, \tag{3.75}$$

$$E\left(\{v(\omega_k)\}\right) = \{0\}, \tag{3.76}$$

then produces the expression

$$E\left(\{\tilde{a}(\omega_k)\}\right) = \{a(\tilde{r}, \omega_k)\} + \{e(\omega_k)\}. \tag{3.77}$$

The measured frequency response function covariance matrix is written by starting with

$$\left[S_{\tilde{a}\tilde{a}}(\omega_k)\right] = E\left(\left(\{\tilde{a}(\omega_k)\} - E\left(\{\tilde{a}(\omega_k)\}\right)\right)\left(\{\tilde{a}(\omega_k)\} - E\left(\{\tilde{a}(\omega_k)\}\right)\right)^T\right), \tag{3.78}$$

then substituting in Eqs. (3.71) and (3.77) and canceling terms to give

$$\left[S_{\tilde{a}\tilde{a}}(\omega_k)\right] = E\left(\{v(\omega_k)\}\{v(\omega_k)\}^T\right). \tag{3.79}$$

Recognizing the definition of zero-mean noise covariance finally produces the relationship

$$\left[S_{\tilde{a}\tilde{a}}(\omega_k)\right] = \left[S_{vv}(\omega_k)\right]. \tag{3.80}$$

The residual force vector, describing the dynamic system imbalance in terms of internal forces when the analytical model is compared to the measured frequency response functions, is defined as

$$\{R(r,\omega_k)\} \triangleq \{i\} - [Z(r,\omega_k)] \cdot \{\tilde{a}(\omega_k)\}. \tag{3.81}$$

Based on the relationship $[Z(r,\omega_k)]\{a(r,\omega_k)\} = \{i\}$ in Eq. (3.9), it is obvious that if $\{\tilde{a}(\omega_k)\} = \{a(r,\omega_k)\}$ then the residual force will equal a vector of zeros, and any deviation from $\{\tilde{a}(\omega_k)\} = \{a(r,\omega_k)\}$ will produce non-zero values.

The residual force vector covariance matrix is defined by the measurement noise, and its value $\left[\underline{S}_{RR}(r_\beta) \right]$ at a parameter point value $\{R(r_\beta,\omega_k)\}$ can be found in terms of the measured frequency response function noise covariance as follows. First, the residual force vector expected value is written in expanded form as

$$E\left(\{R(r_\beta,\omega_k)\}\right) = E\left(\{i\} - \{Z(r_\beta,\omega_k)\}\{\tilde{a}(\omega_k)\}\right). \tag{3.82}$$

The expected value is then brought onto each term and applying

$$E\left(\{i\}\right) = \{i\}, \tag{3.83}$$

$$E\left([Z(r_\beta,\omega_k)]\{\tilde{a}(\omega_k)\}\right) = [Z(r_\beta,\omega_k)]E\left(\{\tilde{a}(\omega_k)\}\right), \tag{3.84}$$

along with Eq. (3.77) gives the expression

$$E\left(\{R(r_\beta,\omega_k)\}\right) = \{i\} - \{Z(r_\beta,\omega_k)\}\left(\{a(\tilde{r},\omega_k)\} + \{e(\omega_k)\}\right). \tag{3.85}$$

The difference between the residual force vector and its expected value can then be written

$$\{R(r_\beta,\omega_k)\} - E\big(\{R(r_\beta,\omega_k)\}\big) = \{Z(r_\beta,\omega_k)\}\{v(\omega_k)\}. \tag{3.86}$$

The residual force vector covariance matrix can be calculated by starting from the basic definition of covariance,

$$[S_{RR}(\omega_k)] = E\left(\big(\{R(r_\beta,\omega_k)\} - E\big(\{R(r_\beta,\omega_k)\}\big)\big)\big(\{R(r_\beta,\omega_k)\} - E\big(\{R(r_\beta,\omega_k)\}\big)\big)^T\right),$$
$$\tag{3.87}$$

substituting in Eq. (3.82), and canceling terms to give

$$[S_{RR}(\omega_k)] = E\left(\big[Z(r_\beta,\omega_k)\big]\{v(\omega_k)\}\{v(\omega_k)\}^T \big[Z(r_\beta,\omega_k)\big]^T\right). \tag{3.88}$$

This expression simplifies to

$$[S_{RR}(\omega_k)] = \big[Z(r_\beta,\omega_k)\big]E\left(\{v(\omega_k)\}\{v(\omega_k)\}^T\right)\big[Z(r_\beta,\omega_k)\big]^T. \tag{3.89}$$

Recognizing the noise covariance allows the residual force vector covariance at parameter point $\{r_\beta\}$ to be written finally as

$$[S_{RR}(\omega_k)] = \big[Z(r_\beta,\omega_k)\big]\big[S_{vv}(\omega_k)\big]\big[Z(r_\beta,\omega_k)\big]^T, \tag{3.90}$$

for each frequency ω_k.

3.6   Least Squares Formulation of Damage Identification Equations

The goal of the damage identification algorithm is to use the model $[Z(r, \omega_k)]$, previously correlated to the baseline state $\{\hat{r}_0\}$, along with $\{\tilde{a}(\omega_k)\}$, measured from a current damaged state, to estimate the mean and covariance of the unknown damage parameter vector $\{\tilde{r}\}$. The quantity $[\Delta Z(r, \omega_k)]$, representing system changes—e.g., from damage—is defined as

$$[\Delta Z(r, \omega_k)] = [Z(\tilde{r}, \omega_k)] - [Z(r_0, \omega_k)], \tag{3.91}$$

where $[Z(\tilde{r}, \omega_k)]$ is the dynamic stiffness matrix evaluated at $\{\tilde{r}\}$. Additionally, the irreducible residual force vector from noise and modeling imperfection can be expressed as

$$\{R(\tilde{r}, \omega_k)\} \triangleq \{i\} - [Z(\tilde{r}, \omega_k)]\{\tilde{a}(\omega_k)\}, \tag{3.92}$$

or equivalently, by expanding the measured frequency response function vector, recognizing $[Z(\tilde{r}, \omega_k)]\{a(\tilde{r}, \omega_k)\} = \{i\}$, and canceling terms, as

$$\{R(\tilde{r}, \omega_k)\} = -[Z(\tilde{r}, \omega_k)]\left(\{e(\omega_k)\} + \{v(\omega_k)\}\right). \tag{3.93}$$

The initial residual force vector for parameter set $\{r_0\}$ can then be seen to equal

$$\{R(r_0, \omega_k)\} = [\Delta Z(r, \omega_k)]\{\tilde{a}(\omega_k)\} + \{R(\tilde{r}, \omega_k)\}. \tag{3.94}$$

Inspection of these expressions revels that as model parameters approach the true physical values—i.e., as $\{r_0\} \to \{\tilde{r}\}$—the reducible system imbalance $\left[\Delta Z(r, \omega_k)\right]$ goes to zero, and $\{R(r_0, \omega_k)\} \to \{R(\tilde{r}, \omega_k)\}$; or, in the case of zero noise or modeling error, $\{R(r_0, \omega_k)\} \to \{0\}$.

In the general case, with noise and modeling error present, $\{R(r_0, \omega_k)\}$ does not go to zero, and the damage identification becomes an optimization problem. To proceed, quantities need to be reconfigured so that all information can be processed together via batch processing, a cost function must be established, and solution equations derived.

3.6.1   Batch Processed Least-Squares

To implement batch processing, quantities with frequency dependency must be stacked with real and imaginary components separated into single large-dimension vectors and matrices so that all available information can be processed at the same time in a single real-valued equation for each iteration step. These batch-processing, or *batch-stacked*, quantities are developed following reference [3-7], and are denoted herein by underbars. The analytical and experimental frequency response function and residual force vector batch-stacked quantities are, respectively,

$$\{\underline{a}(r)\} = \begin{Bmatrix} \text{Re}\big(\{a(r,\omega_1)\}\big) \\ \text{Im}\big(\{a(r,\omega_1)\}\big) \\ \text{Re}\big(\{a(r,\omega_2)\}\big) \\ \text{Im}\big(\{a(r,\omega_2)\}\big) \\ \vdots \\ \text{Re}\big(\{a(r,\omega_{N_\omega})\}\big) \\ \text{Im}\big(\{a(r,\omega_{N_\omega})\}\big) \end{Bmatrix}, \tag{3.95}$$

$$\{\underline{\tilde{a}}\} = \begin{Bmatrix} \text{Re}\big(\{\tilde{a}(\omega_1)\}\big) \\ \text{Im}\big(\{\tilde{a}(\omega_1)\}\big) \\ \text{Re}\big(\{\tilde{a}(\omega_2)\}\big) \\ \text{Im}\big(\{\tilde{a}(\omega_2)\}\big) \\ \vdots \\ \text{Re}\big(\{\tilde{a}(\omega_{N\omega})\}\big) \\ \text{Im}\big(\{\tilde{a}(\omega_{N\omega})\}\big) \end{Bmatrix}, \tag{3.96}$$

$$\{\underline{R}(r)\} = \begin{Bmatrix} \text{Re}\big(\{R(r,\omega_1)\}\big) \\ \text{Im}\big(\{R(r,\omega_1)\}\big) \\ \text{Re}\big(\{R(r,\omega_2)\}\big) \\ \text{Im}\big(\{R(r,\omega_2)\}\big) \\ \vdots \\ \text{Re}\big(\{R(r,\omega_{N_\omega})\}\big) \\ \text{Im}\big(\{R(r,\omega_{N_\omega})\}\big) \end{Bmatrix}, \tag{3.97}$$

$$\{\underline{i}\} = \left\{ \begin{array}{c} \{i\} \\ \{i\} \\ \{i\} \\ \{i\} \\ \vdots \\ \{i\} \\ \{i\} \end{array} \right\}, \qquad (3.98)$$

and the batch-stacked diagonal noise covariance super-matrix is

$$[\underline{S}_{vv}] = \begin{bmatrix} \text{Re}\big([S_{vv}(\omega_1)]\big) & [0] & \cdots & [0] & [0] \\ [0] & \text{Im}\big([S_{vv}(\omega_1)]\big) & \cdots & [0] & [0] \\ \vdots & \vdots & \ddots & \vdots & \vdots \\ [0] & [0] & \cdots & \text{Re}\big([S_{vv}(\omega_{N\omega})]\big) & [0] \\ [0] & [0] & \cdots & [0] & \text{Im}\big([S_{vv}(\omega_{N\omega})]\big) \end{bmatrix}. \qquad (3.99)$$

All other batch-stacked vector and matrix quantities also follow these forms, with the

exception of the non-diagonal dynamic stiffness matrix which must be batch-stacked as

$$[\underline{Z}(r)] = \begin{bmatrix} \text{Re}\big([Z(r,\omega_1)]\big) & -\text{Im}\big([Z(r,\omega_1)]\big) & \cdots & [0] & [0] \\ \text{Im}\big([Z(r,\omega_1)]\big) & \text{Re}\big([Z(r,\omega_1)]\big) & \cdots & [0] & [0] \\ \vdots & \vdots & \ddots & \vdots & \vdots \\ [0] & [0] & \cdots & \text{Re}\big([Z(r,\omega_{N\omega})]\big) & -\text{Im}\big([Z(r,\omega_{N\omega})]\big) \\ [0] & [0] & \cdots & \text{Im}\big([Z(r,\omega_{N\omega})]\big) & \text{Re}\big([Z(r,\omega_{N\omega})]\big) \end{bmatrix} \qquad (3.100)$$

in order to keep information compatible if the batch-stacked equations are expanded back

out into single complex equations for each frequency. (Note: an alternative approach to

batch-processing for parametrically linear systems is *recursive processing*, wherein each

real and imaginary frequency equation is processed independently and the estimate

improves after each iteration [3-7].)

With batch-stacked quantities thus defined, the dynamic system relationships can

be rewritten in a simplified form, giving, for instance, the frequency response system

equation

$$[\underline{Z}(r)] \cdot \{\underline{a}(r)\} = \{\underline{i}\},$$
(3.101)

or

$$\{\underline{a}(r)\} = [\underline{Z}(r)]^{-1} \{\underline{i}\};$$
(3.102)

the residual force vector,

$$\{\underline{R}(r)\} = \{\underline{i}\} - [\underline{Z}(r)] \cdot \{\tilde{\underline{a}}\};$$
(3.103)

and residual force vector covariance,

$$\left[\underline{S}_{RR}(r_\beta)\right] = \left[\underline{Z}(r_\beta)\right]\left[\underline{S}_{vv}\right]\left[\underline{Z}(r_\beta)\right]^{T}.$$
(3.104)

3.6.2 Bayesian Least-Squares Cost Function and Solution

The main damage identification algorithm is now derived as follows. Following

the reasoning of Tarantola and Valette [3-8], it is desired to find an estimate $\{\hat{r}\}$ of

parameter set $\{\tilde{r}\}$ that maximizes the posterior probability distribution (i.e., is most

probable) while also satisfying the governing system equations. When quantities are

assumed to be Gaussian, the posterior parameter distribution $\rho_r(\hat{r})$ can be written as

$$\rho_r(\hat{r}) = D_0 e^{-\frac{1}{2}(\{\hat{r}\}-\{\hat{r}_0\})^T \{S_{r_0 r_0}\}^{-1}(\{\hat{r}\}-\{\hat{r}_0\})}, \tag{3.105}$$

where D_0 is a constant. Maximizing a Gaussian distribution requires minimizing the

exponential terms inside the negative—i.e. minimizing $(\{\hat{r}\}-\{\hat{r}_0\})^T \{S_{r_0 r_0}\}^{-1}(\{\hat{r}\}-\{\hat{r}_0\})$. As

shown by Tarantola and Valette, minimizing the posterior distribution while satisfying

the system equations, here represented through minimizing the residual force vector, is

equivalent to a generalized regularized least-squares minimization problem where the

parameter and system terms each include weighting by the inverse of their respective

covariance matrices. For the residual force vector-based damage detection problem, the

least-squares problem can therefore be defined as the search for the parameter set $\{\hat{r}\}$

minimizing a cost function $J(\hat{r})$, defined as

$$J(\hat{r}) \triangleq \{\underline{R}(\hat{r})\}^T \left[\underline{S}_{RR}(\hat{r}_\beta)\right]^{-1} \{\underline{R}(\hat{r})\} + (\{\hat{r}\}-\{\hat{r}_0\})^T \{S_{r_0 r_0}\}^{-1}(\{\hat{r}\}-\{\hat{r}_0\}), \tag{3.106}$$

where the residual force covariance is calculated at the linearization point $\{\hat{r}_\beta\}$, which is

initially the prior parameter point $\{\hat{r}_0\}$. The cost function can alternatively be viewed in

two parts, as

$$J(\hat{r}) = J_R(\hat{r}) + J_r(\hat{r}), \tag{3.107}$$

where

$$J_R(\hat{r}) \triangleq \{\underline{R}(\hat{r})\}^T \left[\underline{S}_{RR}(r_\beta)\right]^{-1} \{\underline{R}(\hat{r})\}, \tag{3.108}$$

$$J_r(\hat{r}) \triangleq \left(\{\hat{r}\} - \{\hat{r}_0\}\right)^T \left\{S_{r_0 r_0}\right\}^{-1} \left(\{\hat{r}\} - \{\hat{r}_0\}\right). \tag{3.109}$$

Minimization of $J_R(\hat{r})$ corresponds to satisfying the dynamic system equations by minimizing the residual force vector; minimization of $J_r(\hat{r})$ corresponds to maximizing the posterior Gaussian parameter distribution, making the solution more likely in a statistical sense, and providing the updated parameter set with posterior variance values. Compared to a standard deterministic least-squares formulation, which would only seek to minimize the first term (also known as the functional term), the presence of the second term has the practical effect of providing regularization, penalizing the parameters for moving away from their original values and producing a more stable and realistic solution.

The least-squares solution is found by setting the variation of $J(\hat{r})$, taken with respect to $\{\hat{r}\}$, equal to zero, giving

$$\delta J(\hat{r}) = 0 = \{\delta\hat{r}\} \left\{\frac{\partial J}{\partial \hat{r}}\right\} = \{\delta\hat{r}\} \left(\left\{\frac{\partial J_R(\hat{r})}{\partial \hat{r}}\right\} + \left\{\frac{\partial J_r(\hat{r})}{\partial \hat{r}}\right\}\right), \tag{3.110}$$

which, after invoking the variational principle produces

$$0 = \left\{\frac{\partial J_R(\hat{r})}{\partial \hat{r}}\right\} + \left\{\frac{\partial J_r(\hat{r})}{\partial \hat{r}}\right\}. \tag{3.111}$$

The derivative of $J_r(\hat{r})$ can be calculated directly as

$$\left\{\frac{\partial J(\hat{r})}{\partial \hat{r}}\right\} = 2[S_{r_0 r_0}]^{-1}\left(\{\hat{r}\} - \{\hat{r}_0\}\right). \tag{3.112}$$

The derivative of $J_R(\hat{r})$, however, involves an implicit relationship with $\{\hat{r}\}$ and thus the chain rule must be used, producing

$$\left\{\frac{\partial J_R}{\partial \hat{r}}\right\} = 2\left[\frac{\partial \underline{R}(r)}{\partial \hat{r}}\right]^T [S_{RR}(r_0)]^{-1}\{\underline{R}(\hat{r})\}. \tag{3.113}$$

The quantity $\left[\dfrac{\partial \underline{R}(r)}{\partial \hat{r}}\right]^T$ is the transpose of the residual force vector sensitivity defined at the linearization point $\{\hat{r}_\beta\}$ (which is left general for now), and hereafter denoted $\left[\underline{N}_\beta\right]$. For the pth parameter $\hat{r}_p$, it can be calculated from the original definition of the residual force vector as

$$\left\{\left.\frac{\partial \underline{R}(r)}{\partial \hat{r}_p}\right|_{\{\hat{r}_\beta\}}\right\} = \left\{\left.\left(\frac{\partial}{\partial \hat{r}_p}\left(\{i\} - [\underline{Z}(r)]\{\tilde{a}\}\right)\right)\right|_{\{\hat{r}_\beta\}}\right\} = -\left[\left.\frac{\partial \underline{Z}(r)}{\partial \hat{r}_p}\right|_{\{\hat{r}_\beta\}}\right]\{\tilde{a}\}, \tag{3.114}$$

and the sensitivities with respect to each parameter can then be assembled into a single matrix to form

$$\left[\underline{N}_\beta\right] \triangleq -\left\|\left.\frac{\partial \underline{Z}(r)}{\partial \hat{r}}\right|_{\{\hat{r}_\beta\}}\right\|\{\tilde{a}\}. \tag{3.115}$$

In this equation the double-square bracket denotes a 3-dimensional matrix of size $\left(2N_\omega N_d \times 2N_\omega N_d \times N_r\right)$ and multiplication with $\{\tilde{a}\}$ is performed with the second dimension, producing a final batch-stacked sensitivity matrix of size $\left(2N_\omega N_d \times N_r\right)$.

At this point, a linear Taylor Series expansion (1st order) is used to produce an explicit relationship between the objective function $J(\hat{r})$ and all instances of $\{\hat{r}\}$. Following Gura [3-9], linearized iterations serve only to determine a more accurate point from which the final solution may be reached in a single step. The actual parameter estimation is then carried out in one step from this optimal point using the original statistics, meaning that the optimal estimate is only computed once. This interpretation has mathematical relevance since the alternative—having each iteration lead to a more refined estimate of the final solution—requires the implicit assumption that iterations are statistically independent. For a given linearization point, a coupled Taylor series linearization of $[\underline{Z}(\hat{r})]$ is thus written with respect to the most recent linearization point, $\{\hat{r}_\beta\}$, and the initial estimate, $\{\hat{r}_0\}$, as

$$\left[\underline{Z}(\hat{r})\right] = \left[\underline{Z}^*(\hat{r}_0)\right] + \left[\left.\frac{\partial \underline{Z}(r)}{\partial \hat{r}}\right|_{\{\hat{r}_\beta\}}\right]\left(\{\hat{r}\} - \{\hat{r}_0\}\right) \tag{3.116}$$

$$\left[\underline{Z}^*(\hat{r}_0)\right] = \left[\underline{Z}(\hat{r}_\beta)\right] + \left[\left.\frac{\partial \underline{Z}(r)}{\partial \hat{r}}\right|_{\{\hat{r}_\beta\}}\right]\left(\{\hat{r}_0\} - \{\hat{r}_\beta\}\right). \tag{3.117}$$

The quantity $\left[\underline{Z}^*(\hat{r}_0)\right]$ is the most recent linearization evaluated at $\{\hat{r}_0\}$, and is not necessarily equal to $\left[\underline{Z}(\hat{r}_0)\right]$ since the linearization is an approximation of the possibly nonlinear function $\left[\underline{Z}(\hat{r})\right]$.

In the interests of reaching a closed form equation for $\{\hat{r}\}$, Eq. (3.111) can be rewritten by substituting the derivatives and expanding the residual force vector, written with respect to the estimate $\{\hat{r}\}$, to form

$$0 = 2[S_{r_0 r_0}]^{-1}\left(\{\hat{r}\}-\{\hat{r}_0\}\right)+2\left[\underline{N}_\beta\right]^T\left[\underline{S}_{RR}(r_\beta)\right]^{-1}\left(\{\underline{i}\}-[Z(\hat{r},\omega_k)]\{\tilde{a}(\omega_k)\}\right)_.$$

(3.118)

Introducing the linearized dynamic stiffness matrix expression in Eq. (3.116), and collecting terms gives

$$0 = \left[S_{r_0 r_0}\right]^{-1}\left(\{\hat{r}\}-\{\hat{r}_0\}\right)+\left[\underline{N}_\beta\right]^T\left[\underline{S}_{RR}(r_\beta)\right]^{-1}\left(\{\underline{i}\}-\left[\underline{Z}^*(\hat{r}_0)\right]\cdot\{\tilde{a}\}-\left[\underline{N}_\beta\right]\left(\{\hat{r}\}-\{\hat{r}_0\}\right)\right)$$

(3.119)

Solving for $\{\hat{r}\}$, substituting in Eq. (3.117), and rearranging then produces

$$\{\hat{r}\} = \{\hat{r}_0\}-\left(\left[S_{r_0 r_0}\right]^{-1}+\left[\underline{N}_\beta\right]^T\left[\underline{S}_{RR}(r_\beta)\right]^{-1}\left[\underline{N}_\beta\right]\right)^{-1}\cdots$$
$$\cdots\left[\underline{N}_\beta\right]^T\left[\underline{S}_{RR}(r_\beta)\right]^{-1}\left(\{\underline{R}(\hat{r}_\beta)\}-\left[\underline{N}_\beta\right]\left(\{\hat{r}_\beta\}-\{\hat{r}_0\}\right)\right).$$

(3.120)

Finally, it is recognized that this equation will be implemented iteratively, where the most recent parameter estimate is used as the current linearization point—i.e., $\{\hat{r}_\beta\}\rightarrow\{\hat{r}\}_i$. By defining the inverted term in parentheses as $[Q]_{i+1}$, the final coupled iterative estimation equations can be written as

$$\{\hat{r}\}_{i+1} = \{\hat{r}_0\}-[Q]_{i+1}[\underline{N}]_i^T\left[\underline{S}_{RR}(r_i)\right]^{-1}\left([\underline{R}]_i-[\underline{N}]_i\left(\{\hat{r}\}_i-\{\hat{r}_0\}\right)\right),$$

(3.121)

$$[Q]_{i+1} = \left(\left[S_{r_0 r_0} \right]^{-1} + [\underline{N}]_i^T \left[\underline{S}_{RR}(r_i) \right]^{-1} [\underline{N}]_i \right)^{-1}, \tag{3.122}$$

where $\{\hat{r}\}_{i+1}$ becomes the posterior parameter estimate of $\{\tilde{r}\}$, and $[Q]_{i+1}$ becomes the posterior parameter covariance matrix $[S_{\hat{r}\hat{r}}]$, after the final iteration.

The covariance relationship in Eq. (3.122) can be verified following Hemez and Doebling [3-10], where the updated parameter covariance is approximated to the first order as

$$\left[S_{pp} \right]^{new} = \left(\left[S_{p_0 p_0} \right]^{-1} + \left[\frac{\partial \varepsilon}{\partial p} \right]^T \left[S_{\varepsilon\varepsilon} \right]^{-1} \left[\frac{\partial \varepsilon}{\partial p} \right] \right)^{-1} \tag{3.123}$$

for dynamic system imbalance ε and parameters p. Recognizing that in this case the dynamic system imbalance is described by the residual force vector, the expression can be rewritten with respect to the current variables as

$$[S_{\hat{r}\hat{r}}] = \left(\left[S_{\hat{r}_0 \hat{r}_0} \right]^{-1} + \left[\frac{\partial \underline{R}(r)}{\partial \hat{r}} \right]^T [\underline{S}_{RR}]^{-1} \left[\frac{\partial \underline{R}(r)}{\partial \hat{r}} \right] \right)^{-1}. \tag{3.124}$$

This expression is exact for the previously linearized system. It should be noted that the posterior covariance is conditional on the measured data from the damaged system and the subsequent updated parameter estimate; i.e.,

$$[S_{\hat{r}\hat{r}}] \equiv \mathrm{cov}\left(\{r\} \big| E(\{r\}) = \{\tilde{r}\} \right) = E\left((\{r\} - \{\tilde{r}\})(\{r\} - \{\tilde{r}\})^T \right). \tag{3.125}$$

3.6.3 Linearization and Sensitivity Formulations

As described for a generic system in Appendix B, the standard approach for parameter estimation of dynamic systems of the type described herein has been to compare the measured data and analytical model response directly. For noisy frequency response functions the system can be rewritten as

$$\{\tilde{\underline{a}}\} = \{\underline{a}(\tilde{r})\} + \{\underline{v}_e\}, \tag{3.126}$$

where the noise vector and modeling error are combined into $\{\underline{v}_e\}$ for brevity. The batch-stacked form is used here for frequency dependent terms; however, the relationships presented in this section could equivalently be given in terms of frequency. The functional imbalance for a system at point $\{r_\beta\}$ is expressed as

$$\{\tilde{\underline{a}}\} - \{\underline{a}(\hat{r}_\beta)\} = \{\Delta\underline{a}(\hat{r}_\beta)\} + \{\underline{v}_e\}, \tag{3.127}$$

where $\{\Delta\underline{a}(\hat{r}_\beta)\}$ is the analytical system imbalance between the damaged state and system point $\{\hat{r}_\beta\}$,

$$\{\Delta\underline{a}(\hat{r}_\beta)\} = \{\underline{a}(\tilde{r})\} - \{\underline{a}(\hat{r}_\beta)\}. \tag{3.128}$$

The frequency response function system model is inversely related to $[Z(r)]$ and so is nonlinear in the parameters, even if the governing structural model is linear—i.e., qualitatively speaking, if $[Z(r)] = [Z](r)$. To apply parameter estimation the system must

therefore be linearized, and is done so with a first order Taylor series expansion about

point $\{\hat{r}_\beta\}$ as

$$\{\Delta \underline{a}(\hat{r}_\beta)\} = \left[\left. \frac{\partial \underline{a}(r)}{\partial r} \right|_{\hat{r}_\beta} \right] \left(\{\tilde{r}\} - \{\hat{r}_\beta\} \right). \tag{3.129}$$

The gradient or sensitivity matrix $\left[\left. \dfrac{\partial \underline{a}(r)}{\partial r} \right|_{\hat{r}_\beta} \right]$ can be calculated several ways. The

most direct is to use a finite difference method to calculate the gradient estimation

directly, giving

$$\left[\left. \frac{\partial \underline{a}(r)}{\partial r} \right|_{\hat{r}_i} \right] \approx \frac{\{\underline{a}(\hat{r}_i + \Delta)\} - \{\underline{a}(\hat{r}_i)\}}{\Delta}. \tag{3.130}$$

An alternative expression can be found by using the matrix derivative chain rule to write

the derivative of the frequency response function in terms of the derivative of the

dynamic stiffness matrix [3-11]. This approach can be advantageous in the common case

when the dynamic stiffness matrix is linear with update parameters but the frequency

response functions are not. To derive the relationship, the frequency response function is

first written in terms of the dynamic stiffness matrix using $\{a(\tilde{r})\} = [Z(\tilde{r})]^{-1}\{i\}$,

$$\left[\left. \frac{\partial \underline{a}(r)}{\partial r} \right|_{\hat{r}_\beta} \right] = \left(\left. \frac{\partial \left([\underline{Z}(r)]^{-1}\{i\} \right)}{\partial r} \right|_{r_\beta} \right) = \left(\left. \frac{\partial [\underline{Z}(r)]^{-1}}{\partial r} \right|_{\hat{r}_\beta} \right) \{i\}. \tag{3.131}$$

The identity matrix $[I] = [\underline{Z}(r)] \cdot [\underline{Z}(r)]^{-1}$ is then multiplied into the derivative, as

$$\left[\left. \frac{\partial \underline{a}(r)}{\partial r} \right|_{\hat{r}_\beta} \right] = \left(\left. \frac{\partial \left([\underline{Z}(r)]^{-1} [\underline{Z}(r)][\underline{Z}(r)]^{-1} \right)}{\partial r} \right|_{\hat{r}_\beta} \right) \{i\} , \tag{3.132}$$

and the chain rule is used to expand the terms, leading to

$$\left[\left. \frac{\partial \underline{a}(r)}{\partial r} \right|_{\hat{r}_\beta} \right] = \left(\left. \frac{\partial [\underline{Z}(r)]^{-1}}{\partial r} \right|_{\hat{r}_\beta} \right) [\underline{Z}(\hat{r}_\beta)] [\underline{Z}(\hat{r}_\beta)]^{-1} \{i\} + \dots$$

$$\dots [\underline{Z}(\hat{r}_\beta)]^{-1} \left(\left. \frac{\partial [\underline{Z}(r)]}{\partial r} \right|_{\hat{r}_\beta} \right) [\underline{Z}(\hat{r}_\beta)]^{-1} \{i\} + \dots \tag{3.133}$$

$$\dots [\underline{Z}(\hat{r}_\beta)]^{-1} [\underline{Z}(\hat{r}_\beta)] \left(\left. \frac{\partial [\underline{Z}(r)]^{-1}}{\partial r} \right|_{\hat{r}_\beta} \right) \{i\} .$$

Recognizing

$$[I] = [\underline{Z}(\hat{r}_\beta)][\underline{Z}(\hat{r}_\beta)]^{-1} , \tag{3.134}$$

$$[\underline{Z}(\hat{r}_\beta)]^{-1} \{i\} = \{\underline{a}(\hat{r}_\beta)\} , \tag{3.135}$$

and

$$\left(\left. \frac{\partial [\underline{Z}(r)]^{-1}}{\partial r} \right|_{\hat{r}_\beta} \right) \{i\} = \left(\left. \frac{\partial \{\underline{a}(r)\}}{\partial r} \right|_{\hat{r}_\beta} \right) , \tag{3.136}$$

then rearranging and collecting terms, leads to

$$\left[\left. \frac{\partial \underline{a}(r)}{\partial r} \right|_{\hat{r}_\beta} \right] = 2 \left[\left. \frac{\partial \underline{a}(r)}{\partial r} \right|_{\hat{r}_\beta} \right] + [\underline{Z}(r_\beta)]^{-1} \left(\left. \frac{\partial [\underline{Z}(r)]}{\partial r} \right|_{\hat{r}_\beta} \right) \{\underline{a}(\hat{r}_\beta)\} . \tag{3.137}$$

By rearranging further and reverting to the previous double-bracket notation for a three dimensional array, the sensitivity equation can be written in terms of the linearization point as

$$\left[\frac{\partial \underline{a}(r)}{\partial r} \bigg|_{\hat{r}_\beta} \right] = -\left[\underline{Z}(\hat{r}_\beta) \right]^{-1} \left(\left\| \frac{\partial \underline{Z}(r)}{\partial r} \bigg|_{\hat{r}_\beta} \right\| \left\{ \underline{a}(\hat{r}_\beta) \right\} \right). \tag{3.138}$$

The dynamic stiffness sensitivity can then be approximated using finite difference, as

$$\left[\frac{\partial \underline{Z}(r)}{\partial r} \bigg|_{\hat{r}_\beta} \right] \approx \frac{\left[\underline{Z}(\hat{r}_\beta + \Delta) \right] - \left[\underline{Z}(\hat{r}_\beta) \right]}{\Delta}. \tag{3.139}$$

A potentially more accurate formulation, which can be thought of as an *exact* sensitivity formulation, is found by not ever linearizing the frequency response function directly, but instead using the relationship between $\{\underline{a}(r)\}$ and $[\underline{Z}(r)]$ to create an expression for $\{\tilde{a}\}$ in terms of $[\Delta \underline{Z}(r)]$ and then linearizing the less nonlinear dynamic stiffness matrix. Starting with Eq. (3.125), substitute in $\{\underline{a}(\tilde{r})\} = [\underline{Z}(\tilde{r})]^{-1}\{i\}$ and $\{\underline{a}(\hat{r}_\beta)\} = [\underline{Z}(\hat{r}_\beta)]^{-1}\{i\}$, and collect terms to give

$$\{\Delta \underline{a}(\hat{r}_\beta)\} = \{\underline{a}(\tilde{r})\} - \{\underline{a}(\hat{r}_\beta)\} = \left([\underline{Z}(\tilde{r})]^{-1} - [\underline{Z}(\hat{r}_\beta)]^{-1} \right)\{i\}. \tag{3.140}$$

The identity matrix terms $[I] = [\underline{Z}(\hat{r}_\beta)]^{-1}[\underline{Z}(\hat{r}_\beta)]$ and $[I] = [\underline{Z}(\tilde{r})][\underline{Z}(\tilde{r})]^{-1}$ are then added to produce

$$\{\Delta \underline{a}(\hat{r}_\beta)\} = \left([\underline{Z}(\hat{r}_\beta)]^{-1}[\underline{Z}(\hat{r}_\beta)][\underline{Z}(\tilde{r})]^{-1} - [\underline{Z}(\hat{r}_\beta)]^{-1}[\underline{Z}(\tilde{r})][\underline{Z}(\tilde{r})]^{-1} \right)\{i\} \tag{3.141}$$

and collecting terms gives

$$\left\{\Delta\underline{a}(\hat{r}_{\beta})\right\} = \left[\underline{Z}(\hat{r}_{\beta})\right]^{-1}\left(\left[\underline{Z}(\hat{r}_{\beta})\right] - \left[\underline{Z}(\tilde{r})\right]\right)\left[\underline{Z}(\tilde{r})\right]^{-1}\left\{i\right\}. \tag{3.142}$$

This expression can now be substituted back into the original noisy frequency response function difference expression in Eq. (3.128), and recognizing again $\left[\underline{Z}(\tilde{r})\right]^{-1}\left\{i\right\} = \left\{\underline{a}(\tilde{r})\right\}$ produces

$$\left\{\tilde{a}\right\} - \left\{\underline{a}(\hat{r}_{\beta})\right\} = \left[\underline{Z}(\hat{r}_{\beta})\right]^{-1}\left(\left[\underline{Z}(\hat{r}_{\beta})\right] - \left[\underline{Z}(\tilde{r})\right]\right)\left\{\underline{a}(\tilde{r})\right\} + \left\{\underline{v}_{e}\right\}. \tag{3.143}$$

Using the relationship $\left\{\underline{a}(\tilde{r})\right\} = \left\{\tilde{a}\right\} - \left\{\underline{v}_{e}\right\}$, this expression can be expanded and rearranged to

$$\left\{\tilde{a}\right\} - \left\{\underline{a}(\hat{r}_{\beta})\right\} = -\left[\underline{Z}(\hat{r}_{\beta})\right]^{-1}\left(\left[\underline{Z}(\tilde{r})\right] - \left[\underline{Z}(\hat{r}_{\beta})\right]\right)\left\{\tilde{a}\right\} + \left[\underline{Z}(\hat{r}_{\beta})\right]^{-1}\left[\underline{Z}(\tilde{r})\right]\left\{\underline{v}_{e}\right\}$$

$$\tag{3.144}$$

The dynamic stiffness matrix $\left[\underline{Z}(\tilde{r})\right]$ can now be expanded in a 1st order Taylor series expansion about the point $\left\{r_{\beta}\right\}$ for each frequency ω, as

$$\left[\underline{Z}(\tilde{r})\right] - \left[\underline{Z}(\hat{r}_{\beta})\right] = \left\|\left.\frac{\partial\underline{Z}(r)}{\partial r}\right|_{\hat{r}_{\beta}}\right\|\left(\left\{\tilde{r}\right\} - \left\{\hat{r}_{\beta}\right\}\right), \tag{3.145}$$

and substituting into the last equation gives

$$\left\{\tilde{a}\right\} - \left\{\underline{a}(\hat{r}_{\beta})\right\} = -\left[\underline{Z}(\hat{r}_{\beta})\right]^{-1}\left(\left\|\left.\frac{\partial\underline{Z}(r)}{\partial r}\right|_{\hat{r}_{\beta}}\right\|\left\{\tilde{a}\right\}\right)\left(\left\{\tilde{r}\right\} - \left\{\hat{r}_{\beta}\right\}\right) + \left[\underline{Z}(\hat{r}_{\beta})\right]^{-1}\left[\underline{Z}(\tilde{r})\right]\left\{\underline{v}_{e}\right\} \tag{3.146}$$

where the order of $\left(\{\tilde{r}\}-\{\hat{r}_\beta\}\right)$ and $\{\tilde{a}\}$ have been reversed, since they operate on different dimensions of the three dimensional dynamic stiffness sensitivity array.

Comparing this dynamic-stiffness-linearized sensitivity equation to the directly linearized noisy frequency response function expression generated by combining Eqs. (3.128) and (3.129),

$$\{\tilde{a}\}-\{\underline{a}(\hat{r}_\beta)\} = \left[\left.\frac{\partial \underline{a}(r)}{\partial r}\right|_{\hat{r}_\beta}\right]\left(\{\tilde{r}\}-\{\hat{r}_\beta\}\right)+\{v_e\},\tag{3.147}$$

suggests that the new exact sensitivity expression can be written as

$$\left[\left.\frac{\partial \underline{a}(r)}{\partial r}\right|_{\hat{r}_\beta}\right] = -\left[\underline{Z}(\hat{r}_\beta)\right]^{-1}\left(\left\|\left.\frac{\partial \underline{Z}(r)}{\partial r}\right|_{\hat{r}_\beta}\right\|\{\tilde{a}\}\right).\tag{3.148}$$

It can also be seen in this comparison that the noise in Eq. (3.146) is now biased by $\left[\underline{Z}(r_\beta)\right]^{-1}\left[\underline{Z}(\tilde{r})\right]$; however, since the linearized equation is intended for an iterative update, where $\{\hat{r}_\beta\}$ approaches $\{\tilde{r}\}$, this bias will approach unity and can be ignored.

Comparing the two frequency response sensitivity forms in Eqs. (3.138) and (3.148) shows that they only differ by which frequency response function form is used for the post-multiplication—the analytical frequency response function calculated at the most recent linearization point for the direct linearization sensitivity form or the measured frequency response function for the exact sensitivity form. The second expression is the same as that of used by Lin and Ewins [3-12] and Imregun et al. [3-13] for deterministic damage detection work. Lin further showed in a subsequent work [3-14]

that their sensitivity expression can be considered exact compared to a linear gradient eigen-sensitivity approximation. In practice, it leads to faster and more stable convergence than the direct sensitivity form, which in turn is more stable than just applying finite difference directly to the nonlinear analytical frequency response function.

The relationship between frequency response function and residual force vector sensitivities can be examined by left-multiplying Eq. (3.146) by $\left[\underline{Z}(\hat{r}_\beta) \right]$ and rearranging terms, producing

$$\{i\} - \left[\underline{Z}(\hat{r}_\beta) \right]\{\tilde{a}\} = -\left[\underline{Z}(\tilde{r}) \right]\{\underline{v}_e\} + \left(\left\| \left. \frac{\partial \underline{Z}(r)}{\partial r} \right|_{\hat{r}_\beta} \right\| \{\tilde{a}\} \right)\left(\{\tilde{r}\} - \{\hat{r}_\beta\} \right). \qquad (3.149)$$

This expression is equivalent to a Taylor series expansion of the residual force vector calculated around $\{\hat{r}_\beta\}$,

$$\{\underline{R}(\hat{r}_\beta)\} = \{\underline{R}(\tilde{r})\} - \left[\left. \frac{\partial \underline{R}(r)}{\partial r} \right|_{\hat{r}_\beta} \right]\left(\{\tilde{r}\} - \{\hat{r}_\beta\} \right), \qquad (3.150)$$

where $\{\underline{R}(\tilde{r})\} = \{i\} - \left[\underline{Z}(\tilde{r}) \right]\{\tilde{a}\} = -\left[\underline{Z}(\tilde{r}) \right]\{\underline{v}_e\}$, and, as given previously in Eq. (3.115) using the notation $\left[\underline{N}_\beta \right]$,

$$\left[\left. \frac{\partial \underline{R}(r)}{\partial r} \right|_{\hat{r}_\beta} \right] = -\left\| \left. \frac{\partial \underline{Z}(r)}{\partial r} \right|_{\hat{r}_\beta} \right\| \{\tilde{a}\}. \qquad (3.151)$$

Thus, it is seen that the residual force vector sensitivity, which is the same as that developed for the deterministic parameter estimation schemes of Napolitano and

Kosmatka [3-15], is also based on linearization of the dynamic stiffness matrix as opposed to the frequency response function.

Additionally, a direct form of the residual force vector sensitivity can be written, analogously to the frequency response function sensitivity case, as

$$\left[\left. \frac{\partial \underline{R}(r)}{\partial r} \right|_{\hat{r}_\beta} \right] = - \left\| \left. \frac{\partial \underline{Z}(r)}{\partial r} \right|_{\hat{r}_\beta} \right\| \left\{ \underline{a}(\hat{r}_\beta) \right\}. \tag{3.152}$$

The direct and exact sensitivity forms for frequency response based and residual force based parameter estimation are summarized in Table 3-1. The difference between direct and exact methods, as was shown, is related to whether the required Taylor series linearization is applied to the frequency response function, as is done for the direct formulations, or to the dynamic stiffness matrix (or equivalently to the residual force vector), as is done for the exact methods.

3.6.4 Frequency Response Difference Form

Based on the development in Sections (3.5) and (3.6.1-3.6.3) the residual force vector based damage identification algorithm can alternatively be written in a frequency response difference form with exact sensitivity. First, the residual force covariance inverse is written from Eq. (3.101) by the rules of matrix inversion as

$$\left[\underline{S}_{RR}(r_\beta) \right]^{-1} = \left[\underline{Z}(r_\beta) \right]^{-T} \left[\underline{S}_{vv} \right]^{-1} \left[\underline{Z}(r_\beta) \right]^{-1}, \tag{3.153}$$

Table 3-1: Summary of direct and exact formulations for frequency response function and residual force vector based sensitivities.

Dynamic residual	Type	Equation	Expression
Residual force	exact	(3.151)	$\left[\dfrac{\partial R(r)}{\partial r}\bigg|_{\hat{r}_\beta}\right] = -\left\|\dfrac{\partial Z(r)}{\partial r}\bigg|_{\hat{r}_\beta}\right\|\{\tilde{a}\}$
Residual force	direct	(3.152)	$\left[\dfrac{\partial R(r)}{\partial r}\bigg|_{\hat{r}_\beta}\right] = -\left\|\dfrac{\partial Z(r)}{\partial r}\bigg|_{\hat{r}_\beta}\right\|\{a(\hat{r}_\beta)\}$
Frequency response	exact	(3.148)	$\left[\dfrac{\partial a(r)}{\partial r}\bigg|_{\hat{r}_\beta}\right] = -\left[Z(\hat{r}_\beta)\right]^{-1}\left(\left\|\dfrac{\partial Z(r)}{\partial r}\bigg|_{\hat{r}_\beta}\right\|\{\tilde{a}\}\right)$
Frequency response	direct	(3.138)	$\left[\dfrac{\partial a(r)}{\partial r}\bigg|_{\hat{r}_\beta}\right] = -\left[Z(\hat{r}_\beta)\right]^{-1}\left(\left\|\dfrac{\partial Z(r)}{\partial r}\bigg|_{\hat{r}_\beta}\right\|\{a(\hat{r}_\beta)\}\right)$

where superscript $[...]^{-T}$ denotes the inverse of the transpose. Substituting into $J_R(\hat{r})$ in Eq. (3.103) then gives

$$J_R(\hat{r}) = \left(\{\underline{i}\} - [\underline{Z}(\hat{r})]\cdot\{\tilde{a}\}\right)^T \left[\underline{Z}(r_\beta)\right]^{-T}\left[\underline{S}_{vv}\right]^{-1}\left[\underline{Z}(r_\beta)\right]^{-1}\left(\{\underline{i}\} - [\underline{Z}(\hat{r})]\cdot\{\tilde{a}\}\right)$$,

$$(3.154)$$

which, by recognizing $\left[\underline{Z}(r_\beta)\right]^{-1}\{\underline{i}\} = \{\underline{a}(r_\beta)\}$ and rearranging, can alternatively be rewritten

$$J_R(\hat{r}) = \left(\{\underline{a}(r_\beta)\} - \left[\underline{Z}(r_\beta)\right]^{-1}[\underline{Z}(\hat{r})]\{\tilde{a}\}\right)^T \left[\underline{S}_{vv}\right]^{-1}\left(\{\underline{a}(r_\beta)\} - \left[\underline{Z}(r_\beta)\right]^{-1}[\underline{Z}(\hat{r})]\{\tilde{a}\}\right).$$

$$(3.155)$$

It can be seen that as the iterations progress and $\{r_\beta\}$ approaches $\{\hat{r}\}$, $\left[\underline{Z}(r_\beta)\right]^{-1}\left[\underline{Z}(\hat{r})\right]$ will approach the identity matrix, and this functional term will approach

$$J_R(\hat{r}) = \left(\{\underline{a}(\hat{r})\} - \{\tilde{\underline{a}}\}\right)^T \left[\underline{S}_{vv}\right]^{-1} \left(\{\underline{a}(\hat{r})\} - \{\tilde{\underline{a}}\}\right). \tag{3.156}$$

This is the same functional expression as would be found if the problem was set up based on the difference between analytical and measured frequency response functions in the first place. Combining the functional back with $J_r(\hat{r})$ produces the cost function,

$$J_a(\hat{r}) \triangleq \left(\{\underline{a}(\hat{r})\} - \{\tilde{\underline{a}}\}\right)^T \left[\underline{S}_{vv}\right]^{-1} \left(\{\underline{a}(\hat{r})\} - \{\tilde{\underline{a}}\}\right) + \left(\{\hat{r}\} - \{\hat{r}_0\}\right)^T \left\{S_{r_0 r_0}\right\}^{-1} \left(\{\hat{r}\} - \{\hat{r}_0\}\right).$$

$$\tag{3.157}$$

This expression is essentially the same cost function as developed by Martinez [3-7] for model correlation; however, Martinez's sensitivity formulation and Kalman filter based implementation strategy are different from that pursued in this dissertation.

Equivalent frequency response function based damage identification equations can be derived from the residual force versions in Eqs. (3.121) and (3.122) by expanding out the residual force covariance matrix and recognizing that

$$\left[\underline{Z}(r_i)\right]^{-1}\left[\underline{R}\right]_i = \{\underline{a}(r_i)\} - \{\tilde{\underline{a}}\}, \tag{3.158}$$

$$\left[\underline{Z}(r_i)\right]^{-1}\left[\underline{N}\right]_i = \left[\left.\frac{\partial a(r)}{\partial r}\right|_{\hat{r}_i}\right]_{exact}. \tag{3.159}$$

The resulting coupled update equations are

$$\{\hat{r}\}_{i+1} = \{\hat{r}_0\} - [Q]_{i+1}\left[\left.\frac{\partial a(r)}{\partial r}\right|_{\hat{r}_i}\right]^T_{exact} [\underline{S}_{vv}]^{-1}\left(\{\underline{a}(r_i)\} - \{\tilde{\underline{a}}\} - \left[\left.\frac{\partial a(r)}{\partial r}\right|_{\hat{r}_i}\right]_{exact}\left(\{\hat{r}\}_i - \{\hat{r}_0\}\right)\right),$$

$$(3.160)$$

and

$$[Q]_{i+1} = \left(\left[S_{r_0 r_0}\right]^{-1} + \left[\left.\frac{\partial a(r)}{\partial r}\right|_{\hat{r}_i}\right]^T_{exact} [S_{vv}]^{-1}\left[\left.\frac{\partial a(r)}{\partial r}\right|_{\hat{r}_i}\right]_{exact}\right)^{-1}. \qquad (3.161)$$

3.7 Summary of Algorithm

The main damage identification algorithm operates as described in the bulleted lists below. The algorithm is given a set of inputs to start. An iteration loop is then used to calculate required quantities and implement the driving update equations until convergence is reached. The algorithm then returns a set of standardized outputs. Details are as follows:

Algorithm Inputs:

- Damage parameters at initial healthy values:

$$\{r_0\}$$

- Initial damage parameter covariance matrix:

$$\left[S_{r_0 r_0}\right]$$

- Analytical model evaluated at initial damage parameter values:

$$\left[K^*(r_0)\right], \left[M(r_0)\right], \left[C(r_0)\right]$$

- Set of frequency lines over which to perform damage identification:

$$\omega_k, \quad k = 1, 2, ..., N_\omega$$

- Experimental reference data from the damaged structure, batch-stacked over analysis frequency line set:

$$\{\underline{\tilde{a}}\}$$

- Experimental reference data covariance matrix, batch-stacked over analysis frequency line set:

$$\left[\underline{S}_{vv}\right]$$

Iteration Loop i, for $i = 0, 1, 2, \ldots$:

1. Create dynamic stiffness matrix at $\{r_i\}$ in full coordinates using Eq. (3.7):

$$\left[Z(r_i, \omega_k)\right]_f = \left[K^*(r_i)\right]_f + j\omega_k \left[C(r_i)\right]_f - \omega_k^2 \left[M(r_i)\right]_f$$

2. Generate the dynamic reduction transformation matrix using Eq. (3.63) at each frequency ω_k:

$$\left[T(r_i, \omega_k)\right] = \begin{bmatrix} \left[I\right]_{mm} \\ -\left[Z(r_i, \omega_k)\right]_{ss}^{-1} \left[Z(r_i, \omega_k)\right]_{sm} \end{bmatrix}$$

3. Reduce the dynamic stiffness matrix to measurement degree-of-freedom set at each frequency ω_k:

$$\left[Z(r_i,\omega_k)\right]=\left[T(r_i,\omega_k)\right]^T\left[Z(r_i,\omega_k)\right]_f\left[T(r_i,\omega_k)\right]$$

4. Assemble batch-stacked dynamic stiffness matrix over all frequency lines:

$$\left[\underline{Z}(r)\right]=\begin{bmatrix} \mathrm{Re}\left(\left[Z(r_i,\omega_1)\right]\right) & -\mathrm{Im}\left(\left[Z(r_i,\omega_1)\right]\right) & \cdots & [0] & [0] \\ \mathrm{Im}\left(\left[Z(r_i,\omega_1)\right]\right) & \mathrm{Re}\left(\left[Z(r_i,\omega_1)\right]\right) & \cdots & [0] & [0] \\ \vdots & \vdots & \ddots & \vdots & \vdots \\ [0] & [0] & \cdots & \mathrm{Re}\left(\left[Z(r_i,\omega_{N_\omega})\right]\right) & -\mathrm{Im}\left(\left[Z(r_i,\omega_{N_\omega})\right]\right) \\ [0] & [0] & \cdots & \mathrm{Im}\left(\left[Z(r_i,\omega_{N_\omega})\right]\right) & \mathrm{Re}\left(\left[Z(r_i,\omega_{N_\omega})\right]\right) \end{bmatrix}$$

5. Create batch-stacked residual force vector using Eq. (3.103):

$$\{\underline{R}\}_i=\{\underline{i}\}-\left[\underline{Z}(r_i)\right]\cdot\{\underline{\tilde{a}}\}$$

6. Create batch-stacked residual force covariance matrix using Eq. (3.104):

$$\left[\underline{S}_{RR}\right]_i=\left[\underline{Z}(r_i)\right]\left[\underline{S}_{vv}\right]\left[\underline{Z}(r_i)\right]^T$$

7. Generate batch-stacked dynamic stiffness sensitivity using Eq. (3.139) (Note: reduction is performed using $\left[T(r_i,\omega_k)\right]$ on the dynamic stiffness matrix or, equivalently, on the full-coordinate sensitivity matrix):

$$\left[\left. \frac{\partial \underline{Z}(r_i)}{\partial \hat{r}} \right|_{\{\hat{r}_i\}} \right] = \frac{\left[\underline{Z}(r_i + \Delta)\right] - \left[\underline{Z}(r_i)\right]}{\Delta}$$

8. Generate batch-stacked residual force sensitivity matrix using Eq. (3.115):

$$\left[\underline{N}\right]_i = -\left\| \left. \frac{\partial \underline{Z}(r_i)}{\partial \hat{r}} \right|_{\{r_i\}} \right\| \{\tilde{a}\}$$

9. Generate the quantity $\left[Q\right]_{i+1}$ using Eq. (3.121):

$$\left[Q\right]_{i+1} = \left(\left[S_{r_0 r_0} \right]^{-1} + \left[\underline{N}\right]_i^T \left[\underline{S}_{RR}(r_i) \right]^{-1} \left[\underline{N}\right]_i \right)^{-1}$$

10. Generate the updated damage parameter set using Eq. (3.122):

$$\{\hat{r}\}_{i+1} = \{\hat{r}_0\} - \left[Q\right]_{i+1} \left[\underline{N}\right]_i^T \left[\underline{S}_{RR}\right]_i^{-1} \left(\{\underline{R}\}_i - \left[\underline{N}\right]_i \left(\{\hat{r}\}_i - \{\hat{r}_0\} \right) \right)$$

11. Generate the absolute value damage parameter difference mean:

$$\langle \Delta\hat{r} \rangle_{i+1} = mean\left(\left| \{\hat{r}\}_{i+1} - \{\hat{r}\}_i \right| \right)$$

12. Check for parameter convergence:

   a. If $\langle \hat{r} \rangle_{i+1}$ is greater than or equal to the predefined convergence tolerance, increase i and return to the start of the iteration loop.

   b. If $\langle \hat{r} \rangle_{i+1}$ is less than the predefined convergence tolerance, break the iteration loop.

Converged algorithm outputs:

- Updated damage parameter values:

$$\{\hat{r}\}_{i+1} \rightarrow \{\hat{r}_d\}$$

- Updated damage parameter estimation uncertainty:

$$diag\left([Q]_{i+1}\right) \rightarrow \{\sigma_r^2\}_d$$

- Damage correlated analytical model:

$$\left[K^*(r_{i+1})\right] \rightarrow \left[K^*(r_d)\right]$$

$$\left[M(r_{i+1})\right] \rightarrow \left[M(r_d)\right]$$

$$\left[C(r_{i+1})\right] \rightarrow \left[C(r_d)\right]$$

3.8 Algorithm Walk-Through with Damped Mass-Spring System Example

Basic functionality of the current algorithm is now demonstrated using a simple 2-degree-of-freedom mass spring system example with combinations of structural and generalized viscous damping. System details are described first along with derivation of the equations of motion, system matrices, and basic dynamic behavior of the baseline system. The damage cases are then studied, followed by a step-by-step walk-through of

the damage identification algorithm and comparison to results with different levels of damping. The example concludes with a study of approximate methods for modeling generalized damping, including damage identification results compared to the exact damping case.

3.8.1   Baseline System Description

The two degree-of-freedom mass-spring system is designed to approximate the first two modes of a built-up cantilever structure with two masses connected in series via standard linear springs and grounded at one end, as shown in Figure 3-1. Forcing is applied to the first degree-of-freedom for the purpose of generating frequency response functions. Damping is implemented as a combination of structural damping in-line with the springs and viscous spot damping on each degree-of-freedom. There are therefore a total of 10 system parameters: two masses, two spring stiffnesses, two structural damping coefficients, and two viscous damping coefficients. Three specific baseline damping scenarios are considered throughout the study:

(1) Light viscous damping, with modal damping on the order of 3%;

(2) Heavy viscous damping, where all damping parameters are increased by a factor of 10 from the lightly damped case to give modal damping ratios on the order of 30%;

(3) Light viscous damping combined with light structural damping, which could be considered representative of general aerospace structures.
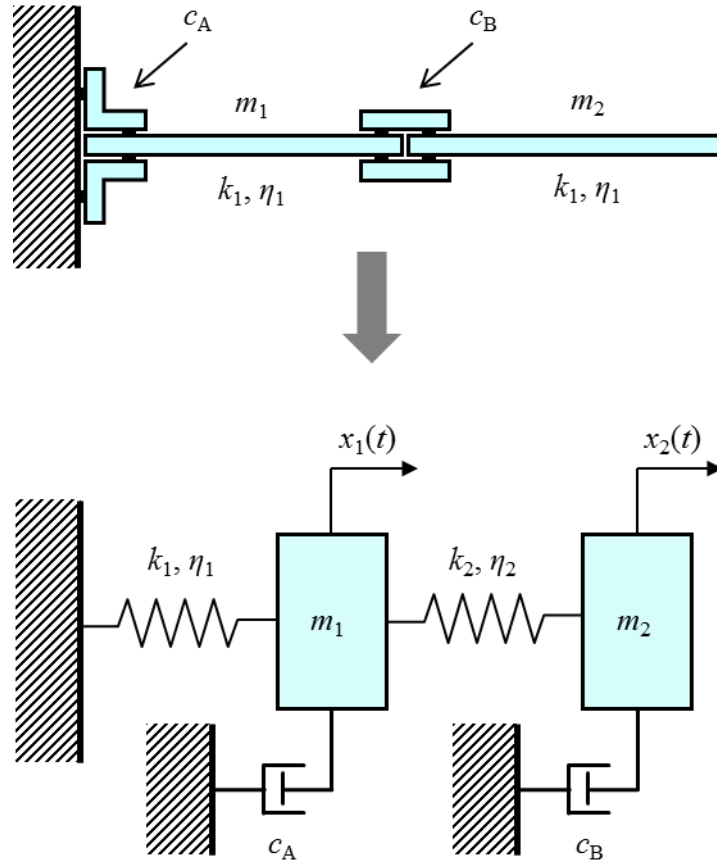
Figure 3-1: Simple wing structure idealized as two degree-of-freedom damped mass-spring system.

The viscous and structural damping values were chosen to produce severely non-proportional damping matrices. Baseline mass, stiffness, and damping parameter values for all cases are provided in Table 3-2.

Basic dynamic quantities for the baseline system are derived as follows. The equations of motion can be written in matrix form as

$$
\begin{bmatrix} m_1 & 0 \\ 0 & m_2 \end{bmatrix} \begin{Bmatrix} \ddot{x}_1(t) \\ \ddot{x}_2(t) \end{Bmatrix} + \begin{bmatrix} c_A & 0 \\ 0 & c_B \end{bmatrix} \begin{Bmatrix} \dot{x}_1(t) \\ \dot{x}_2(t) \end{Bmatrix} + \dots
$$

$$
\dots \begin{bmatrix} k_1(1+j\eta_1)+k_2(1+j\eta_1) & -k_2(1+j\eta_2) \\ -k_2(1+j\eta_2) & k_2(1+j\eta_2) \end{bmatrix} \begin{Bmatrix} x_1(t) \\ x_2(t) \end{Bmatrix} = \begin{Bmatrix} f(t) \\ 0 \end{Bmatrix}
$$

(3.162)

Table 3-2: Baseline parameter values for the 2-degree-of-freedom system.

Parameter	Light Viscous Damping	Heavy Viscous Damping	Light Viscous Damping + Light Structural Damping
m_1	1.000	1.000	1.000
m_2	1.000	1.000	1.000
k_1	1000	1000	1000
k_2	1000	1000	1000
η_1	0.000	0.000	0.02000
η_2	0.000	0.000	0.01000
c_B	4.000	40.00	4.000
c_A	0.1000	1.000	0.1000

which can be further simplified into matrix notation as

$$[M]\{\ddot{x}(t)\} + [C]\{\dot{x}(t)\} + \left[K^*\right]\{x(t)\} = \{f(t)\} \tag{3.163}$$

where

$$\{\ddot{x}(t)\} = \left\{ \begin{array}{c} \ddot{x}_1(t) \\ \ddot{x}_2(t) \end{array} \right\} \tag{3.164}$$

$$\{x(t)\} = \left\{ \begin{array}{c} x_1(t) \\ x_2(t) \end{array} \right\} \tag{3.165}$$

$$\{f(t)\} = \left\{ \begin{array}{c} f(t) \\ 0 \end{array} \right\} \tag{3.166}$$

$$[M] = \begin{bmatrix} m_1 & 0 \\ 0 & m_2 \end{bmatrix} \tag{3.167}$$

$$\left[K^*\right] = \begin{bmatrix} k_1(1+j\eta_1) + k_2(1+j\eta_1) & -k_2(1+j\eta_2) \\ -k_2(1+j\eta_2) & k_2(1+j\eta_2) \end{bmatrix} \tag{3.168}$$

$$[C] = \begin{bmatrix} c_A & 0 \\ 0 & c_B \end{bmatrix} \tag{3.169}$$

The dynamic stiffness matrix is formed following Eq. (3.7) as

$$[Z(\omega_k)] = \begin{bmatrix} k_1(1+j\eta_1) + k_2(1+j\eta_1) & -k_2(1+j\eta_2) \\ -k_2(1+j\eta_2) & k_2(1+j\eta_2) \end{bmatrix} + j\omega_k \begin{bmatrix} c_A & 0 \\ 0 & c_B \end{bmatrix} - \omega_k^2 \begin{bmatrix} m_1 & 0 \\ 0 & m_2 \end{bmatrix},$$

$$\tag{3.170}$$

and the full frequency response function matrix is found by inverting the dynamic

stiffness, producing

$$[A(\omega_k)] = \left(\begin{bmatrix} k_1(1+j\eta_1) + k_2(1+j\eta_1) & -k_2(1+j\eta_2) \\ -k_2(1+j\eta_2) & k_2(1+j\eta_2) \end{bmatrix} + j\omega_k \begin{bmatrix} c_A & 0 \\ 0 & c_B \end{bmatrix} - \omega_k^2 \begin{bmatrix} m_1 & 0 \\ 0 & m_2 \end{bmatrix} \right)^{-1}.$$

$$\tag{3.171}$$

The elements of $[A(\omega_k)]$ correspond to the transfer functions between measurement

degrees-of-freedom in the rows and forcing degrees-of-freedom in the columns (or vice

versa since reciprocity will cause $[A(\omega_k)]$ to be symmetric for linear systems); thus, the

frequency response functions corresponding to forcing on the first degree-of-freedom can

be found in the first column. For this small problem, the inverse in Eq. (3.171) can be

expanded and the frequency response transfer functions for x_1 and x_2 corresponding to

forcing at x_1 written in closed form. To ease understanding of the resulting expressions,

the following parameters are first introduced:

$$\alpha = \frac{k_2}{k_1}, \tag{3.172}$$

$$\bar{\omega}_i = \sqrt{\frac{k_i}{m_i}} \quad \text{for } i = 1, 2, \tag{3.173}$$

$$\beta = \frac{\bar{\omega}_1^2}{\bar{\omega}_2^2}, \tag{3.174}$$

$$\bar{\eta} = \frac{\eta_2}{\eta_1}, \tag{3.175}$$

$$\bar{c}_l = \frac{c_l}{\sqrt{m_1 k_1}} \quad \text{for } l = \text{A, B.} \tag{3.176}$$

The frequency response functions with all damping terms included can then be written as

$$A_{1,1}(\omega) = \frac{X_1(\omega)}{F(\omega)} = \frac{1 - \beta\left(\dfrac{\omega}{\bar{\omega}_1}\right)^2 + j\left(\eta_1\bar{\eta} + \dfrac{\bar{c}_B}{\alpha}\left(\dfrac{\omega}{\bar{\omega}_1}\right)\right)}{k_1 D}, \tag{3.177}$$

and

$$A_{2,1}(\omega) = \frac{X_2(\omega)}{F(\omega)} = \frac{1 + j\eta_1\bar{\eta}}{k_1 D}, \tag{3.178}$$

with

$$
\begin{aligned}
D = {}& 1 - \eta_1^2\bar{\eta} - \eta_1\left(\bar{\eta}\bar{c}_A + \sqrt{\beta}\left(\frac{1}{\alpha} + \bar{\eta}\right)\bar{c}_B\right)\left(\frac{\omega}{\bar{\omega}_1}\right)\dots \\
&\dots - \left(1 + \beta + \alpha\beta + \frac{\sqrt{\beta}}{\alpha}\bar{c}_A\bar{c}_B\right)\left(\frac{\omega}{\bar{\omega}_1}\right)^2 + \beta\left(\frac{\omega}{\bar{\omega}_1}\right)^4 \dots \\
&\dots + j\left(\eta_1 + \eta_1\bar{\eta} + \left(\bar{c}_A + \sqrt{\beta}\left(1 + \frac{1}{\alpha}\right)\bar{c}_B\right)\left(\frac{\omega}{\bar{\omega}_1}\right)\dots\right. \\
&\dots - \eta_1\left(\bar{\eta} + \beta + \alpha\beta\bar{\eta}\right)\left(\frac{\omega}{\bar{\omega}_1}\right)^2 - \left(\beta\bar{c}_A + \sqrt{\beta}\frac{\bar{c}_B}{\alpha}\right)\left(\frac{\omega}{\bar{\omega}_1}\right)^3\right)
\end{aligned}
\tag{3.179}
$$

for x_1 and x_2, respectively. The undamped frequency response functions can be found

from these expressions by setting all damping parameters to zero, producing

$$A_{1,1}(\omega) = \frac{X_1(\omega)}{F(\omega)} = \frac{1 - \beta\left(\frac{\omega}{\overline{\omega}_1}\right)^2}{k_1\left[1 - (1 + \beta + \alpha\beta)\left(\frac{\omega}{\overline{\omega}_1}\right)^2 + \beta\left(\frac{\omega}{\overline{\omega}_1}\right)^4\right]}, \qquad (3.180)$$

and

$$A_{2,1}(\omega) = \frac{X_2(\omega)}{F(\omega)} = \frac{1}{k_1\left[1 - (1 + \beta + \alpha\beta)\left(\frac{\omega}{\overline{\omega}_1}\right)^2 + \beta\left(\frac{\omega}{\overline{\omega}_1}\right)^4\right]}, \qquad (3.181)$$

Before addressing the damping cases, it is useful to calculate the undamped modal

parameters for reference. Performing an eigenvalue analysis on the mass matrix and

stiffness matrix with all damping parameters zero produces natural frequencies

$$\begin{aligned}\omega_1 &= 19.54 \text{ rad/s (3.111 Hz)}\\ \omega_2 &= 51.17 \text{ rad/s (8.143 Hz)}\end{aligned} \qquad (3.182)$$

and mass normalized mode shapes

$$\begin{aligned}\{\phi_1\} &= \begin{Bmatrix} 0.5257 \\ 0.8507 \end{Bmatrix}\\ \{\phi_2\} &= \begin{Bmatrix} -0.8507 \\ 0.5257 \end{Bmatrix},\end{aligned} \qquad (3.183)$$

which are real-valued, as expected.

Inputting values from Table 3-2 for the light viscous damping case produces the following system matrices:

$$[M] = \begin{bmatrix} 1.000 & 0.000 \\ 0.000 & 1.000 \end{bmatrix} \tag{3.184}$$

$$[K^*] = \begin{bmatrix} 2000 & -1000 \\ -1000 & 1000 \end{bmatrix} \tag{3.185}$$

$$[C] = \begin{bmatrix} 4.000 & 0.000 \\ 0.000 & 0.1000 \end{bmatrix} \tag{3.186}$$

Performing a state-space eigenvalue analysis as described in Section 3.2 produces natural frequencies

$$\begin{aligned} \omega_1 &= 19.56 \text{ rad/s } (3.113 \text{ Hz}) \\ \omega_2 &= 51.13 \text{ rad/s } (8.138 \text{ Hz)} \, , \end{aligned} \tag{3.187}$$

and mass normalized mode shapes

$$\begin{aligned} \{\phi_1\} &= \begin{Bmatrix} 0.5259 - 0.04695\,j \\ 0.8524 + 0.02897\,j \end{Bmatrix} \\ \{\phi_2\} &= \begin{Bmatrix} -0.8524 - 0.02897\,j \\ 0.5259 - 0.04695\,j \end{Bmatrix} . \end{aligned} \tag{3.188}$$

The modes shapes have imaginary portions roughly an order of magnitude smaller than the real portion, indicating that the damping is non-proportional as desired. The real portion of the mode shapes is still quite similar to the undamped mode shapes. The modal damping ratios are calculated from the eigenvalues as

$$\zeta_1 = 0.03015$$
$$\zeta_2 = 0.02856,$$

(3.189)

from which the damped natural frequencies are estimated via Eq. (3.46) to be

$$\omega_1^{damped} = 19.55 \text{ rad/s (3.111 Hz)}$$
$$\omega_2^{damped} = 51.11 \text{ rad/s (8.135 Hz)} \ .$$

(3.190)

Frequency lines are required to compute the dynamic stiffness and frequency response function matrices. For the remainder of this study frequency dependent quantities are therefore be calculated at the frequency lines 16.71 rad/s (2.66 Hz) and 52.09 rad/s (8.29 Hz), the values of which were chosen arbitrarily above and below the natural frequencies. The resulting dynamic stiffness and full frequency response function matrices are

$$[Z(\omega = 16.71)] = \begin{bmatrix} 1721 + 66.85j & -1000 \\ -1000 & 720.7 + 1.671j \end{bmatrix}$$
$$[Z(\omega = 52.09)] = \begin{bmatrix} -713.1 + 208.4j & -1000 \\ -1000 & -1713 + 5.209j \end{bmatrix},$$

(3.191)

and

$$[A(\omega = 16.71)] = \begin{bmatrix} 2.875 \times 10^{-3} - 6.048 \times 10^{-4}j & 3.987 \times 10^{-3} - 8.485 \times 10^{-4}j \\ 3.987 \times 10^{-3} - 8.485 \times 10^{-4}j & 6.918 \times 10^{-3} - 1.193 \times 10^{-3}j \end{bmatrix}$$
$$[A(\omega = 52.09)] = \begin{bmatrix} -2.125 \times 10^{-3} - 3.451 \times 10^{-3}j & 3.399 \times 10^{-3} + 1.922 \times 10^{-3}j \\ 1.234 \times 10^{-3} + 2.018 \times 10^{-3}j & -1.301 \times 10^{-3} - 1.182 \times 10^{-3}j \end{bmatrix}$$

(3.192)

respectively. The frequency response functions corresponding to forcing on x_1 are the

first column of each full matrix, producing

$$[a(\omega=16.71)] = \begin{bmatrix} 2.875 \times 10^{-3} - 6.048 \times 10^{-4} j \\ 3.987 \times 10^{-3} - 8.485 \times 10^{-4} j \end{bmatrix}$$

$$[a(\omega=52.09)] = \begin{bmatrix} -2.125 \times 10^{-3} - 3.451 \times 10^{-3} j \\ 1.234 \times 10^{-3} + 2.018 \times 10^{-3} j \end{bmatrix}.$$

(3.193)

The full spectrum frequency response functions are given in Figure 3-2, and it can be

seen that the light viscous damping case has well defined peaks for both modes.

For the heavy viscous damping case the system matrices are

$$[M] = \begin{bmatrix} 1.000 & 0.000 \\ 0.000 & 1.000 \end{bmatrix}$$

(3.194)

$$[K^*] = \begin{bmatrix} 2000 & -1000 \\ -1000 & 1000 \end{bmatrix}$$

(3.195)

$$[C] = \begin{bmatrix} 40.00 & 0.000 \\ 0.000 & 1.000 \end{bmatrix}.$$

(3.196)

The complex eigenvalue analysis produces natural frequencies

$$\begin{aligned} \omega_1 &= 21.22 \text{ rad/s (3.377 Hz)} \\ \omega_2 &= 47.13 \text{ rad/s (7.502 Hz)} \end{aligned}$$

(3.197)

and mass normalized mode shapes

$$\begin{aligned} \{\phi_1\} &= \begin{Bmatrix} 0.8756 - 0.2244 j \\ 0.6198 + 0.3170 j \end{Bmatrix} \\ \{\phi_2\} &= \begin{Bmatrix} -0.6198 - 0.3170 j \\ 0.8756 - 0.2244 j \end{Bmatrix}. \end{aligned}$$

(3.198)
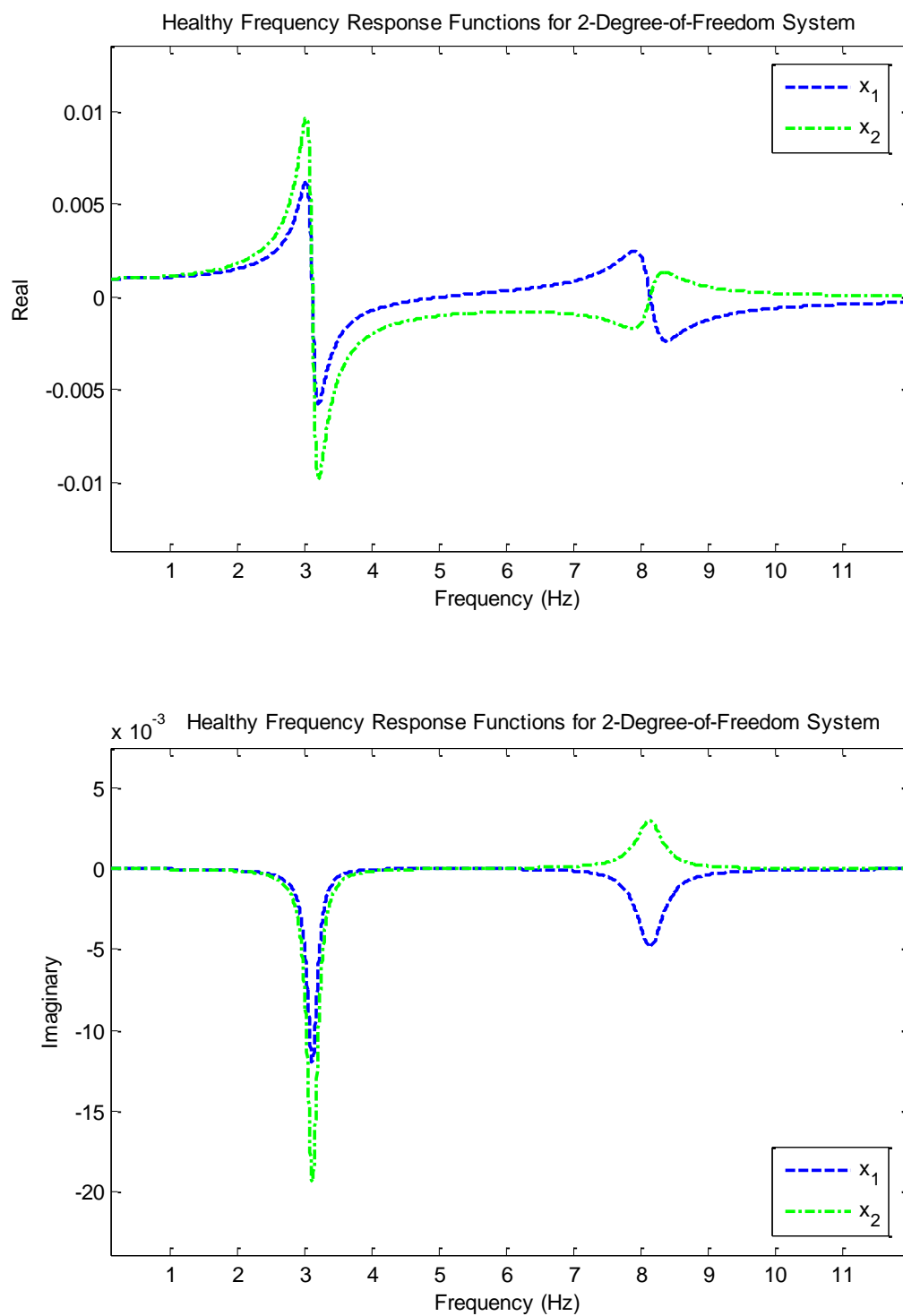
Figure 3-2: Frequency response functions for healthy 2-degree-of-freedom mass-spring system with light viscous damping.

The modal damping ratios are furthermore calculated as

$$\zeta_1 = 0.3132$$
$$\zeta_2 = 0.2939,$$

(3.199)

from which the damped natural frequencies are estimated via Eq. (3.46) to be

$$\omega_1^{damped} = 20.15 \text{ rad/s (3.207 Hz)}$$
$$\omega_2^{damped} = 45.05 \text{ rad/s (7.170 Hz)} .$$

(3.200)

Comparing results between the heavy and light viscous damping cases shows that increasing the damping causes the first natural frequency to increase and the second to decrease. Also, the level of complexity in the mode shapes is much higher in the heavy damping case, with imaginary components on the same order as the real components and the real components now substantially different from the undamped shapes. The dynamic stiffness and full frequency response function matrices for the heavy viscous damping case are

$$[Z(\omega = 16.71)] = \begin{bmatrix} 1721 + 668.5j & -1000 \\ -1000 & 720.7 + 16.71j \end{bmatrix}$$
$$[Z(\omega = 52.09)] = \begin{bmatrix} -713.1 + 2084j & -1000 \\ -1000 & -1713 + 52.09j \end{bmatrix},$$

(3.201)

and

$$[A(\omega=16.71)] = \begin{bmatrix} 5.541\times10^{-4} - 1.163\times10^{-3}\,j & 7.311\times10^{-4} - 1.631\times10^{-3}\,j \\ 7.311\times10^{-4} - 1.631\times10^{-3}\,j & 2.348\times10^{-3} - 2.318\times10^{-3}\,j \end{bmatrix}$$

$$[A(\omega=52.09)] = \begin{bmatrix} -2.931\times10^{-5} - 4.741\times10^{-4}\,j & 8.689\times10^{-6} + 2.770\times10^{-4}\,j \\ 8.689\times10^{-6} + 2.770\times10^{-4}\,j & -5.834\times10^{-4} - 1.794\times10^{-4}\,j \end{bmatrix},$$

(3.202)

respectively. The full spectrum frequency response functions are given in Figure 3-3. It can be seen that the heavy damping causes much larger imaginary components in the frequency response functions than the light damping case, as well as substantial blurring of modal peaks and coupling between the modes.

The system matrices for the case of combined light viscous damping and light structural damping produces system matrices

$$[M] = \begin{bmatrix} 1.000 & 0.000 \\ 0.000 & 1.000 \end{bmatrix}$$

(3.203)

$$[K^*] = \begin{bmatrix} 2000+20.00\,j & -1000-10.00\,j \\ -1000-10.00\,j & 1000+10.00\,j \end{bmatrix}$$

(3.204)

$$[C] = \begin{bmatrix} 4.000 & 0.000 \\ 0.000 & 0.1000 \end{bmatrix}.$$

(3.205)

It can be seen that the stiffness matrix is now complex. Closed form calculation of natural frequencies, mode shapes, and modal damping ratios for the combined damping system is not possible based on the methods described in Section 3.2 and although methods are available for this analysis, for example as described in reference [3-15], they are beyond
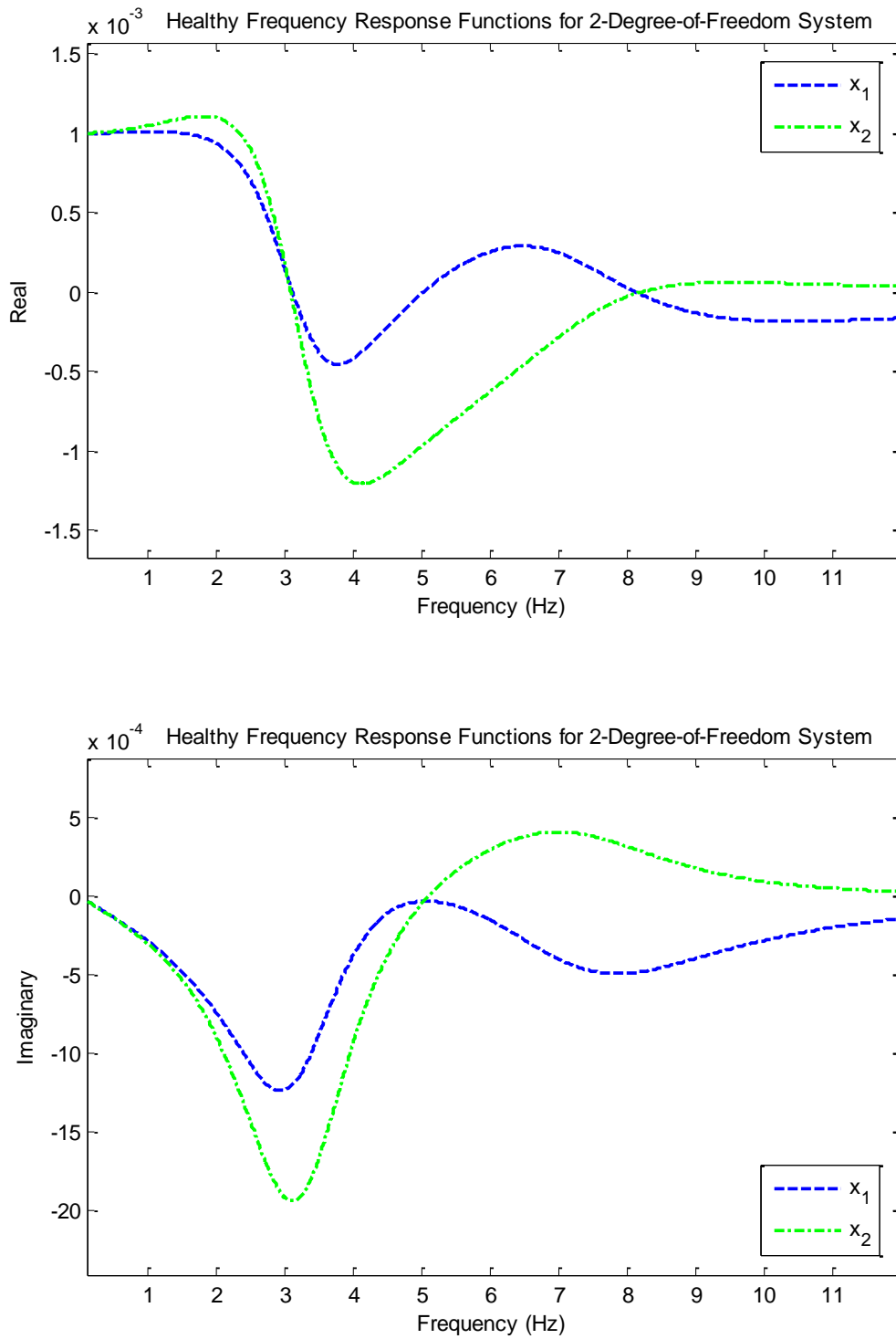
Figure 3-3: Frequency response functions for healthy 2-degree-of-freedom mass-spring system with heavy viscous damping.

the scope of this dissertation. The approximate undamped natural frequencies and mode

shapes can be calculated by assuming zero damping, however, with the same result as

presented in Eqs. (3.182) and (3.183). The dynamic stiffness and frequency response

function matrices can still be calculated without restriction as

$$[Z(\omega=16.71)] = \begin{bmatrix} 1721+96.85j & -1000-10j \\ -1000-10j & 720.7+11.67j \end{bmatrix}$$
$$[Z(\omega=52.09)] = \begin{bmatrix} -713.1+238.4j & -1000-10j \\ -1000-10j & -1713+15.21j \end{bmatrix}$$

$$(3.206)$$

$$[a(\omega=16.71)] = \begin{bmatrix} 2.729\times10^{-3}-7.672\times10^{-4}j & 3.866\times10^{-3}-1.088\times10^{-3}j \\ 3.866\times10^{-3}-1.088\times10^{-3}j & 6.741\times10^{-3}-1.566\times10^{-3}j \end{bmatrix}$$
$$[a(\omega=52.09)] = \begin{bmatrix} -1.582\times10^{-3}-3.115\times10^{-3}j & 8.889\times10^{-4}+1.836\times10^{-3}j \\ 8.889\times10^{-4}+1.836\times10^{-3}j & -1.082\times10^{-3}-1.086\times10^{-3}j \end{bmatrix}.$$

$$(3.207)$$

The full spectrum frequency response functions for this case are given in Figure 3-4. It

should be noted that the damped modal information could be estimated using transfer

function curve-fitting techniques with these full-spectrum frequency response functions

as is commonly performed during experimental modal parameter estimation on measured

data.

Frequency response functions for the three damping cases are plotted together in

Figure 3-5 and Figure 3-6 for x_1 and x_2 respectively. It can be seen that the light viscous

plus light structural damping cases produces effective damping between the other cases.
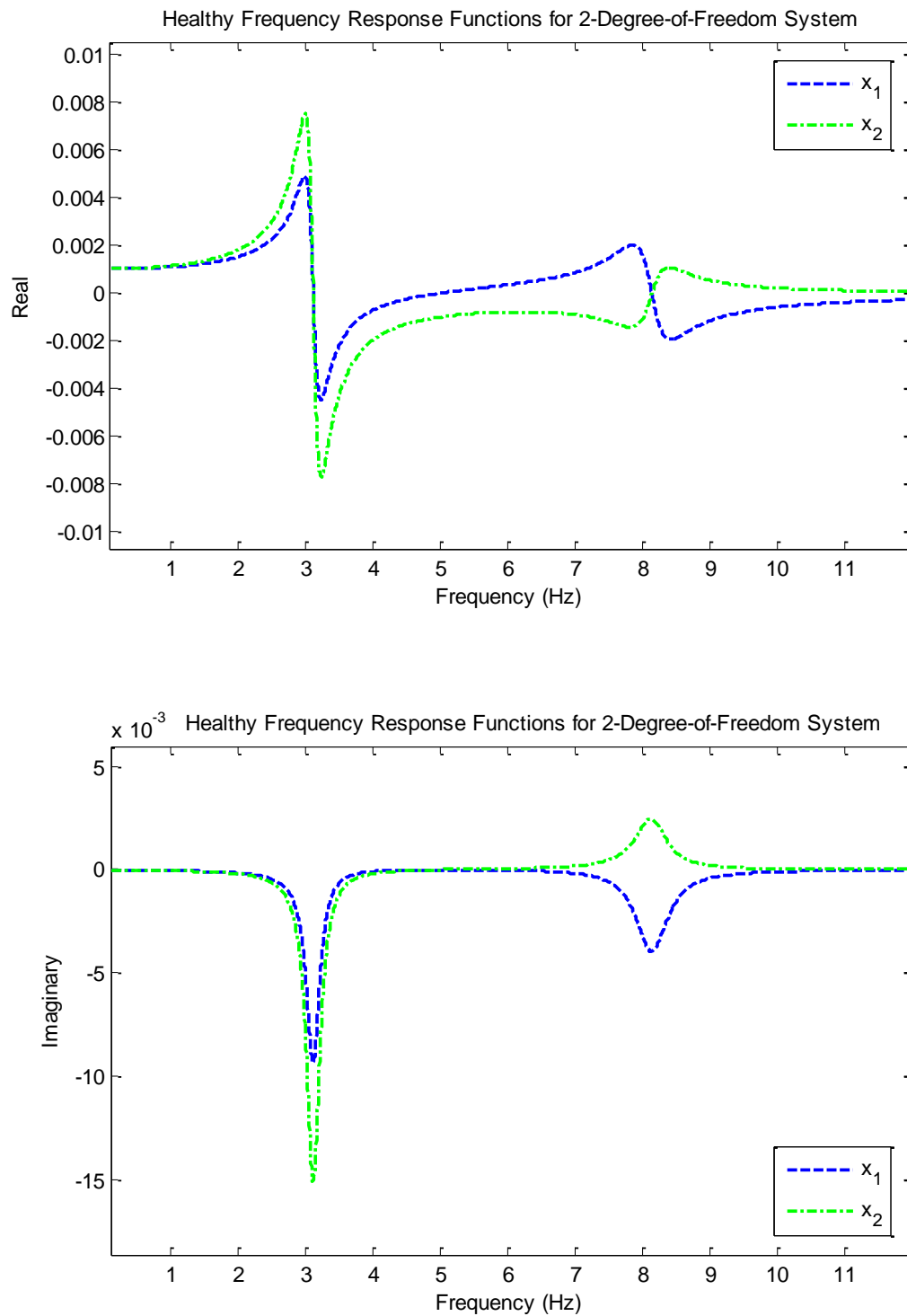
Figure 3-4: Frequency response functions for healthy 2-degree-of-freedom mass-spring system with light viscous plus light structural damping.
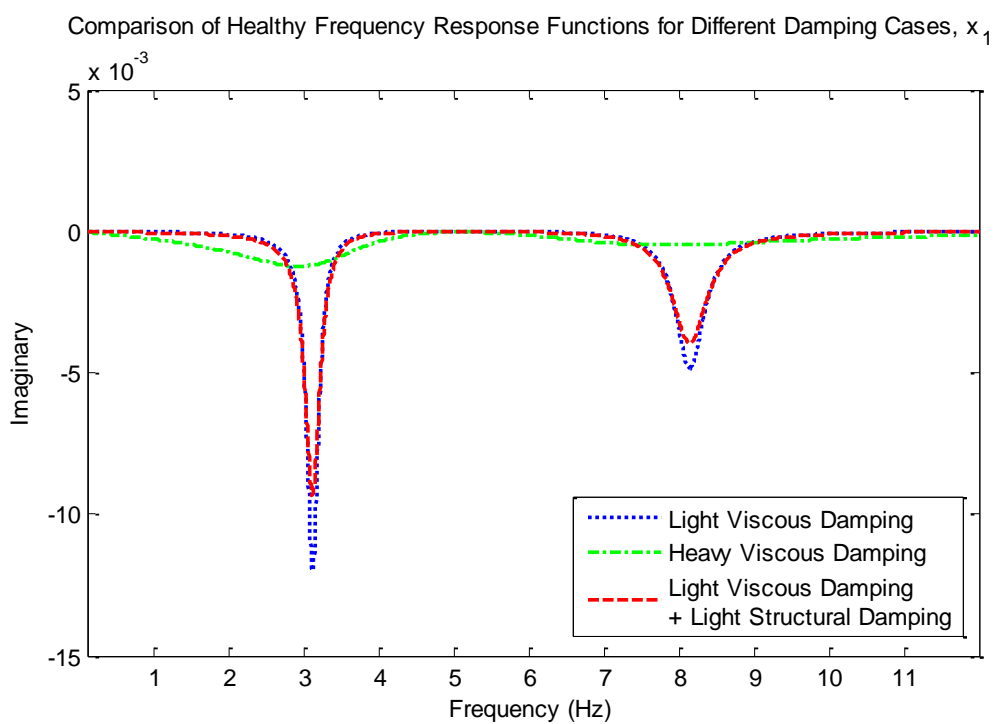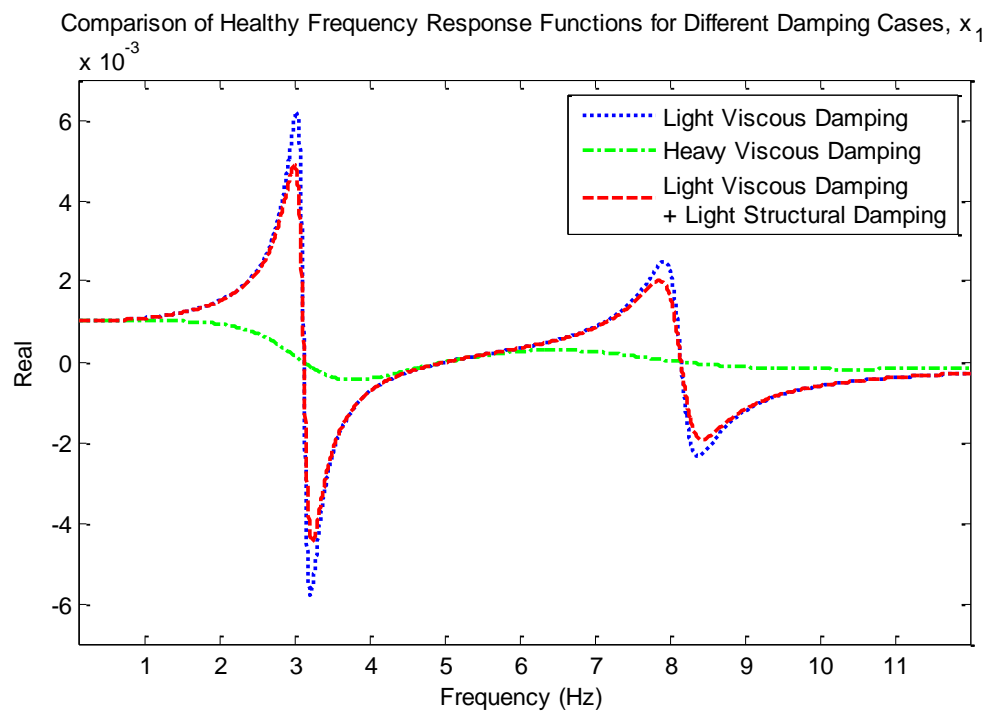
Figure 3-5: Comparison of healthy frequency response functions for three damping cases, x_1.

Comparison of Healthy Frequency Response Functions for Different Damping Cases, x_2
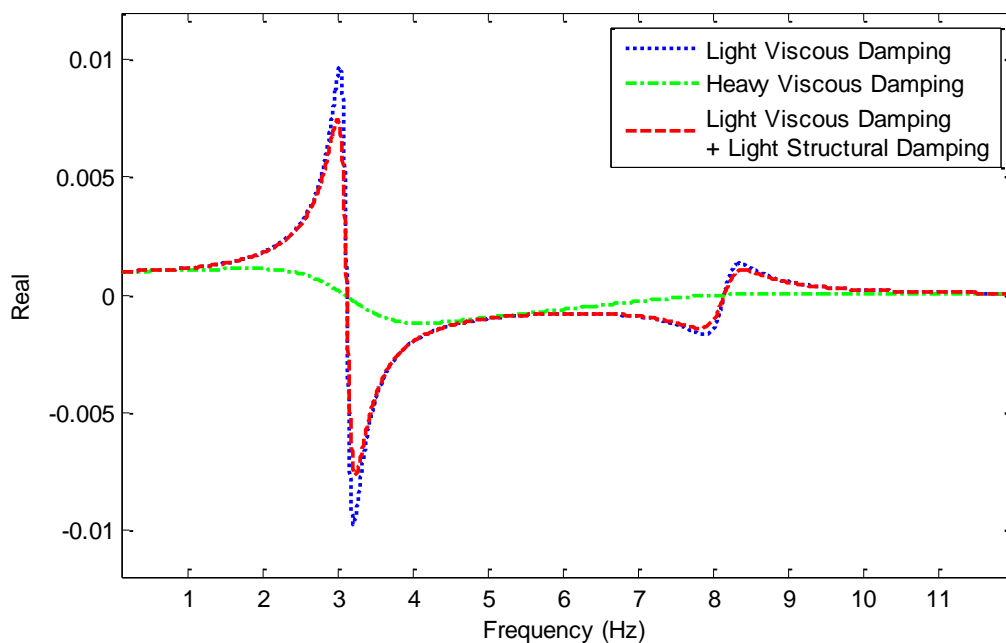
Comparison of Healthy Frequency Response Functions for Different Damping Cases, x_2
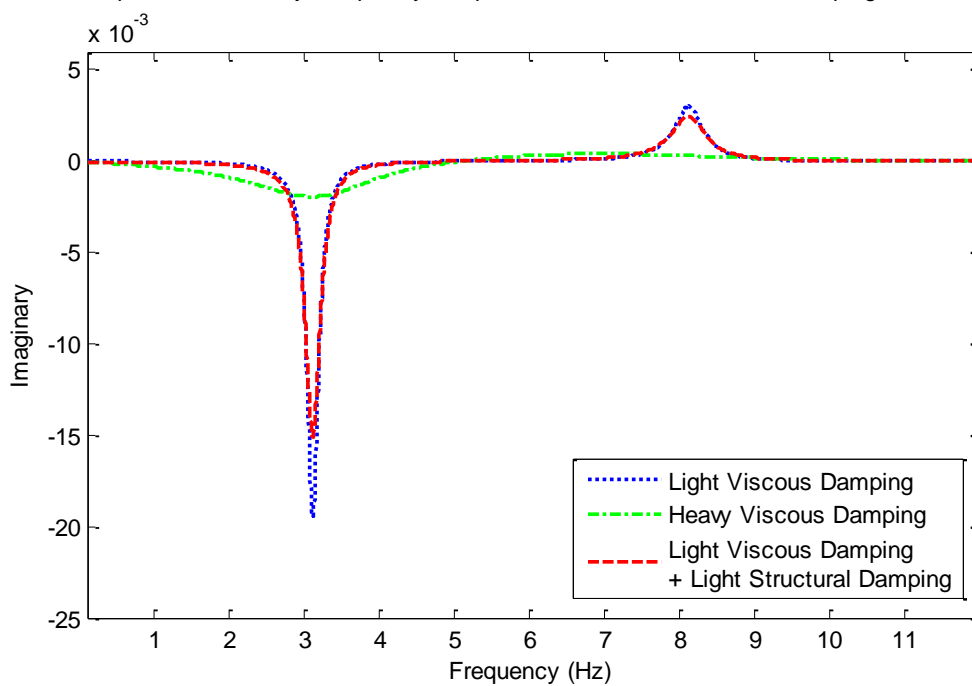
Figure 3-6: Comparison of healthy frequency response functions for three damping cases, x_2.

3.8.2 Damaged System Description

In order to simulate damage, a small decrease in mass and larger decrease in stiffness are introduced into the system for each damping case. Additionally, for the combined viscous and structural damping case one structural damping parameter is increased to simulate increased friction in the damage zone and then for a subsequent case decreased to simulate gapping. Exact parameters for the resulting four damage cases are given in Table 3-3, where the subscript '*d*' on each parameter indicates a damaged value.

Table 3-3: Damaged parameter values for the 2-degree-of-freedom system.

Parameter	Light Viscous Damping	Heavy Viscous Damping	Light Viscous Plus Light Structural Damping, Damping Increase	Light Viscous Plus Light Structural Damping, Damping Decrease
$m_{1,d}$	1.000	1.000	1.000	1.000
$m_{2,d}$	0.990 (-1%)	0.990 (-1%)	0.990 (-1%)	0.990 (-1%)
$k_{1,d}$	900.0 (-10%)	900.0 (-10%)	900.0 (-10%)	900.0 (-10%)
$k_{2,d}$	1000	1000	1000	1000
$\eta_{1,d}$	0.000	0.000	0.024 (+20%)	0.016 (-20%)
$\eta_{2,d}$	0.000	0.000	0.010	0.010
$c_{A,d}$	4.000	40.00	4.000	4.000
$c_{B,d}$	0.1000	1.000	0.1000	0.1000

For each case, damaged reference data, such as would be measured from the damage structure in practice, is created using Eq. (3.171) with only the first column of the full frequency response function matrix retained at each frequency to simulate forcing on the first degree-of-freedom. It should be noted that although acceleration or velocity would most easily be measured on a physical structure the frequency response functions generated for the purpose of the current example are displacement-based. However, acceleration or velocity measurements could be converted to the displacement domain through division by the $j\omega_k$ or $-\omega_k^2$, respectively, at each frequency line so the distinction is a formality. The damaged reference frequency response functions for each case are given below in Figure 3-7 to Figure 3-14 with the healthy frequency response function given in each case for comparison.

The frequency response functions evaluated at the two previously specified analysis frequency lines are as follows.

Light Viscous Damping Case:

$$
\left[a(\omega = 16.71)\right] = \begin{bmatrix} 3.896 \times 10^{-3} - 1.157 \times 10^{-3} \, j \\ 5.402 \times 10^{-3} - 1.618 \times 10^{-3} \, j \end{bmatrix}
$$

$$
\left[a(\omega = 52.09)\right] = \begin{bmatrix} -2.378 \times 10^{-3} - 2.470 \times 10^{-3} \, j \\ 1.384 \times 10^{-3} + 1.446 \times 10^{-3} \, j \end{bmatrix}.
$$

(3.208)
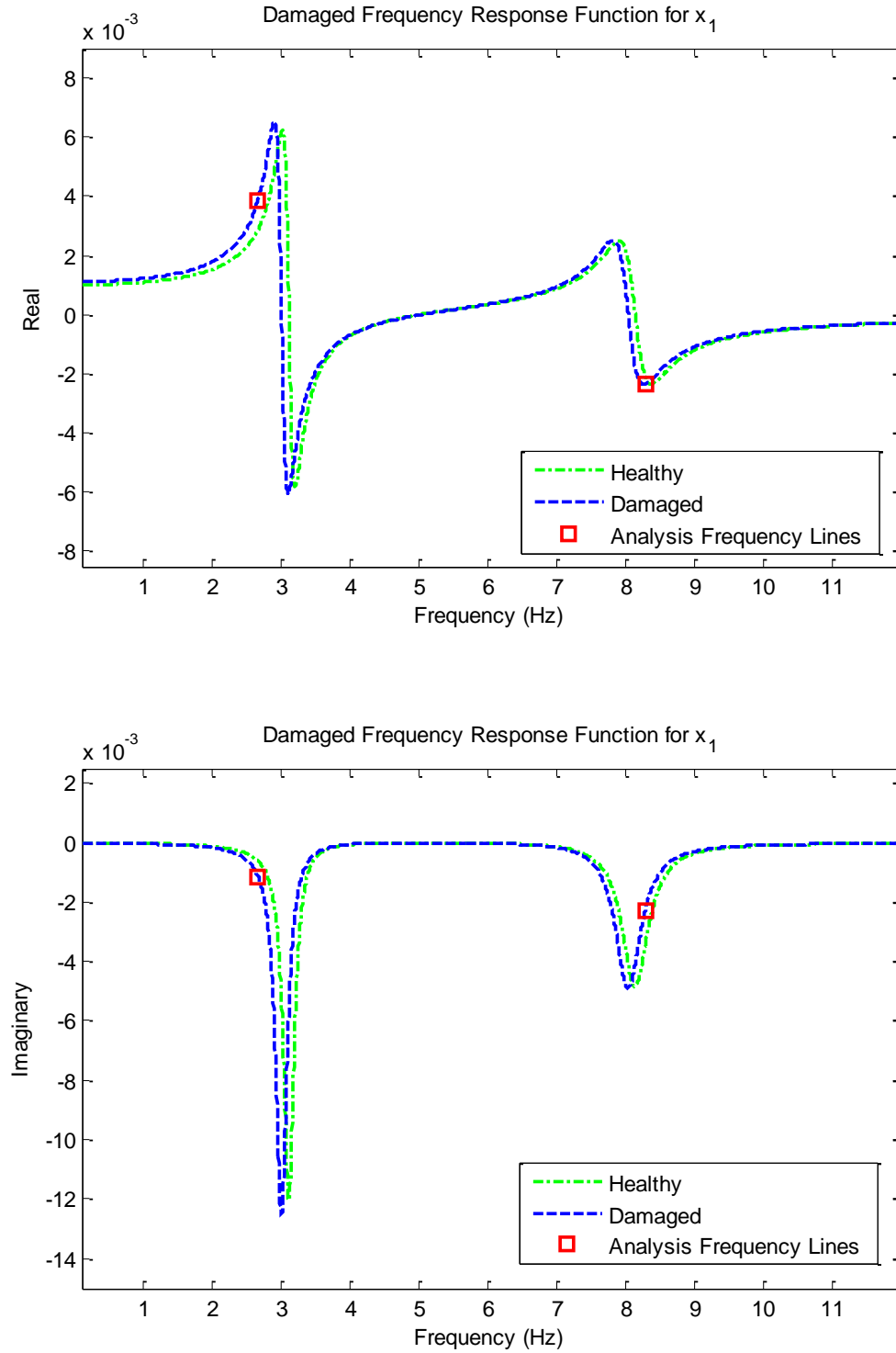
Figure 3-7: Full-spectrum damaged and healthy frequency response functions for the light viscous damping case, x_1.
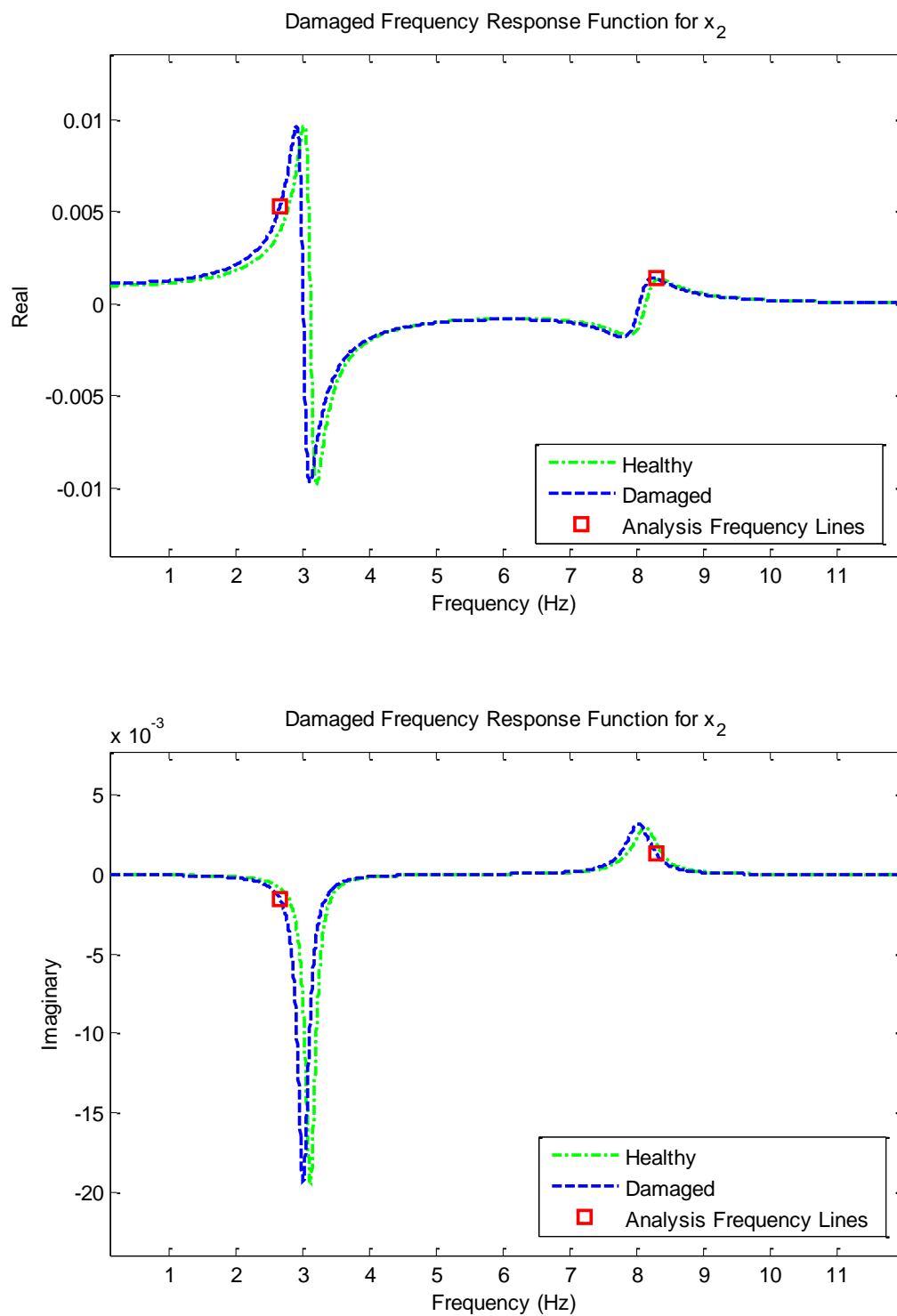
Figure 3-8: Full-spectrum damaged and healthy frequency response functions for the light viscous damping case, x_2.
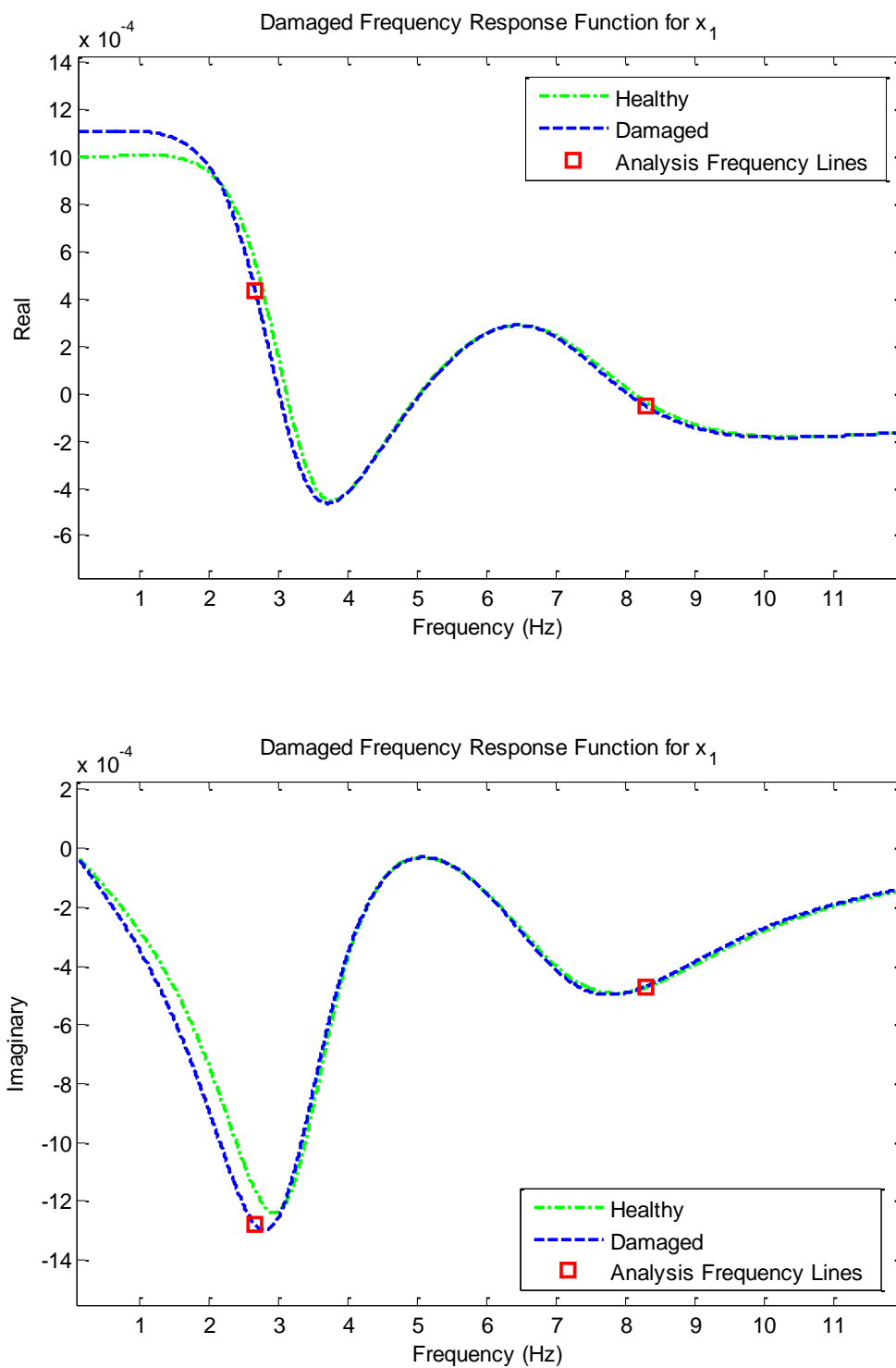
Figure 3-9: Full-spectrum damaged and healthy frequency response functions for the heavy viscous damping case, x_1.
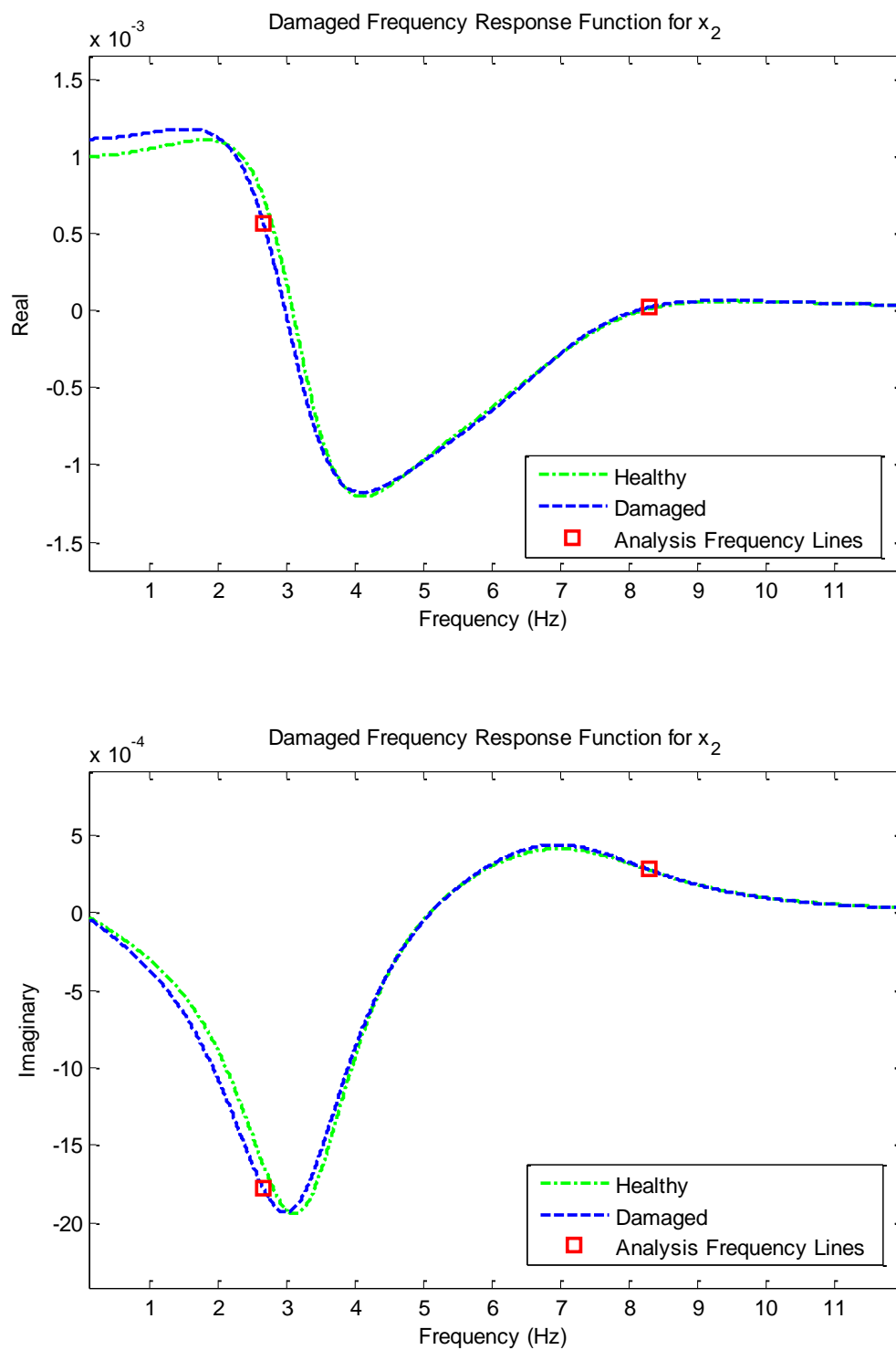
Figure 3-10: Full-spectrum damaged and healthy frequency response functions for the heavy viscous damping case, x_2.
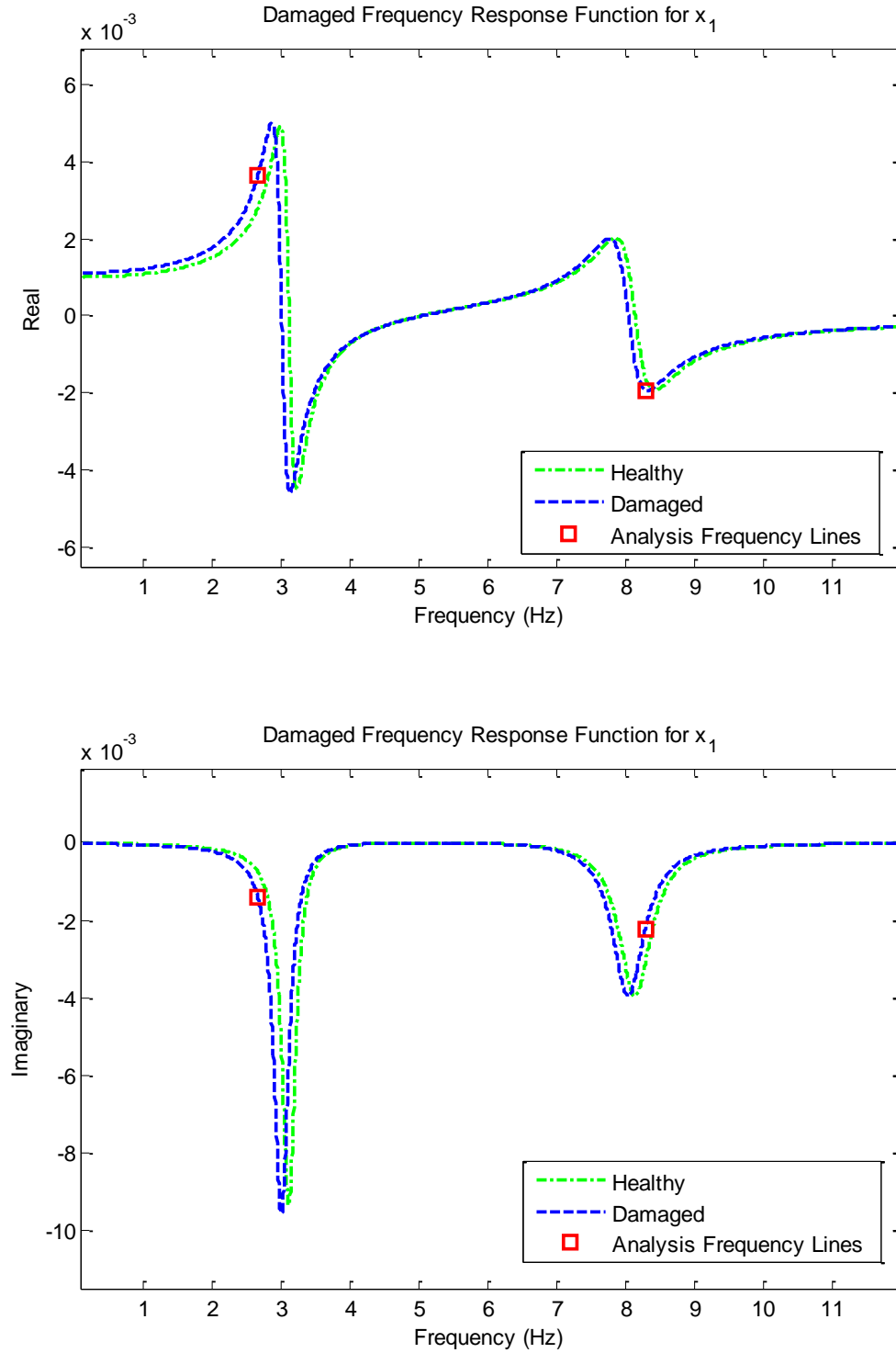
Figure 3-11: Full-spectrum damaged and healthy frequency response functions for the light viscous plus light structural damping with increased structural damping case, x_1.
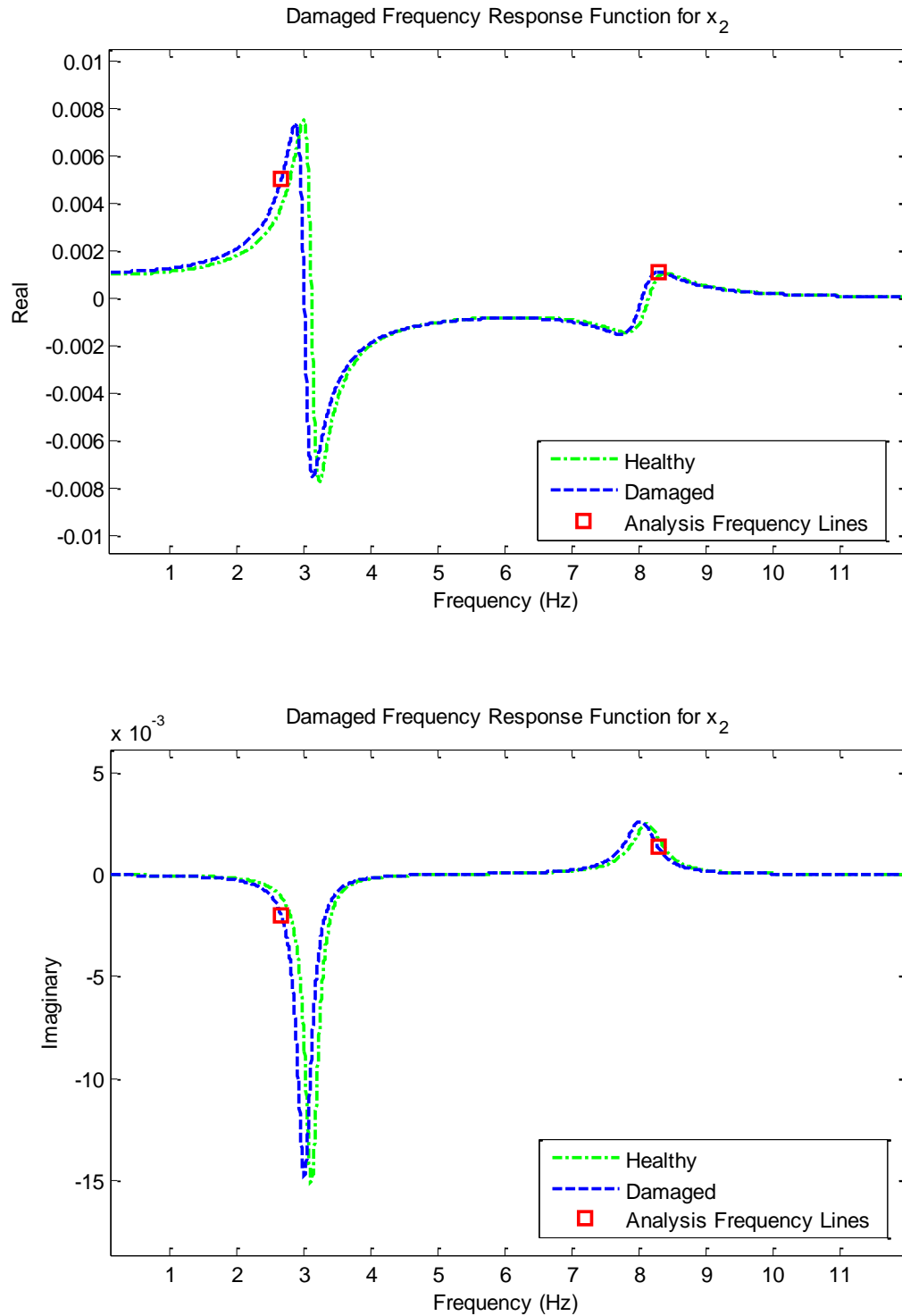
Figure 3-12: Full-spectrum damaged and healthy frequency response functions for the light viscous plus light structural damping with increased structural damping case, x_2.
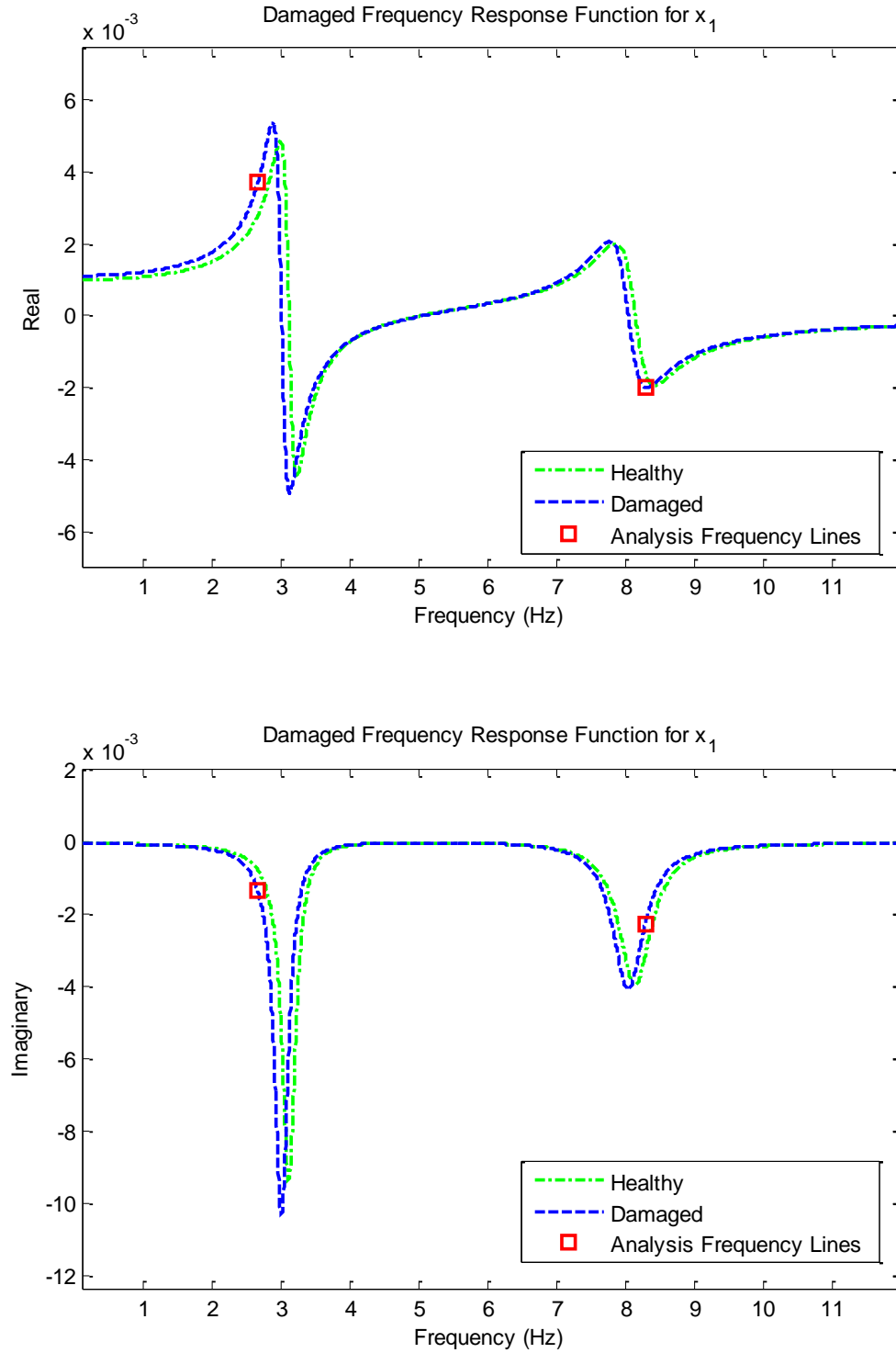
Figure 3-13: Full-spectrum damaged and healthy frequency response functions for the light viscous plus light structural damping with decreased structural damping case, x_1.
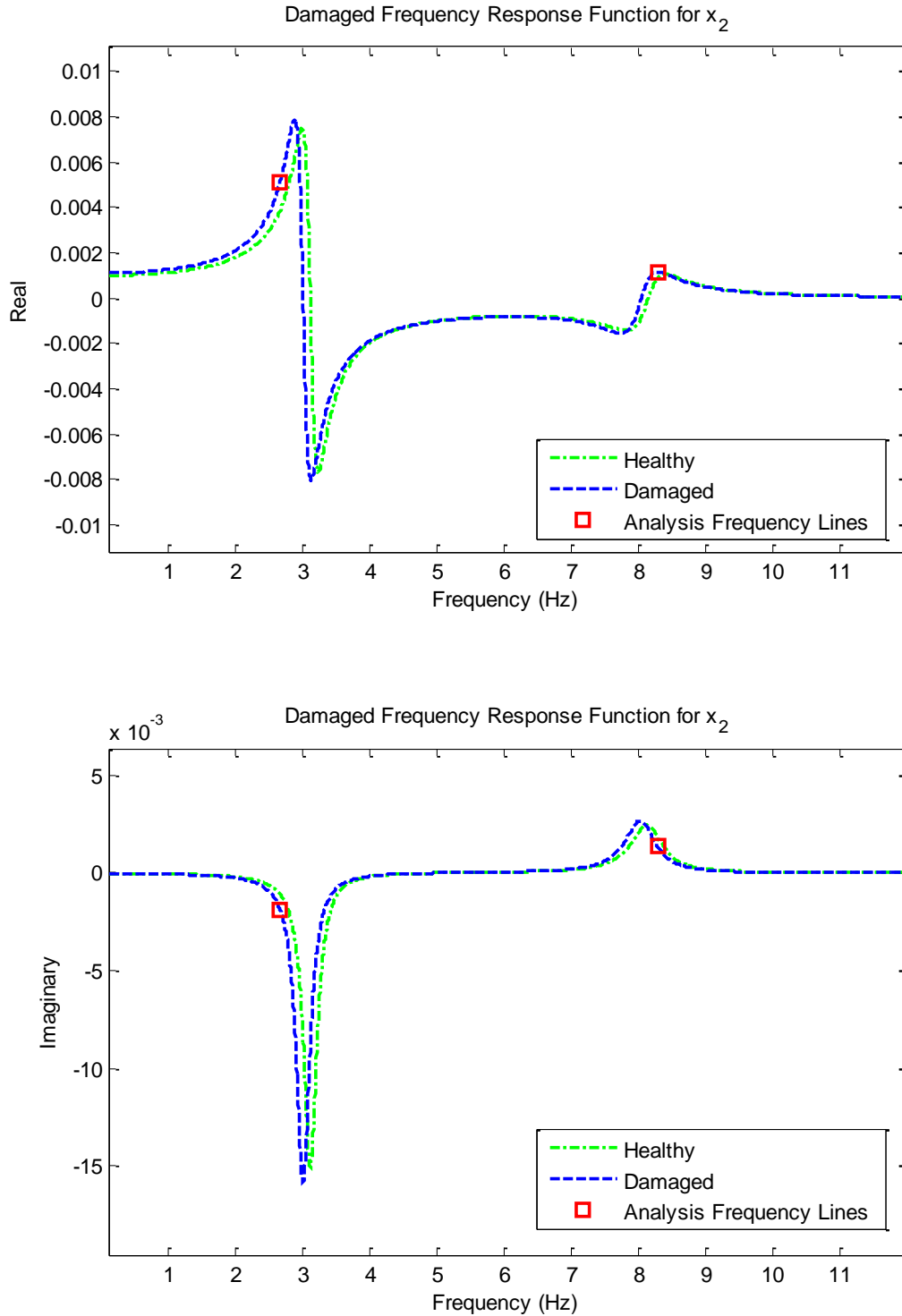
Figure 3-14: Full-spectrum damaged and healthy frequency response functions for the light viscous plus light structural damping with decreased structural damping case, x_2.

Heavy Viscous Damping Case:

$$[a(\omega=16.71)] = \begin{bmatrix} 4.366 \times 10^{-4} - 1.279 \times 10^{-3} j \\ 5.623 \times 10^{-4} - 1.780 \times 10^{-3} j \end{bmatrix}$$

$$[a(\omega=52.09)] = \begin{bmatrix} -4.938 \times 10^{-5} - 4.706 \times 10^{-4} j \\ 2.065 \times 10^{-5} + 2.798 \times 10^{-4} j \end{bmatrix}.$$

(3.209)

Light Viscous plus Light Structural Damping with Increased Damping Case:

$$[a(\omega=16.71)] = \begin{bmatrix} 3.639 \times 10^{-3} - 1.421 \times 10^{-3} j \\ 5.017 \times 10^{-3} - 1.994 \times 10^{-3} j \end{bmatrix}$$

$$[a(\omega=52.09)] = \begin{bmatrix} -1.921 \times 10^{-3} - 2.244 \times 10^{-3} j \\ 1.114 \times 10^{-3} + 1.352 \times 10^{-3} j \end{bmatrix}.$$

(3.210)

Light Viscous plus Light Structural Damping with Decreased Damping Case:

$$[a(\omega=16.71)] = \begin{bmatrix} 3.712 \times 10^{-3} - 1.337 \times 10^{-3} j \\ 5.118 \times 10^{-3} - 1.879 \times 10^{-3} j \end{bmatrix}$$

$$[a(\omega=52.09)] = \begin{bmatrix} -1.984 \times 10^{-3} - 2.253 \times 10^{-3} j \\ 1.151 \times 10^{-3} + 1.358 \times 10^{-3} j \end{bmatrix}.$$

(3.211)

For all four damping cases the change in natural frequency from damage is related only to the changes in mass and stiffness, plus a small amount of damping based scaling. The damaged light viscous damping case produces the following modal parameters.

Natural frequencies:

$$\omega_{1,d} = 18.88 \text{ rad/s (3.005 Hz)}$$
$$\omega_{2,d} = 50.50 \text{ rad/s (8.038 Hz)}$$

(3.212)

Mass normalized mode shapes:

$$\{\phi_{1,d}\} = \begin{Bmatrix} 0.5458 - 0.04870\,j \\ 0.8441 + 0.03180\,j \end{Bmatrix}$$

$$\{\phi_{2,d}\} = \begin{Bmatrix} -.8400 - 0.03165\,j \\ 0.5486 - 0.04894\,j \end{Bmatrix} \tag{3.213}$$

Modal damping ratios:

$$\zeta_{1,d} = 0.03344$$
$$\zeta_{2,d} = 0.02810 \tag{3.214}$$

Damped natural frequencies:

$$\omega_{1,d}^{damped} = 18.87 \text{ rad/s (3.003 Hz)}$$
$$\omega_{2,d}^{damped} = 50.48 \text{ rad/s (8.035 Hz)} \tag{3.215}$$

The damage causes natural frequency changes of -3.465% and -1.231% for mode 1 and

mode 2, respectively, and corresponding mode shape changes of

$$\Delta\,\mathrm{Re}\{\phi_1\} = \begin{Bmatrix} 3.797\% \\ -0.9643\% \end{Bmatrix}, \ \Delta\,\mathrm{Im}\{\phi_1\} = \begin{Bmatrix} -3.723\% \\ 9.808\% \end{Bmatrix}$$

$$\Delta\,\mathrm{Re}\{\phi_2\} = \begin{Bmatrix} 1.461\% \\ 4.320\% \end{Bmatrix}, \quad \Delta\,\mathrm{Im}\{\phi_2\} = \begin{Bmatrix} -9.257\% \\ -4.246\% \end{Bmatrix}, \tag{3.216}$$

where the percentage change has been calculated separately on the real and imaginary

components of the mode shapes.

The damaged heavy viscous damping case produces the following modal

parameters.

Natural frequencies:

$$\omega_{1,d} = 20.60 \text{ rad/s (3.279 Hz)}$$
$$\omega_{2,d} = 46.28 \text{ rad/s (7.365 Hz)}$$

(3.217)

Mass normalized mode shapes:

$$\{\phi_{1,d}\} = \begin{Bmatrix} 0.8976 - 0.1984j \\ 0.5772 + 0.3116j \end{Bmatrix}$$
$$\{\phi_{2,d}\} = \begin{Bmatrix} -0.5743 - 0.3101j \\ 0.9021 - 0.1994j \end{Bmatrix}$$

(3.218)

Modal damping ratios:

$$\zeta_{1,d} = 0.3521$$
$$\zeta_{2,d} = 0.2863$$

(3.219)

Damped natural frequencies:

$$\omega_{1,d}^{damped} = 19.28 \text{ rad/s (3.069 Hz)}$$
$$\omega_{2,d}^{damped} = 44.34 \text{ rad/s (7.057 Hz)}$$

(3.220)

The damage for this case causes natural frequency changes of −2.886% and −1.820% for

mode 1 and mode 2, respectively, and mode shape changes of

$$\Delta \operatorname{Re}\{\phi_1\} = \begin{Bmatrix} 2.510\% \\ -6.876\% \end{Bmatrix}, \ \Delta \operatorname{Im}\{\phi_1\} = \begin{Bmatrix} 11.60\% \\ -1.708\% \end{Bmatrix}$$
$$\Delta \operatorname{Re}\{\phi_2\} = \begin{Bmatrix} 7.343\% \\ 3.027\% \end{Bmatrix}, \quad \Delta \operatorname{Im}\{\phi_2\} = \begin{Bmatrix} -2.201\% \\ 11.16\% \end{Bmatrix},$$

(3.221)

When damping is ignored and modal parameters are calculated from the mass and

stiffness matrices only, natural frequencies for all four damage cases are

$$\omega_{1,d}^{undamped} = 18.87 \text{ rad/s (3.003 Hz)}$$
$$\omega_{2,d}^{undamped} = 50.54 \text{ rad/s (8.044 Hz)} ,$$

(3.222)

with corresponding mass normalized mode shapes

$$\left\{ \phi_{1,d}^{undamped} \right\} = \left\{ \begin{matrix} 0.5455 \\ 0.8423 \end{matrix} \right\}$$
$$\left\{ \phi_{2,d}^{undamped} \right\} = \left\{ \begin{matrix} -0.8381 \\ 0.5483 \end{matrix} \right\}.$$

(3.223)

Viewed in this respect, the damage causes natural frequency changes of −3.469% and

−1.227% for mode 1 and mode 2, respectively, and mode shape changes of

$$\Delta\{\phi_1\} = \left\{ \begin{matrix} 3.764\% \\ -0.9792\% \end{matrix} \right\}$$
$$\Delta\{\phi_2\} = \left\{ \begin{matrix} 1.476\% \\ 4.286\% \end{matrix} \right\} ,$$

(3.224)

On average, the damage cases can therefore be thought of as producing a 3.8% decrease

in ω_1, 1.2% decrease in ω_2, and 2.6% net change in mode shapes compared to the healthy

systems.

3.8.3   Damage Identification Walk-Through and Results

Basic functionality of the damage identification algorithm is now demonstrated on

the damped mass-spring system. In order to clearly illustrate the algorithm mechanics, a

step-by-step walk-through is presented first using the light viscous damping case, with

results of the remaining cases presented directly for comparison. It is assumed for this

example that the generalized damping matrix is known. Only mass and stiffness

parameters are included as damage parameters for the light and heavy viscous damping

cases, with the structural damping parameters included for the final two cases where the

values are not zero, as summarized in Table 3-4.

Additional algorithm variables are as follows:

- Assumed initial parameter standard deviation equal to 10% of initial values.

- Assumed reference data standard deviation equal to 0.01% of mean-square

  average of analysis frequency response function lines.

- Convergence tolerance equal to 0.01% of mean of initial damage parameters

  (equal to 0.0501 for the current case).

Table 3-4: Update parameter selection for damage identification runs on 2-degree-of-freedom damped mass-spring system.

Parameter	Light Viscous Damping	Heavy Viscous Damping	Light Viscous Damping + Light Structural Damping, Damping Increase	Light Viscous Damping + Light Structural Damping, Damping Decrease
m_1	r_1	r_1	r_1	r_1
m_2	r_2	r_2	r_2	r_2
k_1	r_3	r_3	r_3	r_3
k_2	r_4	r_4	r_4	r_4
η_1	N/A	N/A	r_5	r_5
η_2	N/A	N/A	r_6	r_6
c_A	N/A	N/A	N/A	N/A
c_B	N/A	N/A	N/A	N/A

Dynamic stiffness matrix sensitivities are calculated in closed form for this example by first writing the dynamic stiffness matrix with subscript 'i' on parameters to indicate their current value at iteration i,

$$[Z(\omega_k)]_i = \begin{bmatrix} k_{1,i}(1+j\eta_{1,i})+k_{2,i}(1+j\eta_{1,i}) & -k_{2,i}(1+j\eta_{2,i}) \\ -k_{2,i}(1+j\eta_{2,i}) & k_{2,i}(1+j\eta_{2,i}) \end{bmatrix} + j\omega_k \begin{bmatrix} c_A & 0 \\ 0 & c_B \end{bmatrix} - \omega_k^2 \begin{bmatrix} m_{1,i} & 0 \\ 0 & m_{2,i} \end{bmatrix}.$$

(3.225)

The required sensitivities are then calculated as the partial derivative with respect to each parameter. The resulting sensitivity expressions are

$$\left[\frac{\partial Z(\omega_k)}{\partial m_1}\right]_i = \begin{bmatrix} -\omega_k^2 & 0 \\ 0 & 0 \end{bmatrix},$$

(3.226)

$$\left[\frac{\partial Z(\omega_k)}{\partial m_2}\right]_i = \begin{bmatrix} 0 & 0 \\ 0 & -\omega_k^2 \end{bmatrix},$$

(3.227)

$$\left[\frac{\partial Z(\omega_k)}{\partial k_1}\right]_i = \begin{bmatrix} (1+j\eta_{1,i}) & 0 \\ 0 & 0 \end{bmatrix},$$

(3.228)

$$\left[\frac{\partial Z(\omega_k)}{\partial k_2}\right]_i = \begin{bmatrix} (1+j\eta_{2,i}) & -(1+j\eta_{2,i}) \\ -(1+j\eta_{2,i}) & (1+j\eta_{2,i}) \end{bmatrix},$$

(3.229)

$$\left[\frac{\partial Z(\omega_k)}{\partial \eta_1}\right]_i = \begin{bmatrix} jk_{1,i} & 0 \\ 0 & 0 \end{bmatrix},$$

(3.230)

$$\left[\frac{\partial Z(\omega_k)}{\partial \eta_2}\right]_i = \begin{bmatrix} jk_{2,i} & -jk_{2,i} \\ -jk_{2,i} & jk_{2,i} \end{bmatrix}.$$

(3.231)

$$\left[\frac{\partial Z(\omega_k)}{\partial c_A}\right]_i = \begin{bmatrix} j\omega_k & 0 \\ 0 & 0 \end{bmatrix}.$$

(3.232)

$$\left[\frac{\partial Z(\omega_k)}{\partial c_B}\right]_i = \begin{bmatrix} 0 & 0 \\ 0 & j\omega_k \end{bmatrix}. \tag{3.233}$$

The step-by-step damage identification algorithm walk-through is presented in the same bulleted list format as was used for the algorithm summary in Section 3.7 for the light viscous damping case. Results from the remaining damage cases are then presented without step-by-step walk-throughs since the process is identical for each case. Note that for this example the iteration indexing starts at $i = 0$; however, the iterations could equivalently start at $i = 1$ with parameter indexing adjusted accordingly to ensure correct algorithm flow. Additionally, because of the small problem size it is assumed that reference data is available from both degrees-of-freedom with no reduction required.

Light Viscous Damping Case:

Damage Identification Algorithm Inputs:

- Damage parameters at initial healthy values:

$$\{r_0\} = \begin{Bmatrix} 1.000 \\ 1.000 \\ 1000 \\ 1000 \end{Bmatrix}$$

- Initial damage parameter covariance matrix:

$$\left[S_{r_0 r_0} \right] = \begin{bmatrix} 0.01 & 0 & 0 & 0 \\ 0 & 0.01 & 0 & 0 \\ 0 & 0 & 10 & 0 \\ 0 & 0 & 0 & 10 \end{bmatrix}$$

- Analytical model evaluated at initial damage parameter values:

$$\left[M \right]_0 = \begin{bmatrix} 1.000 & 0.000 \\ 0.000 & 1.000 \end{bmatrix}$$

$$\left[K^* \right]_0 = \begin{bmatrix} 2000 & -1000 \\ -1000 & 1000 \end{bmatrix}$$

$$\left[C \right]_0 = \begin{bmatrix} 4.000 & 0.000 \\ 0.000 & 0.1000 \end{bmatrix}$$

- Analysis frequency lines:

$$\{\omega_k\} = \begin{Bmatrix} 16.71 \\ 52.09 \end{Bmatrix} \frac{rad}{s}$$

- Experimental reference data from the damaged structure, batch-stacked

  over analysis frequency line set:

$$\{\tilde{\underline{a}}\} = \begin{Bmatrix} 3.896 \times 10^{-3} \\ 5.402 \times 10^{-3} \\ -1.157 \times 10^{-3} \\ -1.618 \times 10^{-3} \\ -2.378 \times 10^{-3} \\ 1.384 \times 10^{-3} \\ -2.470 \times 10^{-3} \\ 1.446 \times 10^{-3} \end{Bmatrix}$$

- Experimental reference data covariance matrix, batch-stacked over

  analysis frequency line set:

$$[\underline{S}_{vv}] = \begin{bmatrix} 1.028 & 0 & 0 & 0 & 0 & 0 & 0 & 0 \\ 0 & 1.521 & 0 & 0 & 0 & 0 & 0 & 0 \\ 0 & 0 & 0.3221 & 0 & 0 & 0 & 0 & 0 \\ 0 & 0 & 0 & 0.2161 & 0 & 0 & 0 & 0 \\ 0 & 0 & 0 & 0 & 1.028 & 0 & 0 & 0 \\ 0 & 0 & 0 & 0 & 0 & 1.521 & 0 & 0 \\ 0 & 0 & 0 & 0 & 0 & 0 & 0.3221 & 0 \\ 0 & 0 & 0 & 0 & 0 & 0 & 0 & 0.2161 \end{bmatrix} \times 10^{-13}$$

Iteration 1 ($i = 0$):

1. Dynamic stiffness matrix at $\{r_0\}$ using Eq. (3.7):

$$[Z(\omega = 16.71)]_0 = \begin{bmatrix} 1721 + 66.85\,j & -1000 \\ -1000 & 720.7 + 1.671\,j \end{bmatrix}$$

$$[Z(\omega = 52.09)]_0 = \begin{bmatrix} -713.1 + 208.4\,j & -1000 \\ -1000 & -1713 + 5.209\,j \end{bmatrix}$$

2. Assemble batch-stacked dynamic stiffness matrix over all frequency lines:

$$[\underline{Z}]_0 = \begin{bmatrix} 1721 & -1000 & -66.85 & 0 & 0 & 0 & 0 & 0 \\ -1000 & 720.7 & 0 & -1.671 & 0 & 0 & 0 & 0 \\ 66.85 & 0 & 1721 & -1000 & 0 & 0 & 0 & 0 \\ 0 & 1.671 & -1000 & 720.7 & 0 & 0 & 0 & 0 \\ 0 & 0 & 0 & 0 & -713.1 & -1000 & -208.4 & 0 \\ 0 & 0 & 0 & 0 & -1000 & -1713 & 0 & -5.209 \\ 0 & 0 & 0 & 0 & 208.4 & 0 & -713.1 & -1000 \\ 0 & 0 & 0 & 0 & 0 & 5.209 & -1000 & -1713 \end{bmatrix}$$

3. Create batch-stacked residual force vector using Eq. (3.103):

$$\{\underline{R}\}_0 = \begin{Bmatrix} -0.3861 \\ 0.01490 \\ 0.1134 \\ 0.004413 \\ 0.2376 \\ 0.03813 \\ 0.2270 \\ 0.03665 \end{Bmatrix}$$

4. Create batch-stacked residual force covariance matrix using Eq. (3.104):

$$[\underline{S}_{RR}]_0 = \begin{bmatrix} 4565 & -2864 & -81.16 & -18.99 & 0 & 0 & 0 & 0 \\ -2864 & 1817 & 68.34 & -1.571 & 0 & 0 & 0 & 0 \\ -81.16 & 68.34 & 1174 & -709.9 & 0 & 0 & 0 & 0 \\ -18.99 & -1.571 & -709.9 & 434.3 & 0 & 0 & 0 & 0 \\ 0 & 0 & 0 & 0 & 2057 & 3338 & 104.8 & -59.18 \\ 0 & 0 & 0 & 0 & 3338 & 5491 & 213.0 & 11.64 \\ 0 & 0 & 0 & 0 & 104.8 & 213.0 & 424.5 & 599.8 \\ 0 & 0 & 0 & 0 & -59.18 & 11.64 & 599.8 & 956.2 \end{bmatrix} \times 10^{-10}$$

5. Generate batch-stacked dynamic stiffness sensitivity matrix for each damage parameter using the closed form expressions in Eqs. (3.226) to (3.229):

$$\left[\frac{\partial \underline{\underline{Z}}}{\partial \hat{r}_1}\right]_0 = \begin{bmatrix} -279.3 & 0 & 0 & 0 & 0 & 0 & 0 & 0 \\ 0 & 0 & 0 & 0 & 0 & 0 & 0 & 0 \\ 0 & 0 & -2713 & 0 & 0 & 0 & 0 & 0 \\ 0 & 0 & 0 & 0 & 0 & 0 & 0 & 0 \\ 0 & 0 & 0 & 0 & -279.3 & 0 & 0 & 0 \\ 0 & 0 & 0 & 0 & 0 & 0 & 0 & 0 \\ 0 & 0 & 0 & 0 & 0 & 0 & -2713 & 0 \\ 0 & 0 & 0 & 0 & 0 & 0 & 0 & 0 \end{bmatrix}$$

$$\left[\frac{\partial \underline{\underline{Z}}}{\partial \hat{r}_2}\right]_0 = \begin{bmatrix} 0 & 0 & 0 & 0 & 0 & 0 & 0 & 0 \\ 0 & -279.3 & 0 & 0 & 0 & 0 & 0 & 0 \\ 0 & 0 & 0 & 0 & 0 & 0 & 0 & 0 \\ 0 & 0 & 0 & -2713 & 0 & 0 & 0 & 0 \\ 0 & 0 & 0 & 0 & 0 & 0 & 0 & 0 \\ 0 & 0 & 0 & 0 & 0 & -279.3 & 0 & 0 \\ 0 & 0 & 0 & 0 & 0 & 0 & 0 & 0 \\ 0 & 0 & 0 & 0 & 0 & 0 & 0 & -2713 \end{bmatrix}$$

142

$$
\left[\frac{\partial \underline{Z}}{\partial \hat{r}_3}\right]_0 =
\begin{bmatrix}
1000 & 0 & 0 & 0 & 0 & 0 & 0 & 0 \\
0 & 0 & 0 & 0 & 0 & 0 & 0 & 0 \\
0 & 0 & 1000 & 0 & 0 & 0 & 0 & 0 \\
0 & 0 & 0 & 0 & 0 & 0 & 0 & 0 \\
0 & 0 & 0 & 0 & 1000 & 0 & 0 & 0 \\
0 & 0 & 0 & 0 & 0 & 0 & 0 & 0 \\
0 & 0 & 0 & 0 & 0 & 0 & 1000 & 0 \\
0 & 0 & 0 & 0 & 0 & 0 & 0 & 0
\end{bmatrix}
$$

$$
\left[\frac{\partial \underline{Z}}{\partial \hat{r}_4}\right]_0 =
\begin{bmatrix}
1000 & -1000 & 0 & 0 & 0 & 0 & 0 & 0 \\
-1000 & 1000 & 0 & 0 & 0 & 0 & 0 & 0 \\
0 & 0 & 1000 & -1000 & 0 & 0 & 0 & 0 \\
0 & 0 & -1000 & 1000 & 0 & 0 & 0 & 0 \\
0 & 0 & 0 & 0 & 1000 & -1000 & 0 & 0 \\
0 & 0 & 0 & 0 & -1000 & 1000 & 0 & 0 \\
0 & 0 & 0 & 0 & 0 & 0 & 1000 & -1000 \\
0 & 0 & 0 & 0 & 0 & 0 & -1000 & 1000
\end{bmatrix}
$$

6. Generate the batch-stacked residual force sensitivity matrix using Eq.

    (3.115) with parameter contributions corresponding to columns of the final

    matrix:

$$
[\underline{N}]_0 = -
\begin{bmatrix}
-1.078 & 0 & 3.861 & -1.472 \\
0 & -1.490 & 0 & 1.472 \\
0.3168 & 0 & -1.342 & 0.4458 \\
0 & 0.4413 & 0 & -.4458 \\
6.448 & 0 & -2.376 & -3.782 \\
0 & -3.813 & 0 & 3.782 \\
6.160 & 0 & -2.270 & -3.621 \\
0 & -3.665 & 0 & 3.621
\end{bmatrix}
$$

7. Generate the quantity $[Q]_{i+1}$ using Eq. (3.122):

$$[Q]_1 = \begin{bmatrix} 7.826 \times 10^{-5} & 9.449 \times 10^{-5} & 5.282 \times 10^{-2} & 1.094 \times 10^{-2} \\ 9.449 \times 10^{-5} & 1.141 \times 10^{-4} & 6.377 \times 10^{-2} & 1.164 \\ 5.282 \times 10^{-2} & 6.377 \times 10^{-2} & 35.65 & 65.08 \\ 9.643 \times 10^{-2} & 1.164 & 65.08 & 118.8 \end{bmatrix}$$

8. Generate the updated damage parameter set using Eq. (3.121):

$$\{\hat{r}\}_1 = \begin{Bmatrix} 1.001 \\ 0.9908 \\ 900.5 \\ 1001 \end{Bmatrix}$$

9. Generate the absolute value damage parameter difference mean:

$$\langle \Delta \hat{r} \rangle_1 = mean \left| \begin{Bmatrix} 1.001 \\ 0.9908 \\ 900.5 \\ 1001 \end{Bmatrix} - \begin{Bmatrix} 0.9900 \\ 1.000 \\ 900.0 \\ 1000 \end{Bmatrix} \right| = 25.09$$

10. Check for parameter convergence:

$$\left(\langle \Delta \hat{r} \rangle_1 = 25.09 \right) > 0.0501$$

Decision: *Convergence not achieved, increment i and continue.*

Iteration 2 ($i = 1$):

1. Dynamic stiffness matrix at $\{r_1\}$ using Eq. (3.7):

$$[Z(\omega = 16.71)]_1 = \begin{bmatrix} 1622 + 66.85j & -1001 \\ -1001 & 724.1 + 1.671j \end{bmatrix}$$

$$[Z(\omega = 52.09)]_1 = \begin{bmatrix} -813.6 + 208.4j & -1001 \\ -1001 & -1687 + 5.209j \end{bmatrix}$$

2. Assemble batch-stacked dynamic stiffness matrix over all frequency lines:

$$[\underline{Z}]_1 = \begin{bmatrix} 1622 & -1001 & -66.85 & 0 & 0 & 0 & 0 & 0 \\ -1001 & 724.1 & 0 & -1.671 & 0 & 0 & 0 & 0 \\ 66.85 & 0 & 1622 & -1001 & 0 & 0 & 0 & 0 \\ 0 & 1.671 & -1001 & 724.1 & 0 & 0 & 0 & 0 \\ 0 & 0 & 0 & 0 & -813.6 & -1001 & -208.4 & 0 \\ 0 & 0 & 0 & 0 & -1001 & -1687 & 0 & -5.209 \\ 0 & 0 & 0 & 0 & 208.4 & 0 & -813.6 & -1001 \\ 0 & 0 & 0 & 0 & 0 & 5.209 & -1001 & -1687 \end{bmatrix}$$

3. Create batch-stacked residual force vector using Eq. (3.103):

$$\{\underline{R}\}_1 = \begin{Bmatrix} -2.439 \times 10^{-6} \\ 2.044 \times 10^{-6} \\ -1.053 \times 10^{-5} \\ 7.533 \times 10^{-6} \\ -4.180 \times 10^{-6} \\ -6.349 \times 10^{-6} \\ 2.999 \times 10^{-6} \\ 5.721 \times 10^{-6} \end{Bmatrix}$$

4. Create batch-stacked residual force covariance matrix using Eq. (3.104):

$$[\underline{S}_{RR}]_1 = \begin{bmatrix} 4228 & -2770 & -76.50 & -19.01 & 0 & 0 & 0 & 0 \\ -2770 & 1827 & 68.40 & -1.579 & 0 & 0 & 0 & 0 \\ -76.50 & 68.40 & 1068 & -679.4 & 0 & 0 & 0 & 0 \\ -19.01 & -1.579 & -679.4 & 435.9 & 0 & 0 & 0 & 0 \\ 0 & 0 & 0 & 0 & 2218 & 3405 & 119.6 & -59.23 \\ 0 & 0 & 0 & 0 & 3405 & 5359 & 213.2 & 11.47 \\ 0 & 0 & 0 & 0 & 119.6 & 213.2 & 474.2 & 627.2 \\ 0 & 0 & 0 & 0 & -59.23 & 11.47 & 627.2 & 937.9 \end{bmatrix} \times 10^{-10}$$

5. Generate batch-stacked dynamic stiffness sensitivity matrix for each damage parameter using the closed form expressions in Eqs. (3.226) to (3.229):

$$\left[\frac{\partial \underline{Z}}{\partial \hat{r}_1}\right]_1 = \begin{bmatrix} -279.3 & 0 & 0 & 0 & 0 & 0 & 0 & 0 \\ 0 & 0 & 0 & 0 & 0 & 0 & 0 & 0 \\ 0 & 0 & -2713 & 0 & 0 & 0 & 0 & 0 \\ 0 & 0 & 0 & 0 & 0 & 0 & 0 & 0 \\ 0 & 0 & 0 & 0 & -279.3 & 0 & 0 & 0 \\ 0 & 0 & 0 & 0 & 0 & 0 & 0 & 0 \\ 0 & 0 & 0 & 0 & 0 & 0 & -2713 & 0 \\ 0 & 0 & 0 & 0 & 0 & 0 & 0 & 0 \end{bmatrix}$$

$$\left[\frac{\partial \underline{Z}}{\partial \hat{r}_2}\right]_1 = \begin{bmatrix} 0 & 0 & 0 & 0 & 0 & 0 & 0 & 0 \\ 0 & -279.3 & 0 & 0 & 0 & 0 & 0 & 0 \\ 0 & 0 & 0 & 0 & 0 & 0 & 0 & 0 \\ 0 & 0 & 0 & -2713 & 0 & 0 & 0 & 0 \\ 0 & 0 & 0 & 0 & 0 & 0 & 0 & 0 \\ 0 & 0 & 0 & 0 & 0 & -279.3 & 0 & 0 \\ 0 & 0 & 0 & 0 & 0 & 0 & 0 & 0 \\ 0 & 0 & 0 & 0 & 0 & 0 & 0 & -2713 \end{bmatrix}$$

$$\left[\frac{\partial \underline{Z}}{\partial \hat{r}_3}\right]_1 = \begin{bmatrix} 1000 & 0 & 0 & 0 & 0 & 0 & 0 & 0 \\ 0 & 0 & 0 & 0 & 0 & 0 & 0 & 0 \\ 0 & 0 & 1000 & 0 & 0 & 0 & 0 & 0 \\ 0 & 0 & 0 & 0 & 0 & 0 & 0 & 0 \\ 0 & 0 & 0 & 0 & 1000 & 0 & 0 & 0 \\ 0 & 0 & 0 & 0 & 0 & 0 & 0 & 0 \\ 0 & 0 & 0 & 0 & 0 & 0 & 1000 & 0 \\ 0 & 0 & 0 & 0 & 0 & 0 & 0 & 0 \end{bmatrix}$$

$$\left[\frac{\partial \underline{Z}}{\partial \hat{r}_4}\right]_1 = \begin{bmatrix} 1000 & -1000 & 0 & 0 & 0 & 0 & 0 & 0 \\ -1000 & 1000 & 0 & 0 & 0 & 0 & 0 & 0 \\ 0 & 0 & 1000 & -1000 & 0 & 0 & 0 & 0 \\ 0 & 0 & -1000 & 1000 & 0 & 0 & 0 & 0 \\ 0 & 0 & 0 & 0 & 1000 & -1000 & 0 & 0 \\ 0 & 0 & 0 & 0 & -1000 & 1000 & 0 & 0 \\ 0 & 0 & 0 & 0 & 0 & 0 & 1000 & -1000 \\ 0 & 0 & 0 & 0 & 0 & 0 & -1000 & 1000 \end{bmatrix}$$

6. Generate batch-stacked residual force sensitivity matrix using Eq. (3.115)

with parameter contributions corresponding to columns of the final matrix:

$$[\underline{N}]_1 = - \begin{bmatrix} -1.078 & 0 & 3.861 & -1.472 \\ 0 & -1.490 & 0 & 1.472 \\ 0.3168 & 0 & -1.342 & 0.4458 \\ 0 & 0.4413 & 0 & -.4458 \\ 6.448 & 0 & -2.376 & -3.782 \\ 0 & -3.813 & 0 & 3.782 \\ 6.160 & 0 & -2.270 & -3.621 \\ 0 & -3.665 & 0 & 3.621 \end{bmatrix}$$

7. Generate the quantity $[Q]_{i+1}$ using Eq. (3.122):

$$[Q]_2 = \begin{bmatrix} 7.932 \times 10^{-5} & 9.671 \times 10^{-5} & 5.950 \times 10^{-5} & 9.771 \times 10^{-5} \\ 9.671 \times 10^{-5} & 1.179 \times 10^{-4} & 7.255 \times 10^{-5} & 1.191 \times 10^{-4} \\ 5.950 \times 10^{-5} & 7.255 \times 10^{-5} & 4.464 \times 10^{-5} & 7.330 \times 10^{-5} \\ 9.771 \times 10^{-5} & 1.191 \times 10^{-4} & 7.330 \times 10^{-5} & 1.204 \times 10^{-4} \end{bmatrix}$$

8. Generate the updated damage parameter set using Eq. (3.121):

$$\{\hat{r}\}_2 = \begin{Bmatrix} 1.001 \\ 0.9908 \\ 900.5 \\ 1001 \end{Bmatrix}$$

9. Generate the absolute value damage parameter difference mean:

$$\langle \Delta \hat{r} \rangle_2 = mean \left(\begin{Bmatrix} 1.001 \\ 0.9908 \\ 900.5 \\ 1001 \end{Bmatrix} - \begin{Bmatrix} 1.001 \\ 0.9908 \\ 900.5 \\ 1001 \end{Bmatrix} \right) = 5.122 \times 10^{-3}$$

10. Check for parameter convergence:

$$\left(\langle \Delta \hat{r} \rangle_1 = 5.122 \times 10^{-3} \right) < 0.0501$$

Decision: *Convergence achieved, break loop.*

Converged algorithm outputs:

- Iterations to convergence = 2

- Updated damage parameter values:

$$\{\hat{r}_d\} = \begin{Bmatrix} \hat{m}_1 \\ \hat{m}_2 \\ \hat{k}_1 \\ \hat{k}_2 \end{Bmatrix} = \begin{Bmatrix} 1.001 \\ 0.9908 \\ 900.5 \\ 1001 \end{Bmatrix}$$

- Updated damage parameter standard deviation values in terms of real units and percentage of original values:

$$\{\sigma_{\hat{r}_d}\} = \begin{Bmatrix} 8.906 \times 10^{-3} \\ 1.081 \times 10^{-2} \\ 2.004 \\ 3.470 \end{Bmatrix} = \begin{Bmatrix} 8.9\% \\ 11\% \\ 0.20\% \\ 0.35\% \end{Bmatrix},$$

- Damage correlated analytical model:

$$[M(\hat{r}_d)] = \begin{bmatrix} 0.9908 & 0.000 \\ 0.000 & 1.001 \end{bmatrix}$$

$$[K^*(\hat{r}_d)] = \begin{bmatrix} 1901 & -1001 \\ -1001 & 1001 \end{bmatrix}$$

$$[C(\hat{r}_d)] = \begin{bmatrix} 4.000 & 0.000 \\ 0.000 & 0.1000 \end{bmatrix}$$

- Updated parameter error compared to the known solution:

$$\frac{\{\tilde{r}_d\} - \{\hat{r}_d\}}{\{\tilde{r}_d\}} = \begin{Bmatrix} -0.069\% \\ -0.085\% \\ -0.058\% \\ -0.085\% \end{Bmatrix}$$

The correct damage parameter values are reached with low error in a single
iteration, with a second iteration required to verify convergence. Additionally, the update
results in an average of 50% reduction in uncertainty of all four damage parameter values
based on the initial assumptions on parameter and reference data variability.

Repeating the damage identification for the remaining damage cases produces
results as follows.

Heavy Viscous Damping Case:

Converged algorithm outputs:

- Iterations to convergence $= 2$

- Updated damage parameter values:

$$\{\hat{r}_d\} = \begin{Bmatrix} \hat{m}_1 \\ \hat{m}_2 \\ \hat{k}_1 \\ \hat{k}_2 \end{Bmatrix} = \begin{Bmatrix} 1.000 \\ 0.9900 \\ 900.0 \\ 1000 \end{Bmatrix}$$

- Updated damage parameter standard deviation values in terms of real units
  and percentage of original values:

$$\{\sigma_{\hat{r}_d}\} = \begin{Bmatrix} 1.211 \times 10^{-3} \\ 1.398 \times 10^{-3} \\ 2.648 \times 10^{-2} \\ 4.632 \times 10^{-2} \end{Bmatrix} = \begin{Bmatrix} 1.2\% \\ 1.4\% \\ 0.026\% \\ 0.046\% \end{Bmatrix}.$$

- Damage correlated analytical model:

$$[M(\hat{r}_d)] = \begin{bmatrix} 0.9900 & 0.000 \\ 0.000 & 1.000 \end{bmatrix}$$

$$[K^*(\hat{r}_d)] = \begin{bmatrix} 1900 & -1000 \\ -1000 & 1000 \end{bmatrix}$$

$$[C(\hat{r}_d)] = \begin{bmatrix} 40.00 & 0.000 \\ 0.000 & 1.000 \end{bmatrix}$$

- Updated parameter error compared to the known solution:

$$\frac{\{\tilde{r}_d\} - \{\hat{r}_d\}}{\{\tilde{r}_d\}} = \begin{Bmatrix} -0.0012\% \\ -0.0015\% \\ -0.0010\% \\ -0.0015\% \end{Bmatrix}.$$

Light Viscous plus Light Structural Damping with Increased Damping Case:

Converged algorithm outputs:

- Iterations to convergence = 3

- Updated damage parameter values:

$$\{\hat{r}_d\} = \begin{Bmatrix} \hat{m}_1 \\ \hat{m}_2 \\ \hat{k}_1 \\ \hat{k}_2 \\ \hat{\eta}_1 \\ \hat{\eta}_2 \end{Bmatrix} = \begin{Bmatrix} 1.001 \\ 0.9909 \\ 900.6 \\ 1001 \\ 0.02399 \\ 0.009991 \end{Bmatrix}$$

- Updated damage parameter standard deviation values in terms of real units and percentage of original values:

$$
\{\sigma_{\hat{r}_d}\} = \left\{ \begin{array}{c} 5.328 \times 10^{-3} \\ 6.433 \times 10^{-3} \\ 0.1195 \\ 0.2073 \\ 7.635 \times 10^{-4} \\ 6.639 \times 10^{-4} \end{array} \right\} = \left\{ \begin{array}{c} 5.3\% \\ 6.4\% \\ 0.12\% \\ 0.21\% \\ 38\% \\ 66\% \end{array} \right\}.
$$

- Damage correlated analytical model:

$$
[M(\hat{r}_d)] = \begin{bmatrix} 1.001 & 0.000 \\ 0.000 & 0.9909 \end{bmatrix}
$$

$$
\left[K^*(\hat{r}_d) \right] = \begin{bmatrix} 1902 + 31.60j & -1001 - 10.00j \\ -1001 - 10.00j & 1001 + 10.00j \end{bmatrix}
$$

$$
[C(\hat{r}_d)] = \begin{bmatrix} 4.000 & 0.000 \\ 0.000 & 0.1000 \end{bmatrix}
$$

- Updated parameter error compared to the known solution:

$$
\frac{\{\tilde{r}_d\} - \{\hat{r}_d\}}{\{\tilde{r}_d\}} = \left\{ \begin{array}{c} -0.077\% \\ -0.094\% \\ -0.064\% \\ -0.095\% \\ 0.059\% \\ 0.094\% \end{array} \right\}.
$$

Light Viscous plus Light Structural Damping with Decreased Damping Case:

Converged algorithm outputs:

- Iterations to convergence = 3

- Updated damage parameter values:

$$\{\hat{r}_d\} = \begin{Bmatrix} \hat{m}_1 \\ \hat{m}_2 \\ \hat{k}_1 \\ \hat{k}_2 \\ \hat{\eta}_1 \\ \hat{\eta}_2 \end{Bmatrix} = \begin{Bmatrix} 0.9999 \\ 0.9899 \\ 899.9 \\ 999.9 \\ 0.01600 \\ 0.01000 \end{Bmatrix}$$

- Updated damage parameter standard deviation values in terms of real units and percentage of original values:

$$\{\sigma_{\hat{r}_d}\} = \begin{Bmatrix} 5.178 \times 10^{-3} \\ 6.249 \times 10^{-3} \\ 0.1160 \\ 0.2015 \\ 3.889 \times 10^{-4} \\ 6.476 \times 10^{-4} \end{Bmatrix} = \begin{Bmatrix} 5.2\% \\ 6.2\% \\ 0.12\% \\ 0.20\% \\ 19\% \\ 65\% \end{Bmatrix}.$$

- Damage correlated analytical model:

$$[M(\hat{r}_d)] = \begin{bmatrix} 0.9999 & 0.000 \\ 0.000 & 0.9899 \end{bmatrix}$$

$$[K^*(\hat{r}_d)] = \begin{bmatrix} 1900 + 24.40j & -999.9 - 10.00j \\ -999.9 - 10.00j & 999.9 + 10.00j \end{bmatrix}$$

$$[C(\hat{r}_d)] = \begin{bmatrix} 4.000 & 0.000 \\ 0.000 & 0.1000 \end{bmatrix}$$

- Updated parameter error compared to the known solution:

$$\frac{\{\tilde{r}_d\} - \{\hat{r}_d\}}{\{\tilde{r}_d\}} = \begin{Bmatrix} 0.0082\% \\ 0.010\% \\ 0.0068\% \\ 0.010\% \\ -0.0065\% \\ -0.0097\% \end{Bmatrix}.$$

Comparing the results shows successful damage identification for all damage and damping cases, with parameter errors ranging in magnitude from 0.0010% to 0.085%. The non-zero error is primarily a result of the regularization produced by the non-zero ratio of reference data variability to initial parameter variability. If the assumed reference data standard deviation is decreased by a factor of 100 for the light viscous plus light structural damping with increased damping case, the updated parameter error can be seen to decrease by a factor of 100^2 to

$$\frac{\{\tilde{r}_d\} - \{\hat{r}_d\}}{\{\tilde{r}_d\}} = \begin{Bmatrix} -0.0000078\% \\ -0.0000096\% \\ -0.0000065\% \\ -0.0000096\% \\ 0.0000061\% \\ 0.0000096\% \end{Bmatrix}.$$

For an idealized analytical case such as the current 2-degree-of-freedom mass spring

system this trend will continue until machine noise leads to instability from ill-

conditioning during inversion of the residual force covariance matrix.

3.8.4 Approximate Modeling of Generalized Viscous Damping

In the above example it is assumed that the true generalized damping matrix is

known; however, for physical structures this is usually not the case. Whereas mass and

stiffness matrices can be accurately assigned based on knowledge of the structure

geometry and materials, the damping matrix will be more sensitive to loading, operating

regime, environment, and properties that cannot be easily measured such as friction in

structural joints. Sophisticated methods exist for identifying generalized damping

matrices (e.g. as presented in reference [3-15]), but for many structures simple

proportional damping approximations may offer acceptable accuracy for frequency

response function based damage identification.

As discussed in Section 3.2, Rayleigh damping creates a viscous damping matrix

proportional to the global mass matrix, global stiffness matrix, or a summation of both.

The proportionality constants are selected to match selected modal damping ratios. To

reiterate from Section 3.2, the basic Rayleigh equations are

$$[C] = \alpha[K] + \beta[M], \qquad (3.28)$$

and

$$\zeta_n = \frac{1}{2}\left(\alpha\omega_n + \frac{\beta}{\omega_n}\right), \tag{3.30}$$

and proportionality constants α and β are solved for given values of ζ_n and ω_n. For

damping proportional to only the stiffness matrix the constants equal

$$\alpha_{K,n} = \frac{2\zeta_n}{\omega_n}$$
$$\beta_{K,n} = 0 \tag{3.234}$$

where n refers to a single mode that must be selected to be matched. The corresponding

viscous damping matrix is equal to

$$\left[C_{K,n}\right] = \frac{2\zeta_n}{\omega_n}\left[K\right]. \tag{3.235}$$

For damping proportional to only the mass matrix and also referencing a single mode n

the constants equal

$$\alpha_{M,n} = 0$$
$$\beta_{M,n} = 2\zeta_n\omega_n. \tag{3.236}$$

The corresponding viscous damping matrix for this case is equal to

$$\left[C_{M,n}\right] = 2\zeta_n\omega_n\left[M\right]. \tag{3.237}$$

For damping proportional to a combination of both the mass and stiffness matrices, Eq.

(3.30) can be written once for each of two modes, m and n, and solved simultaneously to

produce α and β as

$$\alpha_{Rayleigh} = \frac{2\omega_m\omega_n}{\omega_m^2 + \omega_n^2}\left(\frac{\zeta_m}{\omega_n} - \frac{\zeta_n}{\omega_m}\right) \tag{3.238}$$

$$\beta_{Rayleigh} = \frac{2\omega_m\omega_n}{\omega_m^2 + \omega_n^2}\left(\omega_m\zeta_n - \omega_n\zeta_m\right). \tag{3.239}$$

The viscous damping matrix is then equal to

$$\left[C_{Rayleigh}\right] = \frac{2\omega_m\omega_n}{\omega_m^2 + \omega_n^2}\left(\left(\frac{\zeta_m}{\omega_n} - \frac{\zeta_n}{\omega_m}\right)[K] + \left(\omega_m\zeta_n - \omega_n\zeta_m\right)[M]\right). \tag{3.240}$$

To study the accuracy of using proportional approximations for generalized damping the light viscous damping case was modeled using stiffness proportional damping based on mode 1 (denoted 'K,1'), stiffness proportional damping based on mode 2 (denoted 'K,2'), mass proportional damping based on mode 1 (denoted 'M,1'), mass matrix proportional damping based on mode 2 (denoted 'M,2'), and full stiffness and mass proportional Rayleigh damping based on modes 1 and 2 (denoted '$Rayleigh$'). Results with proportionality factors, viscous damping matrices, modal damping ratios and damped natural frequencies are presented alongside the correct generalized damping results (denoted '$Correct$') as follows:

1) *Correct generalized damping:*

$$[C_{Correct}] = \begin{bmatrix} 4.000 & 0.000 \\ 0.000 & 0.1000 \end{bmatrix} \tag{3.241}$$

$$\begin{aligned} (\zeta_1)_{Correct} &= 0.4077 \\ (\zeta_2)_{Correct} &= 0.09750 \end{aligned}. \tag{3.242}$$

$$\left(\omega_1^{damped}\right)_{Correct} = 19.55 \text{ rad/s (3.111 Hz)}$$
$$\left(\omega_2^{damped}\right)_{Correct} = 51.11 \text{ rad/s (8.135 Hz)} \ . \tag{3.243}$$

2) *Stiffness proportional damping based on mode 1:*

$$\alpha_{K,1} = 0.003083$$
$$\beta_{K,1} = 0 \tag{3.244}$$

$$\left[C_{K,1}\right] = \begin{bmatrix} 6.166 & -3.083 \\ -3.083 & 3.083 \end{bmatrix} \tag{3.245}$$

$$\left(\zeta_1\right)_{K,1} = 0.03015$$
$$\left(\zeta_2\right)_{K,1} = 0.02856 \ . \tag{3.246}$$

$$\left(\omega_1^{damped}\right)_{K,1} = 19.54 \text{ rad/s (3.109 Hz)}$$
$$\left(\omega_2^{damped}\right)_{K,1} = 51.01 \text{ rad/s (8.118 Hz)} \ . \tag{3.247}$$

3) *Stiffness proportional damping based on mode 2:*

$$\alpha_{K,2} = 0.001117$$
$$\beta_{K,2} = 0 \tag{3.248}$$

$$\left[C_{K,2}\right] = \begin{bmatrix} 2.234 & -1.117 \\ -1.117 & 1.117 \end{bmatrix} \tag{3.249}$$

$$\left(\zeta_1\right)_{K,2} = 0.01092$$
$$\left(\zeta_2\right)_{K,2} = 0.02858 \ . \tag{3.250}$$

$$\left(\omega_1^{damped}\right)_{K,2} = 19.54 \text{ rad/s (3.110 Hz)}$$
$$\left(\omega_2^{damped}\right)_{K,2} = 51.15 \text{ rad/s (8.140 Hz)} \ . \tag{3.251}$$

4) *Mass proportional damping based on mode 1:*

$$\alpha_{M,1} = 0$$
$$\beta_{M,1} = 1.179 \tag{3.252}$$

$$\left[C_{M,1} \right] = \begin{bmatrix} 1.179 & 0.000 \\ 0.000 & 1.179 \end{bmatrix} \tag{3.253}$$

$$\left(\zeta_1 \right)_{M,1} = 0.03017$$
$$\left(\zeta_2 \right)_{M,1} = 0.01152 \tag{3.254}$$

$$\left(\omega_1^{damped} \right)_{M,1} = 19.54 \text{ rad/s (3.109 Hz)}$$
$$\left(\omega_2^{damped} \right)_{M,1} = 51.16 \text{ rad/s (8.143 Hz)} \tag{3.255}$$

5) *Mass proportional damping based on mode 2:*

$$\alpha_{M,2} = 0$$
$$\beta_{M,2} = 2.921 \tag{3.256}$$

$$\left[C_{M,2} \right] = \begin{bmatrix} 2.921 & 0.000 \\ 0.000 & 2.921 \end{bmatrix} \tag{3.257}$$

$$\left(\zeta_1 \right)_{M,2} = 0.07473$$
$$\left(\zeta_2 \right)_{M,2} = 0.02854 \tag{3.258}$$

$$\left(\omega_1^{damped} \right)_{M,2} = 19.49 \text{ rad/s (3.102 Hz)}$$
$$\left(\omega_2^{damped} \right)_{M,2} = 51.15 \text{ rad/s (8.140 Hz)} \tag{3.259}$$

6) *Rayleigh damping based on modes 1 and 2:*

$$\alpha_{Rayleigh} = -0.0007804$$
$$\beta_{Rayleigh} = 0.8807 \tag{3.260}$$

$$\left[C_{Rayleigh} \right] = \begin{bmatrix} 2.441 & -0.7804 \\ -0.7804 & 1.661 \end{bmatrix} \qquad (3.261)$$

$$\begin{aligned} (\varsigma_1)_{Rayleigh} &= 0.03016 \\ (\varsigma_2)_{Rayleigh} &= 0.02857 \end{aligned} \qquad (3.262)$$

$$\begin{aligned} \left(\omega_1^{damped} \right)_{Rayleigh} &= 19.54 \text{ rad/s (3.109 Hz)} \\ \left(\omega_2^{damped} \right)_{Rayleigh} &= 51.15 \text{ rad/s (8.140 Hz)} \end{aligned} \qquad (3.263)$$

The modal damping ratios produced by the proportional damping approximations are summarized in Figure 3-15 and a comparison of the frequency response functions resulting from using each method are given in terms of real and imaginary components in Figure 3-16 and Figure 3-17 and in terms of magnitude and phase in Figure 3-18 and Figure 3-19.

Several conclusions can be drawn from these results. Firstly, all of the methods do a good job of modeling the damping ratios for the modes that they are based on. For the single mode methods, the mass-only cases produce reasonable values for the modes that were not modeled compared to the stiffness-only cases which diverge significantly, producing modal damping ratios off by an order of magnitude. Secondly, both the mass-only and stiffness-only methods show noticeable frequency response function error away from the range of the matched mode. Finally, the Rayleigh damping case with both stiffness and mass proportionality fares the best overall—as expected because of the ability to fit both modes—producing low modal damping ratio error and a reasonable approximation of the frequency response functions around both natural frequencies.

However, there is noticeable frequency response function error away from the peaks. It

should be noted that this generalized damping case is severely non-proportional and so

these results are reasonable overall.
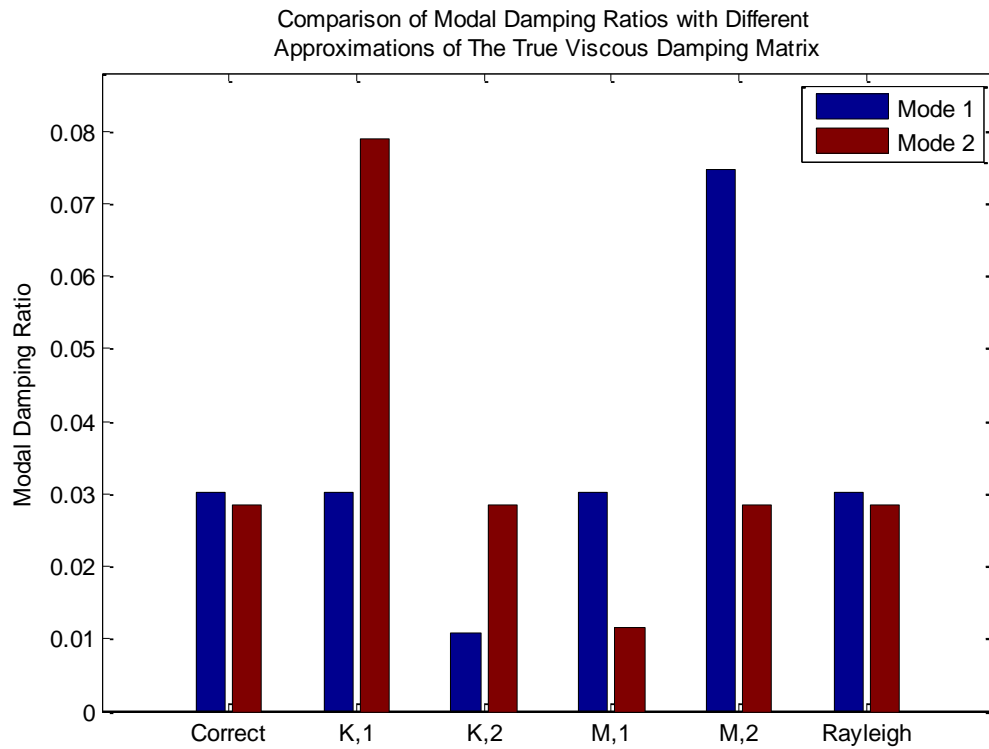
Figure 3-15: Summary of modal damping ratios produced by approximate proportional damping methods compared to the correct values from the generalized damping matrix.
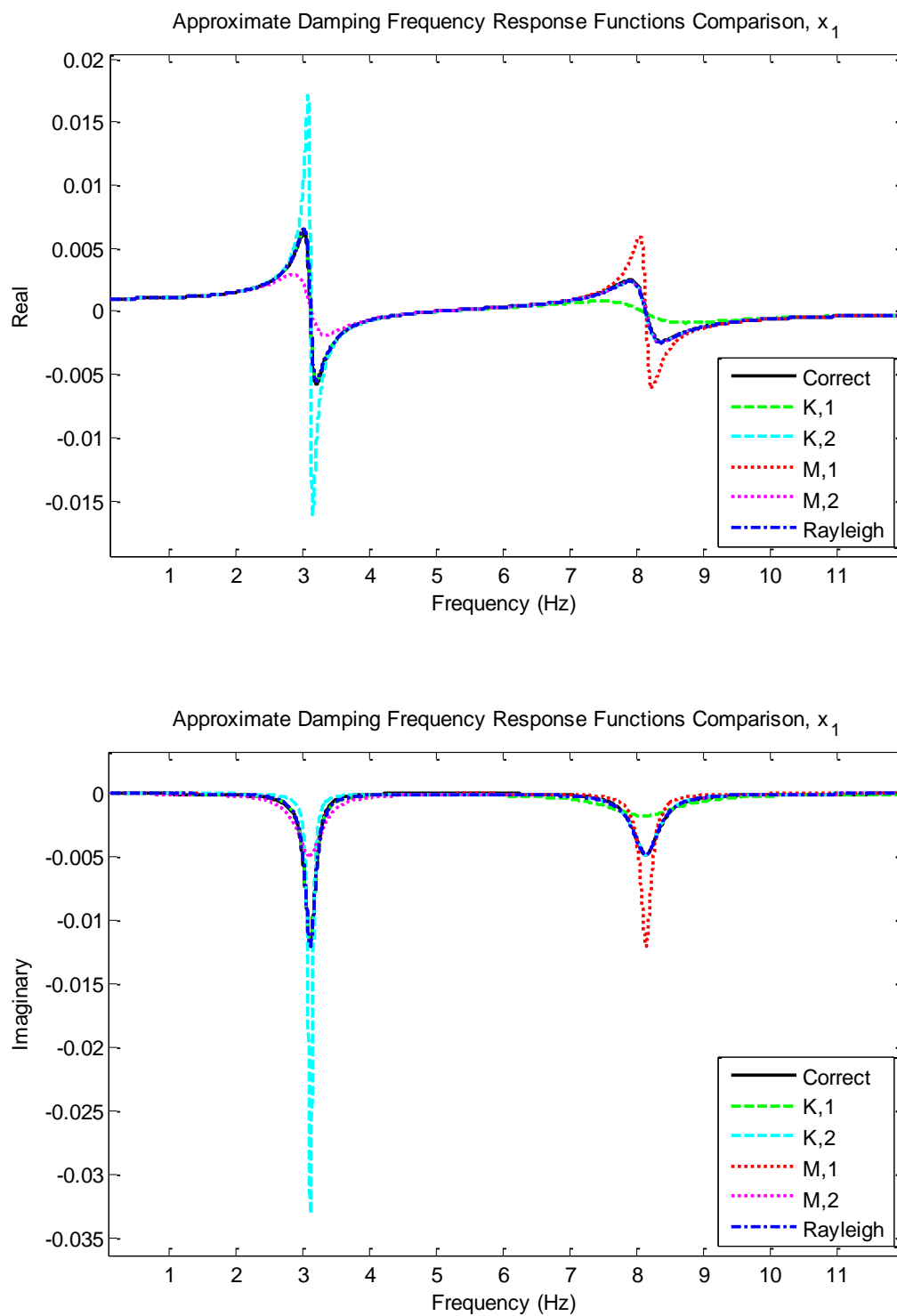
Figure 3-16: Comparison of frequency response functions produced by different approximate proportional damping methods and the correct generalized damping matrix, x_1 (real and imaginary).
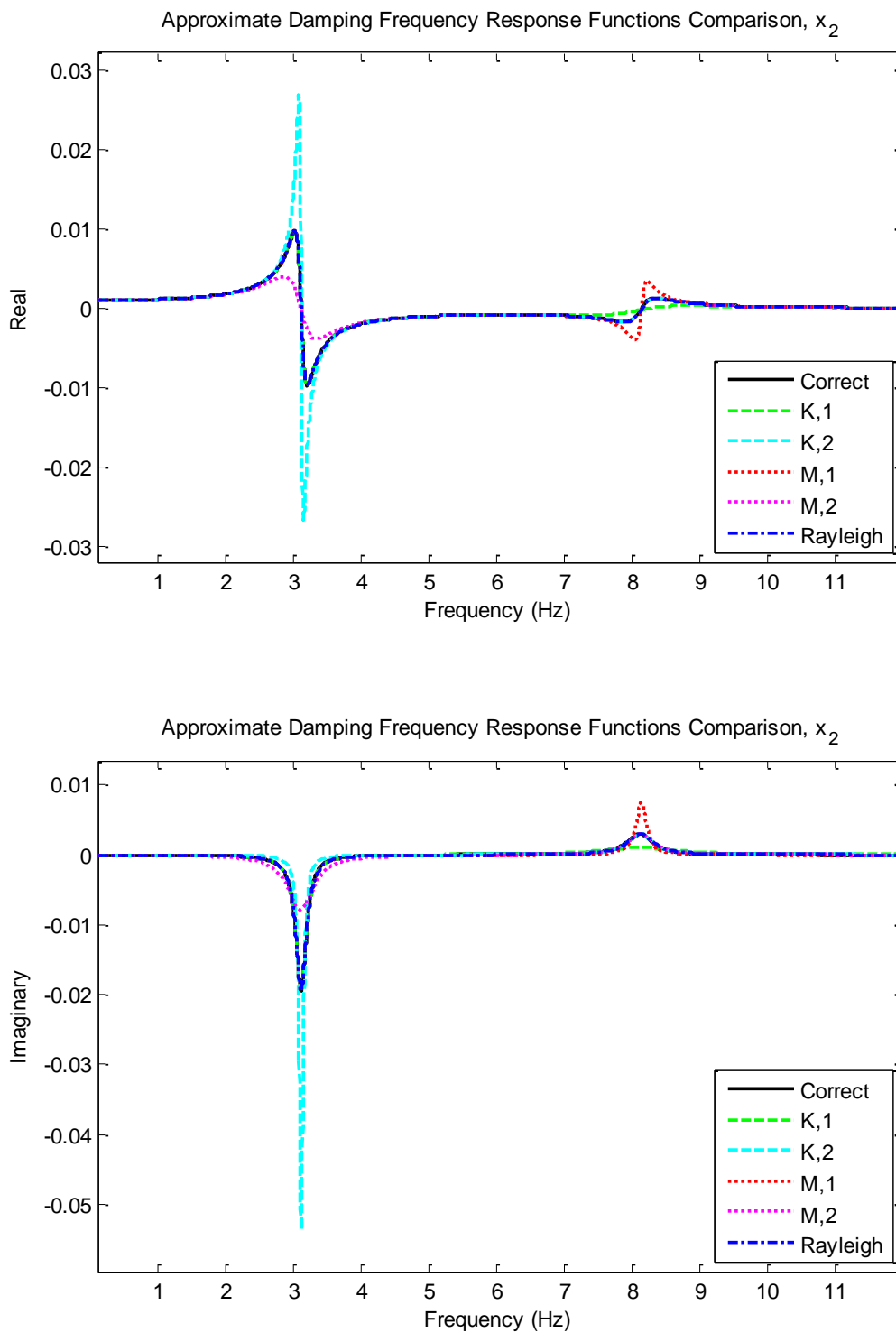
Figure 3-17: Comparison of frequency response functions produced by different approximate proportional damping methods and the correct generalized damping matrix, x_2 (real and imaginary).
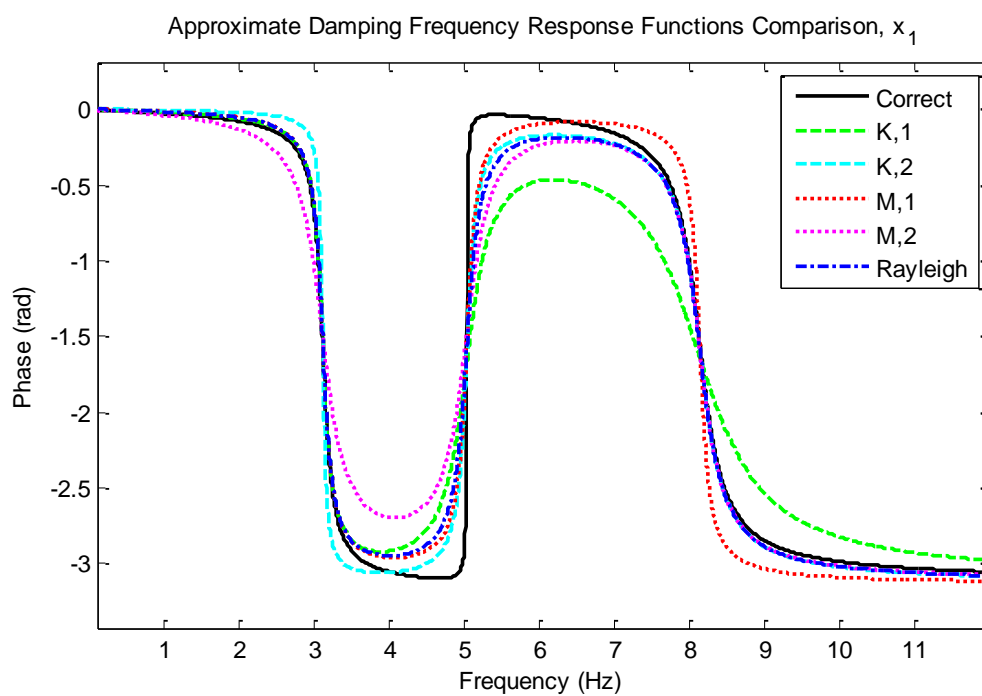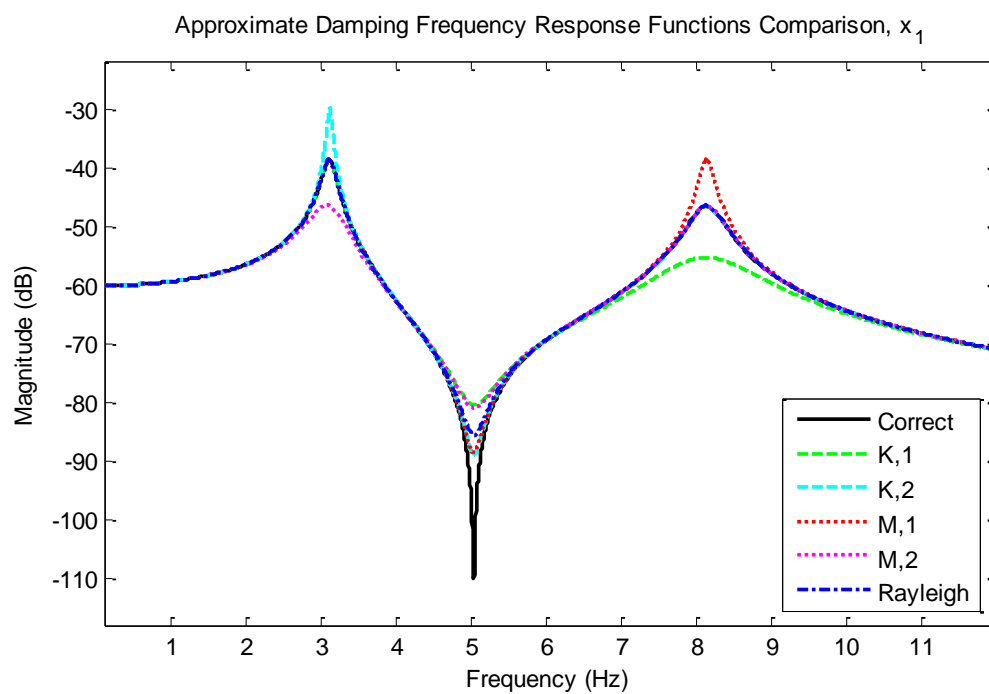
Figure 3-18: Comparison of frequency response functions produced by different approximate proportional damping methods and the correct generalized damping matrix, x_1 (magnitude and phase).
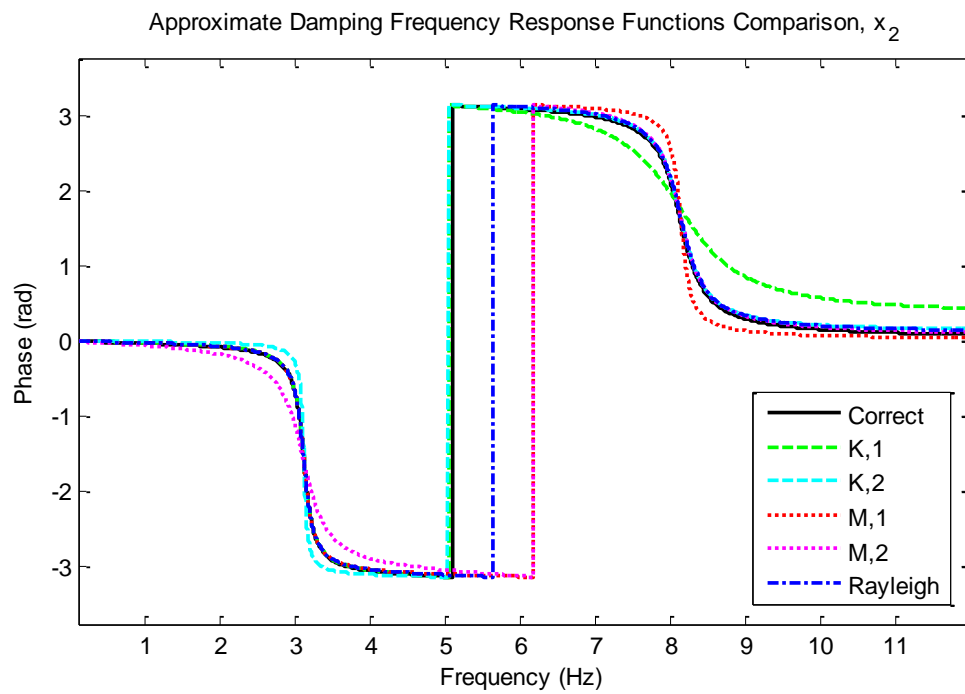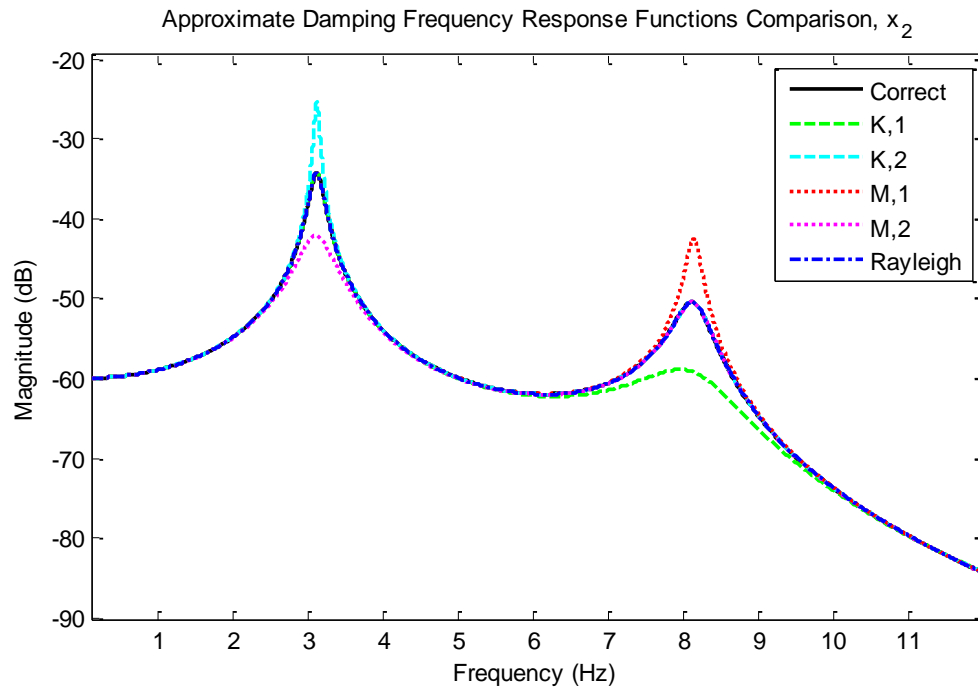
Figure 3-19: Comparison of frequency response functions produced by different approximate proportional damping methods and the correct generalized damping matrix, x_2 (magnitude and phase).

As a final check on the efficacy of using proportional damping to approximate

generalized damping, damage identification is run using the heavy viscous damping

damage case with Rayleigh damping. To simulate a physical situation, the reference

frequency response function data from the damaged system are created using the true

generalized damping matrix but only the mass matrix, stiffness matrix, natural

frequencies, mode shapes, and damping ratios are considered known for the analytical

system. The Rayleigh damping approximation is then formulated and implemented

within the analytical system in place of the true generalized damping matrix to create the

analytical dynamic stiffness matrix at each iteration.

For the first damage identification run, all algorithm parameters are set equal to

their values from the light viscous damping case in Section 3.8.3, including the use of

$N_\omega = 2$ analysis frequency lines at 16.71 rad/s (2.66 Hz) and 52.09 rad/s (8.29 Hz). The

damage identification algorithm fails to converge in this case, oscillating around two

extreme points until the iterations time out.

However, if the damage identification is performed using $N_\omega = 10$ frequency

lines distributed evenly over the frequency domain (0.1 Hz to 12.0 Hz) and all other

parameters unchanged convergence is reached after 3 iterations with the results

- Updated damage parameter values:

$$
\{\hat{r}_d\} = \begin{Bmatrix} \hat{m}_1 \\ \hat{m}_2 \\ \hat{k}_1 \\ \hat{k}_2 \end{Bmatrix} = \begin{Bmatrix} 0.9926 \\ 0.9909 \\ 899.9 \\ 992.8 \end{Bmatrix}
$$

- Updated parameter error compared to the known solution:

$$
\frac{\{\tilde{r}_d\} - \{\hat{r}_d\}}{\{\tilde{r}_d\}} = \begin{Bmatrix} -0.74\% \\ -0.087\% \\ 0.014\% \\ 0.72\% \end{Bmatrix}.
$$

These results include non-negligible error, especially in the two undamaged parameters included in the update. However, it can be seen that the general form of the damaged system is captured well even in the face of initial frequency response function error from the approximate damping model. The improvement from the initial $N_\omega = 2$ case occurs because increasing the number of frequency lines causes the frequency response function error to be averaged out. The result is that the updated system is forced to adhere closer to the true damaged frequency response function form. As can be seen in Figure 3-20 and Figure 3-21, the updated frequency response functions are very similar to the damaged reference data, with only small errors visible.
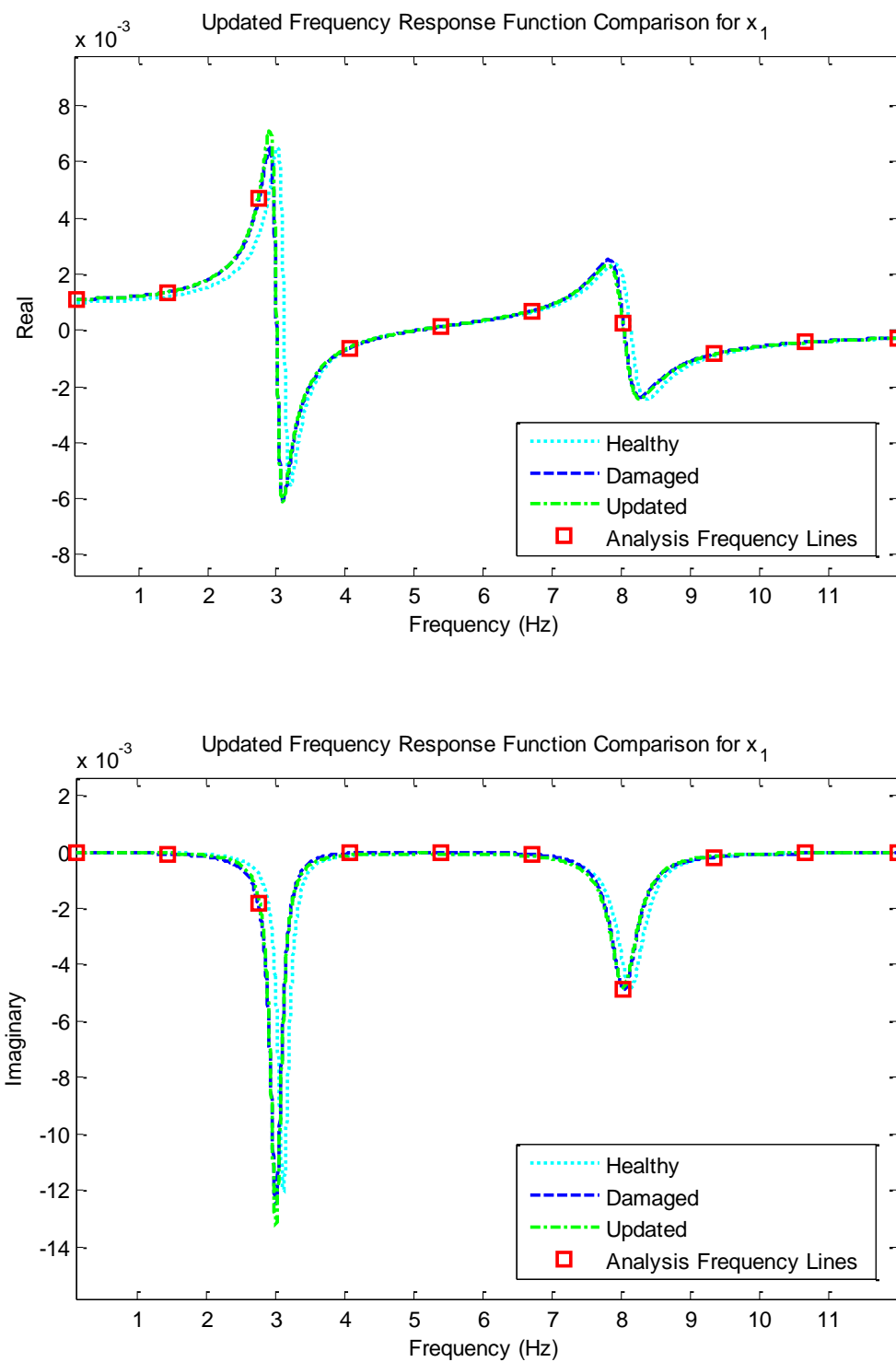
Figure 3-20: Comparison of frequency response functions for the Rayleigh damping damage identification case with $N_\omega = 10$, x_1.
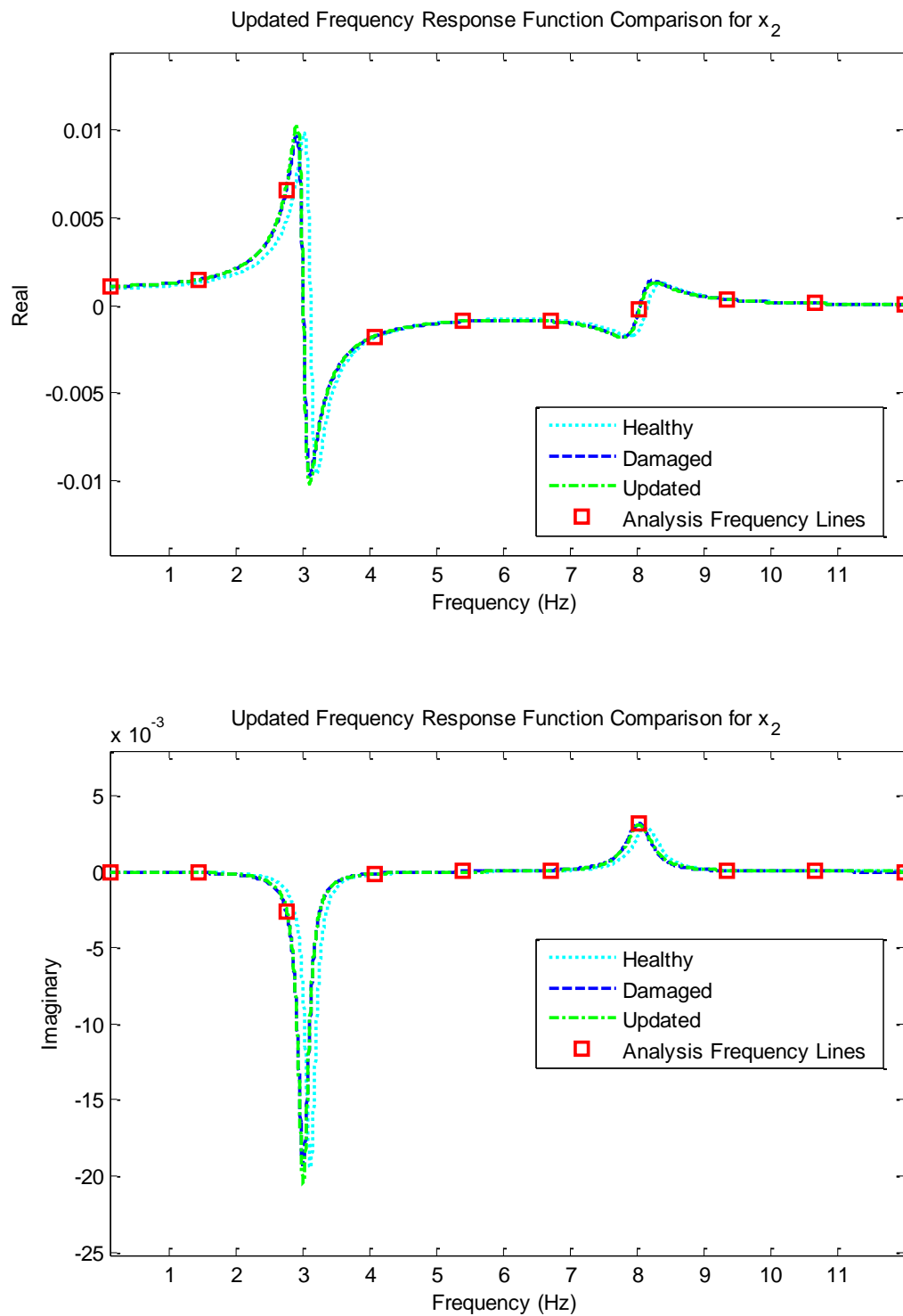
Figure 3-21: Comparison of frequency response functions for the Rayleigh damping damage identification case with $N_\omega = 10$, x_2.

For a final run, the $N_\omega = 10$ case is repeated with the four damping matrix components $C_{1,1}$, $C_{1,2}$, $C_{2,1}$, and $C_{2,2}$, included as damage parameters during the update. The damping matrix components must be used instead of the viscous damping coefficients c_A and c_B in order to allow correction of the off-diagonal matrix terms which are non-zero in the approximate Rayleigh damping matrix. The four damping matrix components have sensitivities as follows:

$$\left[\frac{\partial Z(\omega_k)}{\partial C_{1,1}} \right]_i = \begin{bmatrix} j\omega_k & 0 \\ 0 & 0 \end{bmatrix}, \tag{3.264}$$

$$\left[\frac{\partial Z(\omega_k)}{\partial C_{1,2}} \right]_i = \begin{bmatrix} 0 & j\omega_k \\ 0 & 0 \end{bmatrix}, \tag{3.265}$$

$$\left[\frac{\partial Z(\omega_k)}{\partial C_{2,1}} \right]_i = \begin{bmatrix} 0 & 0 \\ j\omega_k & 0 \end{bmatrix}, \tag{3.266}$$

$$\left[\frac{\partial Z(\omega_k)}{\partial C_{2,2}} \right]_i = \begin{bmatrix} 0 & 0 \\ 0 & j\omega_k \end{bmatrix}, \tag{3.267}$$

The damage identification algorithm is in this case able to correct the damping model and converge with negligible error to the damaged parameters values, with the results

- Updated damage parameter values:

$$
\{\hat{r}_d\} = \begin{Bmatrix} \hat{m}_1 \\ \hat{m}_2 \\ \hat{k}_1 \\ \hat{k}_2 \\ \hat{C}_{1,1} \\ \hat{C}_{1,2} \\ \hat{C}_{2,1} \\ \hat{C}_{2,2} \end{Bmatrix} = \begin{Bmatrix} 0.9900 \\ 1.000 \\ 900.0 \\ 1000 \\ 4.000 \\ -2.262\times10^{-4} \\ 1.012\times10^{-5} \\ 0.1003 \end{Bmatrix}
$$

- Updated parameter error compared to the known solution (N/A denotes a quantity that cannot be calculated because of division by zero):

$$
\frac{\{\tilde{r}_d\}-\{\hat{r}_d\}}{\{\tilde{r}_d\}} = \begin{Bmatrix} -0.000047\% \\ -0.000067\% \\ -0.000020\% \\ -0.000075\% \\ -0.00062\% \\ \text{N/A} \\ \text{N/A} \\ -0.25\% \end{Bmatrix}.
$$

The frequency response function comparisons given in Figure 3-22 and Figure 3-23 confirm that the updated analytical system accurately matches the damaged system.
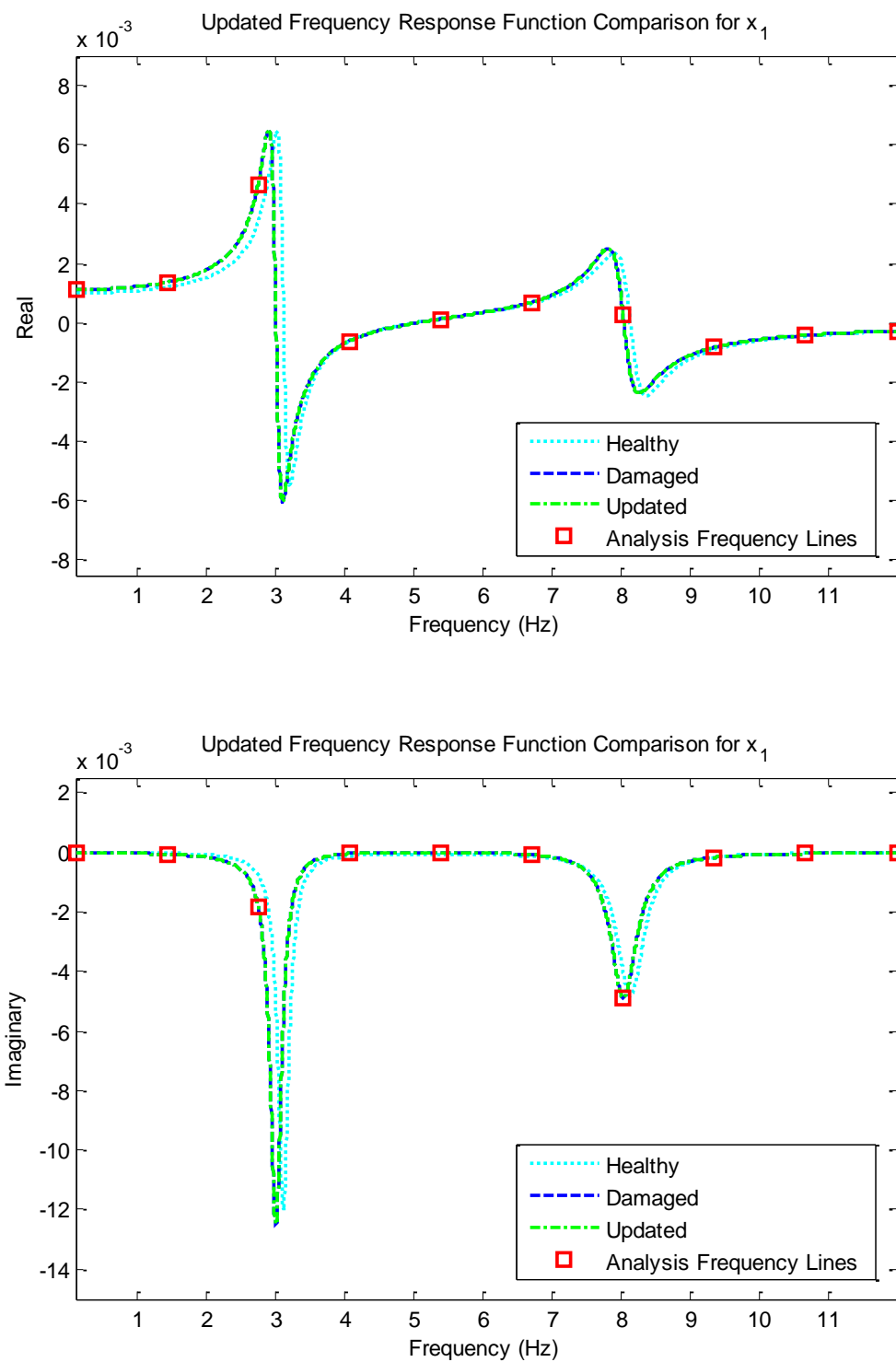
Figure 3-22: Comparison of frequency response functions for the Rayleigh damping damage identification case with $N_\omega = 8$ and damping parameters included in update, x_1.
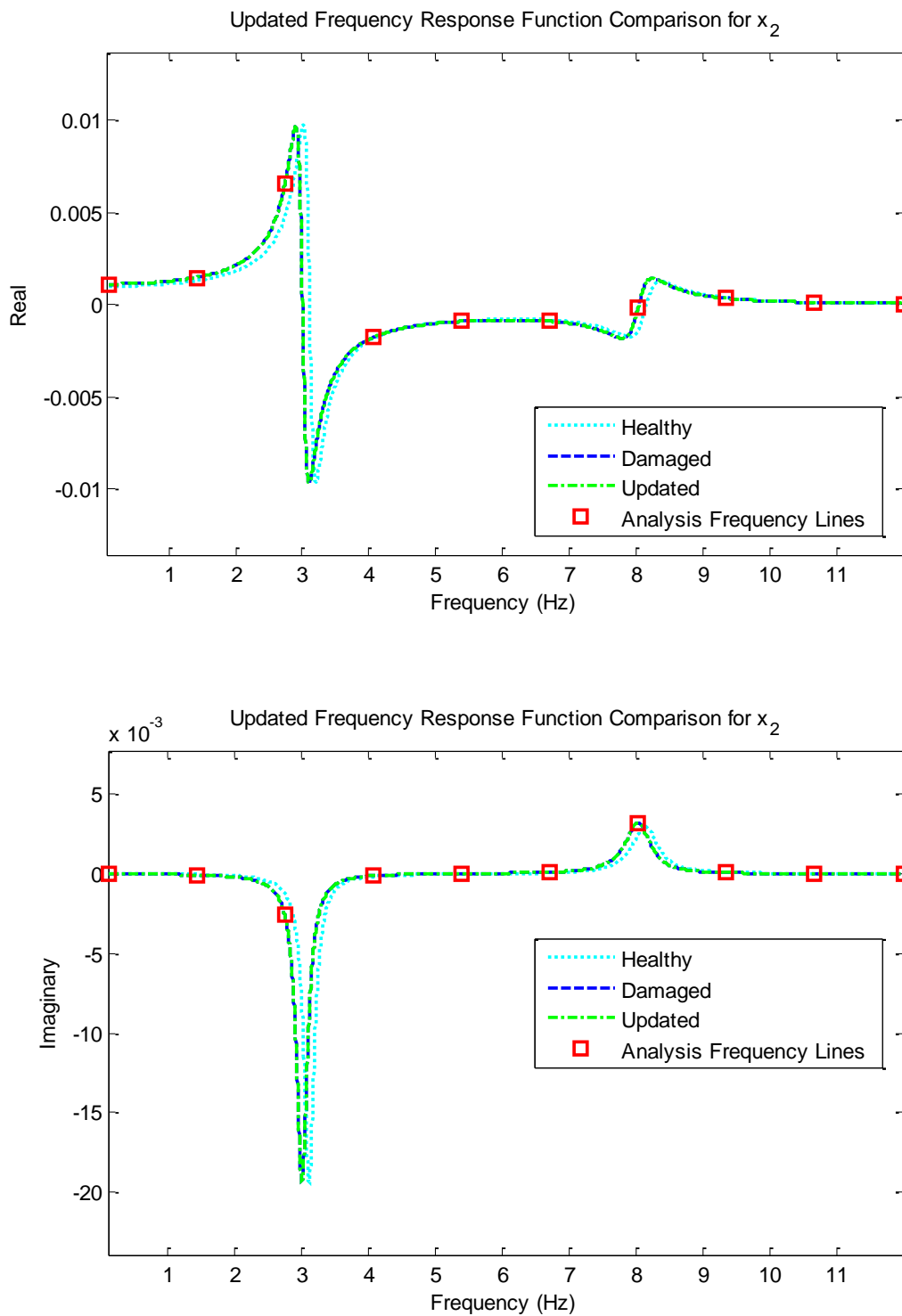
Figure 3-23: Comparison of frequency response functions for the Rayleigh damping damage identification case with $N_\omega = 8$ and damping parameters included in update, x_2.

3.8.5 Discussion

The presented example shows that the basic damage identification algorithm is capable of accurately identifying damage on an analytical 2 degree-of-freedom mass-spring system with combinations of structural and generalized viscous damping. The damage cases presented include a small decrease in mass plus a larger decrease in stiffness with the addition of increases and decreases in structural damping for the problems when structural damping is present, all of which are identified with negligible error when the underlying damping is known. Because of the difficulty in determining generalized viscous damping matrices in physical structures, the example additionally addresses the impact of using simple proportional damping models in place of underlying damping which is severely non-proportional. For the system with light viscous damping, results show that Rayleigh damping model for two modes recreates the desired modal damping ratios well but causes non-negligible error in the frequency response functions. Damage identification performed using the proportional Rayleigh damping model in the analytical system and reference data from the non-proportionally damped damaged system produces erroneous results for the baseline case with two analysis frequency lines. However, when the number of frequency lines is increased the identification error becomes small and when the damping model parameters are included as update parameters the algorithm correctly identifies the damaged parameters with negligible error.

The example provided in this section is idealized, with zero noise and simulated reference data from the damaged system provided for all degrees-of-freedom. As a result the problems presented are linear—meaning the converged solutions generally be reached in a single iteration—with numerical round-off error being the only corrupting influence. Physical damage identification problems are more complicated with more corrupting influences. However, the example presented successfully demonstrates several key points:

(1)   The basic mechanics of the damage identification algorithm function as expected with negligible error.

(2)   The damage identification algorithm can be applied to systems with combinations of generalized viscous damping and structural damping.

(3)   The damage identification algorithm can be applied to systems with concurrent damage changes in stiffness, mass, and damping.

(4)   Moderate levels of non-proportional viscous damping in the reference system can be modeled using approximate proportional methods with acceptable levels of error for damage identification.

(5)   In the case of severely non-proportional viscous damping, assuming proportional damping will lead to corruption in the damage predictions. The algorithm contains features to help mitigate this error, however, including the ability to average out the modeling error by adding analysis frequency lines and the ability to include damping parameters into the update

parameter set and thereby correct the damping model during damage

identification.

The material contained in Chapter 3 was developed in collaboration with Prof. John B. Kosmatka, Prof. Charles Farrar, and Prof. Joel Conte. The dissertation author was the primary investigator and author of this work.

3.9   **Chapter 3 References**

[3-1]   Caughey, T.K., O'Kelly, M.E.J., "Classical Normal Modes in Damped Linear Dynamic Systems", *Journal of Applied Mechanics*, **32**(3), pp.583-588 (1965)

[3-2]   Clough, R.W., Penzien, J., Dynamics of Structures, Second Edition, McGraw Hill, 1993

[3-3]   Hurty, W.C., Rubenstein, M.F., Dynamics of Structures, Prentice-Hall, 1964

[3-4]   He, J., Fe, Z.-F., Modal Analysis, Butterworth-Heinemann, 2001

[3-5]   Kidder, R., "Reduction of Structural Frequency Equations," *AIAA Journal*, **11**(6), (1973)

[3-6]   Guyan, R.J., "Reduction of stiffness and mass matrices," *AIAA Journal*, **3**, pp. 380, (1965)

[3-7]   Martinez, D.R., "Estimation Theory Applied to Improving Structural Dynamics Models," *Sandia National Laboratory Report* SAND82-0572, (1982)

[3-8]   Tarantola, A., Valette, B., "Generalized Nonlinear Inverse Problems Solved Using the Least Squares Criterion," *Reviews of Geophysics and Space Physics*, 20(2), (1982)

[3-9]   Gura, I.A., "Extension of Linear Estimation Techniques to Nonlinear Problems," *Journal of the Astronautical Sciences*, **15**(4) **,** pp.194-205, (1968)

[3-10]   Hemez, F.H., Doebling, S.W., "A Validation of Bayesian Finite Element Model Updating for Linear Dynamics," *17th International Modal Analysis Conference (IMAC)*, Kissimmee, Florida, February 8-11, (1999)

[3-11]   Martinez, D.R., "Parameter Estimation in Structural Dynamics Models," *Ph.D. Dissertation, University of California, Los Angeles*, (1979)

[3-12]   Lin, R.M., Ewins, D.J., "Analytical model improvement using frequency response functions," *Mechanical Systems and Signal Processing*, 8(4), pp.437-458, (1994)

[3-13]   Imregun, M., Visser, V.J., Ewins, D.J., "Finite Element Model Updating Using Frequency Response Function Data—I. Theory and Initial Investigation," *Mechanical Systems and Signal Processing*, **9**(2), pp. 187-202, (1995)

[3-14]   Lin, Lim, "Relationship between Improved Inverse Eigensensitivity and frequency response function Sensitivity Methods for Analytical Model Updating," *Journal of Vibration and Acoustics*, **119**(3), pp. 354-362, (1997)

[3-15]   Napolitano, K., Kosmatka, J.B., "Damage detection of highly damped structures using direct frequency response measurements and residual force vectors," *Proceedings of SPIE*, **2720**, pp. 110-121, (1996)

[3-16]   Adhikari, S., "Damping Models for Structural Vibration," *Ph.D. Dissertation, Cambridge University*, (2000)

4 BASIC IMPLEMENTATION AND VALIDATION WITH NOISE

In addition to the main algorithm equations there are several considerations of implementation which contribute to damage identification effectiveness, especially related to dealing with experimental frequency response reference data and noise. Frequency filtering and measurement noise quantification are discussed in Sections 4.1 and 4.2, followed by a discussion of reference data domain type in Section 4.3. Further validation studies are then performed on an 8 degree-of-freedom damped mass-spring system with added noise in Section 4.4, including comparison to several competing damage identification algorithms.

4.1 **Reference Data and Frequency Line Filtering**

Experimental frequency response functions are usually generated from measured time series over a large number of frequency lines (typically in the thousands), either in the domains of displacement, velocity, or acceleration. Although other options are available, it is often beneficial for experimental vibration data to calculate the H_1 system transfer function estimate and coherence estimate at each data point. In terms of acceleration data, the H_1 frequency response function $\tilde{a}(\omega_k)$ is calculated from measured input and output power-spectrum estimates, $\hat{G}_{xx}(\omega_k)$ and $\hat{G}_{yy}(\omega_k)$ at each measurement point, by

$$\tilde{a}(\omega_k) = \frac{\hat{G}_{xy}(\omega_k)}{\hat{G}_{xx}(\omega_k)},$$ (4.1)

and the coherence $\gamma^2_{xy}(\omega_k)$ is found using

$$\hat{\gamma}^2_{xy}(\omega_k) = \frac{\left|\hat{G}_{xy}(\omega_k)\right|^2}{\hat{G}_{xx}(\omega_k)\hat{G}_{yy}(\omega_k)}.$$ (4.2)

Velocity and displacement data is equivalently converted using the same forms with the only difference being the notation and units.

Although one of the strengths of frequency response based damage identification methods (as compared to modal parameter based methods) is the large amount of data which can be used, it is not advisable, or even possible, to perform damage identification with all available frequency lines. A subset must therefore be selected for the damage identification process. There are four main considerations in selecting frequency lines which help produce accurate solutions while minimizing computational expense. Firstly, the frequency lines should be in regions which promote accuracy with respect to sensitivities and residual force vectors. This usually means they should be in frequency regions with high response—i.e., close to peaks, or at least avoiding flat regions in the frequency response functions. Secondly, there should not be too much difference between the largest and smallest response data. Large disparity in response amplitude will cause high response data to overshadow low response data, potentially to the point where the problem becomes underdetermined with spurious results. Thirdly, frequency lines

corresponding to high levels of measurement noise should be avoided. Finally, the

frequency range of interest needs to be specified—lower frequencies (dominated by

global system modes with larger wavelengths), higher frequencies (dominated by

localized modes with smaller wavelengths), or a combination of both. Damage will affect

response when modal strain energy overlaps the damage region, and small, localized

damage cases will generally be most easily discernible when looking at higher frequency

response—modes with modal strain energy concentrated around the damage. On the

other hand, to maintain a physically meaningful result the updated model should replicate

measured structural response across a large modal frequency range and restricting the

update to too small a frequency band may disturb this result. Update frequency lines

should therefore be spread over a range that includes modes affected by damage and

modes that are not.

In order to meet these criteria the current algorithm employs a frequency line

selection scheme based on three stages.

(1) **Natural Frequency based filtering:** If natural frequency results are available,
a convenient method of initially down-selecting data to avoid low response
regions while ensuring good coverage is to cluster lines around modal peaks.
The recommended method is to form bands around natural frequencies
corresponding to the modes of interest and then choose the initial set of
frequency lines as all of the frequencies within these bands. This step helps
avoid the most erroneous regions while retaining the most useful data. It

should be noted that the modes of interest need to be selected as a preliminary step, an operation requiring operator inspection and input.

(2) **Frequency response function magnitude based filtering:** A secondary method (or alternate first method if modal results are not available) is to average the absolute value magnitude of the frequency response function and establish an amplitude band which avoids excessively low and high response. Any frequency lines corresponding to an averaged absolute value frequency response function magnitude value falling outside of this band is then deleted from the set. This step helps ensure that all of the selected points will be influential and thus not wasted.

(3) **Coherence based filtering:** Finally, coherence values corresponding to the measured frequency response function data can be referenced to identify and exclude regions of high measurement noise and/or system non-linearity. The recommended method is as follows. First, coherence values are either averaged across degree-of-freedom or the minimum coherence value found for each experimental frequency. All frequency lines falling below a specified coherence threshold are rejected. The specified number of update frequency lines are then selected spread evenly from this subset. In the case of fewer than the specified number of frequency lines being available above tolerance, the best available will be selected so that the specified number is still met.

Each of these methods has strengths and weaknesses, and the selection parameters—modal frequency banding, frequency response magnitude level, and coherence threshold—must be tuned for each problem depending on the data set characteristics. The natural frequency based method ensures good coverage, but doesn't discriminate against low magnitude points that won't contribute meaningfully to the update. Magnitude based selection helps ensure that influential data is used; however, the method requires the frequency response functions to be fairly flat so sections are not arbitrarily cut out completely, and large flat regions (highly damped) will tend to either attract too many frequency lines if they are above the threshold, or none at all if they are below, whereas peaky regions will capture only a small number of frequency lines within the acceptance band. Finally, the coherence based method helps avoid corrupt data and tends to push lines towards the high response regions of the peaks, but does not guarantee any sort of even spread coverage for experimental data. The three methods are therefore used in sequence, with natural frequencies ensuring good coverage and in general avoiding the low-response or low-sensitivity regions; frequency response magnitude ensuring there won't be excessively low or high response lines; and coherence based selection allowing the desired number of update lines to be selected from the candidate lines passing the previous criteria.

4.2   Initial Uncertainty Quantification of Data and Parameters

Once update frequency lines are selected, the reference frequency response

function variances can be estimated using a coherence-based method similar to that

presented by Doebling and Farrar [4-1], which was previously developed by Bendat and

Piersol [4-2], and then assembled into $[\underline{S}_{vv}]$. The required modification for the current

algorithm is to use the real and imaginary frequency response function form of Schultz et

al. [4-3] instead of the magnitude and phase frequency response function form specified

by Doebling and Farrar. The required real and imaginary frequency response function

variances are found from the work of Schultz et al. by starting with their equation for the

sample covariance matrix (Eq. 24 in their work),

$$\hat{\sigma}^2_{\text{Re}(\tilde{a}(\omega_k))} = \hat{\sigma}^2_{\text{Im}(\tilde{a}(\omega_k))} = \frac{\left(1 - \hat{\gamma}^2_{xy}(\omega_k)\right) \cdot \hat{G}_{yy}(\omega_k)}{2N_{av} \cdot \hat{G}_{xx}(\omega_k)}, \tag{4.3}$$

where N_{av} is the number of averages used when measuring the initial power spectrums.

Taking the square root and substituting in the power spectrum expressions rearranged

from Eqs. (4.1) and (4.2) then gives

$$\hat{\sigma}^*_{\text{Re}(\tilde{a}(\omega_k))} = \hat{\sigma}^*_{\text{Im}(\tilde{a}(\omega_k))} = \frac{\sqrt{1 - \hat{\gamma}^2_{xy}(\omega_k)} \cdot |\tilde{a}(\omega_k)|}{|\hat{\gamma}_{xy}(\omega_k)| \sqrt{2N_{av}}}. \tag{4.4}$$

Doebling and Farrar state that their magnitude/phase based quantities are actually

estimates of the magnitude/phase confidence bounds, and are related to the desired

population variances through

$$\hat{\sigma} = \hat{\sigma}^* \sqrt{N_{av}} \; . \tag{4.5}$$

This relationship holds also for the real and imaginary case, and thus the final population

variance estimates can thus be finally found by combining Eqs. (4.4) and (4.5) and

squaring again to give

$$\hat{\sigma}^2_{\mathrm{Re}(\tilde{a}(\omega_k))} = \hat{\sigma}^2_{\mathrm{Im}(\tilde{a}(\omega_k))} = \frac{\left(1 - \hat{\gamma}^2_{xy}(\omega_k)\right) \cdot \left|\tilde{a}(\omega_k)\right|^2}{2\left|\hat{\gamma}_{xy}(\omega_k)\right|^2} \; . \tag{4.6}$$

This expression can be used, along with the measured frequency response and coherence

functions, to estimate the variance associated with the data points. The resulting variance

values are then combined into the diagonal measurement covariance matrix $\left[\underline{S}_{vv}\right]$.

Initial parameter variances in the experimental case, however, are less clearly

defined than measured noise variances and have to be estimated based on previous

experiments and/or intuition, or just set to a generic starting quantity. The relative sizes of

the parameter and noise uncertainties affect how the update proceeds since increasing the

amount of parameter uncertainty effectively decreases the level of regularization in the

least-squares update, freeing the algorithm to make greater changes to the parameters.

However, increasing prior parameter uncertainty also increases the posterior uncertainty.

This trade-off must be considered when specifying the parameter variances. Initial

parameter standard deviation values of between 1% and 100% of the initial parameter

values usually seem to give good results (Collins et al. [4-4]). An additional point is that

individual initial parameter variances can be tailored to reflect relative levels of

uncertainty between parameters. For instance, mass parameters may have relatively low

uncertainty, since they can be more easily measured compared to stiffness parameters.

Conversely, damping parameters may have much higher values reflecting how accurately

the values are known in the analytical model.

4.3 **Displacement, Velocity, and Acceleration Domains**

Experimental reference data are usually obtained in the acceleration time domain

using accelerometers placed on the structure during vibration testing or in the velocity

domain using a laser Doppler vibrometer. Data can additionally be obtained, theoretically

at least, in the displacement domain using extensometers, strain gages, or lasers. In each

case, the frequency response functions are calculated using the time series data power

spectrums, as described above. The resulting frequency response functions, denoted here

as $\tilde{a}^A(\omega_k)$ for acceleration, $\tilde{a}^V(\omega_k)$ for velocity, and $\tilde{a}^D(\omega_k)$ for displacement, are

related by multiplication with the circular frequency times the imaginary number, as

$$\left\{\tilde{a}^A(\omega_k)\right\} = j\omega_k\left\{\tilde{a}^V(\omega_k)\right\} = \left(j\omega_k\right)^2\left\{\tilde{a}^D(\omega_k)\right\}. \tag{4.7}$$

The frequency response function vector at frequency ω_k, formed by inverting the

dynamic stiffness matrix in Eq. (3.9) to produce

$$\left\{a(\omega_k)\right\} = \left[Z(r,\omega_k)\right]\left\{i\right\}, \tag{4.8}$$

is in the displacement domain. The standard residual force vector originally presented in

Eq. (3.78),

$$\{R(r,\omega_k)\} = \{i\} - [Z(r,\omega_k)] \cdot \{\tilde{a}(\omega_k)\}$$

therefore also requires that $\{\tilde{a}(\omega_k)\}$ is a displacement frequency response function. If

velocity or acceleration response is measured from the structure, the displacement

domain frequency response function must thus be first calculated using

$$\{\tilde{a}(\omega_k)\} = \left\{\tilde{a}^V(\omega_k)\right\} \Big/ (j\omega_k) \tag{4.9}$$

or

$$\{\tilde{a}(\omega_k)\} = \left\{\tilde{a}^A(\omega_k)\right\} \Big/ \left(-\omega_k^2\right), \tag{4.10}$$

(where squaring the imaginary number produces a negative, giving $\left(j\omega_k\right)^2 = -\omega_k^2$)

before calculating the residual force vector.

Alternatively, a velocity or acceleration based residual vector can be calculated,

as

$$\left\{R^V(r,\omega_k)\right\} \triangleq \{R(r,\omega_k)\}(j\omega_k) = j\omega_k\{i\} - [Z(r,\omega_k)]\left\{\tilde{a}^V(\omega_k)\right\} \tag{4.11}$$

for velocity, and

$$\left\{R^A(r,\omega_k)\right\} \triangleq \{R(r,\omega_k)\}(j\omega_k)^2 = -\omega_k^2\{i\} - [Z(r,\omega_k)]\left\{\tilde{a}^A(\omega_k)\right\} \tag{4.12}$$

for acceleration, and damage identification performed in these respective domains using $\{\tilde{a}^V(\omega_k)\}$ or $\{\tilde{a}^A(\omega_k)\}$, respectively. Inspecting the damage identification equations, however, shows that there is no effective difference between using one domain over another, since the frequency multipliers cancel each other leaving only the original displacement based versions. To see this, the quantity that becomes the updated parameter covariance matrix, previously presented in batch-processing form as

$$[Q]_{i+1} = \left(\left[S_{r_0 r_0} \right]^{-1} + [\underline{N}]_i^T \left[\underline{S}_{RR}(r_i) \right]^{-1} [\underline{N}]_i \right)^{-1}$$
(3.122)
,

is written equivalently as summation over frequency, giving

$$[Q]_{i+1} = \left(\left[S_{r_0 r_0} \right]^{-1} + \sum_{k=1}^{N_\omega} [N(\omega_k)]_i^T \left[S_{RR}(r_i, \omega_k) \right]^{-1} [N(\omega_k)]_i \right)^{-1}.$$
(4.13)

Frequency-explicit expressions can be written for the sensitivity matrix,

$$[N(\omega_k)]_i = \left[\left\| \frac{\partial Z(r, \omega_k)}{\partial r} \right|_{\hat{r}_i} \right\| \{\tilde{a}(\omega_k)\} \right].$$
(4.14)

where the double brackets again denote a three dimensional array of size $(N_d \times N_d \times N_r)$ and inverse residual force vector covariance matrix,

$$[S_{RR}(r_i, \omega_k)]^{-1} = [Z(r_i, \omega_k)]^{-T} [S_{vv}(\omega_k)]^{-1} [Z(r_i, \omega_k)]^{-1},$$
(4.15)

and substituting these into $[Q]_{i+1}$ gives a further expanded form as

$$[Q]_{i+1} = \left(\left[S_{r_0 r_0} \right]^{-1} + \sum_{k=1}^{N_\omega} \left[\left[\left. \frac{\partial Z(r, \omega_k)}{\partial r} \right|_{\hat{r}_i} \right] \{ \tilde{a}(\omega_k) \} \right]^T [Z(r_i, \omega_k)]^{-T} \dots \right.$$
$$\left. \dots [S_{vv}(\omega_k)]^{-1} [Z(r_i, \omega_k)]^{-1} \left[\left[\left. \frac{\partial Z(r, \omega_k)}{\partial r} \right|_{\hat{r}_i} \right] \{ \tilde{a}(\omega_k) \} \right] \right)^{-1}. \tag{4.16}$$

As can be seen in Eq. (4.6), the reference data variances are proportional to the frequency response function magnitude squared, and thus the covariance matrix $[\underline{S}_{vv}]$ will also have a displacement, velocity, or acceleration domain dependency, depending on the domain of the frequency response function, which allows definition of

$$\left[S_{vv}^V(\omega_k) \right] \triangleq (j\omega_k)^2 [S_{vv}(\omega_k)] = -\omega_k^2 [S_{vv}(\omega_k)] \tag{4.17}$$

for velocity and

$$\left[S_{vv}^A(\omega_k) \right] \triangleq (j\omega_k)^4 [S_{vv}(\omega_k)] = \omega_k^4 [S_{vv}(\omega_k)] \tag{4.18}$$

for acceleration. The eventual independency to domain can be seen, by example of velocity domain, by replacing $\{\tilde{a}(\omega_k)\}$ with $\{\tilde{a}^V(\omega_k)\}$ and $\left[S_{vv}(\omega_k) \right]$ with $\left[S_{vv}^V(\omega_k) \right]$, giving the velocity domain version

$$[Q^V]_{i+1} \triangleq \left(\left[S_{r_0 r_0} \right]^{-1} + \sum_{k=1}^{N_\omega} \left[\left[\left. \frac{\partial Z(r, \omega_k)}{\partial r} \right|_{\hat{r}_i} \right] \{ \tilde{a}^V(\omega_k) \} \right]^T [Z(r_i, \omega_k)]^{-T} \dots \right.$$
$$\left. \dots \left[S_{vv}^V(\omega_k) \right]^{-1} [Z(r_i, \omega_k)]^{-1} \left[\left[\left. \frac{\partial Z(r, \omega_k)}{\partial r} \right|_{\hat{r}_i} \right] \{ \tilde{a}^V(\omega_k) \} \right] \right)^{-1}. \tag{4.19}$$

Substituting in $\left\{\tilde{a}^V(\omega_k)\right\} = j\omega_k \left\{\tilde{a}(\omega_k)\right\}$ and $\left[S_{vv}^V(\omega_k)\right] = -\omega_k^{\,2}\left[S_{vv}(\omega_k)\right]$ produces

$$\left[Q^V\right]_{i+1} = \left(\left[S_{r_0 r_0}\right]^{-1} + \sum_{k=1}^{N_\omega}\left[\left[\left.\frac{\partial Z(r,\omega_k)}{\partial r}\right|_{\hat{r}_i}\right]j\omega_k\left\{\tilde{a}(\omega_k)\right\}\right]^T\left[Z(r_i,\omega_k)\right]^{-T}\ldots\right.$$

$$\left.\ldots\left(-\omega_k^{\,2}\right)^{-1}\left[S_{vv}(\omega_k)\right]^{-1}\left[Z(r_i,\omega_k)\right]^{-1}\left[\left[\left.\frac{\partial Z(r,\omega_k)}{\partial r}\right|_{\hat{r}_i}\right]j\omega_k\left\{\tilde{a}(\omega_k)\right\}\right]\right)^{-1},$$

$$(4.20)$$

and by collecting the scalar $j\omega_k$ and $\left(-\omega_k^{\,2}\right)^{-1}$ terms and recognizing

$\left(j\omega_k\right)^2\left(-\omega_k^{\,2}\right)^{-1} = 1$ it can be seen that $\left[Q^V\right]_{i+1} = [Q]_{i+1}$ as claimed. Rewriting the

expression for updated parameter values,

$$\{\hat{r}\}_{i+1} = \{\hat{r}_0\} - [Q]_{i+1}[\underline{N}]_i^T\left[\underline{S}_{RR}(r_i)\right]^{-1}\left([\underline{R}]_i - [\underline{N}]_i\left(\{\hat{r}\}_i - \{\hat{r}_0\}\right)\right), \qquad (3.121)$$

in terms of frequency summation and expanding in the same way produces a similar

equivalency, as does the same process for $[Q]_{i+1}$ and $\{\hat{r}\}_{i+1}$ in the acceleration domain.

Because of the least-squares minimization algorithms' invariance to displacement,

velocity, or acceleration domain, the only effective difference in using one of the

domains over another occurs in the frequency filtering step described in Section 4.1

during frequency response function magnitude based filtering. As described, this method

blocks frequency lines for which the summed magnitude is above or below user-defined

thresholds. Since the frequency response function magnitudes will be higher with

frequency by factors of $j\omega_k$ and $\omega_k^{\,2}$ in the velocity and acceleration domains,

respectively, the thresholds will block different frequency lines in each domain.

Therefore, if lower frequency lines are desired, filtering in the displacement domain may

be preferable, and vice versa for the case of a greater number of high frequencies being

desired. In fact, this fact demonstrates that for filtering the frequency response function

magnitude could be scaled in any desired fashion to change the effect of the thresholds,

so long as the frequency response functions are either transformed back or other related

quantities scaled similarly, although the relative information potency moderation which is

the whole point of this filtering step may then be diminished.

4.4   Analytical Validation on Noisy System with Comparison to Other Methods

The statistical damage identification algorithm is now analytically validated on an

8-degree-of-freedom damped mass-spring system with varying levels of additive noise.

Noise in low levels simulates the ambient noise floor and in higher levels simulates, for

example, faulty sensors or wiring. The current damage identification algorithm is then

compared to four similar methods from the literature on the same system. Programs were

written in Matlab R2009a [4-6] to run all test cases.

4.4.1   Healthy System Description

The structurally damped 8-degree-of-freedom mass-spring system is modified

from the undamped launch vehicle and satellite model developed by Kabe [4-7] as a

challenging test case for system identification algorithms. The system has many

interconnections and a wide range of stiffness and mass parameter values producing

closely-spaced and coupled modes of varying magnitudes and a wide range of parameter

sensitivities. Figure 4-1 shows a schematic of the system expanded into two-dimensions

to show connectivity clearly. Each mass has only 1-degree-of-freedom, however, so a

more accurate visualization is with all masses and their motion on a one-dimensional line,

as in Figure 4-2. This figure also shows a potential breakdown of the system in terms of

launch vehicle systems, including the main primary structure represented by m_2 through

m_7, a component mounted on secondary structure represented by m_1, and the payload

represented by m_8. Changes from the original Kabe system are restricted to the addition

of structural damping and the addition of noise. A structural damping parameter is

included for every spring in the system with damping values chosen to be relatively low

for low-stiffness springs and higher for high stiffness springs to simulate, for instance,

lower damping in the connection between the launch vehicle and payload structure and

higher damping in the interconnected and propellant loaded primary structures. The

distribution of structural damping coefficients from 0.002 to 0.050 also causes the overall

damping to be strongly non-proportional. All parameter values for the healthy system are

given in Table 4-1.
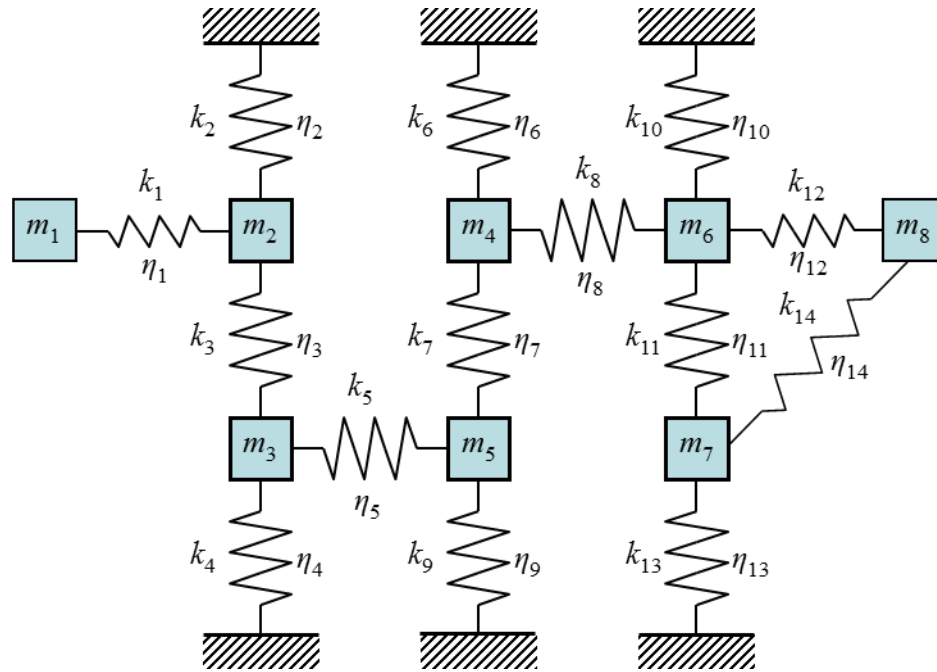
Figure 4-1: Kabe 8-degree-of-freedom mass-spring system, distributed representation.
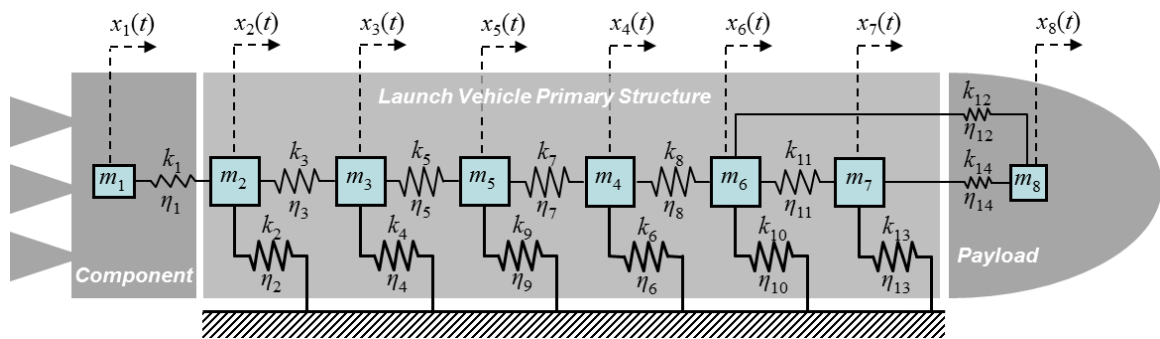
Figure 4-2: Kabe 8-degree-of-freedom mass-spring system, in-line launch vehicle representation.

Table 4-1: Modified Kabe 8-degree-of-freedom healthy system parameters.

Spring stiffness parameters		Spring damping parameters		Mass parameters
$k_1 = 1.50$	$k_9 = 900$	$\eta_1 = 0.005$	$\eta_9 = 0.002$	$m_1 = 0.001$
$k_2 = 1000$	$k_{10} = 1000$	$\eta_2 = 0.050$	$\eta_{10} = 0.020$	$m_2 = 1.00$
$k_3 = 10.0$	$k_{11} = 10.0$	$\eta_3 = 0.010$	$\eta_{11} = 0.005$	$m_3 = 1.00$
$k_4 = 1000$	$k_{12} = 2.00$	$\eta_4 = 0.050$	$\eta_{12} = 0.002$	$m_4 = 1.00$
$k_5 = 100$	$k_{13} = 1000$	$\eta_5 = 0.020$	$\eta_{13} = 0.010$	$m_5 = 1.00$
$k_6 = 900$	$k_{14} = 1.50$	$\eta_6 = 0.002$	$\eta_{14} = 0.002$	$m_6 = 1.00$
$k_7 = 100$		$\eta_7 = 0.010$		$m_7 = 1.00$
$k_8 = 100$		$\eta_8 = 0.010$		$m_8 = 0.002$

The system thus defined in its baseline state has eight modes. Figure 4-3 summarizes the modal information, including unity-scaled mode shape plots and natural frequency and modal damping values given in the plot titles (natural frequency and damping ratio values are also given along with their damaged counterparts in Table 4-2, Section 4.4.2). In the mode shape plots x_4 and x_5 have been swapped to better match the in-line launch vehicle representation of the system presented in Figure 4-2. It can be seen that the modes are closely spaced in frequency, especially in the cases of modes 2 and 3 which occupy the same frequency to three significant figures of accuracy, and the damping varies from light to moderate with modal damping ratios distributed between
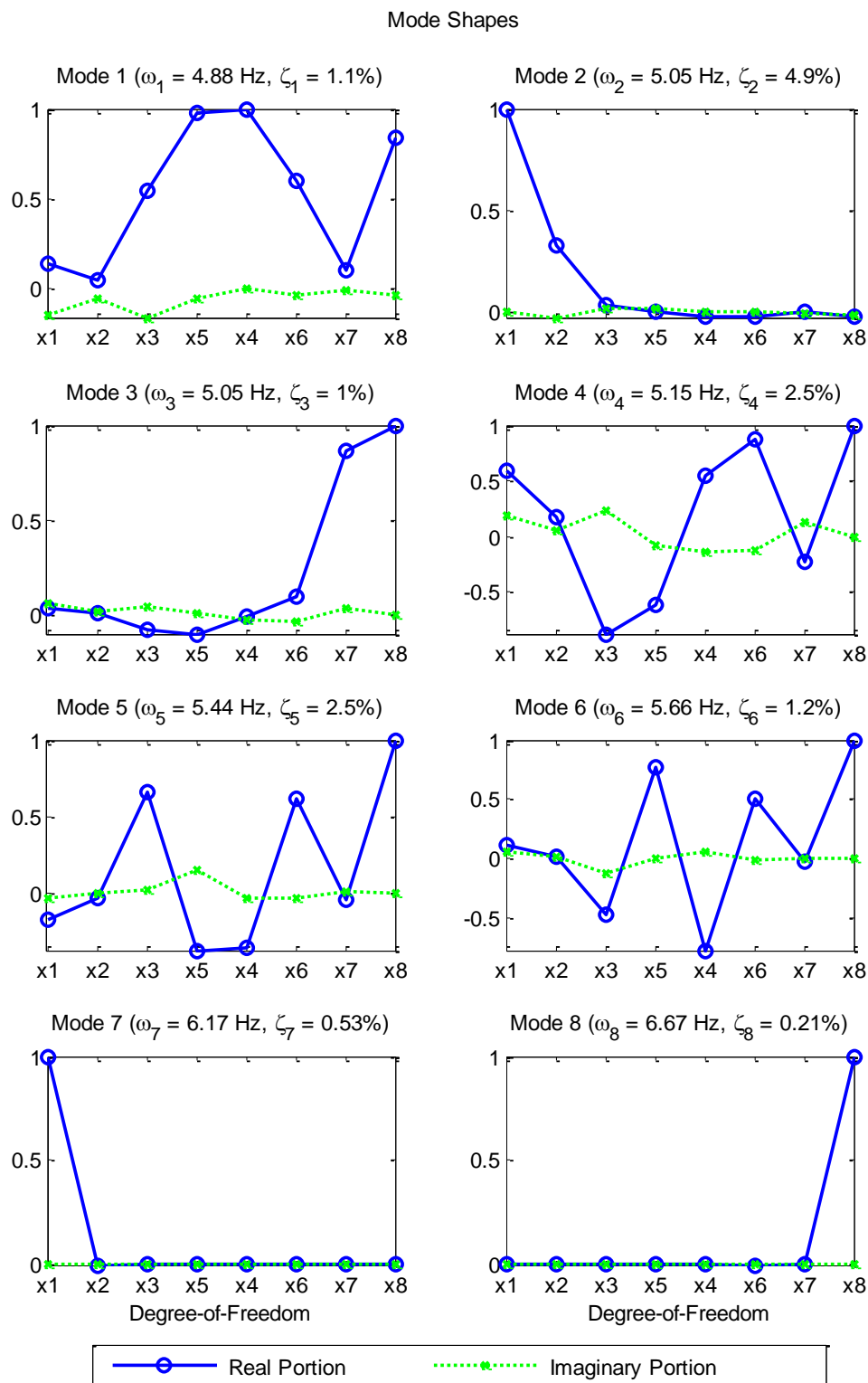
Mode Shapes

Figure 4-3: Modal information for the healthy 8 degree-of-freedom system (with x_4 and x_5 swapped to match the in-line launch vehicle orientation given in Figure 4-2).

0.21% and 4.9% critical damping. Inspection of the mode shapes shows that the first 6 modes are dominated by global system response while mode 7 is dominated by motion of the small mass at x_1 and mode 8 is dominated by motion of the small mass at x_8.

Noise-free healthy frequency response functions, generated at each degree-of-freedom in the displacement domain by forming and inverting the dynamic stiffness matrix $[Z(r, \omega_k)]$ at each of 4096 frequency lines and extracting the column corresponding to x_5, are shown superimposed in Figure 4-4. The damping is heavy enough that modes 1 through 6 are highly coupled with modal peaks blending into each other. Modes 2 and 3 are so closely coupled with each other and the dominant surrounding modes that they cannot be clearly distinguished in the frequency response functions. Modes 7 and 8 appear predominately in the frequency response functions from to x_1 and x_8 which reflects the observation that modes 7 and 8 correspond to motion of the small masses m_1 and m_8 and are largely uncoupled from the rest of the system.

4.4.2   Damaged System Description

Three damage cases are considered for the system as shown in Figure 4-5:

1. Single 10% decrease in the medium sensitivity stiffness parameter k_8 to represent local structural damage (e.g., damage to the launch vehicle structure);
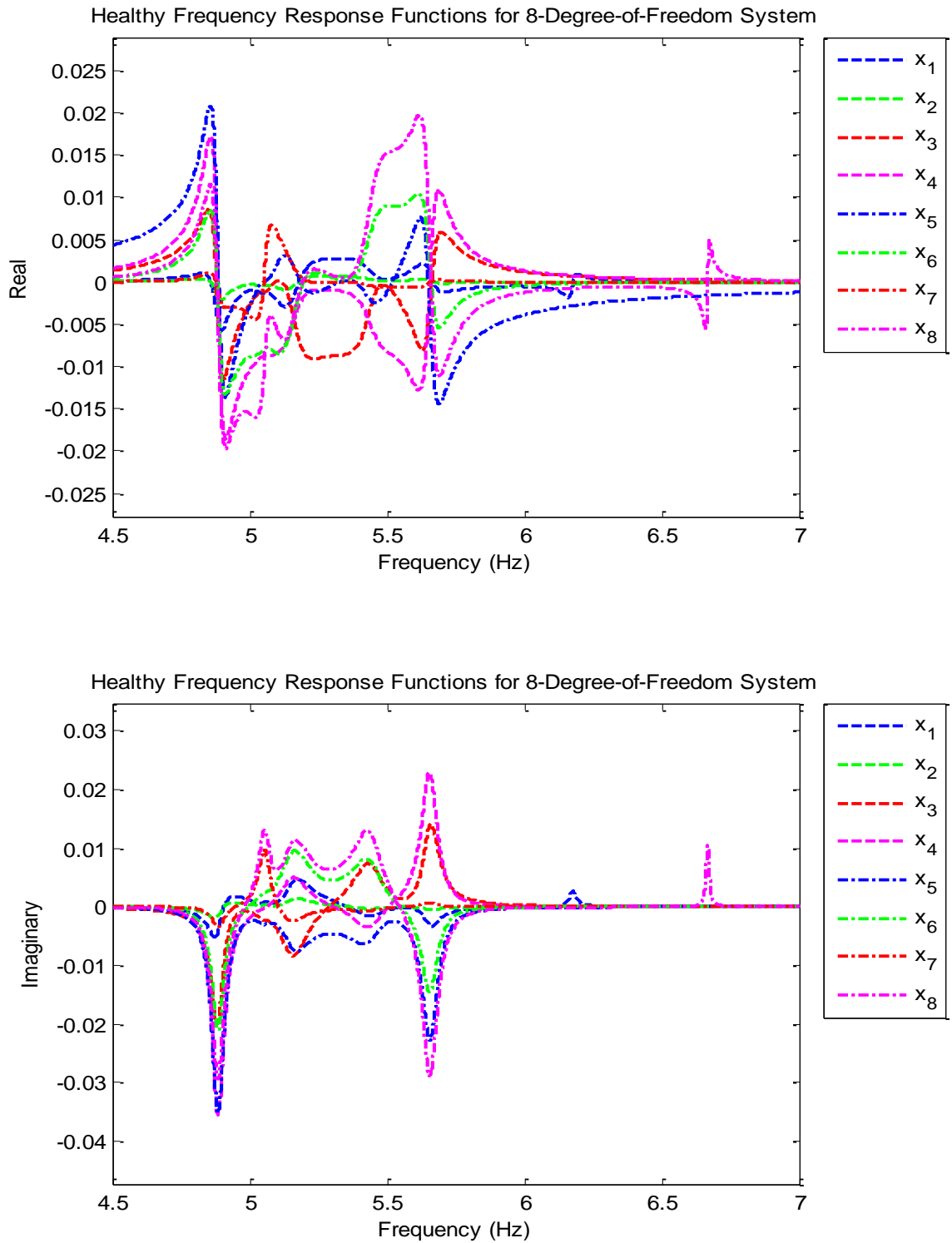
Figure 4-4: Noise-free frequency response functions from the healthy system in terms of real and imaginary components.
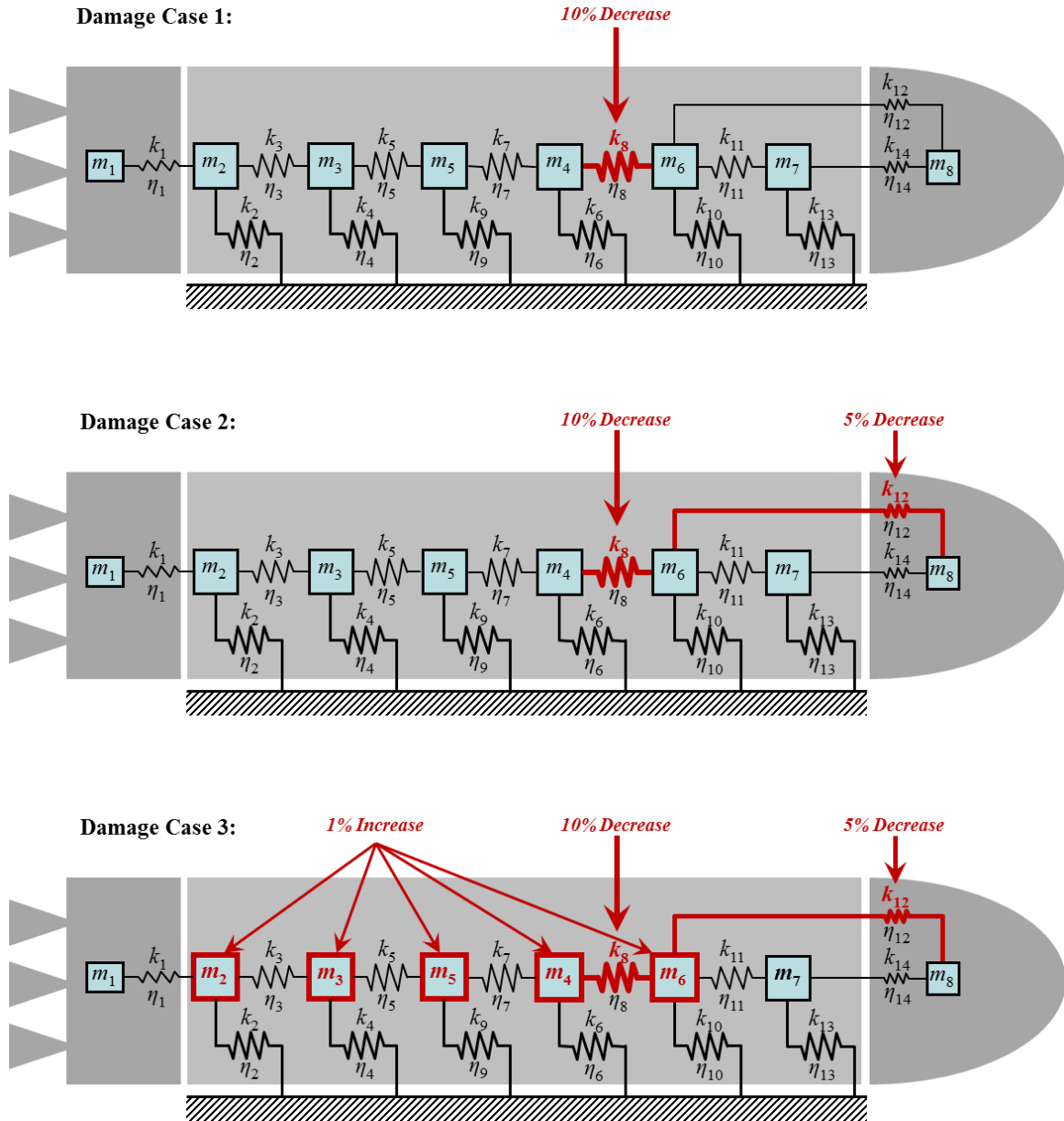
Figure 4-5: Schematic overview of damage cases.

2. Damage case 1 plus a single 5% stiffness decrease in the low sensitivity

   parameter k_{12} to represent local structural damage combined with local

   subsystem damage (e.g., damage to the launch vehicle structure combined

   with damage to the payload mounting structure);

3. Damage case 2 plus a 1% increase in the primary masses m_2, m_3, m_4, m_5, and

   m_6 to represent combined local damage cases in the presence of global mass

   change (e.g., damage to the launch vehicle and payload structures combined

   with an increase in propellant load compared to the baseline case).

The damaged system natural frequencies and damping ratios are given in Table

4-2 along with the healthy system values and the percent change from healthy to

damaged values. The effect of the damage cases is additionally summarized in Figure 4-6

for the natural frequencies, Figure 4-7 for the damping ratios, and Figure 4-8 for the

mode shapes which are presented in terms of unity-scaled magnitude to better show the

comparison on a global level.

The following observations can be made from the figures:

- Damage case 1 primarily affects modes 5 and 6, with smaller influences on

  modes 1 and 4 and negligible influence on modes 2, 3, 7, and 8.

- Damage case 2 is very similar to damage case 1 with the exception of a

  significant and local impact on mode 8.

Table 4-2: Summary of natural frequencies and modal damping ratios for healthy and damaged systems, including percent change from healthy to damaged values.

		Mode							
		1	2	3	4	5	6	7	8
Healthy System	f_n (Hz)	4.88	5.05	5.05	5.15	5.44	5.66	6.17	6.67
	η_n	0.0111	0.0489	0.0104	0.0247	0.0254	0.0124	0.0053	0.0021
Damage Case 1	f_n (Hz)	4.88	5.05	5.05	5.15	5.42	5.64	6.17	6.67
	% change	*-0.034%*	*0.000%*	*-0.007%*	*-0.022%*	*-0.419%*	*-0.354%*	*0.000%*	*-0.002%*
	η_n	0.0109	0.0489	0.0104	0.0245	0.0247	0.0134	0.0053	0.0021
	% change	*-1.724%*	*0.007%*	*0.222%*	*-0.798%*	*-2.680%*	*8.584%*	*0.000%*	*-0.123%*
Damage Case 2	f_n (Hz)	4.88	5.05	5.05	5.15	5.42	5.64	6.17	6.57
	% change	*-0.034%*	*0.000%*	*-0.013%*	*-0.022%*	*-0.420%*	*-0.355%*	*0.000%*	*-1.436%*
	η_n	0.0109	0.0489	0.0104	0.0245	0.0247	0.0134	0.0053	0.0021
	% change	*-1.726%*	*0.007%*	*0.210%*	*-0.804%*	*-2.693%*	*8.585%*	*0.000%*	*0.189%*
Damage Case 3	f_n (Hz)	4.86	5.02	5.05	5.13	5.39	5.61	6.17	6.57
	% change	*-0.528%*	*-0.492%*	*-0.029%*	*-0.504%*	*-0.911%*	*-0.849%*	*-0.004%*	*-1.438%*
	η_n	0.0109	0.0489	0.0107	0.0243	0.0247	0.0134	0.0053	0.0021
	% change	*-1.718%*	*0.034%*	*2.903%*	*-1.898%*	*-2.711%*	*8.577%*	*-0.296%*	*0.036%*

- The mass decreases in damage case 3 have a more broadband effect on the system, affecting modes 1, 2, 4, 5, and 6. Modes 3, 7, and 8 are not influenced significantly in terms of mode shape or natural frequency by the mass increases since these modes are dominated by activity in the unaltered masses.

- Natural frequencies are decreased by all damage cases, with the greatest decrease of approximately 1.4% resulting from the localized stiffness reduction on k_{12} in damage cases 2 and 3. Damage case 1 produces a decrease of approximately 0.4% on modes 5 and 6 while damage case 3 produces a further decrease of approximately 0.5% on modes 1, 2, 4, 5, and 6.
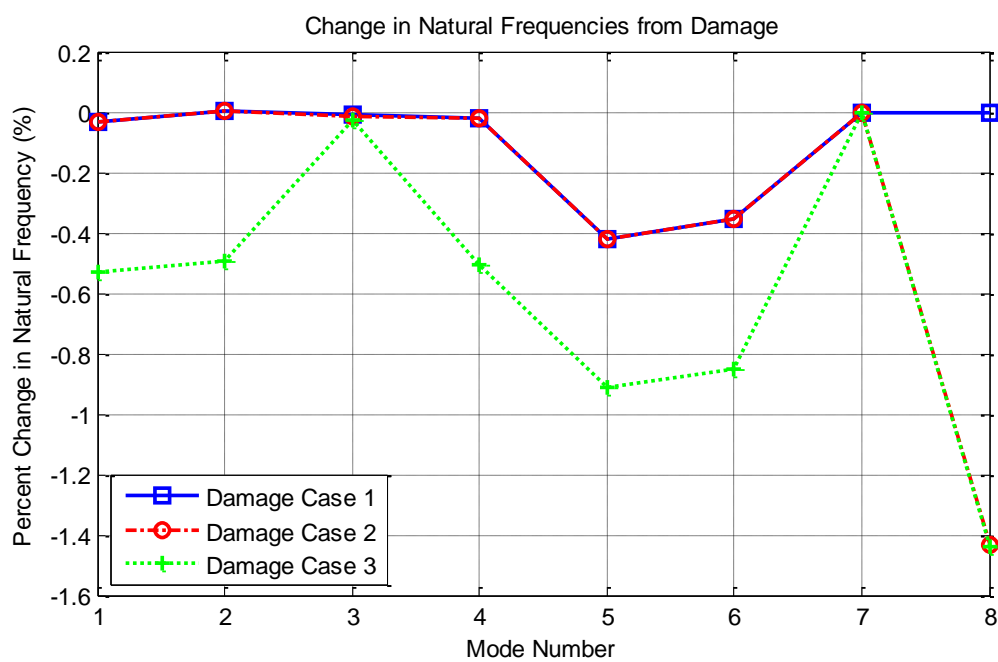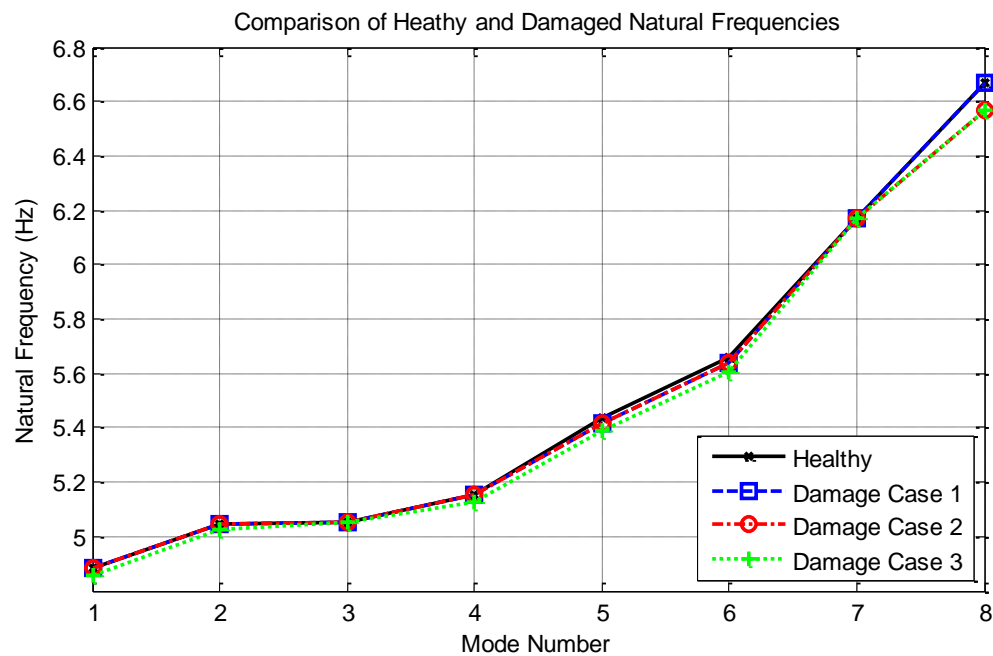
Figure 4-6: Effect of damage cases on system natural frequencies.
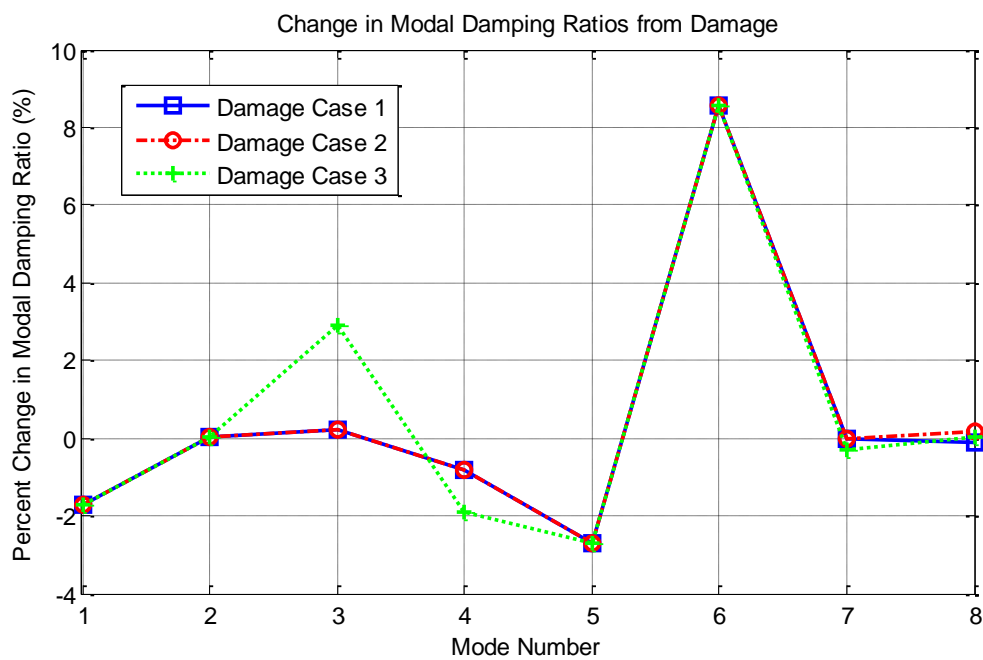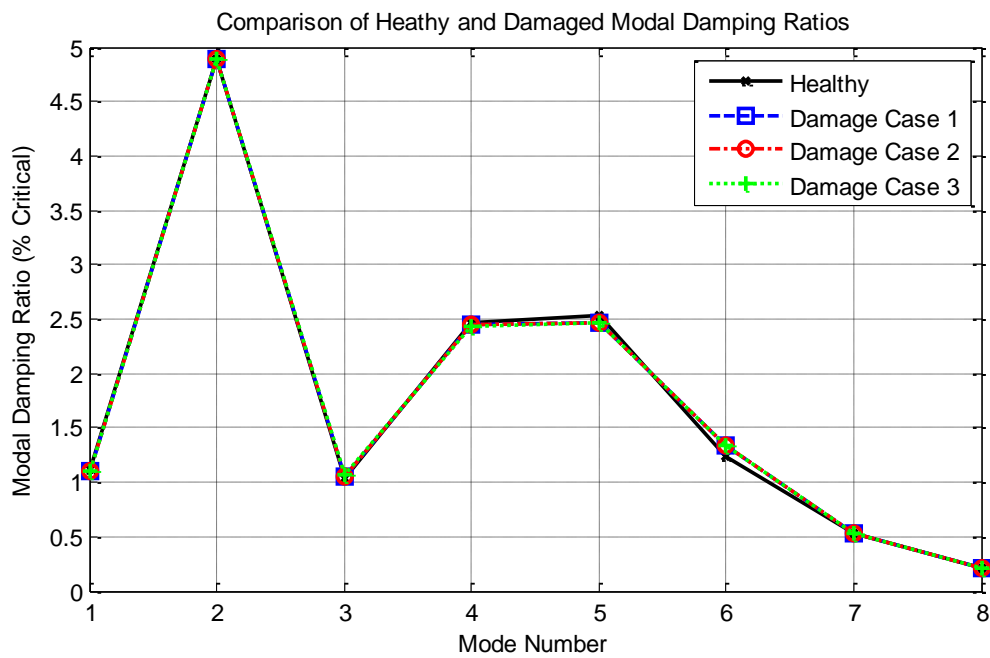
Figure 4-7: Effect of damage cases on system modal damping ratios.

Mode Shape Magnitude for Damage Cases
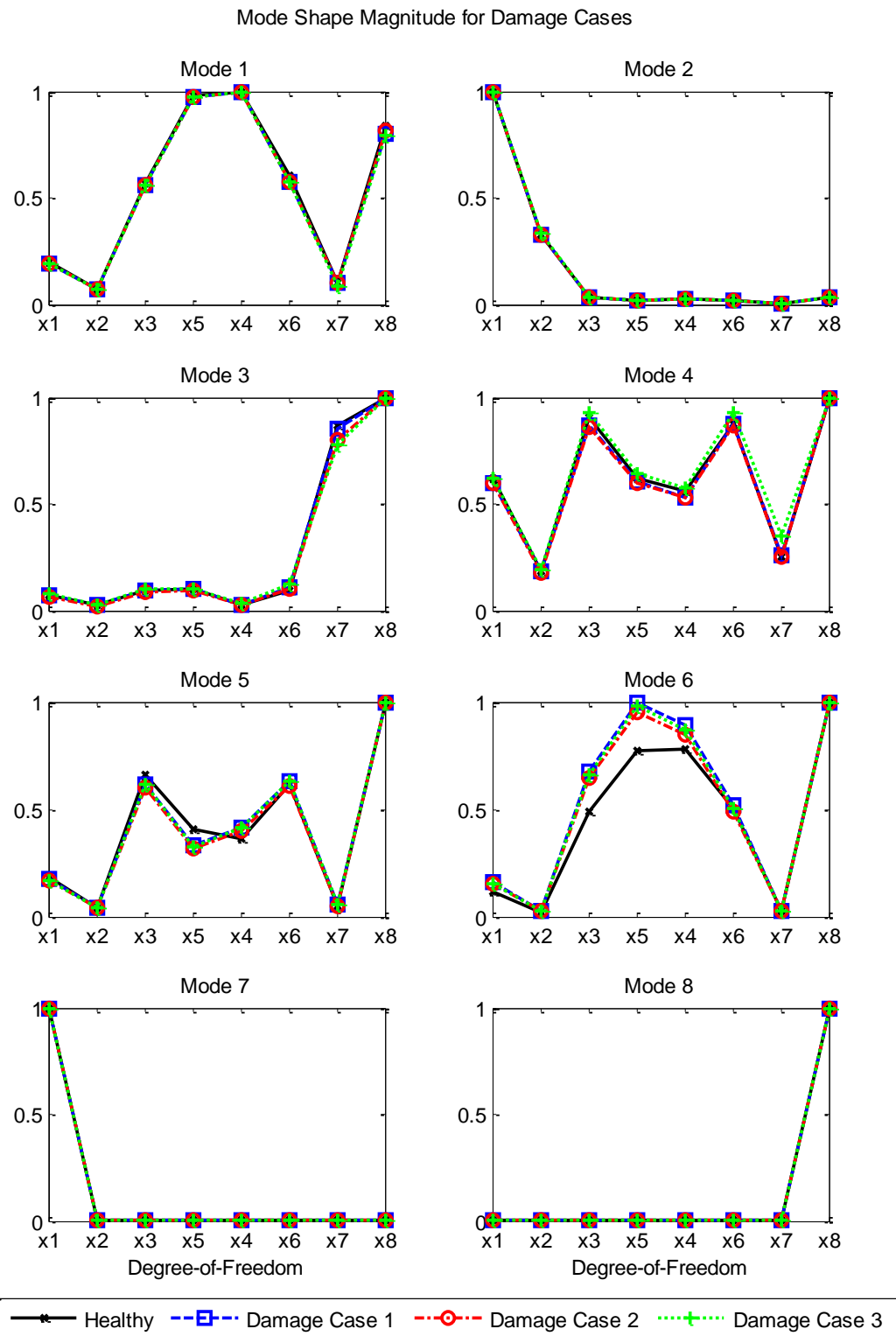
Figure 4-8: Comparison of mode shape magnitudes for the healthy system and three damage cases.

- Modal damping ratios are impacted on the order of 2% to 8% with modes 1, 4, and 5 decreasing slightly for all damage cases, mode 6 damping increasing significantly for all cases, and mode 3 increasing moderately for damage case 3. Damage case 1 has the largest damping impact of all of the damage cases followed by damage case 3 which roughly matches the impact of the damage cases on other modal characteristics.

- The damage cases do not dramatically affect the mode shapes, with the greatest changes occurring on modes 4, 5, and 6 from damage case 1. Mode 3 is also affected locally from damage case 2, although this does not cause a significant change in global natural frequency indicating that the mode is still dominate on a global level by small movements of the heavier masses.

A comparison of frequency response functions from the healthy and damaged systems is given in Figure 4-9 for the driving point degree-of-freedom, x_5, and Figure 4-10 for the small payload simulating mass at degree-of-freedom x_8, both in terms of real and imaginary components. As observed from the mode shapes, damage case 1 primarily affects the frequency zone around modes 5 and 6 while damage case 2 only causes further influence to mode 8, shifting the mode down in frequency without affecting the shape, and damage case 3 has a more broadband impact on the system.
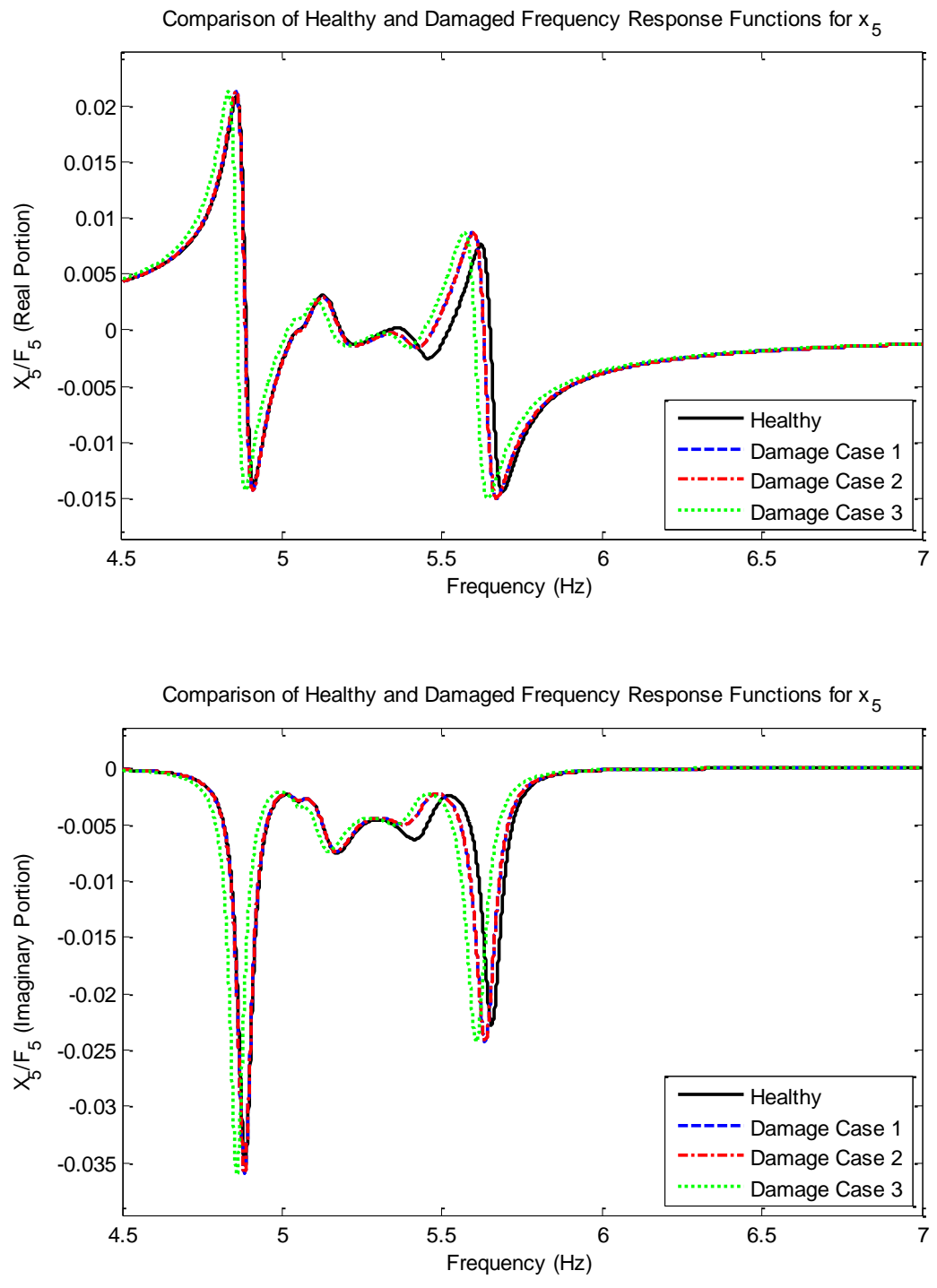
Figure 4-9: Comparison of healthy and damaged frequency response functions for the driving point degree-of-freedom, x_5, in terms of real and imaginary components.
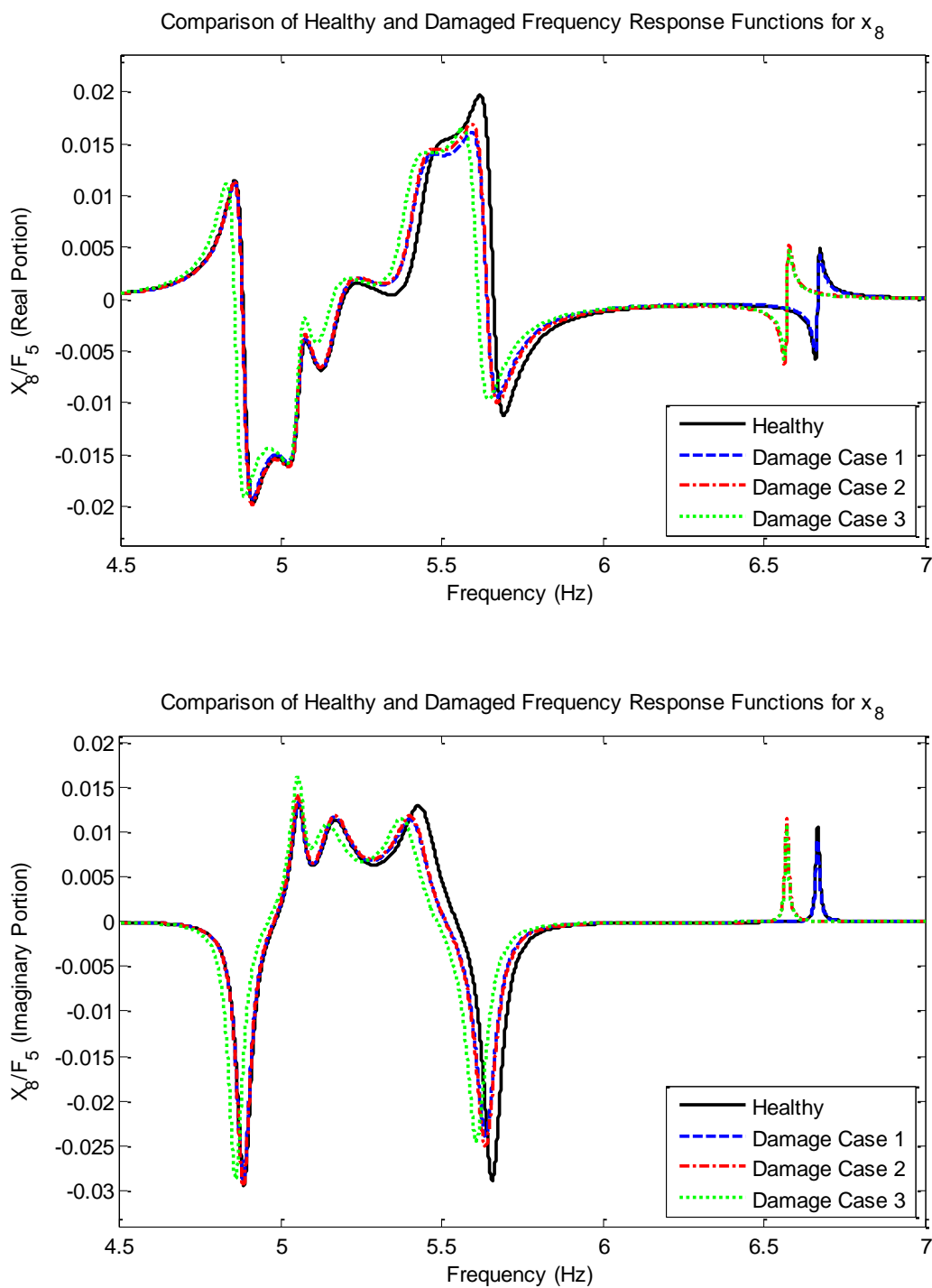
Figure 4-10: Comparison of healthy and damaged frequency response functions for the small payload mass at degree-of-freedom, x_8, in terms of real and imaginary components.

4.4.3   Damage Identification with Noise

The current damage identification algorithm was applied to the three damage

cases with increasing amounts of noise applied to all degrees-of-freedom. The frequency

line filtering criteria based on natural frequency, average frequency response function

magnitude, and coherence discussed in Section 4.1 were applied via an automated

algorithm. Also, the coherence based method for estimating variability in the measured

data described in Section 4.2 was implemented. All calculations were performed in the

displacement domain.

For all runs, noise was added to the system in the time domain by the following

process, as recommended by Zimmerman [4-5]:

(1) Reflect each frequency response function about the vertical axis and remove

the last point in the resulting signal, then apply an inverse Fourier transform to

create an all real time series representation of the data;

(2) Add a vector of Gaussian random noise scaled so that the ratio of system

response signal power to noise signal power matches a specified level;

(3) Transform the noisy time series back into the frequency domain by forward

Fourier Transform.

This process results in noise of constant variance superimposed on the frequency

response function with measurement vectors corresponding to different degrees-of-

freedom having different levels of constant variance (i.e., broadband white) noise and

incoherent noise vectors on different degrees-of-freedom. It should be noted that all 'zero noise' cases actually have a small amount of noise added to avoid numerical instability from having measurement variability values equal perfectly to zero. In these cases a noise vector is created with power equal to 0.000001% of the signal power.

Coherence functions were estimated for the analytical noise cases using

$$\hat{\gamma}_{xy}(\omega_k) = \frac{1}{\left(1 + \dfrac{a(\omega_k) \cdot a(\omega_k)^H}{a_v(\omega_k) \cdot a_v(\omega_k)^H}\right)}, \qquad (4.21)$$

where $a(\omega_k)$ is the noise-free frequency response function, $a_v(\omega_k)$ is the Fourier transform of the pure noise time series, and superscript H indicates the Hermitian transpose.

Since the 8 degree-of-freedom system represents a simple test case compared to the real-world problems for which the algorithm is designed, it was assumed that there was no damage location information available to help down-select the initial set of damage parameters. All runs therefore include damage factors for all mass and stiffness parameters in the system for a total of 22 update parameters—8 mass and 14 stiffness.

The three methods for frequency line selection—natural frequency based screening, average frequency response function magnitude based screening, and coherence based screening—were applied in series. For the first step, frequency lines were chosen which are within 4% of each natural frequency. The second step removed frequency lines corresponding to an average (over degrees-of-freedom) frequency

response function magnitude of -70dB. The third step selected the pre-specified number

of final analysis frequency evenly spaced from the set with minimum coherence values of

0.98 or greater, with the best available lines chosen in the event that not enough candidate

lines meet the criteria. This selection process results in different frequency lines for each

damage and noise case since the frequency response function magnitude and coherence

based criteria are affected by the unique noise in each data set.

Additional test-parameters for all runs are as follows:

- Number of frequency lines equal to the number of update parameters ($N_\omega = N_r$

    = 22);

- All analysis frequency lines restricted to the modal range of 4.5 Hz to 7.0 Hz;

- Initial parameter standard deviation equal to 1.0% of the healthy value;

- Initial sensitivity perturbation equal to 10%;

- Iteration step limit of 0.2 and no parameter bounds;

- Damage factor convergence tolerance equal to 0.0001;

- Maximum number of iterations equal to 100.

The main metric used for assessing damage identification success is relative

parameter error between the algorithm output and the true known values of the damaged

system parameter set. For individual parameters the relative error is calculated using

$$\varepsilon_{r_p} = \left(\frac{\hat{r}_p - \tilde{r}_p}{\tilde{r}_p} \right) \cdot 100\% \,, \tag{4.22}$$

where r_p refers to the parameter being assessed, $\hat{r}_p$ refers to the updated parameter estimate, and $\tilde{r}_p$ refers to the true experimental value. In order to better assess the overall damage identification results the mean relative error across subsets of the parameters is calculated using the equations

$$\varepsilon_{MRE}^d = \left(\frac{1}{N_r^d} \sum_{s=1}^{N_r^d} \left| \frac{\hat{r}_s^d - \tilde{r}_s^d}{\tilde{r}_s^d} \right| \right) \cdot 100\% \,, \tag{4.23}$$

$$\varepsilon_{MRE}^h = \left(\frac{1}{N_r^h} \sum_{s=1}^{N_r^h} \left| \frac{\hat{r}_s^h - \tilde{r}_s^h}{\tilde{r}_s^h} \right| \right) \cdot 100\% \,, \tag{4.24}$$

where the superscript d describes the stiffness parameters that were damaged for that case and the superscript h describes the stiffness parameters which were not damaged. This segregation gives the ability to distinguish between false negative results (increased damaged stiffness parameter error ε_{MRE}^d) and false positive results (increased healthy stiffness parameter error ε_{MRE}^h). Additionally, since mass parameters are included to screen for system mass changes between the baseline and damaged configurations, a third metric that tracks accuracy of mass predictions is defined as

$$\varepsilon_{MRE}^m = \left(\frac{1}{N_r^m} \sum_{s=1}^{N_r^m} \left| \frac{\hat{r}_s^m - \tilde{r}_s^m}{\tilde{r}_s^m} \right| \right) \cdot 100\% \,, \tag{4.25}$$

where superscript m refers to mass parameters.

As an initial screening case the algorithm was first run on all three damage cases with zero noise. Since noise is the only corrupting influence on the measurement vector, the coherence for this case has negligible error to unity for all frequencies and so the frequency lines are evenly distributed across the frequency range 4.5 Hz to 7.0 Hz. In all three cases the algorithm reached the final solution in a single iteration, with a second iteration then used to verify convergence. Inspection of the results shows that the correct result was achieved for all parameters and all damage cases with a maximum parameter error of 0.0003%.

The algorithm was then applied to the three damage cases with varying amounts of noise added to the damaged system reference data. Figure 4-11, Figure 4-12, and Figure 4-13 show examples of the reference data sets from damage case 1 with 0.1%, 1% and 10% added noise, respectively, to give a qualitative visualization of the range of noise cases. The cases of 0.1% and 1% noise represent normal dynamic data whereas 10% noise represents an extreme case which might correspond to very low dynamic response or a malfunctioning data acquisition system. Analysis frequency lines automatically selected for these three examples are shown at the bottom of each coherence plot.

Results are summarized in Table 4-3 for each damage and noise case by way of individual updated parameter error values and the three mean relative error metrics defined in Eqs. (4.21 – 4.24). The results are additionally plotted as absolutely value of relative parameter error in Figure 4-14 for damage case 1, Figure 4-15 for damage case 2,
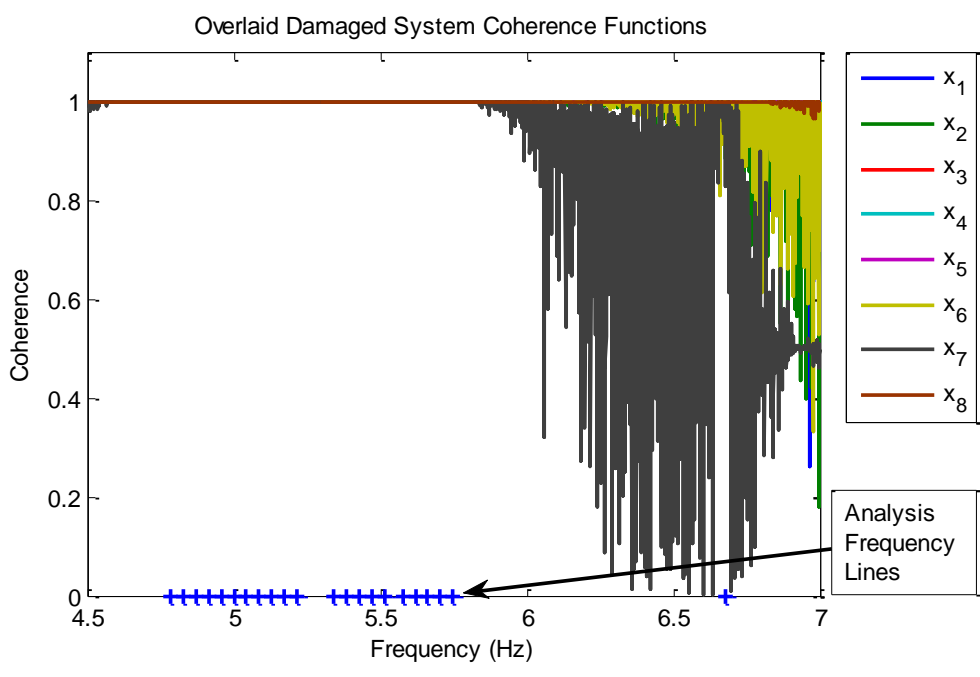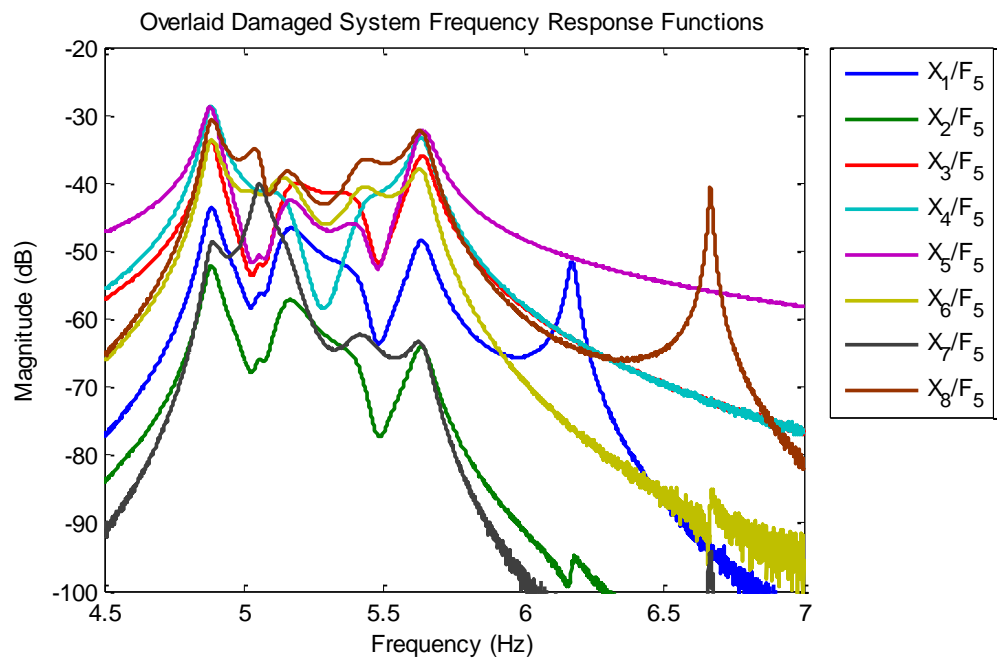
Figure 4-11: Damaged system frequency response functions and coherence functions with 0.1% added noise.
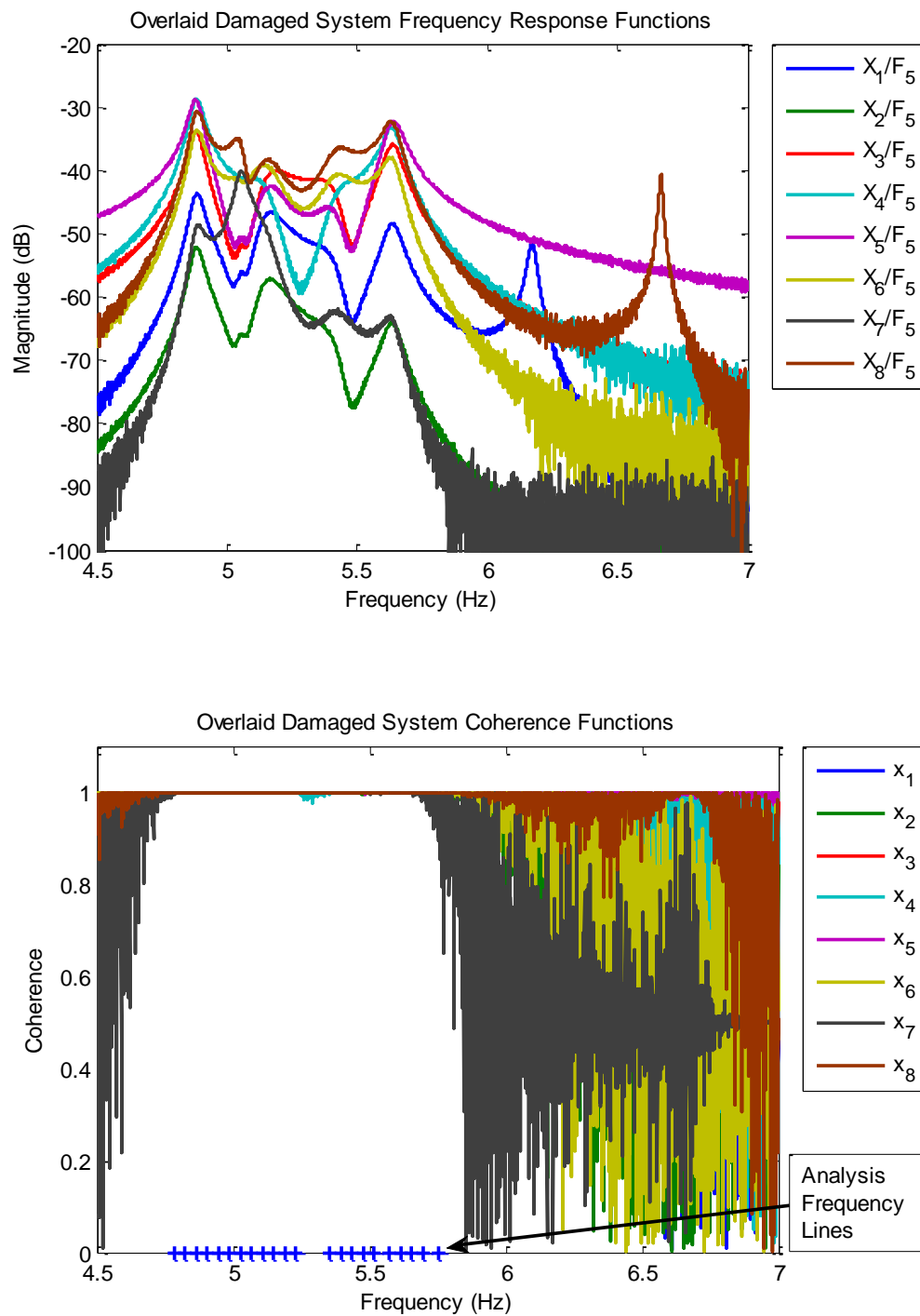
Figure 4-12: Damaged system frequency response functions and coherence functions with 1% added noise.
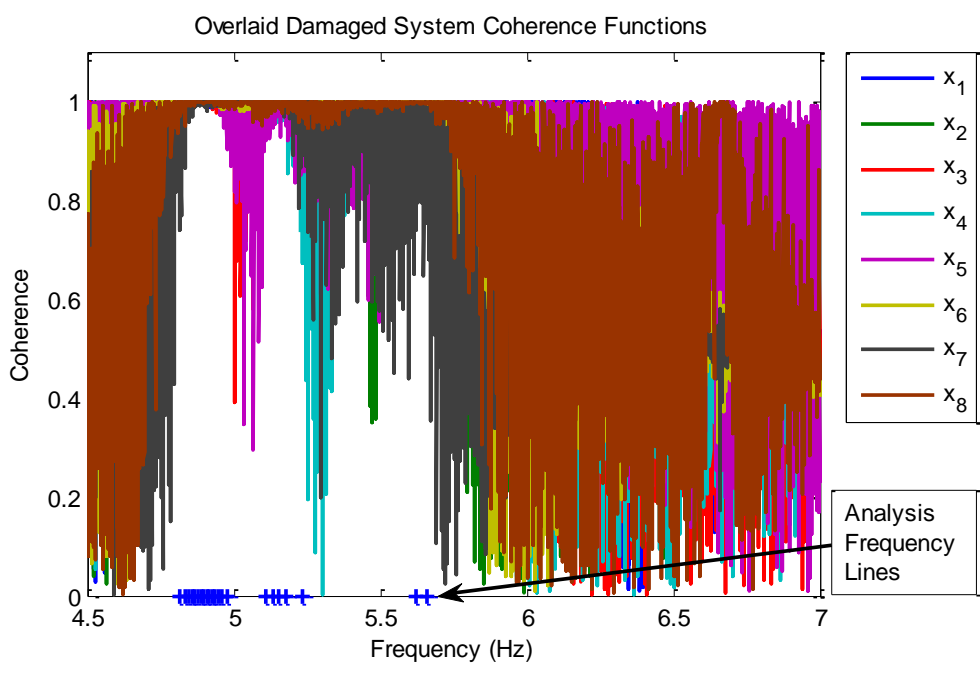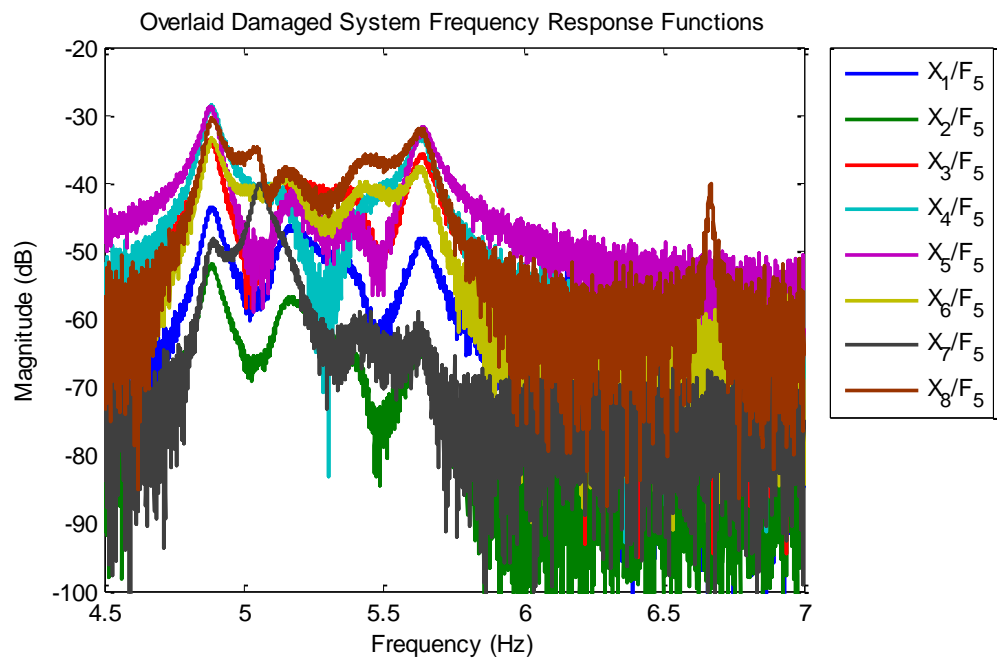
Figure 4-13: Damaged system frequency response functions and coherence functions with 10% added noise.

Table 4-3. Damage identification relative error and mean relative error values.

Parameter	Damage Case 1				Damage Case 2				Damage Case 3			
	Correct	0.1%	1%	10%	Correct	0.1%	1%	10%	Correct	0.1%	1%	10%
ε_{m1}	**0.001**	-0.17%	-0.85%	-1.10%	**0.001**	-0.46%	-1.62%	-0.78%	**0.001**	-0.10%	-0.52%	-2.72%
ε_{m2}	**1.000**	-1.89%	-1.29%	-1.15%	**1.000**	0.05%	-1.81%	-0.07%	**1.010**	0.10%	-2.22%	-7.13%
ε_{m3}	**1.000**	0.02%	0.43%	-1.99%	**1.000**	0.01%	0.03%	-3.33%	**1.010**	-0.02%	0.11%	-5.97%
ε_{m4}	**1.000**	0.04%	-0.37%	-0.33%	**1.000**	0.03%	-0.15%	1.50%	**1.010**	0.02%	0.10%	0.00%
ε_{m5}	**1.000**	-0.02%	-0.29%	-1.01%	**1.000**	0.01%	-0.10%	0.93%	**1.010**	0.03%	-0.09%	0.63%
ε_{m6}	**1.000**	0.09%	0.18%	-1.33%	**1.000**	0.08%	0.03%	0.29%	**1.010**	-0.05%	-0.17%	-3.25%
ε_{m7}	**1.000**	0.46%	2.04%	0.44%	**1.000**	-0.17%	0.55%	-0.31%	**1.000**	0.07%	-4.24%	0.07%
ε_{m8}	**0.002**	-0.05%	-0.22%	0.16%	**0.002**	-0.10%	1.32%	-0.20%	**0.002**	1.57%	0.80%	0.64%
ε_{k1}	**1.500**	-0.18%	-0.87%	-0.58%	**1.500**	-0.46%	-1.73%	-0.56%	**1.500**	-0.09%	-0.45%	-2.67%
ε_{k2}	**1000**	-1.89%	-1.29%	-1.15%	**1000**	0.05%	-1.80%	-0.20%	**1000**	0.10%	-2.22%	-7.14%
ε_{k3}	**10.00**	-1.86%	-1.25%	0.67%	**10.00**	0.06%	-1.82%	-5.78%	**10.00**	0.10%	-2.21%	-5.62%
ε_{k4}	**1000**	0.04%	0.47%	-1.75%	**1000**	0.01%	0.10%	-3.29%	**1000**	-0.02%	0.11%	-6.66%
ε_{k5}	**100.0**	0.00%	0.18%	-3.17%	**100.0**	0.01%	-0.30%	-1.42%	**100.0**	-0.02%	-0.17%	-8.27%
ε_{k6}	**900.0**	0.04%	-0.42%	-0.28%	**900.0**	0.03%	-0.16%	1.55%	**900.0**	0.02%	0.11%	0.16%
ε_{k7}	**100.0**	0.01%	-0.42%	-0.14%	**100.0**	0.02%	0.07%	0.47%	**100.0**	0.03%	0.20%	4.84%
ε_{k8}	**90.00**	0.07%	-0.11%	-0.55%	**90.00**	0.05%	-0.19%	2.33%	**90.00**	0.00%	-0.08%	-2.22%
ε_{k9}	**900.0**	-0.02%	-0.31%	-0.99%	**900.0**	0.01%	-0.11%	1.04%	**900.0**	0.03%	-0.08%	1.35%
ε_{k10}	**1000**	0.08%	0.19%	-1.58%	**1000**	0.09%	0.02%	0.38%	**1000**	-0.05%	-0.12%	-3.76%
ε_{k11}	**10.00**	0.57%	2.79%	-0.07%	**10.00**	-0.13%	0.83%	0.67%	**10.00**	-0.27%	-5.25%	2.23%
ε_{k12}	**2.000**	-0.05%	-0.43%	-1.42%	**1.900**	-0.07%	1.48%	3.65%	**1.900**	1.49%	1.54%	3.64%
ε_{k13}	**1000**	0.46%	2.03%	0.48%	**1000**	-0.17%	0.56%	-0.39%	**1000**	0.07%	-4.23%	0.08%
ε_{k14}	**1.500**	-0.05%	-0.20%	0.72%	**1.500**	-0.14%	1.10%	0.48%	**1.500**	1.64%	0.50%	0.74%
ε^d_{MRE}		0.07%	0.11%	0.55%		0.06%	0.84%	2.99%		0.75%	0.81%	2.93%
ε^h_{MRE}		0.40%	0.83%	1.00%		0.10%	0.72%	1.35%		0.20%	1.30%	3.63%
ε^m_{MRE}		0.34%	0.71%	0.94%		0.11%	0.70%	0.92%		0.25%	1.03%	2.55%

and Figure 4-16 for damage case 3, and the mean relative error metrics are plotted against

noise percentage in Figure 4-17 for damage case 1, Figure 4-18 for damage case 2, and

Figure 4-19 for damage case 3. It can be seen that parameter error increases with noise, as

expected. Damage case 1 produces parameter error values ranging from 0.003% error on
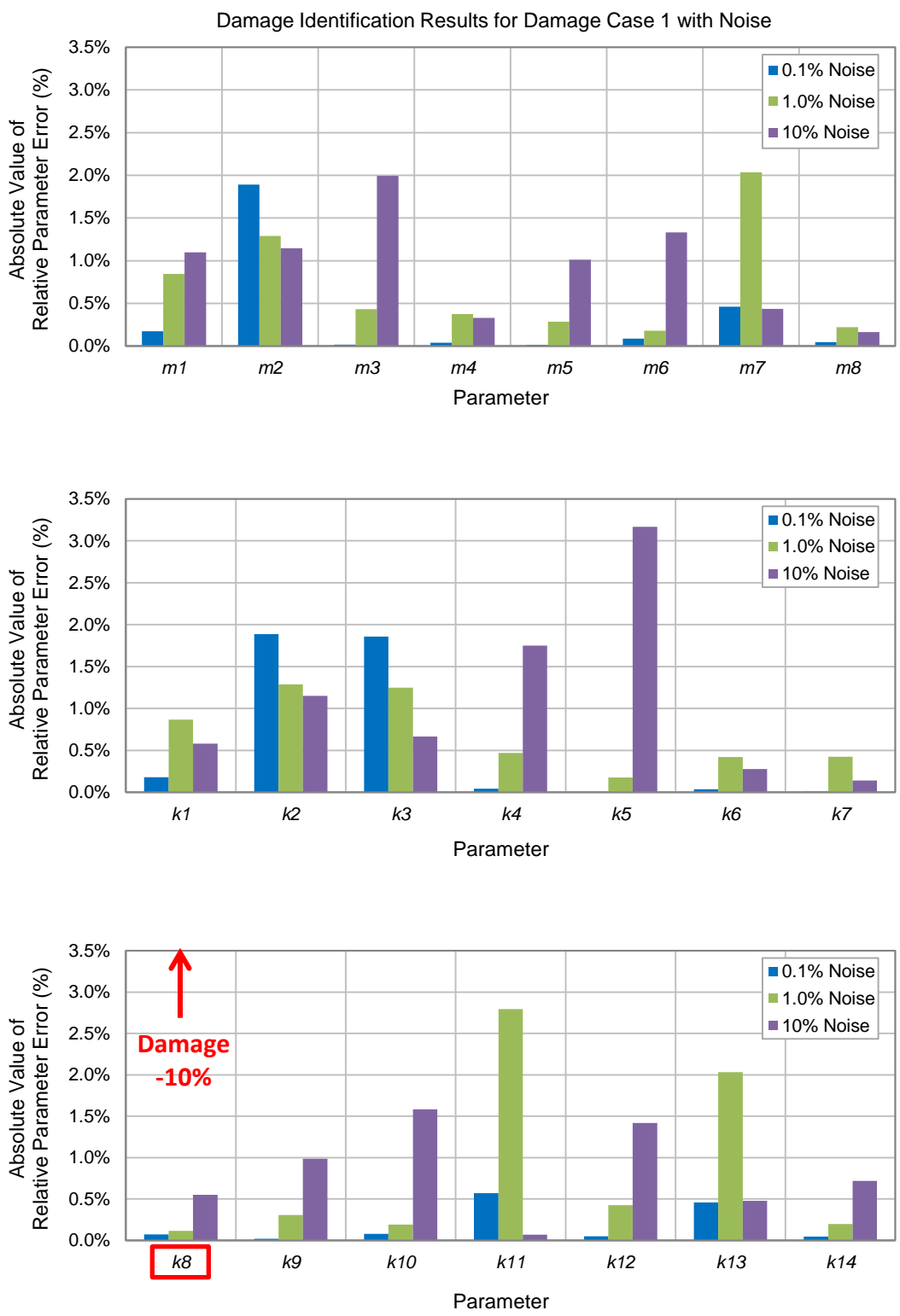
Figure 4-14: Relative parameter error across increasing levels of noise for damage case 1.
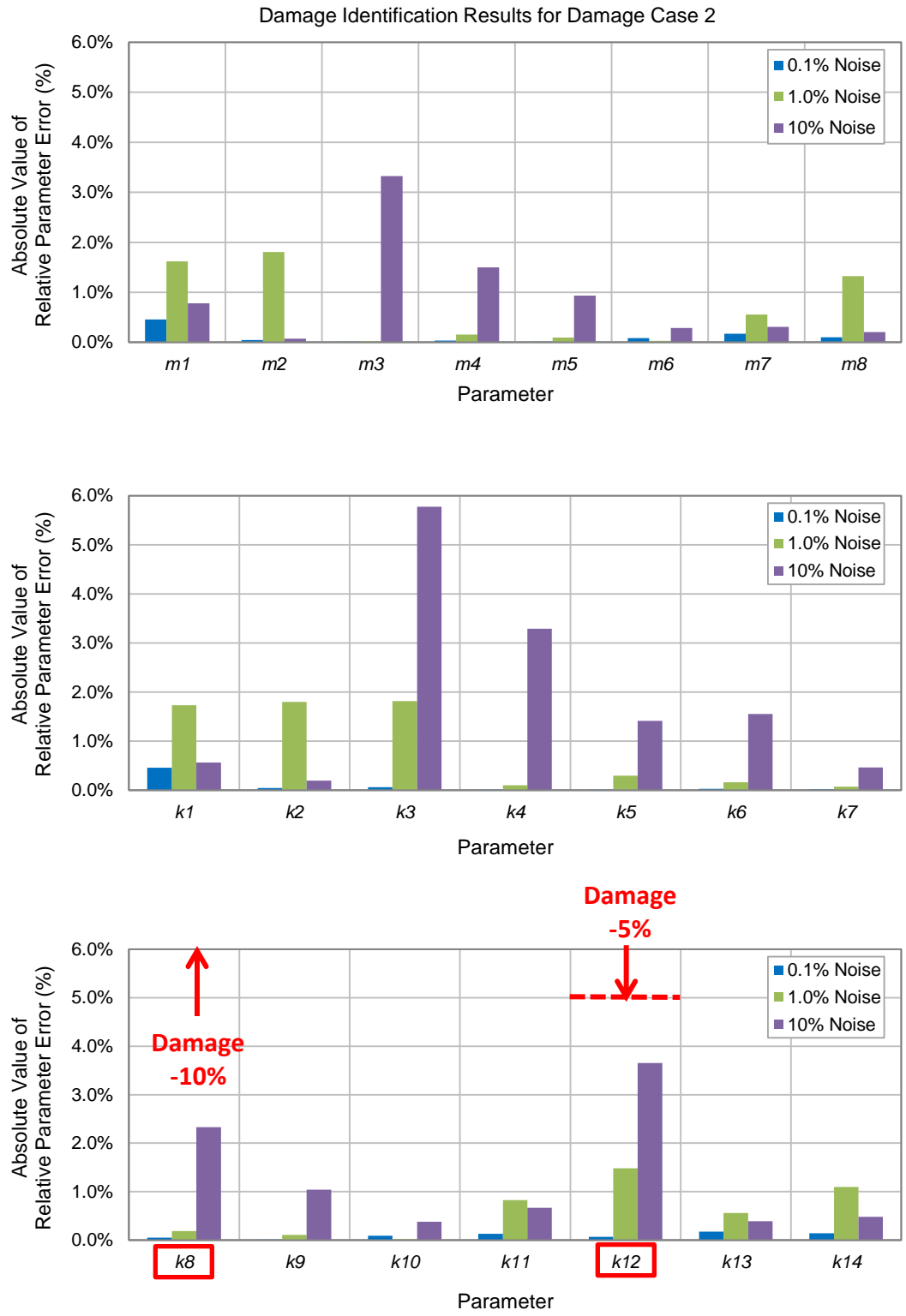
Figure 4-15: Relative parameter error across increasing levels of noise for damage case 2.
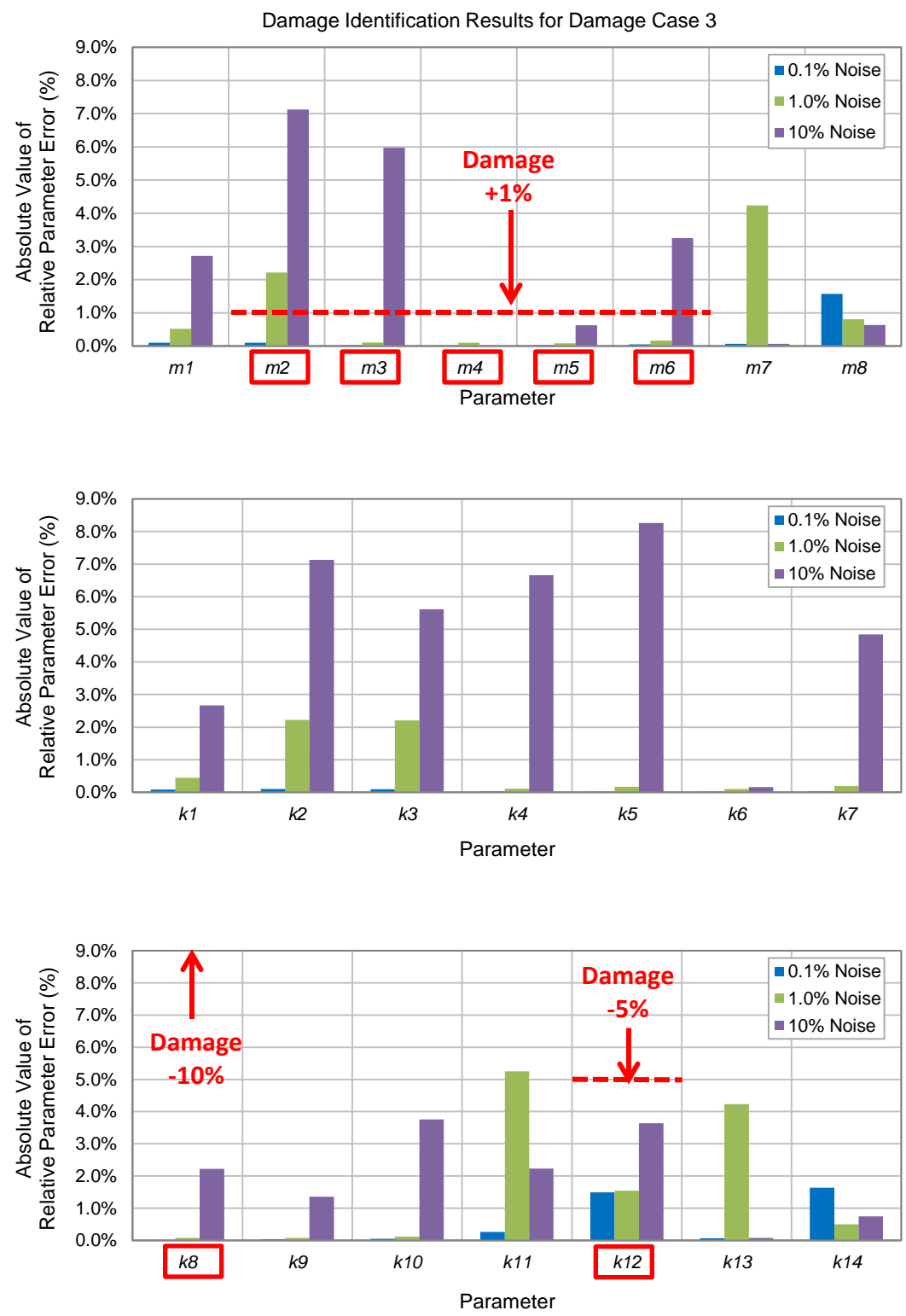
Figure 4-16: Relative parameter error across increasing levels of noise for damage case 3.
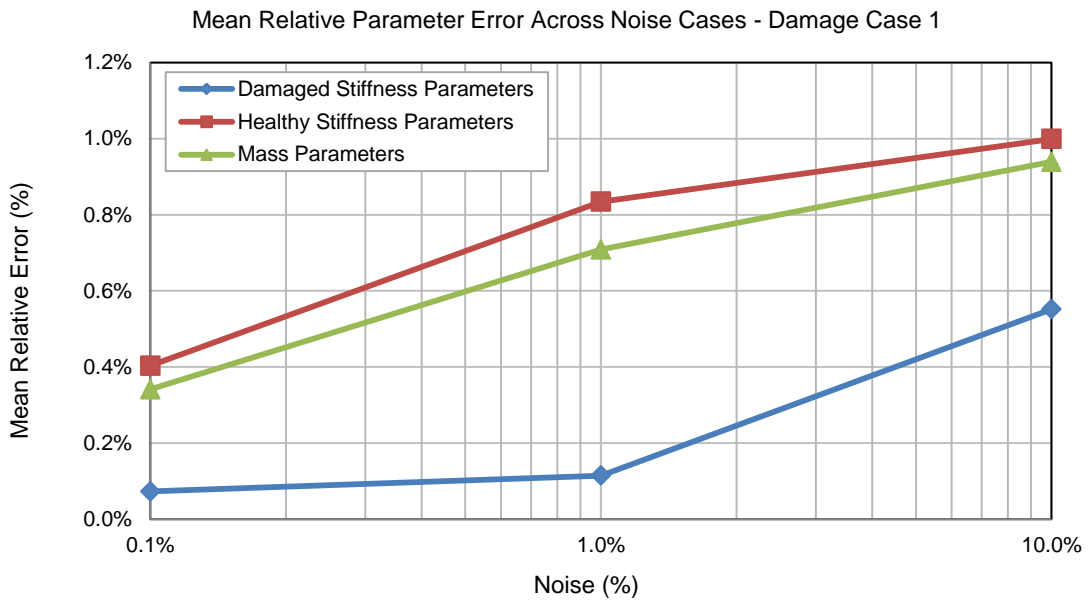
Figure 4-17: Mean relative parameter error as function of noise for damage case 1.
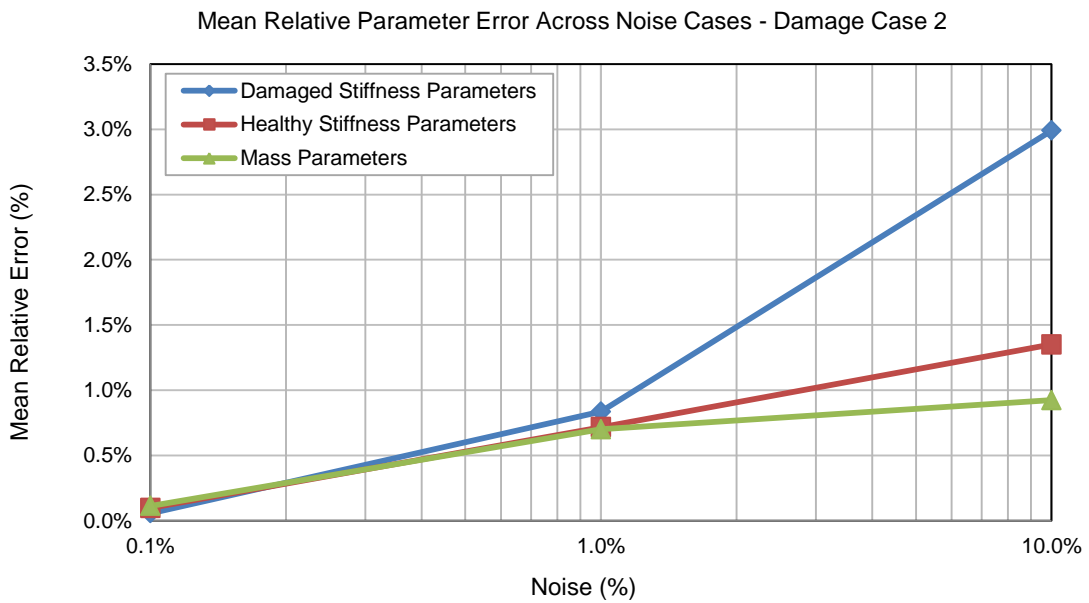
Figure 4-18: Mean relative parameter error as function of noise for damage case 2.
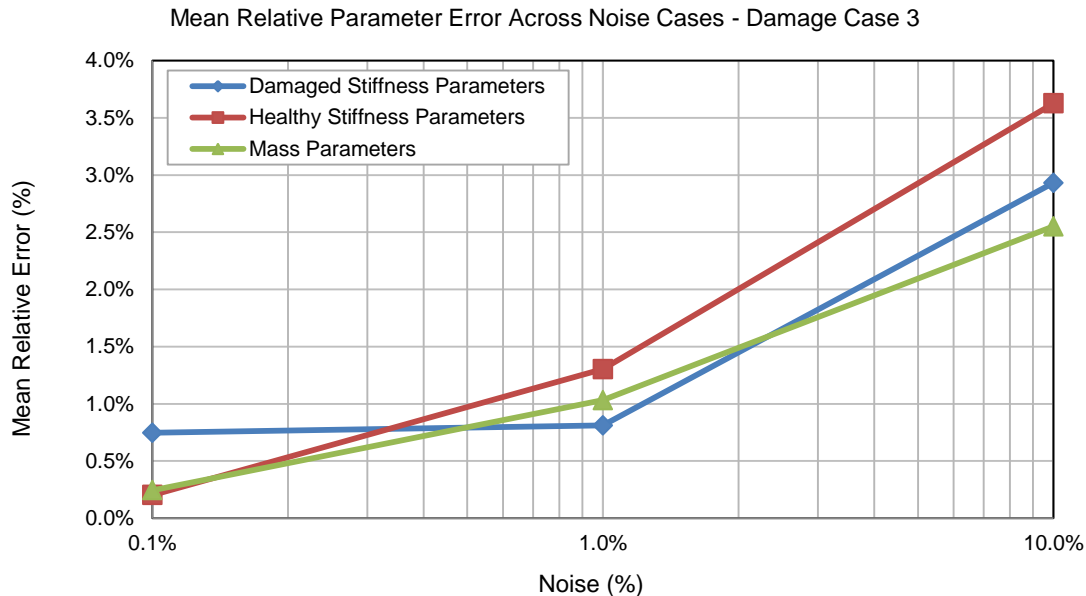
Figure 4-19: Mean relative parameter error as function of noise for damage case 3.

the healthy parameter k_5 in the 0.1% noise case to 3.2% error in the 10% noise case, also

on parameter k_5. Damage case 2 produces parameter error values ranging from 0.011%

error on the mass parameter m_5 in the 0.1% noise case to 5.8% error in the 10% noise

case on healthy parameter k_3. Coincidentally, damage case 3 produces both the overall

lowest parameter error of 0.001% on the damaged parameter k_8 in the 0.1% noise case

and the overall highest parameter error of 8.3%, also on the healthy parameter k_5 in the

10% noise case. The mean relative error metrics give values between 0.06% and 3.0% for

damaged parameters, between 0.2% and 3.63% for healthy parameters, and between

0.11% and 2.55% for mass parameters; however, no clear trends are obvious with the

exception of error increasing with noise level for all cases. Overall the error is very low;

however, for the 10% noise cases the max error approaches or exceeds the amount of damage on some parameters meaning that correct damage identification can only be performed with confidence on cases with commensurately high levels of damage. This limitation is realized on damage cases 2 and 3 where the 5% damage case on the payload simulating parameter k_{12} is identified with a maximum error of 3.7% alongside healthy parameter errors of up to 5.8% for damage case 2 or 8.3% for damage case 3 meaning that the actual damage would not be distinguishable without prior knowledge. For the 1% and 10% noise cases the coherence frequency line selection criteria actually prevents an analysis frequency line being present on the uncoupled mode associated with movement of the payload degree-of-freedom (mode 8 on m_8) so this damage case can only be inferred through the noise by second-order couplings between m_8 and neighboring degrees-of-freedom, creating further disadvantage. A positive observation, however, is that the mass parameters are identified on the same order of accuracy as the stiffness parameters whether or not there were actually changes in mass. Damage identification is therefore possible in the face of changing mass so long as mass parameters are included in the set of update parameters.

4.4.4 Algorithm Comparison

In order to provide further context for the performance of the current damage identification algorithm the runs were repeated with the current algorithm alongside four similar algorithms from literature. The competing algorithms are those of Araujo dos

Santos et al. [4-8], Zang and Imregun [4-9], Zimmerman et al. [4-5], and Ricles and Kosmatka [4-10]. The algorithm of Araujo et al. is essentially a deterministic version of the current algorithm based on least-squares minimization of frequency response function difference. The Zang et al. algorithm is also based on deterministic least-squares minimization but seeks to bring the analytical model into accordance with the reference data by minimizing error in two frequency response correlation functions. The algorithm of Zimmerman et al. applies minimum rank perturbation theory to find in one iteration step the stiffness or mass matrix change responsible for the difference between the analytical model and reference frequency response functions. The Ricles and Kosmatka algorithm is based on probabilistic least-squares minimization of the difference between analytical and reference natural frequencies and mode shapes.

As with the current algorithm, each of these methods includes various specifics for implementation, such as unique criteria for frequency line selection and parameter filtering. Various implementation details are different between the as-published algorithms and can significantly impact the final results. The comparison is therefore homogenized by focusing on the underlying update equations with the same frequency lines used for all algorithms and some other aspects of as-published implementation either discarded or kept constant across all algorithms. Additionally, some aspects of implementation are modified when doing so improves the overall performance of the algorithms. Details of implementation and deviations from the published algorithms include the following.

For the Zang algorithm the weighted least-squares method seemed to overly constrain or otherwise corrupt results for this test case and the direct sensitivity implementation is used instead.

The Zimmerman algorithm as published produces matrix changes instead of parameter changes so a secondary sensitivity method is implemented to reduce the matrix changes to parameter changes.

For the modal parameter based method of Ricles and Kosmatka, analytical modal parameters are produced, where required, using an undamped eigenvalue analysis. Unlike with the frequency response function data, there is no simple connection between measured data and variance for the modal parameters. Standard deviation values are therefore estimated by multiplying the known applied noise percentage (available since the data was created analytically) by the natural frequency values or the largest normalized mode shape values, depending on data type. Finally, an automated routine is used to guard against mode switching at each iteration step by ordering all generated modes as closely as possible with the reference data based on the modal assurance criterion calculated between the two sets. The modal assurance criterion **Error! Reference source not found.** is generated using the equation

$$MAC_{ij} = \frac{\left(\{\tilde{\phi}_i\}^H \{\phi_j\}\right)\left(\{\tilde{\phi}_i\}^H \{\phi_j\}\right)}{\left(\{\tilde{\phi}_i\}^H \{\tilde{\phi}_j\}\right)\left(\{\phi_i\}^H \{\phi_j\}\right)},\tag{4.26}$$

where $\{\tilde{\phi}_i\}$ is the reference mode shape vector for mode i, $\{\phi_j\}$ is the model mode shape

vector for mode j, and $\{...\}^H$ refers to the Hermitian, or complex conjugate transpose, for

the given vector. Additionally, noise is manually propagated from the frequency response

functions to the reference mode shapes and natural frequencies to simulate the error

associated with modal parameter estimation on noisy data. This is accomplished by

creating a noise vector equal to the noise percentage multiplied by the natural frequency

or mode shape variability which is calculated as the maximum value multiplied by the

noise percentage.

For all runs the additional algorithm variables were set equal to their values from

Section 4.4.3 (i.e., iteration parameter step limit of 20% ; 10% parameter perturbation;

initial parameter standard deviation of 1%; the maximum number of iterations equal to

100; convergence dictated by the average parameter change falling below 0.001). The

frequency lines are selected from the subset that is plus or minus 4% of each of the first

six natural frequencies, greater than -70 dB average frequency response function value,

and coherence greater than 0.98 (natural frequencies 7 and 8 were not used for the

comparison since doing so prevented the Zang algorithm from converging for the zero

noise case). All algorithms (besides Ricles and Kosmatka) used identical noisy datasets

for each analysis case. Finally, only stiffness parameter damage cases 1 and 2 are

assessed since the Zimmerman algorithm is limited to either stiffness or mass changes in

one step, but not both.

Results for all algorithms in terms of mean relative error for 0% noise are given in Table 4-4 for damage case 1 and Table 4-5 for damage case 2. The mean relative error results are also plotted in Figure 4-20 for damage case 1 and Figure 4-21 for damage case 2. In both the tables and plots the error metrics calculated from no change in the healthy values are given as a baseline (note that the healthy value relative error metrics are calculated relative to the correct damaged values and so are not equivalent to the percent reductions in stiffness value). The results show that all of the algorithms converge to the correct results with negligible error with the current algorithm and the Araujo dos Santos et al algorithm performing slightly better than the others, both converging in two iterations to similarly low levels of error. The other three algorithms converge to generally similar levels of higher error, requiring 17 and 22 iterations for the algorithm of Zang et al. and 7 and 6 iterations for the algorithm of Ricles and Kosmatka for damage case 1 and 2, respectively (the algorithm of Zimmerman et al. is not iterative).

The algorithms were subsequently run on both damage cases across 0.1%, 1%, and 10% noise. Results are summarized as mean relative error for the healthy and damaged parameter subsets in Figure 4-22. For the cases with added noise all algorithms except for the current algorithm and the algorithm of Araujo dos Santos reach the maximum number of iterations without converging. It can be seen that the Zimmerman et al. and Ricles and Kosmatka algorithms generally do not achieve meaningfully solutions for the cases with added noise. The Zang et al. algorithm achieves reasonable results in some cases despite not converging; however, the results do not appear to be stable.

Table 4-4: Damage identification relative parameter error and mean relative error values for damage case 1 (k8 -10%) with 0% noise (relative error given as value instead of percent error).

Parameter	Healthy Values	Current Algorithm	Araujo dos Santos	Zang et al.	Zimmerman et al.	Ricles & Kosmatka
ε_{k1}	0	1.69E-09	-1.22E-09	1.24E-04	0.00E+00	-1.20E-04
ε_{k2}	0	-1.38E-10	-3.33E-10	2.65E-05	0.00E+00	9.00E-05
ε_{k3}	0	2.94E-10	-1.01E-09	5.25E-04	0.00E+00	-1.02E-02
ε_{k4}	0	-3.27E-10	1.07E-10	-3.90E-06	0.00E+00	-3.60E-05
ε_{k5}	0	3.14E-09	-8.19E-10	2.91E-05	0.00E+00	4.00E-05
ε_{k6}	0	2.03E-10	-6.27E-11	8.01E-06	3.99E-10	-1.29E-04
ε_{k7}	0	-1.13E-09	-6.59E-11	1.88E-05	-3.60E-09	-1.22E-04
ε_{k8}	0.111	3.78E-10	1.22E-09	4.40E-05	-1.11E-05	1.38E-04
ε_{k9}	0	1.32E-10	8.25E-11	-1.11E-05	4.00E-10	1.56E-04
ε_{k10}	0	1.00E-11	-6.25E-11	-2.81E-06	-5.65E-11	-5.20E-05
ε_{k11}	0	7.37E-09	8.58E-10	3.61E-05	5.70E-09	1.43E-02
ε_{k12}	0	6.55E-08	5.81E-09	5.46E-05	4.71E-11	2.30E-03
ε_{k13}	0	-1.14E-10	-6.27E-11	1.87E-07	-5.70E-11	-1.12E-04
ε_{k14}	0	-3.70E-08	-2.38E-09	-7.70E-05	-2.09E-11	-1.77E-03
ε^d_{MRE}	**0.111**	**3.78E-10**	**1.22E-09**	**4.40E-05**	**1.11E-05**	**1.38E-04**
ε^h_{MRE}	**0**	**9.01E-09**	**9.91E-10**	**7.06E-05**	**7.91E-10**	**2.27E-03**
Iterations		2	2	13	N/A	7

Table 4-5: Damage identification relative parameter error and mean relative error values for damage case 2 (k_8 -10%, k_{12} -5%) with 0% noise (relative error given as value instead of % error).

Parameter	Healthy Values	Current Algorithm	Araujo dos Santos	Zang et al.	Zimmerman et al.	Ricles & Kosmatka
ε_{k1}	0	-6.00E-11	7.64E-10	-3.01E-04	0.00E+00	-5.33E-05
ε_{k2}	0	-4.79E-10	-4.90E-11	-8.36E-07	0.00E+00	1.00E-04
ε_{k3}	0	6.92E-10	1.40E-09	-8.48E-04	-1.90E-14	-1.18E-02
ε_{k4}	0	-1.11E-10	5.33E-11	1.07E-05	0.00E+00	-8.70E-05
ε_{k5}	0	-6.41E-09	6.04E-10	9.42E-06	-1.61E-14	2.10E-04
ε_{k6}	0	-3.36E-10	-1.70E-10	-7.95E-07	-2.27E-05	-1.28E-04
ε_{k7}	0	6.01E-09	-5.53E-10	-3.97E-06	-1.78E-10	-1.54E-04
ε_{k8}	0.111	-6.37E-11	4.46E-10	1.80E-05	3.56E-04	-1.11E-06
ε_{k9}	0	2.55E-10	1.45E-10	-1.08E-06	1.98E-11	1.59E-04
ε_{k10}	0	-5.91E-10	-1.84E-11	-3.04E-07	5.11E-06	-1.30E-05
ε_{k11}	0	-1.22E-08	-1.45E-09	4.15E-05	4.42E-09	1.63E-02
ε_{k12}	0.053	-2.81E-08	-2.77E-09	-8.72E-06	8.06E-03	2.38E-03
ε_{k13}	0	1.53E-10	5.60E-11	-1.81E-06	5.11E-06	-1.26E-04
ε_{k14}	0	1.06E-08	6.45E-10	5.87E-06	-3.41E-03	-1.83E-03
ε^d_{MRE}	**0.082**	**1.41E-08**	**1.61E-09**	**1.34E-05**	**4.21E-03**	**1.19E-03**
ε^h_{MRE}	**0**	**3.16E-09**	**4.92E-10**	**1.02E-04**	**2.87E-04**	**2.58E-03**
Iterations		2	2	21	N/A	6
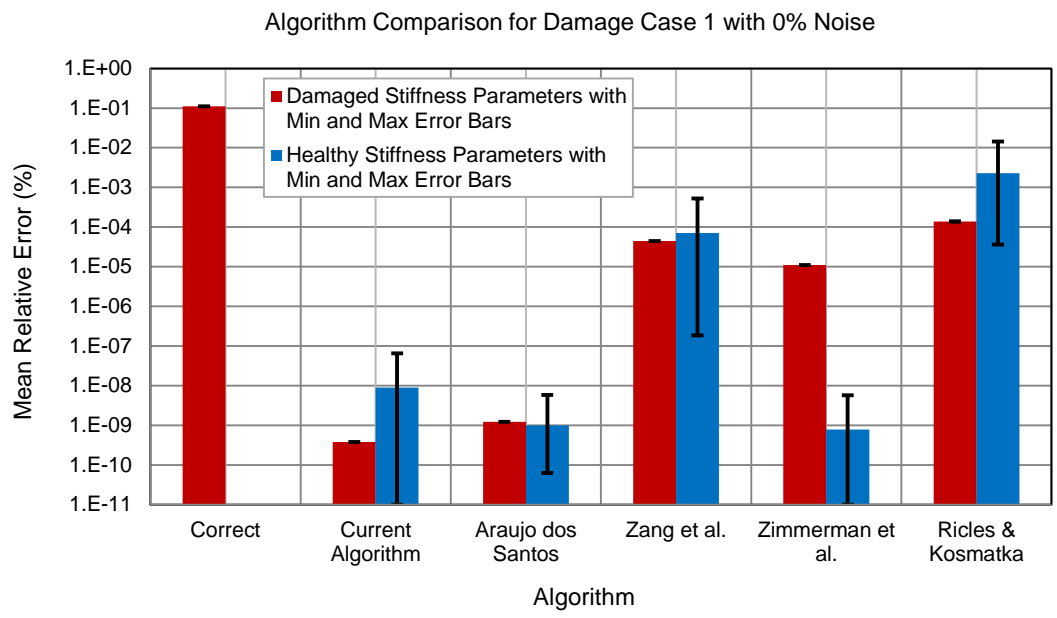
Figure 4-20: Mean relative parameter error for damage case 1 with 0% noise.
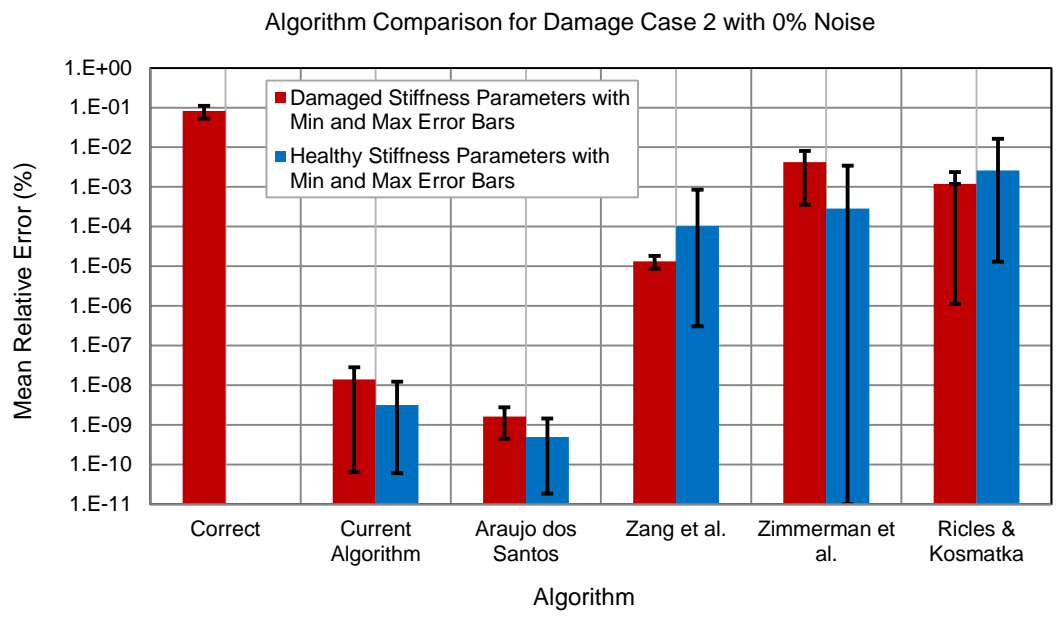
Figure 4-21: Mean relative parameter error for damage case 2 with 0% noise.
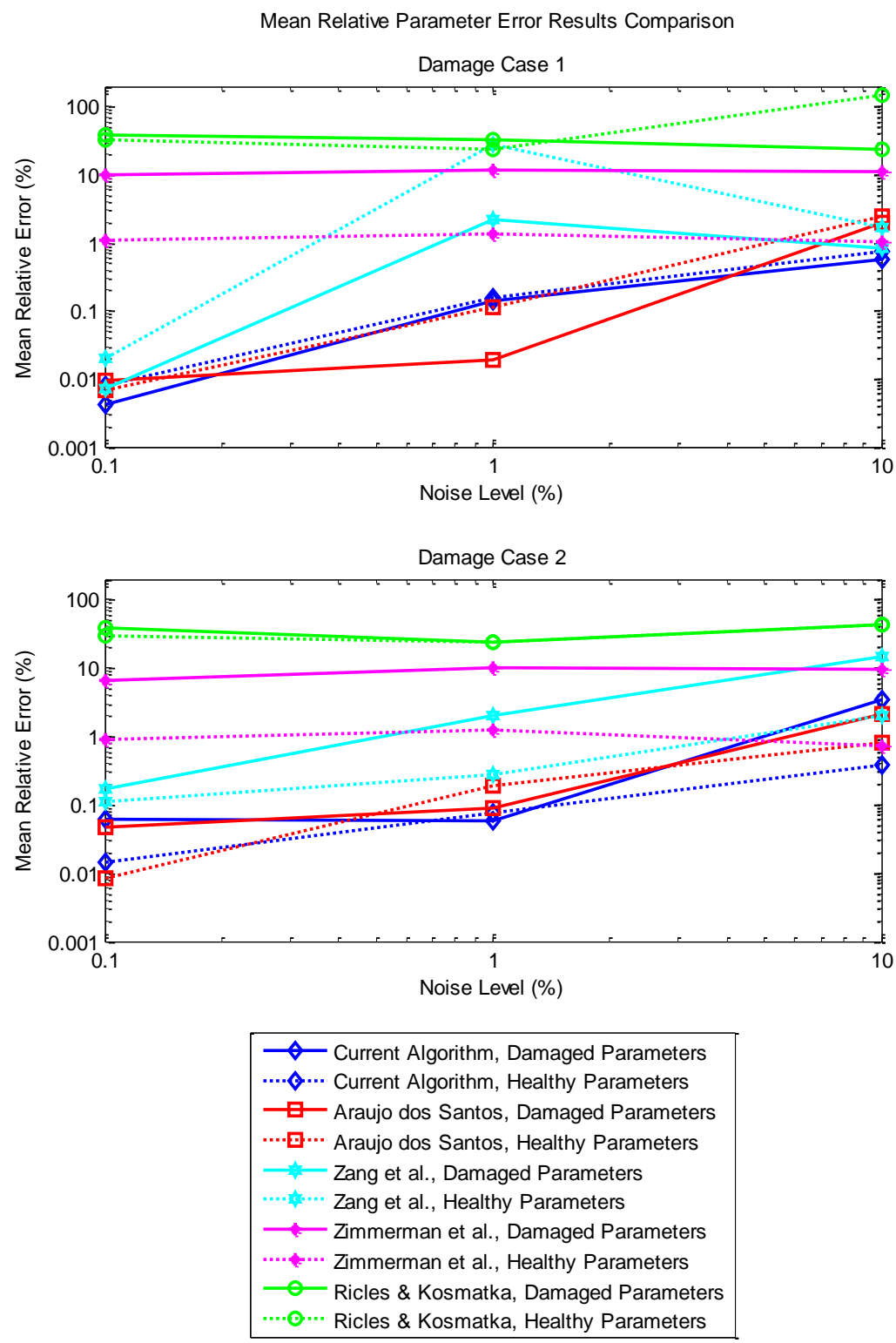
Figure 4-22: Mean relative parameter error for all algorithms across increasing levels of noise.

Additional runs of the noise cases, not presented herein, support this assertion with final

parameter values at the maximum number of iterations being at times severely

erroneous). In all noise cases, the current and Araujo dos Santos et al. algorithms perform

very similarly with error increasing as a function of noise but staying low overall.

Inspection of the converged frequency response functions shows relative frequency

response function error consistent with the amount of parameter error. For example,

frequency response function results from damage case 2 with 10% measurement are

shown in Figure 4-23 for the driving point x_5 and in Figure 4-24 for x_8. In both cases,

updated frequency response functions from the current algorithm and that of Araujo dos

Santos demonstrate the highest fidelity to the reference data although it can be seen that

neither one correctly identifies the mode 8 peak which is visible on the right hand side of

the x_8 plot. Despite having high error metrics for this example, the Zang et al. frequency

response functions are quite accurate for most of the frequency range—possibly a result

of this algorithm being based on matching frequency response function shape and

amplitude metrics. However, the mode 8 peak which relates to the 5% stiffness decrease

in k_{12} is very poorly resolved. The Zimmerman et al. results show noticeable error across

the entire frequency range with a final result that more closely matches the healthy

frequency response functions—a result that suggests a lack of movement in the damage

parameters as a result of the high noise. The Ricles and Kosmatka frequency response

function results bear no resemblance to the target reference data which reflects the

algorithms divergence for this analysis case.
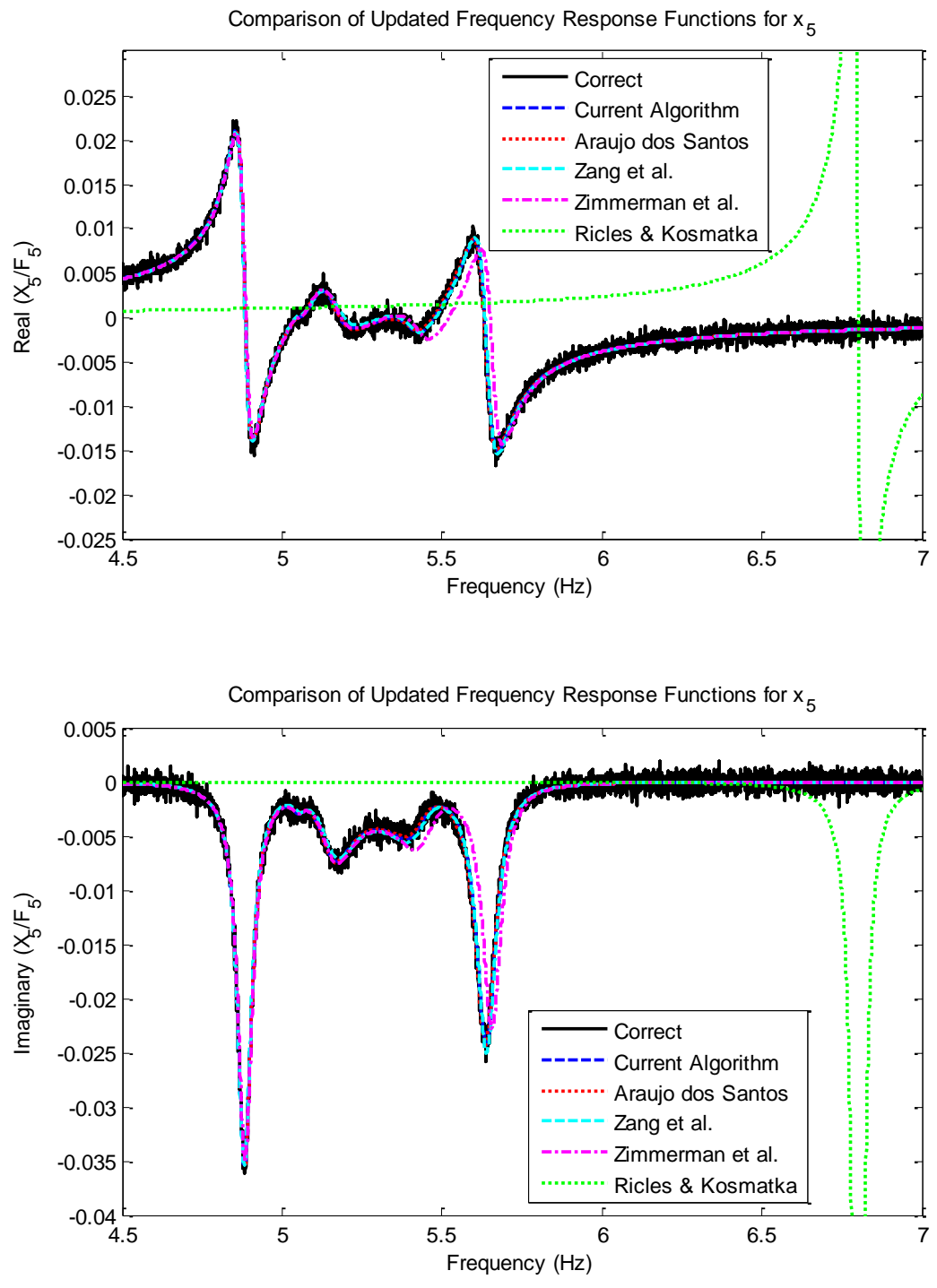
Figure 4-23: Updated frequency response function comparison for damage case 2 with 10% noise, degree-of-freedom x_5.
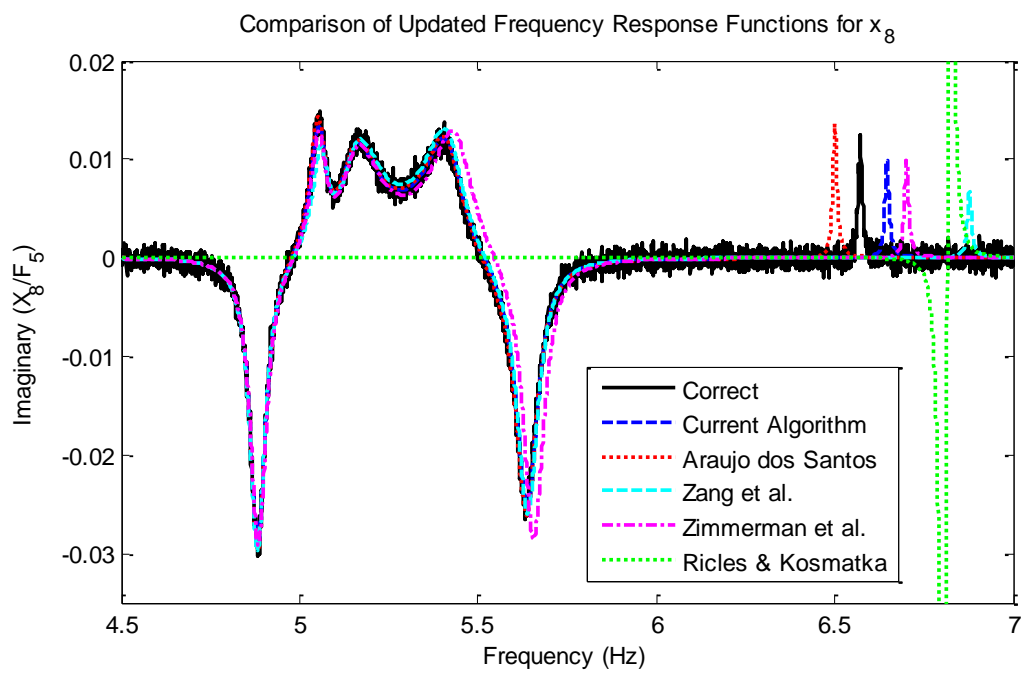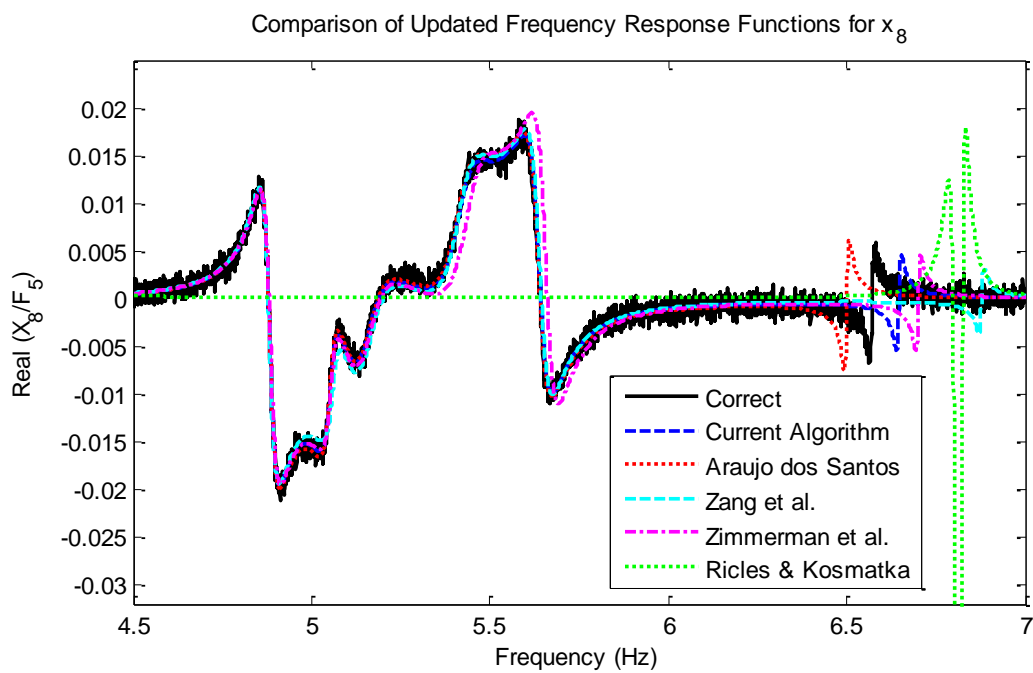
Figure 4-24: Updated frequency response function comparison for damage case 2 with 10% noise, degree-of-freedom x_8.

In order to better compare the Araujo dos Santos et al. algorithm to the current

algorithm both are applied to damage case 3 from Section 4.4.3 across 0.1%, 1% and

10% noise cases. All algorithm variables are kept the same as in the first comparison of

the section with the exception of all mass parameters being included along with all

stiffness parameters for 22 update parameters total, as in Section 4.4.3. Results of the

comparison are summarized in Figure 4-25 and show greatly increased trending of error

with noise for the Araujo dos Santos et al. algorithm compared to the current algorithm.

The difference can be attributed to the increase in number of update parameters and

correspondingly wider variation in parameter sensitivities which lead to decreased

stability during the direct least-squares solutions used by the Araujo dos Santos

algorithm. Regularization provided by the probabilistic formulation of the current

algorithm on the other hand maintains stability even in the face of low and/or varied

parameter sensitivities. This example additionally shows that this stability is maintained

in cases of extremely high levels of noise.

4.4.5   Discussion

The current algorithm for statistical damage identification via frequency response

function-based model correlation, exact sensitivity, and statistically consistent iterative

linearization has been analytically validated on an 8-degree-of-freedom mass-spring

system with nonproportional structural damping and additive broadband white noise on
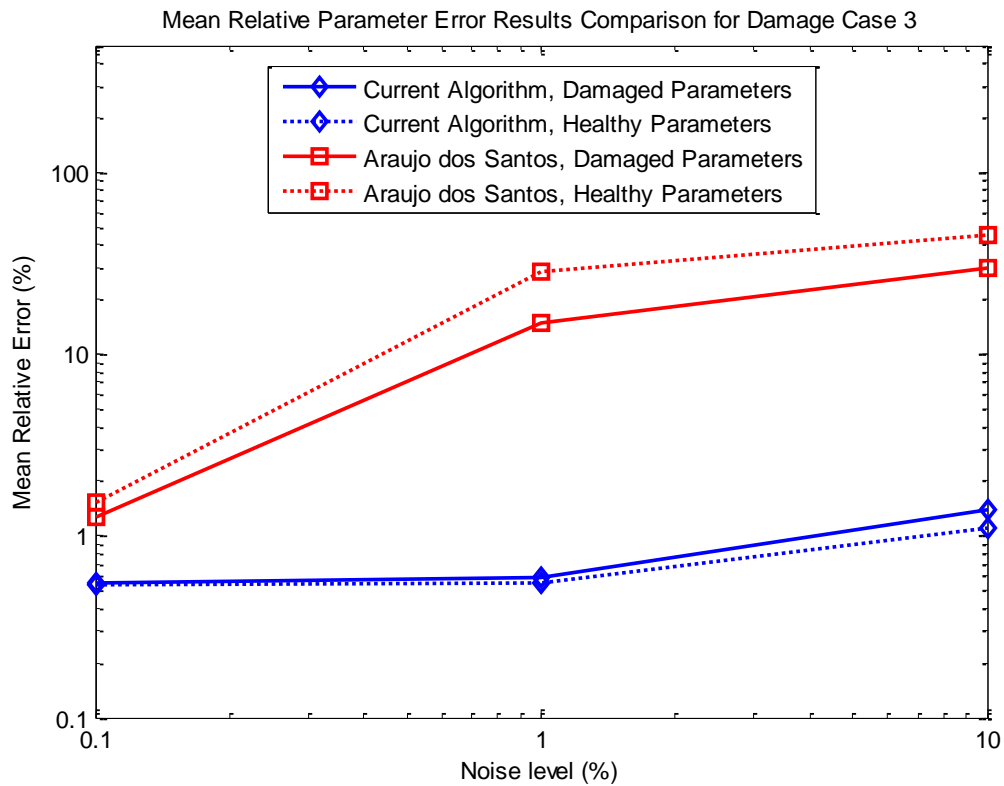
Figure 4-25: Mean relative parameter error for the current and Araujo dos Santos algorithms across increasing levels of noise for damage case 3.

the output ranging from mild to extreme. The analytical studies show that the new

algorithm performs very well for all example damage cases, including those with

concurrent multiple stiffness and mass variations. A direct comparison to four algorithms

from literature further shows the relative accuracy and stability of the current algorithm,

especially for cases with large numbers of damage identification parameters and large

variations of parameter sensitivity. The current algorithm was able to maintain these

favorable traits even in cases of extreme reference data noise when the comparison

algorithms became unstable and divergent. The examples additionally demonstrated the current algorithm's insensitivity to highly coupled system modes.

Author's note: The comparison algorithms were implemented as faithfully as possible within the acknowledged constraints of the comparison example. It is likely that their performance would improve with inclusion of the various additional unique practices discussed in each of the references and that the algorithm authors could find ways to further improve their results on the example system if given the chance.

The material contained in Chapter 4 was developed in collaboration with Prof. John B. Kosmatka, Prof. Charles Farrar, and Prof. Joel Conte. The dissertation author was the primary investigator and author of this work.

4.5   Chapter 4 References

[4-1]   Doebling, S.W., Farrar, C.R., "Estimation of Statistical Distributions for Modal Parameters Identified from Averaged Frequency Response Function Data," Journal of Vibration and Control, 7, pp. 603-604, (2001)

[4-2]   Bendat, J.S. and Piersol, A.G., Engineering Applications of Correlation and Spectral Analysis, John Wiley, New York, (1980)

[4-3]   Schultz, T., Sheplak, M., Cattafesta III, L.N., "Application of Multivariate Uncertainty Analysis to Frequency Response Function Estimates," Journal of Sound and Vibration, 305, pp. 116-133, (2007)

[4-4]   Collins, J.D., Hart, G.C., Hasselman, T.K., and Kennedy, B., "Statistical Identification of Structures," AIAA Journal, 12(2), pp.185–190, (1974)

[4-5]   Zimmerman, D.C., Simmermacher, T., Kaouk, M., "Model Correlation and System Health Monitoring using Frequency Domain Measurements," Structural Health Monitoring, 4(3), pp. 213-227, (2005)

[4-6]   MATLAB version 7.8.0. Natick, Massachusetts: The MathWorks Inc., 2009.

[4-7]   Kabe, A.M., "Stiffness matrix adjustment using mode data," AIAA Journal, 23(9), pp. 1431–1436, (1985)

[4-8]   Araujo dos Santos, J.V., Mota Soares, C.M., Mota Soares, C.A., Maia, N.M.M., "Structural damage identification in laminated structures using frequency response function data," *Composite Structures*, **67**, pp.239-249, (2005)

[4-9]   Zang, C., Imregun, M., "Structural Damage Detection and Localization Using FRF-Based Model Updating Approach," *Key Engineering Materials*, **245-246**, pp. 191-200, (2003)

[4-10]   Ricles, J.M., Kosmatka, J.B., "Damage Detection in Elastic Structures Using Vibratory Residual Forces and Weighted Sensitivity," AIAA Journal, 30(9), pp.2310-2316, (1992)

5   FINITE ELEMENT MODEL IMPLEMENTATION AND VALIDATION

Application of the algorithm to realistically sized structures requires coupling with a finite element model, where the damage is modeled through changes in stiffness, density, lumped masses, and material damping, or other smoothly varying parameters. Given a finite element model which accurately modeled the system in its baseline state, reference data from the damaged system, and information on the approximate damage location the system operates as follows:

(1)   Damage location information is translated into a set of candidate damage parameters (including possible stiffness, mass, and damping changes);

(2)   Frequency filtering is performed to determine analysis frequency lines, and create noise covariance matrix from coherence values;

(3)   The damage identification algorithm is applied to produce damage information, estimation uncertainty, and an updated finite element model.

After damage identification is complete, post-processing can complete the structural health monitoring process. Post-processing activities may include examining updated damage parameter values and variances, damage mapping, structural analysis using the updated model, and refining the damage parameter set for subsequent iterations of the damage identification analysis.

Implementation and code architecture are discussed in Section 5.1 and numerical issues and solutions are discussed in Section 5.2. A finite element model based analytical

validation and parametric studies are presented in Section 5.3. The chapter concludes

with methods for modeling damping in reduced coordinates and supporting examples in

Section 5.4.

5.1   Code Overview and Architecture

Code to implement the damage update algorithm with finite element models was

written in 64-bit Matlab 2009a [5-1] according to the schematic representation given in

Figure 5-1. A cornerstone of the code is its ability to interact automatically with

NASTRAN finite element model decks and the NASTRAN finite element analysis code

to run updated models and read the results as the update progresses. This is handled via

reading and writing the following standard NASTRAN text files:

- '*.BDF' bulk data files—standard NASTRAN input file, used to read model

  parameters (e.g., material and element properties, element connectivity)

- '*.PCH' punch files—optional NASTRAN output file, used to read degree-of-

  freedom information

- '*.OP4' output data files— optional NASTRAN output file, used to read

  system matrices

- '*.F06' files—standard NASTRAN text-based output file, used to read modal

  data results if required.
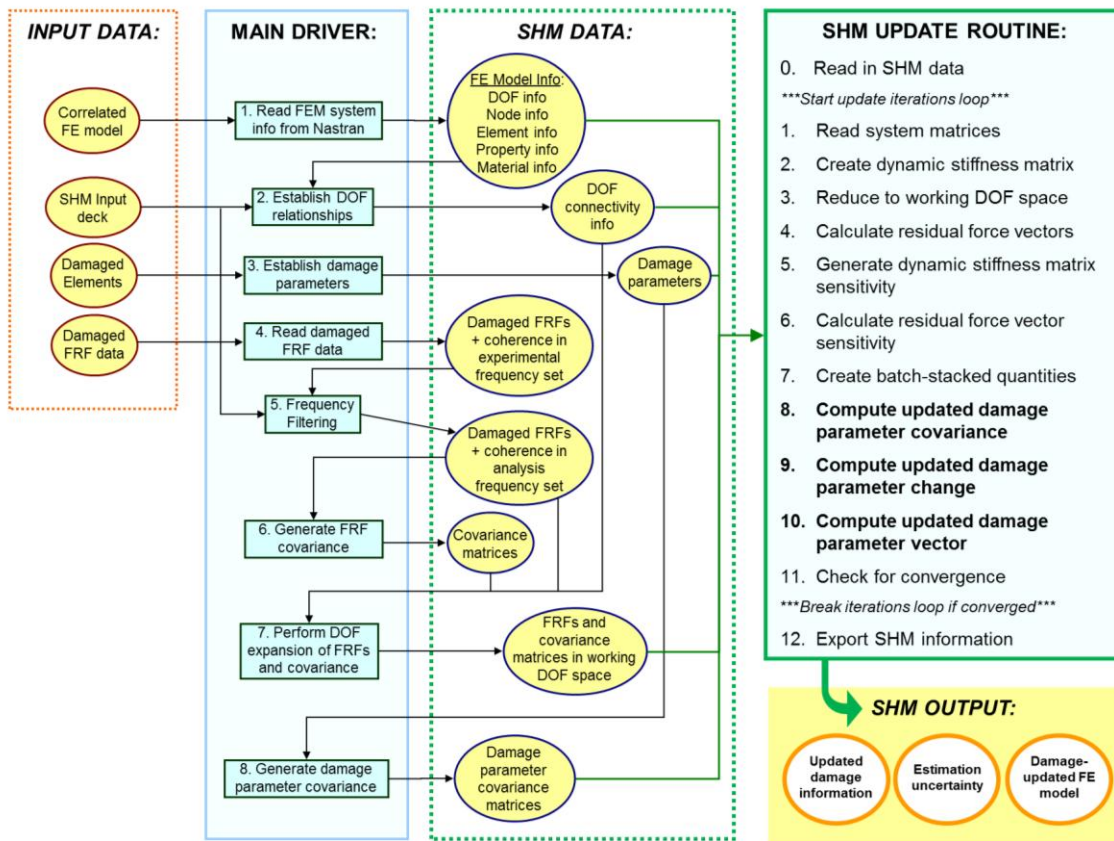
Figure 5-1: Flowchart describing operation of the current algorithm operation (FE ≡ finite element, SHM ≡ structural health monitoring, FRF ≡ frequency response function, DOF ≡ degree-of-freedom).

As can be seen from Figure 5-1, the code is organized around a main driver which

reads in all required information from the finite element model *.BDF* file, structural

health monitoring input deck, damaged elements set, and damaged frequency response

function data, performs preliminary operations, and then calls the damage identification

routine which loops until convergence is reached. The code is primarily written in a

single script, but calls a series of sub-functions for operations that are used repeatedly,

such as degree-of-freedom reduction. The 64-bit implementation allows large variables to

be stored relative to 32-bit Matlab limitations; however, even though the code was configured to maximize storage space and efficiency, it was found that performance was limited on the available PC workstation for models with greater than approximately 12,000 degrees-of-freedom. This is not a large number of degrees-of-freedom compared to the number which would be required for large structures but it is large enough to allow validation of the code for reasonably sized sub-structures.

5.2   **Numerical Issues and Solutions**

There are several challenges involved with applying sensitivity based parameter estimation to realistically sized structures modeled using the finite element method. Potentially continuous physical damage cases must be discretized by the mesh, meaning that the damage definition will be approximate. The model must be created without prior knowledge of the exact damage and so discretization errors may be compounded. Also, the influence on model response from the combined effects of modeling error and noise must be less than the influence of the damage—considerably so for accurate damage identification. The result is that the entire structure must be modeled accurately with respect to not only the healthy condition but unknown damage cases, and thus a large number of elements and analytical degrees-of-freedom may be required, leading to problems with numerical conditioning, low individual parameter sensitivities, truncation

error, and nonlinearity when the model is reduced to the measurement degrees-of-freedom.

Several additions to the algorithm, described in the following paragraphs, help deal with these problems. The additions can be grouped into three categories:

(1) Damage factor scaling;

(2) Iteration step limit;

(3) Methods to combat low-parameter sensitivity.

5.2.1 Damage Factors

Numerical conditioning is improved by using multiplicative *damage factors* for all update parameters instead of the real-unit parameters. These scaled factors equal unity for no change, zero for complete nullification, and fractions and multiples for partial damage, meaning all parameters within the algorithm—whether stiffness, damping, or mass—exist at the same order of magnitude. The real unit parameter values are recovered by multiplying their original value by the current damage factor before being sent back to the finite element model.

5.2.2 Iteration Step Limit

An iteration step limit can be implemented to aid nonlinear convergence. The step limit process functions by scaling down all damage factor changes proportionally at each iteration, if required, until the largest damage change is equal to the limit. The update

process is therefore prevented from moving too far in any iteration and is forced to adhere more closely to the underlying nonlinear convergence curve.

5.2.3 Methods to Combat Low Parameter Sensitivity

Algorithmic additions in the third category help address issues associated with low parameter sensitivity and the machine precision numerical truncation error that can occur as a result. As discussed in Section 3.6, the residual force vector sensitivity matrix is based on the dynamic stiffness sensitivity calculated via finite difference by (1) perturbing each damage factor in turn, (2) subtracting the perturbed dynamic stiffness from the original, and (3) dividing by the perturbation. Although all parameters are the same order of magnitude in the scaled damage factor space they are represented in real units within NASTRAN's internal system matrix definitions. Therefore, if the parameter being perturbed is small compared to additive values in $\underline{Z}(\hat{r}_i)$, the difference will get lost in truncation error and the effective sensitivity will become inaccurate or zero. As available computational numerical precision continues to increase, smaller and smaller sensitivities will be calculable through this method; however, the size of models will also increase and so the problem will persist to some extent. Three approaches are adopted to combat this problem, as detailed in the following paragraphs.

The first method makes use of the fact that many damage cases can be modeled in such a way that the unreduced $\underline{Z}(\hat{r}_i)$ is linear in $\hat{r}_i$—for example by modifying Young's modulus in isotropic materials. The magnitude of multiplicative damage factor change, Δ,

therefore doesn't matter and can be set very large, as opposed to the nonlinear case where it must be kept small enough that the local function behavior is close to linear.

The second method involves grouping elemental parameters together under a single damage factor in such a way that changing the damage factor affects multiple elements. This step helps increase damage factor sensitivities (since a greater number of model parameters are being controlled by each damage factor), thereby decreasing the risk of truncation error in nonlinear parameters and improving numerical conditioning. The total number of parameters is also decreased, which consequently decreases nonuniqueness and computation times. The parameter grouping can be done in any way that makes physical sense; an obvious method is to group local clusters of elements which are likely to be under very similar damage conditions.

The third method is to screen parameters as the update progresses and simply exclude those which fall below a certain sensitivity threshold, holding their current values constant for the remainder of the damage identification update. Even if the parameters are in a damaged area, low sensitivity means they will not contribute in a worthwhile way to the response and so their exclusion is mainly cosmetic.

5.3   Analytical Validation on Composite Sandwich Plate Models

The current damage identification algorithm is now validated analytically using a 2028 degree-of-freedom composite sandwich plate model with simulated measurement

noise. This structure is based on modern all-composite aircraft wing skin design, with thin graphite-epoxy composite laminates bonded to each side of a honeycomb core. The resulting structures are extremely lightweight with high bending stiffness but are susceptible to impact damage which can cause core crushing and laminate damage with little or no external evidence. In order to demonstrate functionality of the algorithm on a quasi-experimental scale, validation damage identification runs were performed using analytically created noisy system transfer and coherence functions from three damage cases with data from a limited number of measurement points. A parametric study was then conducted to investigate relative performance of the algorithm when varying (1) the number of frequency lines used in the update, (2) the coherence threshold for the automatic frequency line selection scheme, (3) the amount of added noise, (4) the ratio of the number of measurement degrees-of-freedom to the number of frequency lines, and (5) the number of update parameters.

A detailed description of the structure is given below followed by details of the validation and parametric studies. All operations were performed in Matlab R2009a [5-1] with finite element analysis performed using MD. NASTRAN 2006a [5-2].

5.3.1   Baseline System Description

The structural system used for all studies is a square composite sandwich plate finite element model with areal dimensions 0.3048 m by 0.3048 m and thickness of 0.004064 m on a 12 x 12 element grid. The 0.003048 m thick Nomex honeycomb core

was modeled as a MAT9 anisotropic material using PSOLID property definitions in

CHEXA solid elements. The laminates were modeled to simulate four 0.000127 m thick

plies of unidirectional graphite-epoxy composite according to the total layup [0/+45/-

45/90/core/90/-45/+45/0]$_T$ (where 0 degree plies are oriented with the x-axis and positive

angles follow the right-hand-rule with the z-axis pointing vertically up) using the MAT8

orthotropic material definition. The plies were combined using a PCOMP laminate

property definition with CQUAD4 plate elements transversely offset away from the

central plane so that they directly share nodes with the core to form a rigid connection.

The model is shown in Figure 5-2 with material properties given in Table 5-1.
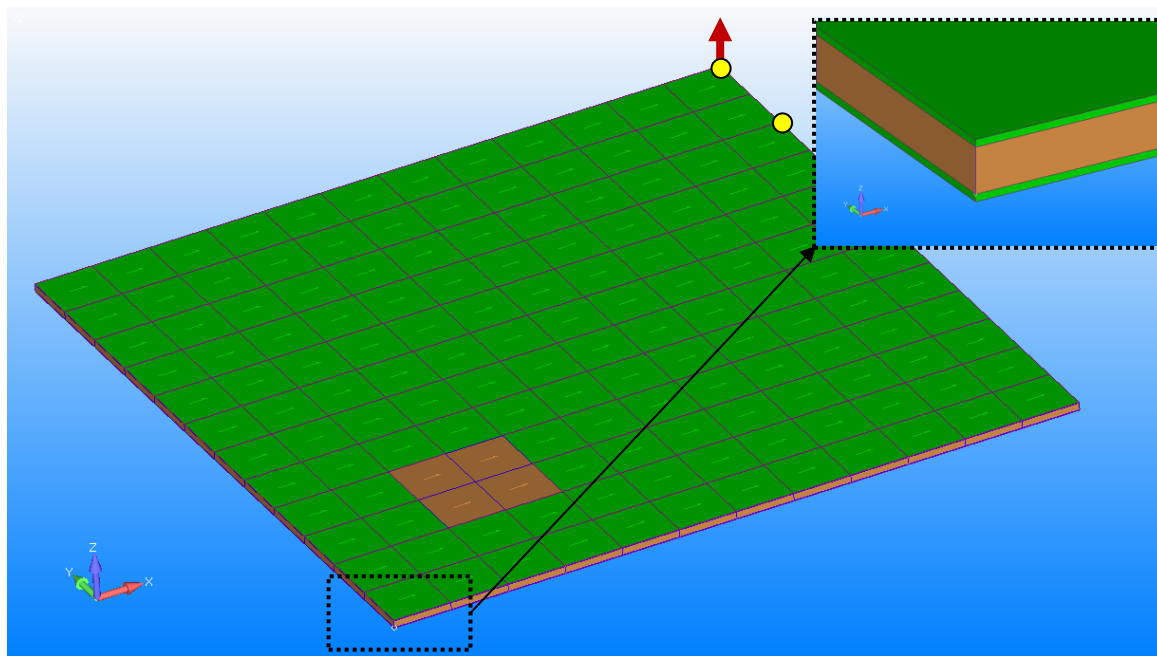
Figure 5-2: Complete view and close up view of the model with 0 degree fiber orientation direction arrows aligned with x-axis, forcing degree-of-freedom as large vertical arrow, and lumped masses represented by solid circles (laminate damage region described in Section 5.3.2 is represented as dark patch in the bottom left quadrant).

Table 5-1: Finite element model material properties for the healthy sandwich plate (note: structural damping constant η and Rayleigh damping constants α and β were applied to the system after exporting undamped system matrices from NASTRAN).

Laminates (3D orthotropic)		Core (3D anisotropic)	
Property	**Healthy Value**	**Property**	**Healthy Value**
E_{11} (GPa)	132.4	G_{11} (GPa)	1.0000×10^{-7}
E_{22} (GPa)	9.1360	G_{22} (GPa)	1.0000×10^{-7}
G_{12} (GPa)	4.5970	G_{33} (GPa)	0.13800
v_{12}	0.30000	G_{44} (GPa)	1.0000×10^{-7}
G_{13} (GPa)	4.5970	G_{55} (GPa)	0.041400
G_{23} (GPa)	3.3000	G_{66} (GPa)	0.024100
ρ (g/cm^3)	1.6608	$G_{ij}, i \neq j$ (GPa)	0
η	0.001	ρ (g/cm^3)	0.25156
α	2×10^{-6}	η	0.001
β	0	α	2×10^{-6}
		β	0

The material property values in Table 5-1 were reached through modal correlation studies on an experimental version of the test plate. In particular, the combined structural and Rayleigh proportional damping model was selected with the given values for η, α, and β based on excellent correlation to the test data. As mentioned in previous chapters, proportional damping is usually not accurate for built-up aerospace structures. However, for the thin plate with free-free boundary conditions in the current example the model is appropriate. The aforementioned correlation is not addressed further in this dissertation since the exact healthy values are not relevant to the objectives of the analytical studies.

In the general experimental case, reference data would be collected by vibration testing the damaged structure at a set number of measurement degrees-of-freedom and experimental frequency lines. For the current analytical validation, pseudo-experimental reference data was created to simulate real experimental data via the following process:

(1)   Apply damage to the baseline finite element model;

(2)   Extract mass and stiffness matrices and assemble the dynamic stiffness matrix at the pre-specified experimental frequency lines;

(3)   Invert the dynamic stiffness matrix at each frequency and save the resulting frequency response functions from the specified forcing degree-of-freedom;

(4)   Add the required amount of noise in the time domain as a percentage-of-time-series power using the process defined in Section 4.4.

The healthy baseline reference frequency response functions were created at 3667 frequency lines over the range 100-1200 Hz, with forcing applied at the top-right corner upper surface normal-to-plate translational degree-of-freedom, as shown in Figure 5-2. Two 0.5 g lumped masses were attached at and near the forcing degree-of-freedom to simulate bonded accelerometers, as also shown in Figure 5-2. Noise at the 0.5% time series power was added to clean analytical frequency response functions to simulate the noise seen when performing experimental hammer-impact vibration testing in a laboratory environment. Coherence functions were calculated using the process described in Section 4.4.3. The resulting driving point baseline displacement frequency response function is given along with coherence in Figure 5-3.
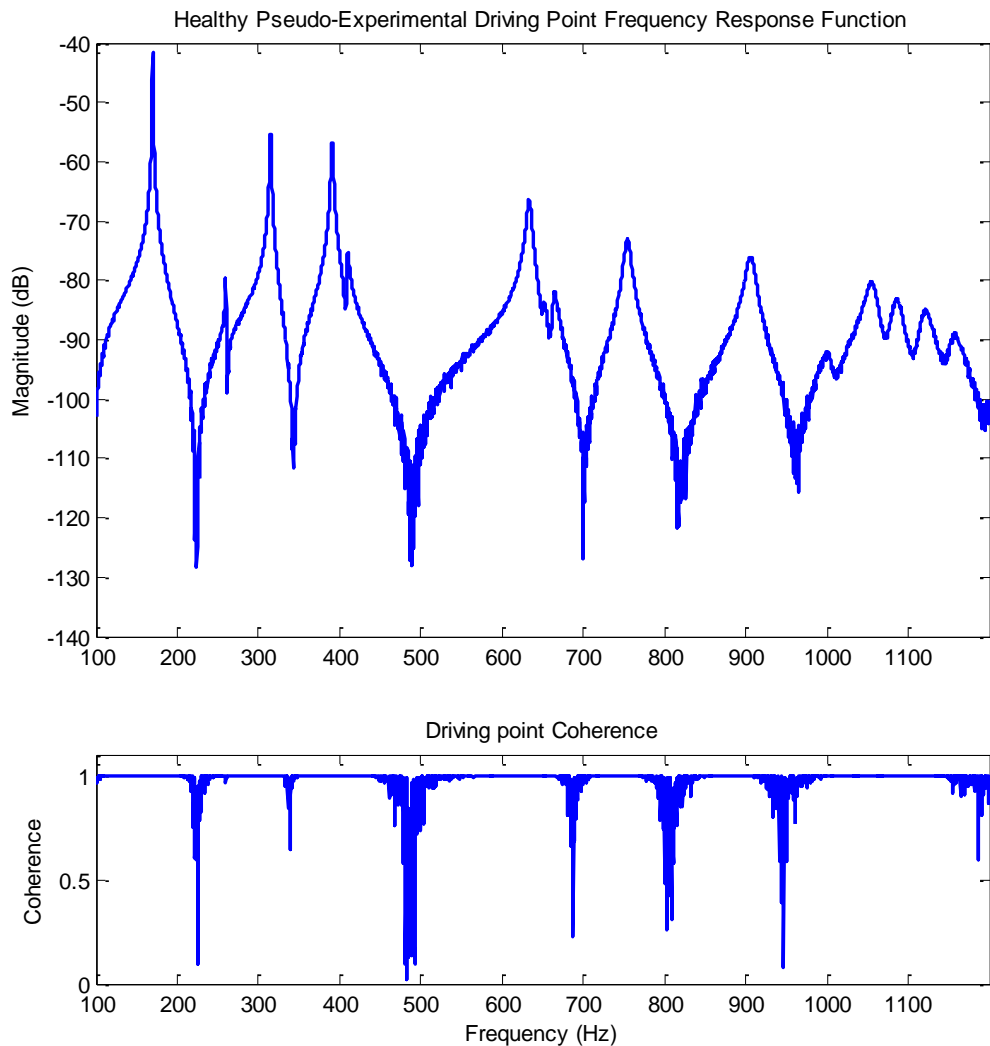
Figure 5-3: Driving point frequency response functions with 0.5% noise from the three damage cases overlaid with the undamaged reference function (top), and coherence function from damage case 3 (bottom), showing typical effects of noise.

5.3.2 Damaged System Description

Three damage cases were created to simulate possible impact damage centered in

the lower left corner of the plate:

- **Damage Case 1:** Pure core crushing over a 4×4 element square region, modeled as a 50% reduction in out-of-plane shear stiffnesses E_{13} and E_{23} in damaged core elements;

- **Damage Case 2:** Laminate damage over a smaller 2×2 element square region, modeled as a 10% reduction of all stiffness parameters in damaged laminate elements (E_{11}, E_{22}, G_{12}, G_{13}, and G_{23});

- **Damage Case 3:** Combined core crushing and laminate damage, modeled by a combination of the first two damage cases.

As with the baseline system, structural damping and viscous damping, both proportional to the global stiffness matrix, were added to the system for all cases. The damage cases are summarized in Figure 5-4 and Table 5-2.
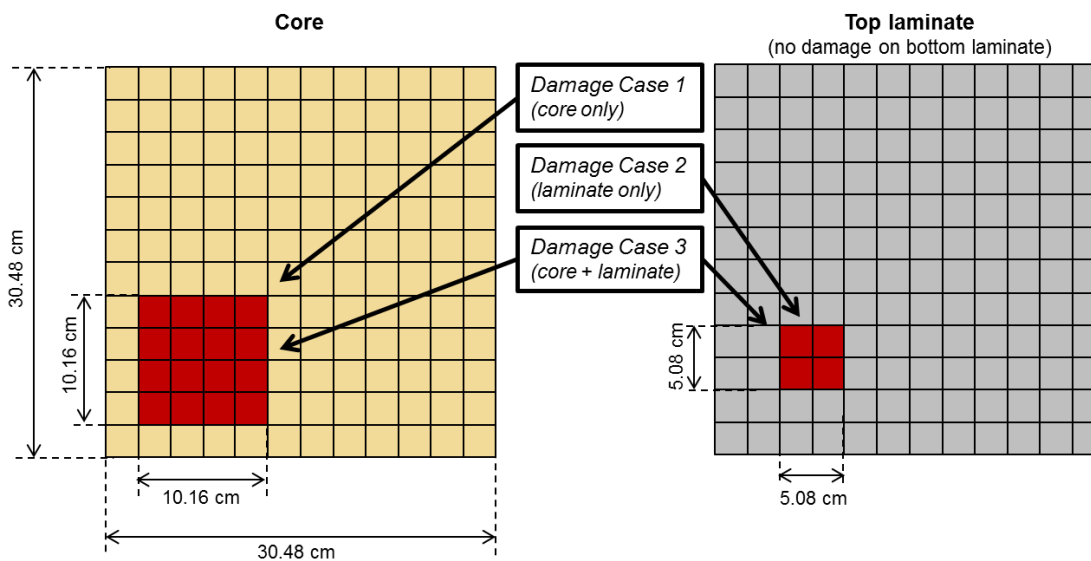
Figure 5-4: Description of in-plane plate dimensions and damage cases.

Table 5-2: Finite element model material properties for healthy sandwich plate and damage cases (note: structural damping constant η and Rayleigh damping constants α and β were applied to the system after exporting undamped system matrices from NASTRAN).

Laminates (3D orthotropic)				
Property	**Baseline Value**	**Damage Case 1**	**Damage Case 2**	**Damage Case 3**
E_{11} (GPa)	132.40	-10%	*no change*	-10%
E_{22} (GPa)	9.1360	-10%	*no change*	-10%
G_{12} (GPa)	4.5970	-10%	*no change*	-10%
v_{12}	0.30000	*no change*	*no change*	*no change*
G_{13} (GPa)	4.5970	-10%	*no change*	-10%
G_{23} (GPa)	3.3000	-10%	*no change*	-10%
ρ (g/cm^3)	1.6608	*no change*	*no change*	*no change*
η	0.001	*no change*	*no change*	*no change*
α	2×10^{-6}	*no change*	*no change*	*no change*
β	0	*no change*	*no change*	*no change*

Core (3D anisotropic)				
Property	**Baseline Value**	**Damage Case 1**	**Damage Case 2**	**Damage Case 3**
G_{11} (GPa)	1.0000×10^{-7}	*no change*	*no change*	*no change*
G_{22} (GPa)	1.0000×10^{-7}	*no change*	*no change*	*no change*
G_{33} (GPa)	0.13800	*no change*	*no change*	*no change*
G_{44} (GPa)	1.0000×10^{-7}	*no change*	*no change*	*no change*
G_{55} (GPa)	0.041400	*no change*	-50%	-50%
G_{66} (GPa)	0.024100	*no change*	-50%	-50%
$G_{ij}, i \neq j$ (GPa)	0	*no change*	*no change*	*no change*
ρ (g/cm^3)	0.251558	*no change*	*no change*	*no change*
η	0.001	*no change*	*no change*	*no change*
α	2×10^{-6}	*no change*	*no change*	*no change*
β	0	*no change*	*no change*	*no change*

Pseudo-experimental frequency response functions from each of the three damage cases were created in the displacement domain using the same process as described for the healthy baseline data in Section 5.3.1, including the addition of 0.5% added noise. The resulting driving point frequency response functions for each damage case are plotted along with a noise-free version of the healthy driving point frequency response function in Figure 5-5. A zoomed view is further given in Figure 5-6. The curves fall into two groups of two overlaid curves each with the healthy case and damage case 2 functions in one group and the damage case 1 and damage case 3 functions in another. By comparing the curves to the known damage cases it can be inferred that the core damage causes an obvious change in vibration response while the smaller laminate damage causes a smaller change. The frequency response functions are further examined by way of mean absolute value frequency response function difference plotted at each of the normal degrees-of-freedom from the top laminate in Figure 5-7, Figure 5-8, and Figure 5-9 for damage cases 1, 2, and 3, respectively. These plots show the spatial distribution of average frequency response function difference on the plate as a result of each damage case. It can be seen that the damage produces predominately global changes in the response of the plate with local effects around the damage region as a second-order effect. The plots additionally support the previous observation that the core damage creates a smaller change in response than the laminate damage.
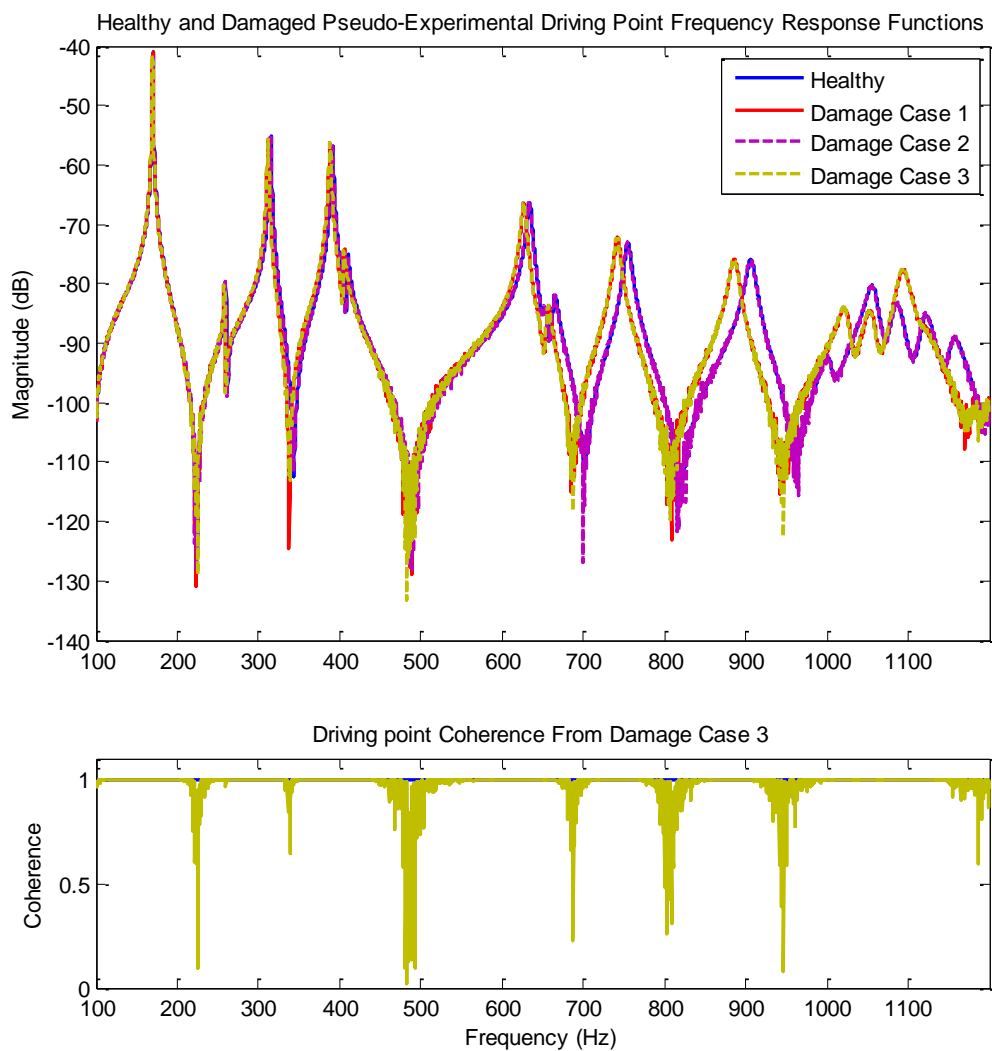
Figure 5-5: Driving point frequency response functions with 0.5% noise from the three damage cases overlaid with the undamaged reference function (top), and coherence function from damage case 3 (bottom), showing typical effects of noise.
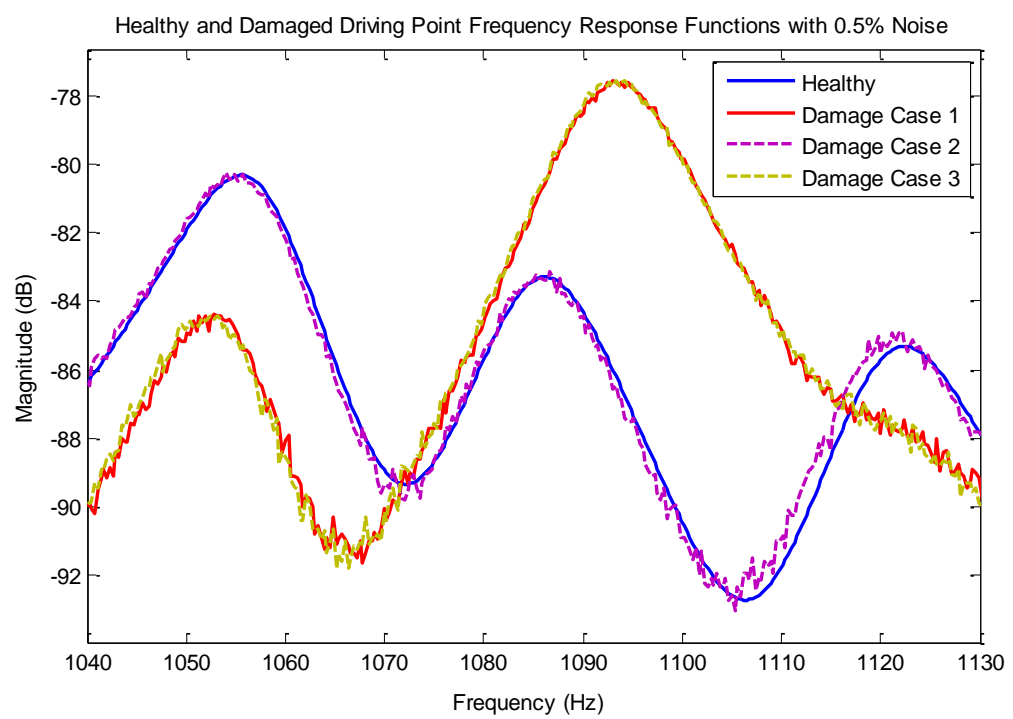
Figure 5-6: Zoomed view of healthy and damaged driving point frequency response functions with 0.5% noise to better show relative impact of damage cases.
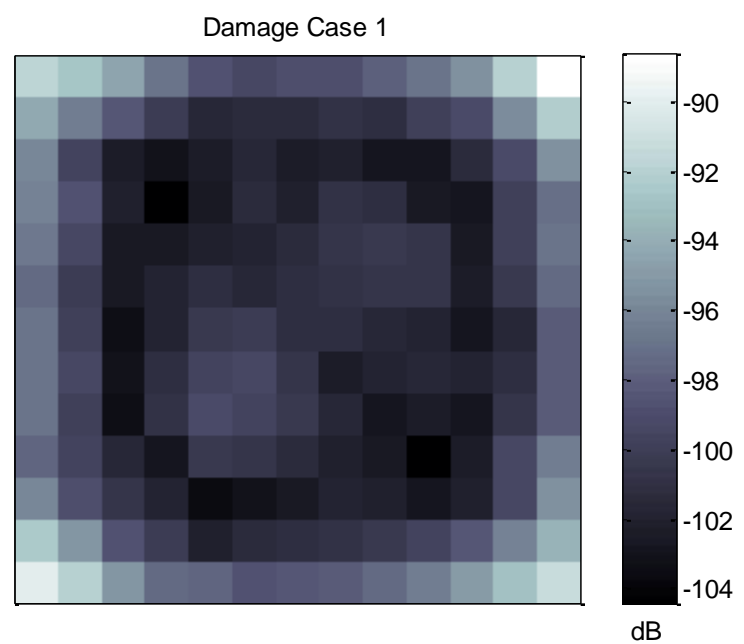
Figure 5-7: Mean absolute value frequency response function difference at top laminate normal degrees-of-freedom for damage case 1 in units of dB.
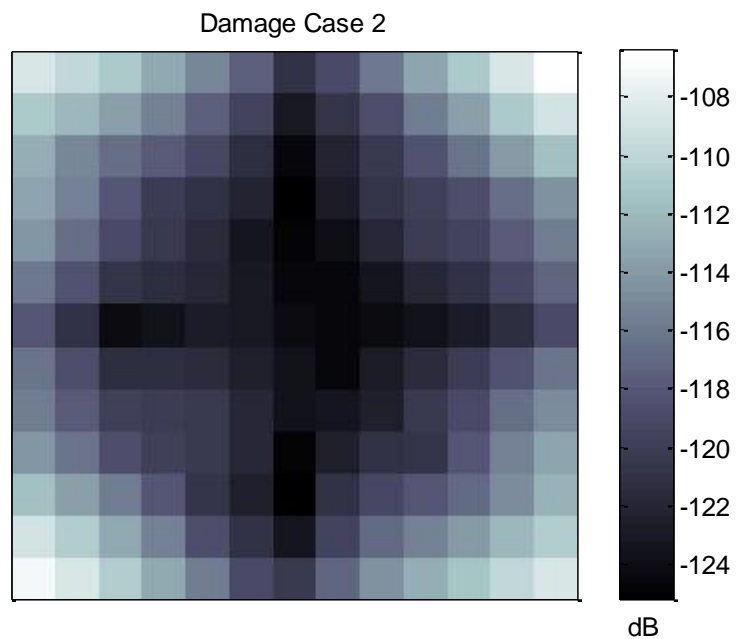
Figure 5-8: Mean absolute value frequency response function difference at top laminate normal degrees-of-freedom for damage case 2 in units of dB.
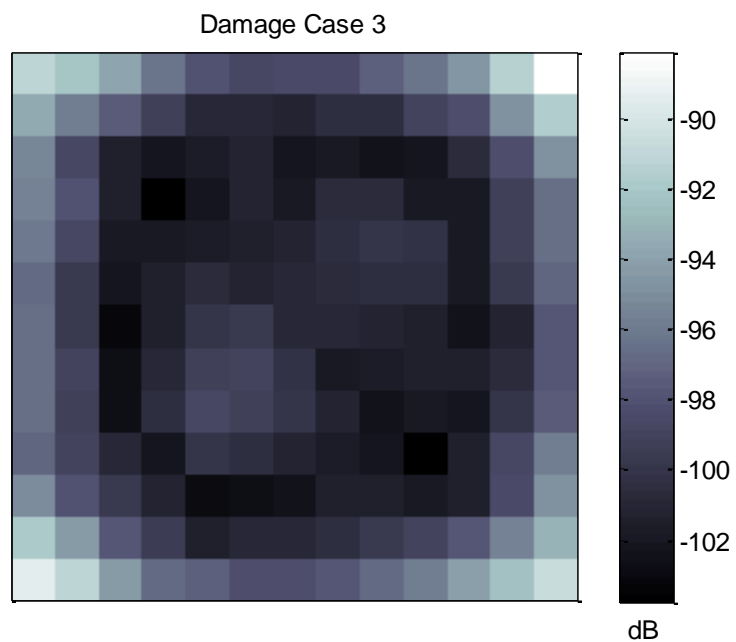
Figure 5-9: Mean absolute value frequency response function difference at top laminate normal degrees-of-freedom for damage case 3 in units of dB.

5.3.3   Finite Element Damage Identification Validation

Damage identification was performed on each of three damage cases with the goal

of validating basic operation of the main algorithm components on a realistic multi-

material composite structure modeling using finite elements. Algorithm parameters used

for the validation runs were set as follows:

- 25 measurement degrees-of-freedom ($N_d = 25$) arranged in an evenly

  distributed 5×5 grid as shown in Figure 5-10.

Top Laminate

● = Analysis degree-of-freedom
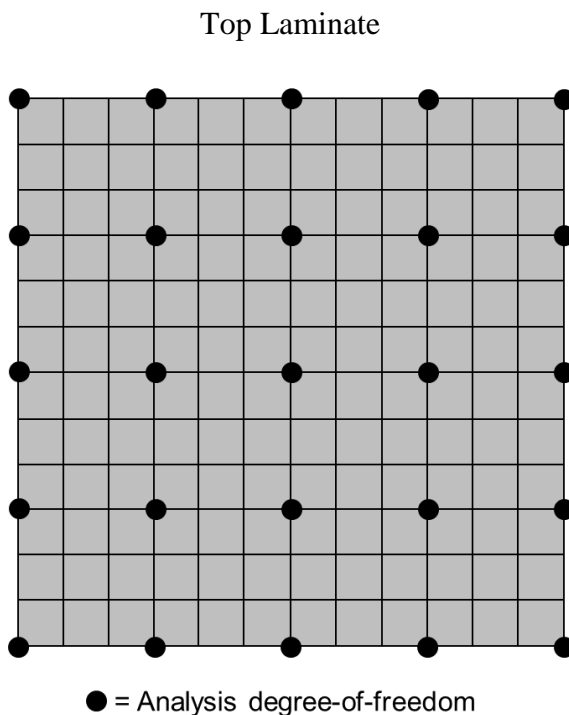
Figure 5-10: Analysis degrees-of-freedom for $N_d = 25$ damage identification validation cases, shown relative to finite element mesh on top laminate (degrees-of-freedom normal to the plate, coming out of the page).

- 20 analysis frequency lines ($N_\omega = 20$) selected from the 3667 frequency lines available in each damaged reference data using the coherence criteria discussed in Section 4.1 with a coherence threshold of 0.999.

- 18 elemental damage factors chosen from the lower left quadrant of the plate according to Figure 5-11, giving a combination of nine core and nine laminate regions with 3 to 5 elements each for a total update parameter count of $N_r =$ 18. In the case of the core elements the damage factor was applied equally to out-of-plane shear stiffnesses E_{13} and E_{23} to model skin-core disbond. For the laminate elements the damage factor was applied equally to all orthotropic stiffness parameters (E_{11}, E_{22}, G_{12}, G_{13}, and G_{23}), to model general laminate damage. In each case, this setup caused the system matrices to be linear with all damage factors, meaning a large perturbation ($\Delta = 1\times10^6$ for all runs herein) could be used to find the dynamic stiffness matrix sensitivities.

- Initial damage parameter standard deviation values of 100% of initial value (i.e., prior variance values equal to 1.0), producing an initial parameter covariance matrix $\left[S_{\hat{r}_0\hat{r}_0} \right]$ equal to the $\left(N_r \times N_r \right)$ sized identity matrix where N_r is the number of damage parameters.

Whole Plate Viewed from Top

Core Sub-Region

Top Laminate Sub-Region
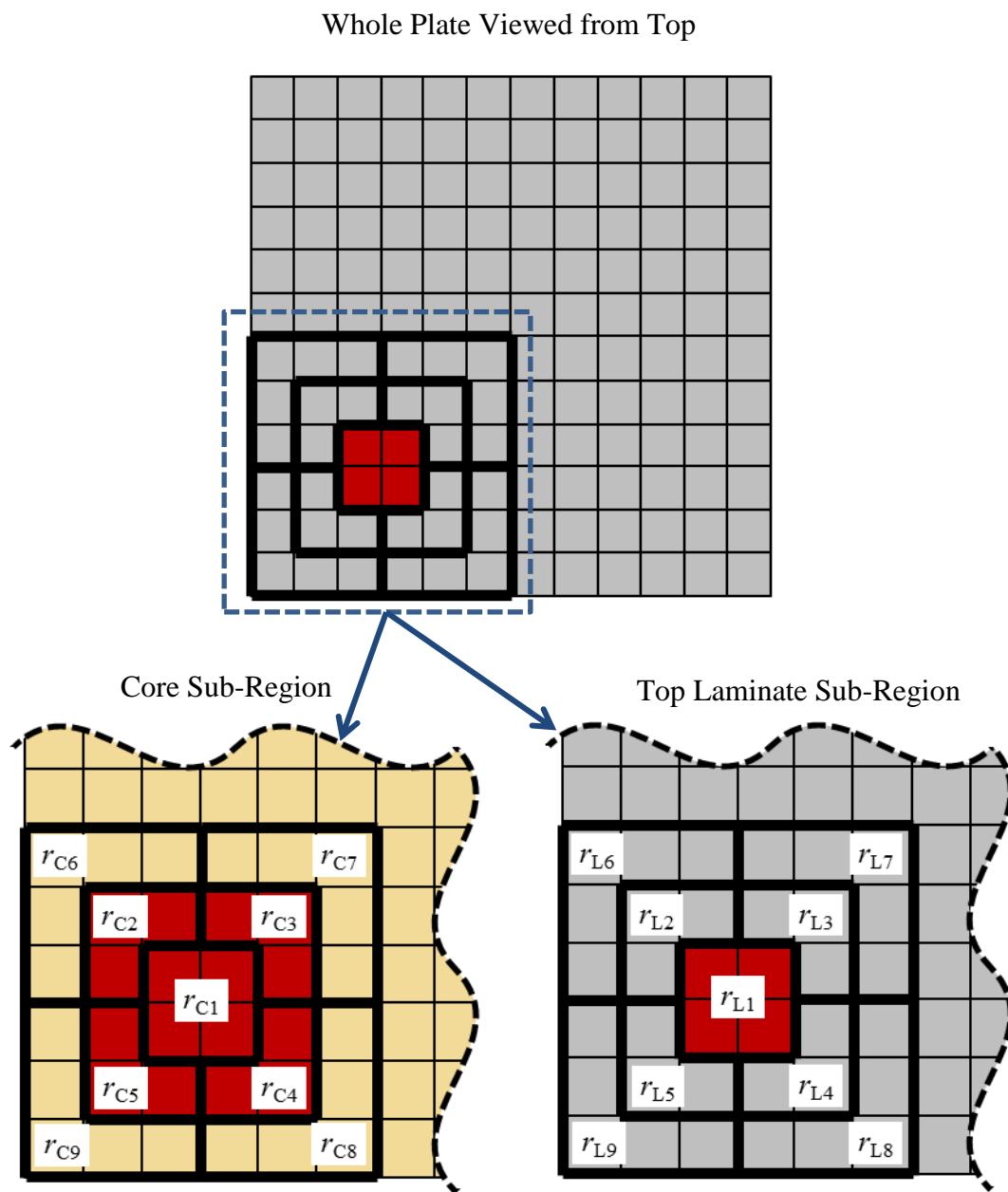
Figure 5-11: Damage factor grouping for the baseline validation case, shown on the full plate at top and on cut-away sections of the core and upper laminate sandwich plate layers on bottom (heavy black lines delineate damage parameter groupings.

- Iteration damage parameter step limit applied such that any parameter attempting to change more than 9% of its original value would cause all parameter changes to be proportionally scaled down until it was below this limit. The particular value of 9% was a compromise between choosing a higher value, which would potentially not constrain the update enough to be stable; choosing a lower value, which would unreasonably slow convergence; and avoiding making the step limit a multiple of the known damage amounts, which would potentially provide an unfair advantage by limiting the damage factors to the exact solution before convergence.

- Convergence criteria set to cause a break from iterations on the second consecutive incidence of mean parameter change less than 0.1% of the original values.

Convergence plots for the baseline validation are given in Figure 5-12 with the correct damage levels shown as dotted lines. Table 5-3 additionally gives the converged values for each case and the amount of relative error for each parameter and mean relative error calculated over all of the updated parameters. The updated damage parameter error ε_i is calculated as

$$\varepsilon_i = \left(\frac{\tilde{r}_i - \hat{r}_i}{\hat{r}_{0,i}} \right) \cdot 100\% \,, \tag{5.1}$$

where $\tilde{r}_i$ refers to the ith correct posterior damage factor value, $\hat{r}_i$ refers to the ith updated posterior damage factor value, and $\hat{r}_{0,i}$ refers to the ith prior damage factor value. Mean relative error is calculated as mean absolute value percentages using

$$\varepsilon = \left(\frac{1}{N_r} \sum_{i=1}^{N_r} |\varepsilon_i| \right) \cdot 100\% \; , \tag{5.2}$$

where N_r refers to the number of damage factors in the set (18 for the baseline validation cases).

The results show successful damage identification for each of the three damage cases with mean relative parameter errors of 0.65%, 0.58%, and 0.34%, respectively. It can be seen that the healthy damage factors move from unity during convergence but then return very close to their undamaged value. The slopes of damaged parameter convergence curves are largely controlled by the iteration step limit causing damage case 2 to converge faster than damage cases 1 or 3 since there is less damage. In each of these cases the parameter uncertainty moves from the prior value of 100% to between 0.02% and 1.2%, with values generally increasing from damage case 1 to damage case 3. Looking qualitatively at updated parameter uncertainties relative to each other leads to the belief that their relative sensitivity is largely a driver for their final value, with low sensitivity parameters having higher posterior uncertainties.

A final trial run was performed on damage case 1 using an $N_r = 9$ update parameter grouping that encompasses the correct damaged region but does not follow the
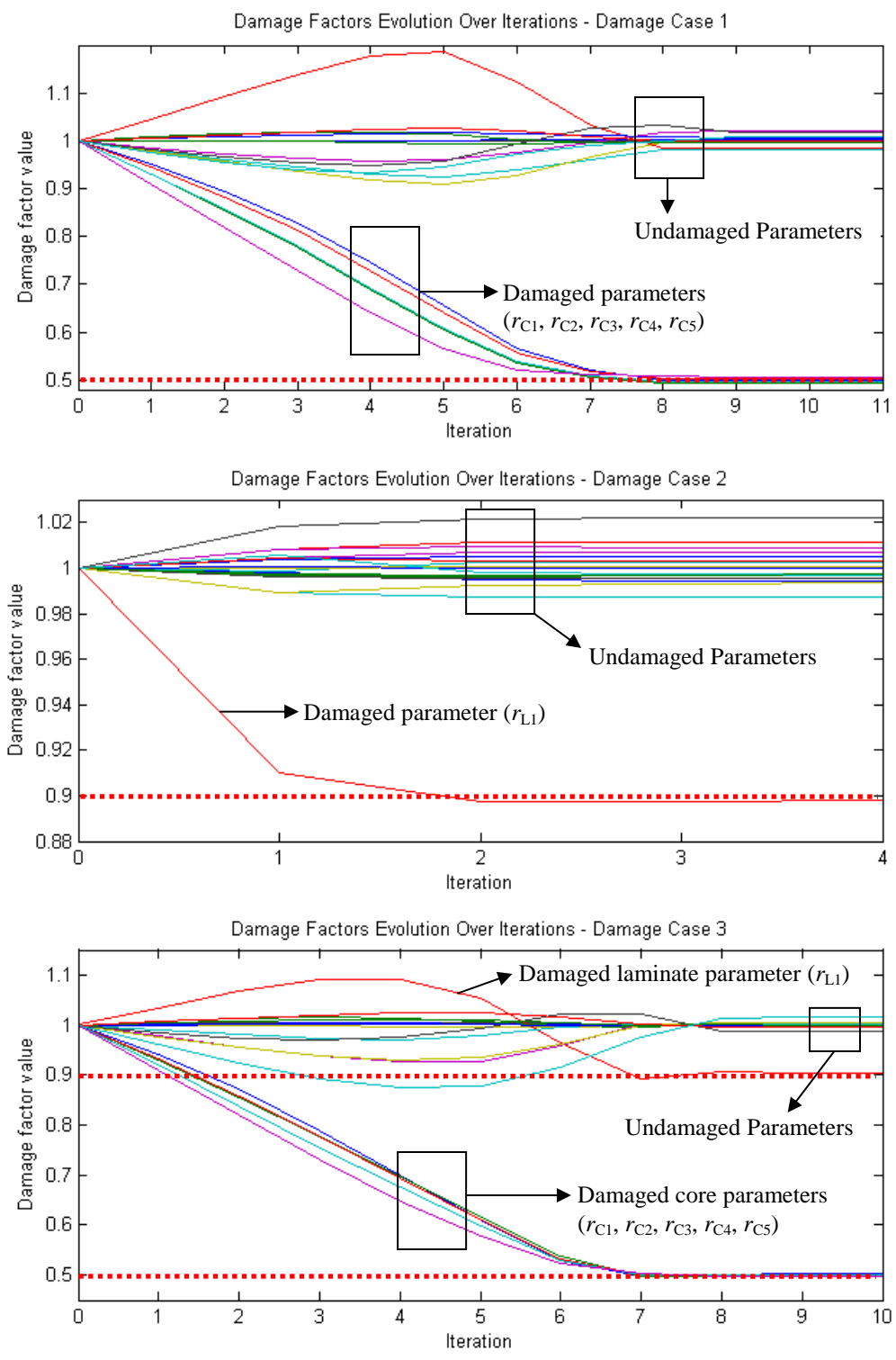
Figure 5-12: Parameter convergence behavior from damage case 1 (top), damage case 2 (center), and damage case 3 (bottom), in the baseline algorithmic parameter state. (Note: an exact legend is not provided because of the large number of curves; converged values are given in Table 5-3).

Table 5-3: Baseline validation results summary.

Parameter r_i	Prior value $\hat{r}_i$	Damage Case 1 Converged value $\hat{r}_i$	Damage Case 1 Error ε_i	Damage Case 2 Converged value $\hat{r}_i$	Damage Case 2 Error ε_i	Damage Case 3 Converged value $\hat{r}_i$	Damage Case 3 Error ε_i
r_{C1}	1.00	0.499	-0.10%	0.994	-0.55%	0.502	0.20%
r_{C2}	1.00	0.494	-0.58%	0.996	-0.44%	0.498	-0.18%
r_{C3}	1.00	0.502	0.21%	1.011	1.11%	0.501	0.10%
r_{C4}	1.00	0.496	-0.37%	1.003	0.27%	0.501	0.08%
r_{C5}	1.00	0.506	0.58%	1.007	0.70%	0.498	-0.19%
r_{C6}	1.00	1.002	0.16%	1.001	0.05%	1.000	0.00%
r_{C7}	1.00	0.999	-0.08%	0.996	-0.43%	0.998	-0.25%
r_{C8}	1.00	1.001	0.12%	1.000	-0.03%	0.999	-0.08%
r_{C9}	1.00	0.998	-0.22%	0.997	-0.33%	1.001	0.11%
r_{L1}	1.00	0.985	-1.45%	0.898	-0.23%	0.905	0.51%
r_{L2}	1.00	0.983	-1.71%	0.987	-1.27%	1.001	0.06%
r_{L3}	1.00	1.022	2.15%	1.009	0.85%	0.996	-0.36%
r_{L4}	1.00	0.998	-0.23%	0.993	-0.67%	1.006	0.58%
r_{L5}	1.00	1.018	1.79%	1.022	2.19%	0.986	-1.41%
r_{L6}	1.00	1.007	0.69%	1.005	0.51%	0.999	-0.08%
r_{L7}	1.00	0.996	-0.40%	0.997	-0.29%	1.000	0.01%
r_{L8}	1.00	1.001	0.06%	1.003	0.28%	0.997	-0.32%
r_{L9}	1.00	1.008	0.80%	0.997	-0.30%	1.016	1.58%
Mean Relative Error ε			0.65%		0.58%		0.34%

damage outline exactly. Details of the parameter grouping are given in Figure 5-13. Since

some of the parameter groupings include both healthy and damaged elements the damage

cannot be modeled exactly and this case therefore more accurately represents a real-world

damage identification problem. The damage factors converged to values of (counting

across rows and then down columns from top left to bottom right) 0.87, 1.1, 0.62, 1.26,
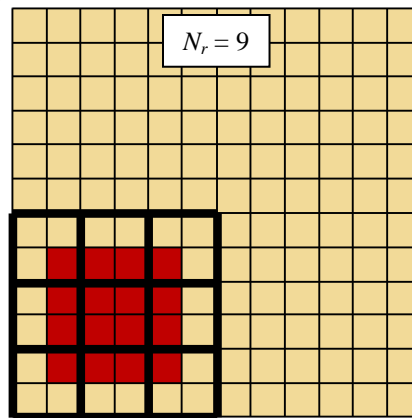
Figure 5-13: Details of a core update parameter group with $N_r = 9$ where the parameter group boundaries do not conform to the damage region.

0.08, 0.84, 0.66, 0.89, and 0.99. Inspection of these results shows a large amount of

stiffness reduction in the center parameter grouping while the surrounding regions vary

from a 38% stiffness decrease to a 26% stiffness increase. While none of the updated

damage parameters correctly identifies the correct damage extent, the overall results

suggest that the damage is centered in the correct location. The results could therefore be

used as a basis for refining the update parameter groupings for a second run.

5.3.4   Parametric Studies

Studies on the effect of specific parameters on algorithm performance are now

presented. The goal of each study was to determine the relationship between specific

algorithm inputs and damage identification results and thereby guide selection of

parameter values for future problems. This was accomplished by performing several identification runs for each study, in each case varying the target parameter(s) while holding all other parameters constant.

All cases were run starting from the damage case 3 configuration with the exception of the 'number of update parameters' study, which was conducted using damage case 1. All parameters besides those being studied were set equal to the values specified in Section 5.3.3 except where noted. Algorithm performance for each study is presented in terms of the mean relative error ε in Eq. (5-2) calculated separately for the total damage parameter set, the damaged parameter set, and the undamaged parameter set. In addition, the time taken to reach convergence is reported with each result normalized to a reference value of 15,000 seconds. Results and observations from these studies are presented in the following sections.

5.3.4.1   Number of Frequency Lines

Results of the study comparing the effect of number of frequency lines on algorithm performance are given in Figure 5-14. It can be seen that decreasing the number of frequency lines increases parameter error while decreasing computation time, reflecting the fact that less information leads to less averaging of the effects of noise and less computation. The $N_\omega = 2$ case did not completely converge, getting stuck oscillating about a local minima as is more likely to happen when fewer data points are used—thus there is no data point plotted in the time-to-convergence plot.

Algorithm Performance as Function of Number of Frequency Lines

Time to Convergence as Function of Number of Frequency Lines
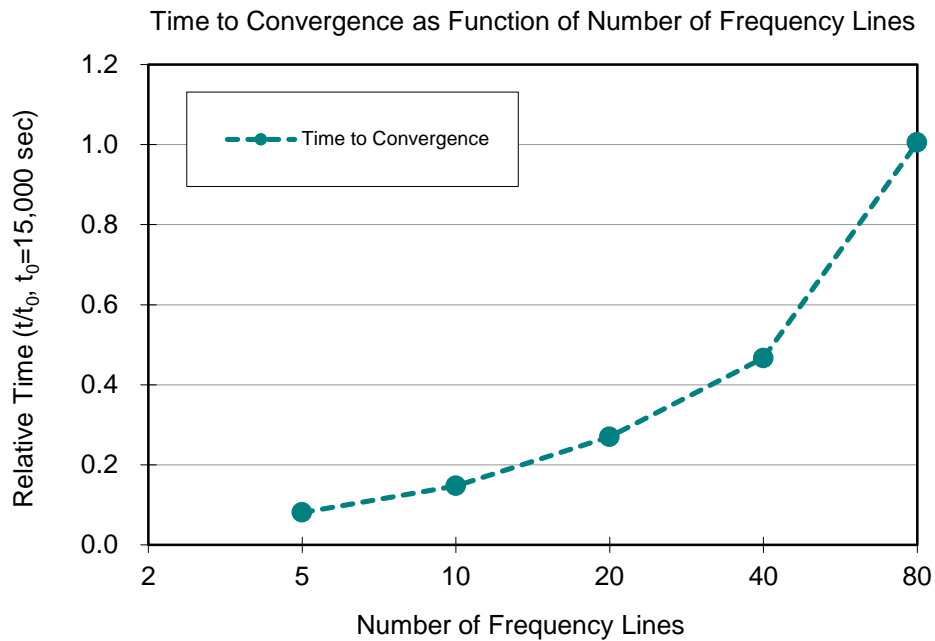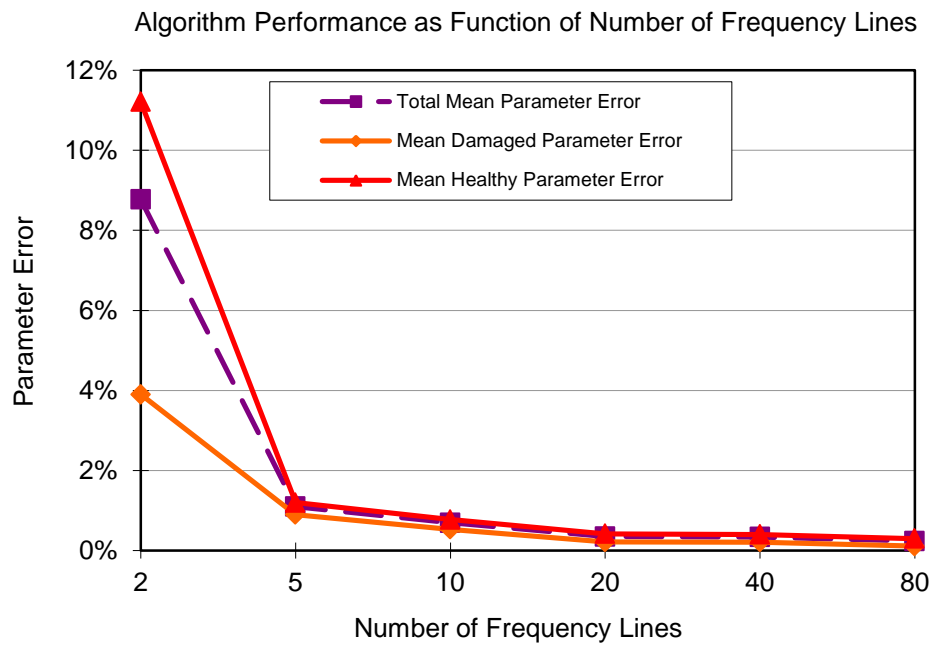
Figure 5-14: Results plots from first parametric study investigating effect of number of frequency lines.

5.3.4.2   Frequency Selection Coherence Tolerance

Results of the frequency selection coherence tolerance study are given in Figure

5-15 and show that increasing frequency selection coherence tolerance decreases

parameter error and computation time. The improvement in performance occurs because

increasing the coherence tolerance decreases the amount of noise in the data being used

for update, leading to lower error and faster convergence. However, at a certain point (in

this case somewhere between 0.999 and 0.9999) the error increases again slightly because

of a lack of diversity in the data as it gets clustered around the most powerful modal

peaks, and finally results remain constant as the same lowest-coherence frequency lines

are used despite increasing frequency selection coherence tolerance.

5.3.4.3   Amount of Noise

Results showing algorithm performance as a function of increasing amounts of

noise in the reference data are presented in Figure 5-16. The plots show that increasing

noise leads to smoothly increased parameter error, while the time to convergence initially

decreases slightly before increasing. These results reflect the fact that increasing noise for

a fixed coherence tolerance drives frequency line selection towards the modal peaks,

where relative noise is lower and differences in the effective residual force vector and

parameter sensitivities are greater, leading to an initial increase in overall algorithm

performance. However, at some point the increasing noise levels overwhelm this benefit

and performance decreases again. The case of zero noise, not shown in the graph, did not
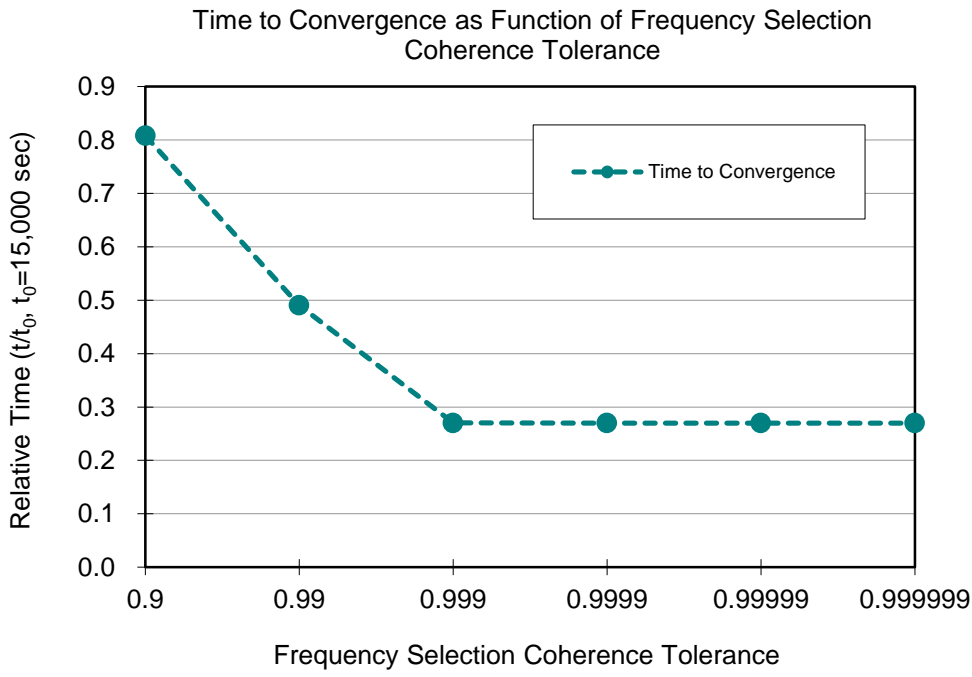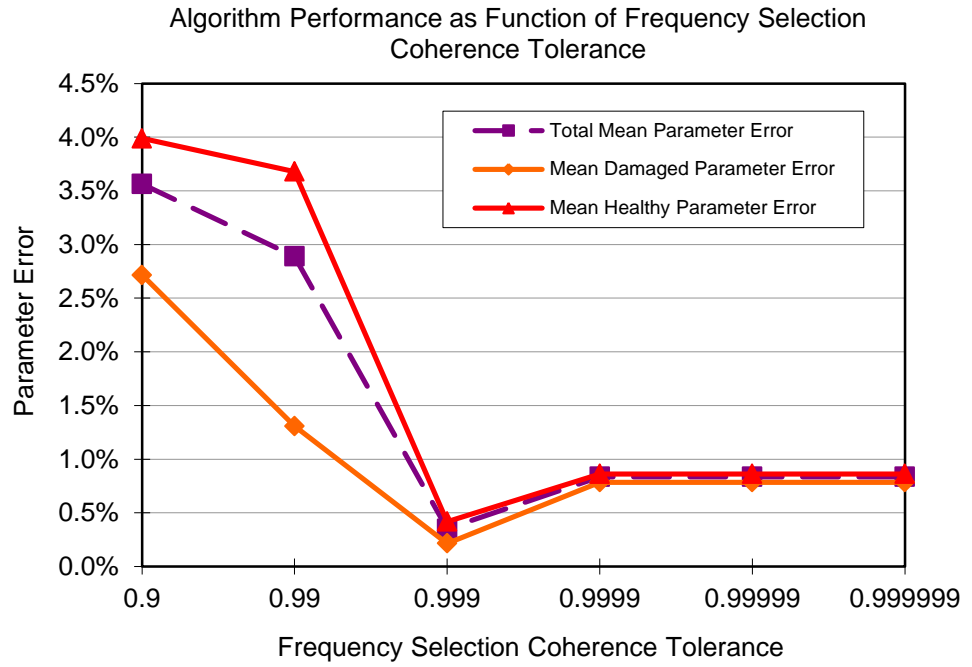
Figure 5-15: Results plots from second parametric study investigating effect of frequency line selection coherence tolerance.
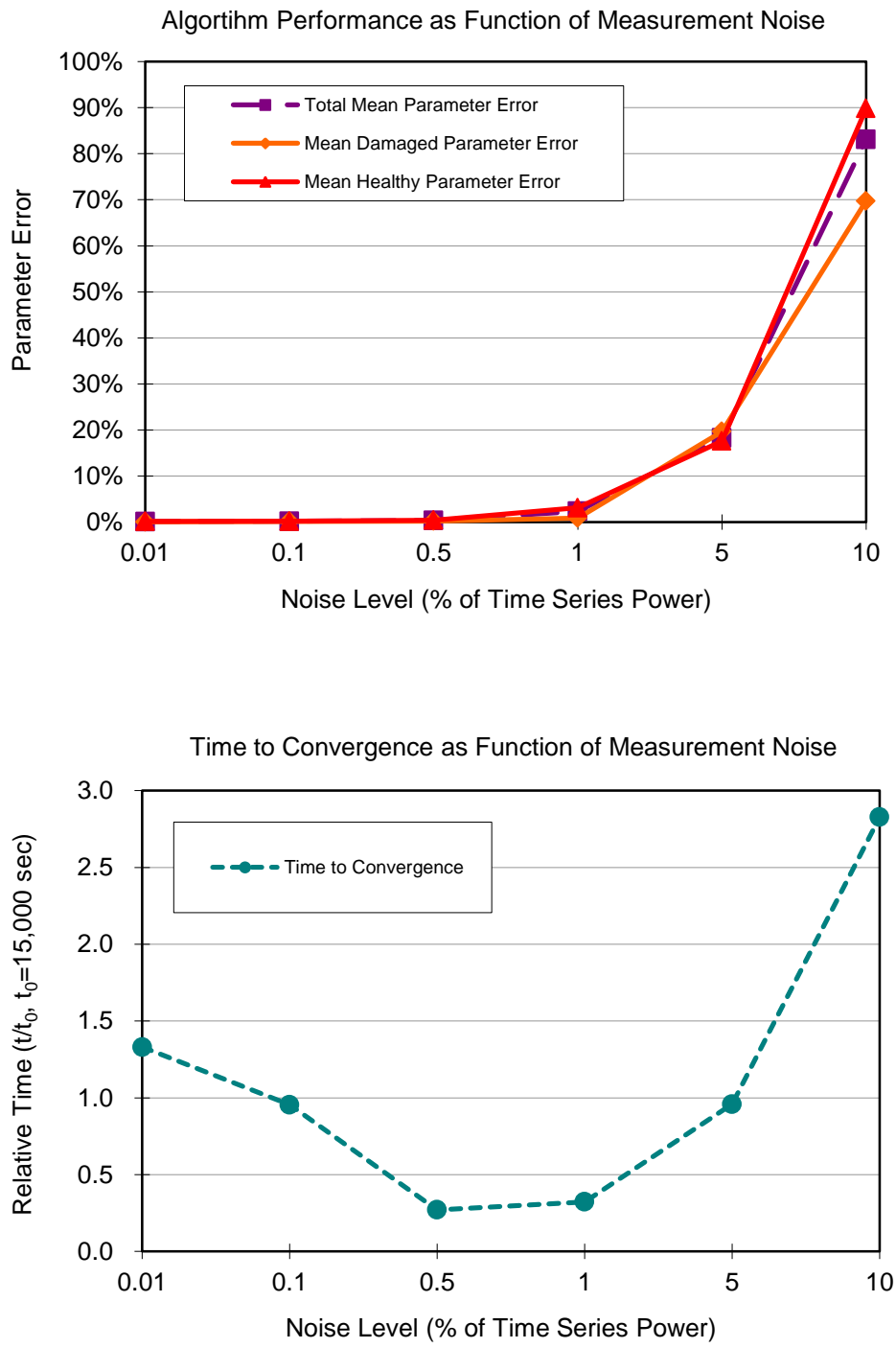
Figure 5-16: Results plots from third parametric study investigating effect of noise level.

converge at all after over 300 iterations, presumably because of too many frequency lines in low-response regions that do not produce accurate sensitivities. This could be fixed in normal use by using one of the other frequency line selection techniques to group frequency lines closer to modal peaks where parameter sensitivities are higher.

5.3.4.4 Ratio of Numbers of Measurement Degrees-of-Freedom to Frequency Lines

The ratio of number of measurement degrees-of-freedom to number of frequency lines study was conducted to show the effect of number of measurement degrees-of-freedom for a given allowable amount of data points. The particular values used are given in Table 5-4 and results are shown in Figure 5-17. The study results show that both parameter error and convergence time initially decrease as the ratio approaches unity before increasing again as the ratio becomes more biased towards the number of frequency lines. The best results occur at the ratio closest to unity. It is believed that the initial increase in performance is driven by the benefit of increasing numbers of

Table 5-4: Algorithm parameters used for ratio of number of measurement degrees-of-freedom to number of frequency lines study.

Ratio (N_r / N_ω)	N_d	N_ω	Number of Data Points	Measurement Points Grid
56.33	169	3	507	13x13
4.90	49	10	490	7x7
1.25	25	20	500	5x5
0.52	16	31	496	4x4
0.16	9	56	504	3x3
0.03	4	125	500	2x2
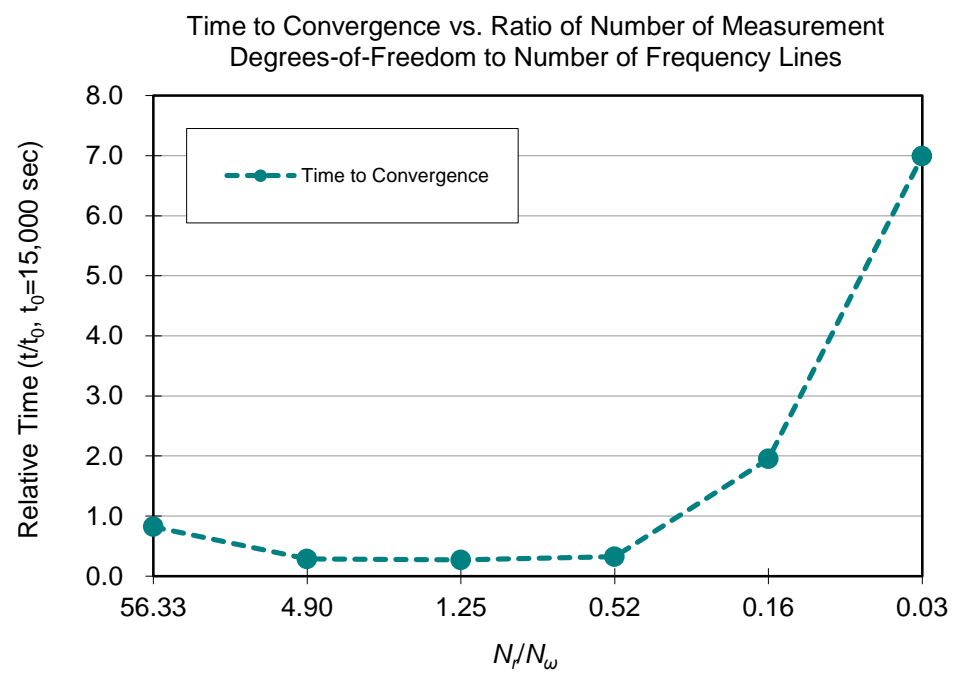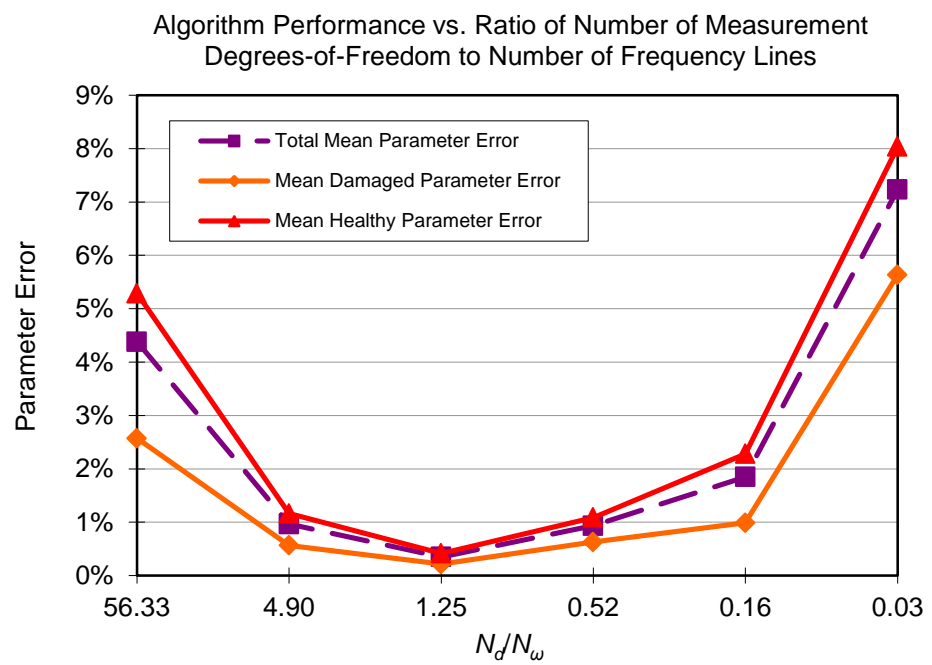
Figure 5-17: Results plots from fourth parametric study investigating the effect of the ratio of number of measurement degrees-of-freedom to number of frequency lines.

frequency lines, which causes the modal data to be better represented across the frequency spectrum. This benefit, however, is then increasingly overshadowed by the detrimental effect of decreasing spatial resolution across the plate and mode shapes. It can be concluded that the modal behavior of the structure needs to be accurately captured both spatially and across frequency for accurate damage identification.

5.3.4.5   Number of Update Parameters

In order to study the effect of the number of update parameters on algorithm performance, several sets of update parameters were specified. Details of the sets are given in Figure 5-18 relative to the core elements. This study was performed on damage case 1 with damage on the core only meaning the update parameter sets were all capable of modeling the damage accurately. Figure 5-19 gives results for the study and it can be seen that both mean relative parameter error and convergence time increase with N_r. This result occurs because increasing the number of update parameters causes more damage factors to have lower individual sensitivities which leads to a loss in numerical accuracy and algorithm stability during update in the presence of noise. The baseline parameter set of 18 damage factors actually presents a relatively difficult case and additional runs, not presented, showed that the lower N_r cases converged very quickly and accurately in all but the most severe noise cases. These easier cases were not used for the parametric studies because of the desire to generate greater parameter errors and provide a better understanding of algorithm performance.
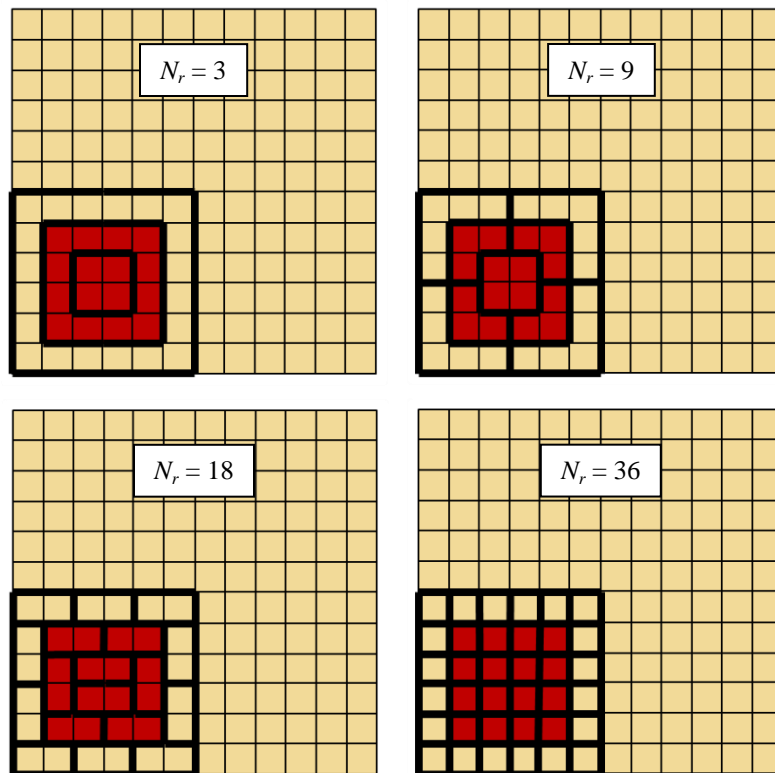
Figure 5-18: Details of core update parameter groups compared to element grid and damaged region for the number of update parameters study for N_r = 3, 9, 18, and 36.

5.3.5 Updated Parameter Uncertainty

Figure 5-20 shows posterior uncertainty values for the noise study presented in Section 5.3.4.3. The uncertainty values are presented in the form of standard deviation percentages averaged for all damage factor parameters, the damaged parameter set, and the healthy parameter set. The values range from a low of 0.03% in the low noise case to 45% in the high noise case. The values generally increase with noise, as would be expected since the noise has a corrupting effect on the damage identification and so should lead to more uncertainty in the solution.
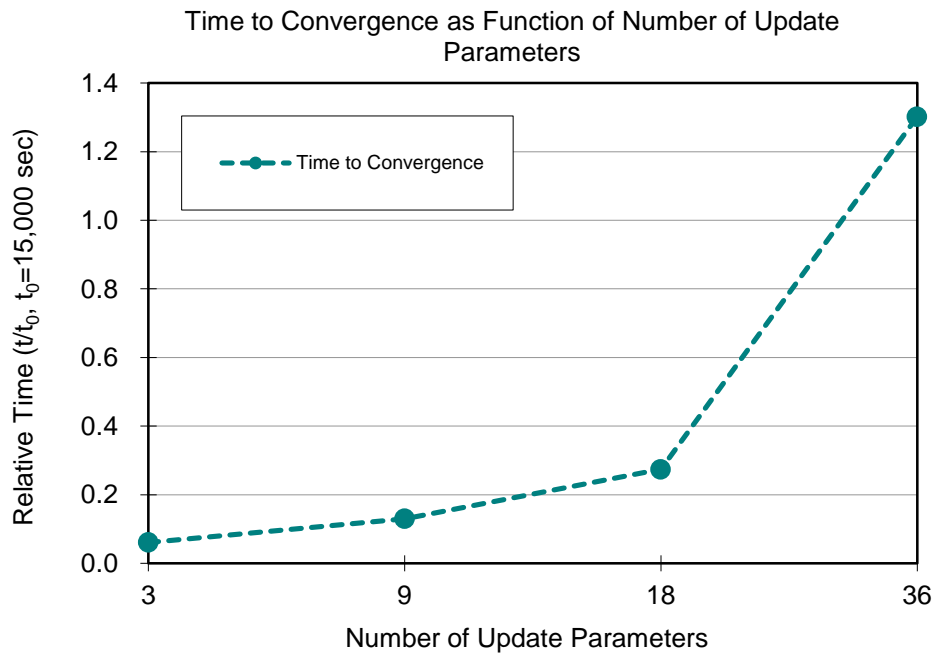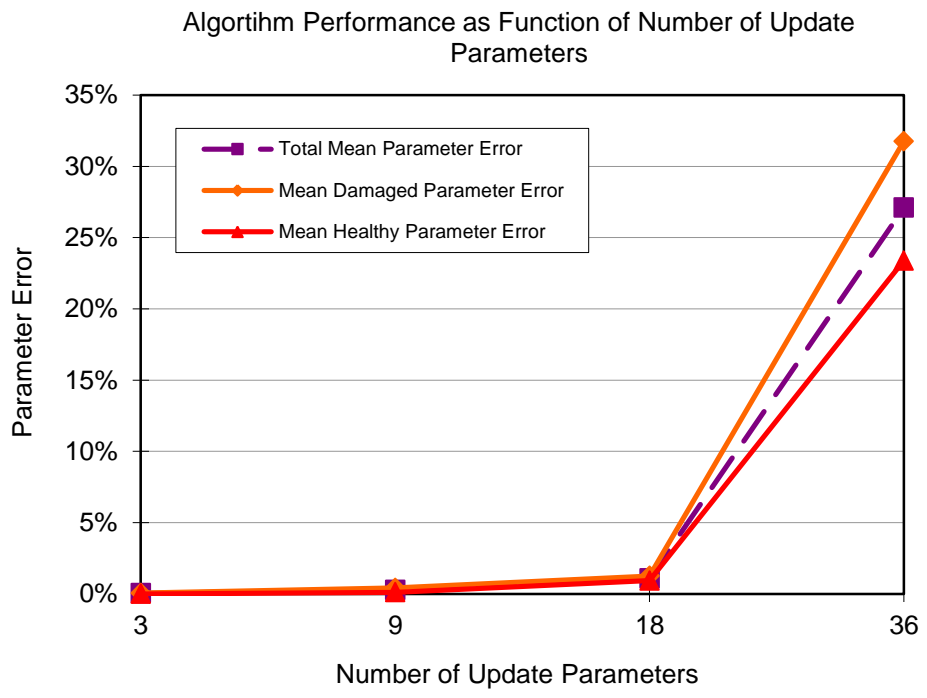
Figure 5-19: Results plots from fifth parametric study investigating effect of number of update parameters.

Algortihm Performance as Function of Measurement Noise
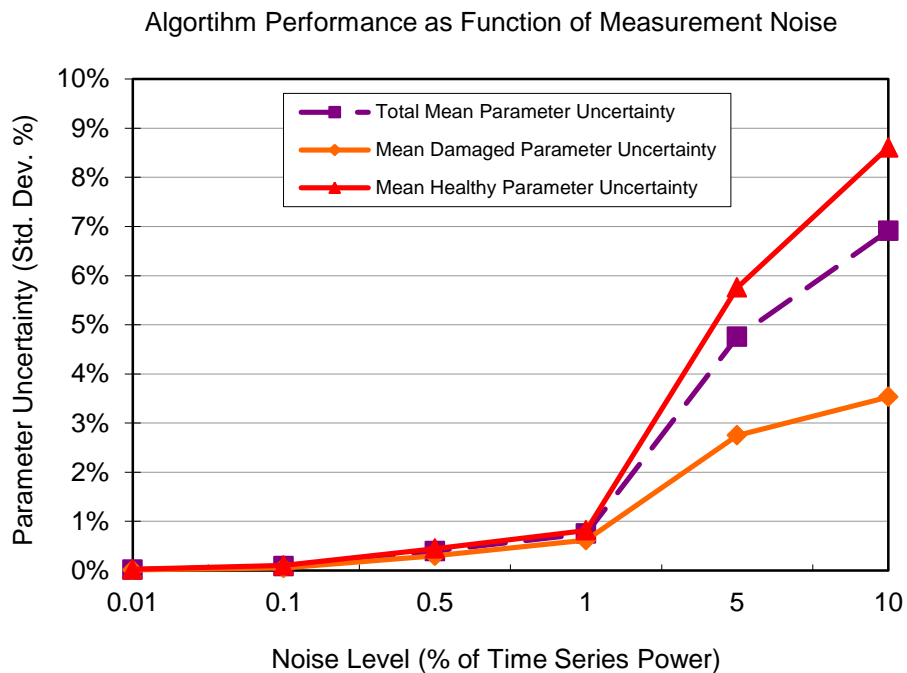
Figure 5-20: Results plots from final parametric study investigating parameter uncertainty as a function of noise level.

5.3.6   Discussion

The algorithm was shown throughout the validation and parametric studies to

perform very well, even in the face of up to 99.8% decrease in degrees-of-freedom

between the analytical model and available measurements, high levels of measurement

noise, and up to 36 individual update parameters. Damage identification performance

could likely be increased by tailoring the various algorithm parameters which were held

fixed during the current study. It can also be seen that the mean relative error for

damaged parameters was lower than that for healthy parameters. This result likely

reflects lower individual parameter sensitivities in the healthy parameter sets.

5.4   **Damping in Reduced Coordinates**

Accurate modeling of damping in the analytical system is required for the current frequency response based damage identification to function properly. For idealized simple systems it is possible to model damping accurately using classical assumptions (e.g., viscous dashpots and/or stiffness proportionality). However, for general real-world aerospace systems damping occurs because of many varied physical phenomena including friction in structural connections, losses generated by the micromechanical behavior of materials, and viscous friction of surrounding fluids. The various damping models for structural dynamic systems are essentially empirical, having been established and accepted over many years to fit various observed responses as opposed to derived from first-principles physics. The result is that there is usually no clear mathematical basis for modeling damping in real-world structures. As discussed in Sections 3.1 and 3.3, some combination of structural and viscous damping is assumed to be adequate for the linear structural dynamic systems considered for the current damage identification algorithm. In particular, one or both of the following quantities must be specified: (1) a complex stiffness matrix $\left[K^* \right]$ for structural damping and/or (2) a viscous damping matrix $\left[C \right]$ in full coordinates.

In the current implementation it is recommended to fit one or both assumed damping matrices to measured data; however, the process is further complicated by the need to work in the reduced coordinate analysis degree-of-freedom set. Approximate

methods for including damping in reduced coordinates using elemental structural

damping or proportional viscous damping are discussed in the following sections.

5.4.1   Elemental Structural Damping

In the finite element modeling framework, structural damping can be included on

the element level through the definition of elemental damping parameters, specified as a

material property for each element and denoted by the symbol η^e. The elemental

complex stiffness matrices are defined through the relationship

$$\left[K^* \right]^e = \left[K \right]^e \left(1 + j\eta^e \right) \tag{5.3}$$

for each element e, where $\left[K \right]^e$ is the elemental stiffness matrix, and then assembled into

the global system complex stiffness matrix $\left[K^* \right]$ through the same element-to-global

level assembly process used for the mass and stiffness matrices. The global system

complex stiffness matrix is then assembled into the dynamic stiffness matrix in full

coordinates and reduced as required using standard dynamic reduction with no loss of

correctness.

For implementation, the damping parameters η_e can be estimated during initial

model building based on knowledge of the element materials, as with mass and stiffness

parameters, and then correlated to the measured frequency response function data if

desired (for example by using the model correlation methods described in Section 6.1).

Modal parameters are not required to implement elemental structural damping which

means the effort and error associated with modal parameter estimation can be avoided. The method can be accurate for true material damping but may be less so for other forms of structural damping, such as when the global damping is dominated by connections which are not explicitly modeled with elements containing damping parameters (e.g., when bonded or bolted joints are modeled using idealized rigid connections). On the other hand, if the finite element model is created with damping in mind it should be possible to account for all major sources of structural damping through this method.

On the global level the elemental structural damping matrix will generally not be proportional to the global stiffness matrix and will therefore produce generalized damping. However, for simple plane structures with no major connections, such as plates made from one material, it may be possible that every element can be modeled with the same structural damping parameter η. In this case the structural damping matrix relationship will simplify to

$$\left[K^* \right] = \left[K \right] \left(1 + j\eta \right) . \tag{5.4}$$

This simplification is included for completeness and is likely to be poor for real-world built-up structures.

5.4.2 Proportional Viscous Damping Methods

Proportional viscous damping matrices can be calculated and added to the system dynamic stiffness matrix in reduced coordinates through several methods, namely the

Rayleigh method, direct modal method, and extended Rayleigh method. In each case they can be applied correctly by being first calculated in the full degree-of-freedom set or on an ad-hoc basis directly in the reduced degree-of-freedom set as described in the following sections.

5.4.2.1   Rayleigh Damping Method

The most straight-forward method for adding proportional viscous damping is through the basic Rayleigh method first discussed in Section 3.3.1. The basic method requires defining proportionality constants α and β in order to define a damping matrix in the full degree-of-freedom set based on stiffness and mass matrices as

$$[C]_f = \alpha[K]_f + \beta[M]_f . \tag{5.5}$$

The dynamic stiffness matrix is then formed in the full degree-of-freedom set using

$$[Z(\omega_k)]_f = \left[K^*\right]_f + j\omega_k[C]_f - \omega_k^2[M]_f , \tag{5.6}$$

and the reduced *m-DOF* system $[Z(r,\omega_k)]_m$ is found by dynamic reduction using Eq. (3.64). The proportionality constants can either be tuned to minimize error between analytical and reference frequency response functions or solved to exactly match one or two modes as described in Section 3.3.1 if modal data are available. However, unless all modes have modal damping ratios that match the relationship in Eq. (3.30) the method will not be accurate.

Rayleigh damping can alternatively be added in the reduced degree-of-freedom

set as follows. The reduced degree-of-freedom stiffness matrix $[K]_m$ and mass matrix

$[M]_m$ are calculated by first calculating the undamped dynamic stiffness matrix

$$\left[Z^u(\omega_k)\right]_f = \left[K^*\right]_f - \omega_k^{\ 2}[M]_f \tag{5.7}$$

and then applying dynamic reduction using Eqs. (3.65) and (3.66), respectively. The

viscous damping matrix is then found as

$$\left[C(\omega_k)\right]_m = \alpha\left[K(\omega_k)\right]_m + \beta\left[M(\omega_k)\right]_m, \tag{5.8}$$

where the reduced coordinate mass and stiffness matrices are functions of frequency as a

result of the reduction process. The *m-DOF* dynamic stiffness matrix is finally

constructed as

$$\left[Z(\omega_k)\right]_m = \left[K^*(\omega_k)\right]_m + j\omega_k\left[C(\omega_k)\right]_m - \omega_k^{\ 2}\left[M(\omega_k)\right]_m. \tag{5.9}$$

5.4.2.2 Direct Modal Damping Method

Measured modal information, if available, can be used to directly create a

proportional viscous damping matrix $[C]$. The relationship is based on the assumption

that the unknown viscous damping matrix can be decoupled using the undamped system

eigenvector matrix, as explained in Section 3.2. To create the matrix a modal damping

matrix is first assembled as

$$[C_n] = \begin{bmatrix} \ddots & & \\ & 2\omega_n \zeta_n M_n & \\ & & \ddots \end{bmatrix} \qquad (5.10)$$

using modal data quantities ω_n, ζ_n, and M_n derived from measured frequency response functions. The viscous damping matrix is then back-calculated using the measured mode shapes $[\Phi]$ and the relationship described in Eq. (3.26), rewritten as

$$[\Phi]^T [C][\Phi] = [C_n]. \qquad (5.11)$$

In the simplest case of a fully populated mode shape matrix, where $N_d = N_D = N_\omega$, the mode shape matrices in Eq. (5.11) can then be inverted producing the viscous damping matrix from the equation

$$[C] = \left([\Phi]^T\right)^{-1} \begin{bmatrix} \ddots & & \\ & 2\omega_n \zeta_n M_n & \\ & & \ddots \end{bmatrix} [\Phi]^{-1}. \qquad (5.12)$$

However, in the usual case of fewer modes than measured degrees-of-freedom the mode shape matrix will not be square and thus cannot be directly inverted. Modes can be removed or degrees-of-freedom reduced to force it square; however, this may lead to an unacceptable loss of information. Alternatively, a pseudo-inverse can be employed in place of the regular inverse producing the relationship

$$[C] = \left([\Phi]^T\right)^{+} \begin{bmatrix} \ddots & & \\ & 2\omega_n \zeta_n M_n & \\ & & \ddots \end{bmatrix}_{(N_\omega, N_\omega)} [\Phi]^{+}. \qquad (5.13)$$

When working in reduced coordinates the viscous damping matrix $[C]$ should be formed in the full degree-of-freedom coordinate system. This is accomplished by first expanding the measured mode shapes into the full degree-of-freedom set using the previously defined

$$\{\phi_n\} = [T_n(r)]\{\phi_n\}_m, \tag{3.70}$$

where $[T_n(r)]$ is the undamped modal transformation matrix defined in Eq. (3.69) for each mode n and r refers to the appropriate analytical model parameter set. Assigning the notation $\{\phi_n\}_f$ to the expanded mode shape for mode n to avoid confusion, the expanded mode shapes can be put into matrix form as

$$[\Phi]_f = \left[\{\phi_1\}_f \ \{\phi_2\}_f \ \cdots \ \{\phi_{N_D}\}_f \right]. \tag{5.14}$$

The modal mass M_n must also be calculated by way of the reduced coordinate mass matrix by combining Eqs. (3.65) and (3.19) to form

$$M_n = \left([\Phi]_m^T\right)^+ [T_n(r)]^T \left[M_f(r)\right][T_n(r)][\Phi]_m^+. \tag{5.15}$$

With these parameters calculated the direct method viscous damping matrix in the full degree-of-freedom set is formed as

$$[C]_f = \left([\Phi]_f^T\right)^+ \begin{bmatrix} \ddots & & \\ & 2\omega_n\zeta_n M_n & \\ & & \ddots \end{bmatrix}_{(N_\omega,N_\omega)} [\Phi]_f^+. \tag{5.16}$$

The full degree-of-freedom $[C]_f$ can then be combined with the mass and stiffness matrices to form the damped dynamic stiffness matrix. When reduction is subsequently applied to the dynamic stiffness matrix, the resulting equation is

$$[Z(\omega_k)]_m = \left[K^*(\omega_k) \right]_m + j\omega_k \left[C(\omega_k) \right]_m - \omega_k^2 \left[M(\omega_k) \right]_m, \tag{5.17}$$

with

$$[C(\omega_k)]_m = [T(\omega_k)]^T \left([\Phi]_f^T \right)^+ \begin{bmatrix} \ddots & & \\ & 2\omega_n\zeta_n M_n & \\ & & \ddots \end{bmatrix} [\Phi]_f^+ [T(\omega_k)]. \tag{5.18}$$

An alternative ad-hoc approach is to calculate $[C(\omega_k)]_m$ directly in the reduced coordinate system using

$$[C]_m = \left([\Phi]_m^T \right)^+ \begin{bmatrix} \ddots & & \\ & 2\omega_n\zeta_n M_n & \\ & & \ddots \end{bmatrix}_{(N_\omega, N_\omega)} [\Phi]_m^+, \tag{5.19}$$

where the modal mass values again need to be calculated first using Eq. (5.15) with the reduced degree-of-freedom mass matrix first calculated by applying dynamic reduction using the undamped dynamic stiffness matrix. Although this approach seems promising, comparison of Eqs. (5.19) and (5.18) shows that the reduced coordinate approach produces a non frequency dependent version of $[C]_m$ which is a disadvantage compared to the version created in full coordinates.

5.4.2.3 Extended Rayleigh Damping Method

A potentially more accurate way to model proportional viscous damping is the extended Rayleigh modal damping method. As with the direct modal method the viscous damping matrix must be formed and added to the dynamic stiffness matrix in full coordinates before being reduced. This process is accomplished by first expanding the measured mode shape matrix into full coordinates using Eq. (3.70) and calculating modal mass values using Eq. (5.15). The full coordinate viscous damping matrix can then be found using the extended Rayleigh damping equation

$$[C]_f = \left(\frac{2\zeta_c}{\omega_c}\right)[K]_f + [M]_f \left[\sum_{n=1}^{c-1} 2\left(\zeta_n - \zeta_c\left(\frac{\omega_n}{\omega_c}\right)\right)\frac{\omega_n}{M_n}\{\phi_n\}_f \{\phi_n\}_f^T\right][M]_f . \quad (5.20)$$

This equation is the same as that discussed in Section 3.3.1, the only change being the addition of '*f*' subscripts to show quantities in the full coordinate system. Once the full coordinates damping matrix is available, the dynamic stiffness matrix can be formed in full coordinates and then reduced normally using Eqs. (3.63) and (3.64).

An extended Rayleigh viscous damping matrix can also be calculated directly in reduced coordinates. This variation requires first calculating the reduced stiffness and mass matrices by forming the undamped coordinate transformation matrix from Eq. (3.63) and then applying Eqs. (3.65) and (3.66). The modal mass values are then calculated from the reduced mass matrix using Eq. (3.19) and the reduced coordinate viscous damping matrix is found as

$$[C(\omega_k)]_m = \left(\frac{2\zeta_c}{\omega_c}\right)[K(\omega_k)]_m \ldots$$

$$\ldots + [M(\omega_k)]_m \left[\sum_{n=1}^{c-1} 2\left(\zeta_n - \zeta_c\left(\frac{\omega_n}{\omega_c}\right)\right)\frac{\omega_n}{M_n}\{\phi_n\}_m\{\phi_n\}_m^T\right][M(\omega_k)]_m. \tag{5.21}$$

As with the reduced coordinate direct modal method this version of $[C]_m$ is not

mathematically consistent compared to the version calculated in full coordinates using

Eq. (5.15) and should not be assumed to be accurate.

5.4.2.4   Further Notes on the Direct Modal and Extended Rayleigh Methods

Even when calculated in full coordinates the direct modal and extended Rayleigh

direct methods involve approximations. Firstly, mode shape expansion is approximate

because (1) the mode shapes must be expanded using an undamped transformation matrix

and (2) the mode shapes are from the damaged system while the available matrices are

from the baseline correlated analytical system (since the damaged system is not yet

known). Secondly, the basic assumption of proportional viscous damping may not be

physically accurate even when combined with structural damping and tuned to each

modal damping ratio. Finally, real modal data must be used for matrix operations even

when the underlying system produces complex modes (potential methods for calculating

equivalent real modes from complex modes are discussed in the next section). As a result

there will be some loss in orthogonality between the real mode shapes and system

matrices.

The need to use real modal data will introduce increasing error as modes increase in complexity and cause the calculated real modes to become less representative of the actual complex modes. Mode shape expansion will increase error for systems which have a lot of damage and modeling error, although this error should decrease as the analytical system converges to the damaged experimental system. Furthermore, the error will generally increase with the amount of damping in the system. The presented methods for assigning proportional viscous damping in the reduced coordinate system will therefore be best suited to systems with relatively light damping. On the other hand, the ability to explicitly match measured damping ratios with no additional correlation is convenient and has the potential to be accurate enough for damage identification.

5.4.3   Real Normal Modes from Complex Measured Modes

In an experimental structure with non-proportional viscous and/or structural damping, measured mode shapes $\{\tilde{\phi}_n\}$ and natural frequencies $\tilde{\omega}_n$ will be complex. However, the proportional viscous damping methods discussed in Sections 5.4.2.2 and 5.4.2.3 are limited to using real normal modes such as would result from the physical system being proportionally damped. Even for lightly damped structures ($\zeta_n \ll 1$) the level of complexity will be non-zero and real-valued approximations of the natural frequencies and mode shapes must be calculated in order to apply either direct modal or extended Rayleigh damping.

Three methods for approximating normal real modes are proposed in this section. The first two are based on rotating each mode shape towards the real axis and then using either the real component or using the sign-preserved absolute value; the third is based on the work of Fuellekrug [5-4]. The methods are ad-hoc and don't guarantee orthogonality, but they may provide an adequate approximation—especially for lightly damped structures. If only elemental structural damping is used then real-valued modal information is not required.

5.4.3.1 Rotated-Real Method

The rotated-real method is implemented by rotating each mode shape so that its largest component is scaled to $(1+0i)$, using

$$\left\{\phi_n^{rot}\right\} = \frac{\left\{\tilde{\phi}_n\right\}}{\max\left(\left\{\tilde{\phi}_n\right\}\right)}, \tag{5.22}$$

where $\max\left(\left\{\tilde{\phi}_n\right\}\right)$ refers to the mode shape vector element with the largest complex modulus (and secondarily with the largest phase if two elements have the same modulus). The real components of the rotated mode shape vectors are then assembled into the matrix form

$$\left[\Phi^{Re}\right] = \left[\mathrm{Re}\left(\left\{\phi_1^{rot}\right\}\right) \quad \mathrm{Re}\left(\left\{\phi_2^{rot}\right\}\right) \quad \dots \quad \mathrm{Re}\left(\left\{\phi_{N_m}^{rot}\right\}\right)\right], \tag{5.23}$$

and the real mode shape matrix $\left[\Phi^{Re}\right]$ or component modes $\left\{\phi_n^{Re}\right\}$ can be used in place of the complex mode shape matrix as required.

The associated real natural frequencies are found by taking the absolute value (complex modulus) of the complex measured values, producing

$$\omega_n^{\text{Re}} = \sqrt{\text{Re}\left(\tilde{\omega}_n\right)^2 + \text{Im}\left(\tilde{\omega}_n\right)^2} . \tag{5.24}$$

5.4.3.2   Rotated Absolute Value Method

The rotated absolute value method is implemented similarly to the rotated-real method, starting with rotated complex mode shapes calculated using Eq. (5.14). The second step involves taking the absolute value of each mode shape value. However, in order to avoid losing the negative part of the shapes a negatives vector $\{P_n\}$ is formed for each shape based on the sign of the real part; i.e., for each element m of each mode shape n,

$$P_{n,m} = \begin{cases} +1, & \text{if } \text{Re}\left(\phi_{n,m}^{rot}\right) \geq 0 \\ -1, & \text{if } \text{Re}\left(\phi_{n,m}^{rot}\right) < 0 \end{cases} . \tag{5.25}$$

The rotated absolute value mode shape matrix is then formed by taking the absolute value of each element of each rotated complex mode shape, performing a point-wise multiplication with the corresponding $\{P_n\}$, and assembling to form

$$\left[\Phi^{abs}\right] = \left[\left|\{\phi_1^{rot}\}\right| \odot P_1 \quad \left|\{\phi_1^{rot}\}\right| \odot P_2 \quad \cdots \quad \left|\{\phi_n^{rot}\}\right| \odot P_n\right], \tag{5.26}$$

where $\odot$ indicates element-by-element (point-wise) multiplication.

The associated real natural frequencies are found, as with the first method, through Eq. (5.24).

5.4.3.3 Fuellekrug Method

The Fuellekrug method is based on the work developed in reference [5-4]. The method uses singular value decomposition to transform the rotated real mode shape array into a reduced coordinate system, if required, and then solves an eigenvalue problem for the modally derived mass modified stiffness matrix. There are three possible scenarios which must be addressed separately in this method based on the relative values of number of modes N_m and number of measurement degrees-of-freedom N_d :

When $N_m < N_d$ the method is implemented as follows:

(1) Rotate mode shapes so largest component of each shape is scaled to $(1+0i)$ using Eq. (5.22) and then assemble the rotated-real mode shape matrix using Eq. (5.23).

(2) Perform a singular value decomposition of the real rotated mode shape array,

$$SVD\left(\left[\Phi^{rot}\right]\right) \rightarrow \left[\Phi^{rot}\right] = [T_m][\Sigma][V]^T,$$
(5.27)

to get an (N_d, N_m) dimensional transformation matrix $[T_m]$, where the additional components $[\Sigma]$ and $[V]^T$ can be discarded.

(3)   Use $[T_m]$ to create a reduced coordinates square mode shape vector (i.e.,

such that the reduced degree-of-freedom set is of length N_m),

$$\left[\Phi^R\right]=\left[T_m\right]^T\left[\Phi^{rot}\right],$$
(5.28)

and separate back into individual mode shapes,

$$\left[\Phi^R\right]=\left[\{\phi_1^R\}\ \ \{\phi_2^R\}\ \ \cdots\ \ \{\phi_{N_m}^R\}\right].$$
(5.29)

(4)   Solve for the mass-modified stiffness matrix, $[K_M]$ by defining two modal

information matrices,

$$[P_A]=\begin{bmatrix}\{\phi_1^R\} & \{\phi_1^R\} & \cdots & \{\phi_{N_m}^R\} & \{\phi_{N_m}^R\} \\ \{\phi_1^R\}\tilde{\omega}_1 & \{\phi_1^R\}\tilde{\omega}_1^* & \cdots & \{\phi_{N_m}^R\}\tilde{\omega}_{N_m} & \{\phi_{N_m}^R\}\tilde{\omega}_{N_m}^*\end{bmatrix},$$
(5.30)

$$[P_B]=\left[\{\phi_1^R\}\tilde{\omega}_1^2\ \ \{\phi_1^R\}\left(\tilde{\omega}_1^*\right)^2\ \ \cdots\ \ \{\phi_{N_m}^R\}\tilde{\omega}_{N_m}^2\ \ \{\phi_{N_m}^R\}\left(\tilde{\omega}_{N_m}^*\right)^2\right],$$
(5.31)

where * indicates the complex conjugate, then solving the equation

$$\left[[K_M]\ \ [C_M]\right]=-[P_A]^{-1}[P_B],$$
(5.32)

and extracting the desired $[K_M]$ from the left hand side.

(5)   Calculate real mode shapes and natural frequencies via eigenvalue

decomposition of $[K_M]$; i.e., by solving

$$[K_M]\{\phi_n^R\}=\omega_n^2\{\phi_n^R\}.$$
(5.33)

(6)   Transform shapes back to full measurement coordinates using the

transformation matrix and the relationship

$$\left[\Phi^{Fuellekrug}\right]=\left[T_m\right]\left[\Phi^R\right].$$
(5.34)

(7)   The Fuellekrug real normal natural frequencies and mode shapes are then

$$\omega_n^{Fuellekrug}=\omega_n \text{ and } \left[\Phi^{Fuellekrug}\right], \text{ respectively.}$$

When $N_m = N_d$ the singular value decomposition coordinate transform to and

from a reduced degree-of-freedom set is not required since $N_m = N_d$. The solution

therefore proceeds as follows:

(1)   Rotate mode shapes so largest component of each shape is scaled to $(1+0i)$

using Eq. (5.22).

(2)   Solve for the mass-modified stiffness matrix, $\left[K_M\right]$ by defining

$$[P_A]=\begin{bmatrix} \{\phi_1^R\} & \{\phi_1^R\} & \cdots & \{\phi_{N_m}^R\} & \{\phi_{N_m}^R\} \\ \{\phi_1^R\}\tilde{\omega}_1 & \{\phi_1^R\}\tilde{\omega}_1^* & \cdots & \{\phi_{N_m}^R\}\tilde{\omega}_{N_m} & \{\phi_{N_m}^R\}\tilde{\omega}_{N_m}^* \end{bmatrix},$$
(5.35)

$$[P_B]=\left[\{\phi_1^R\}\tilde{\omega}_1^2 \quad \{\phi_1^R\}\left(\tilde{\omega}_1^*\right)^2 \quad \cdots \quad \{\phi_{N_m}^R\}\tilde{\omega}_{N_m}^2 \quad \{\phi_{N_m}^R\}\left(\tilde{\omega}_{N_m}^*\right)^2\right],$$
(5.36)

solving the equation

$$\left[\,[K_M]\ \ [C_M]\,\right]=-[P_A]^{-1}[P_B],$$
(5.37)

and extracting the desired $\left[K_M\right]$ from the left hand side.

(3) Calculate real mode shapes and natural frequencies via eigenvalue

decomposition of $[K_M]$; i.e., by solving

$$[K_M]\{\phi_n^R\} = \omega_n^2 \{\phi_n^R\} . \qquad (5.38)$$

The case of $N_m > N_d$ is treated by a combination of the second Fuellekrug

solution and the rotated-real method from Section 5.4.3.1. The procedure is as follows:

(1) Separate the modes into a group of the first N_d modes and a group of all

that remain;

(2) Perform the steps of the second Fuellekrug method on the first group;

(3) Perform the rotated-real method on the remaining group;

(4) Recombine the modes into the full set of N_ω real mode shapes and natural

frequencies.

5.5   Comparative Study for Reduced Coordinate Damping Methods

Performance of the approximate proportional damping methods presented in

Section 5.4 is studied in this section using a composite sandwich plate model with core

damage. The primary interests are to compare the direct modal and extended Rayleigh

methods and to study the loss of accuracy associated with calculating the damping

matrices in reduced coordinates as opposed to full coordinates.

5.5.1   Analytical Sandwich Model and Simulated Experimental Data

The damage case 1 composite sandwich plate model from Section 5.4 was implemented with the material properties in Table 5-5. Reference frequency response functions were calculated using global stiffness matrix proportional Rayleigh damping with $\alpha = 10^{-6}$ and $\beta = 0$ in the plate-normal Z-direction from 100 Hz to 1750 Hz at each of 16 top-surface measurement points. Figure 5-21 shows the model with analysis degrees-of-freedom and the damaged core region. Modal parameter estimation of the reference data was performed using the commercial package ME'scopeVES [5-3] to give natural

Table 5-5: Finite element model material properties for the damping methods study model.

Laminates (3D orthotropic)		Core (3D anisotropic)		
Property	**Healthy Region**	**Property**	**Healthy Region**	**Damaged Region**
E_{11} (Pa)	1.4215×10^{11}	G_{11} (Pa)	100.00	100.00
E_{22} (Pa)	1.4953×10^{10}	G_{22} (Pa)	100.00	100.00
G_{12} (Pa)	1.3828×10^{9}	G_{33} (Pa)	1.3800×10^{8}	1.3800×10^{8}
ν_{12}	3.2039×10^{-6}	G_{44} (Pa)	100.00	100.00
G_{13} (Pa)	4.5970×10^{9}	G_{55} (Pa)	8.3639×10^{7}	2.6763×10^{7}
G_{23} (Pa)	3.3000×10^{9}	G_{66} (Pa)	2.9190×10^{8}	2.9425×10^{7}
ρ (g/cm^3)	1.7391	$G_{ij}, i \neq j$ (Pa)	0	0
η	0	ρ (g/cm^3)	0.24552	0.24552
α	1×10^{-6}	η	0	0
β	0	α	1×10^{-6}	1×10^{-6}
		β	0	0

Figure 5-21: Composite sandwich plate mesh showing $N_d = 16$ analysis degrees-of-freedom on the top laminate (degrees-of-freedom are normal to the plate) and the damaged region of the core.

frequencies, mode shapes, and modal damping ratios for the first 18 modes, as presented

in Table 5-6. Although the underlying damping is proportional, and thus modal data

should be real-valued, the natural frequencies and mode shapes are complex in the third

significant figure (i.e., two-to-three orders of magnitude between real and imaginary

parts). This is a result of the curve-fitting based modal parameter estimation

process being imperfect, even for noise-free analytical data. It should be noted that global

stiffness matrix proportional damping was chosen for the reference data so that error

could be attributed to the degree-of-freedom reduction process and fidelity of the

approximate damping methods without additional error from assuming proportional

damping for a non-proportionally damped system.

Table 5-6: Modal parameter summary of the analytical reference system.

Mode	Mode Shape	Frequency (Hz)	Damping Ratio
1	1-1	-0.109 - 186i	0.06%
2	2-0	-0.232 - 272i	0.09%
3	0-2	-0.380 - 348i	0.11%
4	2-1	-0.640 - 451i	0.14%
5	1-2	-0.694 - 470i	0.15%
6	3-0	-1.67 - 730i	0.23%
7	2-2	-1.96 - 790i	0.25%
8	3-1	-2.20 - 836i	0.26%
9	0-3	-2.23 - 841i	0.27%
10	1-3	-2.93 - 965i	0.30%
11	3-2	-4.29 - 1168i	0.37%
12	2-3	-4.64 - 1231i	0.38%
13	4-0	-5.65 - 1342i	0.42%
14	3-3	-6.32 - 1417i	0.45%
15	4-1	-7.55 - 1549i	0.49%
16	4-2	-7.86 - 1579i	0.50%
17	0-4	-8.40 - 1630i	0.52%
18	1-4	-9.04 - 1696i	0.53%

5.5.2   Damping Study Results

The specific proportional viscous damping methods under study are named in

Table 5-7 along with primary equation references from Section 5.4.2. The damping

methods were implemented using the rotated-real complex-to-real modal transformation

method, where required (i.e., for the direct modal and extended Rayleigh method cases,

since the Rayleigh methods were implemented using known proportionality constants).

The rotated-real method was selected based on the comparison in Appendix C. Frequency

response functions were then generated from the reduced coordinate system for each type

Table 5-7: Damping Method Study Cases.

| Damping Method | Calculation Domain | | Primary Equation Reference |
	Full Degree-of-Freedom Set (*f*-DOF)	Measurement Degree-of-Freedom Set (*m*-DOF)	
Rayleigh Damping in *f*-DOF (Baseline)	X		(5.5)
Rayleigh Damping in *m*-DOF		X	(5.8)
Direct Modal Damping in *f*-DOF	X		(5.18)
Direct Modal Damping in *m*-DOF		X	(5.19)
Extended Rayleigh Damping in *f*-DOF	X		(5.20)
Extended Rayleigh Damping in *m*-DOF		X	(5.21)

of approximate damping and the frequency response functions from the five approximate cases compared to those of the baseline full degree-of-freedom Rayleigh method.

The comparison is presented visually through plots showing the driving point frequency response functions and the following three frequency-based metrics, where $\tilde{C}$ is the baseline damping case, $\hat{C}$ is the approximate damping matrix for the case being evaluated, and angled brackets $\langle ... \rangle$ denote the mean absolute value in each case.

- Mean absolute value frequency response function difference:

$$\left\langle \Delta a(\hat{C}, \omega_k) \right\rangle = \frac{1}{N_d} \sum_{i=1}^{N_d} \left| a(\tilde{C}, \omega_k)_i - a(\hat{C}, \omega_k)_i \right|. \tag{5.39}$$

- Mean absolute value residual force vector:

$$\left\langle R(\hat{C}, \omega_k) \right\rangle = \frac{1}{N_d} \sum_{i=1}^{N_d} \left| f - Z(\tilde{C}, \omega_k)_i a(\hat{C}, \omega_k)_i \right|. \tag{5.40}$$

- Average non-zero damping matrix value:

$$\left\langle \hat{C}(\omega_k) \right\rangle = \frac{1}{N_{els}} \sum_{l=1}^{N_{els}} \left| \left(\hat{C}(\omega_k) \right)_l^{NonZero} \right|,$$ (5.41)

where $\left(\hat{C}(\omega_k) \right)_l^{NonZero}$ is the lth non-zero element of damping matrix $\hat{C}(\omega_k)$

and N_{els} is the number of non-zero elements of $\hat{C}(\omega_k)$.

Driving point frequency response functions from each damping method are

compared to the reference case in Figure 5-22 with average frequency response function

difference in Figure 5-23. It can be seen that both direct modal damping methods give

noticeable error with the direct modal m-DOF method producing too much damping and

the direct modal f-DOF method producing too little damping as frequency increases. The

other methods appear to overlap with the reference data well; however, inspection of the

mean frequency response function difference in Figure 5-23 shows that there is some

error in all of the cases, with the Rayleigh f-DOF method error representing the level of

numerical precision. The extended Rayleigh f-DOF method performs the best, with error

levels averaging approximately -40 dB compared to frequency response function levels

of approximate 40 dB.

The error level trends can be inspected in more detail in Figure 5-24, which gives

the residual force vector calculated between the reference frequency response function

and each of the damping method dynamic stiffness matrices, plotted in decibels (dB).

Several observations can be made. Most importantly, the extended Rayleigh f-DOF

method produces far lower residual force through the mid and high frequencies than the
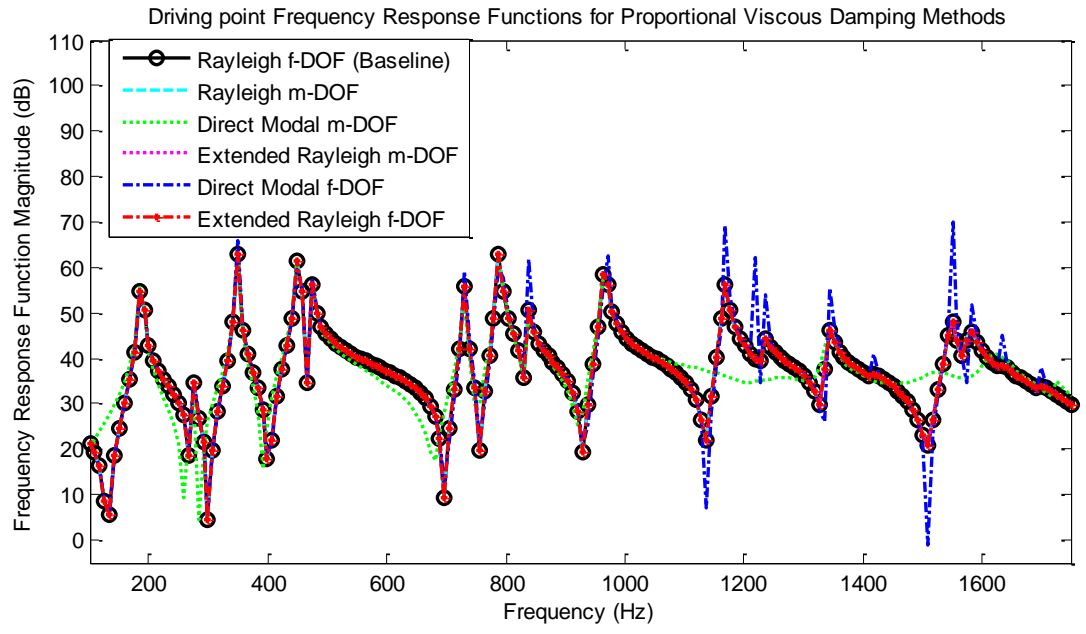
Figure 5-22: Acceleration domain driving point frequency response functions for five damping method cases compared to the exact analytical case and measured reference data.
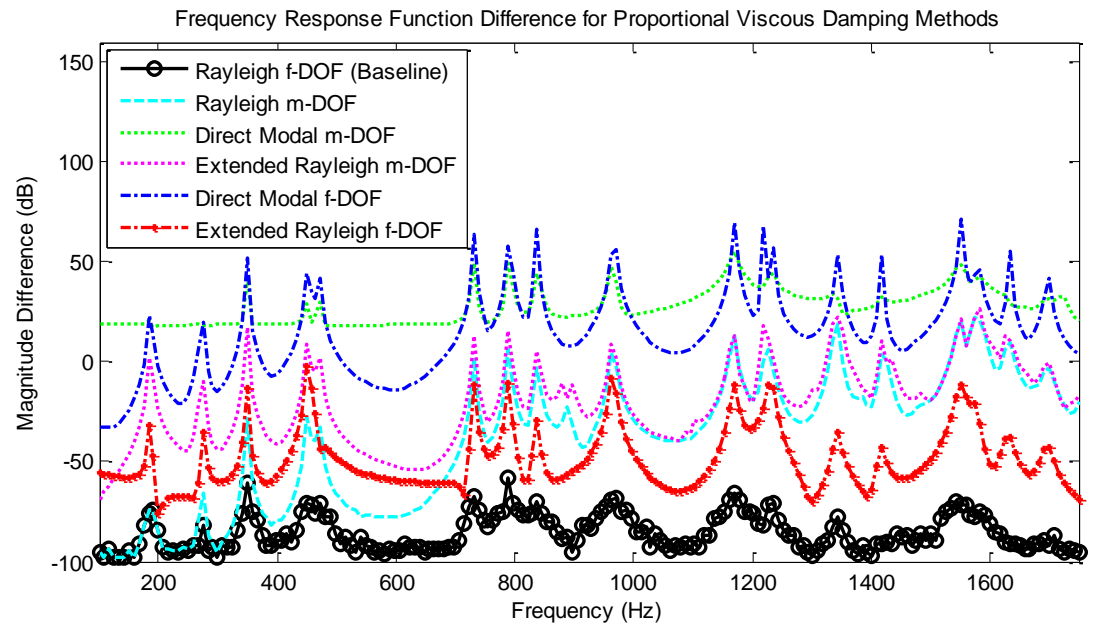
Figure 5-23: Frequency response function difference, mean absolute value over degree-of-freedom, for five damping cases compared to exact analytical case.
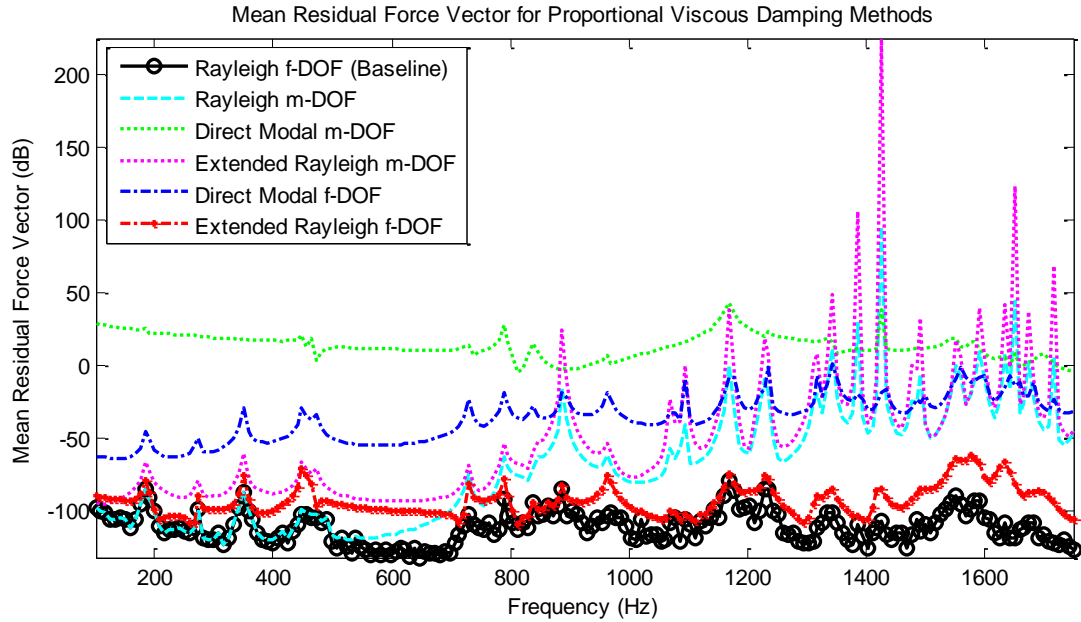
Figure 5-24: Frequency response residual force vector, mean absolute value over degree-of-freedom, for five damping cases compared to exact analytical case.

other methods, while still producing low error at low frequency. Additionally, the

Rayleigh *m*-DOF method produces almost zero error at low frequencies, although the

error grows through higher frequencies. This indicates that if proportional damping is a

fair approximation for the system in question and only low modes are required, the

proportional damping can be added in *m-DOF* space after reducing using the undamped

dynamic stiffness matrix.

Another observation can be seen in the large spikes that develop in the higher

frequencies for the *m-DOF* Rayleigh modal damping case. These spikes correspond to

poles of the inverse slave degree-of-freedom portion of the partitioned dynamic stiffness

matrix, $\left[Z(r,\omega_k)\right]_{ss}^{-1}$, which is required to form the reduction transformation matrix in Eq.

(3.26). It can thus be seen that the *m-DOF* Rayleigh modal damping method can be used

with reasonably low error as long as all frequencies are below the lowest pole of

$$\left[Z(r,\omega_k)\right]_{ss}^{-1}.$$

A final qualitative comparison of the damping methods can be seeing in Figure

5-25, which gives a measure of the magnitude of each damping matrix with respect to

frequency. The magnitude is found by averaging the absolute value of non-zero elements

of each resulting *m-DOF* damping matrix, at each frequency, and thus essentially shows

how each damping matrix varies over frequency, but does not give a meaningful
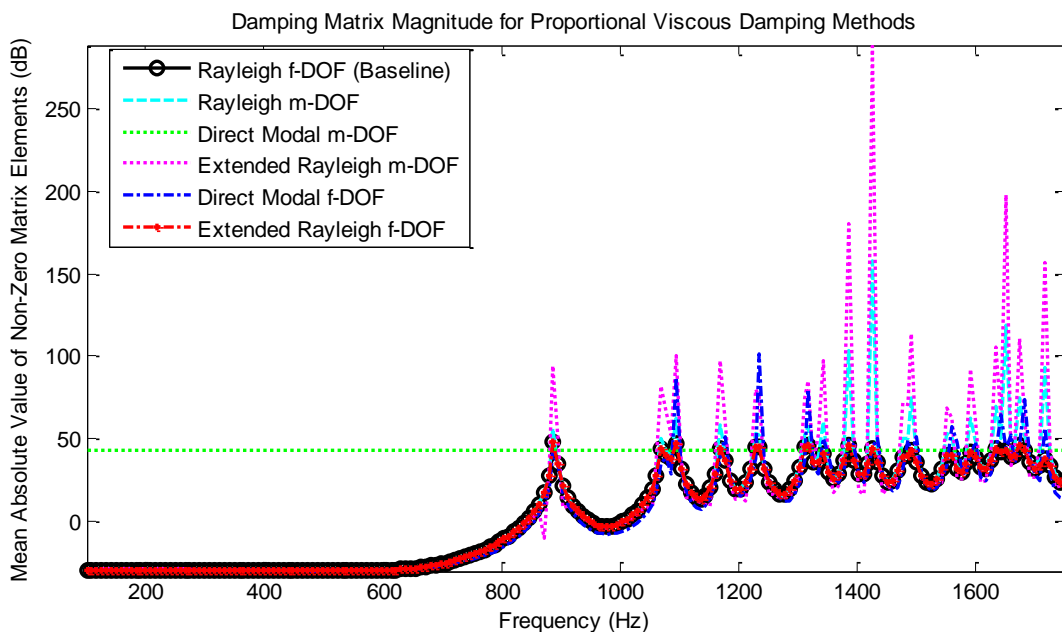
Figure 5-25: Mean absolute value of non-zero reduced degree-of-freedom damping matrix elements for five damping cases compared to exact analytical case.

magnitude comparison between methods. There are large spikes in most of the magnitude

functions which can be shown to again correspond to the poles of $\left[Z(r,\omega_k)\right]_{ss}^{-1}$. The

exception is the *m-DOF* direct modal damping method which is created using the *m-DOF*

mode shape matrix and thus doesn't require additional matrix reduction with the result

that it is the same for each frequency (and as a result, very inaccurate). The Rayleigh *f-*

DOF and extended Rayleigh *f*-DOF cases have very similar matrix values which further

supports the observation that the extended Rayleigh damping method most accurately

models the correct damping for this system.

5.5.3   Discussion

Based on the presented comparison study, using analytically simulated reference

data generated from an experimentally correlated finite element model with known global

stiffness matrix proportional damping and no noise, it can be seen that Extended Rayleigh

modal damping formulated in the full analytical *f-DOF* degree-of-freedom space gives

the best results by every metric. The presented cases simulated a real-world structure and

damping case, with modal parameter estimation performed using commercial software

and the reference data and resulting complex modal parameters used as if they were

measured. This conclusion is therefore meaningful for real-world implementation despite

being drawn from analytical study. Another interesting observation is that the

approximate *m-DOF* methods can potentially produce reasonable results for the lowest

frequencies, with the upper frequency limit imposed by the lowest frequency poles of the

reduction transformation matrix related quantity $\left[Z(r,\omega_k)\right]_{ss}^{-1}$. It can also be seen that the direct modal damping method does not perform acceptably in any case. If all degrees-of-freedom could be measured, it can be assumed that this method would give better results; however, in any real-world situation that is not possible. The Rayleigh modal damping formulations on the other hand produce reasonable results, even with the 99.2% degree-of-freedom reduction studied.

More accurate versions of the modal damping methods can potentially be reached through a two-step method, where approximate proportional viscous damping is fitted as well as possible, and then the approximately damped dynamic stiffness matrix used to expand mode shapes in place of the undamped dynamic stiffness matrix. If the initial proportional viscous damping fit is good then the extended Rayleigh modal damping method could potentially approach the exact damping case (as may the direct modal damping method in the case of $N_d = N_{modes}$).

The material contained in Chapter 5 was developed in collaboration with Prof. John B. Kosmatka, Prof. Charles Farrar, and Prof. Joel Conte. The dissertation author was the primary investigator and author of this work.

5.6 **Chapter 5 References**

[5-1]   MATLAB version 7.8.0. Natick, Massachusetts: The MathWorks Inc., 2009.

[5-2]   MD. NASTRAN 2006 R1. Santa Ana, California: MSC Software., 2006

[5-3]   ME'scopeVES version 4.0.0.53. Scotts Valley, California: Vibrant Technology Inc., 2005

[5-4]   Fuellekrug, U., "Computation of Real Normal Modes from Complex Eigenvectors," *Mechanical Systems and Signal Processing*, **22**, pp. 57-65, (2008)

6   EXPERIMENTAL IMPLEMENTATION AND VALIDATION

The current damage identification algorithm is now extended to experimental

application and validated experimentally on a composite plate test-piece. Techniques for

model correlation techniques are described first, followed by details of additional criteria

for experimental frequency line selection. The full recommended process for

experimental model correlation and damage identification is then outlined. The

subsequent experimental validation includes details of the test-piece, test setup, and

model; details of initial model correlation; and detailed treatment of experimental damage

identification.

6.1   **Baseline Finite Element Model Correlation**

Prior to damage identification, the baseline finite element model must be

correlated to baseline (healthy) data. This step decreases initial modeling error and

increases the accuracy of subsequent damage identification. The basic concept of

correlation is to optimize selected model parameters so that error between the analytical

model response and healthy reference data is minimized. For the current implementation,

any parameters that affect the vibration response of the analytical model can be chosen

for correlation, examples being material stiffnesses, density, laminate ply angles, and

spring stiffnesses. The error to be minimized can likewise be defined based on a range of

vibration criteria. Modal parameters provide a convenient basis for correlation error; however, as will be discussed in more detail below, it is recommended to perform final correlation with respect to frequency domain criteria (e.g., frequency response function error) since the correlated model will be used subsequently for damage identification in the frequency domain.

Common sense dictates that the parameter values being correlated should be kept as physically meaningful as possible. In some cases, however, it may be desirable to update parameters which are known to be physically accurate in the uncorrelated model in order to counter non-parametric inadequacies in the modeling methodology. An example of non-parametric modeling methodology error is increasing levels of natural frequency error as a model's discretization is coarsened relative to the modal wavelengths. This behavior is not related to accuracy of material properties but stems from the basic finite element method assumption of geometrically idealized element shape functions. The resulting error in natural frequency can potentially be corrected for the purposes of damage identification by accepting a baseline value of global density or stiffness which is known to not be physically accurate to the material but which nonetheless increases the fidelity of model to data without overly corrupting subsequent damage identification.

The desire to increase overall fidelity to the baseline data set, however, must be balanced against the desire to have a correlated model which will update accurately to the damage state. One approach to reducing modeling error while keeping parameters

realistic is to update high sensitivity global parameters first (along with parameters related to connections, if applicable), then perform subsequent correlations with increasingly larger sets of variables. This approach serves to first anchor major parameters after which updating additional parameters helps fine-tune the correlation with smaller changes overall. Before progressing to more refined correlation the updated parameters at each step can be inspected to ensure the values are still in an acceptable range.

Another consideration when choosing a correlation technique or series of techniques is how the parameter variability will be defined prior to performing statistical damage identification. It is recommended here to use one or more of the deterministic correlation methods to remove the bulk of the methodology based modeling error, and then to use the statistical method for final correlation in order to provide a set of damage parameter initial variability values that can be referenced during damage identification setup (Note: for detailed analysis of the definition and interpretation of prior and posterior variability on the experimental plate see Section 6.4.4.4).

Four analytical model correlation methods—which can be used independently or consecutively—are now presented and discussed:

(1)   Deterministic least-squares minimization of natural frequencies (a.k.a., modal parameter based pseudo Newton-Raphson method);

(2) Deterministic least-squares minimization of frequency response functions

(a.k.a., frequency response function based pseudo Newton-Raphson

method);

(3) Deterministic least-squares minimization of residual force vectors (a.k.a.,

residual force vector based pseudo Newton-Raphson method);

(4) The current frequency response function based statistical damage

identification algorithm applied to correlation;

The first three methods are deterministic least-squares optimization routines in the

Newton-Raphson style which operate on either modal parameters, frequency response

functions, or residual force vectors, respectively. The fourth method is an application of

the current damage identification algorithm where primarily global parameters are

updated with heavy regularization (low initial parameter variance) to promote a realistic

solution.

Table 6-1: Summary of model correlation methods

Method	Basis			Statistical Optimization Regularization
	Modal Parameters	Frequency Response Functions	Residual Force Vectors	
Modal Parameter Based Pseudo Newton-Raphson	X			No
Frequency Response Function Based Pseudo Newton-Raphson		X		No
Residual Force Vector Based Pseudo Newton-Raphson			X	No
Current Algorithm Applied to Correlation			X	Yes

6.1.1 Modal Parameter Based Pseudo Newton-Raphson

If modal parameters are available, one convenient correlation approach is to update major parameters (e.g., global stiffness and/or density) based on minimizing the difference between measured and analytical natural frequencies. A simple but effective optimization algorithm for implementing this correlation technique is least-squares minimization based on the classical Newton-Raphson method, similar to the algorithm outlined in Ref [6-1]. Implementation of the algorithm for updating N_r parameters is as follows.

(1) Calculate a vector of differences between N_m experimental natural frequencies, $\{\tilde{\omega}_n\}$, and the N_m analytical frequencies for iteration i, $\{\omega_n\}_i$, comparing mode shapes if necessary to ensure correct frequencies are in the correct order:

$$\{\Delta\omega_n\}_i = \{\tilde{\omega}_n\} - \{\omega_n(r_i)\}. \tag{6.1}$$

(2) Generate the natural frequency sensitivity matrix for the pth parameter using finite difference with perturbation Δ:

$$\left\{\frac{\partial\omega_n}{\partial r_p}\right\}_i = \frac{\{\omega_n(r_p + \Delta)\}_i - \{\omega_n(r_p)\}_i}{\Delta}. \tag{6.2}$$

(3) Stack the sensitivity vectors side-by-side into the complete natural frequency sensitivity matrix:

$$\left[\frac{\partial \omega_n}{\partial r}\right]_i = \left[\left\{\frac{\partial \omega_n}{\partial r_1}\right\}_i \left\{\frac{\partial \omega_n}{\partial r_2}\right\}_i \cdots \left\{\frac{\partial \omega_n}{\partial r_{N_m}}\right\}_i\right].$$ (6.3)

(4)   Use the pseudo-inverse least-squares solution for the general case of N_r not

equal to N_m to generate the updated parameter set (the proper Newton-

Raphson solution uses a direct matrix inverse to solve this equation,

requiring a square sensitivity matrix and therefore limiting the number of

correlation modes to the number of parameters being updated):

$$\{r\}_{i+1} = \{r\}_i + \left[\frac{\partial \omega_n}{\partial r}\right]_i^+ \cdot \{\Delta \omega_n\}_i.$$ (6.4)

(5)   Check convergence and either exit the loop or increment i and continue with

the next iteration.

The pseudo Newton-Raphson natural frequency method has the advantage of

avoiding compatibility issues related to units and the number of degrees-of-freedom

between the measured data and analytical model by reducing the comparison to natural

frequencies. Since natural frequencies are relatively insensitive to parameter changes, the

update will also tend to be well behaved, smooth, and unique, so long as there are at least

as many frequencies as parameters (i.e., so long as the problem is not underdetermined).

On the other hand, this simplicity is limiting since damping cannot be correlated, the

number of parameters is limited to the number of available natural frequencies, and

modal parameters need to be available. Also, the curve-fitting process required to derive

modal parameters can potentially add another layer of error to the system, although it should be small in the case of natural frequencies. Note that an iteration step limit can be applied to step (3) to help with convergence if required (depending on the initial discrepancy size and level of parameter nonlinearity).

6.1.2 Frequency Response Function Based Pseudo Newton-Raphson

If modal parameters are not available, and/or if damping needs to be correlated, a similar algorithm can be implemented using the difference between frequency response functions as follows:

(1) For the ith iteration, calculate a vector of differences between batch-stacked experimental and current analytical frequency response functions at N_ω frequency lines using

$$\{\Delta \underline{a}\}_i = \{\underline{\tilde{a}}\} - \{\underline{a}(\hat{r})\}_i,$$ (6.5)

where $\{\Delta \underline{a}\}_i$ is the vector of differences, $\{\underline{\tilde{a}}\}$ is the vector of experimental frequency response functions, and $\{\underline{a}(\hat{r})\}_i$ is the vector of analytical frequency response functions.

(2) Generate the batch-stacked frequency response function sensitivity vector using Eq. (3.150) for the pth parameter, as

$$\left\{\frac{\partial \underline{a}(r)}{\partial r_p}\right\}_i = -[\underline{Z}]_i^{-1}\left(\left[\frac{\partial \underline{Z}(r)}{\partial r_p}\right]_i \{\underline{\tilde{a}}\}\right),$$ (6.6)

where $\left[\underline{Z}\right]_i$ is the batch-stacked dynamic stiffness matrix at iteration i and dynamic stiffness matrix sensitivity can be approximated using finite difference for perturbation Δ as

$$\left[\frac{\partial \underline{Z}(r)}{\partial r_p}\right] \approx \frac{\left[\underline{Z}(r_p + \Delta)\right] - \left[\underline{Z}(r_p)\right]}{\Delta}. \tag{6.7}$$

(3) Calculate the full frequency response function sensitivity matrix by stacking the individual parameter sensitivity vectors side-by-side into the complete matrix:

$$\left[\frac{\partial \underline{a}}{\partial r}\right]_i = \left[\left\{\frac{\partial \underline{a}(r)}{\partial r_1}\right\}_i \left\{\frac{\partial \underline{a}(r)}{\partial r_2}\right\}_i \cdots \left\{\frac{\partial \underline{a}(r)}{\partial r_{N_p}}\right\}_i\right]. \tag{6.8}$$

(4) Use the pseudo-inverse least-squares solution to generate the updated parameter set:

$$\{r\}_{i+1} = \{r\}_i + \left[\frac{\partial \underline{a}}{\partial r}\right]_i^+ \cdot \{\Delta \underline{a}\}_i. \tag{6.9}$$

(5) Check convergence using averaged parameter change and either exit the loop or increment i and continue with next iteration.

As with the modal parameters version, this unregularized algorithm tends to work best with a small number of global parameters so that the parameter sensitivities are strongly defined and the optimization is more stable. Similarly to the main damage detection algorithm, frequency line selection must be performed prior to beginning the

update. It should be noted that the algorithm is presented in its most simple form above,

and implementation complications arising from reduced degree-of-freedom measurement

set and the desired inclusion of measured modal damping can be solved using the

methods developed in the preceding chapters for the main damage identification

algorithm.

6.1.3 Residual Force Vector Based Pseudo Newton-Raphson

A similar algorithm can be alternatively formed to minimize residual force

vectors through the pseudo Newton Raphson approach as follows:

(1) For the ith iteration, calculate the batch-stacked vector of residual force

vectors $\{\underline{R}\}_i$ at N_ω frequency lines using

$$\{\underline{R}\}_i = \{\underline{i}\} - \left[\underline{Z}(r_i)\right]\{\tilde{\underline{a}}\}, \tag{6.10}$$

where $\left[\underline{Z}(r_i)\right]$ is the dynamic stiffness matrix and $\{\tilde{\underline{a}}\}$ is the vector of

experimental frequency response functions.

(2) Generate the batch-stacked residual force vector sensitivity vector using Eq.

(3.115) for the pth parameter, as

$$\left[\underline{N}\right]_i = -\left[\left.\frac{\partial \underline{Z}(r_i)}{\partial r}\right|_{\{r_i\}}\right]\{\tilde{\underline{a}}\}, \tag{6.11}$$

where the batch-stacked dynamic stiffness matrix sensitivity $\left\| \left. \dfrac{\partial \underline{Z}(r_i)}{\partial r} \right|_{\{r_i\}} \right\|$

can be built from the dynamic stiffness matrix sensitivity for each of the pth

parameters using finite difference for perturbation Δ as

$$\left[\frac{\partial \underline{Z}(r)}{\partial \hat{r}_p} \right] \approx \frac{\left[\underline{Z}(\hat{r}_p + \Delta) \right] - \left[\underline{Z}(\hat{r}_p) \right]}{\Delta} . \tag{6.12}$$

(3) Use the pseudo-inverse least-squares solution to generate the updated

parameter set:

$$\{r\}_{i+1} = \{r\}_i + \left[\underline{N} \right]_i^+ \{\underline{R}\}_i . \tag{6.13}$$

(4) Check convergence using averaged parameter change and either exit the

loop or increment i and continue with next iteration.

6.1.4 Statistical Model Correlation Using the Current Algorithm

The current statistical frequency response function based damage identification

algorithm can additionally be used for model correlation when configured properly,

allowing robust correlation in the frequency domain. The statistical basis of the algorithm

presents two distinct benefits to correlation. First, the statistical output gives variability

values for parameters which would otherwise be missing. Second, the statistical

formulation provides regularization during optimization, meaning that the algorithm will

be stable for larger numbers of concurrent update parameters and parameters with a wider

range of sensitivities—correlation goals which will often cause the previously described deterministic techniques to fail. It is recommended to perform final correlation using this algorithm.

Implementation of the current algorithm for correlation is similar to the implementation for damage identification. The main exception is that the primary outputs are real-valued healthy parameter values, parameter variability, and the healthy correlated model instead of damage factor values, damage factor variability, and the damage-correlated model. Additionally, the following algorithm configuration options should be considered:

- The selection of global parameters as opposed to local element parameters for bulk material structures or subsystems will help keep the correlation more physically meaningful.

- Using a large number of widely distributed frequency lines will help increase correlation fidelity.

- Relatively tight regularization (i.e., starting with higher assumed parameter variability values) will help keep values from varying too far from their physically realistic values.

- Multiple consecutive runs may increase the final fidelity of correlation while keeping parameter values physically meaningful.

6.2   **Damage Identification Frequency Selection Based on Modal Correlation**

During frequency line selection for damage identification, an additional and optional criterion based on modal correlation in the healthy model can be established to further decrease post-correlation modeling error and potentially improve damage identification accuracy. In an ideal situation, correlation would produce an updated healthy model with zero effective modeling error. However, in experimental practice the correlated model will not be perfect and it is desirable to minimize as far as possible the amount of modeling error that actually propagates into the damage identification step.

The proposed method involves selecting the subset of modes with the highest correlation to the healthy data set and then selecting the update frequencies to be clustered around those same modes in the damaged data set. The selection can be based on one of three criteria:

(1)   Minimum error in natural frequency;

(2)   Minimum error in mode shapes;

(3)   A combined metric that ranks the modes in terms of both error in natural frequency and error in mode shapes and selects the subset of modes with the lowest combined ranking, choosing the lowest of available modes in the event of equal combined ranking.

The mode shape error criterion could be judged based on either cross-correlation or modal assurance criterion, and in the current studies the modal assurance criterion

option is chosen for simplicity since it requires only the two shape vectors for each mode and no mass matrix. After the modes are selected based on healthy correlation, the subset is passed to the mode based frequency selection routine described in Section 4.1.

6.3   **Complete Experimental Correlation and Damage Identification Process**

The complete experimental damage identification process includes vibration testing, model correlation, and damage identification as summarized in Figure 6-1.

Details of the process steps are as follows:

(1)   Perform a vibration test on the structure in its healthy or baseline state to produce frequency response and correlation functions. Perform modal parameter estimation to the frequency response functions to produce healthy natural frequencies, mode shapes, and modal damping ratios if possible.

(2)   Correlate the baseline analytical model to the healthy measurement set to minimize modeling error and establish healthy baseline parameters and parameter uncertainty. The following multi-step correlation procedure is recommended, including one or both of the optional non-statistical initial correlation methods described in Section 6.1:

    a)   (*Optional*) If modal parameters are available, correlate the original finite element model to the healthy modal data using the pseudo
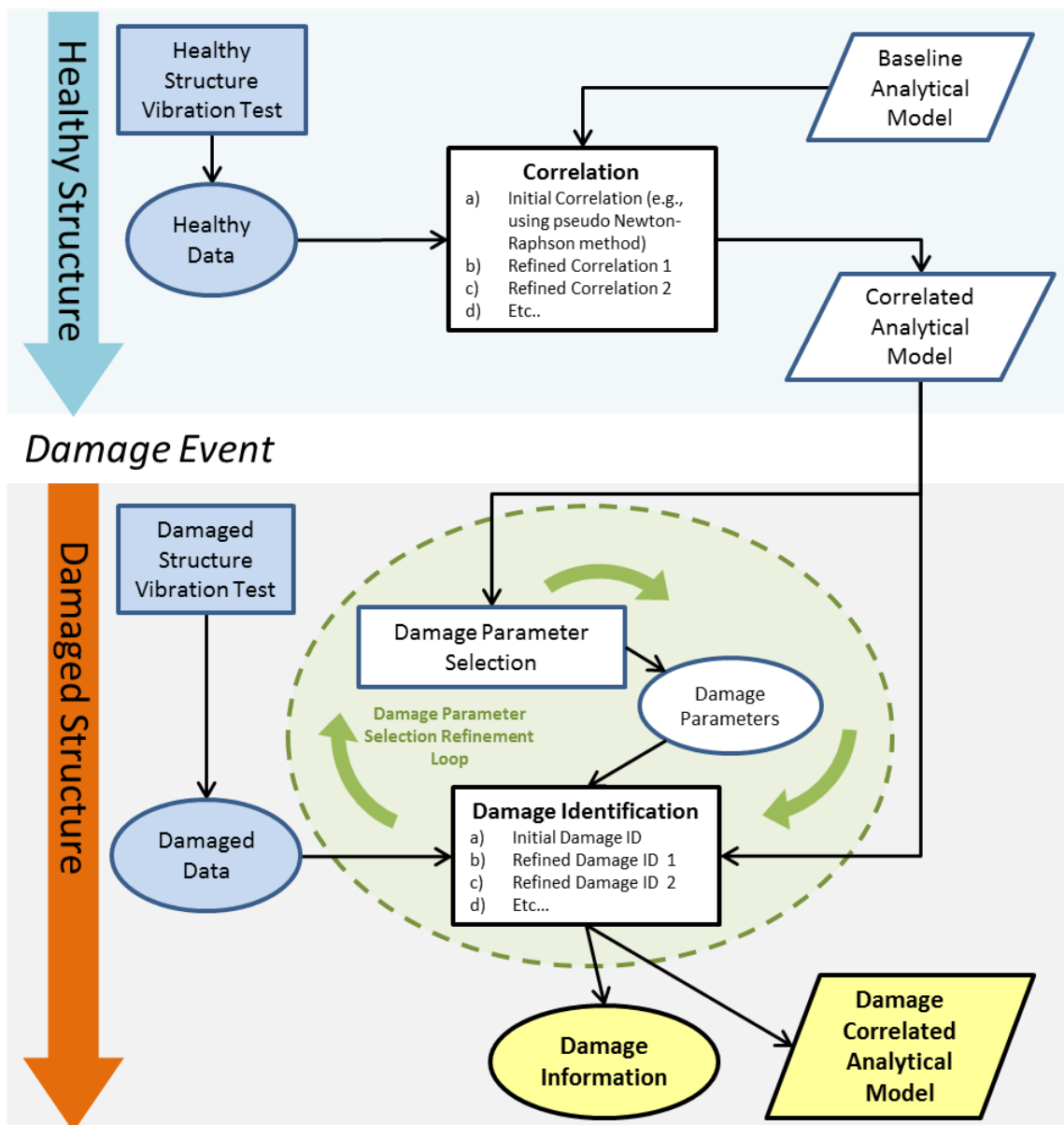
Figure 6-1: Flowchart of the full correlation and damage identification process.

Newton-Raphson natural frequency method. The correlation should be

performed with a small number of global parameters and natural

frequencies over the expected damage identification frequency range.

b) (*Optional*) If modal parameters are not available, the frequency response function damping model requires correlation, or large frequency response function correlation changes are required, perform correlation using the pseudo Newton-Raphson frequency response function or residual force method. The correlation should be performed with a small number of global parameters and natural frequencies over the expected damage identification frequency range. Additional damping parameters can be included if desired.

c) Perform one or more correlation runs using the current statistical damage identification algorithm. These runs may be performed with a large number of parameters in order to fine-tune the model in the frequency domain if desired.

(3) After the structure has sustained damage, perform a vibration test on the structure in its damaged state to produce damaged reference frequency response and correlation functions. Perform modal parameter estimation to the frequency response functions to produce damaged natural frequencies, mode shapes, and modal damping ratios if possible.

(4) By referencing the analytical model, perform damage parameter selection using any available damage location information to establish an initial parameter set for damage identification. Select *prior* parameter variance values based on correlated values and knowledge of expected damage state.

(5)   Perform damage identification using the current statistical frequency domain algorithm to produce updated damage factor values, estimates of damage factor uncertainty, and the damage correlated finite element model. The procedure can be optionally extended iteratively by using the results to select a new and likely smaller set of damage parameters at each step, thereby zeroing in on the damage. This approach is essentially provides coupled damage location and damage identification, and may help overcome modeling error and improve final damage identification results.

It should be noted that measured modal data will generally be complex because of damping in the structure. Equivalent normal modal information can be derived using the methods outlined in Section 5.4.3 where required.

6.4   **Experimental Validation on a Composite Plate**

Experimental validation of the damage identification algorithm on a composite laminate plate with induced damage is presented. The composite plate test-piece was manufactured from a commercially produced stock laminate plate and vibration tested using the roving hammer impact method to produce healthy reference data. A finite element model of the plate was constructed and correlated to the baseline data. Damage was induced into a small region of the structure test-piece and the plate was vibration tested a second time to produce damaged reference data. The finite element model and

damaged data sets were then used to validate the damage identification algorithm and explore performance.

6.4.1 Baseline System Description

All experimental validation was performed using a cross-ply graphite-epoxy composite plate with 12 plies arranged in the layup $[(0/90)_3]_S$. The test-piece was cut using a wet diamond tile-saw from a stock plate with product name *0.060" thickness Carbon Fiber Plate, 12" x 48" sheet* purchased from CST Composites [6-2]. The plate was then stored for several months in the air-conditioned laboratory where all further testing was conducted. The completed test-piece plate was measured to be nominally square with edge lengths of 0.2995±0.001 m. Mass was measured using a digital scale to be 0.231 kg in the plate's baseline vibration testing configuration. Thickness was measured using calipers to a thickness of 0.00165±0.001 m.

Vibration testing was performed using a Dactron Focus 24-bit signal analyzer and Lenovo T64s 64-bit laptop computer with RT Pro v6.21 data acquisition software [6-3]. The test-piece was suspended vertically during testing using lengths of thin surgical tubing attached to the plate in two locations along the top edge via fishing line and small pieces of masking tape to approximate free-free boundary conditions with minimal additional mass-loading as shown in Figure 6-2. The plate was excited using roving impacts from a modal force-hammer (PCB model 086E80 miniature instrumented impulse hammer, range 0–50 lbf) at 36 locations arranged in an evenly spaced 6 x 6 grid

of pre-defined measurement points. Acceleration response was measured at two locations (primary and back-up) using tear-drop AC accelerometers (PCB model 352C22/AC miniature 10 mV/g ceramic shear ICP accelerometer, mass 0.5 gram). The force input and acceleration response sensors were connected to the signal analyzer through a PCB 481A series signal conditioning unit. A schematic of the vibration testing setup showing measurement locations is given in Figure 6-3.
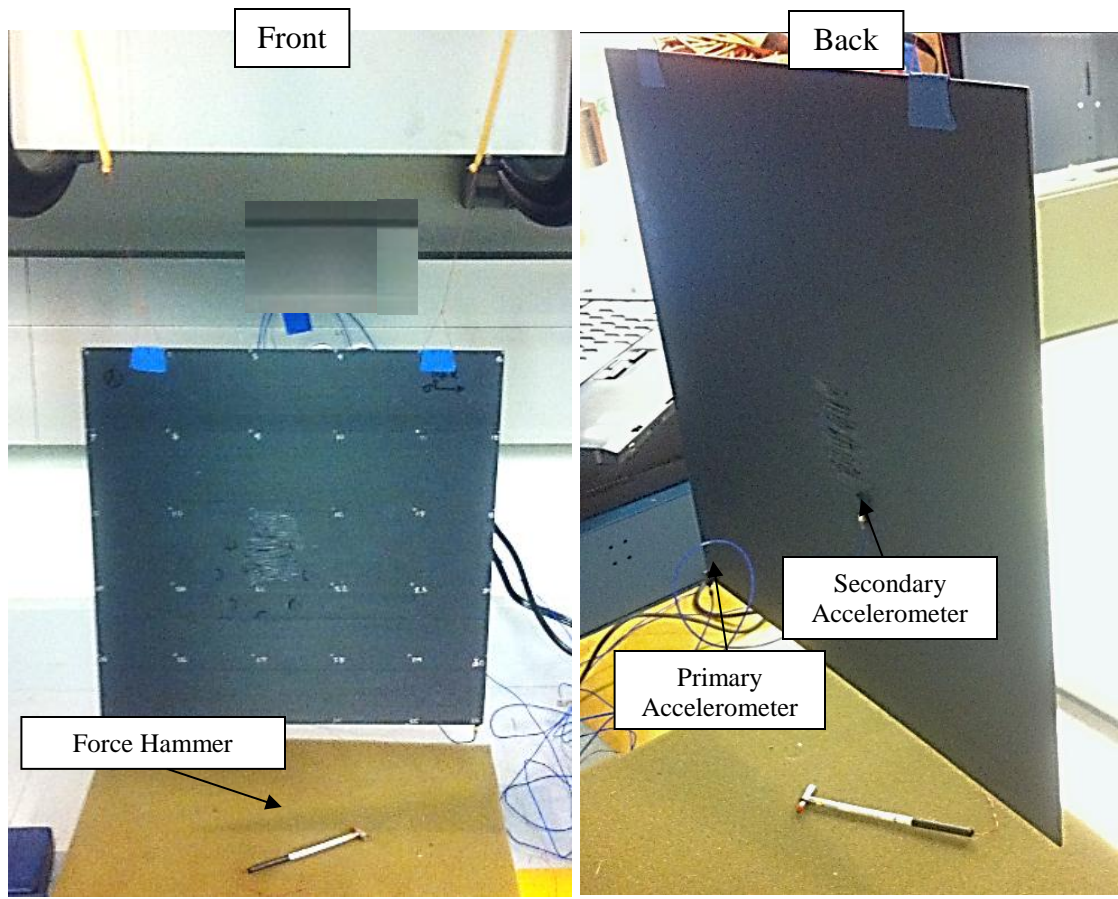
Figure 6-2: Experimental vibration testing setup for the composite plate test-piece.

For each measurement point, the data acquisition system acquired and stored
frequency response functions and frequency coherence functions at 3600 frequency lines
from 0 Hz to 3218 Hz as the average of 5 successful hammer hits through the following
standard process: (1) acquire times time series from the hammer force sensor and each
accelerometer; (2) apply a force exponential window, predefined to bring each time series
to approximately zero by the end of the acquired signal; (3) calculate auto power
spectrum estimates for each time series and cross power spectrum estimates between the
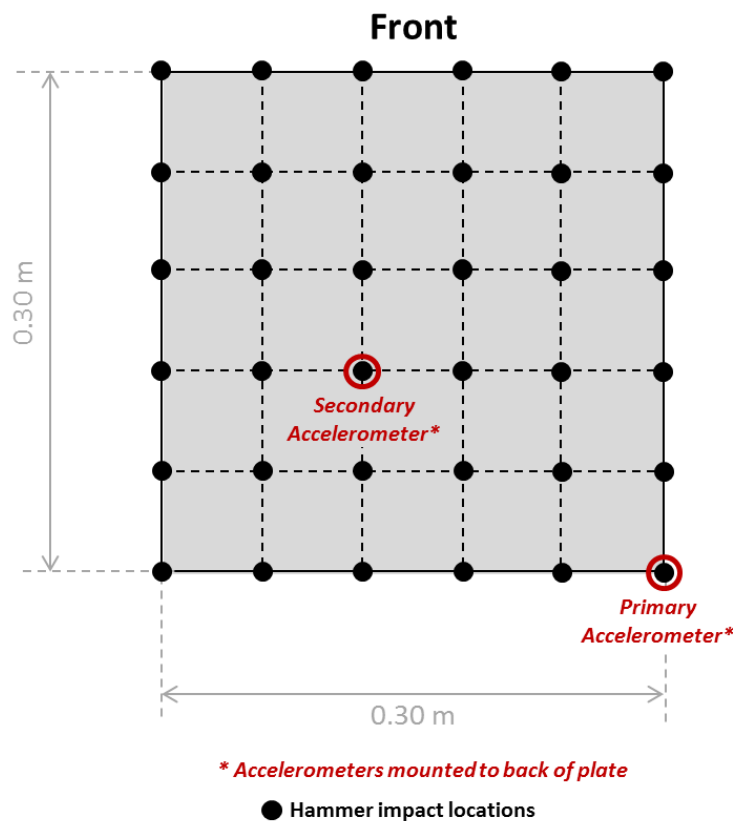
Figure 6-3: Vibration testing setup schematic from plate front showing hammer impact locations (plate front side) and primary and secondary response locations (plate back side).

force time series and each acceleration time series; (4) calculate the H_1 transfer function and coherence function estimates between the force input and each acceleration response; and (5) average the current transfer function and coherence function estimate into the running group average. The output after each complete vibration test was 36 frequency response transfer functions and 36 coherence functions for each response location. The driving point frequencies corresponding to the primary accelerometer location (bottom right corner of the plate) are given in Figure 6-4 and Figure 6-5.

Modal parameter estimation was performed on the baseline frequency response functions using ME'scopeVES v5.1 [6-4] with the modal peaks modal indicator function and ortho-polynomial curve-fitting options. Mode shapes, natural frequencies, and modal damping ratios for the first 12 modes are given in Table 6-2 along with a description of mode type. Since the test-piece is a plane free-free plate the modes follow a predicable pattern and can be described by the number of vertical and hozizontal node lines following Figure 6-6. Visual representations of the mode shapes are given in Figure 6-7. It can be seen in Table 6-2 that damping is generally higher for the torsion modes than for the bending modes. This occurs because torsion in $[(0/90)_N]_S$ cross-ply laminates is dominated by matrix shearing while bending is dominated by fiber deformation. This distinction decreases with increasing modal frequuency as the wavelength decreases and bending involves increasing amounts of matrix shear.

(a)

(b)
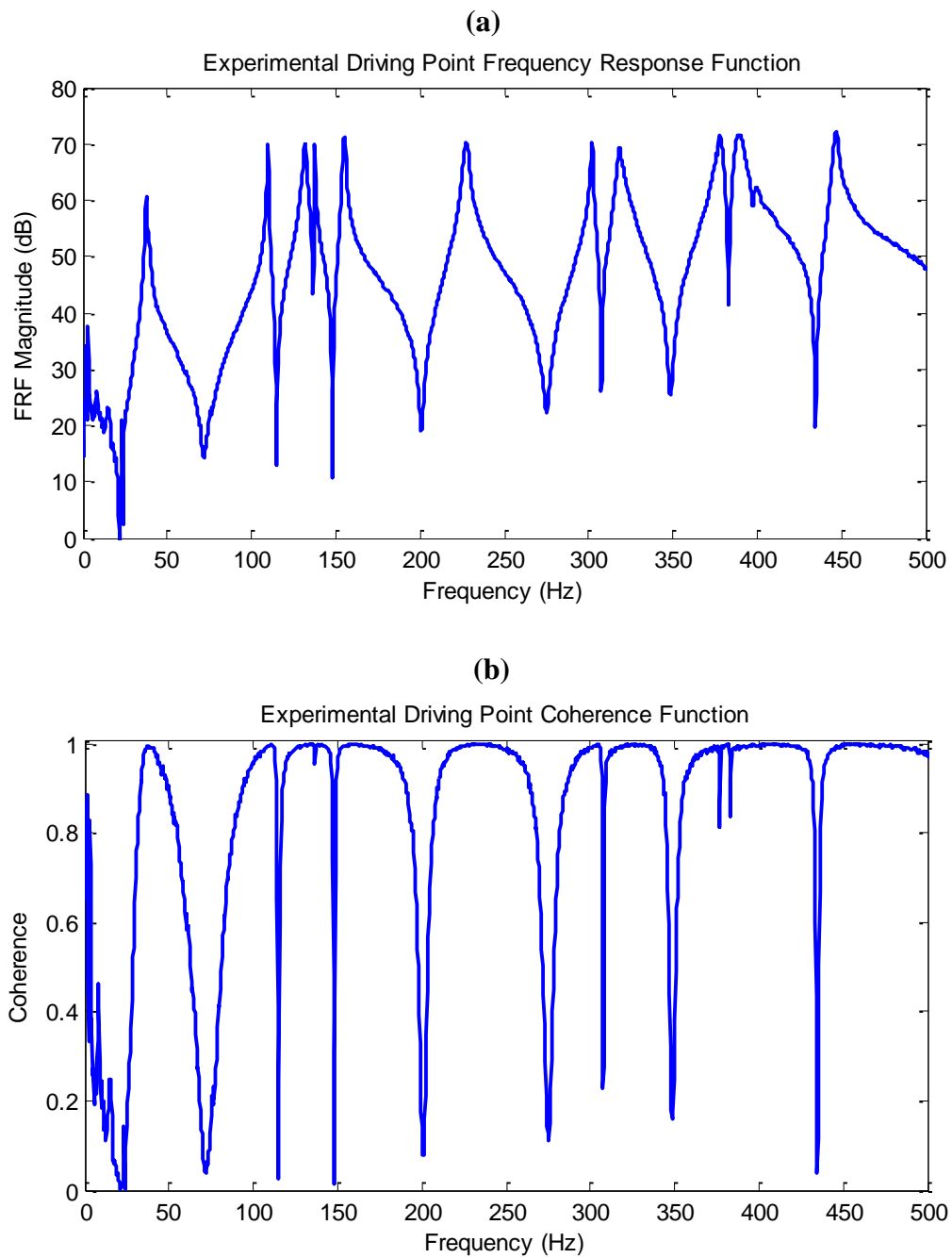
Figure 6-4: Driving point frequency response function from the baseline test-piece: (a) magnitude, (b) coherence.

(a)

(b)
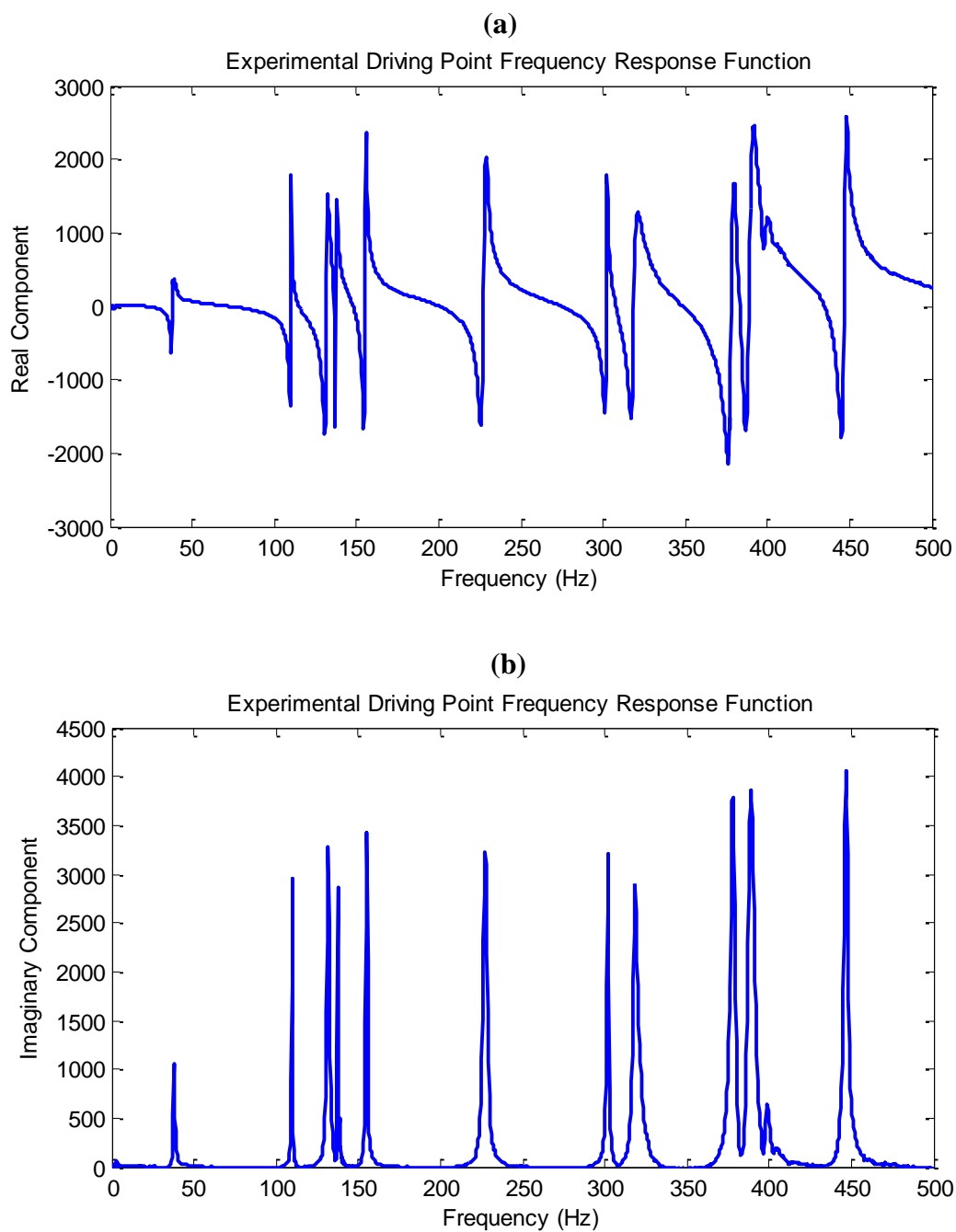
Figure 6-5: Driving point frequency response function from the baseline test-piece: (a) real component, (b) imaginary component.

Table 6-2: Modal summary of the experimental baseline system

Mode	Mode Type	Mode Shape	Frequency (Hz)	Damping Ratio
1	Torsion	*1-1*	37.7	0.78%
2	Bending	*0-2*	109.9	0.24%
3	Bending-Torsion	*1-2*	131.7	0.68%
4	Bending	*2-0*	137.6	0.17%
5	Bending-Torsion	*2-1*	155.1	0.41%
6	Torsion	*2-2*	227.5	0.65%
7	Bending	*0-3*	302.1	0.20%
8	Bending-Torsion	*1-3*	318.4	0.49%
9	Bending	*3-0*	378.1	0.51%
10	Bending-Torsion	*3-1*	388.6	0.61%
11	Bending-Torsion	*2-3*	398.0	0.27%
12	Bending-Torsion	*3-2*	446.6	0.34%
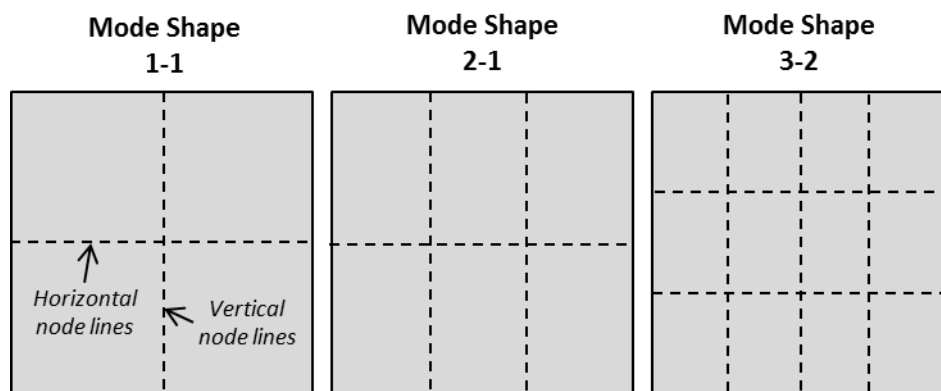
Figure 6-6: Examples of the mode shape description scheme based on node-lines (Number of vertical node lines – Number of horizontal node lines).
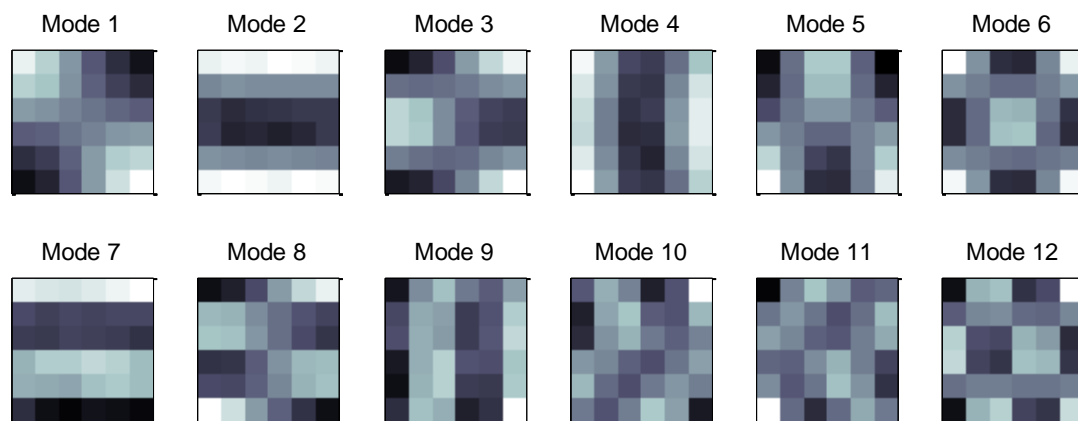
Figure 6-7: Experimental mode shapes measured from baseline plate (white equals a scaled mode shape value of 1, black equals a value of -1, and medium grey equals a value of zero).

A structural finite element model of the test-piece plate was created for MSC. NASTRAN [6-5] (see Appendix D for bulk data file). The structure was discretized into 400 equally sized square plate elements in a 20 x 20 grid producing a 21×21 grid of regularly spaced nodes for a total of 2646 degrees-of-freedom. This mesh was chosen to keep the total number of degrees-of-freedom relatively low while still leaving adequate resolution for capturing the damage. Additionally, the selected mesh provided a close correspondence between the 36 measurement points and node locations. shows the finite element model structure in translucent configuration, aligned as if viewing the test-piece in vibration testing configuration (*x*-axis horizontal, *y*-axis vertical). Nodes corresponding to the vibration testing measurement points are shown with small squares, and the 0° fiber direction, aligned with the global *x*-axis, can be seen as an arrow centered on each element and corresponding to the local element coordinate system 0° direction. The
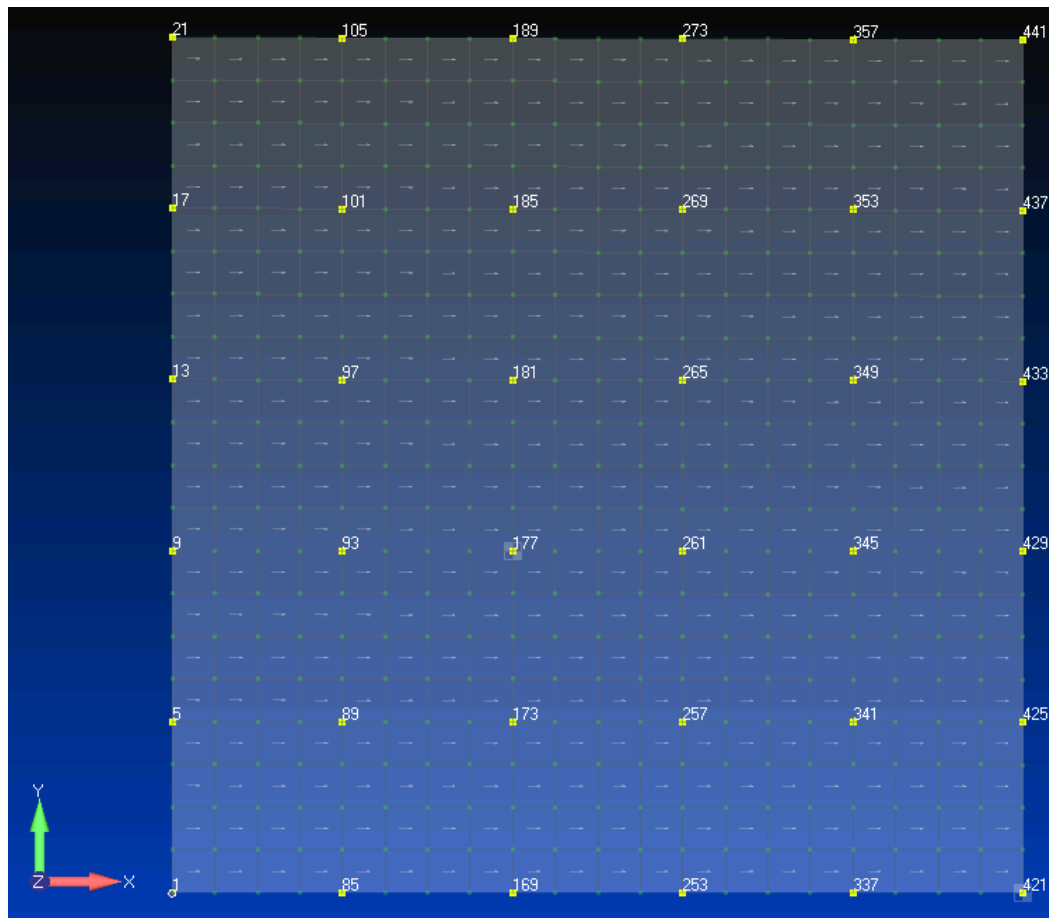
Figure 6-8: Composite plate finite element model (nodes corresponding to measurement points indicated with yellow squares on nodes).

elements were modeled using CQUAD4 plates with PCOMP laminate property definitions and MAT8 material definitions, with all 12 plies through the thickness using the same material definition for each element. The accelerometers were additionally modeled as 0.5 gram point masses, centered on nodes 177 and 421.

Initial ply level material properties were derived from static material coupon testing of the bulk laminate by fellow student Eduardo Velazquez and are presented along

with correlated material properties in Table 6-3 (table located in Section 6.4.2.2). The baseline ply material properties were derived by manually adjusting values in the NASTRAN laminate builder until bulk cross-ply laminate stiffness values matched the measured coupon values and so are only approximations of their true values (i.e., as would have been derived from unidirectional laminate tensile coupons, had they been available). Because of the availability of modal damping ratios, damping was modeled in the plate using the full-coordinates extended Rayleigh method described in Section 5.4.2.3. This method matches measured modal damping ratios by creating a superposition of scaled Rayleigh damping matrices, one for each mode. Since the extended Rayleigh method completely matches the measured damping (within the limits of proportional damping) it was not attempted to additionally define and correlate material damping in the finite element model.

Figure 6-9 shows natural frequencies and mode shapes from the uncorrelated finite element model response. The plate shows expected mode shape response, with modes 10 and 11 deviating slightly from the clean node-line pattern. Figure 6-10 through Figure 6-12 additionally show comparisons to the measured baseline data, with natural frequencies in Figure 6-10, relative natural frequency error in Figure 6-11, and modal assurance criterion diagonal values in Figure 6-12. It can be seen that in the uncorrelated baseline state there is a regular natural frequency error up to 4.9%, with most modes deviating by less than ±2%. The modal assurance criterion is greater than 0.97 for all
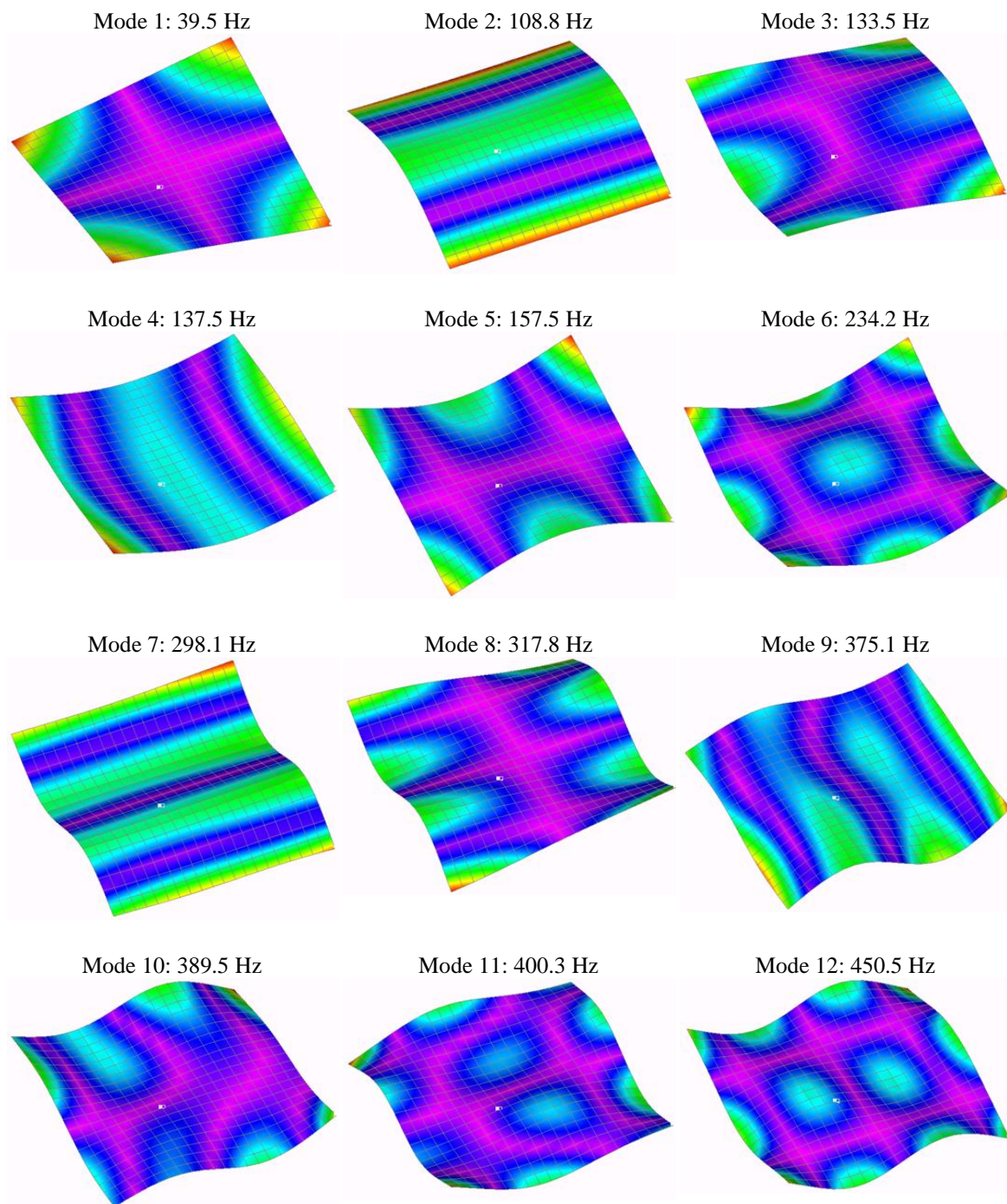
Figure 6-9: Natural frequencies and mode shapes from the uncorrelated finite element model (the white dot near the center of each picture is one of the two accelerometer mass-elements).
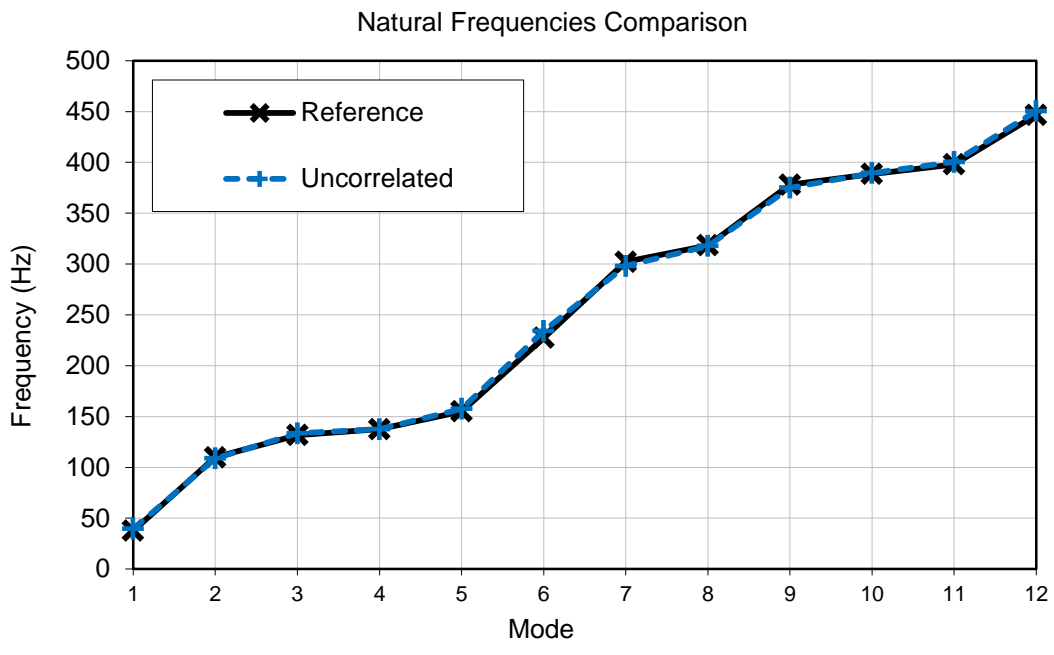
Figure 6-10: Natural frequencies from the uncorrelated baseline finite element model compared to those from the measured healthy data set.
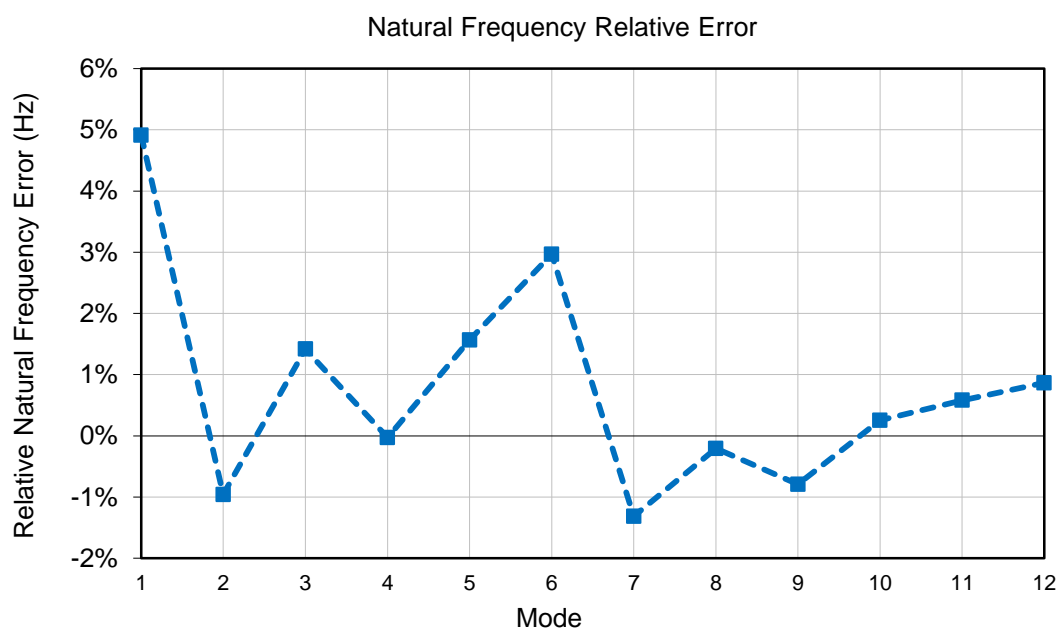
Figure 6-11: Mean relative error in natural frequencies between the uncorrelated baseline finite element model and measured healthy data set (analytical set lower than the baseline reference set).
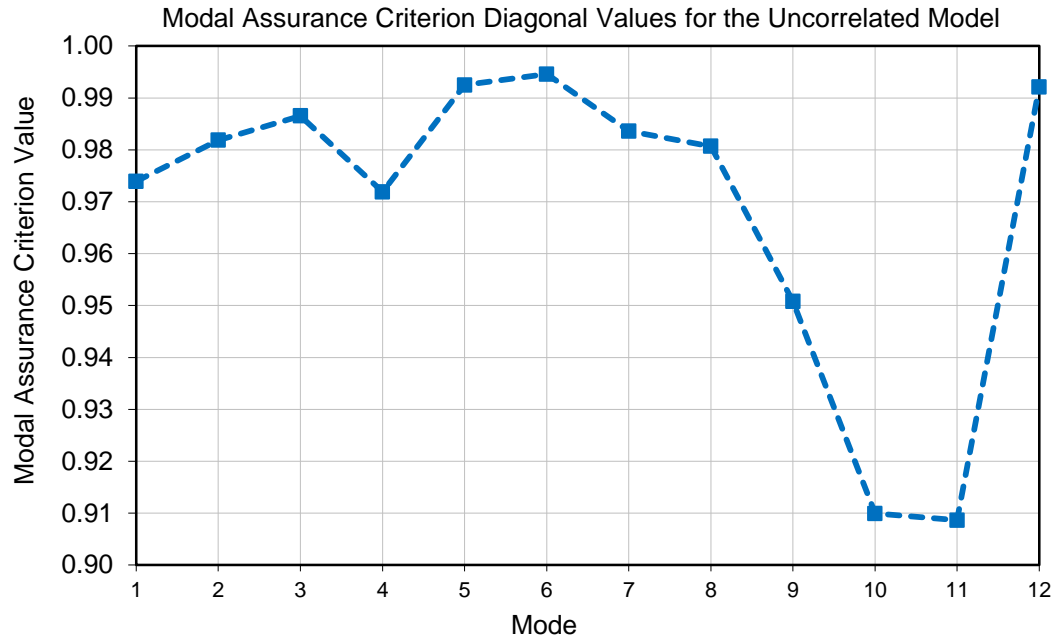
Figure 6-12: Modal assurance criterion diagonal values calculated between the uncorrelated finite element model and measured baseline data.

modes except for 9, 10 and 11, which have modal assurance criterion values of 0.95, 0.91 and 0.91, respectively. This indicates excellent mode shape correlation overall with small but non-negligible error in modes 10 and 11. The visual mode shape representations in Figure 6-7 and Figure 6-9 each indicate a slight loss of symmetry in the experimental and analytical mode shapes, respectively, of modes 10 and 11 which suggests that these modes are not as clearly resolved in the structure as the others.

To investigate mesh discretization error the baseline finite element model was recreated with the same parameters on a 10×10 element mesh, 40×40 element mesh, 80×80 element mesh, and 160×160 element mesh. Natural frequencies from the five total models (including the baseline 20×20 element mesh) are compared in Figure 6-14, and

the natural frequency error between the 160×160 mesh and each coarser mesh is shown in

Figure 6-15. It can be seen from these figures that there is a substantial mesh

discretization error in the 10×10 element mesh with natural frequency differences ranging

from 1.5% at mode 1 to 8.4% at mode 12. The 20×20 element model also has a

noticeable but smaller mesh discretization error, with natural frequency differences

ranging from 0.22% at mode 1 to 2.3% at mode 12. The 40×40 mesh error is smaller

again, ranging from 0.07% to 0.46%, and the 80×80 element model error is negligible at

0.01% to 0.07%. Overall the natural frequency convergence is within expectations,

showing smoothly decreasing natural frequency error with mesh refinement. Mode shape

modal assurance criterion values calculated over the 36 measurement points relative to

the 160×160 element model are given in Figure 6-16. These results show improvement

with each successive refinement; however, the convergence is not smooth, as expected,

with asymptotic reduction in error in the first three refinements up to 40×40 elements and

then a sudden jump to near perfect mode shape correlation in the 80×80 element model.

The jump may indicate some subtlety of modal solution in NASTRAN, or round-off

error,or there may be an undiscovered modeling error. In any case, the 20×20 element

model mode shapes are highly correlated to those of the 40×40 element model with a

maximum modal assurance criterion difference of 0.0001 up to mode 8 and a maximum

overall difference of 0.006 at mode 10. The 10×10 element model shows noticeable more

shape error with a maximum modal assurance criterion difference of 0.28 at mode 10. A

final mesh convergence comparison is made in Figure 6-17 which shows natural
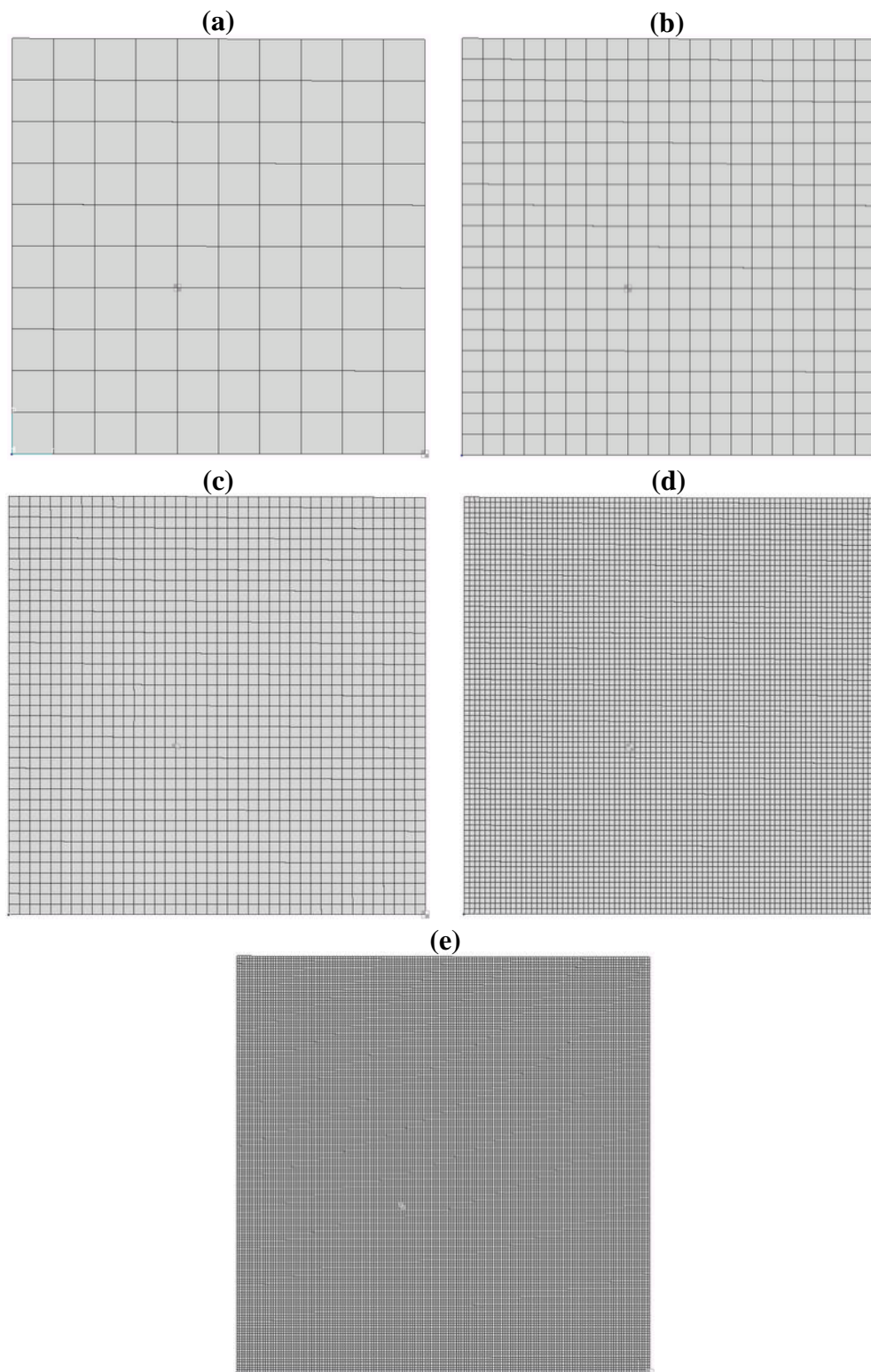
Figure 6-13: Images of the baseline finite element model with varying mesh densities: (a) 10×10; (b) 20×20; (c) 40×40; (d) 80×80; (e) 160×160.
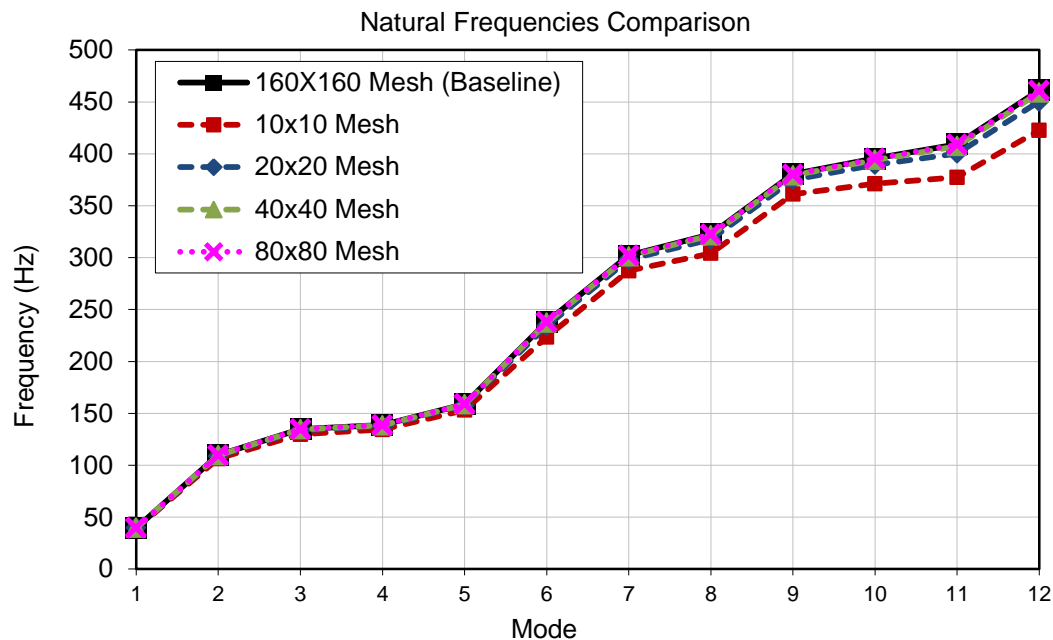
Figure 6-14: Comparison of natural frequencies from the baseline model with varying mesh density.
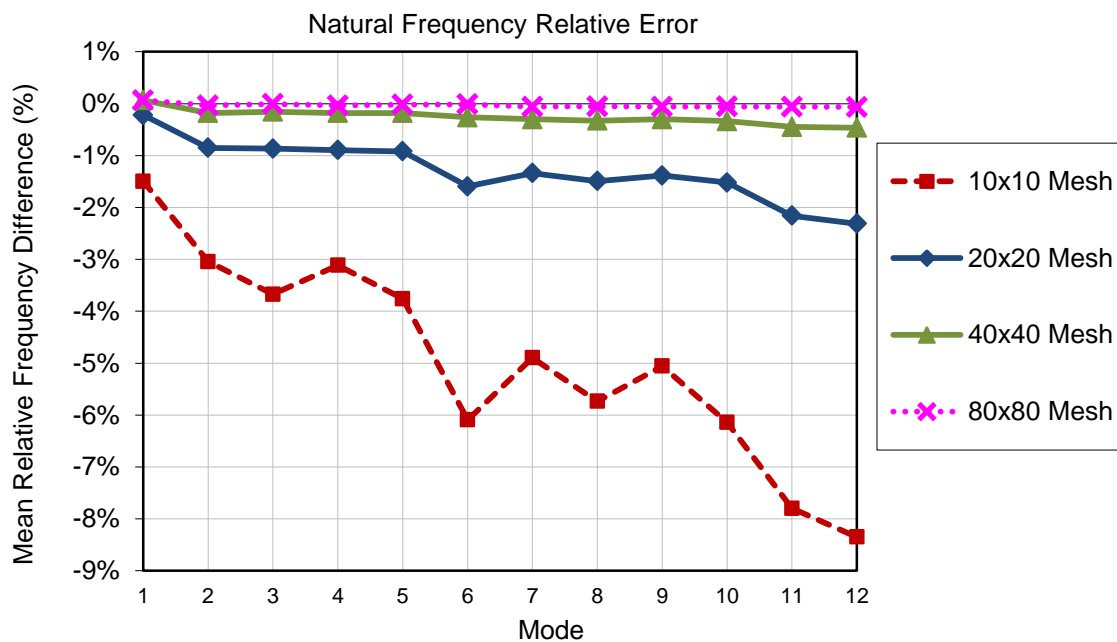
Figure 6-15: Natural frequency difference between the baseline model with varying mesh densities and the 160x160 mesh (highest mesh density).
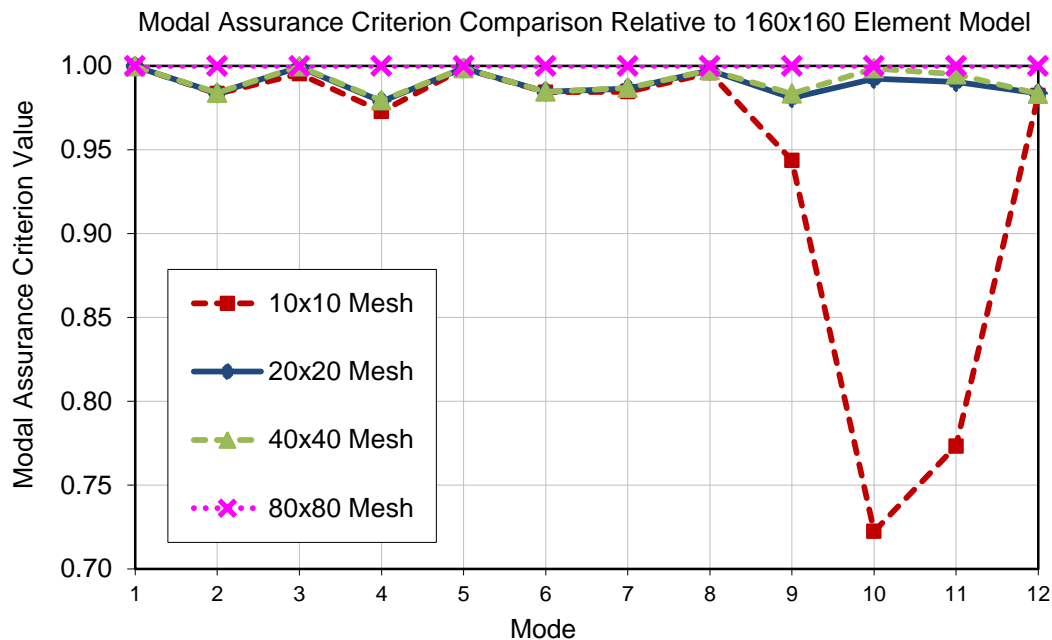
Figure 6-16: Comparison of modal assurance criterion values between the baseline model with varying mesh densities and the 160x160 mesh (highest mesh density).
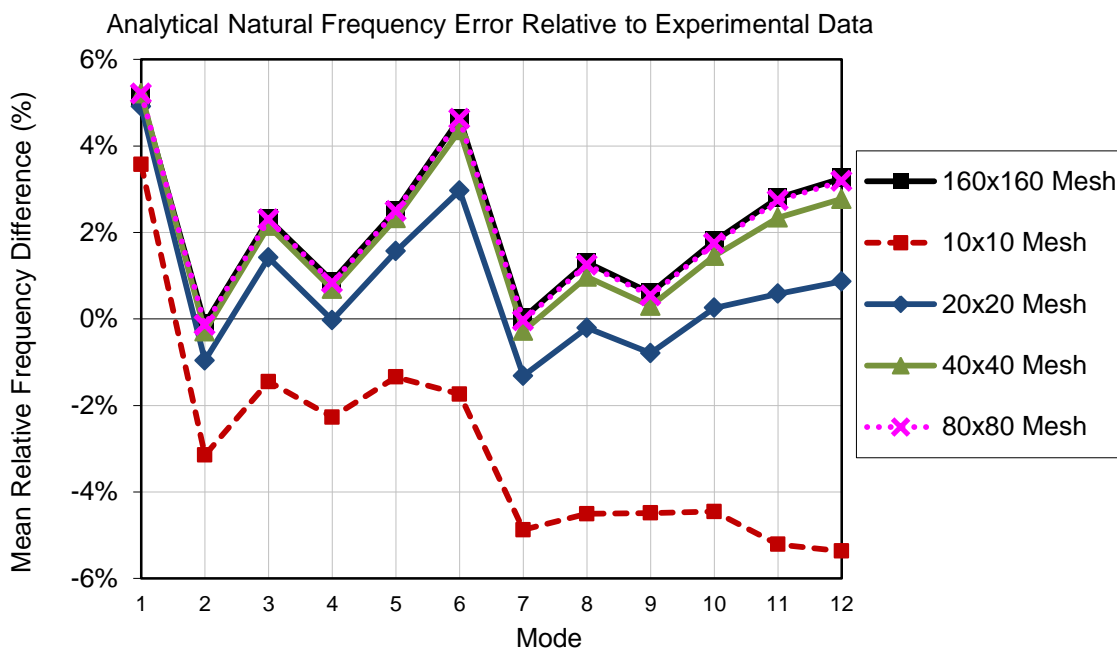
Figure 6-17: Natural frequency difference between the baseline model with varying mesh densities and the baseline experimental data.

frequency error between each model and the baseline experimental data. It can be seen that all of the models have intrinsic error to the experimental data of up to approximately 5%. The mesh discretization error in the baseline 20×20 element model was used since it most closely correlates to the experimental data.

In conclusion, the 20×20 element model has non-negligible mesh discretization error in addition to the baseline material property error compared to the experimental data, but to a level that appears manageable. Given the expectation to perform model correlation to the baseline data before damage identification and the desire to validate the current algorithm within the limitations of real-world models, which will almost always be limited in size and therefore have mesh discritization error, the 20×20 element model is an adequate baseline for the current study.

6.4.2   Baseline Model Correlation

Correlation of the initial plate model was accomplished in two main stages: first using the pseudo Newton-Raphson algorithm to minimize natural frequency error by updating primary global stiffness parameters, and secondly using the damage detection algorithm configured for correlation to update a larger selection of global material properties along with the laminate ply angles. The first correlation step was considered optional but was included, since modal parameters were available, to validate the algorithm and deterministically address the known mesh discretization error.

6.4.2.1 Correlation Approach and Details of Implementation

An initial correlation run was performed using the deterministic pseudo Newton-Raphson natural frequency algorithm described in Section 6.1.1 to remove the bulk of the initial modeling error. Because of the trend of decreased mode shape fidelity in higher modes, correlation was applied to only the first 8 modes. Correlation parameters were chosen to be the primary laminate stiffness properties E_{11}, E_{22}, and G_{12}. Finite difference sensitivity calculations were performed using a perturbation of 1% and an iteration parameter step limit of 0.4 was enforced (i.e., all parameter changes scaled when necessary to a largest parameter change of 40% of the original value).

Three additional correlation runs were subsequently performed using the current statistical damage identification algorithm with variables arranged to support global model correlation. The goal of these correlation runs was to fine-tune the model with respect to the frequency response functions which would form the basis of the subsequent statistical damage identification runs. Although the four correlation runs could have used different combinations of parameters and algorithm variables at each step, it was found that adequate correlation was achieved by using the same setup for all runs. Algorithm variables were assigned as follows:

- Same parameters as in the initial correlation were used plus the addition of ρ, ν_{12}, and the layup angles of the outermost 8 laminate plies for 13 update parameters total: E_{11}, E_{22}, G_{12}, ρ, ν_{12}, θ_1, θ_2, θ_3, θ_4, θ_9, θ_{10}, θ_{11}, and θ_{12}.

- The first statistical correlation run was seeded with assumed initial parameter standard deviation values equal to 1% of the initially correlated stiffness parameter values (primary laminate stiffnesses E_{11}, E_{22}, and G_{12}) and 0.1% of all other parameter values (ρ, v_{12}, θ_1, θ_2, θ_3, θ_4, θ_9, θ_{10}, θ_{11}, and θ_{12}). Each of the subsequent runs was then started from the final parameter and standard deviation values from the previous run. This setup served to reset the effective regularization provided by the statistical formulation allowing the update to fine-tune further at each step until additional runs would not appreciably improve the correlation.

- Measured modal damping from the healthy reference data set was applied to the analytical frequency response functions using the reduced coordinate extended Rayleigh modal damping process described in Section 5.4.

- $N_\omega = 48$ update frequency lines were automatically selected using the process described in Section 4.1 to be evenly distributed from the subset of experimental lines satisfying the following criteria:

  o Falling within ±8 Hz of modes 1 through 8 (selected to capture the majority of individual modal peaks while excluding neighboring modes);

  o Mean frequency response function magnitude value of between -5 and -10 dB in the velocity domain (where the limit values were chosen to capture frequencies in the band just exclusive of the peak values at each mode

while still being clustered around the selected natural frequencies and the

velocity domain was selected to make the average frequency response

function peaks approximately level);

- o Minimum average coherence value of 0.96 across all measurement

  degrees of freedom.

- The finite difference sensitivity calculation perturbation value was set to 2%

  of the current parameter value at each iteration.

- An iteration step limit was enforced at each iteration so that, when limited, all

  parameter values would be scaled down until the maximum change was 5% of

  its initial value.

- Convergence criteria was set such that the iteration process would break on

  the second consecutive incidence of mean parameter change of less than 0.1%

  of the original values.

The final frequency lines used are shown relative to the baseline measured driving

point magnitude frequency response function in Figure 6-18.

Ply angle correlation factors (i.e., the damage factors applied to correlation)

cannot be assigned according to the simple multiplicative relationship used for other

material properties since ply angles range around 0° and 90° instead of between 0 and

their maximum value. Physical ply angle values were therefore recovered from the
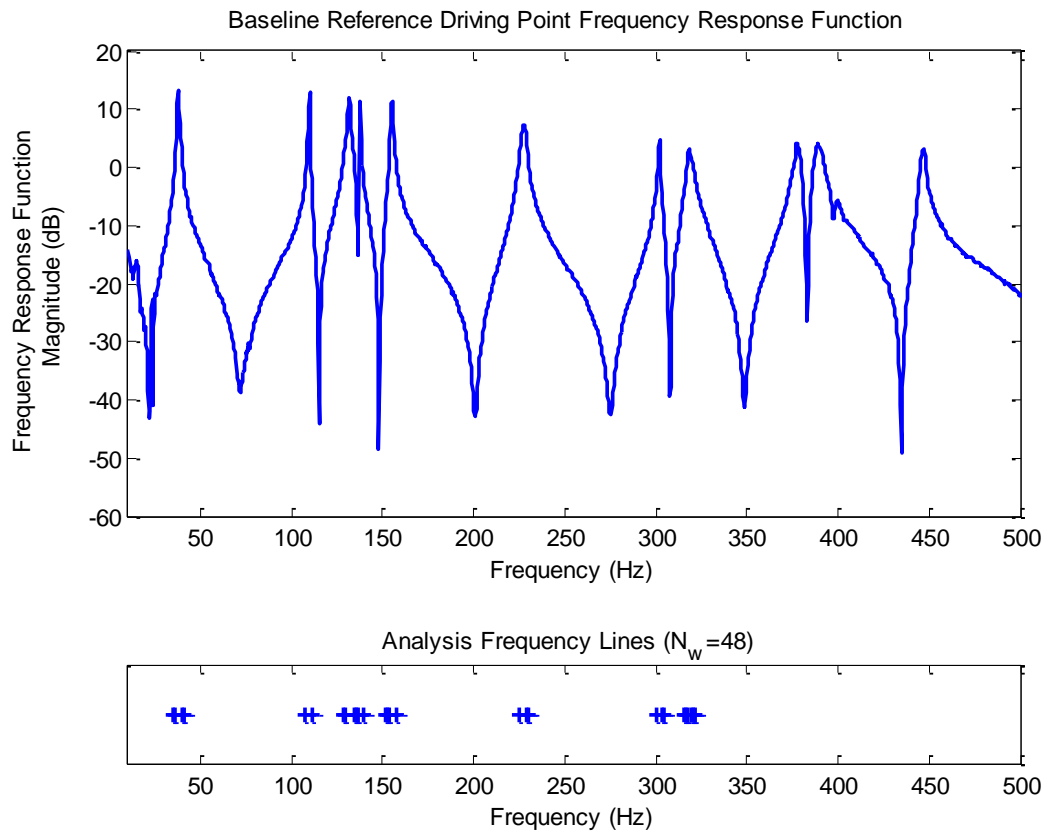
Figure 6-18: Correlation frequency lines shown relative to driving point measured baseline frequency response function magnitude.

correlation factors according to the relationship

$$\theta_1 = \theta_0 + (CorrelationFactor - 1) \times 90°, \qquad (6.14)$$

where θ_0 is the baseline ply angle value (0° or 90° for the current plate) and θ_1 is the updated ply angle value. In other words, correlation factors were assumed to reference 90°, with the resulting change then added or subtracted from the correct baseline ply

angle. A correlation factor value of 0.9 would therefore cause a baseline ply angle of 0°
to update to -9° and a baseline ply angle of 90° to update to 81°.

6.4.2.2   Correlation Results and Discussion

The initial pseudo Newton-Raphson natural frequency correlation run converged
after 3 iterations, producing an improvement in natural frequency correlation from 1.67%
initial error to 0.42% final error over the optimization mode set (modes 1 through 8). The
four subsequent correlation runs using the statistical damage detection algorithm in series
converged in 5, 3, and 3 iterations respectively, with the first run achieving the majority
of convergence and the next two serving to minimally fine-tune the correlation.

Plots comparing driving point frequency response functions from the correlated
analytical model and healthy reference set are shown in Figure 6-20, Figure 6-21, and
Figure 6-22, with each plot giving either frequency response magnitude in units of dB or
the real and imaginary representations at varying levels of zoom in the velocity domain.
In all plots, the measured modal damping from the healthy reference data has been added
to the undamped analytical frequency response functions in both uncorrelated and fully
correlated forms, and the baseline experimental frequency response function is shown for
reference. It can be seen that the initial uncorrelated model had a small amount of error
compared to the reference data but that this error was reduced through the correlation
process, especially in terms of the peak amplitude of the higher modes. The correlated
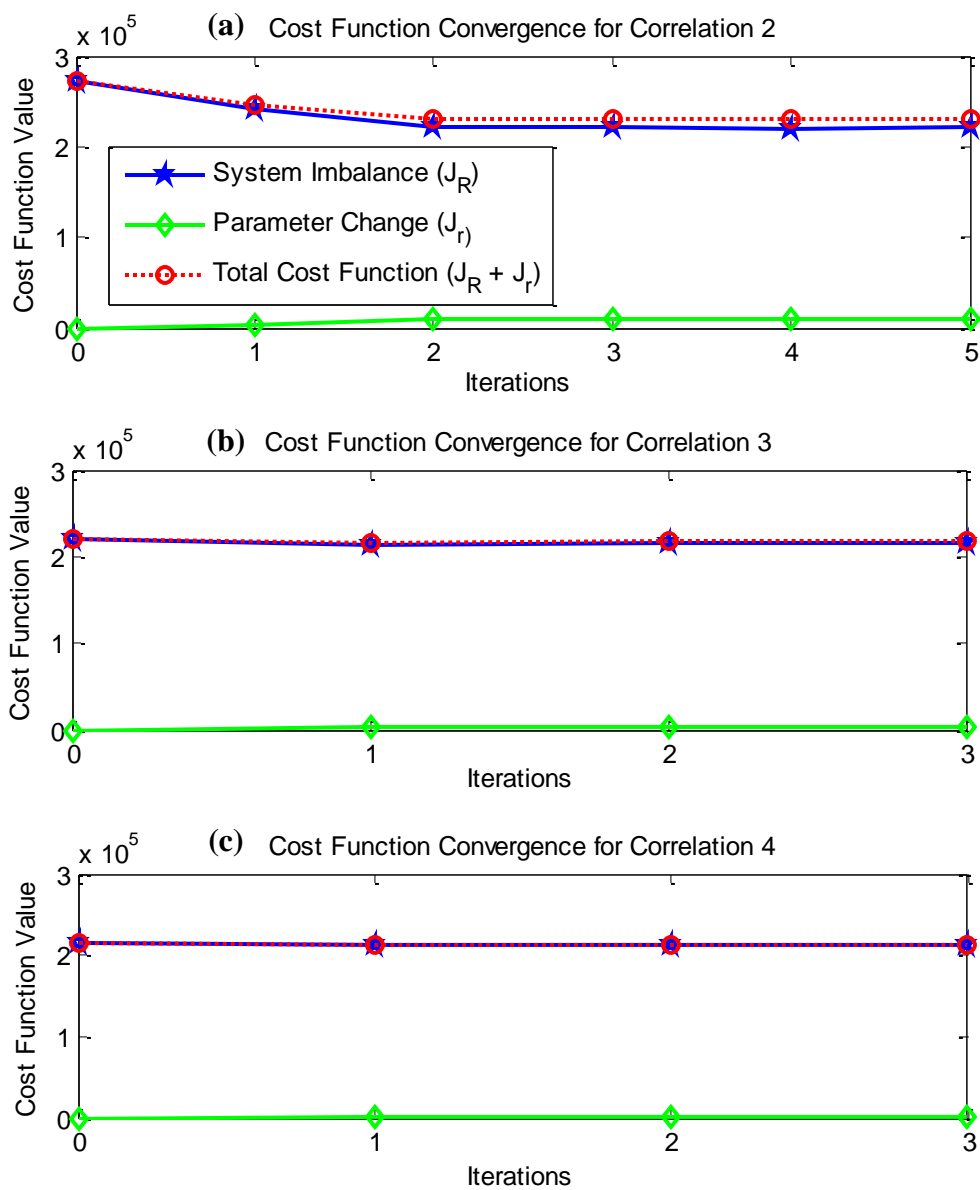
Figure 6-19: Correlation cost function convergence for statistical damage identification algorithm correlation runs: (a) correlation run 2; (b) correlation run 3; (c) correlation run 4.
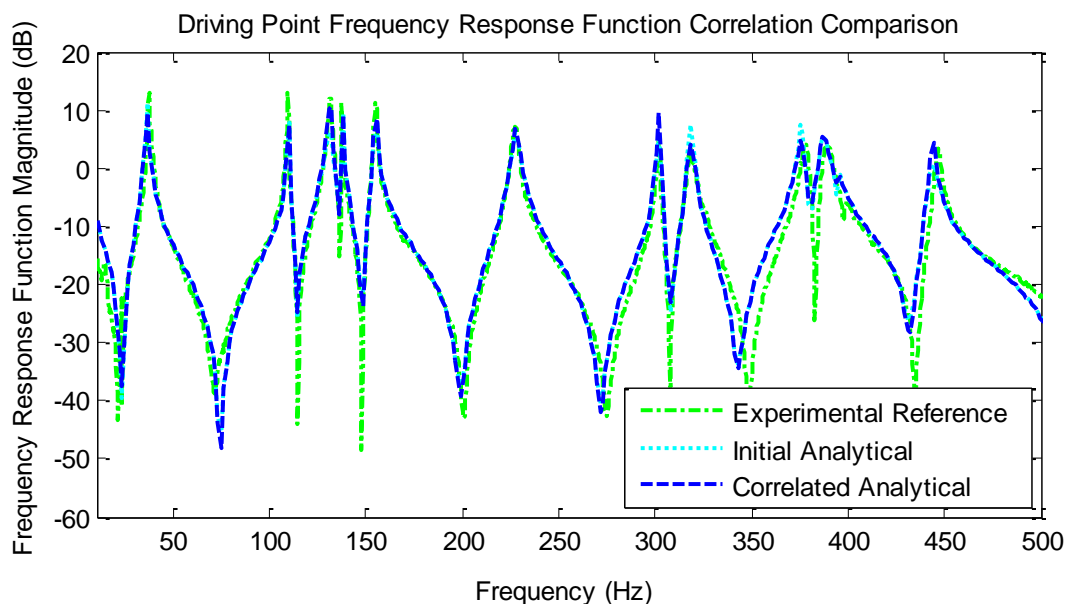
Figure 6-20: Comparison of driving point frequency response function magnitude before and after correlation to healthy experimental reference data.

frequency response function achieves a high degree of fidelity to the experimental

reference data over the first 8 modes—extending from 10 Hz to approximately 340 Hz—

where the frequency response function based correlation was performed.

Modal parameter metrics were compiled in order to further assess the degree of

correlation after each step. The results are presented in plot format with Figure 6-23

showing a comparison of natural frequencies between the healthy experimental reference

set and the correlation run results, Figure 6-24 showing the relative change in natural

frequencies, and Figure 6-25 showing a comparison of the modal assurance criterion

values between the healthy experimental reference set and the result of each correlation

(a)

Driving Point Frequency Response Function Correlation Comparison

(b)

Driving Point Frequency Response Function Correlation Comparison
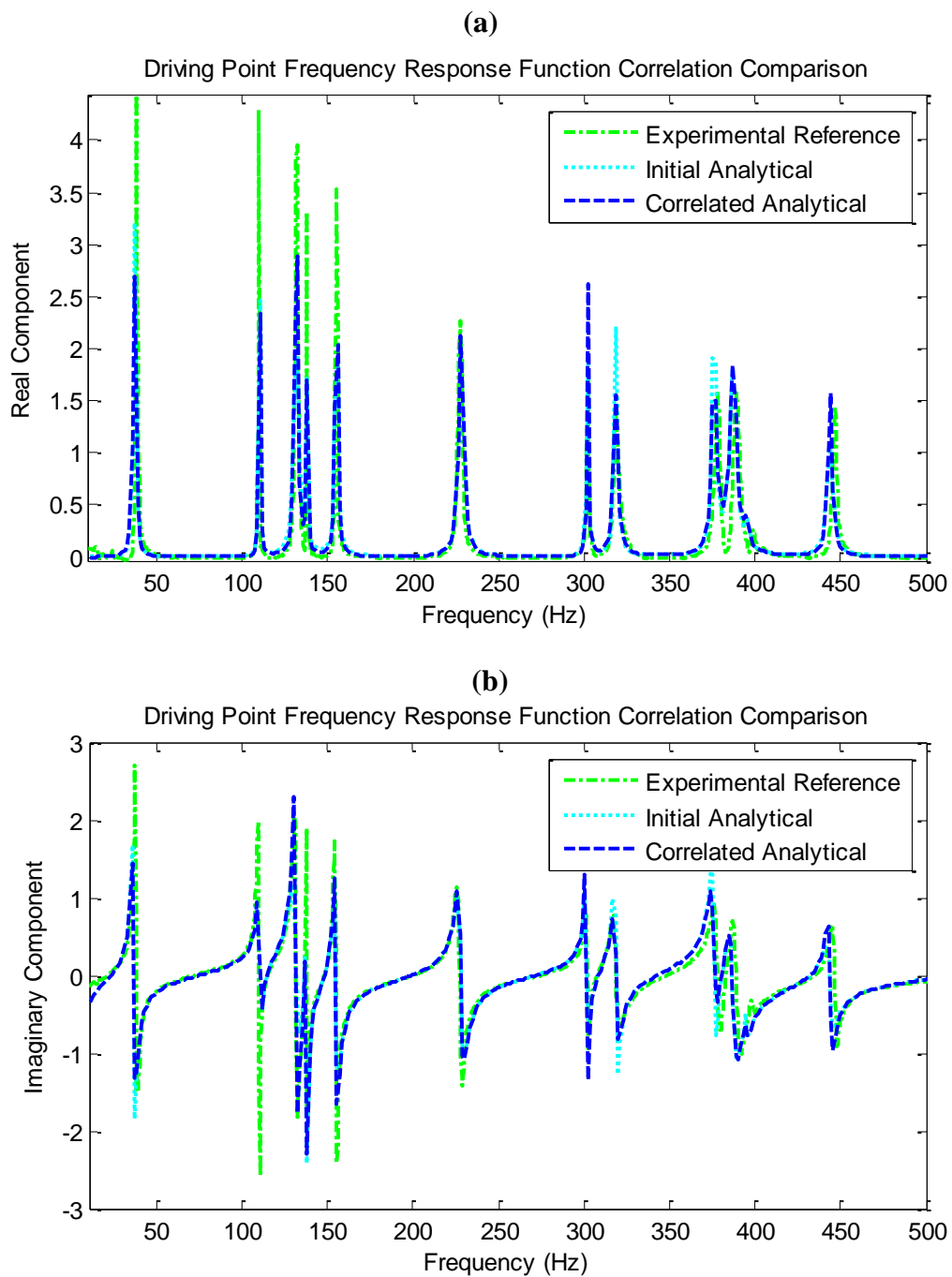
Figure 6-21: Comparison of driving point frequency response functions before and after correlation to healthy experimental reference data: (a) real component, (b) imaginary component.

(a)

Driving Point Frequency Response Function Correlation Comparison (Zoomed)

(b)

Driving Point Frequency Response Function Correlation Comparison (Zoomed)
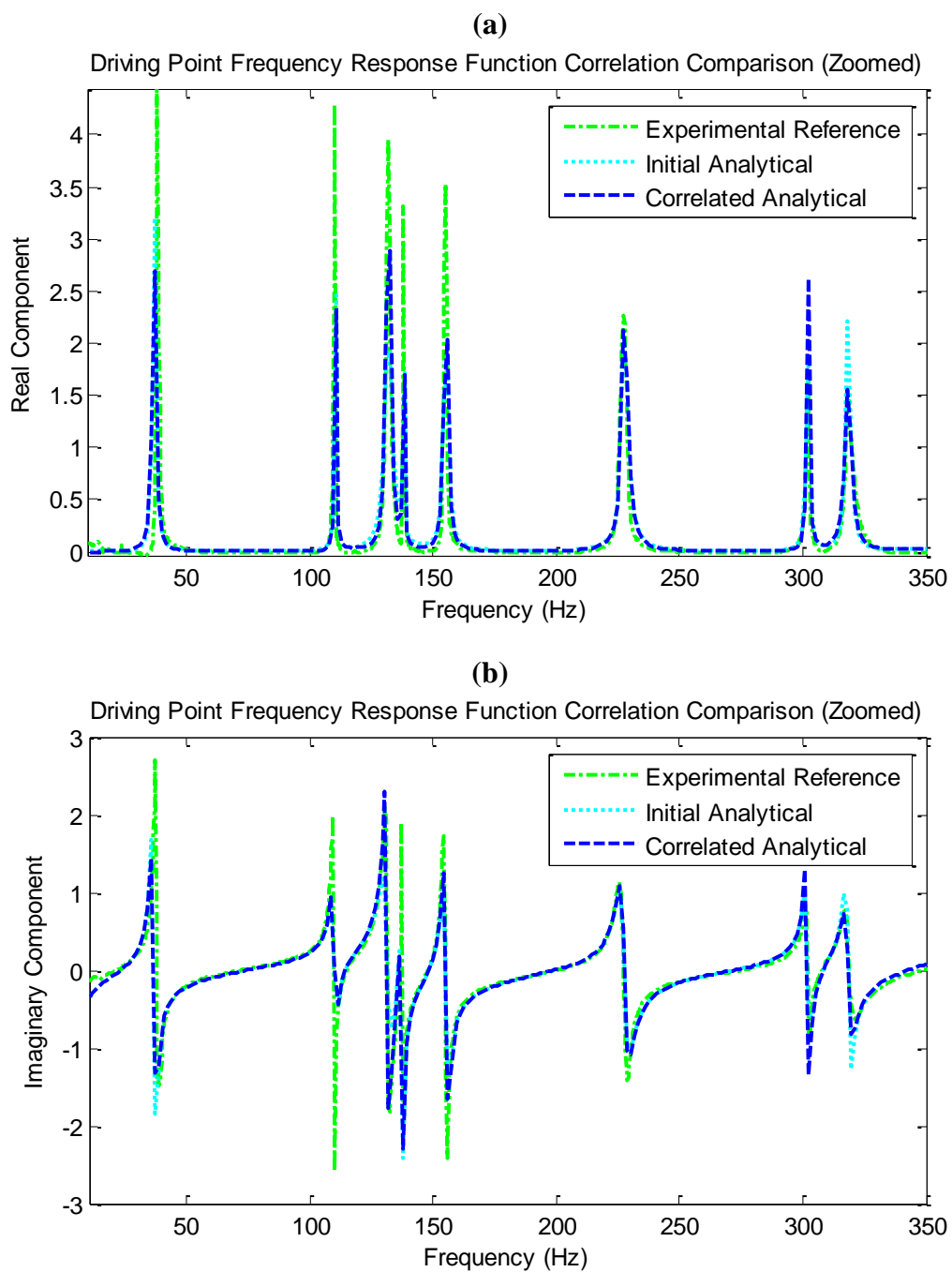
Figure 6-22: Comparison of driving point frequency response functions before and after correlation to healthy experimental reference data, zoomed to the frequency range containing modes 1 through 8: (a) real component, (b) imaginary component.
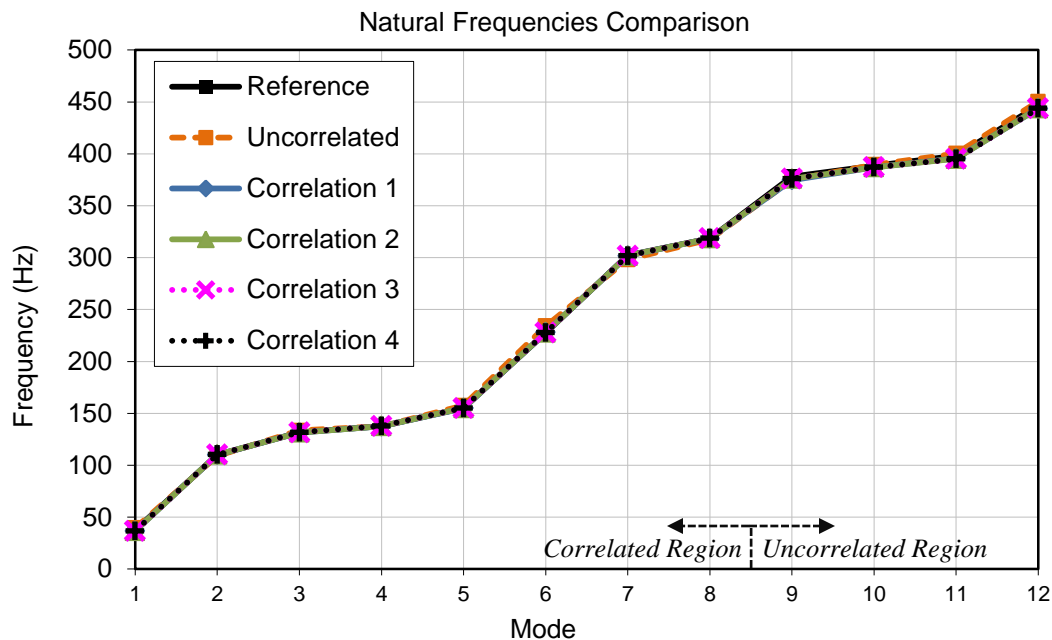
Figure 6-23: Comparison of natural frequencies between the healthy experimental reference set and the correlation run results.
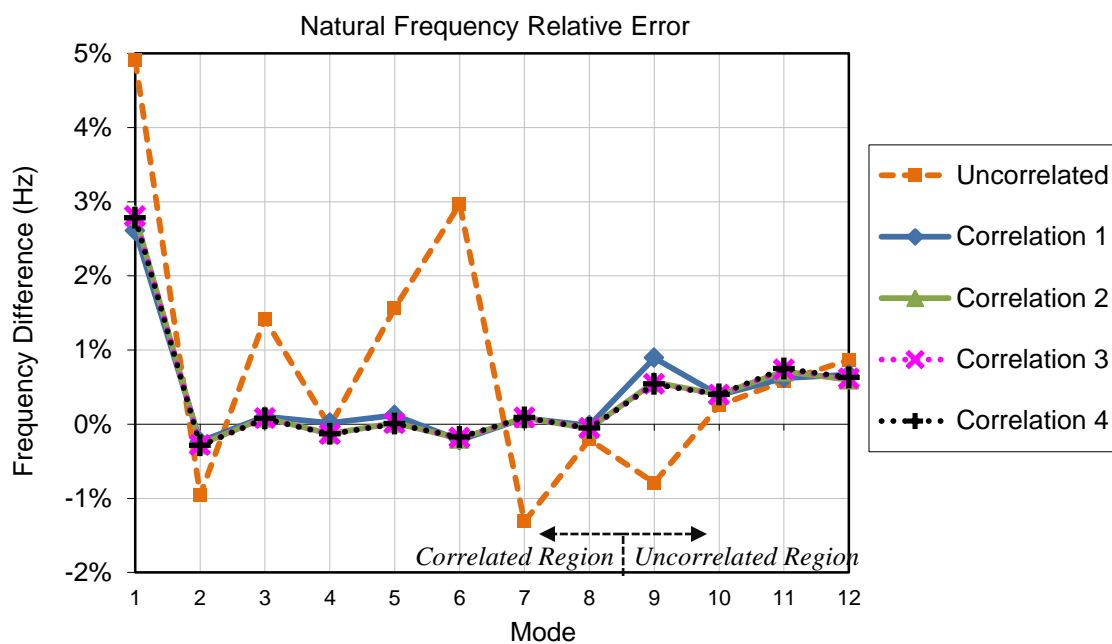
Figure 6-24: Relative change in natural frequencies between the healthy experimental reference set and the correlation run results.
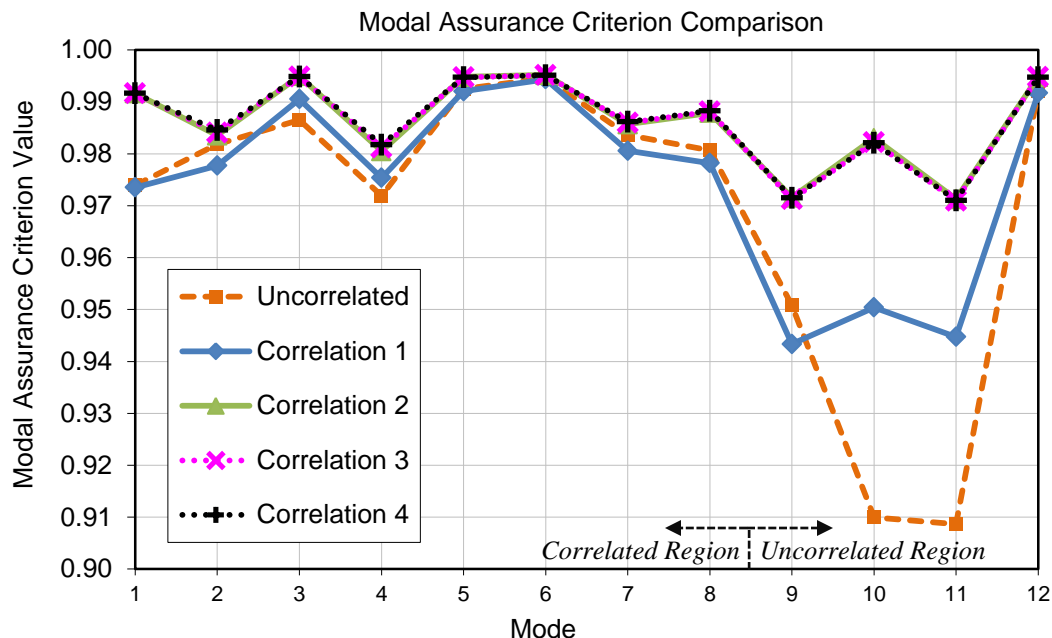
Figure 6-25: Comparison of modal assurance criterion values between the healthy experimental reference set and the correlation run results.

run. It can be seen from these plots that the initial natural frequency based correlation run produced a substantial reduction in natural natural frequency error and the subsequent frequency domain correlation runs further refined the correlation to close to zero natural frequency error for the first 8 modes, with the exception of mode 1 which maintained an error of close to 3%. The correlation process also increased mode shape correlation for all modes, with the initial natural frequency based correlation run producing similar mode shape correlation to the reference data and the frequency-domain correlation runs then refining the mode shape correlation to above 0.98 for correlation frequency range.

Inspection of the updated material properties and ply angles for each correlation run, which are given in Table 6-3 along with the original baseline values and percentage

Table 6-3: Material properties for baseline test-piece finite element model (percent change relative to the baseline values is given in italics below each value).

Property	Baseline	Correlation 1	Correlation 2	Correlation 3	Correlation 4
E_{11} (GPa)	129	127	138	140	140
% change		*-1.73%*	*+7.06%*	*+8.41%*	*+8.78%*
E_{22} (GPa)	7.72	11.1	11.5	11.6	11.6
% change		*43.3%*	*48.7%*	*49.9%*	*50.3%*
G_{12} (GPa)	6.41	5.49	5.90	5.97	5.99
% change		*-14.3%*	*-7.87%*	*-6.82%*	*-6.51%*
v_{12}	0.323	0.323	0.307	0.295	0.284
% change		*0.0%*	*-4.87%*	*-8.85%*	*-12.3%*
G_{13} (GPa)	2.63	2.63	2.63	2.63	2.63
% change		*+0.0%*	*+0.0%*	*+0.0%*	*+0.0%*
G_{23} (GPa)	2.63	2.63	2.63	2.63	2.63
% change		*+0.0%*	*+0.0%*	*+0.0%*	*+0.0%*
ρ (g/cm^3)	1.561	1.561	1.689	1.709	1.713
% change		*+0.0%*	*+8.23%*	*+9.48%*	*+9.80%*
θ_1 (°)	0.0	0.0	-0.95	-1.03	-1.03
% change		*0.0%*	*-1.06%*	*-1.15%*	*-1.15%*
θ_2	90.0	90.0	88.9	88.8	88.8
% change		*0.0%*	*-1.28%*	*-1.28%*	*-1.28%*
θ_3	0.0	0.0	-4.0	-2.82	-2.82
% change		*0.0%*	*-0.44%*	*-0.31%*	*-0.31%*
θ_4	90.0	90.0	89.4	89.4	89.4
% change		*0.0%*	*-0.69%*	*-0.69%*	*-0.69%*
θ_9	90.0	90.0	89.4	89.4	89.4
% change		*0.0%*	*-0.69%*	*-0.69%*	*-0.69%*
θ_{10}	0.0	0.0	-4.0	-2.82	-2.82
% change		*0.0%*	*-0.44%*	*-0.31%*	*-0.31%*
θ_{11}	90.0	90.0	88.9	88.8	88.8
% change		*0.0%*	*-1.28%*	*-1.28%*	*-1.28%*
θ_{12}	0.0	0.0	-0.95	-1.03	-1.03
% change		*0.0%*	*-1.06%*	*-1.15%*	*-1.15%*

change for each correlation run, shows acceptable changes from baseline values. In

detail, E_{11} increased by 8.8%, E_{22} increased by 50%, G_{12} decreased by 6.5%, Poisson's

ration decreased by 12.3%, density increased by 9.8%, and ply angles changed from

between -1.2% to -0.3%. The large change in E_{22}, as well as the smaller changes in other

stiffness properties, can be attributed to the approximately derived origin of the baseline

values. These properties were reached by first testing tensile coupons of the bulk 12-ply

cross-ply laminate and then manually modifying the ply-level stiffness properties using

the NASTRAN laminate builder until resulting laminate properties approximately

matched the test results. There was therefore relatively low confidence in the baseline

properties prior to starting correlation and the resulting correlated stiffness values are

within physical expectations. The correlated ply angle values are close to the nominal

perfect values and represent expected manufacturing error from a manual layup. The

correlated density represents a 23 gram variation from the measured mass of the

experimental plate, which is outside of the ±0.5 gram tolerance of the digital scale used to

originally measure the plate mass. The most likely explanation for the discrepency is that

the plate finite element model retained some error to the physical plate because of the

known mesh discretization error plus manufacturing imperfections and model theory

error and the correlation process corrected some of this error through pushing the density

slightly beyond the measured physical value. The density could have been held fixed as a

known quantity; however, the goal was to reduce correlation error for subsequent damage

identification and so the change in density was accepted as a reasonable compromise.

Parameter standard deviation updated from the initial values of 1% of the initially

correlated stiffness parameter values (primary laminate stiffnesses E_{11}, E_{22}, and G_{12}) and

0.1% of all other parameter values to similar values between 0.00095 and 0.00020 after the final correlation. Interestingly, the prior value assigned to each parameter did not have a noticeable bearing on its final value.

Overall, the current plate model was deemed to be a reasonable test case for larger systems with their own challenges with the justification that if the algorithm can be shown to work on an imperfect subscale model, chances for successful implementation on a realistically sized complex system are improved.

6.4.3   Damaged System Description

Damage was induced into a sub-region of the test-piece by repeated impacts with a metal wedge such as could occur from equipment or other vehicles impacting the external surface of an aircraft or from interference of an internal mechanism with the primary structure. The goal of the damage was to randomly degrade fiber and matrix stiffness to negligible levels in a target region approximately 0.04 m x 0.06 m in size and centered at the center of the vertical axis and 0.02 m to the left-of-center of the horizontal axis of the plate when the plate is viewed from the front. The damage was imparted by manually striking the plate with the sharp edge of a hammer until the desired damage state had been achieved. The plate with the damaged region indicated using dashed lines is shown in Figure 6-26 with close-up views of the damage region shown in Figure 6-27.
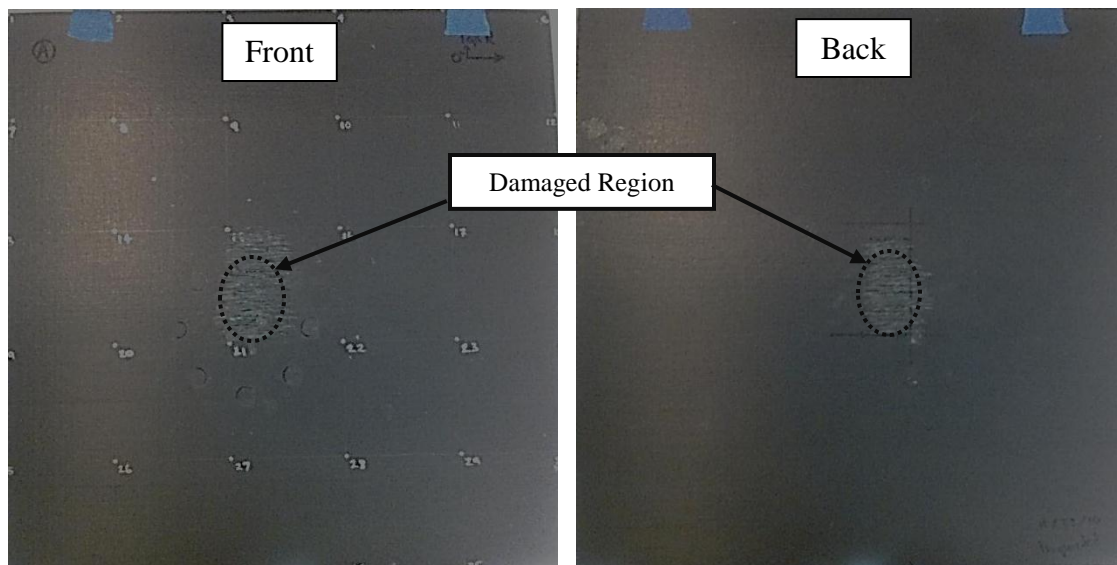
Figure 6-26: Experimental composite plate test-piece showing front and back sides and damaged region.
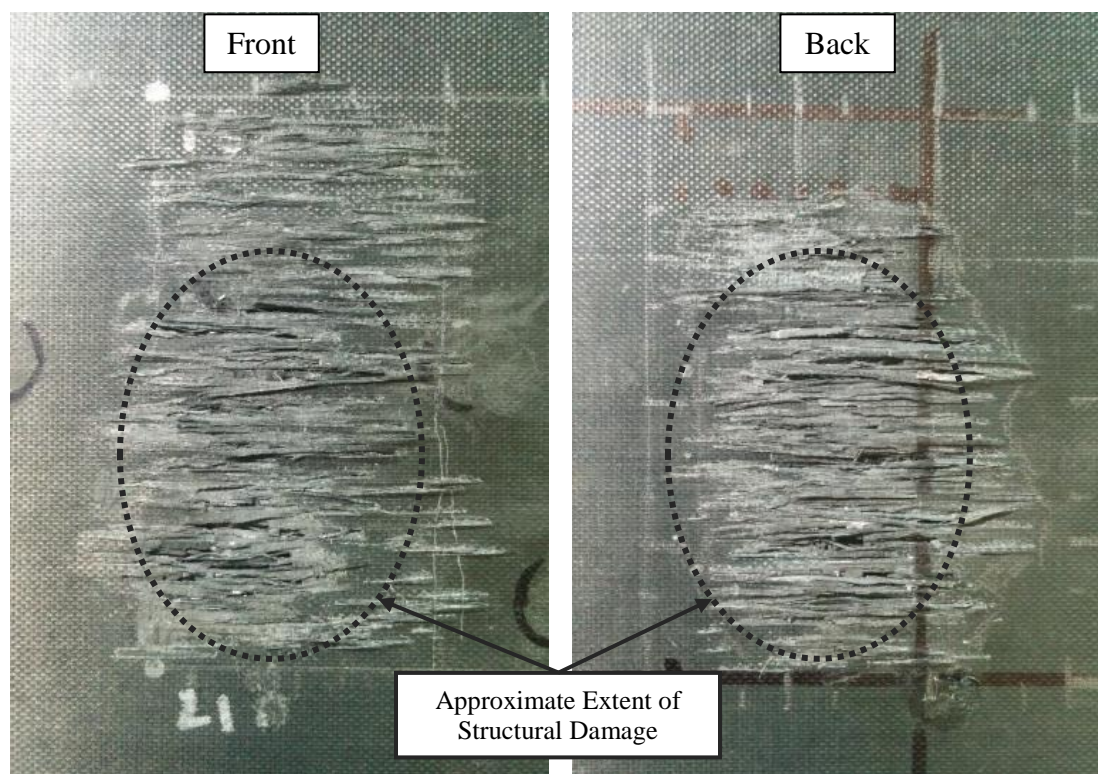
Figure 6-27: Close-up views of damage in experimental composite plate test-piece.

A comparison of healthy and damaged driving point vibration data is given in Figure 6-28, with frequency response functions compared in plot (a) and the corresponding coherence functions compared in plot (b). The frequency response functions are additionally presented in real/imaginary form in Figure 6-29. The modal data derived from these frequency response function sets through modal parameter estimation are presented in Table 6-4 and compared in terms of relative change in natural frequency in Figure 6-30, relative change in modal damping ratios in Figure 6-31, and modal assurance criterion diagonal values in Figure 6-32. It can be seen from these figures that the damage has changed the structural vibration response, but not dramatically. The frequency response functions show small shifts in the modal peaks but maintain a high degree of similarity overall. The natural frequencies decreased between 0% and 3.2% with the highest changes occurring in the low twisting and bending modes, small changes in the first three coupled twist-bend modes, and a moderate changes in the higher modes. Modal damping values show changes ranging from a 54% decrease on mode 11 to an 83% increase on mode 3 (note that modal damping ratios are sensitive to damping values and also changes in stiffness and mass). The mode shapes show similarly low changes from the damage with modal assurance criterion values of 0.93 on mode 10, 0.95 on modes 1 and 8, 0.96 on modes 9 and 11, and either 0.98 or 0.99 on the remaining modes. Overall, the damage does not appear to have affected the modes with any clear pattern and all modes show some aspect of change. The two vibration tests were

(a)

Experimental Driving Point Frequency Response Function Comparison (Zoomed)

(b)

Experimental Driving Point Coherence Function Comparison (Zoomed)
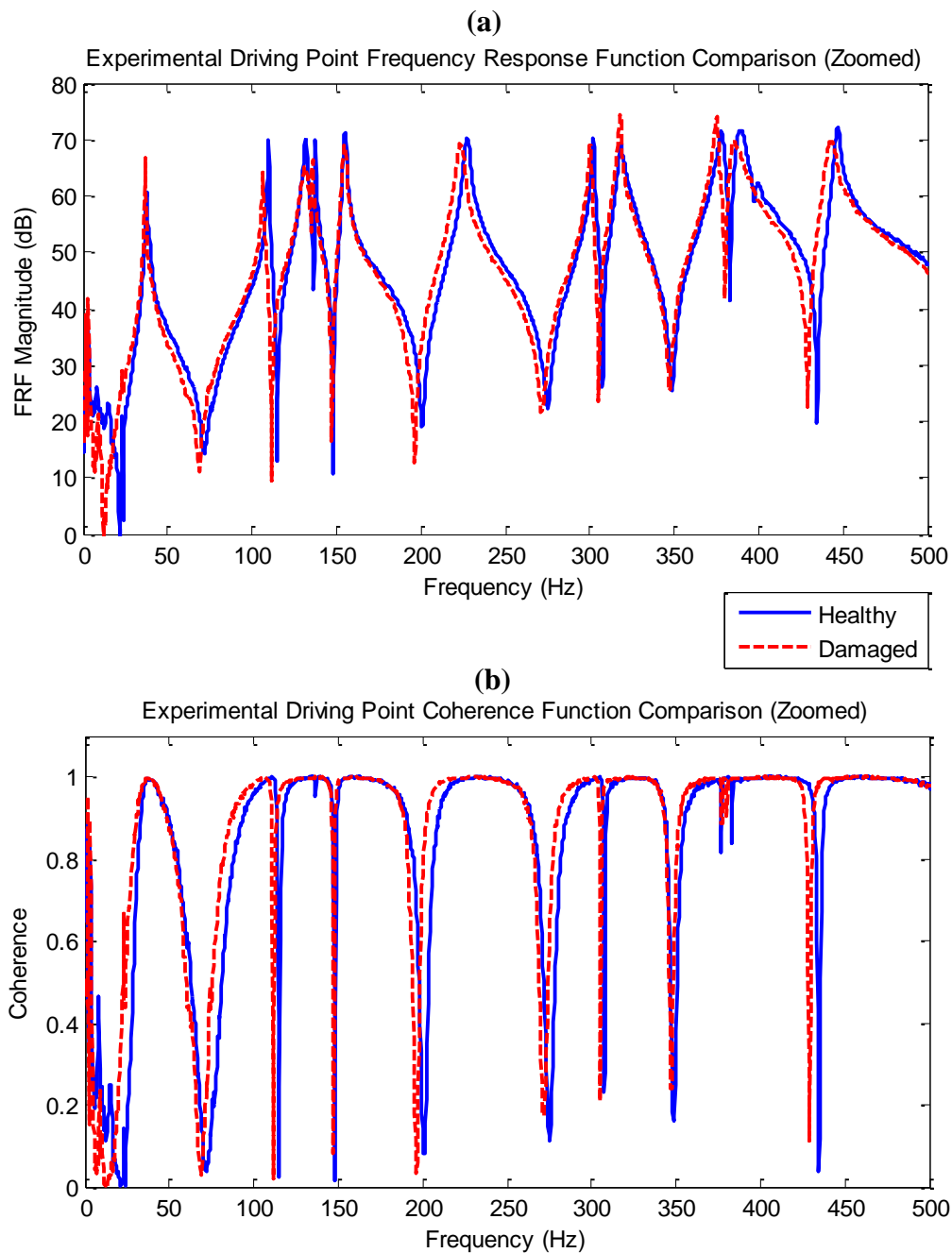
Figure 6-28: Comparison of driving point frequency response function data from the healthy and damaged plates zoomed to the frequency range containing modes 1 through 12: (a) frequency response function manitude in units of dB, (b) frequency response function phase.

(a)

Experimental Driving Point Frequency Response Function Comparison (Zoomed)

(b)

Experimental Driving Point Frequency Response Function Comparison (Zoomed)
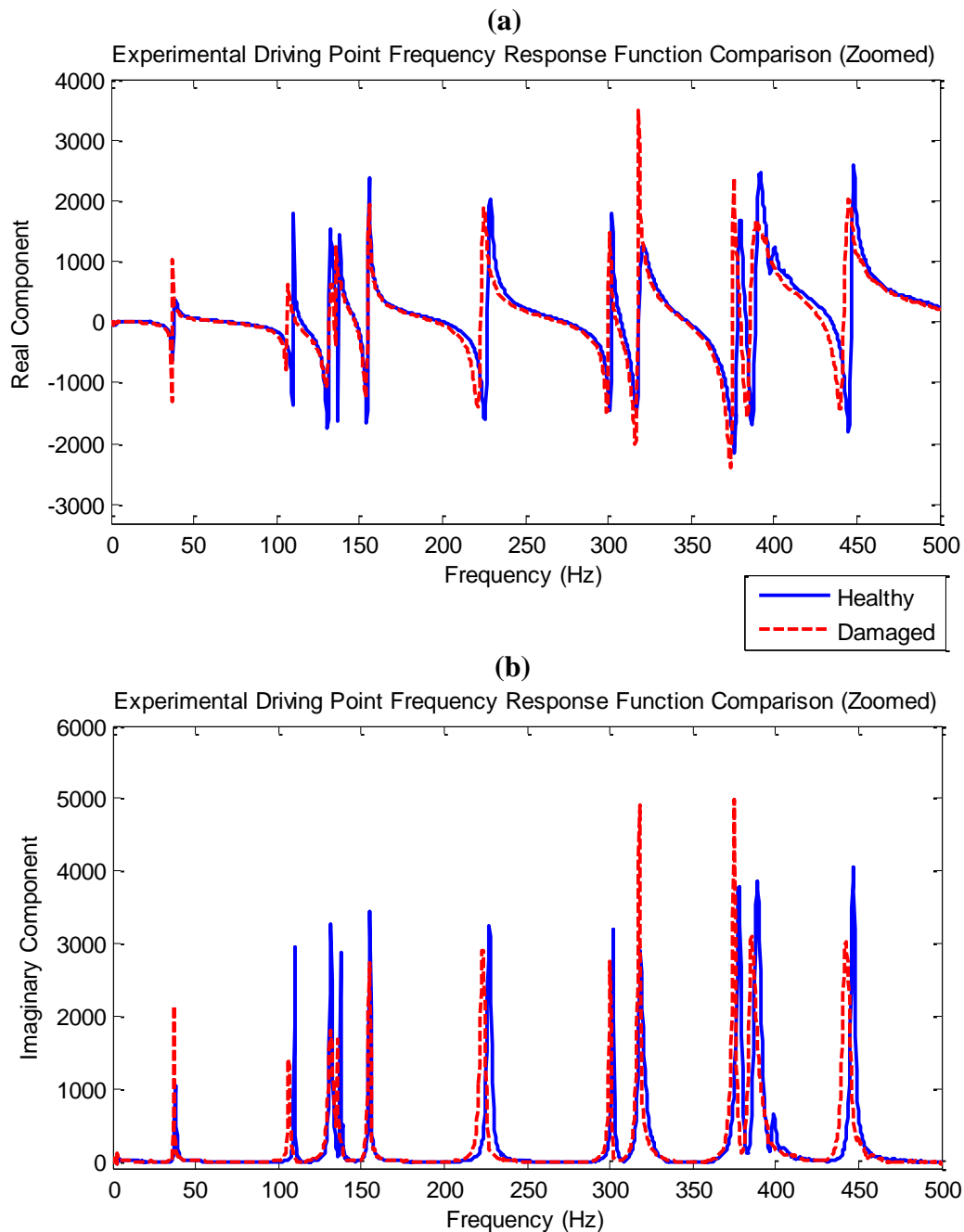
Figure 6-29: Comparison of driving point vibration data from the healthy and damaged plates zoomed to the frequency range containing modes 1 through 12: (a) real component, (b) imaginary component.

Table 6-4: Modal summary of the experimental test-piece after damage.

mode	Mode Type	Mode Shape	Damaged Test Data		Change From Baseline	
			Frequency (Hz)	Damping Ratio	Natural Frequency Change	Modal Assurance Criterion
1	Torsion	*1-1*	36.9	0.49%	-2.07%	0.95
2	Bending	*2-0*	106.4	0.35%	-3.19%	0.98
3	Torsion-Bending	*2-1*	131.8	1.27%	0.13%	0.98
4	Bending	*0-2*	135.6	0.15%	-1.42%	0.98
5	Torsion-Bending	*1-2*	154.7	0.58%	-0.22%	0.99
6	Torsion	*2-2*	223.2	0.76%	-1.86%	0.99
7	Bending	*3-0*	300.2	0.24%	-0.63%	0.99
8	Torsion-Bending	*3-1*	318.0	0.26%	-0.13%	0.95
9	Bending	*0-3*	375.0	0.29%	-0.82%	0.96
10	Torsion-Bending	*1-3*	385.0	0.63%	-0.93%	0.93
11	Torsion-Bending	*3-2*	395.3	0.12%	-0.68%	0.96
12	Torsion-Bending	*2-3*	442.1	0.50%	-1.01%	0.99
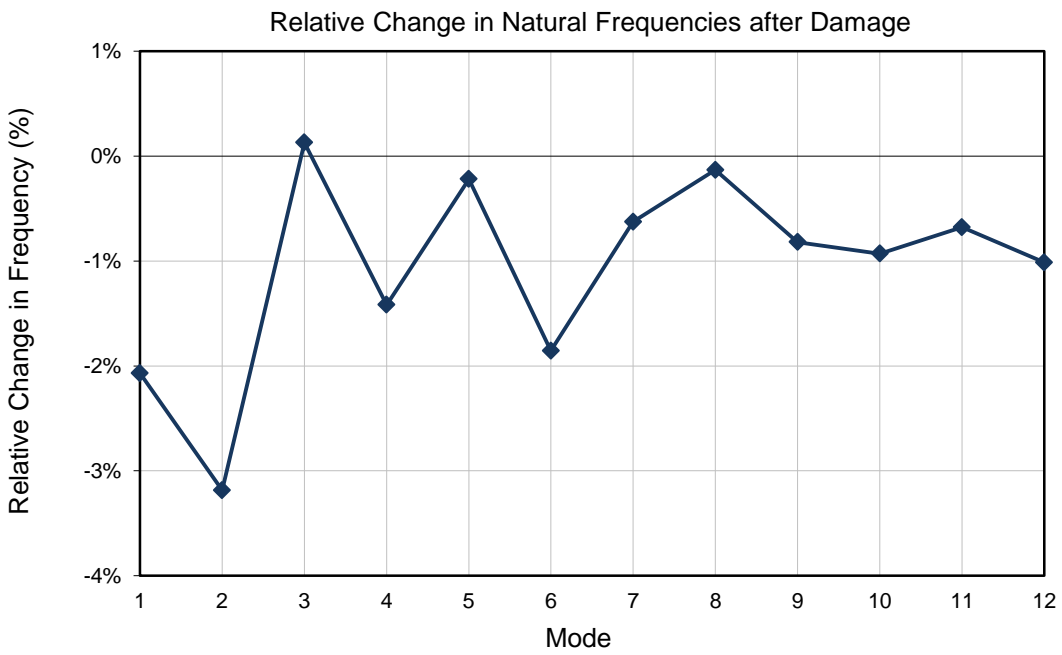
Figure 6-30: Relative change in natural frequencies between healthy and damaged plate data sets.
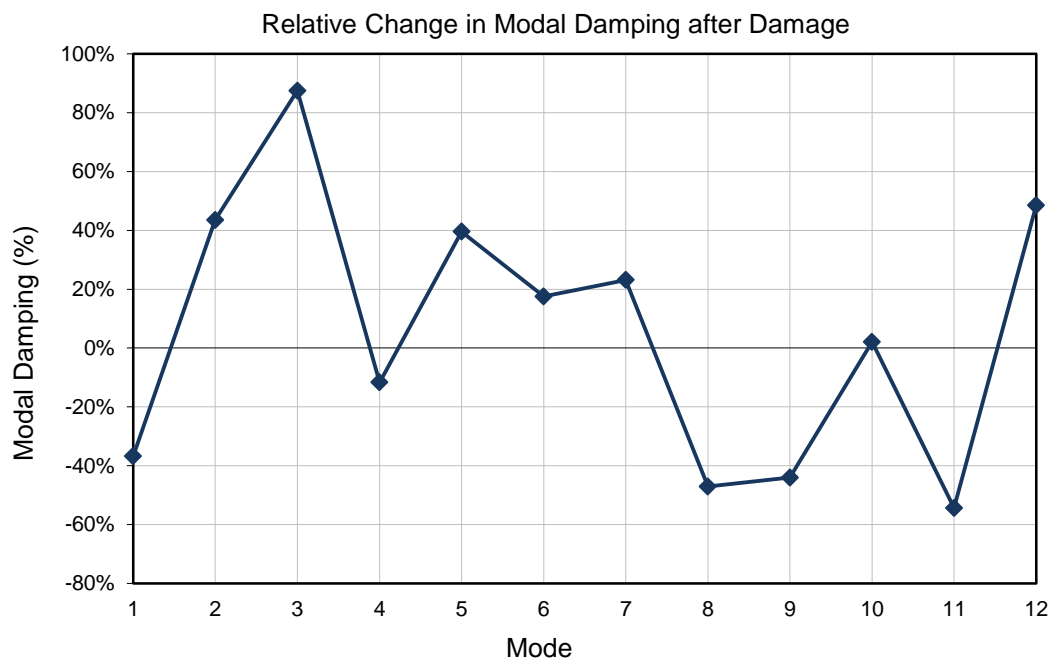
Figure 6-31: Comparison of modal damping ratios between healthy and damaged plate data sets.
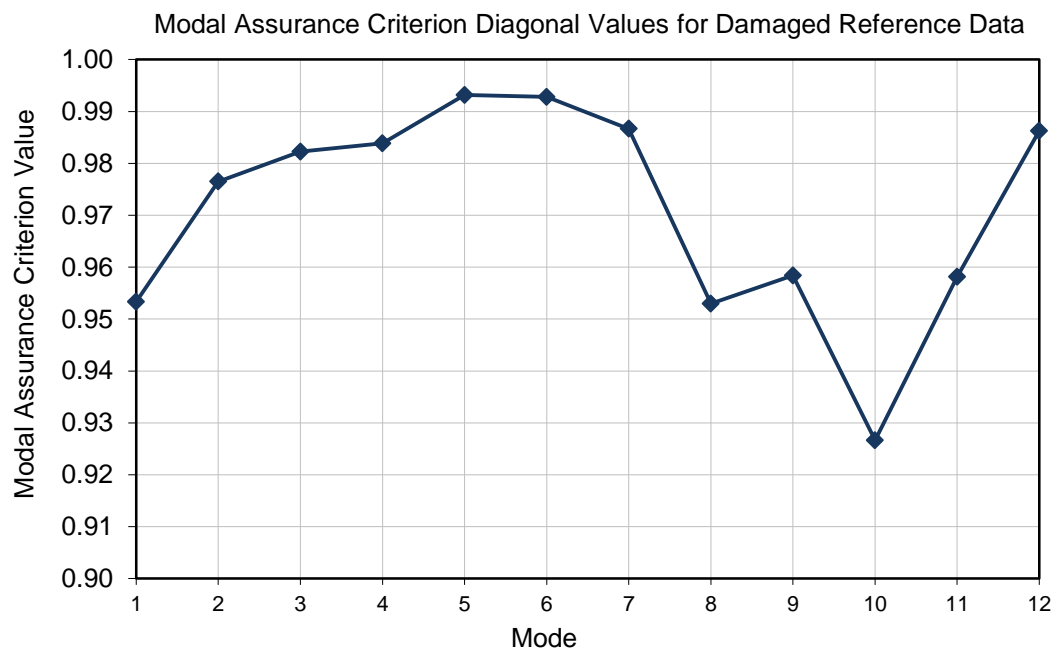
Figure 6-32: Modal assurance criterion diagonal values between the baseline and damaged measured reference data.

conducted within several hours of each other with negligible changes in experimental set-up or environment so it can be assumed that the observed changes are due to the damage.

6.4.4 Damage Identification

The correlated finite element model was used to perform damage identification using the experimentally measured damaged plate vibration data and the current damage identification algorithm. The approach and algorithm parameters used are given first, followed by results of the primary experimental damage identification validation. Three studies are then presented, including the effect of a secondary correlation targeting the damage identification frequency range, element level material properties damage factors, and an investigation into updated and final parameter variability.

6.4.4.1   Primary Damage Identification Validation

Damage identification was run multiple times from the correlated finite element model with varying numbers of candidate damage elements to investigate performance under different conditions. Because of the large number of elements in the model, the damage factors were applied to a 10×10 grid of 4-element groupings, each arranged in 2×2 squares, for a total of 100 potential damage element groups. For each damage group, a single damage factor was applied to all stiffness parameters (E_{11}, E_{22}, G_{12}, G_{13}, and G_{23}) in all four elements, meaning a total of 100 potential damage factors for the entire model (or proportionally fewer for cases of damage identification on a restricted region). To

recap from previous chapters, after damage identification the damage factor value represents the level of damage for the properties to which it is assigned on a scale of 0 for fully damaged, 1 for no change, and greater than 1 for increases in properties, the last being a potentially nonphysical side effect of the unconstrained optimization algorithm driving the update.

Additional algorithm variables common to all runs were assigned as follows:

- Initial parameter standard deviation values were set equal to 1% of the initial correlated parameter values.

- Measured modal damping from the damaged reference data set was applied to the analytical frequency response functions using the reduced coordinate extended Rayleigh modal damping process described in Section 5.4.

- $N_\omega = 24$ update frequency lines were automatically selected using the processes described in sections 4.1. The lines were selected to be evenly distributed from the subset of experimental lines satisfying the following criteria:

  o Falling within ±8 Hz of the most highly correlated two modes out of the first 8 modes of the damaged reference set, where the correlation was assessed between the correlated analytical modes and the healthy reference modes using the mode shape selection criteria discussed in Section 6.2 (note: mode 3 was excluded from consideration because close

proximity to the poorly correlated mode 4 caused mode 3 frequency lines to be corrupted);

- o Mean frequency response function magnitude value of between -3 and -13 dB in the velocity domain (where the limit values were chosen to capture frequencies in the band just exclusive of the peak values at each mode while still being clustered around the selected natural frequencies and the velocity domain was selected to make the average frequency response function peaks approximately level);

- o Minimum coherence value of 0.8 across all measurement degrees of freedom.

- The finite difference sensitivity calculation perturbation value was set to 2% of the current parameter value at each iteration.

- An iteration step limit was enforced so that the parameter change vector at each iteration would be scaled down to a maximum parameter change of 5% of its initial value.

- Convergence criteria was set such that the iteration process would break on the second consecutive incidence of mean parameter change of less than 0.1% of the original values.

The mode shape correlation frequency selection criteria selected modes 5 and 6 around which to cluster the initial sub-group of update frequency lines. Down selection of

frequency lines to be clustered around only two out of the eight modal peaks was

performed after trial-and-error runs showed improved performance by focusing on the

regions surrounding the most highly shape correlation. From Table 6-4 and Figure 6-32 it

can be seen that modes 5 and 6 also have the least mode shape change due to damage,

although it is not known if this was important. The final 24 frequency lines used for the

subsequent damage identification runs are shown relative to the damaged system driving

point magnitude frequency response function in Figure 6-33.

Although in general practice it is assumed that there would be some form of

damage location available to pre-screen candidate elements, the first damage

identification run was performed using all 100 element groups in order to present a more

challenging validation case and test the algorithm's potential for global damage location.

The damage identification run converged after 30 iterations. The damage results are

shown in Figure 6-34 in the form of a visual damage map, where each square corresponds

to a damage element group of four identically updated finite elements, and the shade

indicates the updated damage factor value, with healthy values of 1 indicated by white

and zero-stiffness damaged values of 0 indicated by black. It can be seen that there is a

region near the center of the plate with reduced damage factor values. The central

element group located at mesh coordinates (X=5, Y=5) in particular updated to a damage

factor value of 0.1, indicating stiffness based damage in that localized region of the

structure.
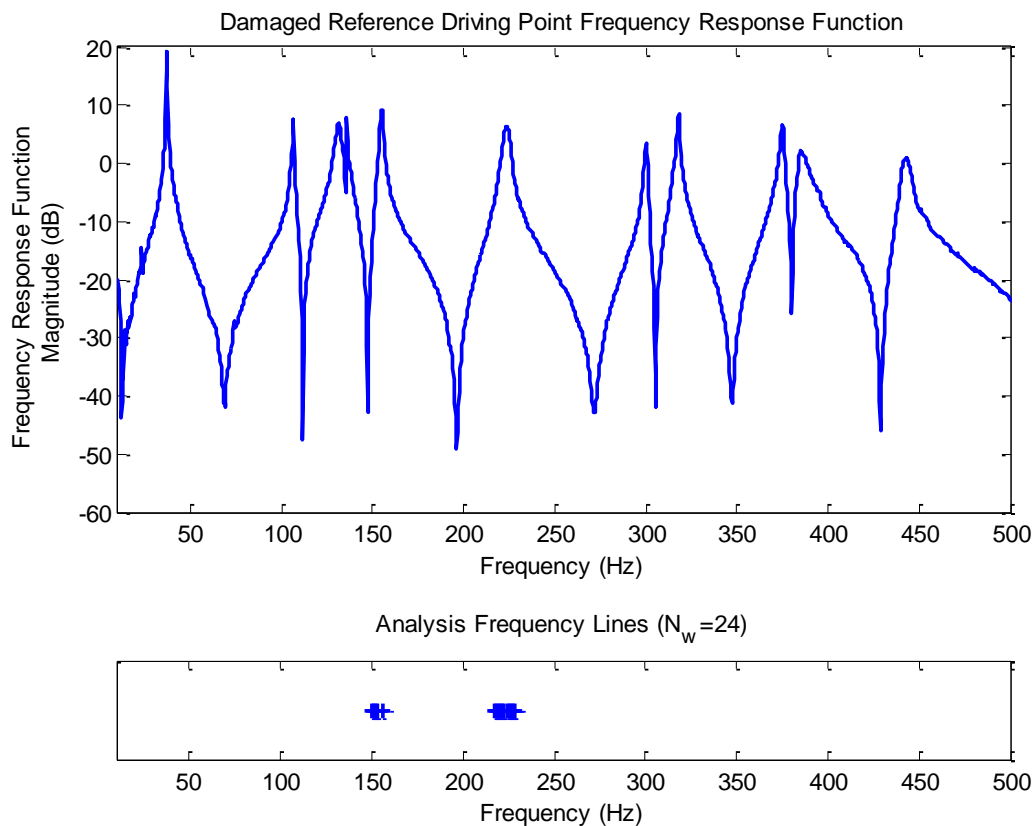
Figure 6-33: Analysis frequency lines for the primary damage identification validation runs shown relative to driving point measured baseline frequency response function magnitude.

The damage identification process was repeated using 30 element groups arranged in a grid 6 element groups high and 5 wide centered on the damage zone using the same algorithm parameters. Figure 6-35 shows the resulting damage map from the second damage identification run, including a dashed line around the region of damage parameters. Elements not included in the update set are shown with an effective damage factor value of 1 for visualization purposes. The element group most closely
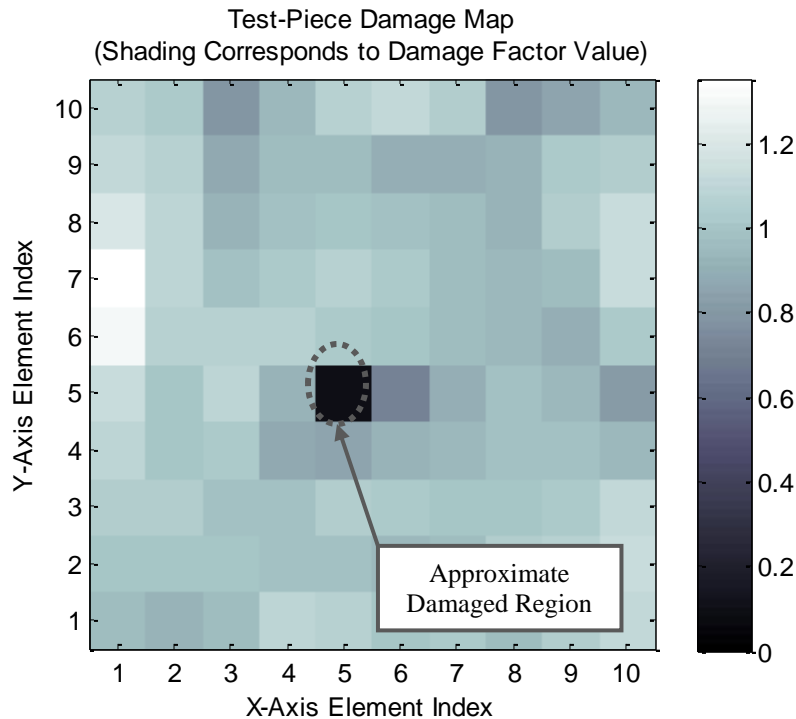
Figure 6-34: Damage map for 100 element group damage identification case.

corresponding to the damage location (X=5, Y=5) updated to a damage factor value of

0.26 and the remaining 10 damage factor values range from 0.77 to 1.13, indicating

successful damage location and identification compared to expectations.

The damage identification procedure was performed a third time with a further

reduced candidate set of 12 damage factors arranged in a grid 4 element groups high and

3 wide and centered on the damage region. The resulting damage map is shown in Figure

6-36 with a dashed line encompassing the candidate damage element groups. Inspection
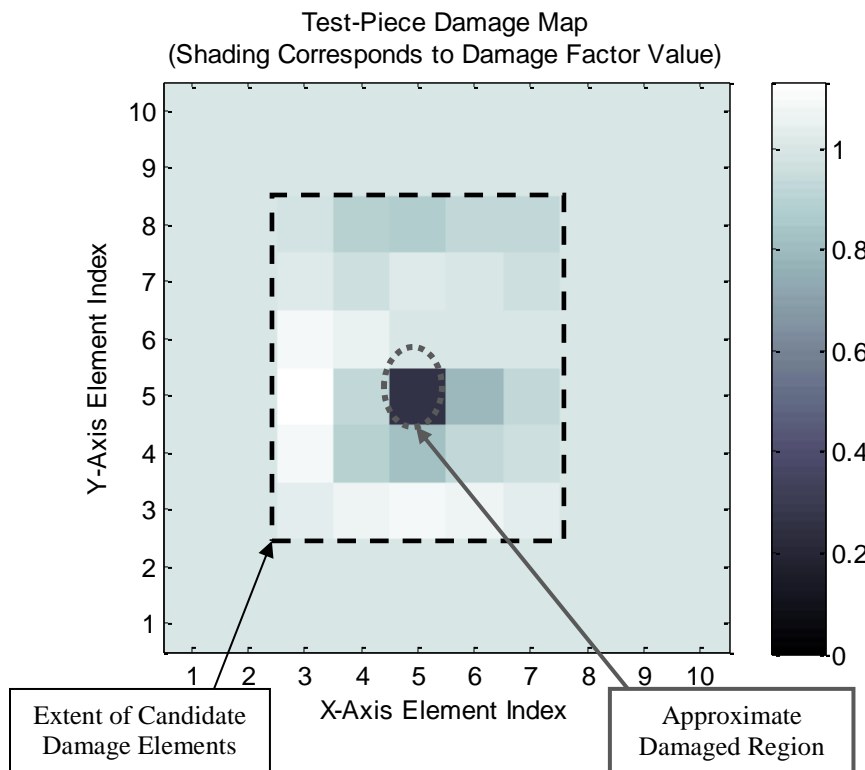
Figure 6-35: Damage map for 30 element group damage identification case.

of results shows that the element group most closely corresponding to the damage

location at (X=5, Y=5) updated to the reduced value of 0.34, indicating damage, while

surrounding groups updated to between 0.78 and 1.0. Corresponding updated damage

factor standard deviations updated from initial values of 0.01 for all parameters to 0.0054

for the damaged elements and between 0.0072 and 0.0097 for the 10 undamaged

elements.

Visually comparing these results to the damaged experimental test-piece indicates

that the damage identification algorithm successfully identified the damage location. It
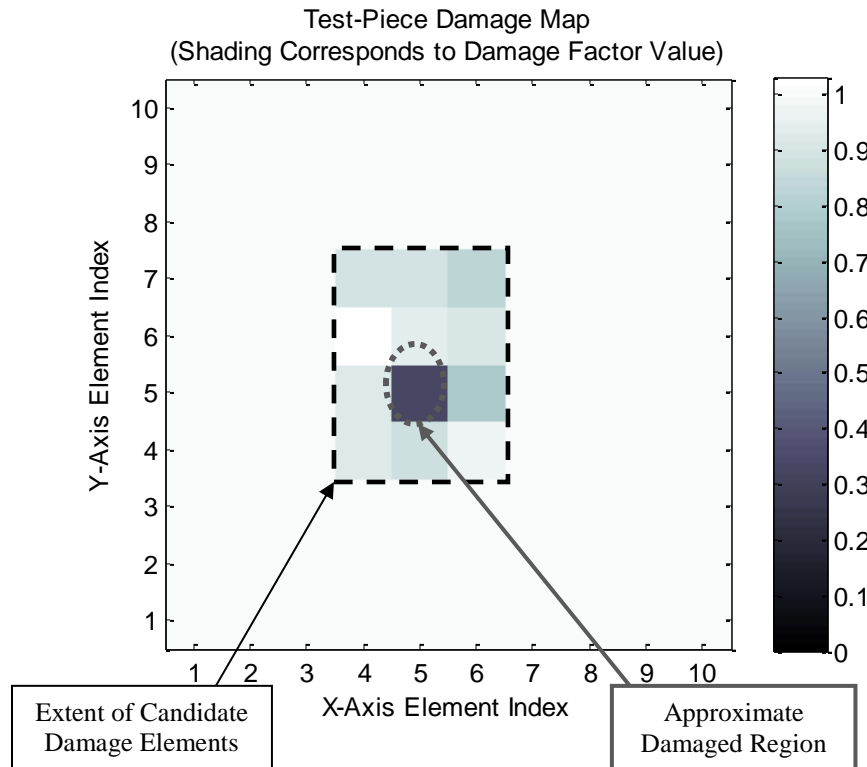
Figure 6-36: Damage map for 12 element group damage identification case.

should be noted that the 'correct' updated damage factor values for the two element

groups that encompass the primary damaged region and the surrounding elements cannot

be precisely defined. The reason is that the element boundaries do not coincide exactly

with the damaged region, and also because the exact effect of the damage on element

stiffness parameters would be irregularly distributed over the element regions whereas

the damage identification results are averaged constants over the element region.

However, visual inspection of the damaged region suggests that the damage was most

severe and widespread in the region covered by the lower primary damaged element

group and minimal in surrounding elements. The physical damage did appear to partially overlap with the element group at (X=5, Y=6) and the expectation was to see partial damage indicated in that element group also. The deviation from expectations reflects the effect of irreducible modeling error retained post-correlation as well as the approximate nature of damage modeling for the current example.

The residual force vectors calculated between the correlated analytical model and damaged reference data are presented visually in Figure 6-37, with the residual force values root-mean-square averaged over the update frequency points and the map representing the 36 measurement points as they appear on the experimental plate (where 1, 1 in the figure corresponds to the top-left corner of the plate). Non-zero residual forces are spread around the plate, as expected, but not in a pattern that obviously corresponds to the damaged region. This occurs because the residual forces capture the effects of measurement noise and modeling error in addition to those of damage. There is additionally likely a blurring effect from the degree-of-freedom reduction process from 2646 analytical degrees-of-freedom to the 36 measurement degrees-of-freedom. When the residual force vector difference is calculated from the updated model after damage identification there is an improvement of up to approximately 20% which is also spread around the plate but biased towards the damage region of the structure, as shown in Figure 6-38. The current algorithm can thus separate the effects of damage from those of unrelated modeling error and noise; however, the effect is blurred by the degree-of-freedom reduction process and existing error in the correlated model.
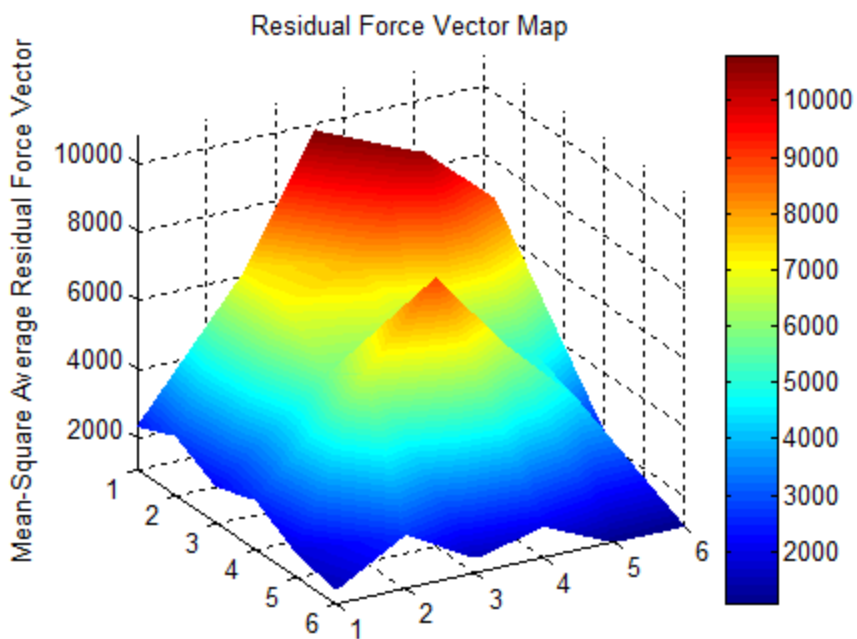
Figure 6-37: Map of frequency averaged residual forces before damage identification at 36 measurement points.
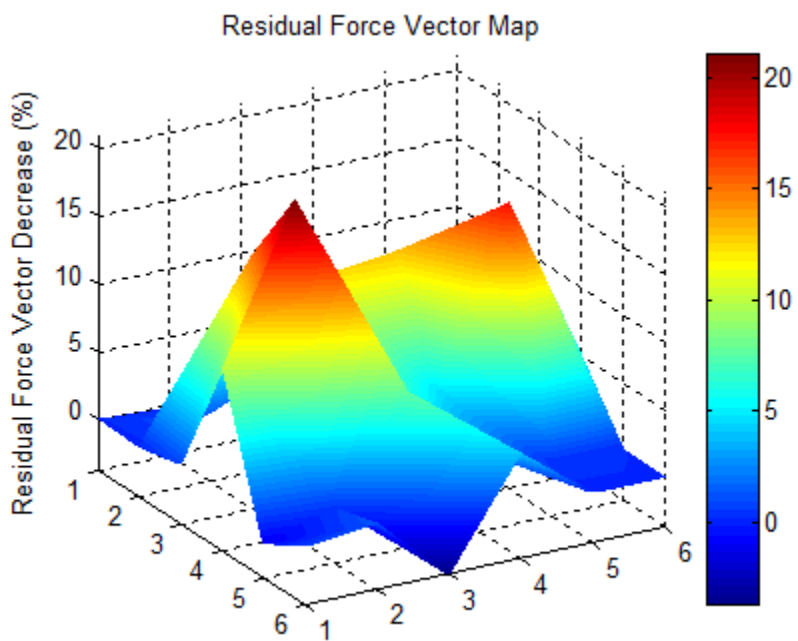
Figure 6-38: Relative decrease in averaged residual forces at 36 measurement points during damage.

6.4.4.2   Effect of Secondary Targeted Correlation

A secondary targeted correlation was performed from the previously correlated model focusing on modes 5 and 6 to investigate the effect of correlating the model only in the frequency region being used for damage identification. The correlation setup described in Section 6.4.2.1 was used again, including 13 global update parameters and parameter standard deviation values loaded from the previous correlation. 48 frequency lines were selected around modes 5 and 6. Because of the restricted frequency range (25% of the previous correlation runs) the frequency response function magnitude bounds were removed and the selection tolerance widened to ±16 Hz around each mode. The correlation converged after 3 iterations. Parameter movement was minimal with density, E_{11}, and the ply angles remaining unchanged to within four significant figures and E_{22}, G_{12}, and ν_{12} decreasing by 0.3%, 0.2%, and 0.3%, respectively.

The 12 element damage identification process was run again from the secondarily correlated model using the setup described in Section 6.4.4.1, additionally following the correlation setup for frequency line selection of no frequency response function magnitude bounds and selection tolerance of ±16 Hz around each of modes 5 and 6. The resulting damage map given in Figure 6-39 shows generally improved resolution of the expected damage state, with clear indication of damage in the main damaged element group (X=5, Y=5), indication of damage in the secondary upper damage element group (X=5, Y=6), and damage factor values generally very close to unity for other element groups. The two element groups to the right of the damage region show indications of

degradation which may indicate internal structural degradation in the damaged plate or

(more likely) reflect lingering modeling error. Final damage factor values converged to

0.47 for the primarily lower damage element group, 0.75 for the secondary upper damage

element group, and between 0.77 and 1.03 for other damage factors.
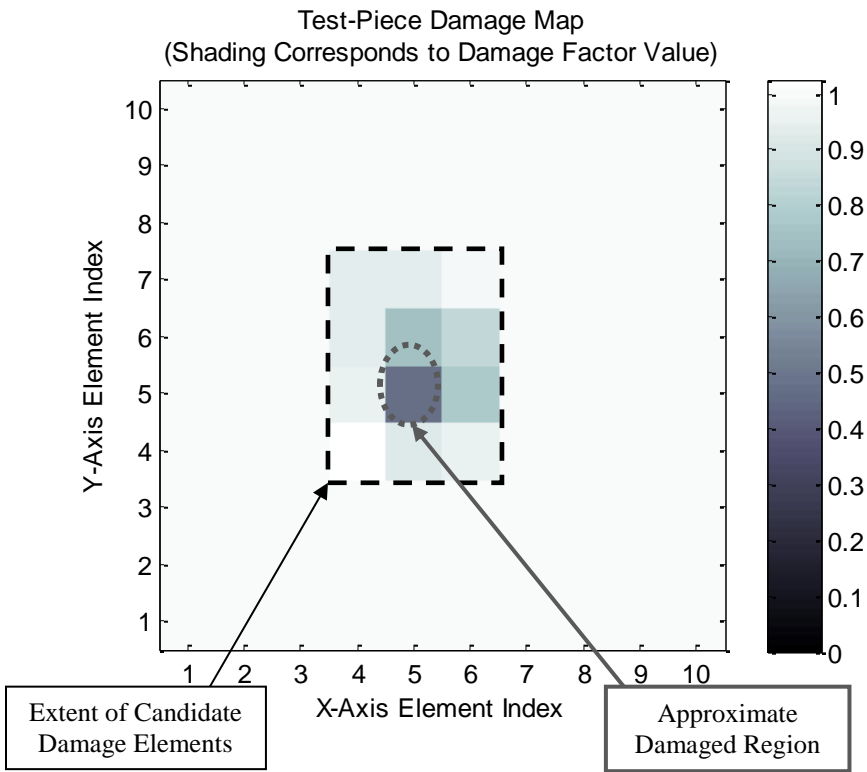
Figure 6-39: Damage map for 12 element group damage identification case after secondary correlation.

6.4.4.3   Damage Identification Using Element Material Properties

To test the damage identification process on the level of individual element

material parameter results the algorithm was rerun from the secondary targeted

correlation model with damage factors assigned to E_{11}, E_{22}, and G_{12} of each of the two

identified damaged elements, creating a total of six damage parameters for the update.

From the point of view of the complete algorithm this optional step would occur

subsequently to damage identification runs performed using elemental damage factors.

The material parameter runs could therefore be confined to a reduced set of candidate

damaged elements resulting in a reasonably small number of distinct material parameters

for the final update.

The damage identification algorithm was run using the same setup described for

the primary runs of Section 6.4.4.1. The resulting damage factors are represented in

Figure 6-40 using a separate damage map plot for each of the elemental stiffness

parameters. Updated damage factor values were 0.1, 0.89, and 0.99 for the lower

damaged element E_{11}, E_{22}, and G_{12} parameters, respectively; and 0.86, 1.0, and 0.99 for

the upper damaged element E_{11}, E_{22}, and G_{12} parameters, respectively. The corresponding

damage factor standard deviation values updated from 0.01 each to 0.0018, 0.0098, and

0.01 for the lower damaged element E_{11}, E_{22}, and G_{12} parameters, respectively; and

0.0049, 0.01, and 0.01 for the upper damaged element E_{11}, E_{22}, and G_{12} parameters,

respectively. Despite the accuracy of the element-global damage factor values achieved

Test-Piece Damage Map for Element Parameter E_{11}
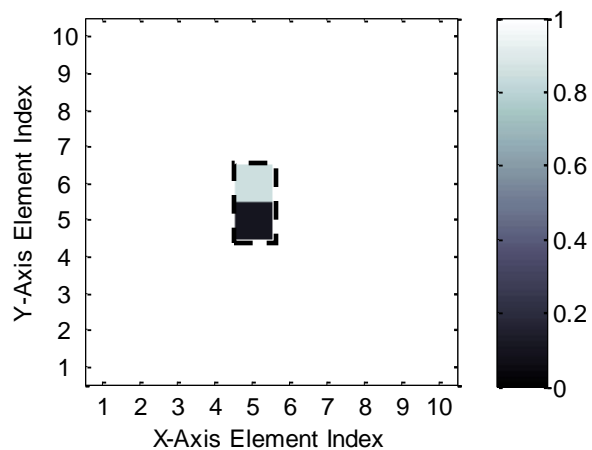
Test-Piece Damage Map for Element Parameter E_{22}
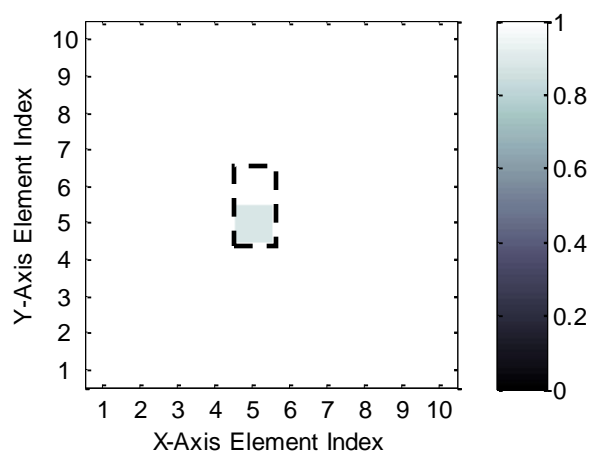
Test-Piece Damage Map for Element Parameter G_{12}
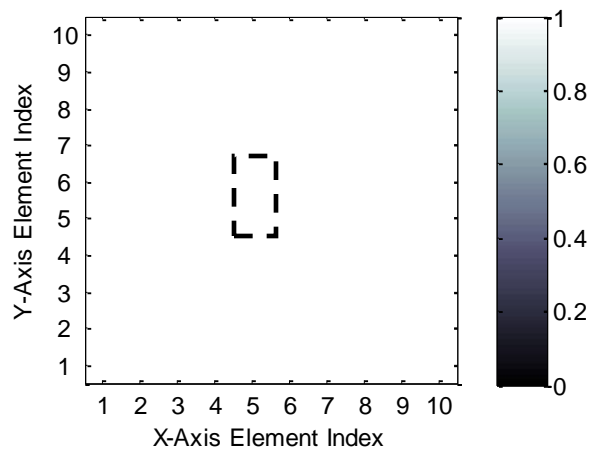
Figure 6-40: Damage map for 2 element group multi-element parameter damage identification case (dashed line indicates approximate limit of damaged elements).

by the end of the 12 element run these final damage identification results likely have a non-negligible amount of error. This is especially true for the lower sensitivity E_{22} and G_{12} parameters as the physical damage case would likely have reduced all three of the candidate stiffnesses to lower values for both elements. It is expected that the remaining noise in the experimental data and modeling error is too high for accuracy at this level of resolution. However, standard deviation did not change for these parameters indicating that information was not gained and the updated values should not be trusted.

6.4.4.4 Investigation into Initial and Updated Parameter Variability

The values of initial damage factor variability specified at the beginning of a damage identification run influence both the final updated variability values and, through regularization, the ability of the damage factors to update to values much different from their original values. Regularization has a strong influence on the outcome of the damage identification optimization process, especially for cases seeking to update a large number of parameters with varying sensitivities. In these cases, unregularized optimization may lead to some parameters, usually those with low sensitivity coefficients, being adjusted to values which are far removed from their initial and physically realistic levels. Regularization effectively establishes a penalty component in the optimization cost function that discourages parameters from traveling too far. The net effect is that (1) parameters stay within reasonable bounds; and (2) the optimization becomes smoother, more stable, and more likely to converge. On the other hand, regularization introduces a

restoring force which may prevent parameters from reaching values that could produce the lowest possible error.

It is one of the fundamental assumptions of the current algorithm that the regularization applied for each parameter is proportional to the inverse of its initial variance, as can be seen from the previously defined underlying cost function definition,

$$J(\hat{r}) \triangleq \{\underline{R}(\hat{r})\}^T \left[\underline{S}_{RR}(\hat{r}_\beta) \right]^{-1} \{\underline{R}(\hat{r})\} + \left(\{\hat{r}\} - \{\hat{r}_0\} \right)^T \left\{ S_{r_0 r_0} \right\}^{-1} \left(\{\hat{r}\} - \{\hat{r}_0\} \right), \quad (3.111)$$

where $J(\hat{r})$ refers to the total cost function value, $\{\hat{r}\}$ refers to the current parameter values, $\{\hat{r}_0\}$ refers to the initial parameter values, $\left\{ S_{r_0 r_0} \right\}$ refers to the initial parameter variance values, and the remaining variables are as defined in Chapter 3. The initial variability values therefore correspond directly to how far the damage factors will be able to change from their initial values. This makes sense on a conceptual level—that parameters known to be accurate at their initial values (i.e., low variability) should remain at similar values while those values with less associated knowledge (i.e., high variability) should be less constrained. In practice, however, the best choice of actual values for initial parameter variance is not obvious. Likewise, the resulting posterior variance values can be interpreted in different ways.

The original expectation for the current algorithm had been to use the parameter standard deviation values generated from the final correlation run. The effectiveness of this approach was investigated by repeating the standard 12 element damage identification from Section 6.4.4.2 with initial parameter standard deviation set to

0.00040, which was the average of updated stiffness parameters from the secondary

targeted correlation run. The result is shown in Figure 6-41. It can be seen that the

damage parameters fail to update to any reasonable approximation of the physical

damage state, with the lowest updated damage factor having a value of 0.96. The lack of

change in any of the parameters suggests that the damage identification was over-

constrained, meaning the initial standard deviation values were too low and resulting

regularization too strong.

Even without this experimental evidence, the original concept of carrying

correlated variability values into the damage identification can be faulted conceptually as

Test-Piece Damage Map
(Initial Param. Std. Dev. = 0.0004)
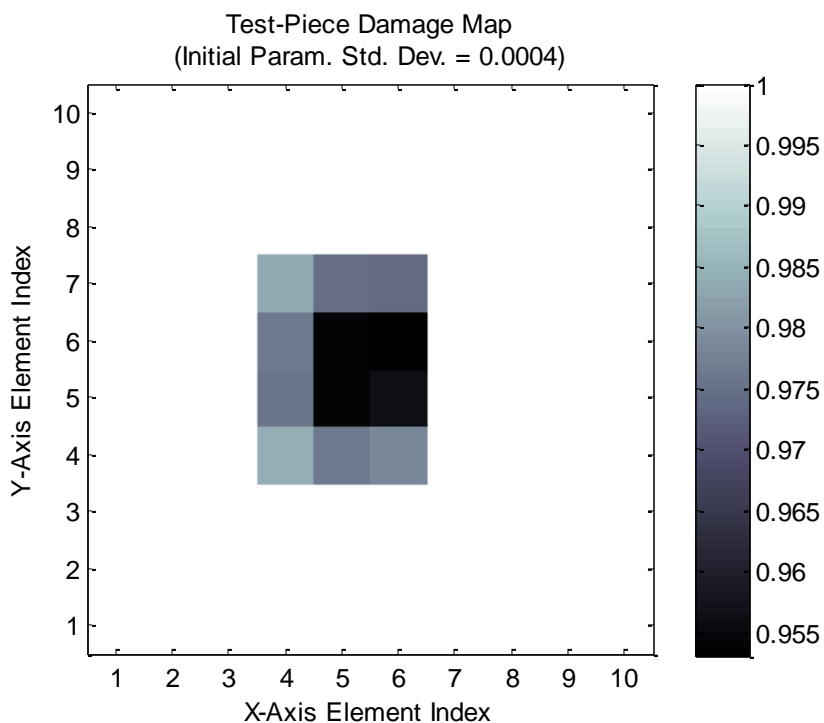
Figure 6-41: Damage map results for case with initial parameter variability loaded from final statistical correlation output.

follows. In a healthy structure parameters can be initially measured independently from the structure and then further correlated to measured data as part of the healthy analytical model. This process produces a high degree of confidence in the appropriateness of the resulting parameter value and subsequently the parameter variability is low. However, when the structure then endures a damaging event that changes its structural configuration by some unknown amount, it cannot be reasonable to assume that the associated analytical parameter values are still known with the same degree of confidence. The initial parameter variability values must therefore be reestablished post-damage, taking into account both the new lack-of-knowledge about the current parameter values and the consideration that they will strongly influence damage identification regularization.

To further investigate trends between initial parameter variability values and algorithm performance, additional damage identification runs were performed using the standard 12 update parameters damage identification case from Section 6.4.4.2. With all other algorithm variables being held constant, initial damage factor standard deviation values were set to 1.0000, 0.1000, 0.0100, 0.0010, 0.0001, and the final average correlated value of 0.0004 for all damage factors. Updated damage factor values from these runs are presented by way of damage maps in Figure 6-42 with specific values plotted against initial standard deviation in Figure 6-43. The number of iterations to convergence for each case is additionally plotted against initial standard deviation in Figure 6-44.
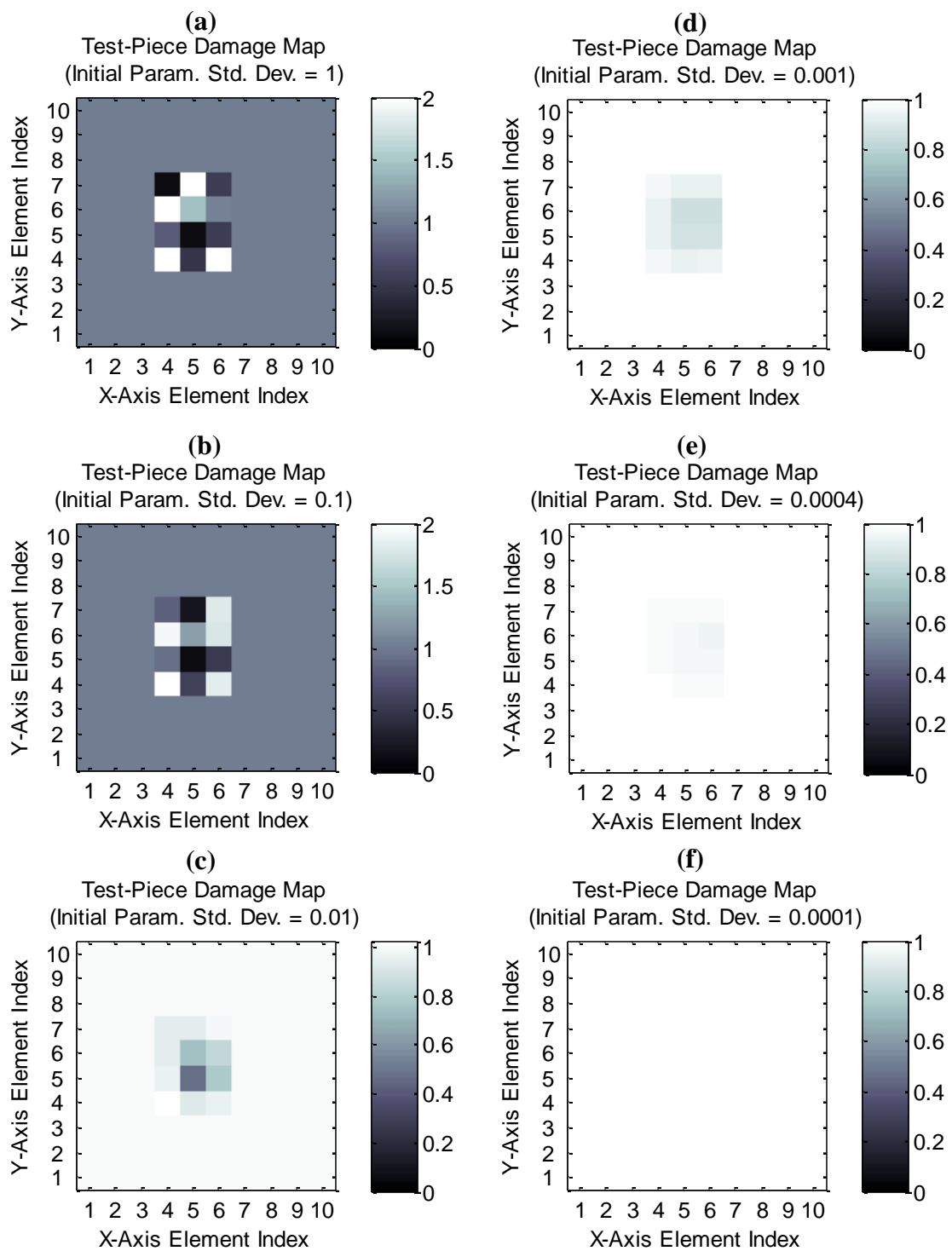
Figure 6-42: Damage map results for initial parameter standard deviation study, where subplots show results from runs with initial parameter standard deviation values set to (a) 1, (b) 0.1, (c) 0.01, (d) 0.001, (e) 0.0004 (average of posterior correlated values), (f) 0.0001.
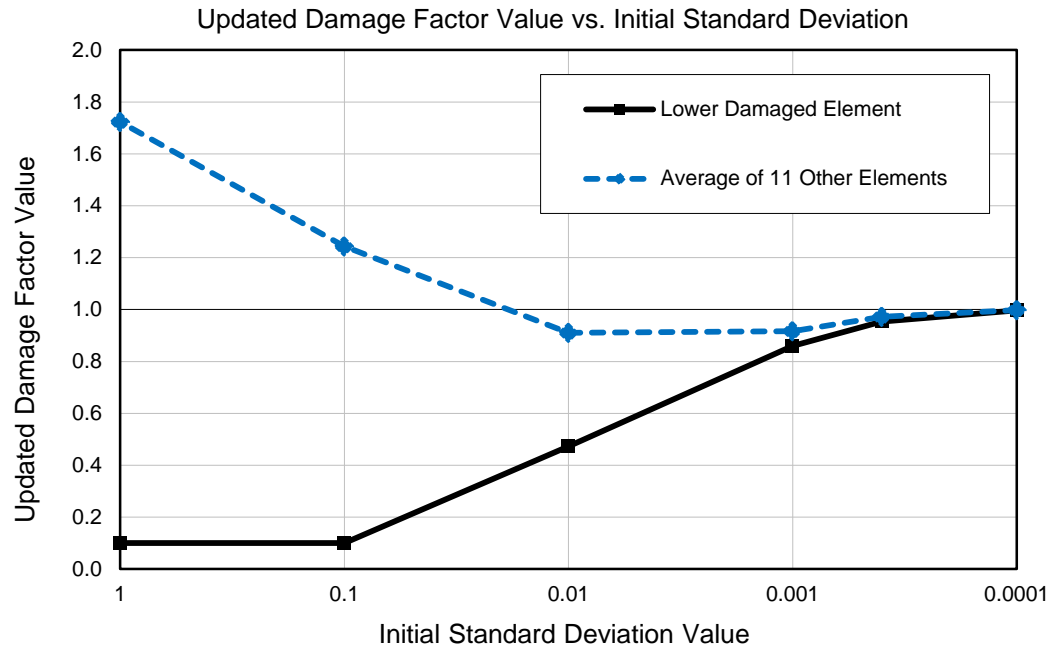
Figure 6-43: Updated damage factor results from initial parameter variability study.
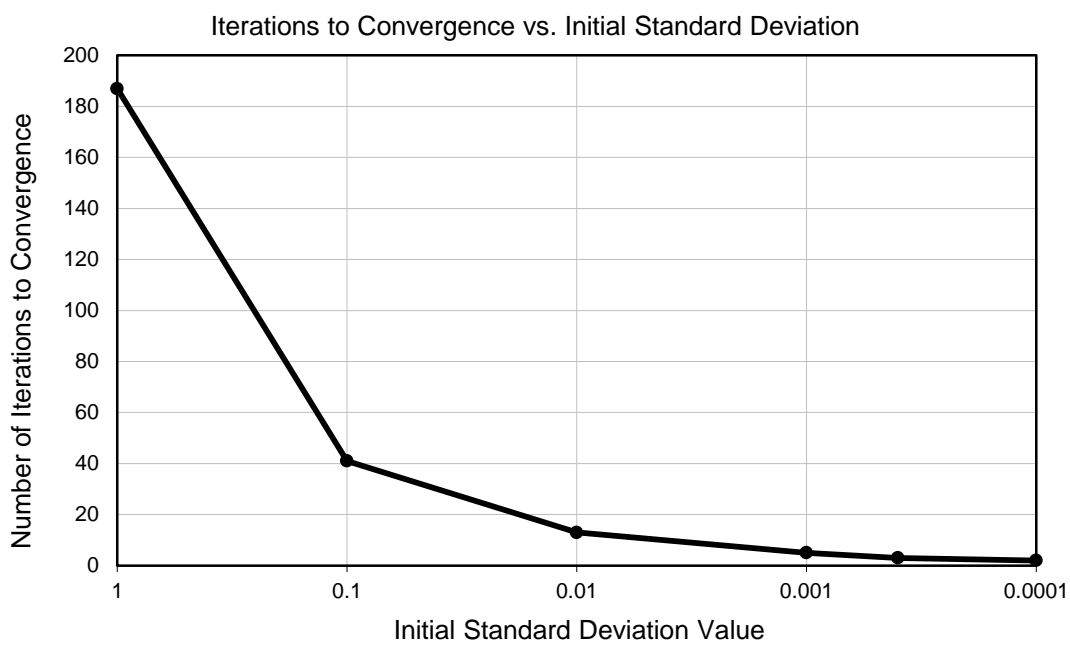
Figure 6-44: Number of iterations to convergence for initial parameter variability study.

It can be seen from these results that the runs with initial standard deviation values of 0.1000 and 1.0000 required increasingly high numbers of iterations to reach convergence and produced erroneous final damage factor values. This result is indicative of the optimization parameters experiencing wide-ranging movement through the solution-space before converging—a behavior common to runs with a high range of parameter sensitivities and low regularization. The run with initial standard deviation value of 0.01 produced a successful damage identification result, similar to that reached by the nearly identical 12 element damage identification case presented in Section 6.4.4.1. The remaining test cases, with increasingly low values of initial parameter variability, were increasingly overconstrained by regularization to the point that the damage factors could not move appreciably at all in the cases of initial parameter variability loaded from the model correlation output and initial standard deviation equal to 0.0001.

From the point of view of damage identification, there is obviously an optimal region where regularization allows meaningful convergence without overconstraining the optimization. For the current study case, the value of 0.01 for initial damage factor standard deviation produced acceptable results, with higher and lower values leading to degrading results as a result of either too much or too little regularization. For problems with different ranges of parameter sensitivity and measurement noise, acceptable values for initial damage factor standard deviation could be different. At this stage it is not clear if there is an available means of accurately establishing initial parameter variability based

on absolute criteria. It is thus recommended that operator intuition and experience be used to set initial values with adjustments made subsequently based on algorithm convergence and the amount of apparent regularization until a suitable range of values is established for the given problem.

Corresponding updated damage factor standard deviation results from the six runs described above are plotted against initial standard deviation in Figure 6-45, with relative decrease in standard deviation value given in Figure 6-46. From these results it can be seen that lower initial parameter standard deviation values lead to lower updated parameter standard deviation values, and also that the relative amount of change decreases with decreasing initial value. Further insight is provided by rewriting the expression for updated parameter variance given in Eq. (3.129) from Section 3.6.2 by expanding and canceling terms as

$$[S_{\hat{r}\hat{r}}] = \left(\left[S_{\hat{r}_0 \hat{r}_0} \right]^{-1} + \left[\frac{\partial \underline{a}}{\partial r} \right]^T [\underline{S}_{vv}]^{-1} \left[\frac{\partial \underline{a}}{\partial r} \right] \right)^{-1}, \qquad (6.15)$$

where $[S_{\hat{r}\hat{r}}]$ is the updated parameter covariance matrix, $\left[S_{\hat{r}_0 \hat{r}_0} \right]$ is the updated parameter covariance matrix, $\left[\frac{\partial \underline{a}}{\partial r} \right]$ is the parameter sensitivity with respect to the frequency response functions, and $[\underline{S}_{vv}]$ is the measurement noise variance. Inspection of the resulting relationship verifies that updated parameter variance should decrease with decreasing initial variance value, as demonstrated in Figure 6-45. The equation
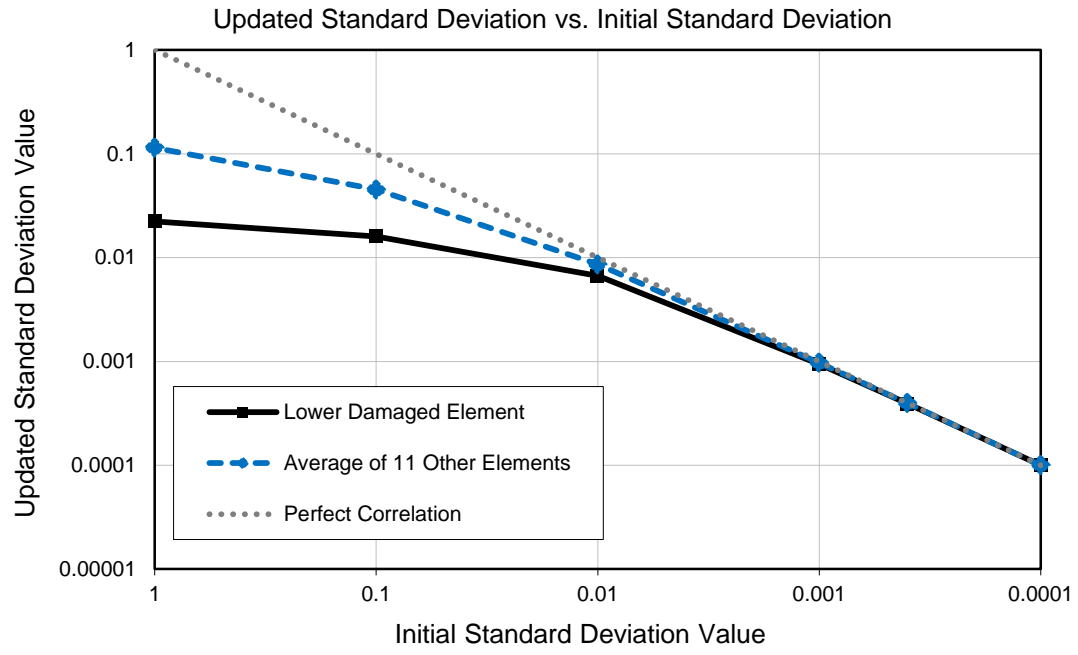
Figure 6-45: Updated damage factor standard deviation value plotted against initial damage factor standard deviation value from initial parameter variability study.
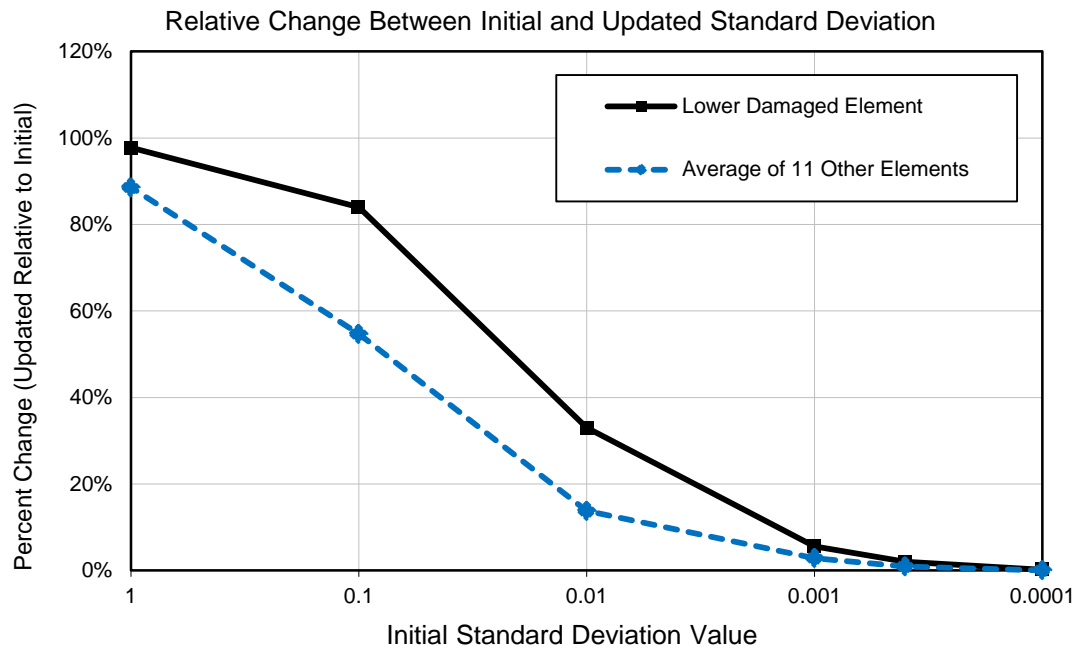
Figure 6-46: Relative change between initial and updated damage factor standard deviation values with respect to initial value from initial parameter variability study results.

additionally shows that updated parameter standard deviation will decrease with

decreasing measurement noise variance and increasing parameter sensitivity. The

trending of updated parameter standard deviation with measurement noise makes

conceptual sense, dictating that more noise will lead to higher updated parameter

variability. The inverse relationship with sensitivity shows that higher sensitivity

parameters should end up with lower updated variability, and vice versa. This

relationship makes physical sense from the point of view that high sensitivity parameters

will stand out more strongly above the noise and therefore become more accurately

known. An additional interesting point to be taken from inspecting Eq. (6.10) is that the

decreasing relative standard deviation change observed in Figure 6-46 is likely related to

the relative magnitude of $\left[S_{\hat{r}_0 \hat{r}_0} \right]^{-1}$ compared to $\left[\dfrac{\partial \underline{a}}{\partial r} \right]^{T} \left[\underline{S}_{vv} \right]^{-1} \left[\dfrac{\partial \underline{a}}{\partial r} \right]$. For any given

parameter, this means that the amount of relative decrease in parameter variability

depends on how high the initial parameter variance is compared to the ratio of noise

variance to parameter sensitivity squared. The noise variance and parameter sensitivity

are fixed for a given update problem; therefore, insight into reasonable values of initial

damage factor variance could potentially be gained by inspecting its relative magnitude

compared to the ratio of parameter sensitivity and noise variance.

The meaning of updated parameter variance values is not definite; however some

clarity is offered by the above observations and analysis. Quantitatively, the updated

damage factor values describe the uncertainty associated with the parameters and can

therefore be used with respect to subsequent analyses, such as the extension to prognosis

as discussed in Chapter 1. It should be considered that the operator-specified initial

variability values will influence the final variability values. Independent of their

individual values in an absolute sense, however, the relative updated variability values

are useful in a qualitative sense when viewing damage identification results since they

give an indication of parameter sensitivity to the measurement noise and, therefore,

confidence in the updated parameter values.

6.4.5   Discussion

The statistical damage identification algorithm developed through previous

chapters has been extended to experimental implementation and successfully validated on

an experimental composite plate with laminate damage. The composite plate test-piece

was manufactured from a commercially produced stock laminate plate and vibration

tested using the roving hammer impact method to produce healthy reference data. A finite

element model was built and correlated using a combination of deterministic pseudo

Newton-Raphson minimization of natural frequency error and a correlation

implementation of the statistical damage identification algorithm. The correlated model

was subsequently used with measured vibration data from the damaged plate to

successfully perform damage location and damage identification. The effect of a

secondary correlation targeted to the damage identification frequency range was

additionally studied, along with damage identification using individual material

properties. Finally, the implementation and interpretation of damage factor variability was explored.

The algorithm was able to successfully correlate initial approximate baseline finite element model and subsequently identify the damage in the face of experimental measurement noise and modeling error. There remain open questions with respect to damage identification of low-sensitivity parameters and with establishing and interpreting parameter variability. However, the current algorithm's ability to successfully perform realistic experimental damage identification has been demonstrated.

The material contained in Chapter 6 was developed in collaboration with Prof. John B. Kosmatka, Prof. Charles Farrar, and Prof. Joel Conte. The dissertation author was the primary investigator and author of this work.

6.5   **Chapter 6 References**

[6-1]   Tillerson, J.R., Stricklin, J.A., Haisler, W.E., "Numerical Methods for the Solution of Nonlinear Problems in Structural Analysis," *Numerical Solution of Nonlinear Structural Problems*, ASME, 1973

[6-2]   CST Composites (http://www.cstsales.com/carbon_plate.html)

[6-3]   RT Pro v6.21 (http://www.lds-group.com)

[6-4]   ME'scopeVES version 5.1.2011.0225. Scotts Valley, California: Vibrant Technology Inc., 2011

[6-5]   MD.NASTRAN 2010.1. Santa Ana, California: MSC Software., 2010

7   DEVELOPMENT OF A COMPOSITE WING TEST-BED

The final chapter diverges from the primary damage identification algorithm to present the author's contribution towards development of a composite aircraft wing structural health monitoring test-bed. The development was part of a multi-team collaborative effort lead by Los Alamos National Laboratory focused on furthering technology for structural health monitoring and prognosis. The test-bed is comprised of a lightweight composite main wing structure based on modern unmanned aerial vehicle design practices, a family of detailed structural finite element models, and a laboratory setup for modal vibration testing.

An explanation of the project motivation is provided first along with details of the test-bed design. The finite element models are described followed by an analysis of modal behavior and an analytical damage study. Physical manufacturing of the wings is presented followed by details and results from vibration testing and model correlation. The chapter concludes with recommendations for future work.

7.1   Composite Wing Test-Bed Project

As discussed in Chapter 1, a distinct area of interest for structural health monitoring is composite airframes, in particular the all-composite lightweight structures used for certain modern unmanned aerial vehicles. Composite airframes are susceptible to

both fatigue and impact damage and unmanned aerial vehicle airframes in particular are more likely than their manned counterparts to be operated close to or past the point of structural failure. There is an economical advantage to be gained from developing structural health monitoring and prognosis capability for unmanned aerial vehicles and these systems likewise offer a platform for testing developmental structural health monitoring and prognosis systems.

In the interests of forwarding structural health monitoring technology for unmanned aerial vehicles and other aerospace structures, components of a specialized test-bed were developed to facilitate studies on damage location, damage identification, and structural health prognosis. The test-bed development was part of a multi-team project lead by Dr. Charles Farrar at Los Alamos National Laboratory with three research groups at the University of California, San Diego (UCSD). The UCSD groups consisted of the current author and Prof. John Kosmatka tasked with developing and testing the physical scaled wing test-bed and methods for damage identification, a team lead by Howard Matt and Prof. Francesco Lanza di Scalia tasked with developing piezo-electric sensor networks and methods for ultrasonic damage location, and a team lead by Maurizio Gobbato and Prof. Joel Conte focusing on structural health prognosis. The damage location work of Matt and Lanza di Scalia is summarized in reference [7-1]. The prognosis work of Gobbato and Conte is summarized in reference [7-2]. Development of the test-bed and methods for damage identification is presented in the current dissertation.

7.2 Test-Bed Scaled Wing Design

The physical test-bed is loosely based on the wing structure of the Predator A unmanned aerial vehicle produced by General Atomics in San Diego, CA. An example of the Predator A aircraft is shown in Figure 7-1. The Predator vehicle wings are structurally independent from the rest of the vehicle and can be detached, as shown in in Figure 7-2. Each wing has a protruding main spar with the spars on port and starboard wings offset in the vehicle longitudinal direction to enable the wing spars to overlap while the wing surfaces remain symmetrical. Each wing additionally has a pin protruding from the wing root aft of the main spar which reacts against the fuselage to counteract torsional wing loads. For flight the wings are inserted into the main aircraft fuselage and bolted through the fuselage primary structure in a cantilevered configuration. This configuration means the aircraft can be transported in a low-profile shipping container but also results in high loads in the skin spar bond at the wing root when the aircraft is in operation. These loads lead to disbond damage cases near the wing root and, combined with the susceptibility of the main composite main wing surface to impact damage, results in the potential for the wing structures to age faster than the rest of the aircraft structure. The removable wings can be replaced when they become damaged or reach the end of their fatigue life. Despite the high cost of new wings, replacement can be more economical than regular structural inspection as the wings age, whether or not they are actually damaged. Structural health

Figure 7-1: General Atomics' Predator A Unmanned Aerial Vehicle in flight.

Figure 7-2: Predator UAV wings removed from the rest of the aircraft.

monitoring could allow a more nuanced approach to managing the life-cycle of these and similar aircraft, with an obvious extension to economical and safety benefits in manned aircraft.

Following the example of this aircraft the test-bed structure was designed in adherence to the principles of modern composite structural design, using graphite epoxy composite in a tailored layup with sandwich structures in unsupported regions of the wing skins to provide simple load paths with a minimum of redundancy and waste. The wing was designed with geometry visually similar to the Predator wing at approximately 1/3 scale with a constantly tapering cross-section and protruding main spar. Additionally the Predator's duel-spar and sandwich composite skin architecture was adopted. Apart from approximate form-factor and basic structural design, however, the test-bed structure deviated significantly from the Predator design. An SD-7062 airfoil was selected for the outer mold line of the wing—both for the finite element models and physical manufacturing of the wing. The leading edge was formed by designing a dog-leg style joggle into the lower skin so that the top skins could overlap by several millimeters and form a bondline. The trailing edge structure was formed by bonding the top and bottom skins to a wedge of lightweight structural closed-cell foam. The laminate system was chosen to be a woven high-modulus graphite-epoxy prepreg system, based on the specific stiffness requirements of airframes and material availability, with Nomex honeycomb for the sandwich core.

A schematic of the design with major dimensions is presented in Figure 7-3 and views of the Solidworks computer aided design model shown in Figure 7-4. To meet the design constraints discussed above the test-bed wing structure was formed from four independently manufactured primary components: top skin, bottom skin, main spar, and aft spar. The two spars provide the primary load path for wing bending and are similar to each other in design and construction—C-section type beams with the horizontal top and bottom structures including built-up regions of unidirectional graphite composite to carry tension and compression loads and the vertical web structure being constructed of angled weave to carry shear. The wing skins were designed to transmit aerodynamic wing loads into the rest of the structure and provide torsional stiffness and load carrying capability. The skins were constructed primarily of angled weave for carrying global wing torsional loads and included honeycomb core co-cured through unsupported regions of the wing skin structure to provide local stiffness for aero surface loads. The sandwich core regions were tapered down to plain-laminate close-out through bondline regions with a 45° chamfer in the core to decrease stress concentrations. The four wing components were designed to be co-cured as a single independent piece and then bonded together along with a wedge-shaped piece of foam at the trailing edge in a secondary step. This overall design approach meets the necessary wing torsional and bending stiffness/strength requirements with low mass compared to conventional metallic wing designs with regularly-spaced ribs and stringers. Certain details of a full-scale wing, such
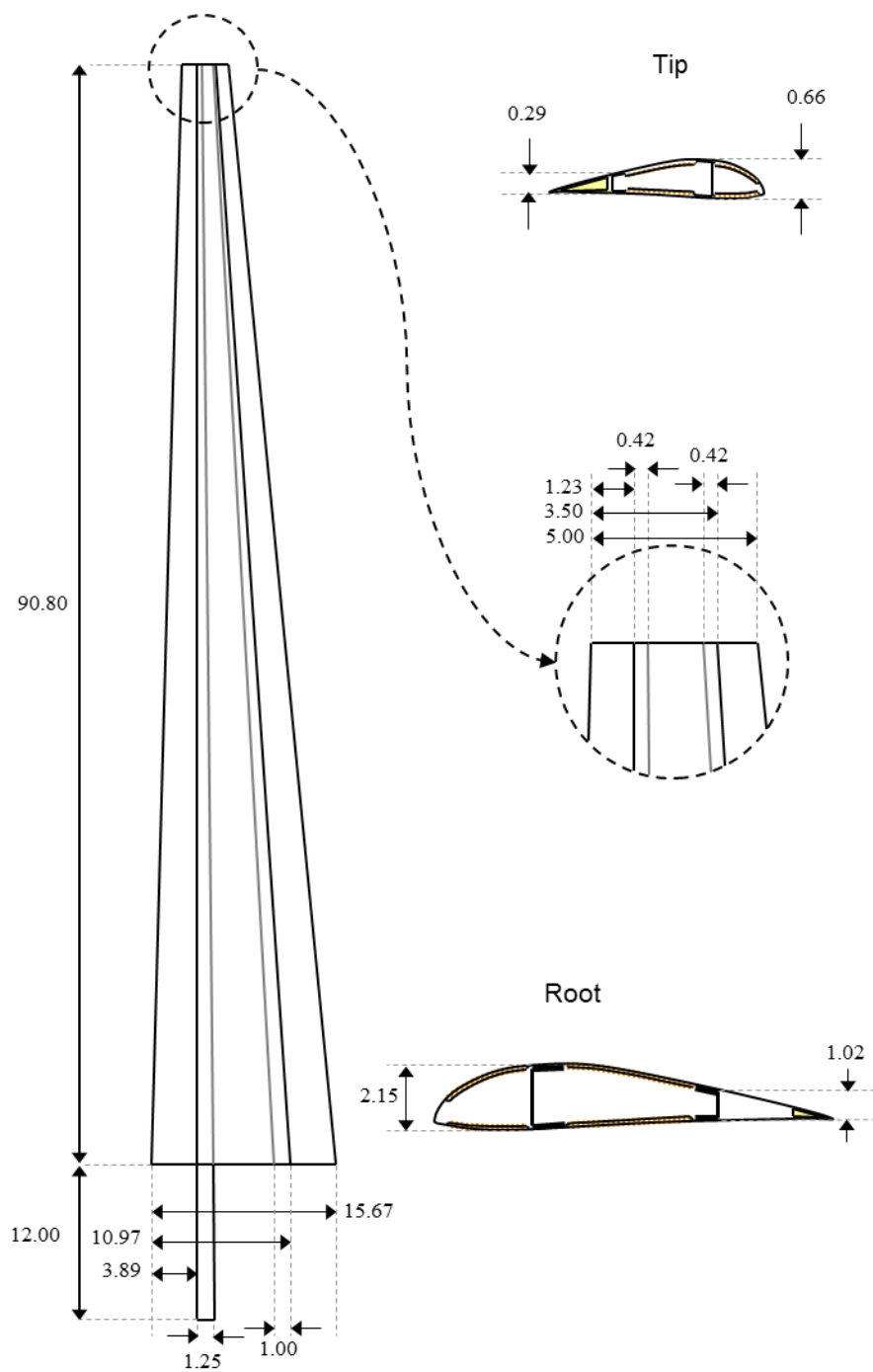
Figure 7-3: Test piece dimensions (dimensions in cm).

Isometric View

Plan View
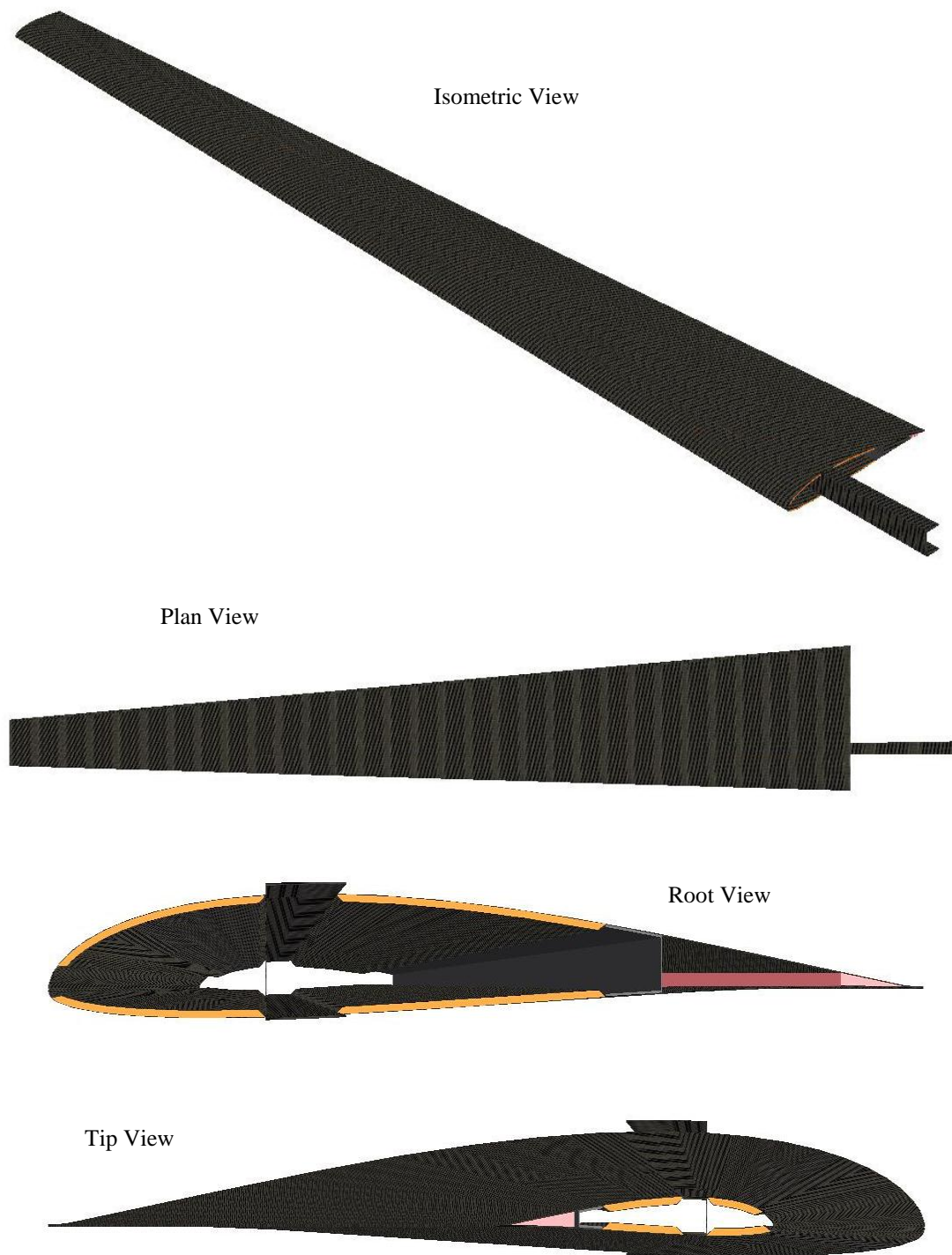
Root View

Tip View

Figure 7-4: Computer aided design renderings of the test-bed wing structure from various viewpoints (from top down): isometric view, plan view, root view, tip view.

as articulating control surfaces, fuel tanks, and associated plumbing and harnessing were not included for the scaled-down test-bed for practical manufacturing reasons and to maintain focus on response of the primary structure. It should be noted in Figure 7-4 that the core is shown exposed at the wing root and tip but was closed-out by a chamfered section of laminate in the physical case. Layup details are given in Table 7-1.

Table 7-1: Layup details.

Region	Layup
Skin closeout	$[45]_2$
Skin sandwich	$[45/core/45]_T$
Spar cap	$[45/0/0/45]_T$
Spar web	$[45]_2$

7.3 Analytical Development

A detailed finite element model of the wing structure was constructed as part of the test-bed and to facilitate studying dynamic response of the system. The finite element model was constructed with the capability to model the wing structure in its healthy state and with various types of damage. Following the requirements for finite element model based damage identification outlined in Chapter 5, the finite element mesh had to be detailed enough to approximate realistic damage cases while maintaining a reasonably

low degree-of-freedom count for damage identification algorithm viability and computation efficiency. The damage cases considered during model development were primarily skin-spar disbonds, which can occur as a result of operational fatigue, and skin-core disbonds, which can occur from blunt impact to the external wing surface.

The baseline models were constructed primarily of shell elements for all laminate regions with solid elements representing the sandwich core and aft-edge bonding foam. Rigid links were used as a first-order idealization of bondlines between spar and skin, for the first damage type, and between skin laminate and skin core, for the second. Damage could then be simulated by removing rigid links through the affected region. This modeling technique additionally allowed the potential for modeling the bondlines as separate solid elements with properties that could be adjusted to represent various levels of damage—for example, elements with reduced Young's modulus to represent micro fatigue cracks in the adhesive or manufacturing discrepancies in the adhesive mixture.

Details of the finite element model are provided in the first subsection followed by analysis of the wing modes and an investigation into wing response in various cases of spar-skin disbond damage at the wing root.

7.3.1   Finite element model development

The wing test-bed finite element model was made for MD.NASTRAN [7-3] using Femap [7-4] as a pre- and post-processor. Four independent component finite element models were created to match the four wing pieces, with each component model able to

be analyzed independently for correlation purposes. The four models were then attached

using RBE2 rigid links to simulate the ideally bonded physical case. Isoparametric

CQUAD4 quadrilateral shell elements with two-dimensional orthotropic MAT8 material

properties defined using the PCOMP laminate property set were used for all laminate

regions. Laminate nodes were situated at element mid-planes with element mid-planes

positioned such that the exterior element surface, including element thickness, formed the

smooth airfoil mold-line. Sandwich sections were modeled as shells connected with

RBE2 rigid links to the solid core which was modeled using 8-node cubic CHEXA solid

elements with PSOLID property sets and 3-dimensional MAT9 anisotropic material

cards. Honeycomb material only has appreciable stiffness properties in transverse shear

directions (G_{13} and G_{23}) and the transverse extensional direction (E_{33}) and all other

properties were set non-zero, but several orders of magnitude lower. The bondlines at the

leading edge, top and bottom of both spars, and top and bottom of the trailing edge were

modeled using RBE2 rigid links and additionally included non-structural mass-

membranes modeled with CQUAD elements, PSHELL property cards, and MAT1

material cards. The foam wedge used to create the trailing edge bonding surfaces was

modeled using CPENTA elements, PSOLID property cards, and MAT1 material cards.

Longitudinal primary element boundaries were set to follow the main wing

geometry lines, including the lines of sandwich region closeouts and both spars.

Additionally, a constant leading-to-trailing edge element count was maintained down the

length of the wing producing a similarly tapered grid of elements for each layer. The

mesh structure visible on the top skin surface was therefore closely matched through all element layers—outside and inside laminates of the top and bottom skins, top and bottom caps of both spars, and the solid mesh of the sandwich core—meaning that nodes requiring rigid link connections were automatically positioned close together.

The assembled wing model is shown from the plan view in Figure 7-5. A view from the wing root is given in Figure 7-6 showing the tapered wing interior surfaces receding into the page and the open wing tip visible at the deepest point. A close-up view of the top spar-skin joint is given in Figure 7-7 showing rigid links connecting the skin to the spar cap and a layer of non-structural membrane providing adhesive mass to the bondline. Views of the model leading and trailing edges are given in Figure 7-8 and Figure 7-9, respectively. The chamfered sandwich core is also visible in Figure 7-7 as white blocks to the left and right of the spar-skin bondline, with laminate skins following the contour of the core and attached at their corners via rigid links. Overall model mesh details are given in Table 7-2, including the number of elements in each model and the number of nodes and structural nodes, where the latter count disregards one of each pair of nodes sharing rigidly linked degrees-of-freedom. Table 7-3 provides structural material properties used for the laminates and honeycomb core in the baseline finite element models. It should be noted that the G_{13} and G_{13} properties for the laminate are included for completeness but have negligible influence on model response.
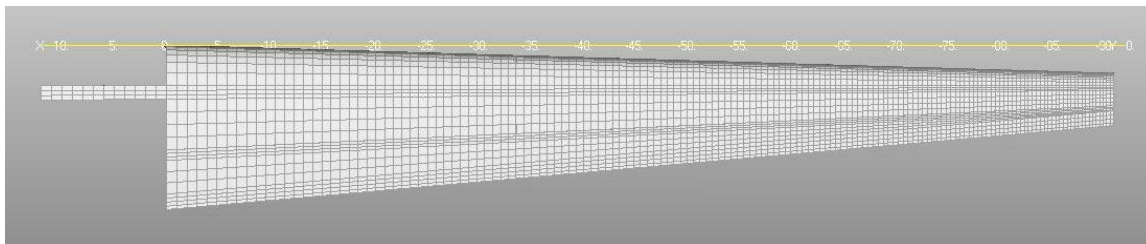
Figure 7-5: Assembled finite element model, plan view, showing mesh distribution.
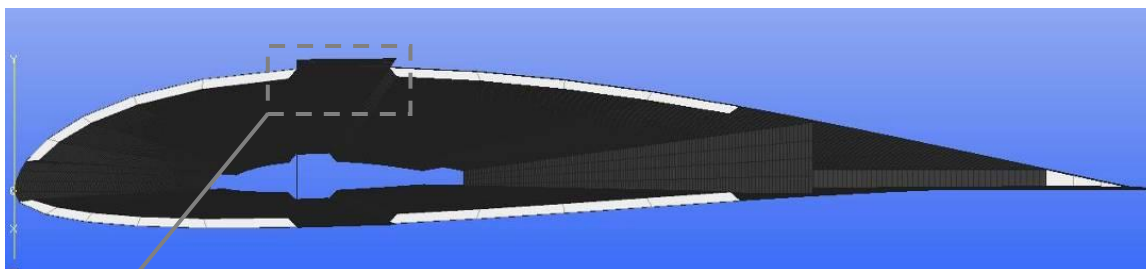
Figure 7-6: View of model cross section and interior, from the root.
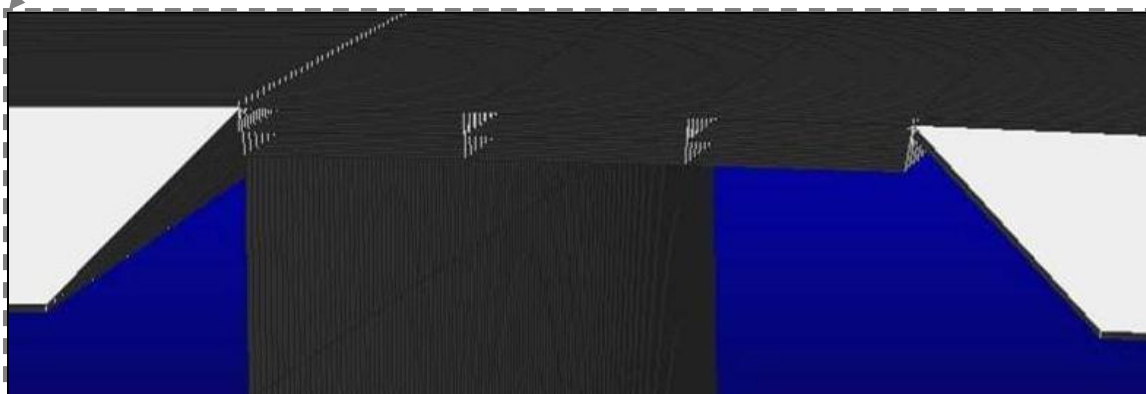
Figure 7-7: Close-up view of spar-skin bondline modeling.
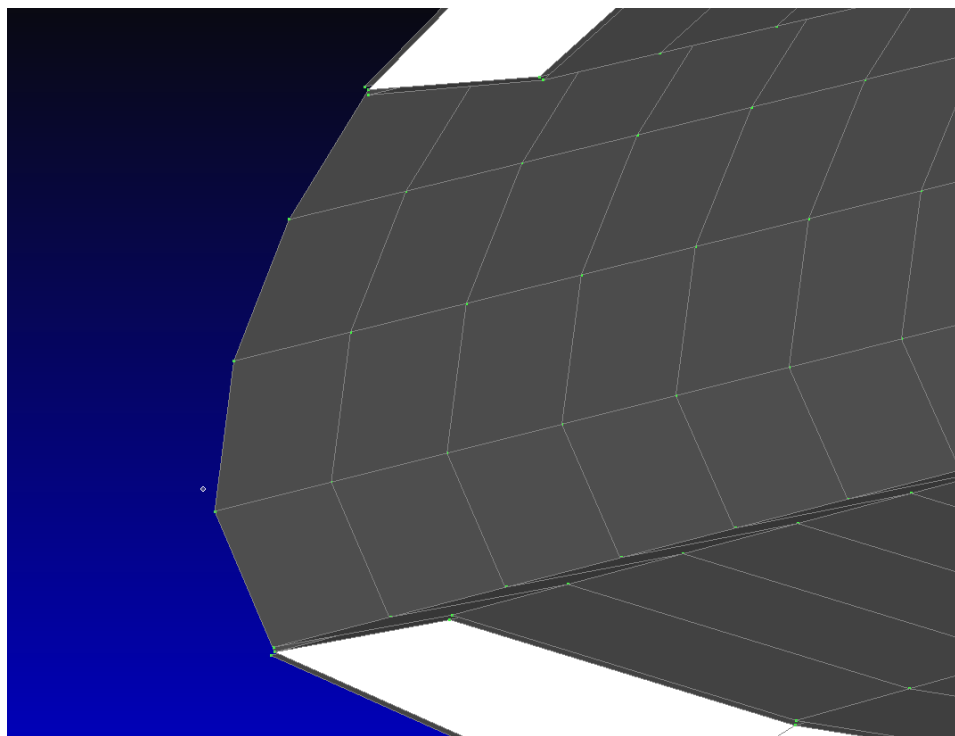
Figure 7-8: Close-up view of the leading edge.
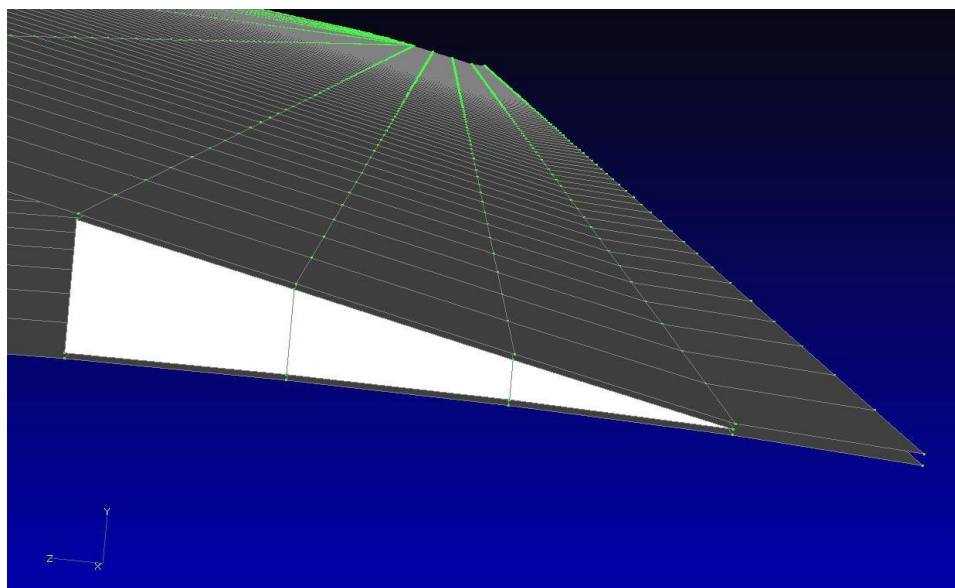
Figure 7-9: Close-up view of the trailing edge.

Table 7-2: Finite element mesh information for wing and component models.

	Number of Elements	**Number of Nodes (Structural Nodes)**
Assembled wing	27,370	36,246 (17,600)
Top skin	9,486	10,970 (5624)
Bottom skin	9,486	10,970 (5624)
Main spar	1,815	1,640
Aft spar	1,683	1,520

Table 7-3: Finite element model material properties for the baseline finite element model.

Laminates (3D orthotropic)		**Core (3D anisotropic)**		**Foam (Isotropic)**	
E_{11} (Pa)	1.11×10^{11}	G_{11} (Pa)	6.89×10^3	E (Pa)	0.0700
E_{22} (Pa)	1.11×10^{11}	G_{22} (Pa)	6.89×10^3	G (Pa)	0.0191
G_{12} (Pa)	4.83×10^9	G_{33} (Pa)	1.38×10^8	v	-0.45*
v_{12}	0.02	G_{44} (Pa)	6.89×10^3	ρ (g/cm^3)	0.0521
G_{13} (Pa)	4.14×10^9	G_{55} (Pa)	41.4×10^7		
G_{23} (Pa)	4.14×10^9	G_{66} (Pa)	24.1×10^7		
ρ (g/cm^3)	1.660	G_{12} (Pa)	6.89		
		G_{13} (Pa)	6.89	*Negative value was used in error (correct value is 0.45). Material was used in low-load region and the error is not believed to have impacted results.*	
Ply t (mm)	0.25	G_{23} (Pa)	6.89		
		G_{ij}, $i{\neq}j$ (Pa)	0		
		ρ (g/cm^3)	0.1403		

7.3.2   Analytical Study of Modes

Undamped modes for baseline wing finite element model were calculated using

the normal mode solution in NASTRAN in several boundary condition configurations.

The cantilevered-pinned configuration used in the physical Predator aircraft wings was

first modeled by constraining all degrees-of-freedom for the nodes on the top and bottom

surfaces of the protruding portion of the main and pinning all degrees-of-freedom for the

root aft-spar nodes. Modes were then calculated with the wing structure in a free-free

configuration and, additionally, with grounded springs of varying stiffness attached to the

root cantilever nodes to investigate response with a non-ideal cantilever configuration.

The first 14 undamped normal modes of the cantilevered configuration are

summarized in Table 7-4 in terms of mode order, natural frequency, and mode shape

description. The first eight mode shapes are additionally shown in Figure 7-10, where the

deformation and contours represents total translation of each node. In order of ascending

natural frequency the fundamental modes are 1st bending, 2nd bending, 1st transverse

bending, 3rd bending, 4th bending, 2nd transverse bending, 1st torsion, and a mode

dominated by local skin deformation in the root trailing edge region. The fact that the

wing has four out-of-plane bending modes and two transverse bending modes before the

first torsional mode occurs as a result of the long aspect ratio of the wing combined with

the high torsional stiffness afforded by the $\pm 45°$ ply structure of the skin laminate. It

Table 7-4: Normal modes for baseline finite element model in cantilevered configuration.

Mode	Natural Frequency (Hz)	Mode Description
1	8.6	1st Bending
2	35.4	2nd Bending
3	39.0	1st Transverse Bending
4	85.2	3rd Bending
5	152.1	4th Bending
6	159.5	2nd Transverse Bending
7	164.0	1st Torsion
8	203.9	Trailing Edge Skin Mode
9	221.8	1st Chordwise Mixed
10	240.2	2nd Chordwise Mixed
11	252.6	2nd Torsion Mixed
12	259.6	Skin Mode
13	284.8	Mixed
14	297.1	5th Bending Mixed

would have been desirable to place a distinct torsional wing mode more closely interspaced with the first two wing bending modes to better simulate the conditions of a standard high-aspect wing structure; however, the physical scaling process limited options with respect to ply layup so this was accepted as a necessary deviation.

A selection of the fundamental modes for the baseline wing model in free-free configuration is given in Table 7-5 and a selection of eight mode shapes are shown in Figure 7-11, where deformation and contours again represent total translation of each

Mode 1 – 8.6 Hz (1st Bending)

Mode 2 – 35.4 Hz (2nd Bending)

Mode 3 – 39.0 Hz (1st Transverse Bending)

Mode 4 – 85.2 Hz (3rd Bending)

Mode 5 – 152.1 Hz (4th Bending)

Mode 6 – 159.5 Hz (2nd Transverse Bending)

Mode 7 – 164.0 Hz (1st Torsion)

Mode 8 – 203.9 Hz (1st Skin Mode)
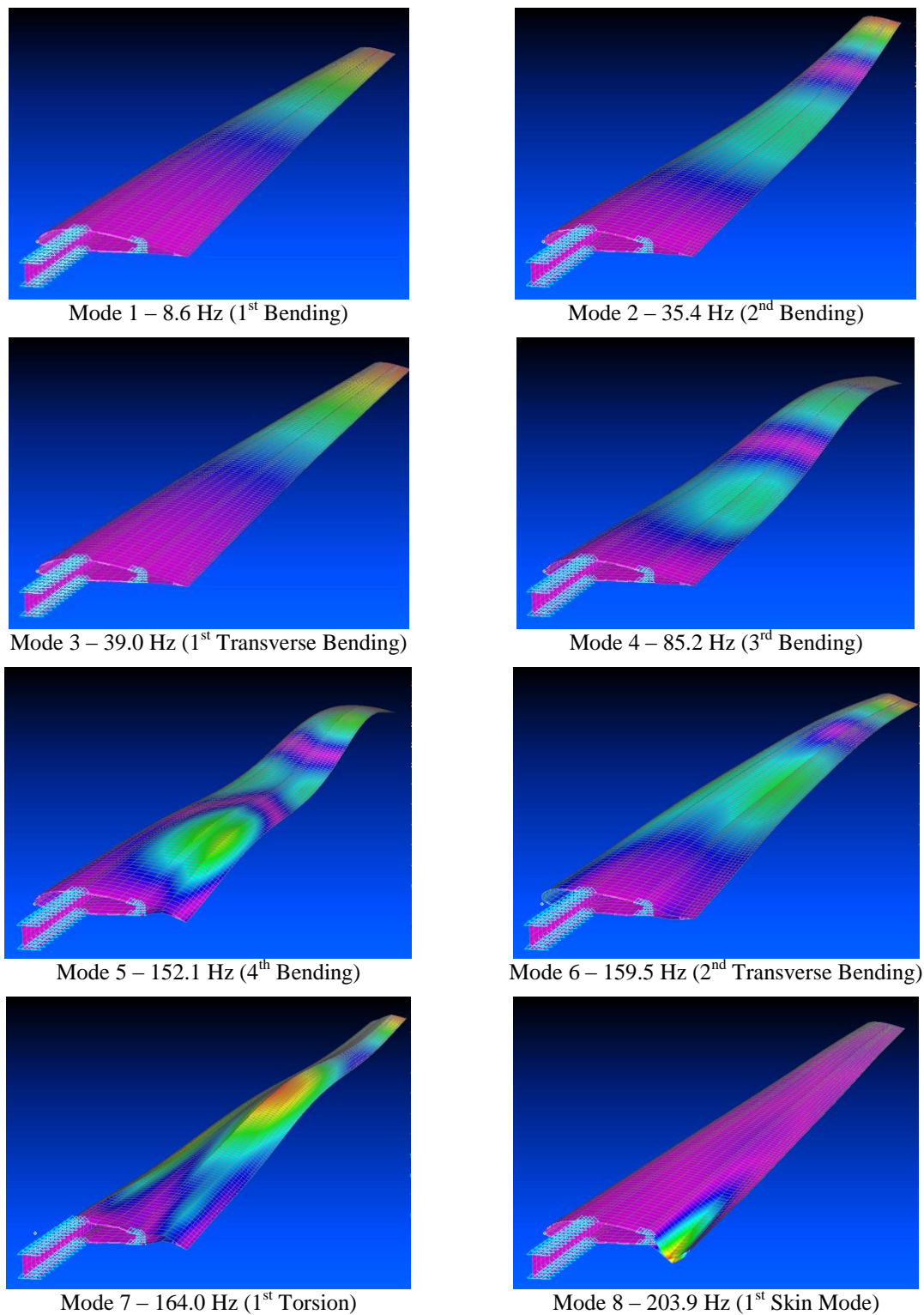
Figure 7-10: First eight modes from the baseline finite element model in cantilever configuration.

Table 7-5: Normal modes for baseline finite element model in free-free configuration.

Mode	Natural Frequency (Hz)	Mode Description
1	30.1	1st Bending
2	78.4	2nd Bending
3	111.4	1st Chordwise Bending
4	142.1	1st Transverse Bending
5	144.9	3rd Bending
6	184.8	4th Bending/Spar Mode Mixed
7	193.4	Spar Mode
8	210.8	Trailing Edge Skin Mode
9	223.1	2nd Chordwise Bending
10	231.9	Spar + Skin Mode
11	234.8	5th Bending
12	268.4	1st Torsion Mixed
13	288.4	3rd Torsion Mixed
14	292.6	Chordwise Mixed

node. Although the ordering of primary bending modes is similar to the cantilever configuration, the torsion mode is less distinct and is both higher in frequency and mixed with skin and spar deformation. Conversely, chordwise bending occurs with more freedom and at a lower frequency since the spars are free to move at the root. It should be noted that the '1st' bending/torsion modes in the free-free configuration are actually more similar to the '2nd' bending/torsion modes in the cantilevered case, with two low-deformation nodal lines instead of one. Because of a lack of constraints for force reaction,

Mode 1 – 30.1 Hz (1st Bending)

Mode 2 – 78.4 Hz (2nd Bending)

Mode 3 – 111.4 Hz (1st Chordwise Bending)

Mode 4 – 142.1 Hz (1st Transverse Bending)

Mode 5 – 144.9 Hz (3rd Bending)

Mode 6 – 184.8 Hz (4th Bending/Spar Mode)

Mode 9 – 223.1 Hz (2nd Chordwise)

Mode 12 – 268.4 Hz (1st Torsion Mixed)
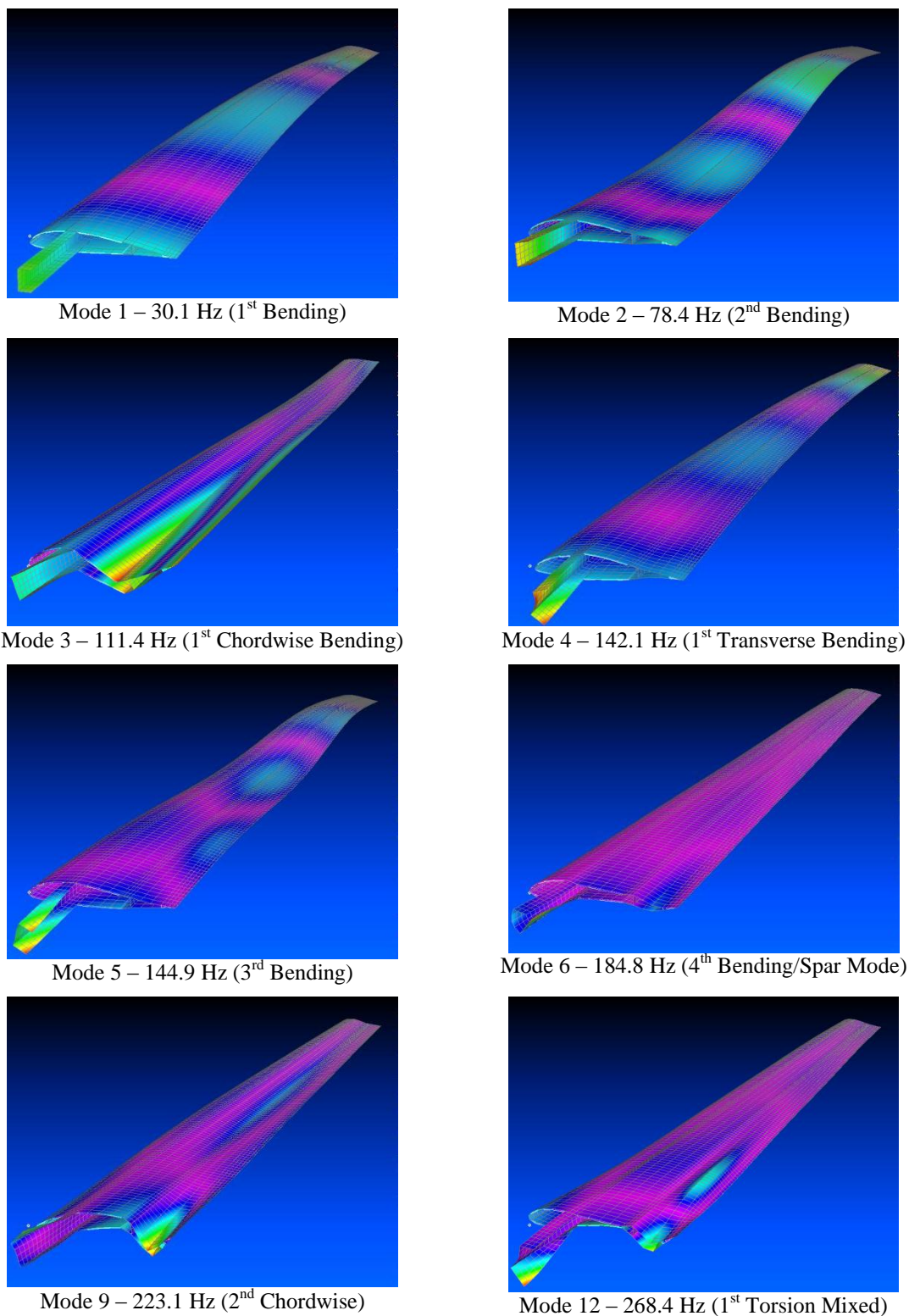
Figure 7-11: Selection of modes from the baseline finite element model in free-free configuration.

the free-free case can't support modes with a single nodal line. The free-free modes most similar to the cantilevered '1st' bending and torsion modes in terms of overall structural motion are rigid body modes at close to zero natural frequency (the six rigid body modes for the cantilever case are not presented in Table 7-5 and Figure 7-11 but do exist in the solution).

An installed physical wing will not have an idealized cantilever constraint with zero displacement and rotation at its root because of compliance in the aircraft fuselage structure. Instead, the physical boundary condition for a wing will be somewhere between cantilevered and free-free. In order to investigate wing response with a non-ideal cantilevered boundary condition the wing was modeled with undamped springs for all cantilever nodes. The springs were grounded to free-floating nodes which were then constrained in all degrees-of-freedom for the main spar cantilever connections and in translational degrees-of-freedom for the aft spar pin connections. Thus defined, the spring stiffness could be varied from a very high value, to simulate a cantilevered boundary condition, to a very low value, to simulate a free-free boundary condition. The finite element model with root springs is shown in Figure 7-12 and a description of the cases used for comparison is given in Table 7-6. The spring stiffnesses were varied from values of 10^{10} N/m to 1 N/m in power increments of 2 for all degrees-of-freedom. The results, plotted in Figure 7-13, are given in terms of 7 primary modes of the structure, including the first four bending modes, 1st torsion, 1st chordwise bending, and the skin mode
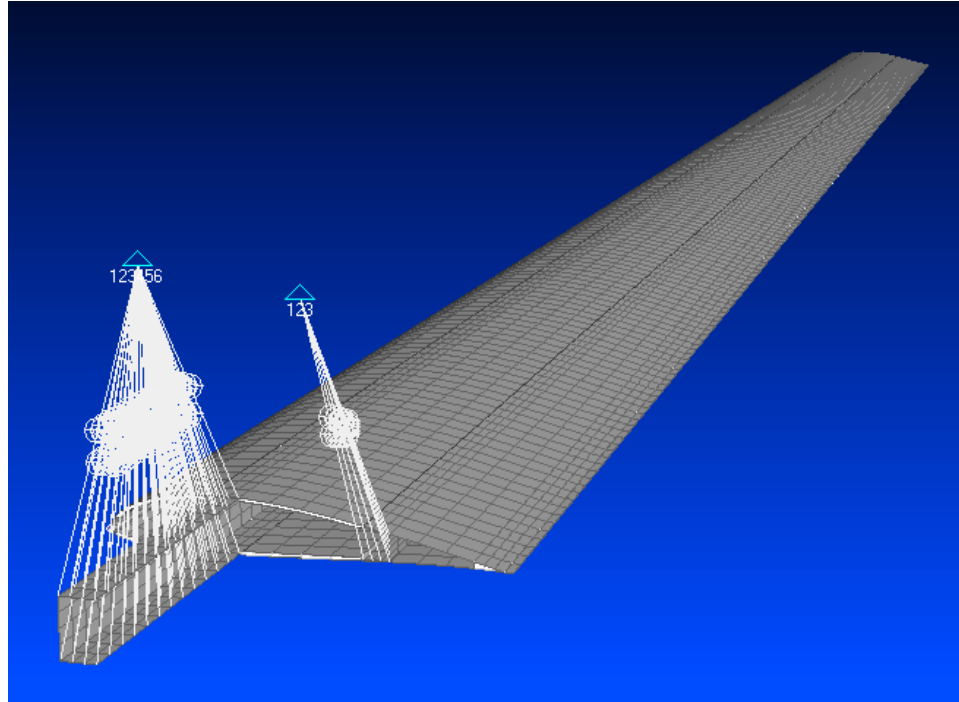
Figure 7-12: View of wing root springs for boundary condition study.

Table 7-6: Description of cases for boundary condition study.

Case	Spring Stiffness (N/m)	Boundary Condition Description
1	∞	Cantilevered
2	10^{10}	Spring Order 10
3	10^{8}	Spring Order 8
4	10^{6}	Spring Order 6
5	10^{4}	Spring Order 4
6	10^{2}	Spring Order 2
7	1.0	Spring Order 0
8	0	Free-Free

characterized by local deformation of the root trailing edge. The bending and torsion

mode naming convention used for all cases of the boundary condition study is based on

that of the cantilevered configuration—i.e., with the 1st mode for each type characterized

by a single nodal line—to allow smooth tracking from the cantilevered to free-free

configurations. The descriptive numbering for modes approaching a free-free

configuration is therefore offset by one from that presented in Table 7-5 and Figure 7-11

since the 1st bending and torsion modes approach rigid body motion as spring stiffness

decreases. Figure 7-13 shows that 2nd and higher out-of-plane bending modes are not

greatly influenced by boundary condition stiffness; however, the torsion and chordwise
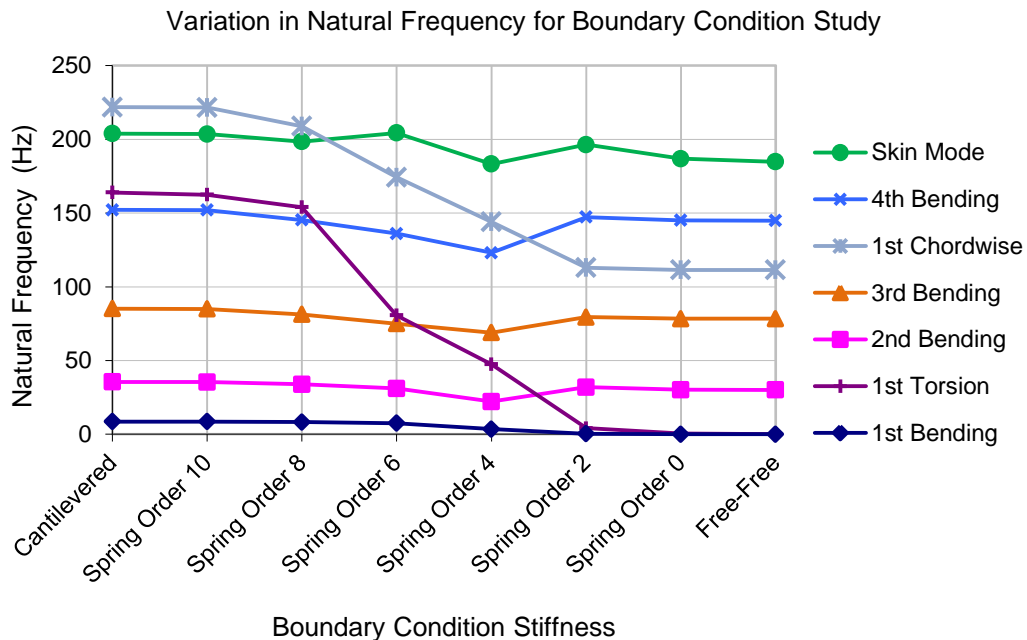
Figure 7-13: Summary of natural frequencies for boundary condition study with boundary condition stiffness varying from cantilevered to free-free.

bending modes decrease dramatically with boundary condition stiffness, with the 1st torsion mode in particular decreasing in frequency from 164 Hz to approximately zero and the 1st chordwise bending mode decreasing by a factor of two from 222 Hz to 111 Hz. The 1st bending mode additionally decreases in frequency to approximately zero, as expected. A notable observation is that the bending modes all trend slowly downward until the 1st bending mode is mode is dominated by rigid body motion (at spring order 2), at which point the remaining bending modes increase in frequency slightly to values that then remain approximately constant as the spring stiffness is decreased to the free-free configuration. The change in trending is a result of the primary force reaction mechanism switching from being dominated by the spring stiffness to being dominated by the inertia of the unconstrained root region of the structure, with a corresponding alteration in mode shapes and natural frequencies. This explanation is supported by the observation that mode shapes in this spring stiffness region are less clearly defined in terms of either the cantilevered or free-free descriptions and approach more coupled representation.

The observed trending of torsional natural frequency towards zero with decreasing boundary condition stiffness represents a real-life risk for operational aircraft in the form of aeroelastic instability—known as *divergence* if the instability is static and *flutter* if the instability is oscillatory. The lift generated by a wing depends on angle-of-attack (i.e., angle of the wing chord relative to the direction of chordwise air flow), with lift generally increasing with angle of attack and vice versa. The angle-of-attack in turn is affected by activity of the torsional mode of the wing. In a properly designed wing

operated within design envelopes the internal elastic and damping forces will effectively

react the aerodynamic lift and torsional rotation forces to create a stable system.

However, if the primary torsion mode couples with a primary bending mode of the wing

the interaction of wing bending and angle-of-attack can lead to greatly increased external

forces and divergence or flutter. Divergence is characterized as the condition where static

lift forces increase the wing's angle-of-attack, creating further lift and rotation until the

aerodynamic forces exceed internal elastic forces and the structure fails—essentially the

wing twists off of the aircraft. In the case of flutter, the internal elastic forces react the

increasing lift on the upward vibrational bending cycle but in doing so cause negative

wing rotation and increasingly negative lift on the downward bending cycle. If the lift is

in phase with the bending oscillations the result is a constructive feedback loop that can

rapidly overcome internal damping forces and lead to structural failure after several

cycles. The current boundary condition study shows that, even for a wing with well

separated primary torsion and bending modes in the idealized cantilever condition, the

modes will couple as the boundary condition softens leading to conditions for instability.

Based on the results in Figure 7-13, the 1st torsion mode appears to cross the 2nd

bending mode for the current wing model at a root spring stiffness of approximately 10^3

N/m. This is additionally the region where a shift in the trending of bending natural

frequencies is observed. The model was run at with spring stiffness set to 10^3 to further

investigate the modes and coupling under a mixed cantilever/free-free boundary

condition. The modal results, presented in terms of natural frequencies and mode shapes

in Figure 7-14, show significant modal coupling. The mode corresponding to 1st bending

in the cantilever case is now a pure spring bending mode at 1.45 Hz with negligible

elastic bending in the wing structure. Rigid torsional rotation of the wing occurs in two

modes—the first at 12.8 Hz with the axis of rotation near the center of gravity of the wing

structure and the second, corresponding more properly to 1st torsion in the bending case,

at 25.9 Hz. The mode that turns into 2nd bending in the free-free configuration is

dominated by 1st cantilevered bending mode elastic deformation at 19.3 Hz. Mode 6 is

heavily coupled between 2nd bending and 1st torsion and, at 27.3 Hz, the natural

frequency is very close to the crossing point between 1st torsion and 2nd bending observed

in Figure 7-13. If the current wing was flown and lower rigid bending and torsion modes

were adequately constrained, this coupled mode could be a dangerous case for flutter.

The coupled modes at this spring stiffness level also corroborate the change in bending

mode trending noted previously in Figure 7-13.

7.3.3   Analytical Damage Studies

The impact of spar-skin disbond damage starting from the root was investigated

by running several cases with increasing levels of damage. Damage was applied to the

bottom spar-skin bondline based on the assumption that operational fatigue would

manifest first on the tension side of the wing. The damage was modeled by disconnecting

the spar-skin rigid links in the regions shown, with each row of spar-skin rigid links

Mode 2 – 1.45 Hz (1st Bending, Rigid)

Mode 3 – 12.8 Hz (1st Torsion, Rigid 1)

Mode 4 – 19.3 Hz (Coupled 1st/2nd Bending)

Mode 5 –25.9 Hz (1st Torsion, Rigid 2)

Mode 6 – 27.3 Hz (Coupled Bending/Torsion)

Mode 6 – 58.3 Hz (2nd Bending)

Mode 8 – 100.0 Hz (3rd Bending)

Mode 11 – 161.9 Hz (4th Bending)
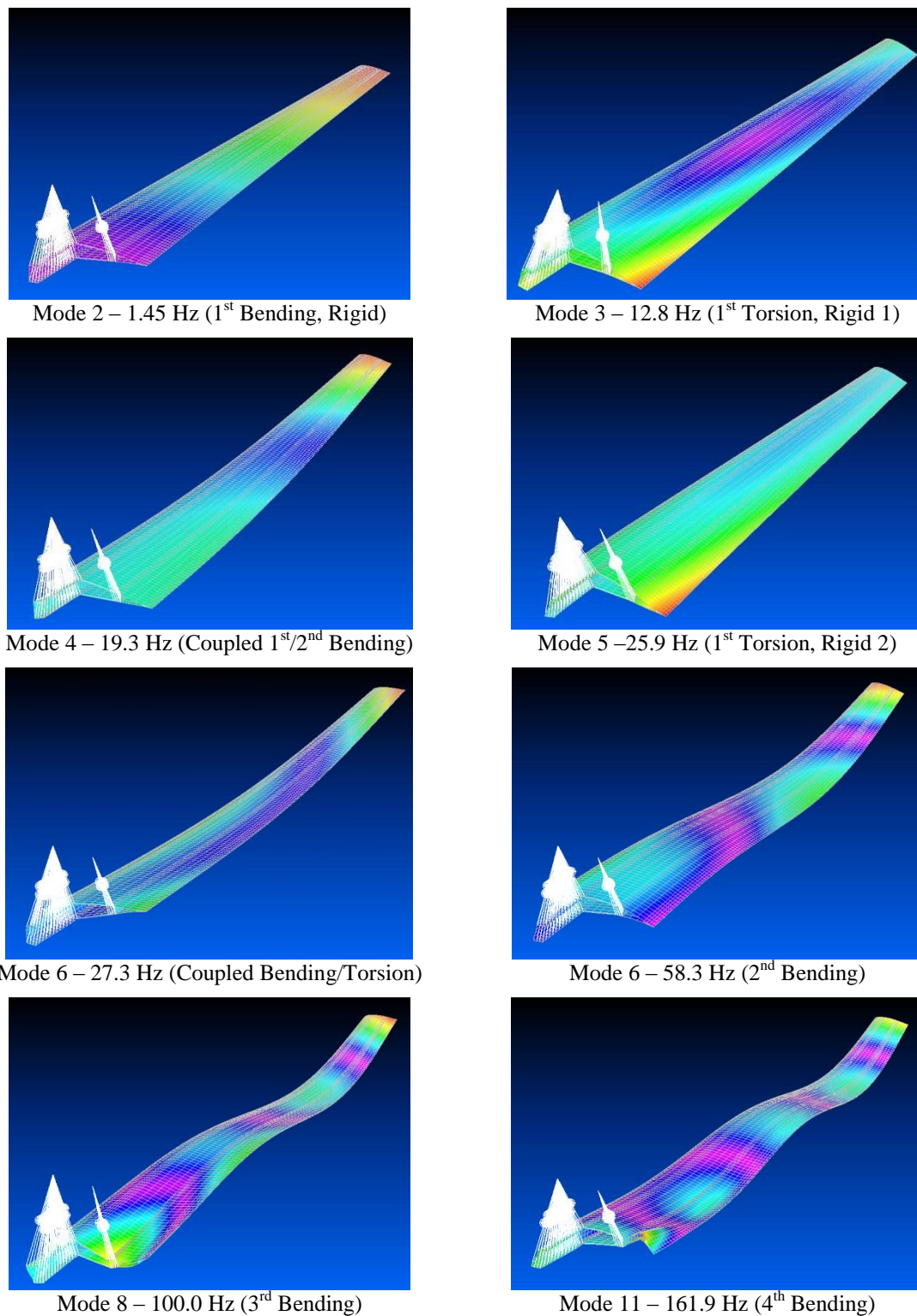
Figure 7-14: Modal results from the baseline model in mixed cantilever/free-free configuration.

increasing the effective damage length by approximately 0.025 m when disconnected.

The following five damage cases were analyzed:

1. 0.025 m (1 row of rigid links removed)

2. 0.05 m (2 rows of rigid links removed)

3. 0.10 m (4 rows of rigid links removed)

4. 0.20 m (8 rows of rigid links removed)

5. 0.41 m (16 rows of rigid links removed)

Figure 7-15 shows the five damage cases overlaid on the wing mesh viewed from the bottom. For each damage case the appropriate number of rows of spar-skin rigid links were disconnected and the model run for undamped normal modes. Seven of the primary
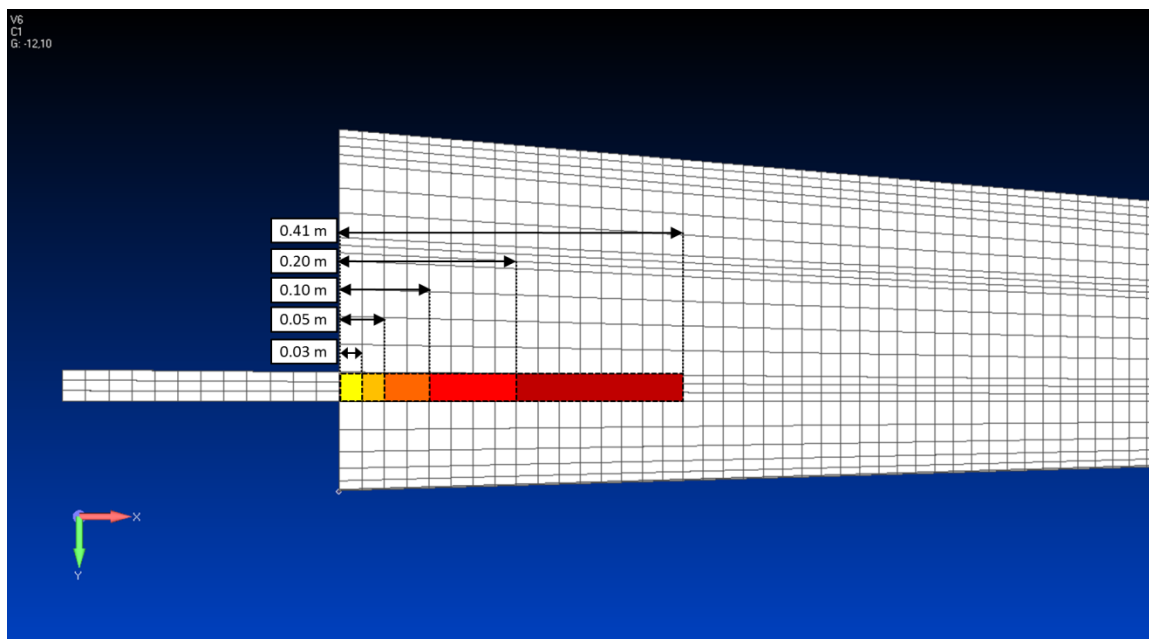
Figure 7-15: Summary of spar-skin disbond damage cases (wing viewed from bottom).

wing modes—1st bending, 2nd bending, 3rd bending, 4th bending, 1st torsion, the first skin

mode, and 1st chordwise bending—were then tracked across damage cases. The change in

response for each case compared to the undamaged cantilevered response was evaluated

based on change in natural frequency, expressed as the absolute value percentage change,

and mode shape modal assurance criterion, calculated from 80 normal (z-axis) degrees of

freedom from the bottom external wing surface such as would be measured during

vibration testing on a real wing structure. The nodes used to calculate the modal

assurance criterion are shown in Figure 7-16.

Results from the spar-skin disbond damage study are presented in terms of change

in natural frequency in Figure 7-17, modal assurance criterion in Figure 7-18, and

trending of natural frequency over increasing damage size for each mode in Figure 7-19.

It can be seen that the change in natural frequency is spread fairly uniformly across the

observed modes, with changes ranging from a 0.16% decrease in the skin mode to a
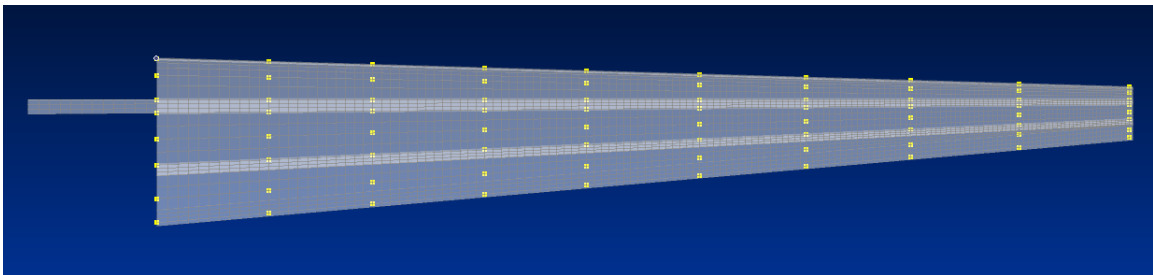
Figure 7-16: Bottom wing skin nodes used to calculate modal assurance criterion values for damage studies.
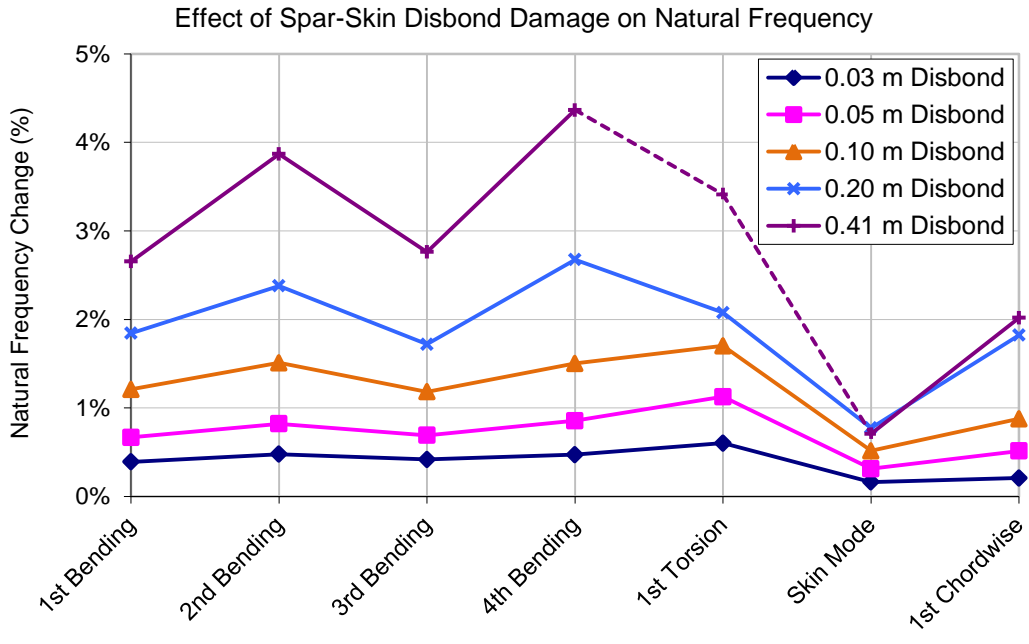
Figure 7-17: Change in natural frequency for select modes over spar-skin disbond cases (dashed line indicates mode shape varying from description).
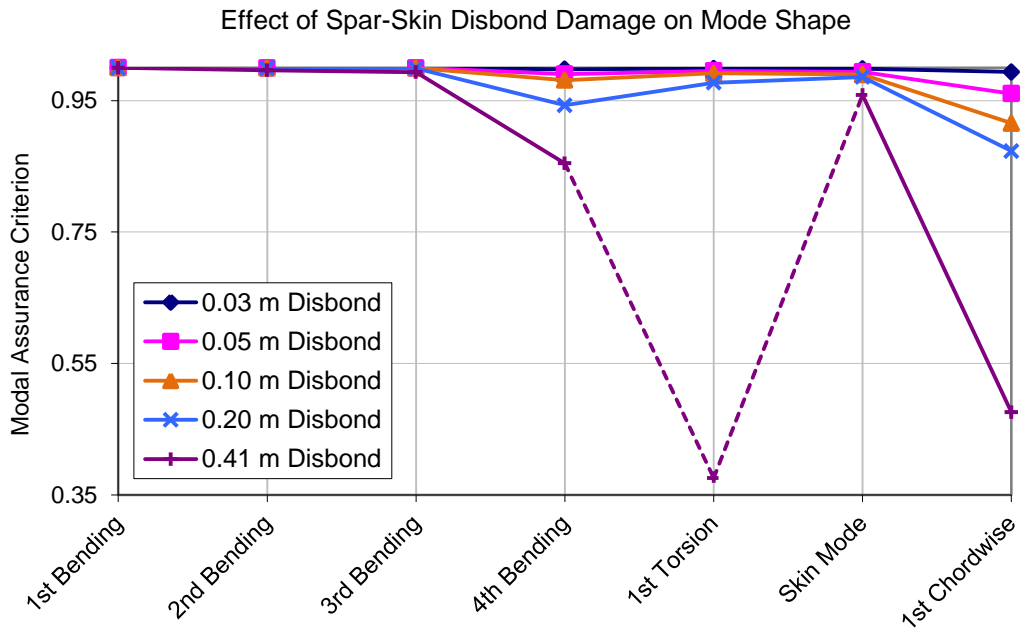
Figure 7-18: Modal assurance criterion values for select modes over spar-skin disbond cases (dashed line indicates mode shape varying from description.

Variation in Natural Frequency with Spar-Skin Disbond Length
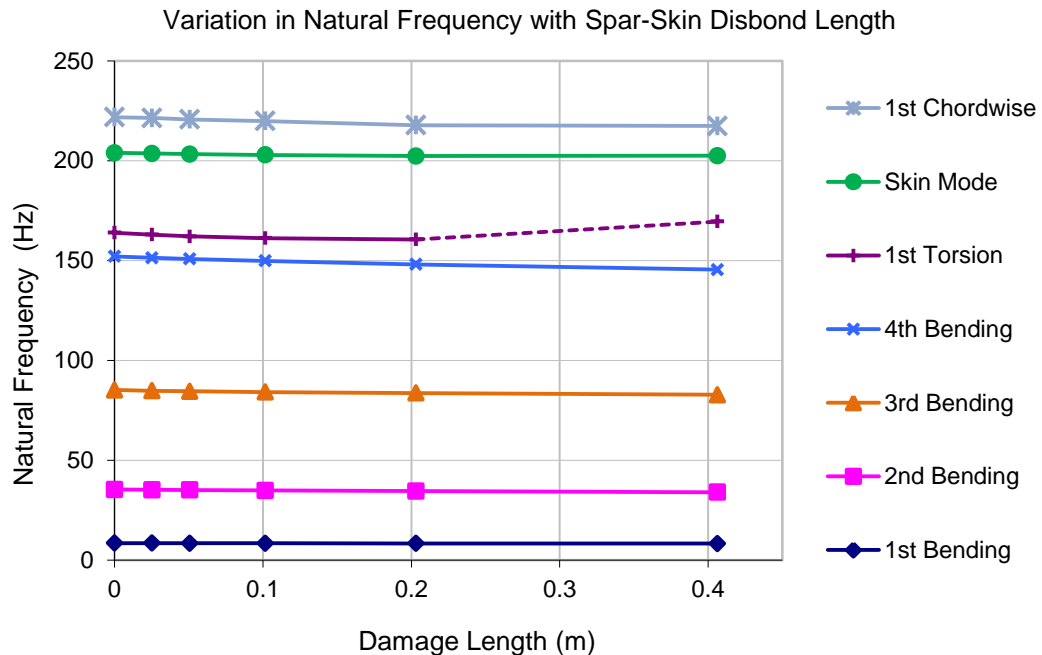
Figure 7-19: Trending of select wing modes over increasing spar-skin disbond length in baseline finite element model (dashed line indicates mode shape varying from description).

4.73% decrease in the 4th bending mode. The torsion mode was affected on the same order as the bending modes but did not exhibit pronounced changes of the sort that would present a risk for flutter. It should be noted, however, that in the 0.41 m damage case the torsion mode shape was significantly altered by the damage with the torsional activity coupled with local deformation of the disbanded skin region (indicated with a dashed line in the results figures). The coupled torsion mode increased in frequency compared to frequency decreases in all of the other cases. With the exception of the coupled torsional mode and 4th bending mode in the 0.41 m damage case, the damage produced relatively low changes in mode shape, with modal assurance criterion values ranging from 0.95 to

1.0. These results together show that the localized damage softens the system response but does not have a high impact on the global mode shapes, even as the damage gets large. The discrepancy occurs because the natural frequency is heavily dependent on localized strain energy activity at the wing root, where the damage is located, but overall mode shape is primarily influenced by distributed system properties, which are not highly impacted by the localized damage.

A second set of damage cases was analyzed to study the effect of skin-core disbonds in the plane skin regions of the wing. This sort of damage can result from blunt force impact on the plane composite sandwich structures which causes the core to crush, degrade, and/or disbond from the skin while leaving the skin laminates intact. Operational aircraft see many opportunities for impact to their external primary structures during ground operations. Blunt-force impact in particular is dangerous in practice for composite aircraft since even large internal damage cases can be invisible from the exterior and may go undetected.

Five damage cases were introduced sequentially by disconnecting rigid links between the inner and outer sandwich structure laminates and core from the top wing skin in the regions shown in Figure 7-20. The top wing was chosen because of the greater chance of a falling object causing the damage as opposed to the impact coming from underneath the wing. In each case, rigid links were disconnected in rows of three nodes leaving the skin and core uncoupled across the entire width of the between-spar sandwich
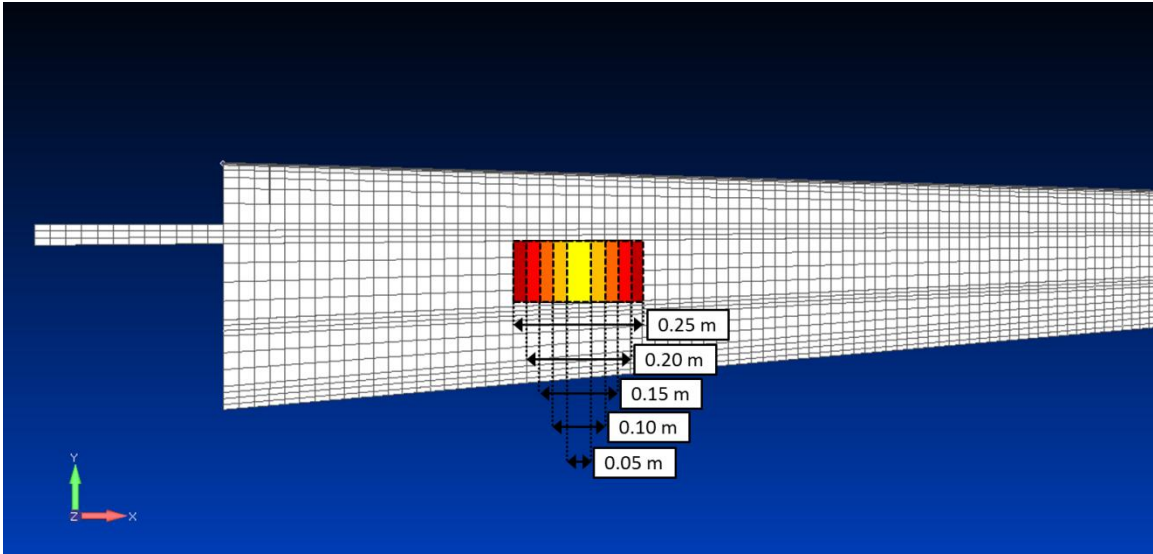
Figure 7-20: Summary of laminate-core disbond damage cases (wing viewed from top).

region (approximately 0.10 m in width). The first row of nodes disconnected was situated

approximately 0.64 from the wing root and for each subsequent damage case two rows of

nodes were disconnected spreading out from the initial row. The resulting damage cases

were rectangular in shape with width approximately 0.10 m and length as follows:

1. 0.05 m (1 row of rigid links removed)

2. 0.10 m (3 rows of rigid links removed)

3. 0.15 m (5 rows of rigid links removed)

4. 0.20 m (7 rows of rigid links removed)

5. 0.25 m (9 rows of rigid links removed)

As with the spar-skin disbond damage study the impact on system response was

evaluated based on change in natural frequency, expressed as the absolute value

percentage change, and mode shape modal assurance criterion, calculated using the

normal degrees of freedom from the 80 bottom external wing surface nodes shown in

Figure 7-16.

The results are presented in terms of in terms of change in natural frequency in

Figure 7-21, modal assurance criterion in Figure 7-22, and trending of natural frequency

over increasing damage size for each mode in Figure 7-23. The laminate-core disbond

damage cases show a lower-level impact to the system modes compared to the spar-skin

damage cases, despite similar or larger overall areas of damage in each case. Natural

frequencies for the seven modes of interest are decreased by at most 1.6% for the
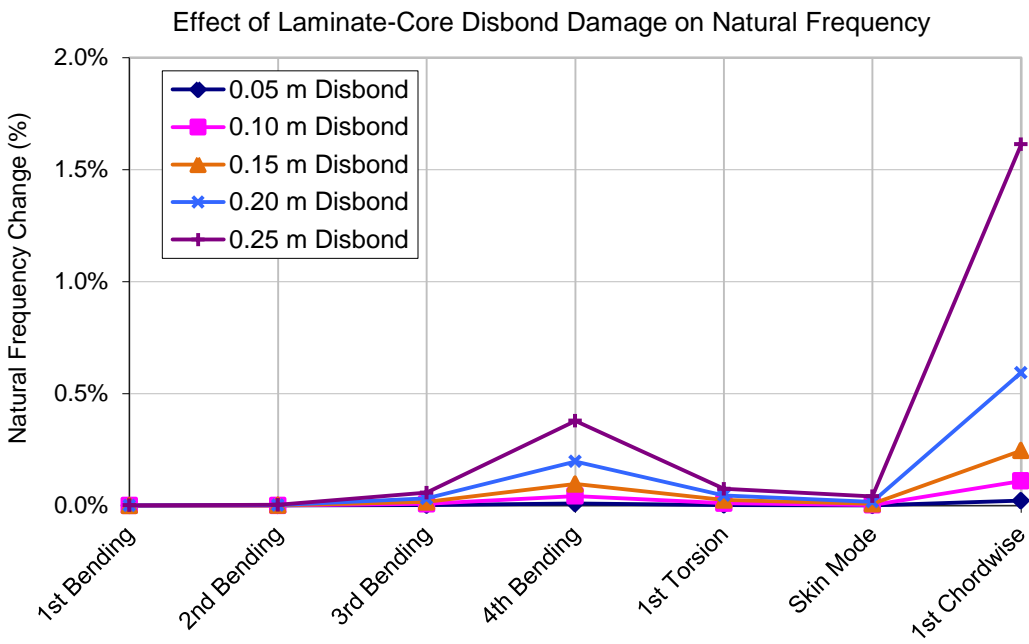
Figure 7-21: Change in natural frequency for select modes over laminate-core disbond cases.

Effect of Laminate-Core Disbond Damage on Mode Shape
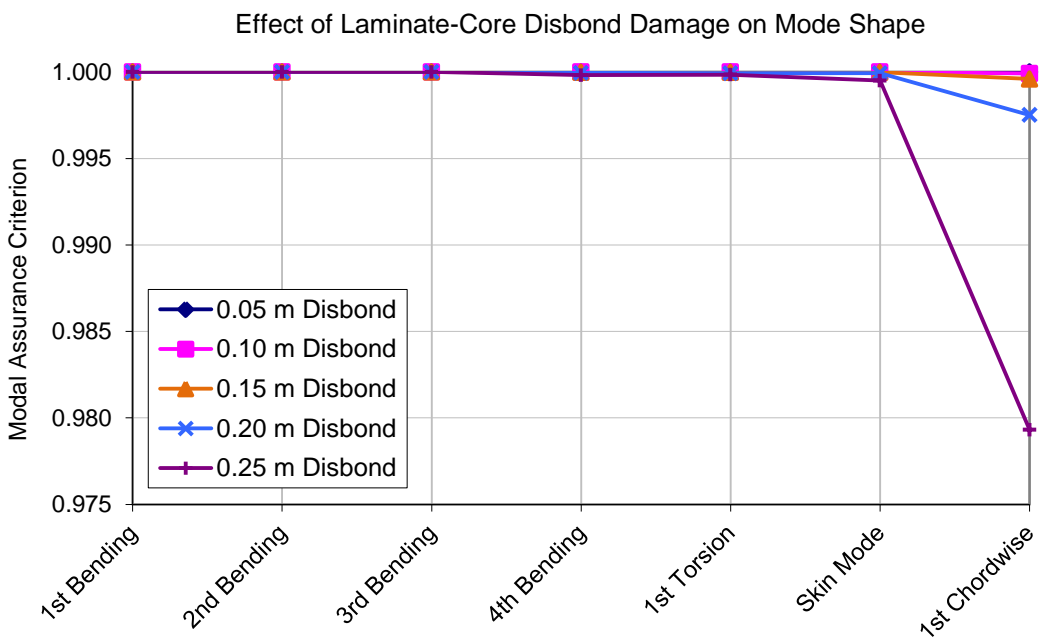
Figure 7-22: Modal assurance criterion values for select modes over laminate-core disbond cases.

Variation in Natural Frequency with Laminate-Core Disbond Length
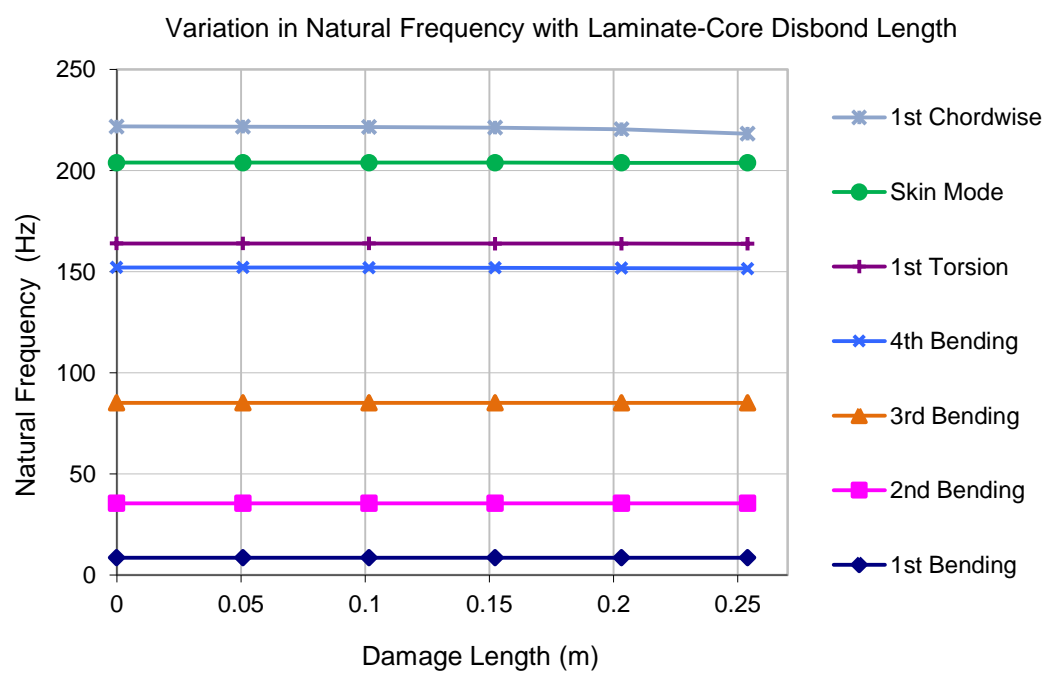
Figure 7-23: Trending of select wing modes over increasing laminate-core disbond length in baseline finite element model.

chordwise mode and at most by 0.4% for the other modes. The global mode shapes (as measured on the bottom skin) are minimally altered, with the lowest modal assurance criterion value calculated to be 0.98 on the 1st chordwise bending mode and most other modes seeing effective modal assurance criterion values of unity. The primary reason for these relatively small changes is because the damage cases do not interact with regions of high strain energy in the structure, such as spar regions at the root or in-plane laminate properties in the external wing skin laminates. In practice, this type of damage will impact local bending of the otherwise unsupported wing skins and will thus affect the ability for the wing to react aero loads and to maintain airfoil shape in operation—both consequences which will affect aircraft performance and could lead to full system failure in the event that operational loads cause the damage to propagate. The local nature of the damage will, however, show increasingly greater impact on higher order, especially those related to bending of the sandwich skin regions.

Both of the studied damage scenarios will change natural frequencies and mode shapes to some extent. The physical damage, however, will also change damping characteristics in the region of damage and will cause new local modes to develop. The result is that, even for the smaller damage cases, the system frequency response functions will be impacted, especially in regions near the damage. The current damage detection algorithm can therefore be expected to perform well on these and similar damage cases for the composite wing structure.

7.4   **Experimental Manufacturing**

The physical test-bed scaled wings were manufactured at UCSD's Composites and Aerospace Structures Laboratory by the author with help from a rotating team of UCSD undergraduate and graduate students. The laminates were cured at Pratt & Whitney Composites in San Diego, CA. After curing, the components pieces were individually vibration tested in free-free configuration and quasi-static coupon tests were conducted to produce material properties for the material systems.

7.4.1   Manufacturing of Component Pieces and Assembly

All laminate pieces were made from a Hexcel graphite-epoxy prepreg system (Toray M46J graphite fibers with Hexcel HexPly 6376 epoxy resin matrix) in a 5-harness satin weave, with the bulk material stored at -14F in 1.52 meter wide rolls. The skins were built using Hexcel Nomex honeycomb core (HRH-10-1/8-3.0) co-cured with Cytec 1515 epoxy film adhesive through their sandwich areas. The components were cured using one-sided aluminum molds which were machined from purpose-built CAD reference files. Figure 7-24 shows the skin molds which were each fabricated from two sealed pieces because of part-size limitations of the mill.

Figure 7-24: Machined aluminum molds for layup and cure of the composite wing skins.

The lay-up manufacturing process for all laminate components proceeded through the following steps:

1. Prepreg plies were cut to shape using plastic templates and razor blades, with backing paper and protective surface film layers retained, as shown in Figure 7-25.

2. Full-size sandwich structure core pieces were cut to shape out of single pieces using templates and a hand-held razor. The edges were cut with a 45° chamfer for laminate close-outs as shown in Figure 7-26.

3. Film adhesive pieces, one for each side of the sandwich core, were cut using straight-edges and a razor with backing paper and protective surface film layers retained on the pieces.

Figure 7-25: Wing skin laminate plies being cut to shape using a custom-made plastic template.

4. Mold surfaces were cleaned using isopropyl alcohol and then prepared using 3 to 5 coats of Chemlease 41 mold release agent and allow to dry.

5. Vacuum bagging material cut to shape, including peel-ply, perforated release film, breather material, and vacuum bagging material.
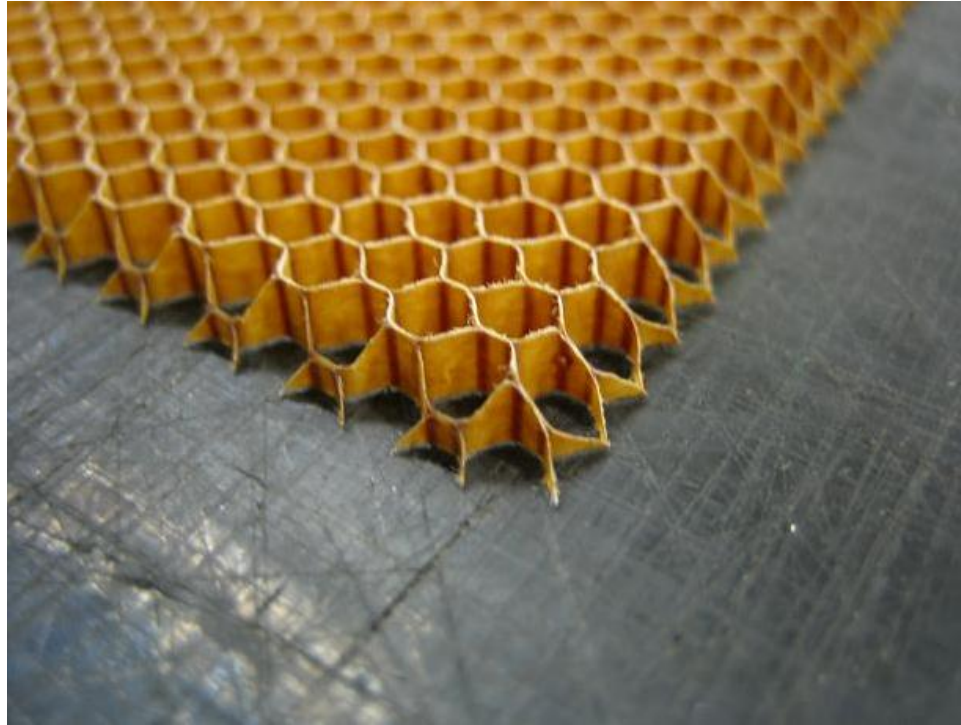
Figure 7-26: Close-up view of Nomex honeycomb sandwich core with chamfered edges.

6. The first ply for each component piece were applied to the mold by aligning the pre-cut pieces along a common edge, removing backing paper, and pressing the ply down from the alignment edge across the full surface to remove large pockets of air. Edges were compressed and the ply smoothed using hand-pressure as the play was laid down to prevent bridging and air pockets. For the lower wing skin the leading edge was formed around the joggle tool bolted to the edge of the mold, as shown in Figure 7-27, to form the overlapping leading edge bondline.

Figure 7-27: Close-up view of bottom wing skin ply formed against the leading-edge joggle tool.

7. Vacuum sealant tape (a.k.a., chromate) was applied around the edges of the mold with backing paper left intact on the exposed surface. Vacuum cup base pieces were installed between the breather material and vacuum bag on an exposed portion of the mold inside the sealant tape boundary. Debulking was then applied by applying peel-ply, breather, and temporary vacuum bag onto the ply stack; removing the sealant tape backing paper; loosely sealing the vacuum bag to the mold; and drawing vacuum for 5 minutes. This step was applied after application of every one to three laminate plies.

8. After each debulking procedure the vacuum layers were removed, the layup process continued. For the sandwich skins, after application of the first ply the core alignment tool was installed, as shown in Figure 7-28. The lower film adhesive layer, core layer, and top film adhesive layer were then applied for the fore and aft sandwich regions, and alignment tool removed. The correctly placed core layers are shown in Figure 7-29 for the top wing skin. For the spars, the built-up 0° spar caps were added to the laminates before addition of the final full ply, as shown in Figure 7-30 for the main spar (with the bare aft spar mold shown to the right).

9. After the final ply was added to each component laminate, thermo-couple wires were installed by butting several millimeters of exposed thermo-couple wire up against the edge of the laminate stack in several distributed locations. Several centimeters of strain relief slack were retained inside the vacuum bag area and the insulated thermocouple wire was sandwiched against the sealant tape with an additional piece of sealant tape. The exterior thermocouple wire casing was stripped through the sealing region in each case to prevent a leak path. The top ply surface film was removed and peel ply, release film, and breather added to the laminate surface. Vacuum cup bases were installed on additional padding layers of breather in distributed locations around the layup. The final cure vacuum bag was applied to the mold, sealant tape backing paper removed, and the vacuum bag sealed to the exposed sealant tape with
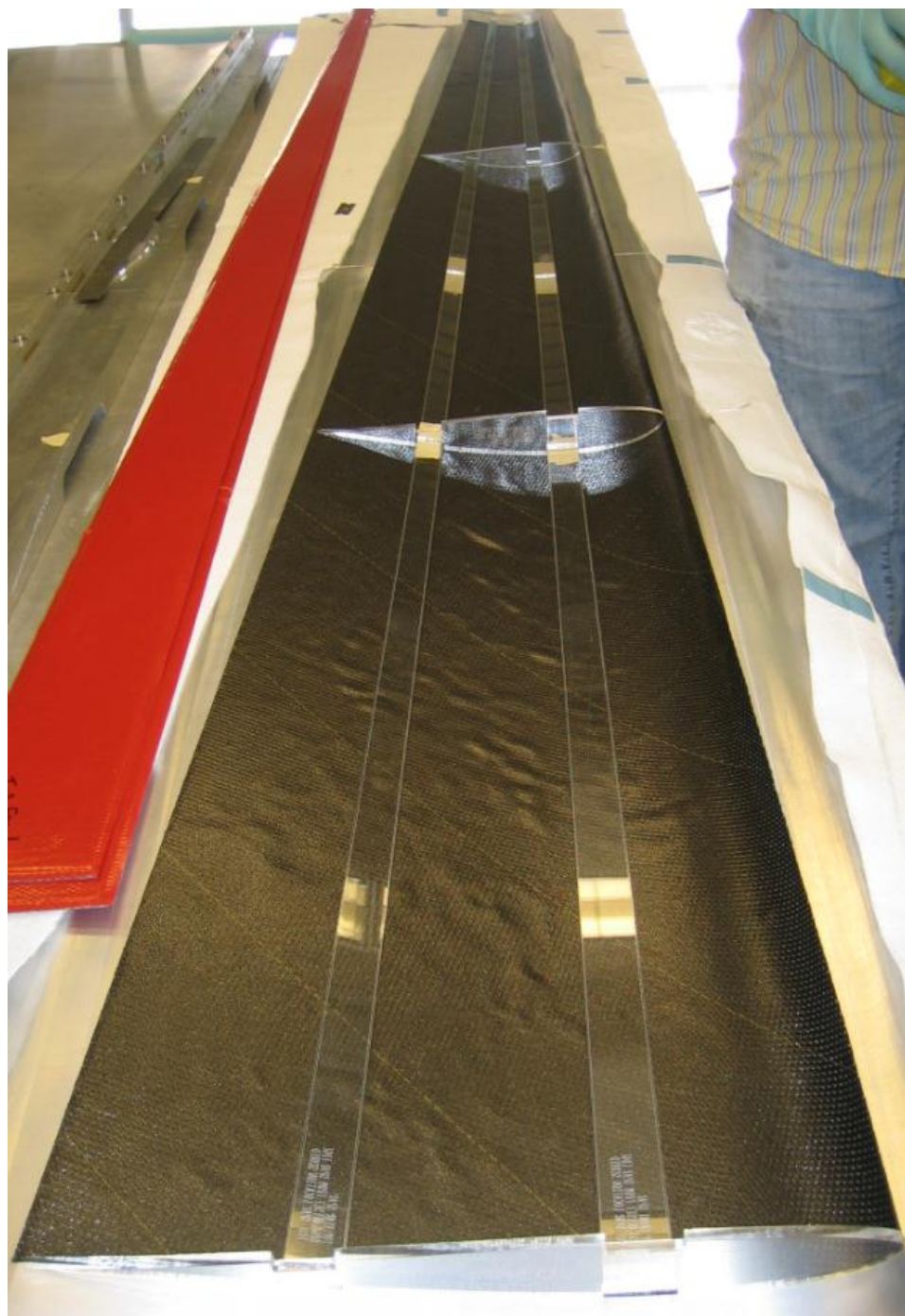
Figure 7-28: Top wing skin core location tools temporarily placed on laminate during layup.
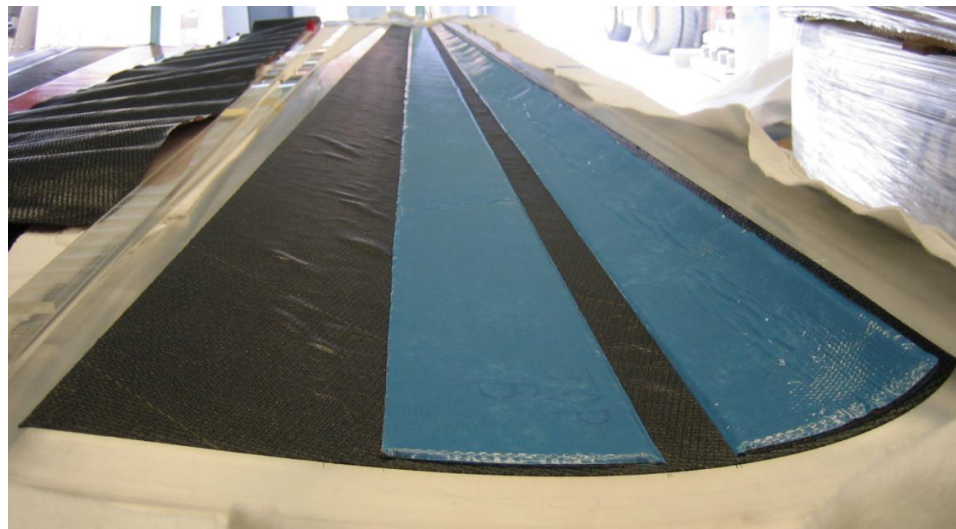
Figure 7-29: Top wing skin core sections with honeycomb encased in film-adhesive after placement and before addition of the top sandwich ply.
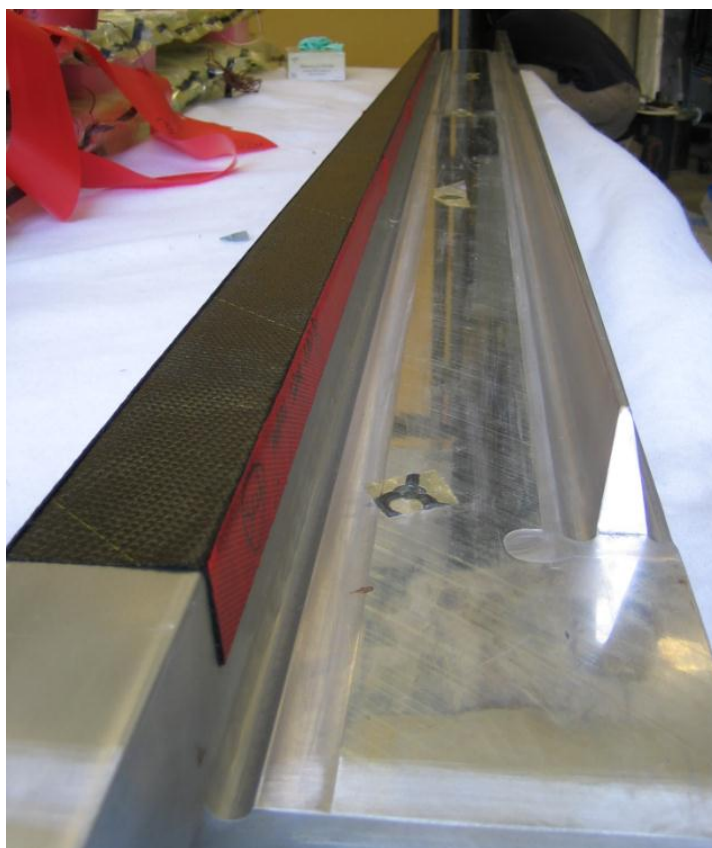
Figure 7-30: Main spar laminate on the mold on the left side with the bare aft spar mold on the right during layup.

regularly spaced 'rabbit-ear' folds for strain relief in the vacuum bag to prevent bridging of the vacuum bag. In some cases, the vacuum bag was applied as an folded envelope of the entire mold with the bag then sealed to itself instead of to the mold (envelope bagging).

10. Vacuum was applied to each complete mold-laminate setup slowly while ensuring all plies and vacuum cure materials remained aligned properly as the vacuum settled.

11. Vacuum carrying capability was tested for each part using a vacuum gauge on one of the vacuum ports, with vacuum deemed to be adequate when the part would at a maximum lose 5 in-Hg in 5 minutes. In cases of inadequate vacuum the leaks were investigated using an acoustic leak detector and either fixed or the vacuum bag replaced until adequate vacuum could be achieved. The parts were then stored under vacuum until transportation and cure.

Cure was performed for all pieces in a large autoclave at Pratt & Whitney Composites in San Diego, CA. The cure location was several miles from the layup location and the molds were transported via covered truck and then reattached to vacuum lines at the cure facility. Once placed together in the autoclave, shown in Figure 7-31, autoclave vacuum lines were attached to the molds and vacuum holding capability verified through the autoclave vacuum system. Following manufacturer instructions for the laminate system, each cure was performed at 180°C and 0.62 MPa with controlled

Figure 7-31: Wing components being prepared for cure in an autoclave at Pratt & Whitney Composites.

ramps and a dwell time of 2 hours. After internal autoclave pressure had reached 1 atm

the vacuum lines were vented to the atmosphere to allow gasses produced during the

exothermic resin cure process to escape from the laminates. After completion of the cure

cycle the cooled parts, still bagged on the molds as shown in Figure 7-32, were removed

from the autoclave and transported to UCSD. The spots which can be seen on cured parts

in Figure 7-32 are from excess laminate resin bleeding through the perforated release film

and into the breather material during cure. This process increases fiber volume fraction

and, therefore, structural performance of the parts. The cured wing component pieces

were finally removed from the molds and the resin flashing lightly sanded from the

Figure 7-32: Bagged wing components on molds post-cure.

laminate edges to reduce excess mass and make the parts safe for handling. Examples of the completed component pieces are shown along with an assembled wing in Figure 7-33. Measuring representative pieces with calipers showed that the prepreg plies cured to an average of 0.25 mm thick each and the honeycomb remained approximately 3.0 mm thick.

After modal testing of the individual components—described in Section 7.4.2—the components were assembled in a secondary adhesive bonding step. Before starting assembly a small constant right-angle triangle cross section wedge 0.036 m wide was cut from Rohacel 51IG foam to provide a bonding surface down the length of the trailing edge. Bonding of the wing components was then accomplished through the following procedure for each wing.

1. All laminate bonding surfaces were prepared by wiping with isopropyl alcohol using lint-free rags, scrubbing with Scotchbrite scouring pads, and wiping again with isopropyl alcohol until all surfaces could pass a water break test. The water break test was administered by wiping a small quantity of distilled water on the surface and verifying that the water wets evenly out across the surface without beading. Beading of the water indicates oil-based contamination on the bonding surface down to the microscopic level which can prevent an adequate bond. Regions of the bonding surface failing the

Figure 7-33: An assembled wing (far left), and four component wing pieces (from left-to-right): top skin, main spar, aft spar, bottom skin.

water break test were subject to additional cleaning and scouring using the same isopropyl alcohol wipe, Scotchbrite scour, isopropyl alcohol wipe process until they passed the water break test.

2. Both sides of all bonding surfaces, including those of the trailing edge foam wedge, were coated with a layer of layer Hysol EA9394 structural adhesive approximately 1 to 3 mm thick applied using flat wooden applicator sticks, as shown in Figure 7-34.

3. The parts were assembled using the lower wing skin mold as a tool, as shown in Figure 7-35, and sandbags applied on top of the to the top wing skin to provide constant distributed compressive force. The bonding assembly was left to cure for at least 24 hours to reach handling strength and at least 7 days to reach full structural strength.

After curing to at least handling strength the assembled wing was removed from the bonding assembly and excess adhesive flashing sanded from exposed boundaries where required. Views of completed wings are shown in Figure 7-36 and along with the author in Figure 7-37. The final assembled wing mass was measured to be approximately 2.12 kg for each wing.

Figure 7-34: Application of structural adhesive onto wing component bondlines.
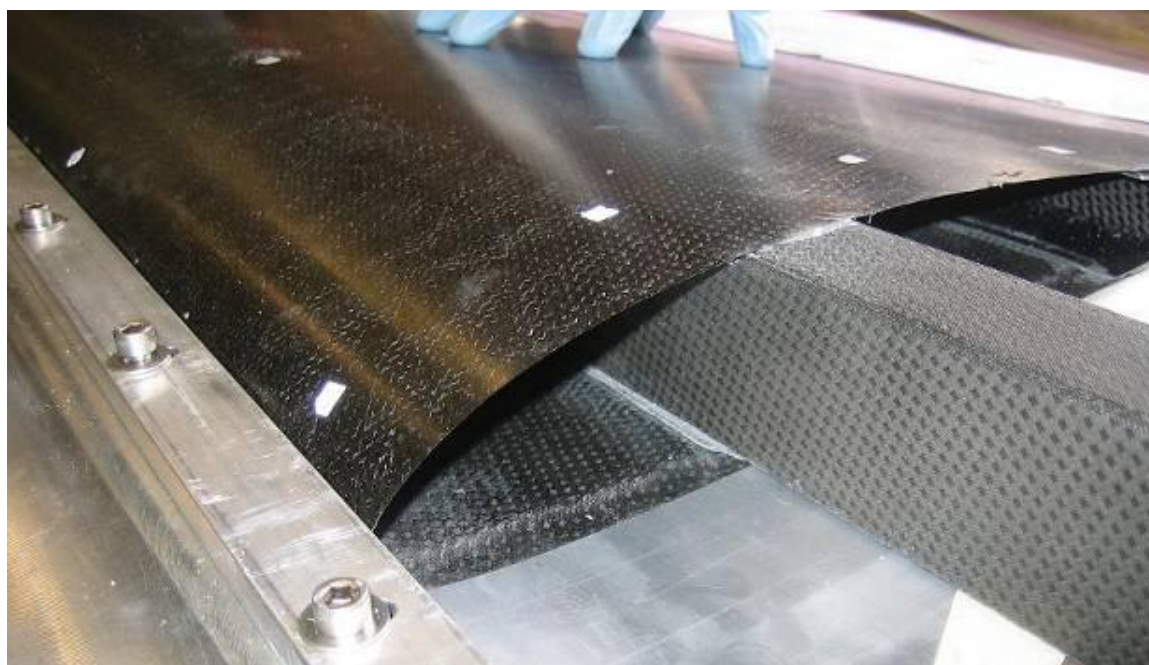
Figure 7-35: Assembly of component pieces with adhesive applied into the bonding assembly.

(a)

(b)

(c)
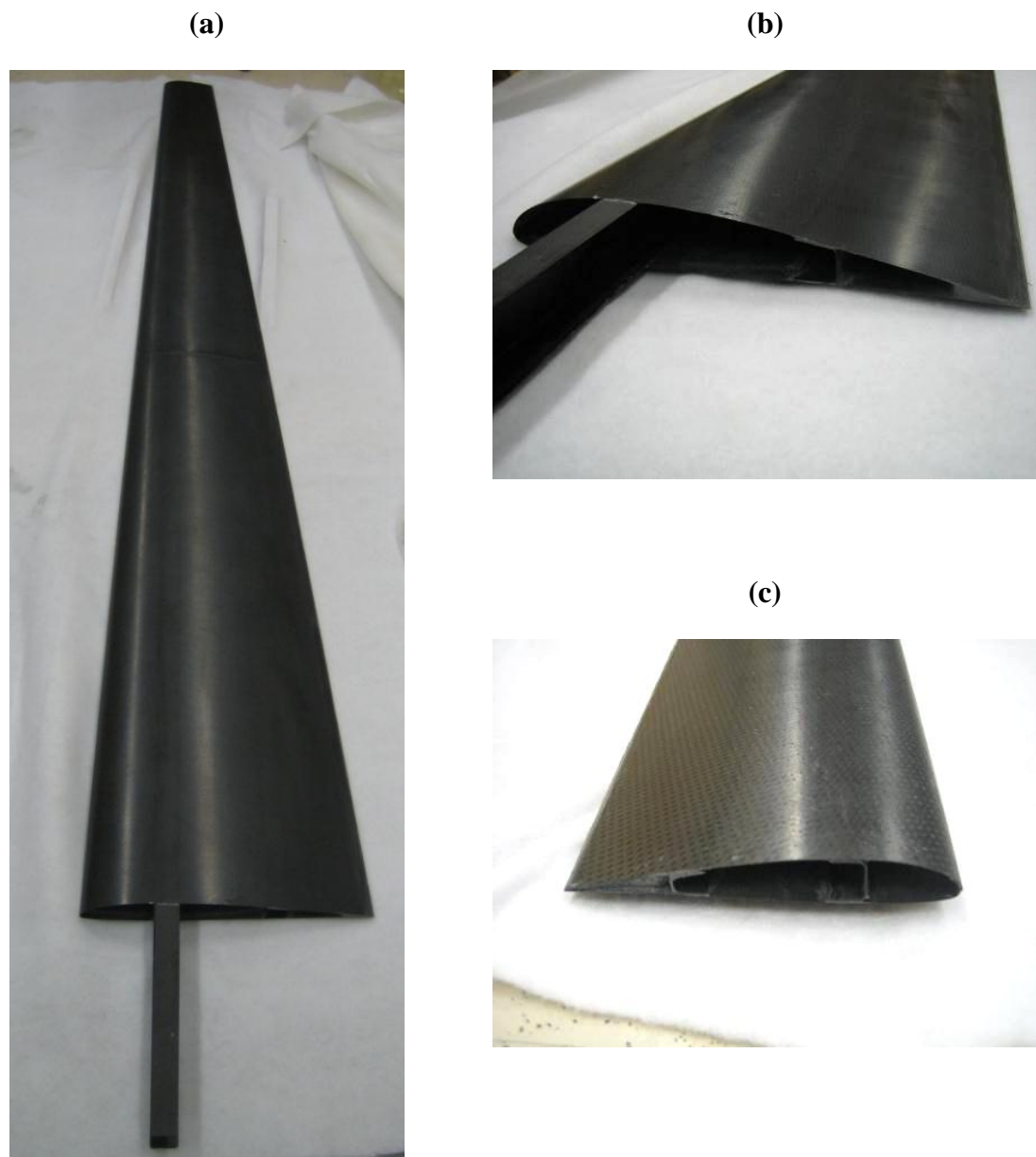
Figure 7-36: Views of the assembled test-bed wing structure: (a) entire wing (shown in perspective plan view), (b) wing root, (c) wing tip.

Figure 7-37: A complete assembled wing held by the author for scale.

7.4.2 Coupon Testing

A series of material-property testing tensile coupons were fabricated and tested

according to ASTM: D 3039 [7-5] to produce strength and stiffness data for modeling.

Sixteen coupons were tested in total, each with duel longitudinal strain gauges to monitor

longitudinal strain and bending and a single transverse strain gauge to monitor transverse

strain. The coupons were given constant displacement loading to failure using a hydraulic

tensile load actuator. These measurements were averaged and combined to give in-plane

axial stiffness and strength data (E_{11}, E_{22}; X_{T1}, X_{T2}) and Poisson's ratios (v_{12}, v_{21}).

Additionally, a 0.254×0.305 m flat sandwich plate made was manufactured with

the same laminate, core, adhesive and cure as the wing components. Vibration testing and

a preliminary model correlation by the Newton Raphson method to convergence with

mean relative error of 0.5% over the first 10 modes produced an estimate of effective

material property values for the sandwich structure (E_{11}, E_{22}, v_{12}, G_{12}, for the laminate;

E_{23}, E_{13} for the core). These physical material properties were assumed to be more

accurate than using the plain laminate properties for the sandwich skin laminates which

can lose stiffness because of co-cure with the cell-structure honeycomb.

Results for each material test are provided in Table 7-7 and Table 7-8

respectively. The plane laminate properties are higher than the properties assumed for the

baseline finite element model. Additionally, the plate correlation suggests reduced

stiffness in the sandwich laminates. Both material tests agree that, despite this prepreg

system having a symmetric weave, properties in the tow (11) direction of the prepreg

were higher than their transverse (22) counterparts.
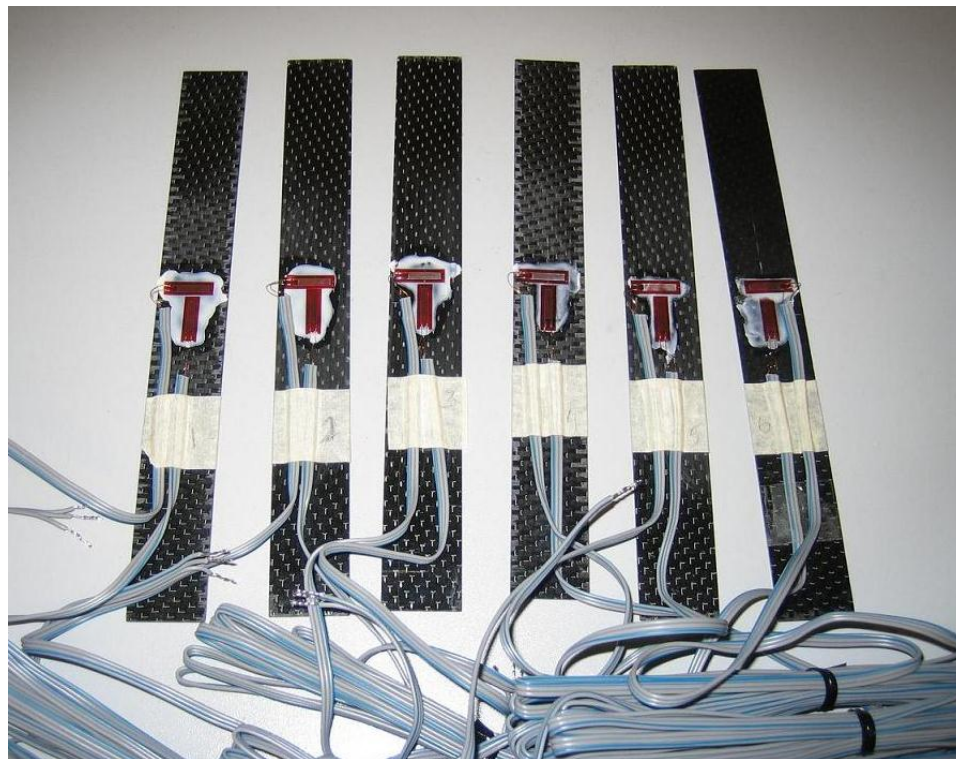
Figure 7-38: Material property testing coupons with strain gauges.

Table 7-7: Material coupon testing results for plain laminate regions.

	Average results	Standard deviation	Samples
E_{11} (GPa)	128	3.94	3
E_{22} (GPa)	123	0.779	3
v_{12}	0.039	0.016	3
v_{21}	0.030	0.015	3
X_{T1} (GPa)	0.717	0.0751	3
X_{T2} (GPa)	0.621	0.0198	3

Table 7-8: Material properties for sandwich structure derived from correlation of a representative plate structure and finite element model.

		E_{11} (GPa)	E_{22} (GPa)	v_{12}	G_{12} (GPa)	G_{23} (GPa)	G_{13} (GPa)	ρ (g/cm^3)
Sandwich Structure	Skin	93.8	84.8	0.15	5.68	4.14*	4.14*	1.77
	Core	6.89×10^{-6}	6.89×10^{-6}	0.001	6.89×10^{-6}	.0288	.0556	0.140

Properties are very low sensitivity, so generic value was assumed; values have negligible impact on response

7.5 Vibration Testing

The final component of the composite wing test-bed is a vibration testing setup configured to modally characterize both independent wing components in free-free configuration before assembly and the assembled wings in cantilevered configuration. Vibration testing of the wing component structures before assembly was performed to produce data for part-to-part variability studies and finite element model correlation on the component level. Once wings were assembled, vibration testing in a flight-like cantilevered configuration was enabled with the expectation to provide data for studying manufacturing variability of the structural assemblies, model correlation, sensor studies, damage analysis, and structural health monitoring algorithm development and evaluation.

All vibration testing was performed using a Polytec scanning laser Doppler vibrometer (PSV-200 system; Vibrascan OFV 055 scanning head), with excitation provided by a 1.36 kg LDS-V203 electrodynamic shaker. The shaker-part connection was made using a 0.152 m stinger with low bending stiffness and high axial stiffness attached

to a Kistler 9712A50 force transducer, which was super-glued to the driving point surface via a small bolt section as shown in Figure 7-39. Predetermined measurement points were marked on the exterior measurement surfaces of the test-pieces using small squares of diffusely reflective adhesive tape measuring approximately 5 mm on a side to increase reflectivity and effectiveness of the laser. For all measurement points only the degree-of-freedom facing the laser was measured. This setup produced vibration corresponding to primary bending and torsional modes of the wings, as desired, and also allowed each test to be performed in a single run without repositioning the laser. A schematic representation of a generic laser vibrometer vibration test setup is shown in Figure 7-40.

For each test the test-piece was situated in the desired orientation with the test surface facing horizontally, the shaker was suspended behind the test-piece with the stinger lightly touching the excitation degree-of-freedom, and the laser vibrometer scanning head situated perpendicularly facing the nominal measurement degree-of-freedom plane at a distance of approximately $5 - 8$ m. The scan points were programmed into the acquisition software and matched to the video feed of the test-piece using the built-in acquisition software module. The test was run by starting the shaker excitation, allowing the test-piece to reach steady-state vibration, and enabling the scan and acquisition program. The acquisition software then automatically took data at each point for the specified number of averages sequentially for all measurement points. H1 mobility (velocity) average system transfer functions were saved at each measurement point in the frequency domain. Modal parameter estimation of the measured vibration

data was performed using ME'scopeVES [7-6] to produce experimental frequencies,

mode shapes, and damping ratios. Vibration test parameters for each component and the

assembled are given in Table 7-9.
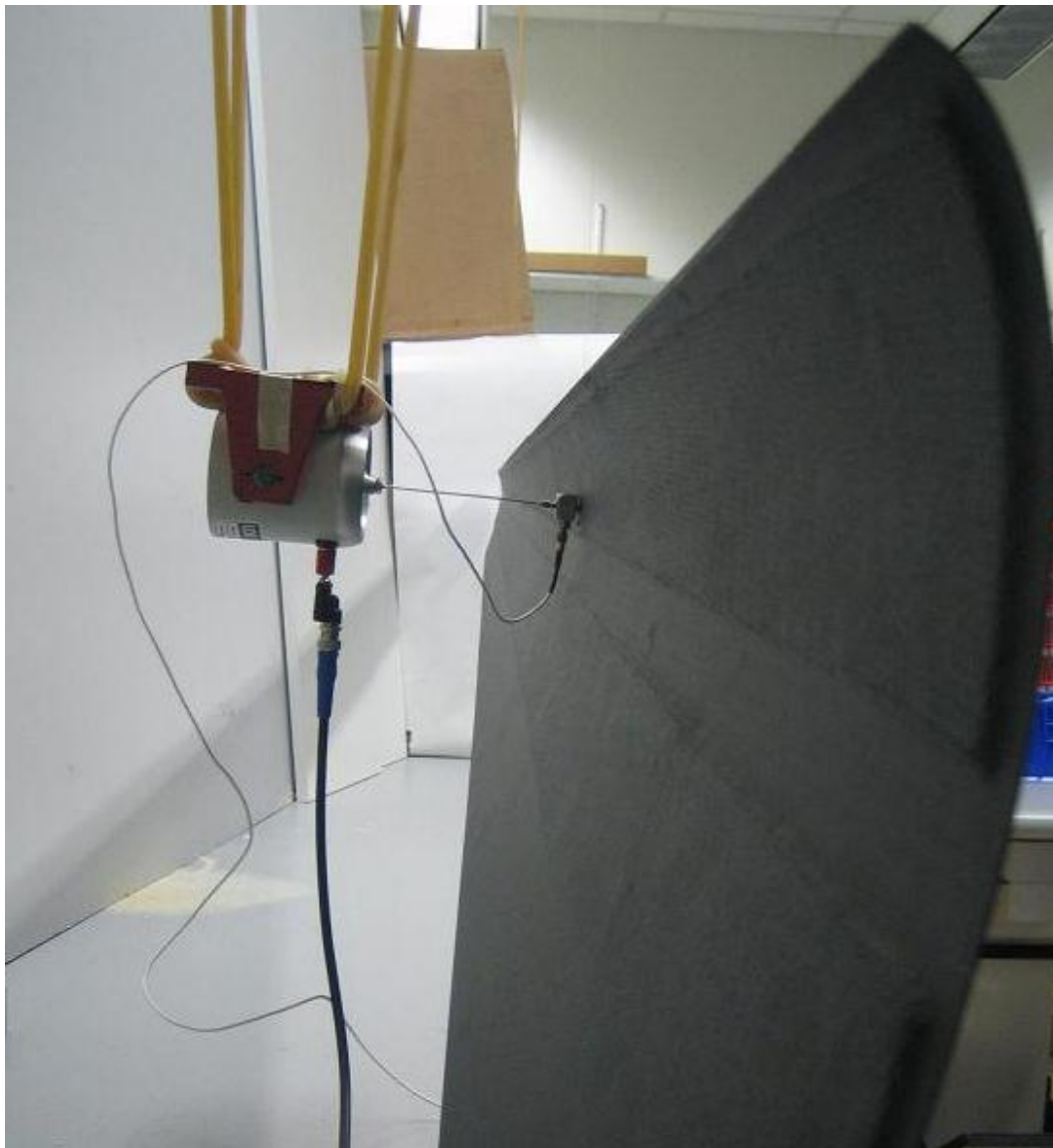
Figure 7-39: View of the electrodynamic shaker and force transducer attachment method, shown during component vibration testing of the top wing skin.
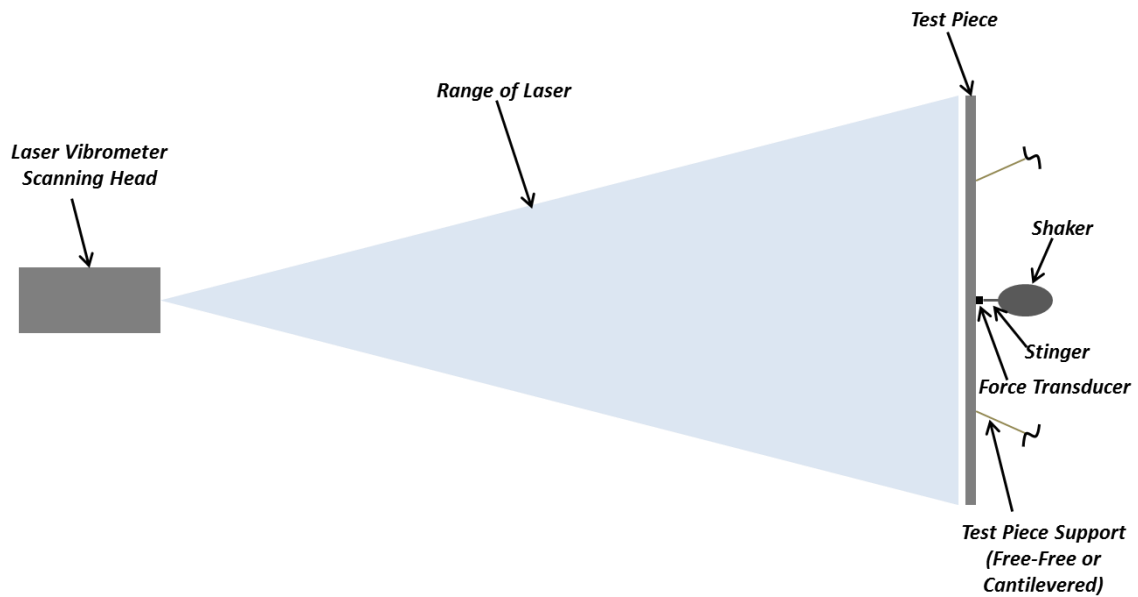
Figure 7-40: Schematic representation of a generic laser vibrometer vibration test setup.

Table 7-9: Modal test parameters for wing components and the assembled wing.

	Frequency Range (Hz)	Resolution (Hz)	Number of averages	Number of scan-points
Top skin	5 – 200	0.0625	6	80
Bottom skin	5 – 200	0.0625	6	80
Main spar	10 – 400	0.1250	8	36
Aft spar	10 – 400	0.1250	8	36
Assembled wing	5 – 500	0.1563	6	80

7.5.1 Wing Component Vibration Testing

The wing component pieces were tested individually with free-free boundary conditions approximated by suspending each piece using approximately 1.22 m of 0.00635 m thick elastic surgical tubing and 0.2 m of 2.72 kg–weight fishing line. The lines were connected to the test pieces using super-glue for the skins and elastic bands for the spars. The two skins were each assigned 80-point measurement grids with 8-points across wing width and 10-points down wing length following the bond line geometry, as shown in Figure 7-41. The measurement point locations were chosen to approximately match external surface nodes in the finite element model. The spars were assigned 36-point scan grids—12 points evenly spaced down the length with 3 points across the width—with response measured normal to the top cap to emphasize assembled-wing bending behavior, as shown in Figure 7-42. Resulting measured natural frequencies for the four wing components are given in Table 7-10. A screen shot of the modal parameter estimation process for the top wing skin is given in Figure 7-43. The figure shows curve-fit magnitude frequency response functions in red superimposed on the black frequency response functions with the curve-fit functions and measured functions from all degrees-of-freedom overlaid on the same plot. Operational deflection shapes matching the first three bending modes are additionally shown inlaid at the top of the figure with arrows pointing to the peaks they represent.
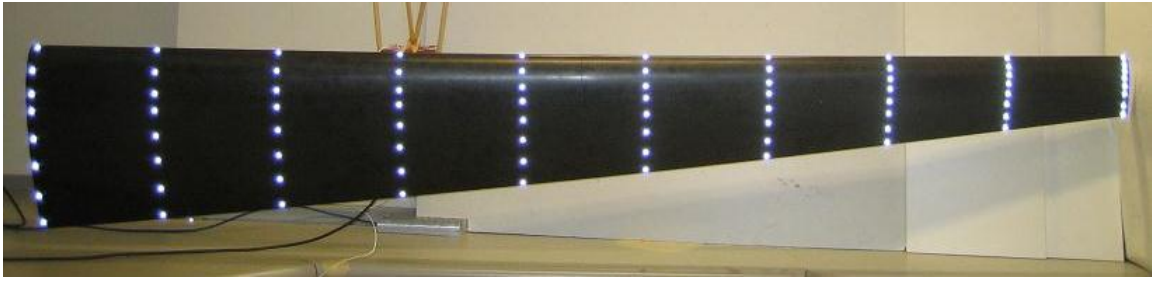
Figure 7-41: Top wing skin components in free-free scanning laser Doppler vibrometer modal testing configuration.
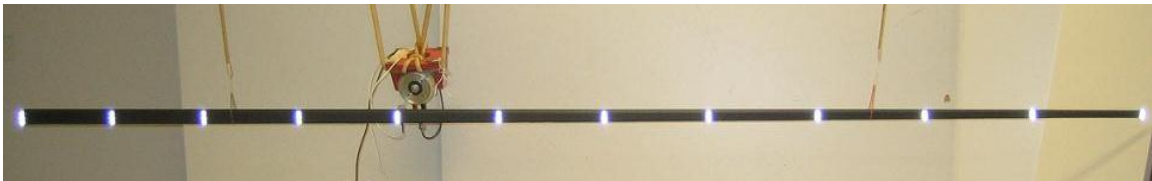
Figure 7-42: Main spar component in free-free scanning laser Doppler vibrometer modal testing configuration.
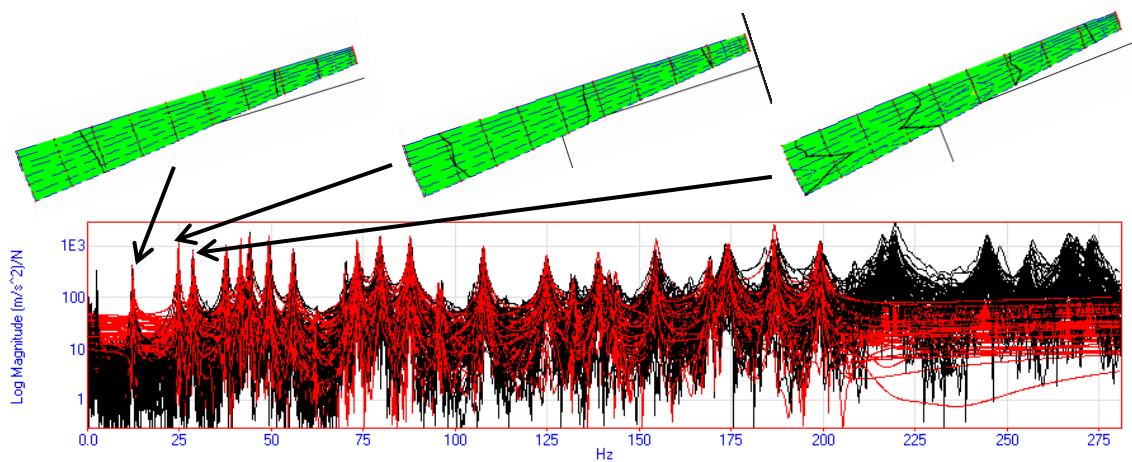
Figure 7-43: Example of curve-fit frequency response functions during modal parameter estimation for the top wing skin.

Table 7-10: Measured natural frequencies for wing components.

Mode	Top skin (Hz)	Bottom skin (Hz)	Main spar (Hz)	Aft spar (Hz)
1	12.4	4.4	22.2	11.9
2	23.9	11.5	33.8	24.4
3	28.7	21.8	46.1	48.3
4	35.0	23.4	59.0	62.3
5	40.6	34.2	70.2	75.2
6	42.3	35.6	101.9	103.5
7	48.8	41.6	116.4	133.5
8	51.8	47.6	131.7	137.4
9	59.0	49.5	154.4	151.0
10	66.7	61.4	175.3	187.7
11	73.8	63.6	186.8	239.8
12	75.6	76.6	222.3	314.6
13	80.9	83.4	240.0	308.8
14	82.7	88.3	251.7	357.7
15	88.6	90.2	282.3	333.9
16	91.4	102.9	308.9	385.4
17	99.9	106.3	343.6	*
18	108.6	115.2	359.5	*
19	118.8	*	*	*
20	124.6	*	*	*

7.5.2   Assembled Wing Vibration Testing

A cantilever mounting fixture was developed for vibration testing of the assembled wing. The fixture was designed to emulate the fuselage attachment of detachable wings in an operational unmanned aerial vehicle—fixed on the main spar by clamping of the spar caps and pinned on the aft spar by contact at a point. The fixture is shown with the assembled wing installed in test configuration in Figure 7-44. The fixture

was built on a section of steel I-beam which could be attached to a table by fixing the bottom flange. A piece of aluminum machined to match the interior surface of the protruding portion of main spar was bolted to the top surface of the I-beam. The wing was fixed to the machined piece of aluminum by placing flat pieces of aluminum on the exposed outer surfaces of the spar caps which were covered in a thin soft layer of cardboard to protect the laminate surfaces and aid with load distribution. The aluminum plates were then clamped at several locations to sandwich the spar caps as shown in Figure 7-45. A small block of aluminum machined to match the interior surface of the aft spar was inserted 25 mm into the aft spar cavity and fitted to the vertical wing-side surface of the I-beam web with a pin to resist torsional motion of the wing.

Vibration testing of the assembled wing was performed with the wing mounted on the cantilever fixture as shown in Figure 7-44 with the bottom skin facing the laser vibrometer. Vibration measurements were made using the same the degrees-of-freedom set used for the bottom wing skin component vibration test. The measurement point coordinates are given relative to an origin at the wings leading edge root in Table 7-11 based on the numbering scheme shown schematically in Figure 7-46. Vibration test parameters were previously presented in Table 7-9.

Table 7-12 gives the first five natural frequencies, modal damping ratios, and mode shape descriptions for the assembled wing. The mode shapes are additionally presented in Table 7-13 for all measurement degrees-of-freedom. The modes can be seen to generally agree with the results of the finite analysis presented in Section 7.3.2, albeit
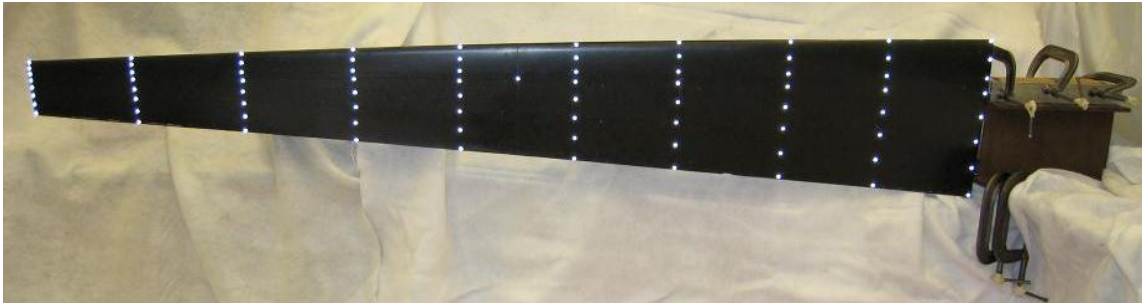
Figure 7-44: View of assembled wing in cantilever test configuration.

Figure 7-45: Detail of cantilever test fixture.

Table 7-11: Degree-of-freedom locations for cantilevered wing vibration test (DOF = degree-of-freedom).

DOF	x (m)	y (m)	DOF	x (m)	y (m)
1	0.010	-0.010	41	0.013	-0.188
2	0.274	-0.015	42	0.272	-0.184
3	0.516	-0.022	43	0.519	-0.177
4	0.784	-0.030	44	0.781	-0.170
5	1.023	-0.038	45	1.022	-0.166
6	1.290	-0.045	46	1.290	-0.159
7	1.536	-0.053	47	1.533	-0.152
8	1.794	-0.064	48	1.796	-0.148
9	2.051	-0.071	49	2.051	-0.141
10	2.297	-0.079	50	2.298	-0.138
11	0.008	-0.051	51	0.017	-0.250
12	0.272	-0.055	52	0.273	-0.239
13	0.518	-0.059	53	0.520	-0.229
14	0.783	-0.060	54	0.782	-0.218
15	1.023	-0.067	55	1.023	-0.211
16	1.290	-0.075	56	1.292	-0.197
17	1.536	-0.075	57	1.532	-0.186
18	1.794	-0.083	58	1.795	-0.176
19	2.052	-0.087	59	2.051	-0.166
20	2.298	-0.094	60	2.298	-0.155
21	0.010	-0.096	61	0.019	-0.316
22	0.272	-0.096	62	0.278	-0.301
23	0.518	-0.096	63	0.522	-0.290
24	0.783	-0.097	64	0.782	-0.273
25	1.023	-0.100	65	1.022	-0.259
26	1.291	-0.100	66	1.291	-0.241
27	1.537	-0.101	67	1.535	-0.224
28	1.795	-0.104	68	1.794	-0.207
29	2.054	-0.105	69	2.050	-0.193
30	2.297	-0.105	70	2.297	-0.176
31	0.009	-0.131	71	0.019	-0.384
32	0.271	-0.131	72	0.278	-0.366
33	0.518	-0.128	73	0.522	-0.348
34	0.783	-0.124	74	0.781	-0.330
35	1.023	-0.124	75	1.022	-0.310
36	1.292	-0.124	76	1.291	-0.286
37	1.535	-0.120	77	1.534	-0.265
38	1.794	-0.123	78	1.794	-0.241
39	2.052	-0.120	79	2.050	-0.217
40	2.299	-0.120	80	2.294	-0.196
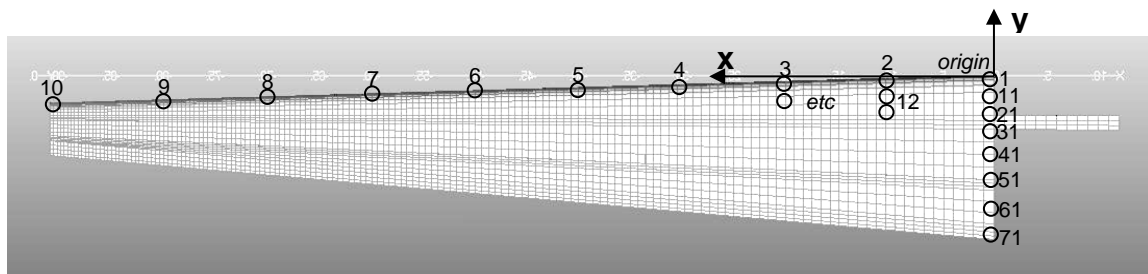
Figure 7-46: Degree-of-freedom numbering scheme and coordinate system orientation for cantilevered wing vibration test.

Table 7-12: Description of modes for cantilevered wing vibration test .

Mode	1	2	3	4	5
ω_n (Hz)	7.4	31.7	67.6	110	262
ζ_n (%)	0.62	0.86	0.48	1.1	0.21
Description	1st Bending	2nd Bending	3rd Bending	4th Bending	Torsion mixed

with slightly lower frequencies for all modes. The decrease in natural frequency can be

attributed to two main factors: material properties and boundary condition. The coupon

testing presented in Section 7.4.2 suggest that the primary laminate stiffness properties in

the wing spars are actually slightly higher than those assumed for the baseline finite

element model studies, even though the sandwich laminate stiffnesses may be lower.

Overall measured wing mass also had negligible error compared to the finite element model and so material properties alone do not explain the difference. The physical wing bondlines on the other hand are not likely to be as stiff as the idealized rigid links used in the finite element model which could have an effect, although not enough to fully explain the difference in natural frequencies. The most likely factor is therefore compliance in the cantilevered boundary condition compared to the fixed constraint used in the finite element model which is believable considering that the cantilever mount was clamped to a table and included a thin but compliant layer of cardboard protection around the spar laminates. Comparing the measured modes to results of the boundary condition stiffness study presented in Section 7.3.2 suggests that, if the effect of material property differences is ignored, the true physical cantilever mound had an effective stiffness on the order of 10^3 N/m. The relatively high frequency of the first measured torsion mode also suggests that the true 1st torsion mode was not correctly measured. This could have occurred because of the vibration test excitation being inadvertently placed at a region of low activity in the 1st torsion mode which would have caused response of that mode to be similarly low. Inspection of the baseline finite element model mode shapes and natural frequencies further suggests that the first measured torsion mode is in fact 2nd torsion.

Table 7-13: Measured mode shapes for cantilevered wing (DOF = degree-of-freedom).

DOF	Mode 1	2	3	4	5	DOF	Mode 1	2	3	4	5
1	0.01	0.06	0.08	0.14	0.03	41	0.25	0.34	0.41	0.34	0.62
2	0.01	0.09	0.05	0.10	0.15	42	0.27	0.49	0.21	0.14	0.19
3	0.27	1.00	0.93	1.00	0.28	43	0.14	0.52	0.13	0.42	0.24
4	0.77	1.00	0.95	0.99	0.37	44	0.07	0.45	0.37	0.29	0.12
5	0.03	0.03	0.18	0.09	0.36	45	0.04	0.32	0.46	0.05	0.35
6	0.09	0.16	0.25	0.10	0.42	46	0.03	0.20	0.39	0.29	0.26
7	0.09	0.29	0.17	0.35	0.18	47	0.84	0.96	1.00	0.96	0.94
8	0.21	0.36	0.03	0.44	0.18	48	0.39	0.46	0.23	0.07	0.07
9	0.13	0.35	0.32	0.21	0.30	49	0.03	0.07	0.26	0.20	0.25
10	0.31	0.22	0.50	0.20	0.24	50	0.15	0.32	0.22	0.32	0.13
11	0.48	0.08	0.38	0.43	0.50	51	0.27	0.06	0.34	0.46	0.23
12	0.40	0.52	0.16	0.02	0.63	52	0.50	0.50	0.19	0.01	0.42
13	0.00	0.04	0.37	0.49	0.04	53	0.18	0.40	0.01	0.42	0.19
14	0.00	0.01	0.24	0.37	0.01	54	0.09	0.27	0.15	0.37	0.18
15	0.01	0.03	0.11	0.17	0.04	55	0.04	0.02	0.17	0.06	0.46
16	0.07	0.19	0.31	0.03	0.39	56	0.40	1.00	0.92	1.00	0.17
17	0.48	0.24	0.47	0.23	0.06	57	0.56	0.51	0.19	0.02	0.53
18	1.00	0.98	0.96	1.00	0.51	58	0.42	0.23	0.48	0.21	0.10
19	0.51	0.98	0.98	0.99	0.67	59	0.07	0.17	0.27	0.06	0.37
20	0.55	0.96	0.99	0.98	0.81	60	0.17	0.37	0.31	0.20	0.22
21	0.03	0.11	0.36	0.30	0.28	61	0.03	0.05	0.21	0.14	0.25
22	0.04	0.23	0.40	0.04	0.39	62	0.08	0.30	0.20	0.33	0.16
23	0.14	0.35	0.30	0.29	0.08	63	0.22	0.38	0.01	0.42	0.17
24	0.18	0.43	0.06	0.42	0.24	64	0.28	0.07	0.35	0.44	0.36
25	0.23	0.41	0.26	0.18	0.02	65	0.16	0.38	0.29	0.19	0.14
26	0.31	0.26	0.45	0.25	0.31	66	0.53	0.03	0.32	0.53	0.18
27	0.46	0.05	0.33	0.49	0.04	67	0.01	0.11	0.03	0.08	0.25
28	0.46	0.49	0.21	0.02	0.28	68	0.55	0.53	0.15	0.03	0.73
29	0.01	0.02	0.24	0.29	0.34	69	0.58	0.09	0.39	0.43	0.61
30	0.02	0.17	0.48	0.40	0.82	70	0.19	0.21	0.52	0.19	0.35
31	0.05	0.31	0.57	0.14	0.56	71	0.32	0.34	0.34	0.23	0.38
32	0.09	0.43	0.42	0.31	0.46	72	0.09	0.35	0.05	0.45	0.19
33	0.13	0.50	0.16	0.45	0.64	73	0.06	0.14	0.22	0.13	0.46
34	0.24	0.47	0.22	0.17	0.25	74	0.01	0.15	0.47	0.38	0.18
35	0.28	0.31	0.43	0.33	0.85	75	0.08	0.27	0.49	0.09	0.27
36	0.38	0.02	0.31	0.57	0.34	76	0.13	0.39	0.37	0.27	0.05
37	0.00	0.10	0.27	0.35	0.20	77	0.12	0.46	0.11	0.40	0.27
38	0.40	0.93	1.00	0.93	1.00	78	0.25	0.43	0.23	0.16	0.12
39	0.38	0.45	0.24	0.10	0.12	79	0.23	0.29	0.44	0.28	0.57
40	0.38	0.03	0.29	0.59	0.31	80	0.53	0.47	0.22	0.04	0.12

7.6 **Discussion**

The motivation for creating the composite wing test-bed was threefold: (1) to investigate composite unmanned aerial vehicle wing response under various structural conditions, including with evolving damage; (2) to study efficacy of certain experimental distributed sensor systems, including those based on piezo-electric elements and fiber optic sensors, and understand their effect on wing response; and (3) to guide development of hardware systems and algorithms for structural health monitoring and prognosis. The author's role in this project was focused on developing, modeling, analyzing, and testing the test-bed structure (presented throughout the current chapter) and, separately, developing technology for damage identification that could be applied to the test-bed as an analog for similar operational structures (developed throughout the remainder of the dissertation). Other aspects of the project, especially those related to distributed sensor systems and structural health prognosis, were pursued by project team-members.

Although aspects of the original test-bed goals were realized at the time of writing, more can be accomplished towards development and refinement of structural health monitoring and prognosis technology through further development and study of the test-bed . Recommendations for future work include the following.

1. Assemble the remaining wings, including installation of candidate distributed sensor systems following the development in [7-1].

2. Perform further modal vibration testing to quantify the manufacturing variability inherent to the wings and assess the impact of embedded sensor systems on response.

3. Perform damage identification studies using the algorithm presented in the previous chapters of this dissertation to further validate the algorithm and guide future improvements.

4. Use results of progressive impact and fatigue based damage to further study, develop, and validate the algorithms for structural health prognosis technology developed by the team lead by Gobbato and Conte [7-2].

This general roadmap shows the potential of the flexible experimental test-bed for structural health monitoring and prognosis developed by the Los Alamos National Laboratory and UCSD research teams. The extension beyond analytical capability and simple laboratory experiments is a necessary step towards reaching mature technology that can then be implemented on operational systems for refinement and validation.

The material contained in Chapter 7 was developed in collaboration with Prof. John B. Kosmatka, Prof. Charles Farrar, Prof. Joel Conte, and Prof. Francesco Lanza di Scalea. The dissertation author was the primary investigator and author of this work.

7.7   Chapter 7 References

[7-1]   Matt, H., "Structural Diagnostics of CFRP Composite Aircraft Components by Ultrasonic Guided Waves and Built-In Piezoelectric Transducers,' *Ph.D. Dissertation, Department of Structural Engineering, University of California, San Diego,* (2006)

[7-2]   Gobbato, M., "Reliability-Based Framework for Fatigue Damage Prognosis of Bonded Structural Elements in Aerospace Composite Structures,' *Ph.D. Dissertation, Department of Structural Engineering, University of California, San Diego,* (2011)

[7-3]   MD. NASTRAN 2006 R1. Santa Ana, California: MSC Software., 2006

[7-4]   Femap Version 9.3. Plano, Texas: UGS Corp., 2007

[7-5]   ASTM International, D 3039, Standard Test Method for Tensile Properties of Polymer Matrix Composite Materials, 2005

[7-6]   ME'scopeVES version 4.0.0.53. Scotts Valley, California: Vibrant Technology Inc., 2005

8 CONCLUSION

Conclusions for the dissertation are presented in five parts. First, the dissertation is summarized, including motivations, overarching definitions, an overview of the damage detection algorithm, and chapter organization. Second, primary technical conclusions are reiterated, roughly in the order they were reached in the dissertation. Third, specific novel contributions developed through the dissertation are presented. Fourth, recommendations for future work are presented. The final section gives closing remarks.

8.1 Dissertation Summary

The current dissertation has developed and validated technologies related to structural health monitoring and prognosis under the motivation of increasing safety and life-cycle efficiency of aerospace structures. Structural health monitoring is defined in this context as the process of regularly detecting, localizing, and identifying structural damage. Prognosis is defined as the process of using knowledge of the current damage state along with statistical assumptions on future operational conditions to predict useful life remaining. Damage identification is defined as the process of damage quantification, estimation of the prediction uncertainty, and structural model update. In this context, damage identification can be viewed either as a standalone process for understanding a

450

structure's current damage state or as part of a larger system for ongoing structural health monitoring and prognosis of an operational structure.

The primary innovation is a statistical least-squares algorithm for *damage identification* based in concepts of parameter estimation and model update. The dissertation's damage identification algorithm requires the following limiting assumptions to be met:

1. The target physical system must be analytically modeled as a multiple degree-of-freedom system in the linear frequency domain.

2. Frequency response function reference data must be available across multiple frequency lines and degrees-of-freedom in a way that can be replicated by the analytical model with acceptably low error. Environmental factors affecting structural and model response, for example temperature, must be normalized between the structural test configuration and model. For practical implementation, for instance on an aircraft, this likely requires testing the structural in a controlled environment where boundary conditions and environmental factors can be controlled and measured with sufficient accuracy to be replicated precisely in the analytical model.

3. System properties and potential damage parameters must be modeled as implicit, smoothly varying parameters which are tied to dynamic system response in the same regime as the reference data.

4. The system damping must be able to be captured using a linear combination of structural and viscous damping matrices (albeit with no restrictions on proportionality).

5. The model must be capable of producing the global frequency domain dynamic response of the physical structure in the baseline and damaged states with a lower level of error than is caused by the target damage cases being identified.

Required algorithmic inputs are a structural model, a set of reference data from the baseline structure if the model is not sufficiently correlated to the baseline state, and a set of reference data from the damaged system. Any information on damage location and form can be included as an input, if available, but is not strictly required since the algorithm also determines (or refines) damage location during standard operation. If the analytical model does not have high enough fidelity to the baseline data it can be correlated using optimization based techniques, including a modified version of the damage identification algorithm. Once the analytical model is correlated to the baseline state, the damage identification algorithm uses a statistically weighted least-squares minimization of frequency response function based residual force vectors to update the structural model, thereby producing refined location information, quantification of the damage, estimation uncertainty, and an updated structural model.

Damage identification has been an active field of study for approximately 40 years at the time of writing; however, the current algorithm demonstrates advantages

compared to competing approaches. Since the algorithm uses frequency response functions as a reference data basis, it can be applied to systems with generalized and/or heavy damping. This ability sets the current algorithm apart from methods based on modal parameters, among others. Because of the connection to full-system structural models—e.g., dynamic finite element models—the only limitation in terms of structural applicability is related to computational processing power (which scales as a function of number of degrees-of-freedom). Large amounts of reference data can be incorporated into the damage identification process, producing a resilience to incoherent noise. In combination with the integrated method for degree-of-freedom reduction, the algorithm also supports successful implementation in cases where the number of degrees-of-freedom in the model is far greater than in the reference data—a situation which is unavoidable for realistically sized aerospace structures.

The dissertation began with an introduction in Chapter 1 and review of foundational literature in Chapter 2. The primary algorithm was developed theoretically in Chapter 3, including elements of damping, noise, and degree-of-freedom reduction, and was validated analytically on a 2 degree-of-freedom mass-spring system with generalized damping. The methodology was expanded to allow realistically large amounts of noisy data and was further validated in comparison to a selection of competing algorithms with positive results in Chapter 4. In Chapter 5 the algorithm was extended for use with finite element models and reduced degree-of-freedom reference data sets and was validated on a composite sandwich plate model, including parametric

studies and an investigation of methods for modeling damping in reduced coordinates. The algorithm was further extended for experimental implementation, including operations for initial model correlation, and was validated experimentally using a composite laminate plate with impact damage and a reduced coordinate data set in Chapter 6. Chapter 7 finally presented development of a composite unmanned aerial vehicle scaled-wing structural health monitoring and prognosis test bed developed as part of a collaborative project between Los Alamos National Laboratory and the University of California, San Diego.

8.2   **Technical Conclusions**

Analytical validation studies showed that the basic mechanics of the damage identification algorithm function as expected with low error and that the algorithm is capable of accurately identifying damage in the form of concurrent changes in mass, stiffness, and damping. The algorithm additionally functions accurately when the target system includes structural damping, proportional viscous damping, and/or non-proportional generalized viscous damping. This functionality extends to potentially severe cases of generalized damping, so long as the damping can be modeled accurately using a viscous or structural damping matrix using the same degree-of-freedom basis as the mass and stiffness matrices.

Methods for approximating generalized damping using proportional models, including by the so-called extended Rayleigh method, can be implemented effectively in place of the exact damping formulations. The accuracy of these approximate methods can be increased by using a larger number of analysis frequency lines and/or including damping parameters during the identification process. In the case of severely non-proportional viscous damping, assuming proportional damping will lead to corruption in the damage predictions. The algorithm contains features to help mitigate this error, including (1) the ability to average out the modeling error by adding analysis frequency lines and (2) the ability to include damping parameters into the update parameter set and thereby correct the damping model during damage identification.

As shown through analytical studies on a damped eight degree-of-freedom mass-spring system, the algorithm is capable of accurately identifying damage in cases with significant corruption of the reference data by incoherent noise, large numbers of damage identification parameters, large variations of parameter sensitivity, and coupled and/or overlapping modes in the underlying system. This includes when damping is non-proportional and damage involves concurrent changes in mass, stiffness, and damping. Success of the algorithm in these cases is aided by several additional algorithms for selecting analytical frequency lines and combating numerical issues. Accuracy of the current algorithm was also shown to be superior to that of a selection of competing algorithms from the literature when they were all given the same advantages with respect to frequency line selection and numerical stability. Advantages of the current algorithm

are amplified in extreme cases of data corruption, number of damage identification parameters, and low parameter sensitivity.

As shown through examples on an analytical composite sandwich plate, the algorithm is effective when coupled with finite element models on the order of thousands of degrees-of-freedom. The results include accurate damage identification in cases of up to 99.8% decrease in degrees-of-freedom between the analytical model and available measurements, high levels of measurement noise, and up to 36 individual update parameters. Parameter estimation error increases as relative parameter sensitivity decreases, meaning that low-sensitivity parameters are less likely to be identified accurately. Through parametric studies on the same analytical test structure, the following conclusions can additionally be drawn:

- Increasing the number of frequency lines decreases damage identification error and increases computation time (number of iterations and time per iteration).

- Increasing the frequency selection coherence tolerance decreases parameter error and computation time.

- Damage identification error increases smoothly with increasing noise.

- The dynamic behavior of the structure needs to be accurately captured both spatially and across frequency for accurate damage identification.

- Mean relative parameter error and convergence time increase with number of update parameters.

- Posterior parameter uncertainty increases with noise.

Further studies on the composite sandwich plate model show that the extended Rayleigh damping method formulated in the full analytical degree-of-freedom space can provide an accurate method for directly modeling unknown damping in reduced coordinates in a realistically-sized structure when modal parameters are available.

Based on experimental studies on a composite laminate plate, the primary algorithm can successfully perform damage identification on a real structure with realistic levels of measurement noise and modeling error. Initial model correlation to a baseline dataset can successfully be used to reduce initial modeling error sufficiently below the level of changes caused by the damage, even when the initial model has underlying deficiencies. Deterministic pseudo Newton-Raphson optimization techniques with cost functions based on change in natural frequencies, frequency response functions, or residual force vectors can be used for initial model correlation. This family of methods is computationally efficient but will become unstable for more than a small number of update parameters and/or when there is a wide variation in parameter sensitivity. It is therefore recommended that these methods only be used as an optional preliminary step on realistically sized physical structures. The primary damage identification algorithm can also be successfully used for baseline model correlation when global model parameters are selected as update variables. Assuming a low-level of parameter variability in this context will have the effect of constraining the parameters to a restricted range, as desired. Inclusion of the primary algorithm during the correlation

process also helps produce an updated baseline model which is accurate in the domain to be queried for damage identification.

The algorithm can accurately determine which elements correspond most closely to the damaged region by updating elemental damage factors—with the effect of reducing all element stiffnesses—to close to zero for elements fully contained in the damage region and to a value between one and zero for elements partially contained in the damage region and/or partially damaged. Damage factors on elements which are fully out of the damage region are successfully maintained close to unity. The algorithm may produce false positives; however, additional damage identification runs using a subset of the original update damage parameters can identify the error. In this case, the algorithm benefits from operator judgment to assign and interpret additional diagnostic damage identification runs.

Relative parameter sensitivity with respect to global response and noise will dictate the detail to which damage can be identified. For instance, damage which is small compared to the size of the structure and/or located in an area of low strain-energy may only be quantifiable in terms of major element properties, or not at all.

Using more frequency lines during damage identification increases both accuracy and computational expense, with the increase in accuracy offering diminishing returns after a certain point. Accuracy can also be improved by selecting specific analysis frequency lines from the pool surrounding modes with a high level of fidelity between the correlated analytical model and reference data. Three methods for determining this

correlation were trialed with the result that the level of mode shape correlation between the healthy reference data set and correlated analytical model appears to be the best choice.

The values of initial damage factor variability specified at the beginning of a damage identification run influence both the final updated variability values and, through regularization, the ability of the damage factors to update to values much different from their original values. Updated parameter variability will decrease with decreasing initial variance value and increasing parameter sensitivity. The amount of relative decrease in parameter variability depends on how high the initial parameter variance is compared to the ratio of noise variance to parameter sensitivity squared. The noise variance and parameter sensitivity are fixed for a given update problem; therefore, insight into reasonable values of initial damage factor variability could potentially be gained by inspecting its relative magnitude compared to the ratio of parameter sensitivity and noise variance. The impact of regularization also needs to be taken into account when specifying initial variability since too low of an initial value may over-constrain the optimization. Although insight into reasonable values may be gained through the methods and observations just mentioned, no rigorous quantitative means of establishing the best prior variability numbers for a particular problem is currently known.

The following conclusions can be drawn regarding development efforts towards a scaled composite wing test-bed for structural health monitoring technology. A scaled architecture representing the primary wing structure of a composite unmanned aerial

vehicle was successfully designed, modeled using finite elements, manufactured, and vibration tested. The test-bed captures the fundamental modal behavior of the target vehicle structure. Damage cases representing progressive spar-skin and skin-core disbond damage were modeled to a first-order by the removal of rigid links with an acceptable effect on fundamental modes compared to expectations. Top-to-bottom manufacturing practices for layup, cure, and assembly of the wing structure were detailed, as were the methods and results of component and system level vibration testing using a scanning laser Doppler vibrometer. Vibration testing results show reasonable fidelity to the finite element model, with the primary variations explainable through differences in boundary conditions and bondline stiffness.

8.3   Specific Contributions

The following is a list of contributions developed through the current dissertation which, to the best of the author's knowledge, are partially or wholly novel.

- Adaptation of the frequency domain equations for statistical least-squares iterative parameter estimation to structural health monitoring on the basis of frequency response function based residual force vectors (or equivalently, frequency response function difference). *Ref: Section 3.6.*

- Novel derivation of the exact frequency response function sensitivity equation (Note: the resulting equation has been presented previously but, to the best of

the author's knowledge, the derivation presented herein is novel). *Ref: Section 3.6.3.*

- Algorithmic approaches for selecting frequency lines by consecutive discrimination based on natural frequency (if modal parameters are available), average frequency response function magnitude (in displacement, velocity, or acceleration domains), and coherence. *Ref: Section 4.1.*

- A method for estimating reference frequency response function covariance matrices from measured frequency response coherence functions. *Ref: Section 4.2.*

- Proof of equivalence between displacement, velocity, and acceleration domains in frequency response function reference data for use of the current damage identification algorithm. *Ref: Section 4.3.*

- Development of approaches to dealing with numerical issues stemming from low parameter sensitivity, including the use of scaled damage factors, large sensitivity perturbations for linear parameters, and grouping of damaged elements. *Ref: Section 5.2.*

- Development of methods for accurately modeling proportional damping in reduced coordinates, including adaptation of the extended Rayleigh method for approximating generalized damping for frequency response function based damage identification when modal information is available. *Ref: Section 5.4.2.*

- Development of three methods for calculating real-valued modal data for use with modeling proportional damping in reduced coordinates when modal information is available (one of which is heavily based on the work of the cited author). *Ref: Section 5.4.3.*

- Detail of four methods for analytical model correlation, including three methods based on the Newton-Raphson method and minimization of error in natural frequencies, frequency response functions, or frequency response residual force vectors, and the final method using a modified form of the primary damage identification algorithm. (Note: the classical Newton-Raphson optimization algorithms are not claimed to be novel, although foundational references for the specific presentation and application herein were not located.) *Ref: Section 6.1*

- Integration of model correlation and damage identification, including iterative brute-force update of a potentially deficient model for damage identification, frequency line selection based on correlated modes, and recommendations for parameter prior variability assignment. *Ref: Section 6.3*

- Dissection of prior and posterior parameter variability in the context of model correlation and damage identification, in term of both prior variability assignment and posterior variability interpretation. *Ref: Section 6.4.4.4*

- Detailed description and values of experimental modal data from a composite wing structure representing the primary structure of a modern unmanned aerial vehicle wing at 1/3 scale. *Ref: Section 7.5.*

8.4   **Future Work**

The following topics are recommended for future development of the current algorithm towards full-vehicle structural health monitoring and prognosis:

- Investigate the algorithm's performance and behavior with noise on the input and colored, frequency-varying noise.

- Investigate the algorithm's performance and behavior to additional cases of parametric nonlinearity.

- Investigate the algorithm's potential application to cases of nonlinearity with respect to loading. In this case, the structural testing and model formulation and analysis would need to, at a minimum, be capable of producing matching frequency response functions in the baseline and damaged configurations.

- Investigate the use of multiple-input multiple-output methods for data acquisition with respect to increasing algorithm performance.

- Incorporate additional algorithms for automatically down selecting update parameters to reduce non-uniqueness in the final solution.

- Recode algorithm implementation for higher numerical efficiency, more general application on complex structures with varying element and material types, and automation.

- Incorporate exact finite element model parameter sensitivities where possible as opposed to relying on finite difference approximations.

- Couple the algorithm with upstream systems for detailed damage location and downstream prognosis.

- Further explore the meaning and behaviors of parameter uncertainty in terms of both defining prior uncertainty values and understanding the meaning of posterior uncertainty values and their application to downstream prognosis activities.

- Apply the algorithm to the scaled-wing structural health monitoring test-bed presented in Chapter 7 of the dissertation.

- Experimentally apply and validate the algorithm on increasingly large and realistic structures with controlled and then operationally-generated damage cases.

8.5   **Closing Remarks**

The completed dissertation has presented the development and validation of an integrated top-to-bottom algorithm architecture for damage identification of realistically

sized and damped structures, including initial model correlation, damage location (if required), identification of multiple concurrent damage cases of varying non-specific types (including, but not limited to, changes in stiffness, mass, and damping), and estimation of updated parameter uncertainty. The algorithm is appropriate for systems with unspecified and potentially severe levels of structural, proportional, and/or generalized damping and with significantly reduced degree-of-freedom reference sets. The algorithm is also robust to measurement noise, large variations in parameter sensitivity, and the various numerical complications associated with application to realistically sized structures.

The current effort follows decades of research and development towards structural health monitoring technology by engineers, researchers, and students around the world, and the result is a system that—in the author's opinion—has significant potential for application to real-world aerospace structures. The next steps in continuing work would be to experimentally apply and validate the algorithm on increasingly large and realistic structures with controlled and then operationally-generated damage cases. Application to the structural health monitoring scaled-wing test-bed presented in Chapter 7 would be a natural start. However, the algorithm is generalized enough in its construction that application could be made to a very many structures, both within and outside of the world of aerospace. As discussed in Chapter 1, the primary interest is to end up with fully integrated systems for regular and accurate structural health monitoring of operational structures, and then to extend the analysis to prognosis so that the damage propagation

and the useful life of the structure may be understood and tracked. The day will inevitably come when the majority of airplanes, spacecraft, unmanned aerial vehicles, automobiles, buildings, bridges, and the other aerospace and civil infrastructure that form the foundation of our civilization will know at any given second their state of health, the details of any anomalies, and life-expectancy. In the beginning, this will be a small evolution from the detail currently provided by regular inspection. In the long run, the structures we live with and depend on will operate with fully integrated sophisticated health systems that rival and even surpass the biological nervous systems that are their inspiration.

APPENDIX A. EXTENDED RAYLEIGH DAMPING DERIVATION

It is assumed that N_D degree-of-freedom stiffness matrix $[K]$ and mass matrix $[M]$ are known from the analytical model and that natural frequencies ω_n, N_D degree-of-freedom mode shapes $\{\phi_n\}$, and modal damping ratios ζ_n have been measured for $n = 1...c$ modes, where ω_c, $\{\phi_c\}$, and ζ_c correspond to the highest mode in the set. Derivation of a viscous damping matrix $[C]$ by the extended Rayleigh damping method, following Clough and Penzien (2003), then proceeds as follows.

The goal is to calculate $[C]$ which replicates measured model damping at specified modes and is orthogonal to the mode shapes. Orthogonality is guaranteed by forming the damping matrix as a summation of scaled mass and stiffness matrices, which are assumed to be orthogonal with the properties

$$\{\phi\}_m^T [M] \{\phi\}_n = \begin{cases} M_n, & \text{if } m = n \\ 0, & \text{if } m \neq n \end{cases}, \tag{A.1}$$

$$\{\phi\}_m^T [K] \{\phi\}_n = \begin{cases} K_n, & \text{if } m = n \\ 0, & \text{if } m \neq n \end{cases}, \tag{A.2}$$

and

$$\omega_n^2 = \frac{K_n}{M_n}. \tag{A.2}$$

The damping matrix will thus obey the relationship

$$\{\phi\}_m^T [C]\{\phi\}_n = \begin{cases} C_n, & \text{if } m = n \\ 0, & \text{if } m \neq n \end{cases}$$

(A.3)

where C_n is defined in terms of the modal damping ratio as

$$C_n = 2\omega_n \zeta_n M_n$$

(A.4)

for each mode n. Defining $[C_n]$ as the diagonal matrix containing the components C_n, the orthogonality relationship can alternatively be written in matrix form as

$$[\Phi]^T [C][\Phi] = \begin{bmatrix} \ddots & & \\ & 2\omega_n \zeta_n M_n & \\ & & \ddots \end{bmatrix} = [C_n]$$

(A.5)

(Note: For the derivation it is assumed that the mode shape matrix is fully populated, with dimensions equal to system matrices, even though only select modes will end up being used to populate the damping matrix). Similarly, the diagonal model mass matrix $[M_n]$ can be written as

$$[M_n] = [\Phi]^T [M][\Phi],$$

(A.6)

If Eq. (A.6) is pre-multiplied by $[M_n]^{-1}$ and the post-multiplied by $[\Phi]^{-1}$ the relationship

$$[\Phi]^{-1} = [M_n]^{-1}[\Phi]^T [M],$$

(A.7)

is established. Similarly, pre-multiplying Eq. (A.6) by $[\Phi]^{-T}$ (where superscript $[...]^{-T}$ denotes the inverse of the transpose of the matrix) and then post-multiplying by $[M]^{-1}$ produces

$$[\Phi]^{-T} = [M][\Phi][M_n]^{-1}. \tag{A.8}$$

Equation (A.5) is now inverted to produce

$$[C] = [\Phi]^{-T}[C_n][\Phi]^{-1}, \tag{A.9}$$

and combining with Eqs. (A.7) and (A.8) and recognizing symmetry of the mass matrix (i.e., $[M]^T = [M]$) gives the relationship

$$[C] = [M][\Phi][M_n]^{-1}[C_n][M_n]^{-1}[\Phi]^T[M]. \tag{A.10}$$

The central three matrices on the right hand side of this equation are all diagonal and thus can be combined into a single diagonal matrix $[D_n]$ with non-zero components

$$D_n = \frac{2\omega_n \zeta_n}{M_n}. \tag{A.11}$$

Equation (A.10) can therefore be rewritten

$$[C] = [M][\Phi][D_n][\Phi]^T[M]. \tag{A.12}$$

Inspecting the form of this equation, it can be seen that each mode effectively makes an independent contribution to the damping matrix equal to $[M]\{\phi\}_n D_n \{\phi\}_n^T [M]$ and the damping matrix can therefore be written as a summation of these parts:

$$[C] = [M]\left(\sum_{n=1}^{c} \{\phi\}_n D_n \{\phi\}_n^T \right)[M].$$

(A.13)

This equation could be used to generate the damping matrix; however, if the number of modes used is less than the total number present in the system, i.e. if $c < N_D$, then undamped modes above $n = c$ will be amplified by the lack of analytical damping and may distort response in the range of interest. This effect can be mitigated by adding in stiffness proportional damping at the highest mode of interest. The reasoning can be seen by imagining a single mode with viscous damping proportional to the stiffness matrix by a constant a_1, $[C] = a_1 [K]$, which leads to the relationship

$$C_n = a_1 \{\phi\}_n^T [K]\{\phi\}_n = a_1 K_n = a_1 \omega_n^2 M_n.$$

(A.14)

Substituting in Eq. (A.4) then produces

$$\zeta_n = \frac{a_1 \omega_n}{2}.$$

(A.15)

and it can be seen that modal damping increases linearly with natural frequency.

If the proportionality constant a_1 is set to produce the desired damping ratio at the highest mode of interest, then

$$a_1 = \frac{2\zeta_c}{\omega_c}. \tag{A.16}$$

Each mode will now have a damping ration equal to the sum of stiffness-proportional damping, designated as $(\zeta_n)_K$, and mass-proportional damping given in Eq. (A.13), designated as $(\zeta_n)_M$. The stiffness contribution is equal to

$$(\zeta_n)_K = \frac{a_1 \omega_c}{2} = \zeta_c \left(\frac{\omega_n}{\omega_c} \right). \tag{A.17}$$

Hence, in order to achieve a total combined damping ratio of ζ_n, the mass-proportional damping ratio must be

$$(\zeta_n)_M = \zeta_n - \zeta_c \left(\frac{\omega_n}{\omega_c} \right). \tag{A.18}$$

The final equation for the extended Rayleigh proportional damping matrix is thus

$$[C] = a_1 [K] + [M] \left(\sum_{n=1}^{c-1} \{\phi\}_n \frac{2\omega_c (\zeta_n)_M}{M_n} \{\phi\}_n^T \right) [M], \tag{A.19}$$

or, after substituting in Eqs. (A.16) and (A.18) and rearranging,

$$[C] = \left(\frac{2\zeta_c}{\omega_c} \right)[K] + [M] \left[\sum_{n=1}^{c-1} 2 \left(\zeta_n - \zeta_c \left(\frac{\omega_n}{\omega_c} \right) \right) \frac{\omega_n}{M_n} \{\phi_n\} \{\phi_n\}^T \right] [M], \tag{A.20}$$

A.2   Appendix A References

[A-1]   Clough, R.W., Penzien, J., Dynamics of Structures, Second Edition, McGraw Hill, (1993)

APPENDIX B. BAYESIAN OPTIMAL ESTIMATE FOR LINEAR SYSTEMS

Parameter estimation in a system which is nonlinear in its parameters can be accomplished by iteratively applying small linear updates—repeatedly linearizing the system and updating. One method for achieving a best linear unbiased estimate is minimization of the variance of the difference between measured and analytical response quantities and can be derived as follows (following Collins et al. (1974) and Martinez (1982) for a general response residual). To start, a general linear system, where the random measured response vector $\{Y\}$ is modeled as the system $[A]$ multiplied by random parameters in $\{x\}$ plus a vector of measurement noise $\{v\}$, is written

$$\{Y\} = [A]\{x\} + \{v\} \tag{B.1}$$

The prior statistical information for the random variables can be defined as $\{x\} \rightarrow \mathsf{N}\left(\{\hat{x}_0\}, \left[S_{\hat{x}_0\hat{x}_0}\right]\right)$ and $\{v\} \rightarrow \mathsf{N}\left(\{\mu_v\}, [S_{vv}]\right)$, where $\{\alpha\} \rightarrow \mathsf{N}\left(\{\mu_\alpha\}, [S_{\alpha\alpha}]\right)$ denotes generic quantity $\{\alpha\}$ as a Gaussian normal random quantity with mean

$$\{\mu_\alpha\} = E\{\alpha\} \tag{B.2}$$

and covariance

$$[S_{\alpha\alpha}] = E\left[(\{\alpha\} - E\{\alpha\})(\{\alpha\} - E\{\alpha\})^T\right], \tag{B.3}$$

472

a *caret* denotes an estimated point value of a random quantity, and $E(...)$ refers to the expected value (with $E[...], E\{...\}$ occasionally used for brevity, depending on the dimensionality.

The random variance covariance matrices can be written explicitly as

$$\left[S_{\hat{x}_0 \hat{x}_0} \right] = E\left[\left(\{x\} - \{\hat{x}_0\} \right)\left(\{x\} - \{\hat{x}_0\} \right)^T \right], \tag{B.4}$$

$$\left[S_{vv} \right] = E\left[\left(\{v\} - \{\mu_v\} \right)\left(\{v\} - \{\mu_v\} \right)^T \right]. \tag{B.5}$$

At a given time the model will be in a state represented by the prior mean set $\{\hat{x}_0\}$, with corresponding response

$$\{Y_0\} = [A]\{x_0\} \tag{B.6}$$

Given a new measured response $\{\tilde{Y}\}$, a new set of parameters are desired such at the model response matches the measured response as closely as possible, given the noise; i.e., such it satisfies the system

$$\{\tilde{Y}\} = [A]\{x\} + \{v\}. \tag{B.7}$$

Subtracting the initial estimate response equation from the measured response equation leads to

$$\{\tilde{Y}\} - \{Y_0\} = [A]\{x\} + \{v\} - [A]\{\hat{x}_0\}, \tag{B.8}$$

and can be further simplified to

$$\{\Delta Y_0\} = [A]\{\Delta x_0\} + \{v\} \tag{B.9}$$

where

$$\{\Delta Y_0\} = \{\tilde{Y}\} - \{Y_0\}, \tag{B.10}$$

$$\{\Delta x_0\} = \{x\} - \{\hat{x}_0\} \tag{B.11}$$

are the prior measurement residual and prior estimation error, respectively.

The prior parameter expected value is still the prior parameter estimate vector, and thus the prior estimation error mean is zero, as shown by the following succession:

$$E\{\Delta x_0\} = E(\{x\} - \{\hat{x}_0\}) = E(\{x\}) - E(\{\hat{x}_0\}) = \{\hat{x}_0\} - \{\hat{x}_0\} = 0. \tag{B.12}$$

Based on this result, the prior estimation error can be written simply

$$\left[S_{\Delta x_0 \Delta x_0}\right] = E\left[\{\Delta x_0\}\{\Delta x_0\}^T\right], \tag{B.13}$$

and substituting in $\{\Delta x_0\} = \{x\} - \{\hat{x}_0\}$ shows it to equal the original prior parameter covariance:

$$\left[S_{\Delta x_0 \Delta x_0}\right] = E\left[(\{x\} - \{\hat{x}_0\})(\{x\} - \{\hat{x}_0\})^T\right] = \left[S_{\hat{x}_0 \hat{x}_0}\right]. \tag{B.14}$$

The prior measurement residual mean is first written in terms of the expected value, and then expanded to give

$$E\{\Delta Y_0\} = E\left([A]\{\Delta x_0\} + \{v\}\right) = [A]E\{\Delta x_0\} + E\{v\}. \tag{B.15}$$

Recognizing that $E\{\Delta x_0\} = 0$ and $E\{v\} = \mu_v$ from above, the expression reduces to

$$E\{\Delta Y_0\} = \{\mu_v\}. \tag{B.16}$$

The prior measurement residual covariance is calculated by plugging the system difference equation along with $E\{\Delta Y_0\} = \{\mu_v\}$ into the formulation for covariance, to give

$$\begin{aligned}
\left[S_{\Delta Y_0 \Delta Y_0}\right] &= E\left[\left(\{\Delta Y_0\} - E\{\Delta Y_0\}\right)\left(\{\Delta Y_0\} - E\{\Delta Y_0\}\right)^T\right] \\
&= E\left[\left([A]\{\Delta x_0\} + \{v\} - \{\mu_v\}\right)\left([A]\{\Delta x_0\} + \{v\} - \{\mu_v\}\right)^T\right].
\end{aligned} \tag{B.17}$$

Expanding the quadratic and bringing the expected value onto each term produces

$$\begin{aligned}
\left[S_{\Delta Y_0 \Delta Y_0}\right] &= E\left([A]\{\Delta x_0\}\{\Delta x_0\}^T [A]^T\right) + E\left([A]\{\Delta x_0\}\left(\{v\} - \{\mu_v\}\right)^T\right) + \ldots \\
&\quad \ldots E\left(\left(\{v\} - \{\mu_v\}\right)\{\Delta x_0\}^T [A]^T\right) + E\left(\left(\{v\} - \{\mu_v\}\right)\left(\{v\} - \{\mu_v\}\right)^T\right).
\end{aligned} \tag{B.18}$$

By expanding and recognizing the parameter covariance the first term becomes

$$E\left([A]\{\Delta x_0\}\{\Delta x_0\}^T [A]^T\right) = [A]E\left(\{\Delta x_0\}\{\Delta x_0\}^T\right)[A]^T = [A]\left[S_{\hat{x}_0 \hat{x}_0}\right][A]^T. \tag{B.19}$$

The second and third terms equal zero because $\{\Delta x_0\}$ and $\{v\}$ are statistically independent, and thus

$$E\Big([A]\{\Delta x_0\}\big(\{v\}-\{\mu_v\}\big)^T\Big)=[A]E\Big(\{\Delta x_0\}\big(\{v\}-\{\mu_v\}\big)^T\Big)=[0], \tag{B.20}$$

$$E\Big(\big(\{v\}-\{\mu_v\}\big)\{\Delta x_0\}^T[A]^T\Big)=E\Big(\big(\{v\}-\{\mu_v\}\big)\{\Delta x_0\}^T\Big)[A]^T=[0]. \tag{B.21}$$

Finally, the last term is the previously defined noise covariance. The full expression is therefore

$$\big[S_{\Delta Y_0 \Delta Y_0}\big]=[A]\big[S_{\hat{x}_0 \hat{x}_0}\big][A]^T+[S_{vv}]. \tag{B.22}$$

The covariance between response and parameters can similarly be calculated by first writing

$$\begin{aligned}
\big[S_{\Delta Y_0 \Delta x_0}\big] &= E\Big[\big(\{\Delta Y_0\}-\{\mu_v\}\big)\big(\{\Delta x_0\}\big)^T\Big] \\
&= E\Big[\big([A]\{\Delta x_0\}+\{v\}-\{\mu_v\}\big)\big(\{\Delta x_0\}\big)^T\Big],
\end{aligned} \tag{B.23}$$

then expanding to

$$\big[S_{\Delta Y_0 \Delta x_0}\big]=[A]E\Big[\{\Delta x_0\}\{\Delta x_0\}^T\Big]+E\Big[\big(\{v\}-\{\mu_v\}\big)\big(\{\Delta x_0\}\big)^T\Big]. \tag{B.24}$$

By recognizing the parameter covariance and that $E\Big[\big(\{v\}-\{\mu_v\}\big)\big(\{\Delta x_0\}\big)^T\Big]=0$ because of statistical independence, the final expression can be written as

$$\big[S_{\Delta Y_0 \Delta x_0}\big]=[A]\big[S_{\hat{x}_0 \hat{x}_0}\big]. \tag{B.25}$$

Similarly, the transposed case can be written

$$\left[S_{\Delta x_0 \Delta Y_0} \right] = \left[S_{\hat{x}_0 \hat{x}_0} \right] [A]^T . \tag{B.26}$$

Because $\left[S_{\hat{x}_0 \hat{x}_0} \right]$ is symmetric, it can additionally be observed that

$$\left[S_{\Delta x_0 \Delta Y_0} \right] = \left[S_{\Delta Y_0 \Delta x_0} \right]^T . \tag{B.27}$$

It is desired to find $\{\hat{x}\}$, the optimal estimate of $\{x\}$, based on measured $\{\tilde{Y}\}$ and the prior estimate $\{\hat{x}_0\}$. As demonstrated in Martinez (1982), under a few very general assumptions several common Bayesian estimators—including maximum a posteriori, maximum likelihood, and minimum mean square error (i.e., unbiased minimum variance)—are equivalent. In particular, if the conditional distribution of $\{x\}$ given $\{\tilde{Y}\}$, $f(\{x\}|\{\tilde{Y}\})$, is symmetric about the mean and convex for argument values less than or equal to the mean, then the optimal estimate is also the conditional mean; i.e.,

$$\{\hat{x}\} = E\left(\{x\}|\{\tilde{Y}\}\right) = E\{x\} + \left[S_{x\tilde{Y}} \right] \left[S_{\tilde{Y}\tilde{Y}} \right]^{-1} \left(\{\tilde{Y}\} - E\{\tilde{Y}\} \right) . \tag{B.28}$$

For symmetric unimodal density functions (e.g., Gaussian) the maximum a posteriori estimation will also produce the optimal estimate. Furthermore, the minimum mean square error estimate, which is also the unbiased minimum variance estimate (where an unbiased estimator is one for which the expected value of the estimator and the true variable are the same; i.e., $E\{\hat{x}\} = E\{x\}$), is equivalent to the conditional mean for continuous density functions. The minimum mean square error estimate is equivalent to

an extended weighted least-squares minimization, where the inverse covariance matrices are used to weight the system residual error and parameter regularization terms, and it can be shown that the appropriately formulated least-squares minimization also produces the optimal estimate.

The optimal estimate $\{\hat{x}\}$ can be found, as stated above, via the unbiased minimum variance estimator. In other words, it is desired to find G in the equation

$$\{\Delta\hat{x}\} = [G]\{\Delta Y_0\} \tag{B.29}$$

where $[G]$ minimizes the variance of the difference between the true parameter difference $\{\Delta x_0\} = \{x\} - \{\hat{x}_0\}$ and estimated parameter difference $\{\Delta\hat{x}\} = \{\hat{x}\} - \{\hat{x}_0\}$. Note that the difference forms $\{\Delta x_0\}$ and $\{\Delta\hat{x}\}$ are used instead of the pure parameters $\{x\}$ and $\{\hat{x}\}$ because the update requires differences to drive it, as evidenced by the form of Eq. (B.1). Because the estimator is unbiased, by definition, the expected values of $\{x\}$ and $\{\hat{x}\}$ will be equal; therefore, the minimization problem can be presented as

$$\min_{[G]}[Q], \text{ where } [Q] = E\left(\left(\{\Delta x_0\} - \{\Delta\hat{x}\}\right)\left(\{\Delta x_0\} - \{\Delta\hat{x}\}\right)^T\right). \tag{B.30}$$

Substituting the system equations into $[Q]$ and expanding gives

$$Q = E\left(\left(\{\Delta x_0\} - [G]\{\Delta Y_0\}\right)\left(\{\Delta x_0\} - [G]\{\Delta Y_0\}\right)^T\right), \tag{B.31}$$

$$Q = E\left([G]\{\Delta Y_0\}\{\Delta Y_0\}^T[G]^T - [G]\{\Delta Y_0\}\{\Delta x_0\}^T - \ldots \right. $$
$$\left. \ldots\{\Delta x_0\}\{\Delta Y_0\}^T[G]^T + \{\Delta x_0\}\{\Delta x_0\}^T\right). \tag{B.32}$$

The expected value can then be expanded, and covariance matrices recognized, to produce

$$[Q] = [G]\left[S_{\Delta Y_0 \Delta Y_0}\right][G]^T - [G]\left[S_{\Delta Y_0 \Delta x_0}\right] - \left[S_{\Delta x_0 \Delta Y_0}\right][G]^T + \left[S_{\Delta x_0 \Delta x_0}\right],$$ (B.33)

The minimization problem is solved by setting the first variation equal to zero, producing

$$[\delta Q]\big|_{\delta G} = 0 = \delta [G]\left[\frac{\partial Q}{\partial G}\right] + \left[\frac{\partial Q}{\partial G^T}\right]\delta [G]^T,$$ (B.34)

and, by taking the derivatives and substituting in,

$$0 = \delta [G]\left(-\left[S_{\Delta Y_0 \Delta x_0}\right] + \left[S_{\Delta Y_0 \Delta Y_0}\right][G]^T\right) + \left(-\left[S_{\Delta x_0 \Delta Y_0}\right] + [G]\left[S_{\Delta Y_0 \Delta Y_0}\right]\right)\delta [G]^T.$$ (B.35)

Invoking the principal of variations gives the equivalent expressions

$$0 = -\left[S_{\Delta Y_0 \Delta x_0}\right] + \left[S_{\Delta Y_0 \Delta Y_0}\right][G]^T,$$
$$0 = -\left[S_{\Delta x_0 \Delta Y_0}\right] + [G]\left[S_{\Delta Y_0 \Delta Y_0}\right],$$ (B.36)

and rearranging finally produces the estimator solution,

$$[G] = \left[S_{\Delta x_0 \Delta Y_0}\right]\left[S_{\Delta Y_0 \Delta Y_0}\right]^{-1},$$ (B.37)

or equivalently,

$$[G] = \left[S_{\Delta Y_0 \Delta x_0}\right]^T \left[S_{\Delta Y_0 \Delta Y_0}\right]^{-1},$$ (B.38)

with a transpose of

$$[G]^T = \left[S_{\Delta Y_0 \Delta Y_0} \right]^{-1} \left[S_{\Delta Y_0 \Delta x_0} \right].$$

(B.39)

The update equation can now be written in terms of covariance quantities by combining the estimator solution with Eq. (B.29) to give

$$\{\Delta \hat{x}\} = \left[S_{\Delta Y_0 \Delta x_0} \right]^T \left[S_{\Delta Y_0 \Delta Y_0} \right]^{-1} \{\Delta Y_0\};$$

(9.40)

expanding the variables and rearranging then leads to

$$\{\hat{x}\} = \{\hat{x}_0\} + \left[S_{\Delta Y_0 \Delta x_0} \right]^T \left[S_{\Delta Y_0 \Delta Y_0} \right]^{-1} \left(\{\tilde{Y}\} - \{Y_0\} \right).$$

(B.41)

Notice that if $E\{\hat{x}\} = \{\hat{x}_0\}$ and $E\{\tilde{Y}\} = \{Y_0\}$, consistent with prior assumptions, then this result equals the conditional mean as described above in Eq. (B.28). In the current general formulation with non-zero mean noise, this equivalence would not be true because then $E\{\tilde{Y}\} = \{Y_0\} + \{\mu_v\}$; however, non-zero noise introduces bias in which case the minimum variance estimator and conditional mean are not expected to be equivalent.

Substituting in previously derived expressions for the covariance quantities leads to the final expression for the optimal estimate:

$$\{\hat{x}\} = \{\hat{x}_0\} + \left[S_{\hat{x}_0 \hat{x}_0} \right] [A]^T \left[[A] \left[S_{\hat{x}_0 \hat{x}_0} \right] [A]^T + [S_{vv}] \right]^{-1} \left(\{\tilde{Y}\} - \{Y_0\} \right).$$

(B.42)

The posterior parameter covariance is given by the expression

$$\left[S_{xx}^* \right] = E\left(\left(\{x\} - \{\hat{x}\} \right)\left(\{x\} - \{\hat{x}\} \right)^T \right), \tag{B.43}$$

and can be found following reference Collins et al. [B-1]. Its equality to the parameter difference covariance, previously represented by $[Q]$, is first shown by subtracting the prior estimate from each vector, as

$$\left[S_{xx}^* \right] = E\left(\left(\left(\{x\} - \{\hat{x}_0\} \right) - \left(\{\hat{x}\} - \{\hat{x}_0\} \right) \right)\left(\left(\{x\} - \{\hat{x}_0\} \right) - \left(\{\hat{x}\} - \{\hat{x}_0\} \right) \right)^T \right), \tag{B.44}$$

and then recognizing the parameter difference expressions, to give

$$\left[S_{xx}^* \right] = E\left(\left(\{\Delta x_0\} - \{\Delta\hat{x}\} \right)\left(\{\Delta x_0\} - \{\Delta\hat{x}\} \right)^T \right). \tag{B.45}$$

The expanded version of $[Q]$ given in Eq. (B.33) can now be combined with the solution of $[G]$, giving

$$\left[S_{xx}^* \right] = \left[S_{\Delta Y_0 \Delta x_0} \right]^T \left[S_{\Delta Y_0 \Delta Y_0} \right]^{-1} \left[S_{\Delta Y_0 \Delta Y_0} \right]\left[S_{\Delta Y_0 \Delta Y_0} \right]^{-1} \left[S_{\Delta Y_0 \Delta x_0} \right] - \dots$$
$$\dots \left[S_{\Delta Y_0 \Delta x_0} \right]^T \left[S_{\Delta Y_0 \Delta Y_0} \right]^{-1} \left[S_{\Delta Y_0 \Delta x_0} \right] - \left[S_{\Delta x_0 \Delta Y_0} \right]\left[S_{\Delta Y_0 \Delta Y_0} \right]^{-1} \left[S_{\Delta Y_0 \Delta x_0} \right] + \left[S_{\Delta x_0 \Delta x_0} \right], \tag{B.46}$$

and canceling terms then leads to

$$\left[S_{xx}^* \right] = \left[S_{\Delta x_0 \Delta x_0} \right] - \left[S_{\Delta x_0 \Delta Y_0} \right]\left[S_{\Delta Y_0 \Delta Y_0} \right]^{-1} \left[S_{\Delta Y_0 \Delta x_0} \right]. \tag{B.47}$$

Substituting in the previously derived expressions for various covariance matrices leads to the following final expression:

$$\left[S_{xx}^* \right] = \left[S_{\hat{x}_0 \hat{x}_0} \right] - \left[S_{\hat{x}_0 \hat{x}_0} \right][A]^T \left([A]\left[S_{\hat{x}_0 \hat{x}_0} \right][A]^T + [S_{vv}] \right)^{-1} [A]\left[S_{\hat{x}_0 \hat{x}_0} \right]. \tag{B.48}$$

An alternative representation of this expression, consistent with Gura [B-2] and Martinez [B-3], can be found, for matrices B, U, C, and V, by invoking the matrix inversion lemma,

$$\left(B+UCV\right)^{-1} = B^{-1} - B^{-1}U\left(C^{-1}+VB^{-1}U\right)^{-1}VB^{-1} \tag{B.49}$$

producing

$$\left[S_{xx}^{*}\right] = \left(\left[S_{\hat{x}_0\hat{x}_0}\right]^{-1} + \left[A\right]^{T}\left[S_{vv}\right]^{-1}\left[A\right]\right)^{-1}. \tag{B.50}$$

Likewise, the estimate equation can be written in an alternate form which is more easily compared to similar equations from the literature, as

$$\{\hat{x}\} = \{\hat{x}_0\} + \left(\left[S_{\hat{x}_0\hat{x}_0}\right]^{-1} + \left[A\right]^{T}\left[S_{vv}\right]^{-1}\left[A\right]\right)^{-1}\left[A\right]^{T}\left[S_{vv}\right]^{-1}\left(\{\tilde{Y}\}-\left[A\right]\{\hat{x}_0\}\right); \tag{B.51}$$

or, in terms of the posterior parameter covariance, as

$$\{\hat{x}\} = \{\hat{x}_0\} + \left[S_{xx}\right]^{-1}\left[A\right]^{T}\left[S_{vv}\right]^{-1}\left(\{\tilde{Y}\}-\left[A\right]\{\hat{x}_0\}\right). \tag{B.52}$$

To prove equivalence to the original estimate expression in Eq. (B.42), first expand Eq. (B.52) using the matrix inversion lemma on the inverse quantity to form

$$\{\hat{x}\} = \{\hat{x}_0\} + \left(\left[S_{\hat{x}_0\hat{x}_0}\right] - \left[S_{\hat{x}_0\hat{x}_0}\right]\left[A\right]^{T}\left(\left[A\right]\left[S_{\hat{x}_0\hat{x}_0}\right]\left[A\right]^{T} + \left[S_{vv}\right]\right)^{-1}\left[A\right]\left[S_{\hat{x}_0\hat{x}_0}\right]\right)\dots$$
$$\dots\left[A\right]^{T}\left[S_{vv}\right]^{-1}\left(\{\tilde{Y}\}-\left[A\right]\{\hat{x}_0\}\right). \tag{B.53}$$

Subtracting this quantity from Eq. (B.42) and rearranging leaves the expression

$$\left(\left[S_{\hat{x}_0\hat{x}_0}\right]-\left[S_{\hat{x}_0\hat{x}_0}\right][A]^T\left([A]\left[S_{\hat{x}_0\hat{x}_0}\right][A]^T+[S_{vv}]\right)^{-1}[A]\left[S_{\hat{x}_0\hat{x}_0}\right]\right)[A]^T[S_{vv}]^{-1}\ldots$$
$$\ldots=\left[S_{\hat{x}_0\hat{x}_0}\right][A]^T\left([A]\left[S_{\hat{x}_0\hat{x}_0}\right][A]^T+[S_{vv}]\right)^{-1}. \tag{B.54}$$

Expanding and canceling $\left[S_{\hat{x}_0\hat{x}_0}\right][A]^T$ from the left leaves

$$[S_{vv}]^{-1}-\left([A]\left[S_{\hat{x}_0\hat{x}_0}\right][A]^T+[S_{vv}]\right)^{-1}[A]\left[S_{\hat{x}_0\hat{x}_0}\right][A]^T[S_{vv}]^{-1}\ldots$$
$$\ldots=\left([A]\left[S_{\hat{x}_0\hat{x}_0}\right][A]^T+[S_{vv}]\right)^{-1}. \tag{B.55}$$

Multiplying from the left by $\left([A]\left[S_{\hat{x}_0\hat{x}_0}\right][A]^T+[S_{vv}]\right)$ and canceling terms produces

$$[I]=[I] \tag{B.56}$$

and thus proves the equivalence.

B.2   Appendix B References

[B-1]   Collins, J.D., Hart, G.C., Hasselman, T.K., and Kennedy, B., "Statistical Identification of Structures," AIAA Journal, **12**(2), pp. 185–190, (1974)

[B-2]   Gura, I.A., "Extension of Linear Estimation Techniques to Nonlinear Problems," Journal of the Astronautical Sciences, **15**(4) , pp.194-205, (1968)

[B-3]   Martinez, D.R., "Estimation Theory Applied to Improving Structural Dynamics Models," Sandia National Laboratory Report SAND82-0572, (1982)

APPENDIX C. COMPLEX-TO-REAL MODE TRANSFORMATION STUDY

A comparison study is presented to evaluate the methods detailed in Section 5.4.3 for acquiring real mode shapes and natural frequencies from measured complex data. These methods are required for implementing the modal damping methods discussed in Section 5.4. The Rayleigh modal damping method implemented in full coordinates (Eq. 5-5 from Section 5.4.2.1) is used for all cases so differences between results are only related to which complex-to-real method was used. In each case, the methods are evaluated against the known exact analytical damping solution calculated using stiffness proportional viscous damping and representing the error generated by machine precision. An additional comparison is made to a result gained by using straight complex modal data without performing the complex-to-real conversion. The complex-to-real methods under consideration (with references to their previous descriptions in parentheses where applicable) are

    (A)   Rotated-real method (Section 5.4.3.1)

    (B)   Rotated absolute value method (Section 5.4.3.2)

    (C)   Fuellekrug method (Section 5.4.3.3)

    (D)   Complex modal data with no complex-to-real transformation

    (E)   Exact analytical solution, using known proportional damping

Figures C-1 through C-4 present results in terms of the driving point frequency response functions, frequency response function difference, residual force vector, and non-zero matrix element averaged magnitude over frequency, respectively. It can be seen by looking at these results that the Fuellekrug and rotated absolute value methods perform very similarly, with a very slight increase in accuracy being gained from the Fuellekrug method, and both methods giving acceptably low error. The rotated-real method, however, gives a substantially lower error and is thus clearly the better choice for these cases. On the other hand, using the complex data directly gives very inaccurate results, both in terms of the residual force vector and frequency response functions. All methods produce similar variations in damping matrix non-zero element magnitude across frequency, with the spikes corresponding to the poles of $\left[Z(r,\omega_k)\right]_{ss}^{-1}$ as observed and discussed in Section 5.5.2.
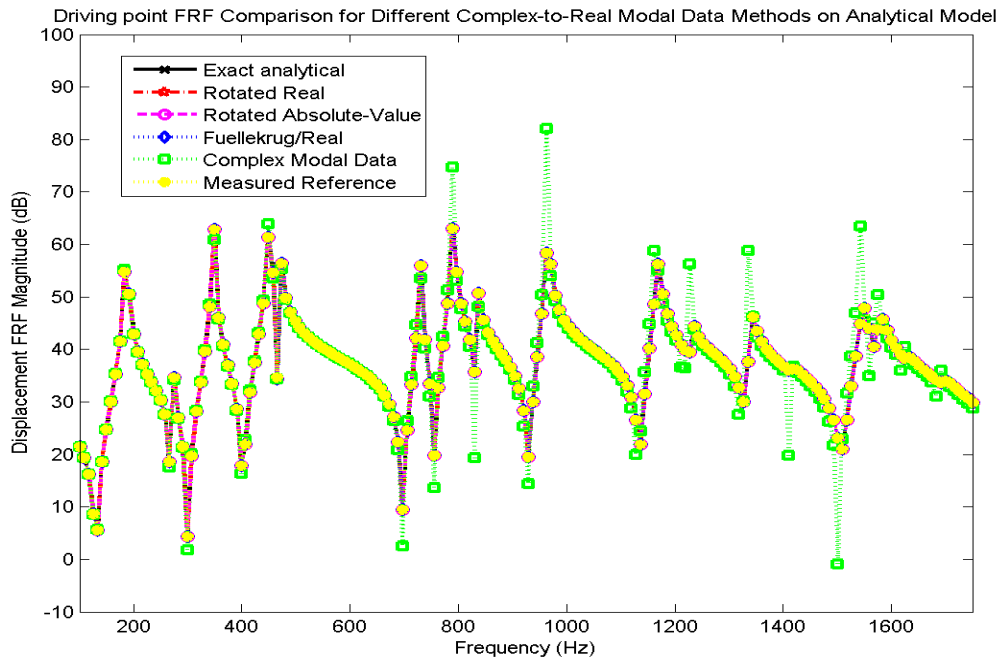
Figure C-1: Acceleration domain driving point frequency response functions of five complex-to-real modal transformation cases compared to exact analytical case (all using extended Rayleigh modal damping in *f-DOF*) and simulated reference frequency response function.
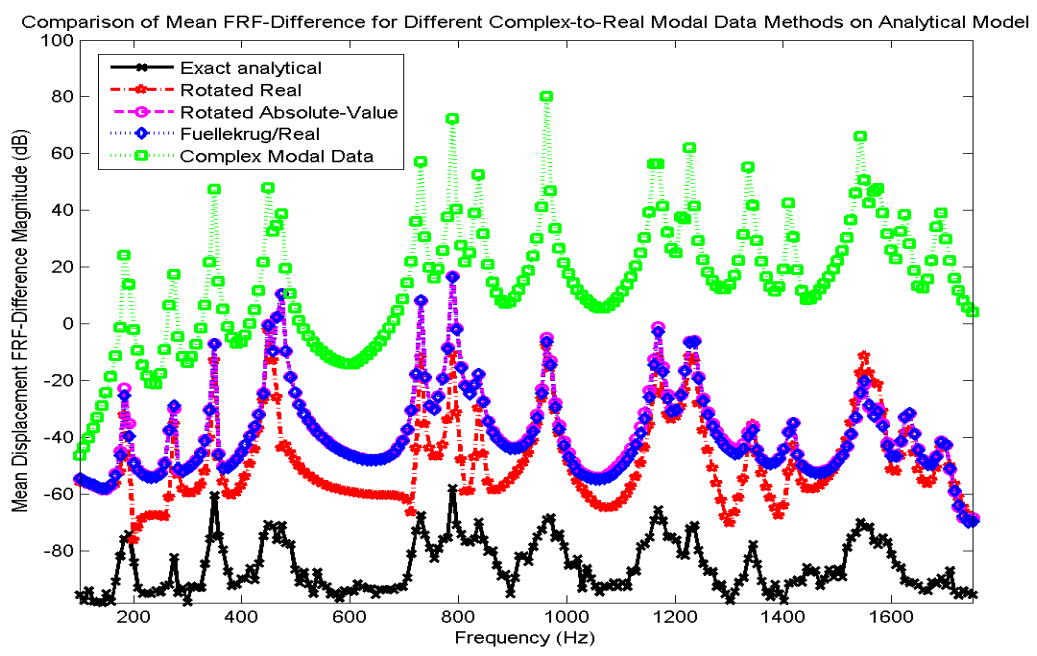
Figure C-2: Frequency response function difference, mean absolute value over degree-of-freedom, for five complex-to-real modal transformation cases compared to exact analytical case.
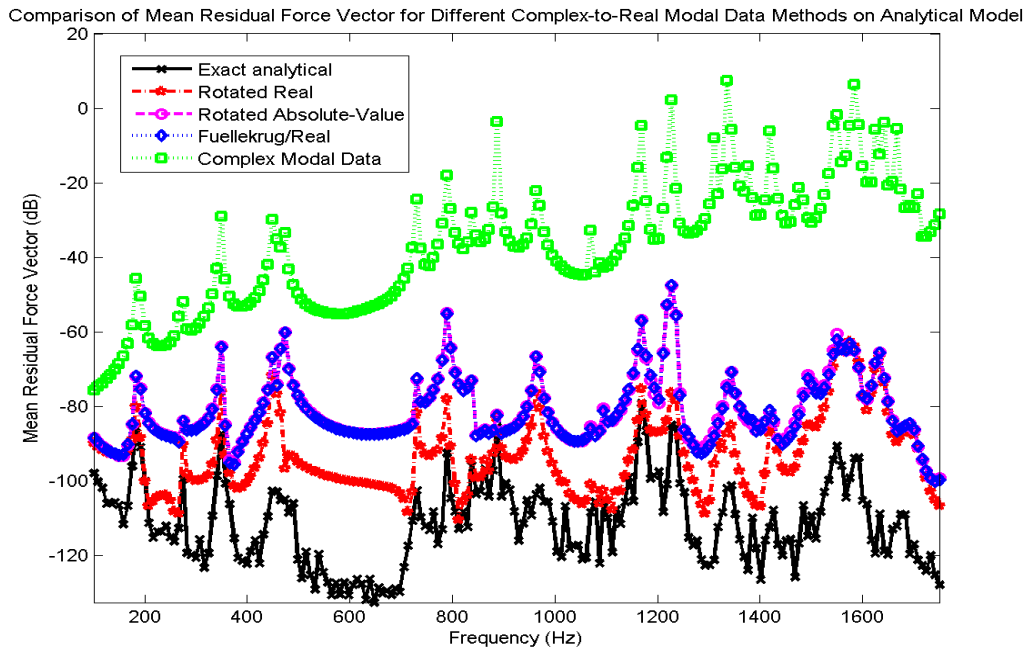
Figure C-3: Frequency response residual force vector, mean absolute value over degree-of-freedom, for five complex-to-real modal transformation cases compared to exact analytical case.
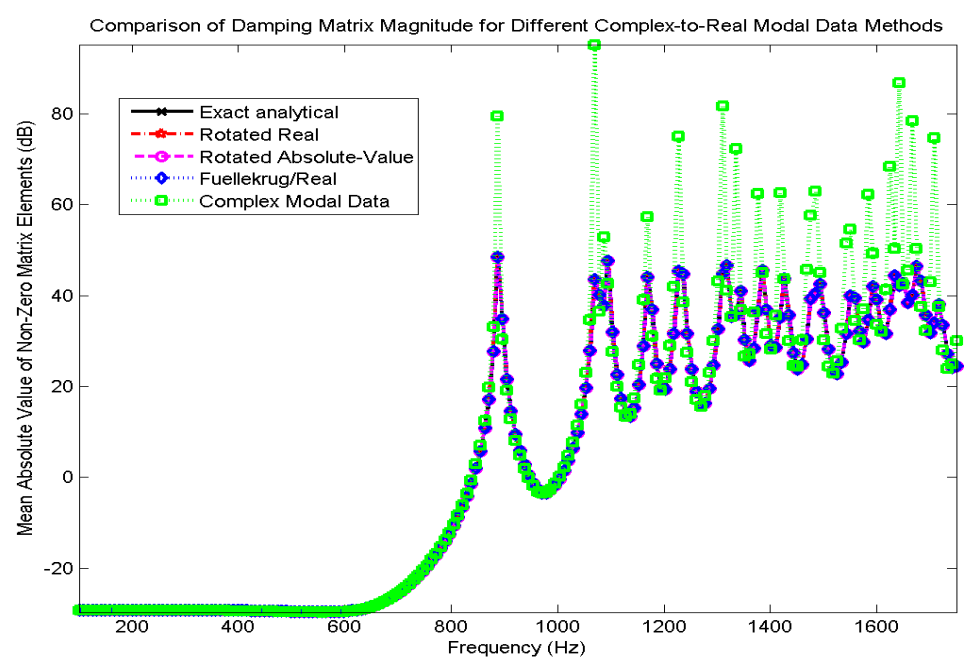
Figure C-4: Mean absolute value of non-zero reduced degree-of-freedom damping matrix elements for five complex-to-real modal transformation cases compared to exact analytical case (all using extended Rayleigh modal damping in *f-DOF*).

APPENDIX D. BULK DATA FILE FOR LAMINATE PLATE

```
INIT MASTER(S)
NASTRAN SYSTEM(442)=-1, SYSTEM(319)=1
SOL SEMODES
TIME 10000
CEND
  TITLE = NXNAS_HVT36_LFF_30MODES
  ECHO = NONE
  SET 1 = 1,5,9,13,17,21,85,89,93,97,101,105,169,173,177,181,185,189,253,257,
    261,265,269,273,337,341,345,349,353,357,421,425,429,433,437,441
  DISPLACEMENT(PRINT) = 1
  METHOD = 1
BEGIN BULK
PARAM,POST,-1
PARAM,OGEOM,NO
PARAM,AUTOSPC,YES
PARAM,MAXRATIO,1.+8
PARAM,GRDPNT,0
EIGRL          1                      36       0                      MASS
CORD2C*                1               0      0.                     0.
*                     0.              0.              0.              1.*
*                     1.              0.              1.
CORD2S*                2               0      0.                     0.
*                     0.              0.              0.              1.*
*                     1.              0.              1.
$ Femap with NX NASTRAN Property 1 : CST_Xply12_GrEp
PCOMP*                 1                              0.
*                                                                      *
*                      1       0.0001375              0.             YES
*                      1       0.0001375             90.             YES*
*                      1       0.0001375              0.             YES
*                      1       0.0001375             90.             YES*
*                      1       0.0001375              0.             YES
*                      1       0.0001375             90.             YES*
*                      1       0.0001375             90.             YES
*                      1       0.0001375              0.             YES*
*                      1       0.0001375             90.             YES
*                      1       0.0001375              0.             YES*
*                      1       0.0001375             90.             YES
*                      1       0.0001375              0.             YES
$ Femap with NX NASTRAN Material 1 : Composite Material
MAT8*                  1   129100000000.     7715200000.           0.3232
*            6407200000.     2630400000.     2630400000.        1560.505*
*                     0.              0.              0.
*                                                                      *
*
GRID           1       0      0.      0.      0.       0
GRID           2       0      0. .015025      0.       0
GRID           3       0      0.  .03005      0.       0
GRID           4       0      0. .045075      0.       0
GRID           5       0      0.   .0601      0.       0
GRID           6       0      0. .075125      0.       0
GRID           7       0      0.  .09015      0.       0
GRID           8       0      0.  .10517      0.       0
GRID           9       0      0.   .1202      0.       0
GRID          10       0      0.  .13522      0.       0
GRID          11       0      0.  .15025      0.       0
GRID          12       0      0.  .16528      0.       0
GRID          13       0      0.   .1803      0.       0
GRID          14       0      0.  .19533      0.       0
GRID          15       0      0.  .21035      0.       0
GRID          16       0      0.  .22537      0.       0
GRID          17       0      0.   .2404      0.       0
GRID          18       0      0.  .25542      0.       0
```

```
GRID        19      0      0.   .27045      0.      0
GRID        20      0      0.   .28547      0.      0
GRID        21      0      0.    .3005      0.      0
GRID        22      0  .01495      0.       0.      0
GRID        23      0  .01495 .015023      0.      0
GRID        24      0  .01495 .030045      0.      0
GRID        25      0  .01495 .045068      0.      0
GRID        26      0  .01495 .060091      0.      0
GRID        27      0  .01495 .075114      0.      0
GRID        28      0  .01495 .090136      0.      0
GRID        29      0  .01495  .10516      0.      0
GRID        30      0  .01495  .12018      0.      0
GRID        31      0  .01495   .1352      0.      0
GRID        32      0  .01495  .15023      0.      0
GRID        33      0  .01495  .16525      0.      0
GRID        34      0  .01495  .18027      0.      0
GRID        35      0  .01495   .1953      0.      0
GRID        36      0  .01495  .21032      0.      0
GRID        37      0  .01495  .22534      0.      0
GRID        38      0  .01495  .24036      0.      0
GRID        39      0  .01495  .25539      0.      0
GRID        40      0  .01495  .27041      0.      0
GRID        41      0  .01495  .28543      0.      0
GRID        42      0  .01495  .30045      0.      0
GRID        43      0   .0299      0.       0.      0
GRID        44      0   .0299 .015021      0.      0
GRID        45      0   .0299 .030041      0.      0
GRID        46      0   .0299 .045061      0.      0
GRID        47      0   .0299 .060082      0.      0
GRID        48      0   .0299 .075102      0.      0
GRID        49      0   .0299 .090123      0.      0
GRID        50      0   .0299  .10514      0.      0
GRID        51      0   .0299  .12016      0.      0
GRID        52      0   .0299  .13518      0.      0
GRID        53      0   .0299   .1502      0.      0
GRID        54      0   .0299  .16523      0.      0
GRID        55      0   .0299  .18025      0.      0
GRID        56      0   .0299  .19527      0.      0
GRID        57      0   .0299  .21029      0.      0
GRID        58      0   .0299  .22531      0.      0
GRID        59      0   .0299  .24033      0.      0
GRID        60      0   .0299  .25535      0.      0
GRID        61      0   .0299  .27037      0.      0
GRID        62      0   .0299  .28539      0.      0
GRID        63      0   .0299  .30041      0.      0
GRID        64      0  .04485      0.       0.      0
GRID        65      0  .04485 .015018      0.      0
GRID        66      0  .04485 .030036      0.      0
GRID        67      0  .04485 .045055      0.      0
GRID        68      0  .04485 .060073      0.      0
GRID        69      0  .04485 .075091      0.      0
GRID        70      0  .04485 .090109      0.      0
GRID        71      0  .04485  .10513      0.      0
GRID        72      0  .04485  .12015      0.      0
GRID        73      0  .04485  .13516      0.      0
GRID        74      0  .04485  .15018      0.      0
GRID        75      0  .04485   .1652      0.      0
GRID        76      0  .04485  .18022      0.      0
GRID        77      0  .04485  .19524      0.      0
GRID        78      0  .04485  .21026      0.      0
GRID        79      0  .04485  .22527      0.      0
GRID        80      0  .04485  .24029      0.      0
GRID        81      0  .04485  .25531      0.      0
GRID        82      0  .04485  .27033      0.      0
GRID        83      0  .04485  .28535      0.      0
GRID        84      0  .04485  .30036      0.      0
GRID        85      0   .0598      0.       0.      0
GRID        86      0   .0598 .015016      0.      0
GRID        87      0   .0598 .030032      0.      0
```

```
GRID          88        0    .0598 .045048      0.        0
GRID          89        0    .0598 .060064      0.        0
GRID          90        0    .0598  .07508      0.        0
GRID          91        0    .0598 .090096      0.        0
GRID          92        0    .0598  .10511      0.        0
GRID          93        0    .0598  .12013      0.        0
GRID          94        0    .0598  .13514      0.        0
GRID          95        0    .0598  .15016      0.        0
GRID          96        0    .0598  .16518      0.        0
GRID          97        0    .0598  .18019      0.        0
GRID          98        0    .0598  .19521      0.        0
GRID          99        0    .0598  .21022      0.        0
GRID         100        0    .0598  .22524      0.        0
GRID         101        0    .0598  .24026      0.        0
GRID         102        0    .0598  .25527      0.        0
GRID         103        0    .0598  .27029      0.        0
GRID         104        0    .0598   .2853      0.        0
GRID         105        0    .0598  .30032      0.        0
GRID         106        0   .07475      0.       0.        0
GRID         107        0   .07475 .015014      0.        0
GRID         108        0   .07475 .030027      0.        0
GRID         109        0   .07475 .045041      0.        0
GRID         110        0   .07475 .060055      0.        0
GRID         111        0   .07475 .075069      0.        0
GRID         112        0   .07475 .090082      0.        0
GRID         113        0   .07475   .1051      0.        0
GRID         114        0   .07475  .12011      0.        0
GRID         115        0   .07475  .13512      0.        0
GRID         116        0   .07475  .15014      0.        0
GRID         117        0   .07475  .16515      0.        0
GRID         118        0   .07475  .18016      0.        0
GRID         119        0   .07475  .19518      0.        0
GRID         120        0   .07475  .21019      0.        0
GRID         121        0   .07475  .22521      0.        0
GRID         122        0   .07475  .24022      0.        0
GRID         123        0   .07475  .25523      0.        0
GRID         124        0   .07475  .27025      0.        0
GRID         125        0   .07475  .28526      0.        0
GRID         126        0   .07475  .30028      0.        0
GRID         127        0    .0897      0.       0.        0
GRID         128        0    .0897 .015012      0.        0
GRID         129        0    .0897 .030023      0.        0
GRID         130        0    .0897 .045035      0.        0
GRID         131        0    .0897 .060046      0.        0
GRID         132        0    .0897 .075057      0.        0
GRID         133        0    .0897 .090069      0.        0
GRID         134        0    .0897  .10508      0.        0
GRID         135        0    .0897  .12009      0.        0
GRID         136        0    .0897   .1351      0.        0
GRID         137        0    .0897  .15012      0.        0
GRID         138        0    .0897  .16513      0.        0
GRID         139        0    .0897  .18014      0.        0
GRID         140        0    .0897  .19515      0.        0
GRID         141        0    .0897  .21016      0.        0
GRID         142        0    .0897  .22517      0.        0
GRID         143        0    .0897  .24018      0.        0
GRID         144        0    .0897   .2552      0.        0
GRID         145        0    .0897  .27021      0.        0
GRID         146        0    .0897  .28522      0.        0
GRID         147        0    .0897  .30023      0.        0
GRID         148        0   .10465      0.       0.        0
GRID         149        0   .10465 .015009      0.        0
GRID         150        0   .10465 .030018      0.        0
GRID         151        0   .10465 .045028      0.        0
GRID         152        0   .10465 .060037      0.        0
GRID         153        0   .10465 .075046      0.        0
GRID         154        0   .10465 .090056      0.        0
GRID         155        0   .10465  .10506      0.        0
GRID         156        0   .10465  .12007      0.        0
```

```
GRID        157      0  .10465  .13508     0.        0
GRID        158      0  .10465  .15009     0.        0
GRID        159      0  .10465   .1651     0.        0
GRID        160      0  .10465  .18011     0.        0
GRID        161      0  .10465  .19512     0.        0
GRID        162      0  .10465  .21013     0.        0
GRID        163      0  .10465  .22514     0.        0
GRID        164      0  .10465  .24015     0.        0
GRID        165      0  .10465  .25516     0.        0
GRID        166      0  .10465  .27017     0.        0
GRID        167      0  .10465  .28518     0.        0
GRID        168      0  .10465  .30018     0.        0
GRID        169      0   .1196      0.     0.        0
GRID        170      0   .1196 .015007     0.        0
GRID        171      0   .1196 .030014     0.        0
GRID        172      0   .1196 .045021     0.        0
GRID        173      0   .1196 .060028     0.        0
GRID        174      0   .1196 .075035     0.        0
GRID        175      0   .1196 .090042     0.        0
GRID        176      0   .1196  .10505     0.        0
GRID        177      0   .1196  .12006     0.        0
GRID        178      0   .1196  .13506     0.        0
GRID        179      0   .1196  .15007     0.        0
GRID        180      0   .1196  .16508     0.        0
GRID        181      0   .1196  .18008     0.        0
GRID        182      0   .1196  .19509     0.        0
GRID        183      0   .1196   .2101     0.        0
GRID        184      0   .1196  .22511     0.        0
GRID        185      0   .1196  .24011     0.        0
GRID        186      0   .1196  .25512     0.        0
GRID        187      0   .1196  .27013     0.        0
GRID        188      0   .1196  .28513     0.        0
GRID        189      0   .1196  .30014     0.        0
GRID        190      0  .13455      0.     0.        0
GRID        191      0  .13455 .015005     0.        0
GRID        192      0  .13455   .03001     0.        0
GRID        193      0  .13455 .045014     0.        0
GRID        194      0  .13455 .060019     0.        0
GRID        195      0  .13455 .075024     0.        0
GRID        196      0  .13455 .090028     0.        0
GRID        197      0  .13455  .10503     0.        0
GRID        198      0  .13455  .12004     0.        0
GRID        199      0  .13455  .13504     0.        0
GRID        200      0  .13455  .15005     0.        0
GRID        201      0  .13455  .16505     0.        0
GRID        202      0  .13455  .18006     0.        0
GRID        203      0  .13455  .19506     0.        0
GRID        204      0  .13455  .21007     0.        0
GRID        205      0  .13455  .22507     0.        0
GRID        206      0  .13455  .24008     0.        0
GRID        207      0  .13455  .25508     0.        0
GRID        208      0  .13455  .27009     0.        0
GRID        209      0  .13455  .28509     0.        0
GRID        210      0  .13455   .3001     0.        0
GRID        211      0   .1495      0.     0.        0
GRID        212      0   .1495 .015003     0.        0
GRID        213      0   .1495 .030005     0.        0
GRID        214      0   .1495 .045008     0.        0
GRID        215      0   .1495  .06001     0.        0
GRID        216      0   .1495 .075012     0.        0
GRID        217      0   .1495 .090015     0.        0
GRID        218      0   .1495  .10502     0.        0
GRID        219      0   .1495  .12002     0.        0
GRID        220      0   .1495  .13502     0.        0
GRID        221      0   .1495  .15002     0.        0
GRID        222      0   .1495  .16503     0.        0
GRID        223      0   .1495  .18003     0.        0
GRID        224      0   .1495  .19503     0.        0
GRID        225      0   .1495  .21003     0.        0
```

```
GRID       226      0  .1495  .22504     0.       0
GRID       227      0  .1495  .24004     0.       0
GRID       228      0  .1495  .25504     0.       0
GRID       229      0  .1495  .27004     0.       0
GRID       230      0  .1495  .28505     0.       0
GRID       231      0  .1495  .30005     0.       0
GRID       232      0  .16445     0.     0.       0
GRID       233      0  .16445   .015     0.       0
GRID       234      0  .16445    .03     0.       0
GRID       235      0  .16445 .045001    0.       0
GRID       236      0  .16445 .060001    0.       0
GRID       237      0  .16445 .075001    0.       0
GRID       238      0  .16445 .090002    0.       0
GRID       239      0  .16445   .105     0.       0
GRID       240      0  .16445    .12     0.       0
GRID       241      0  .16445   .135     0.       0
GRID       242      0  .16445    .15     0.       0
GRID       243      0  .16445   .165     0.       0
GRID       244      0  .16445    .18     0.       0
GRID       245      0  .16445   .195     0.       0
GRID       246      0  .16445    .21     0.       0
GRID       247      0  .16445   .225     0.       0
GRID       248      0  .16445    .24     0.       0
GRID       249      0  .16445   .255     0.       0
GRID       250      0  .16445    .27     0.       0
GRID       251      0  .16445   .285     0.       0
GRID       252      0  .16445  .30001    0.       0
GRID       253      0  .1794      0.     0.       0
GRID       254      0  .1794 .014998     0.       0
GRID       255      0  .1794 .029996     0.       0
GRID       256      0  .1794 .044994     0.       0
GRID       257      0  .1794 .059992     0.       0
GRID       258      0  .1794  .07499     0.       0
GRID       259      0  .1794 .089988     0.       0
GRID       260      0  .1794  .10499     0.       0
GRID       261      0  .1794  .11998     0.       0
GRID       262      0  .1794  .13498     0.       0
GRID       263      0  .1794  .14998     0.       0
GRID       264      0  .1794  .16498     0.       0
GRID       265      0  .1794  .17998     0.       0
GRID       266      0  .1794  .19497     0.       0
GRID       267      0  .1794  .20997     0.       0
GRID       268      0  .1794  .22497     0.       0
GRID       269      0  .1794  .23997     0.       0
GRID       270      0  .1794  .25497     0.       0
GRID       271      0  .1794  .26996     0.       0
GRID       272      0  .1794  .28496     0.       0
GRID       273      0  .1794  .29996     0.       0
GRID       274      0  .19435     0.     0.       0
GRID       275      0  .19435 .014996    0.       0
GRID       276      0  .19435 .029991    0.       0
GRID       277      0  .19435 .044987    0.       0
GRID       278      0  .19435 .059983    0.       0
GRID       279      0  .19435 .074979    0.       0
GRID       280      0  .19435 .089975    0.       0
GRID       281      0  .19435  .10497    0.       0
GRID       282      0  .19435  .11997    0.       0
GRID       283      0  .19435  .13496    0.       0
GRID       284      0  .19435  .14996    0.       0
GRID       285      0  .19435  .16495    0.       0
GRID       286      0  .19435  .17995    0.       0
GRID       287      0  .19435  .19494    0.       0
GRID       288      0  .19435  .20994    0.       0
GRID       289      0  .19435  .22494    0.       0
GRID       290      0  .19435  .23993    0.       0
GRID       291      0  .19435  .25493    0.       0
GRID       292      0  .19435  .26992    0.       0
GRID       293      0  .19435  .28492    0.       0
GRID       294      0  .19435  .29991    0.       0
```

```
GRID         295     0    .2093      0.       0.       0
GRID         296     0    .2093 .014994      0.       0
GRID         297     0    .2093 .029987      0.       0
GRID         298     0    .2093 .044981      0.       0
GRID         299     0    .2093 .059974      0.       0
GRID         300     0    .2093 .074967      0.       0
GRID         301     0    .2093 .089961      0.       0
GRID         302     0    .2093  .10495      0.       0
GRID         303     0    .2093  .11995      0.       0
GRID         304     0    .2093  .13494      0.       0
GRID         305     0    .2093  .14993      0.       0
GRID         306     0    .2093  .16493      0.       0
GRID         307     0    .2093  .17992      0.       0
GRID         308     0    .2093  .19492      0.       0
GRID         309     0    .2093  .20991      0.       0
GRID         310     0    .2093   .2249      0.       0
GRID         311     0    .2093   .2399      0.       0
GRID         312     0    .2093  .25489      0.       0
GRID         313     0    .2093  .26988      0.       0
GRID         314     0    .2093  .28488      0.       0
GRID         315     0    .2093  .29987      0.       0
GRID         316     0   .22425      0.       0.       0
GRID         317     0   .22425 .014991      0.       0
GRID         318     0   .22425 .029982      0.       0
GRID         319     0   .22425 .044974      0.       0
GRID         320     0   .22425 .059965      0.       0
GRID         321     0   .22425 .074956      0.       0
GRID         322     0   .22425 .089948      0.       0
GRID         323     0   .22425  .10494      0.       0
GRID         324     0   .22425  .11993      0.       0
GRID         325     0   .22425  .13492      0.       0
GRID         326     0   .22425  .14991      0.       0
GRID         327     0   .22425   .1649      0.       0
GRID         328     0   .22425  .17989      0.       0
GRID         329     0   .22425  .19489      0.       0
GRID         330     0   .22425  .20988      0.       0
GRID         331     0   .22425  .22487      0.       0
GRID         332     0   .22425  .23986      0.       0
GRID         333     0   .22425  .25485      0.       0
GRID         334     0   .22425  .26984      0.       0
GRID         335     0   .22425  .28483      0.       0
GRID         336     0   .22425  .29982      0.       0
GRID         337     0    .2392      0.       0.       0
GRID         338     0    .2392 .014989      0.       0
GRID         339     0    .2392 .029978      0.       0
GRID         340     0    .2392 .044967      0.       0
GRID         341     0    .2392 .059956      0.       0
GRID         342     0    .2392 .074945      0.       0
GRID         343     0    .2392 .089934      0.       0
GRID         344     0    .2392  .10492      0.       0
GRID         345     0    .2392  .11991      0.       0
GRID         346     0    .2392   .1349      0.       0
GRID         347     0    .2392  .14989      0.       0
GRID         348     0    .2392  .16488      0.       0
GRID         349     0    .2392  .17987      0.       0
GRID         350     0    .2392  .19486      0.       0
GRID         351     0    .2392  .20985      0.       0
GRID         352     0    .2392  .22484      0.       0
GRID         353     0    .2392  .23982      0.       0
GRID         354     0    .2392  .25481      0.       0
GRID         355     0    .2392   .2698      0.       0
GRID         356     0    .2392  .28479      0.       0
GRID         357     0    .2392  .29978      0.       0
GRID         358     0   .25415      0.       0.       0
GRID         359     0   .25415 .014987      0.       0
GRID         360     0   .25415 .029974      0.       0
GRID         361     0   .25415  .04496      0.       0
GRID         362     0   .25415 .059947      0.       0
GRID         363     0   .25415 .074934      0.       0
```

```
GRID       364     0   .25415 .089921     0.       0
GRID       365     0   .25415  .10491     0.       0
GRID       366     0   .25415  .11989     0.       0
GRID       367     0   .25415  .13488     0.       0
GRID       368     0   .25415  .14987     0.       0
GRID       369     0   .25415  .16485     0.       0
GRID       370     0   .25415  .17984     0.       0
GRID       371     0   .25415  .19483     0.       0
GRID       372     0   .25415  .20981     0.       0
GRID       373     0   .25415   .2248     0.       0
GRID       374     0   .25415  .23979     0.       0
GRID       375     0   .25415  .25477     0.       0
GRID       376     0   .25415  .26976     0.       0
GRID       377     0   .25415  .28475     0.       0
GRID       378     0   .25415  .29974     0.       0
GRID       379     0   .2691       0.     0.       0
GRID       380     0   .2691  .014985     0.       0
GRID       381     0   .2691  .029969     0.       0
GRID       382     0   .2691  .044954     0.       0
GRID       383     0   .2691  .059938     0.       0
GRID       384     0   .2691  .074922     0.       0
GRID       385     0   .2691  .089907     0.       0
GRID       386     0   .2691   .10489     0.       0
GRID       387     0   .2691   .11988     0.       0
GRID       388     0   .2691   .13486     0.       0
GRID       389     0   .2691   .14984     0.       0
GRID       390     0   .2691   .16483     0.       0
GRID       391     0   .2691   .17981     0.       0
GRID       392     0   .2691    .1948     0.       0
GRID       393     0   .2691   .20978     0.       0
GRID       394     0   .2691   .22477     0.       0
GRID       395     0   .2691   .23975     0.       0
GRID       396     0   .2691   .25474     0.       0
GRID       397     0   .2691   .26972     0.       0
GRID       398     0   .2691   .28471     0.       0
GRID       399     0   .2691   .29969     0.       0
GRID       400     0   .28405      0.     0.       0
GRID       401     0   .28405 .014982     0.       0
GRID       402     0   .28405 .029964     0.       0
GRID       403     0   .28405 .044947     0.       0
GRID       404     0   .28405 .059929     0.       0
GRID       405     0   .28405 .074911     0.       0
GRID       406     0   .28405 .089894     0.       0
GRID       407     0   .28405  .10488     0.       0
GRID       408     0   .28405  .11986     0.       0
GRID       409     0   .28405  .13484     0.       0
GRID       410     0   .28405  .14982     0.       0
GRID       411     0   .28405   .1648     0.       0
GRID       412     0   .28405  .17979     0.       0
GRID       413     0   .28405  .19477     0.       0
GRID       414     0   .28405  .20975     0.       0
GRID       415     0   .28405  .22473     0.       0
GRID       416     0   .28405  .23972     0.       0
GRID       417     0   .28405   .2547     0.       0
GRID       418     0   .28405  .26968     0.       0
GRID       419     0   .28405  .28466     0.       0
GRID       420     0   .28405  .29964     0.       0
GRID       421     0    .299       0.     0.       0
GRID       422     0    .299   .01498     0.       0
GRID       423     0    .299   .02996     0.       0
GRID       424     0    .299   .04494     0.       0
GRID       425     0    .299   .05992     0.       0
GRID       426     0    .299    .0749     0.       0
GRID       427     0    .299   .08988     0.       0
GRID       428     0    .299   .10486     0.       0
GRID       429     0    .299   .11984     0.       0
GRID       430     0    .299   .13482     0.       0
GRID       431     0    .299    .1498     0.       0
GRID       432     0    .299   .16478     0.       0
```

```
GRID         433      0    .299   .17976   0.       0
GRID         434      0    .299   .19474   0.       0
GRID         435      0    .299   .20972   0.       0
GRID         436      0    .299   .2247    0.       0
GRID         437      0    .299   .23968   0.       0
GRID         438      0    .299   .25466   0.       0
GRID         439      0    .299   .26964   0.       0
GRID         440      0    .299   .28462   0.       0
GRID         441      0    .299   .2996    0.       0
CQUAD4         1      1      2       1      22      23      90.
CQUAD4         2      1      3       2      23      24      90.
CQUAD4         3      1      4       3      24      25      90.
CQUAD4         4      1      5       4      25      26      90.
CQUAD4         5      1      6       5      26      27      90.
CQUAD4         6      1      7       6      27      28      90.
CQUAD4         7      1      8       7      28      29      90.
CQUAD4         8      1      9       8      29      30      90.
CQUAD4         9      1     10       9      30      31      90.
CQUAD4        10      1     11      10      31      32      90.
CQUAD4        11      1     12      11      32      33      90.
CQUAD4        12      1     13      12      33      34      90.
CQUAD4        13      1     14      13      34      35      90.
CQUAD4        14      1     15      14      35      36      90.
CQUAD4        15      1     16      15      36      37      90.
CQUAD4        16      1     17      16      37      38      90.
CQUAD4        17      1     18      17      38      39      90.
CQUAD4        18      1     19      18      39      40      90.
CQUAD4        19      1     20      19      40      41      90.
CQUAD4        20      1     21      20      41      42      90.
CQUAD4        21      1     23      22      43      44      90.
CQUAD4        22      1     24      23      44      45      90.
CQUAD4        23      1     25      24      45      46      90.
CQUAD4        24      1     26      25      46      47      90.
CQUAD4        25      1     27      26      47      48      90.
CQUAD4        26      1     28      27      48      49      90.
CQUAD4        27      1     29      28      49      50      90.
CQUAD4        28      1     30      29      50      51      90.
CQUAD4        29      1     31      30      51      52      90.
CQUAD4        30      1     32      31      52      53      90.
CQUAD4        31      1     33      32      53      54      90.
CQUAD4        32      1     34      33      54      55      90.
CQUAD4        33      1     35      34      55      56      90.
CQUAD4        34      1     36      35      56      57      90.
CQUAD4        35      1     37      36      57      58      90.
CQUAD4        36      1     38      37      58      59      90.
CQUAD4        37      1     39      38      59      60      90.
CQUAD4        38      1     40      39      60      61      90.
CQUAD4        39      1     41      40      61      62      90.
CQUAD4        40      1     42      41      62      63      90.
CQUAD4        41      1     44      43      64      65      90.
CQUAD4        42      1     45      44      65      66      90.
CQUAD4        43      1     46      45      66      67      90.
CQUAD4        44      1     47      46      67      68      90.
CQUAD4        45      1     48      47      68      69      90.
CQUAD4        46      1     49      48      69      70      90.
CQUAD4        47      1     50      49      70      71      90.
CQUAD4        48      1     51      50      71      72      90.
CQUAD4        49      1     52      51      72      73      90.
CQUAD4        50      1     53      52      73      74      90.
CQUAD4        51      1     54      53      74      75      90.
CQUAD4        52      1     55      54      75      76      90.
CQUAD4        53      1     56      55      76      77      90.
CQUAD4        54      1     57      56      77      78      90.
CQUAD4        55      1     58      57      78      79      90.
CQUAD4        56      1     59      58      79      80      90.
CQUAD4        57      1     60      59      80      81      90.
CQUAD4        58      1     61      60      81      82      90.
CQUAD4        59      1     62      61      82      83      90.
CQUAD4        60      1     63      62      83      84      90.
```

```
CQUAD4        61      1      65      64      85      86      90.
CQUAD4        62      1      66      65      86      87      90.
CQUAD4        63      1      67      66      87      88      90.
CQUAD4        64      1      68      67      88      89      90.
CQUAD4        65      1      69      68      89      90      90.
CQUAD4        66      1      70      69      90      91      90.
CQUAD4        67      1      71      70      91      92      90.
CQUAD4        68      1      72      71      92      93      90.
CQUAD4        69      1      73      72      93      94      90.
CQUAD4        70      1      74      73      94      95      90.
CQUAD4        71      1      75      74      95      96      90.
CQUAD4        72      1      76      75      96      97      90.
CQUAD4        73      1      77      76      97      98      90.
CQUAD4        74      1      78      77      98      99      90.
CQUAD4        75      1      79      78      99     100      90.
CQUAD4        76      1      80      79     100     101      90.
CQUAD4        77      1      81      80     101     102      90.
CQUAD4        78      1      82      81     102     103      90.
CQUAD4        79      1      83      82     103     104      90.
CQUAD4        80      1      84      83     104     105      90.
CQUAD4        81      1      86      85     106     107      90.
CQUAD4        82      1      87      86     107     108      90.
CQUAD4        83      1      88      87     108     109      90.
CQUAD4        84      1      89      88     109     110      90.
CQUAD4        85      1      90      89     110     111      90.
CQUAD4        86      1      91      90     111     112      90.
CQUAD4        87      1      92      91     112     113      90.
CQUAD4        88      1      93      92     113     114      90.
CQUAD4        89      1      94      93     114     115      90.
CQUAD4        90      1      95      94     115     116      90.
CQUAD4        91      1      96      95     116     117      90.
CQUAD4        92      1      97      96     117     118      90.
CQUAD4        93      1      98      97     118     119      90.
CQUAD4        94      1      99      98     119     120      90.
CQUAD4        95      1     100      99     120     121      90.
CQUAD4        96      1     101     100     121     122      90.
CQUAD4        97      1     102     101     122     123      90.
CQUAD4        98      1     103     102     123     124      90.
CQUAD4        99      1     104     103     124     125      90.
CQUAD4       100      1     105     104     125     126      90.
CQUAD4       101      1     107     106     127     128      90.
CQUAD4       102      1     108     107     128     129      90.
CQUAD4       103      1     109     108     129     130      90.
CQUAD4       104      1     110     109     130     131      90.
CQUAD4       105      1     111     110     131     132      90.
CQUAD4       106      1     112     111     132     133      90.
CQUAD4       107      1     113     112     133     134      90.
CQUAD4       108      1     114     113     134     135      90.
CQUAD4       109      1     115     114     135     136      90.
CQUAD4       110      1     116     115     136     137      90.
CQUAD4       111      1     117     116     137     138      90.
CQUAD4       112      1     118     117     138     139      90.
CQUAD4       113      1     119     118     139     140      90.
CQUAD4       114      1     120     119     140     141      90.
CQUAD4       115      1     121     120     141     142      90.
CQUAD4       116      1     122     121     142     143      90.
CQUAD4       117      1     123     122     143     144      90.
CQUAD4       118      1     124     123     144     145      90.
CQUAD4       119      1     125     124     145     146      90.
CQUAD4       120      1     126     125     146     147      90.
CQUAD4       121      1     128     127     148     149      90.
CQUAD4       122      1     129     128     149     150      90.
CQUAD4       123      1     130     129     150     151      90.
CQUAD4       124      1     131     130     151     152      90.
CQUAD4       125      1     132     131     152     153      90.
CQUAD4       126      1     133     132     153     154      90.
CQUAD4       127      1     134     133     154     155      90.
CQUAD4       128      1     135     134     155     156      90.
CQUAD4       129      1     136     135     156     157      90.
```

```
CQUAD4     130     1     137     136     157     158     90.
CQUAD4     131     1     138     137     158     159     90.
CQUAD4     132     1     139     138     159     160     90.
CQUAD4     133     1     140     139     160     161     90.
CQUAD4     134     1     141     140     161     162     90.
CQUAD4     135     1     142     141     162     163     90.
CQUAD4     136     1     143     142     163     164     90.
CQUAD4     137     1     144     143     164     165     90.
CQUAD4     138     1     145     144     165     166     90.
CQUAD4     139     1     146     145     166     167     90.
CQUAD4     140     1     147     146     167     168     90.
CQUAD4     141     1     149     148     169     170     90.
CQUAD4     142     1     150     149     170     171     90.
CQUAD4     143     1     151     150     171     172     90.
CQUAD4     144     1     152     151     172     173     90.
CQUAD4     145     1     153     152     173     174     90.
CQUAD4     146     1     154     153     174     175     90.
CQUAD4     147     1     155     154     175     176     90.
CQUAD4     148     1     156     155     176     177     90.
CQUAD4     149     1     157     156     177     178     90.
CQUAD4     150     1     158     157     178     179     90.
CQUAD4     151     1     159     158     179     180     90.
CQUAD4     152     1     160     159     180     181     90.
CQUAD4     153     1     161     160     181     182     90.
CQUAD4     154     1     162     161     182     183     90.
CQUAD4     155     1     163     162     183     184     90.
CQUAD4     156     1     164     163     184     185     90.
CQUAD4     157     1     165     164     185     186     90.
CQUAD4     158     1     166     165     186     187     90.
CQUAD4     159     1     167     166     187     188     90.
CQUAD4     160     1     168     167     188     189     90.
CQUAD4     161     1     170     169     190     191     90.
CQUAD4     162     1     171     170     191     192     90.
CQUAD4     163     1     172     171     192     193     90.
CQUAD4     164     1     173     172     193     194     90.
CQUAD4     165     1     174     173     194     195     90.
CQUAD4     166     1     175     174     195     196     90.
CQUAD4     167     1     176     175     196     197     90.
CQUAD4     168     1     177     176     197     198     90.
CQUAD4     169     1     178     177     198     199     90.
CQUAD4     170     1     179     178     199     200     90.
CQUAD4     171     1     180     179     200     201     90.
CQUAD4     172     1     181     180     201     202     90.
CQUAD4     173     1     182     181     202     203     90.
CQUAD4     174     1     183     182     203     204     90.
CQUAD4     175     1     184     183     204     205     90.
CQUAD4     176     1     185     184     205     206     90.
CQUAD4     177     1     186     185     206     207     90.
CQUAD4     178     1     187     186     207     208     90.
CQUAD4     179     1     188     187     208     209     90.
CQUAD4     180     1     189     188     209     210     90.
CQUAD4     181     1     191     190     211     212     90.
CQUAD4     182     1     192     191     212     213     90.
CQUAD4     183     1     193     192     213     214     90.
CQUAD4     184     1     194     193     214     215     90.
CQUAD4     185     1     195     194     215     216     90.
CQUAD4     186     1     196     195     216     217     90.
CQUAD4     187     1     197     196     217     218     90.
CQUAD4     188     1     198     197     218     219     90.
CQUAD4     189     1     199     198     219     220     90.
CQUAD4     190     1     200     199     220     221     90.
CQUAD4     191     1     201     200     221     222     90.
CQUAD4     192     1     202     201     222     223     90.
CQUAD4     193     1     203     202     223     224     90.
CQUAD4     194     1     204     203     224     225     90.
CQUAD4     195     1     205     204     225     226     90.
CQUAD4     196     1     206     205     226     227     90.
CQUAD4     197     1     207     206     227     228     90.
CQUAD4     198     1     208     207     228     229     90.
```

```
CQUAD4       199     1     209     208     229     230     90.
CQUAD4       200     1     210     209     230     231     90.
CQUAD4       201     1     212     211     232     233     90.
CQUAD4       202     1     213     212     233     234     90.
CQUAD4       203     1     214     213     234     235     90.
CQUAD4       204     1     215     214     235     236     90.
CQUAD4       205     1     216     215     236     237     90.
CQUAD4       206     1     217     216     237     238     90.
CQUAD4       207     1     218     217     238     239     90.
CQUAD4       208     1     219     218     239     240     90.
CQUAD4       209     1     220     219     240     241     90.
CQUAD4       210     1     221     220     241     242     90.
CQUAD4       211     1     222     221     242     243     90.
CQUAD4       212     1     223     222     243     244     90.
CQUAD4       213     1     224     223     244     245     90.
CQUAD4       214     1     225     224     245     246     90.
CQUAD4       215     1     226     225     246     247     90.
CQUAD4       216     1     227     226     247     248     90.
CQUAD4       217     1     228     227     248     249     90.
CQUAD4       218     1     229     228     249     250     90.
CQUAD4       219     1     230     229     250     251     90.
CQUAD4       220     1     231     230     251     252     90.
CQUAD4       221     1     233     232     253     254     90.
CQUAD4       222     1     234     233     254     255     90.
CQUAD4       223     1     235     234     255     256     90.
CQUAD4       224     1     236     235     256     257     90.
CQUAD4       225     1     237     236     257     258     90.
CQUAD4       226     1     238     237     258     259     90.
CQUAD4       227     1     239     238     259     260     90.
CQUAD4       228     1     240     239     260     261     90.
CQUAD4       229     1     241     240     261     262     90.
CQUAD4       230     1     242     241     262     263     90.
CQUAD4       231     1     243     242     263     264     90.
CQUAD4       232     1     244     243     264     265     90.
CQUAD4       233     1     245     244     265     266     90.
CQUAD4       234     1     246     245     266     267     90.
CQUAD4       235     1     247     246     267     268     90.
CQUAD4       236     1     248     247     268     269     90.
CQUAD4       237     1     249     248     269     270     90.
CQUAD4       238     1     250     249     270     271     90.
CQUAD4       239     1     251     250     271     272     90.
CQUAD4       240     1     252     251     272     273     90.
CQUAD4       241     1     254     253     274     275     90.
CQUAD4       242     1     255     254     275     276     90.
CQUAD4       243     1     256     255     276     277     90.
CQUAD4       244     1     257     256     277     278     90.
CQUAD4       245     1     258     257     278     279     90.
CQUAD4       246     1     259     258     279     280     90.
CQUAD4       247     1     260     259     280     281     90.
CQUAD4       248     1     261     260     281     282     90.
CQUAD4       249     1     262     261     282     283     90.
CQUAD4       250     1     263     262     283     284     90.
CQUAD4       251     1     264     263     284     285     90.
CQUAD4       252     1     265     264     285     286     90.
CQUAD4       253     1     266     265     286     287     90.
CQUAD4       254     1     267     266     287     288     90.
CQUAD4       255     1     268     267     288     289     90.
CQUAD4       256     1     269     268     289     290     90.
CQUAD4       257     1     270     269     290     291     90.
CQUAD4       258     1     271     270     291     292     90.
CQUAD4       259     1     272     271     292     293     90.
CQUAD4       260     1     273     272     293     294     90.
CQUAD4       261     1     275     274     295     296     90.
CQUAD4       262     1     276     275     296     297     90.
CQUAD4       263     1     277     276     297     298     90.
CQUAD4       264     1     278     277     298     299     90.
CQUAD4       265     1     279     278     299     300     90.
CQUAD4       266     1     280     279     300     301     90.
CQUAD4       267     1     281     280     301     302     90.
```

```
CQUAD4      268     1     282     281     302     303     90.
CQUAD4      269     1     283     282     303     304     90.
CQUAD4      270     1     284     283     304     305     90.
CQUAD4      271     1     285     284     305     306     90.
CQUAD4      272     1     286     285     306     307     90.
CQUAD4      273     1     287     286     307     308     90.
CQUAD4      274     1     288     287     308     309     90.
CQUAD4      275     1     289     288     309     310     90.
CQUAD4      276     1     290     289     310     311     90.
CQUAD4      277     1     291     290     311     312     90.
CQUAD4      278     1     292     291     312     313     90.
CQUAD4      279     1     293     292     313     314     90.
CQUAD4      280     1     294     293     314     315     90.
CQUAD4      281     1     296     295     316     317     90.
CQUAD4      282     1     297     296     317     318     90.
CQUAD4      283     1     298     297     318     319     90.
CQUAD4      284     1     299     298     319     320     90.
CQUAD4      285     1     300     299     320     321     90.
CQUAD4      286     1     301     300     321     322     90.
CQUAD4      287     1     302     301     322     323     90.
CQUAD4      288     1     303     302     323     324     90.
CQUAD4      289     1     304     303     324     325     90.
CQUAD4      290     1     305     304     325     326     90.
CQUAD4      291     1     306     305     326     327     90.
CQUAD4      292     1     307     306     327     328     90.
CQUAD4      293     1     308     307     328     329     90.
CQUAD4      294     1     309     308     329     330     90.
CQUAD4      295     1     310     309     330     331     90.
CQUAD4      296     1     311     310     331     332     90.
CQUAD4      297     1     312     311     332     333     90.
CQUAD4      298     1     313     312     333     334     90.
CQUAD4      299     1     314     313     334     335     90.
CQUAD4      300     1     315     314     335     336     90.
CQUAD4      301     1     317     316     337     338     90.
CQUAD4      302     1     318     317     338     339     90.
CQUAD4      303     1     319     318     339     340     90.
CQUAD4      304     1     320     319     340     341     90.
CQUAD4      305     1     321     320     341     342     90.
CQUAD4      306     1     322     321     342     343     90.
CQUAD4      307     1     323     322     343     344     90.
CQUAD4      308     1     324     323     344     345     90.
CQUAD4      309     1     325     324     345     346     90.
CQUAD4      310     1     326     325     346     347     90.
CQUAD4      311     1     327     326     347     348     90.
CQUAD4      312     1     328     327     348     349     90.
CQUAD4      313     1     329     328     349     350     90.
CQUAD4      314     1     330     329     350     351     90.
CQUAD4      315     1     331     330     351     352     90.
CQUAD4      316     1     332     331     352     353     90.
CQUAD4      317     1     333     332     353     354     90.
CQUAD4      318     1     334     333     354     355     90.
CQUAD4      319     1     335     334     355     356     90.
CQUAD4      320     1     336     335     356     357     90.
CQUAD4      321     1     338     337     358     359     90.
CQUAD4      322     1     339     338     359     360     90.
CQUAD4      323     1     340     339     360     361     90.
CQUAD4      324     1     341     340     361     362     90.
CQUAD4      325     1     342     341     362     363     90.
CQUAD4      326     1     343     342     363     364     90.
CQUAD4      327     1     344     343     364     365     90.
CQUAD4      328     1     345     344     365     366     90.
CQUAD4      329     1     346     345     366     367     90.
CQUAD4      330     1     347     346     367     368     90.
CQUAD4      331     1     348     347     368     369     90.
CQUAD4      332     1     349     348     369     370     90.
CQUAD4      333     1     350     349     370     371     90.
CQUAD4      334     1     351     350     371     372     90.
CQUAD4      335     1     352     351     372     373     90.
CQUAD4      336     1     353     352     373     374     90.
```

```
CQUAD4       337       1     354     353     374     375     90.
CQUAD4       338       1     355     354     375     376     90.
CQUAD4       339       1     356     355     376     377     90.
CQUAD4       340       1     357     356     377     378     90.
CQUAD4       341       1     359     358     379     380     90.
CQUAD4       342       1     360     359     380     381     90.
CQUAD4       343       1     361     360     381     382     90.
CQUAD4       344       1     362     361     382     383     90.
CQUAD4       345       1     363     362     383     384     90.
CQUAD4       346       1     364     363     384     385     90.
CQUAD4       347       1     365     364     385     386     90.
CQUAD4       348       1     366     365     386     387     90.
CQUAD4       349       1     367     366     387     388     90.
CQUAD4       350       1     368     367     388     389     90.
CQUAD4       351       1     369     368     389     390     90.
CQUAD4       352       1     370     369     390     391     90.
CQUAD4       353       1     371     370     391     392     90.
CQUAD4       354       1     372     371     392     393     90.
CQUAD4       355       1     373     372     393     394     90.
CQUAD4       356       1     374     373     394     395     90.
CQUAD4       357       1     375     374     395     396     90.
CQUAD4       358       1     376     375     396     397     90.
CQUAD4       359       1     377     376     397     398     90.
CQUAD4       360       1     378     377     398     399     90.
CQUAD4       361       1     380     379     400     401     90.
CQUAD4       362       1     381     380     401     402     90.
CQUAD4       363       1     382     381     402     403     90.
CQUAD4       364       1     383     382     403     404     90.
CQUAD4       365       1     384     383     404     405     90.
CQUAD4       366       1     385     384     405     406     90.
CQUAD4       367       1     386     385     406     407     90.
CQUAD4       368       1     387     386     407     408     90.
CQUAD4       369       1     388     387     408     409     90.
CQUAD4       370       1     389     388     409     410     90.
CQUAD4       371       1     390     389     410     411     90.
CQUAD4       372       1     391     390     411     412     90.
CQUAD4       373       1     392     391     412     413     90.
CQUAD4       374       1     393     392     413     414     90.
CQUAD4       375       1     394     393     414     415     90.
CQUAD4       376       1     395     394     415     416     90.
CQUAD4       377       1     396     395     416     417     90.
CQUAD4       378       1     397     396     417     418     90.
CQUAD4       379       1     398     397     418     419     90.
CQUAD4       380       1     399     398     419     420     90.
CQUAD4       381       1     401     400     421     422     90.
CQUAD4       382       1     402     401     422     423     90.
CQUAD4       383       1     403     402     423     424     90.
CQUAD4       384       1     404     403     424     425     90.
CQUAD4       385       1     405     404     425     426     90.
CQUAD4       386       1     406     405     426     427     90.
CQUAD4       387       1     407     406     427     428     90.
CQUAD4       388       1     408     407     428     429     90.
CQUAD4       389       1     409     408     429     430     90.
CQUAD4       390       1     410     409     430     431     90.
CQUAD4       391       1     411     410     431     432     90.
CQUAD4       392       1     412     411     432     433     90.
CQUAD4       393       1     413     412     433     434     90.
CQUAD4       394       1     414     413     434     435     90.
CQUAD4       395       1     415     414     435     436     90.
CQUAD4       396       1     416     415     436     437     90.
CQUAD4       397       1     417     416     437     438     90.
CQUAD4       398       1     418     417     438     439     90.
CQUAD4       399       1     419     418     439     440     90.
CQUAD4       400       1     420     419     440     441     90.
CONM2        401     421       0     5.-4      0.      0.      0.             +
+             0.      0.      0.      0.      0.      0.
CONM2        403     177       0     5.-4      0.      0.      0.             +
+             0.      0.      0.      0.      0.      0.
ENDDATA
```

APPENDIX E. META-MODEL BASED TEST-ANALYSIS CORRELATION

This section presents a method for modal correlation based on different principles than those of the primary damage identification algorithm. The described process, referred to as the meta-model based test-analysis correlation method, is based on training and optimizing fast-running meta-models in place of a detailed physical model, and could be used as a preliminary step before damage identification or solely for the general correlation task of bettering a model's adherence to measured data. The chapter summarizes work previously presented with co-authors in references [E-1] and [E-2].

The basics of the meta-model based test-analysis correlation method are outlined first followed by a discussion of general implementation considerations. Although the method is initially described with reference to general application, subsequent detail is given with specific reference to updating a finite element model using modal data and polynomial meta-models. Three issues encountered in practical implementation are discussed along with additional algorithmic routines to help address these issues. To test the meta-model test-analysis correlation technique multi-stage correlation was performed on the lightweight composite wing structure discussed in Chapter 7. Material stiffness and density properties were selected as correlation variables and modal frequencies selected as algorithm features. Polynomials up to the quadratic level were used to form the required meta-models, one for each feature, and central-composite design-of-experiments were used to create all meta-model training data. Correlation was applied to

the wing pieces independently and then the assembled wing model compared to measured data. Results from the meta-model are compared to the same correlation performed using a traditional Newton-Raphson based approach.

E.2 Method Overview

The meta-model based test-analysis-correlation method presented herein is based on standard practices from the larger methodology of model *verification and validation*, for example as presented in references [E-3], [E-4], and [E-5]. The basic concept is to fit fast running meta-models (a.k.a. numerical emulators, response surfaces, or surrogate models) to a set of physical model response data, and then numerically optimize the meta-models in place of the slow-running physical model. Implementation requires the following steps:

(1) Select correlation variables and response features;

(2) Run the models with specific combinations of variable perturbations according to a predefined design-of-experiments and store results as training data;

(3) Fit meta-models to the training data, one for each response feature (*meta-model optimization*);

(4) Optimize the meta-models to match the experimental response features (*test-analysis optimization*);

(5) Return the optimized meta-model variables to the original physical model, check correlation, and repeat iteratively if necessary;

In addition to the main correlation algorithm, there are three algorithmic routines which help address issues with implementation. The first is a routine to ensure the correct modes are always being used as they switch order during variable variation. The second is a routine to help avoid local minima when the meta-models are being optimized by a standard line-search optimization function. The third is iterative capability to address lack of fit between the meta-models and physical model as well other errors and shortcomings.

There are benefits to the meta-model test-analysis correlation method compared to more traditional methods for model correlation, such as those based on direct application of least-squares optimization (e.g., the pseudo Newton Raphson techniques described in Section 6.1). One benefit is that the meta-model test-analysis correlation method has the capability to update a large number of different variables, and to do so on the basis of minimizing (or maximizing) a large assortment of different response features, while remaining stable. This is largely due to the main update optimization being performed on meta-models instead of the physical model, meaning sophisticated optimization algorithms can be efficiently applied including options for variable constraints, weighting, and regularization. Another benefit is that the correlated meta-models can be subsequently used to propagate statistical uncertainty and variability information through the model, providing a much more complete understanding of the model and structure than allowed by most standard correlation methods.

The fundamental requirements of the meta-model based test-analysis correlation method are now discussed. In remaining discussions *variable* refers to any of the physical model input parameters used for the correlation process (e.g., material properties), and *feature* refers to a model output quantity used to create a metric for quantifying and evaluating response (e.g., a modal frequency). The word *parameter*, when used, generally refers to the various input quantities of the correlation algorithm itself.

E.2.1   Meta-Model Training Data

The first task involved in meta-model based test-analysis correlation is to identify physical model variables and features—the model input and output sets, respectively—to be used during correlation. For example, if trying to correlate an aluminum plate finite-element model with vibration data, the selected variables might be Young's modulus, shear modulus, density, and plate thickness, and the selected features might be the first ten natural frequencies and mode shape deflections at specified points. Each variable then requires an expected perturbation level—which is referenced to ensure finite element model input-output behavior is modeled over a meaningful range—and global bounds—which stop variable values from becoming non-physical during test-analysis-optimization.

After the variable space and feature sets are defined, a *design-of-experiments* is established in order to define sets of variable value combinations which represent the

variable-space of interest. The functional form of the design-of-experiment is an array of specified combinations of variable values. The finite element model is run at each of these design-of-experiment variable combinations and the resulting feature sets saved. This database of finite element input-output cases, initially ordered by the design-of-experiments, is what is used to then train the meta-models.

E.2.2   Meta-Model Type and Training

The basic concept of a meta-model—a numerical response surface—is given in Figure E-1 for two variables. There are potentially unlimited forms that a meta-model can take, and few limits provided that it combines numerical representations of the chosen physical model variables (input) to give numerical representations of the required physical model features (output), thereby modeling the physical model input-output relationship over the desired range. In addition, meta-models should be computationally efficient compared to the physical model, ideally by many orders of magnitude in order to expose the benefits of the method with respect to optimization and potential post-processing computations (e.g., Monte-Carlo based uncertainty propagation). Simple mathematical equations are desired, including polynomials, nonlinear functions, Gaussian process models, or artificial neural networks.
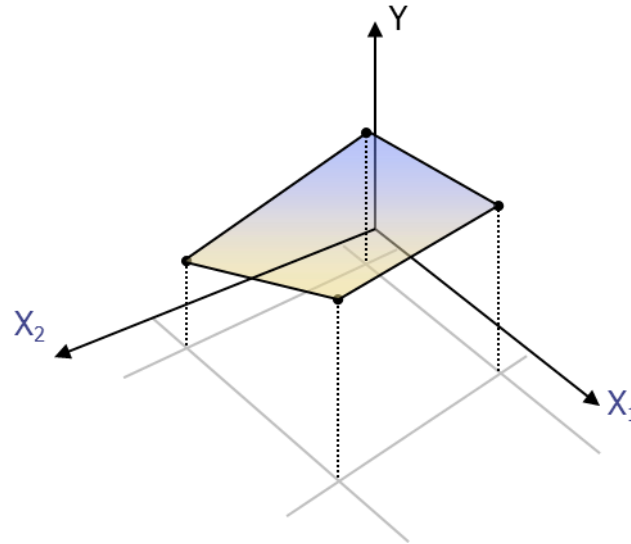
Figure E-1: Schematic representation of a meta-model response surface for two variables.

One simple but powerful meta-model form, and the one investigated for the remainder of this chapter, is families of polynomials, with each correlation feature modeling using an independent polynomial in terms of the physical model variables. For example, if N variables are represented by X_i, $i = 1...N$, and M features are represented by Y_k, $k = 1...M$, then the most basic family of polynomials, including direct linear dependencies and no interactions, will take the form

$$
\begin{aligned}
Y_1 &= c_{11} + c_{12}X_1 + c_{13}X_2 + ... + c_{1N}X_N \\
Y_2 &= c_{21} + c_{22}X_1 + c_{23}X_2 + ... + c_{2N}X_N \\
&... \\
Y_M &= c_{M1} + c_{M2}X_1 + c_{M3}X_2 + ... + c_{MN}X_N.
\end{aligned}
\tag{E.1}
$$

If $N = 2$ and $M = 3$, adding the interaction term $X_1 X_2$ and quadratic terms X_1^2 and X_2^2 gives the more capable polynomial family

$$Y_1 = c_{11} + c_{12}X_1 + c_{13}X_2 + c_{14}X_1X_2 + c_{15}X_1^2 + c_{16}X_2^2$$

$$Y_2 = c_{21} + c_{22}X_1 + c_{23}X_2 + c_{24}X_1X_2 + c_{25}X_1^2 + c_{26}X_2^2 \qquad \text{(E.2)}$$

$$Y_3 = c_{31} + c_{32}X_1 + c_{33}X_2 + c_{34}X_1X_2 + c_{35}X_1^2 + c_{36}X_2^2.$$

These equations can be further collected into matrix form as

$$\{Y\} = [c]\{X\}, \qquad \text{(E.3)}$$

where

$$\{Y\} = \begin{Bmatrix} Y_1 \\ Y_2 \\ Y_3 \end{Bmatrix} \qquad \text{(E.4)}$$

is the vector of model features,

$$\{X\} = \begin{Bmatrix} 1 \\ X_1 \\ X_2 \\ X_1X_2 \\ X_1^2 \\ X_2^2 \end{Bmatrix} \qquad \text{(E.5)}$$

is the vector of model variables, and

$$[c] = \begin{bmatrix} c_{11} & c_{12} & c_{13} & c_{14} & c_{15} & c_{16} \\ c_{21} & c_{22} & c_{23} & c_{24} & c_{25} & c_{26} \\ c_{31} & c_{32} & c_{33} & c_{34} & c_{35} & c_{36} \end{bmatrix} \qquad \text{(E.6)}$$

is the matrix of polynomial coefficients which are trained to define the meta-model. It is

also possible to add higher order direct dependency terms up to X_1^m and X_2^m for an mth

order polynomial and interaction terms $X_1^i X_2^j$ for each combination of i and j up to m, for an mth order polynomial, with each additional term requiring another polynomial coefficient for each feature. Training the meta-models then requires determining the matrix $[c]$ such that the relationship between $\{X\}$ and $\{Y\}$ in the physical model is approximately reproduced.

Before training the polynomial meta-models, the physical model is run for different combinations of variables according to a design-of-experiment and the resulting feature values are stored, creating a database of the input-output behavior of the physical model. The minimum number of physical model runs required is determined by the number of variables, polynomial order, and number of interactions being pursued. However, meta-model accuracy will increase with the amount of information available for training, and so the actual number of physical runs should be dictated primarily by computational budget limitations, with extra runs above the minimum used to increase meta-model fidelity and range. Once the training data is available, the meta-model coefficient matrix $[c]$ is determined row-by-row (i.e., feature by feature) by unconstrained numerical optimization. For each feature, the numerical optimization scheme seeks the corresponding $[c]$ row values which best reproduce the training features output for corresponding training variables as input.

E.2.3   Test-Analysis Optimization

A second optimization step, referred to herein as *test-analysis optimization*, is performed directly on the trained meta-models to find a set of variables which minimizes a cost function between the meta-model output features and a set of reference features. This step is essentially the same as normal model correlation optimization except the meta-models are used in place of the physical model. Whereas the previous meta-model training optimization step is applied to establish values for the meta-model coefficients in $[c]$, the test-analysis optimization step leaves $[c]$ fixed, and instead updates the meta-model variables in $\{X\}$ in order to match the experimental feature values $\{\tilde{Y}\}$ in the equation

$$\{\tilde{Y}\} = [c]\{X\}. \tag{E.7}$$

The optimized variables are then returned to the finite element model to produce the correlated model and a set of correlated features which can be used to evaluate success.

One major benefit of the meta-model based test-analysis correlation method compared to standard direct correlation optimization methods is the ability to apply sophisticated optimization algorithms, including the use of constraints, weighting, regularization, and higher-order convergence approaches. Additionally, global optimization techniques become more easily available, and, in fact, it can be computationally realistic to apply multiple optimization techniques either sequentially or

in parallel to increase the chance of success. Applying these algorithms directly to the correlation of realistically sized and detailed physical models is generally not possible because of computational constraints and the difficulty in obtaining second-order (i.e., hessian) and higher sensitivity relationships for physical models. However, with meta-models the computational requirements are minimal and sensitivity relationships can be produced easily to high order. Additionally, once the meta-models have been formed, the optimization can potentially be performed very accurately because of the potential for deriving sensitivity relationships in closed form instead of relying on finite-difference methods. Because the entire model is now represented by a series of polynomials or similar there are very few, if any, constraints on the type or sophistication of test-analysis correlation which can be used.

E.3   Implementation Considerations and Algorithmic Additions

In order to implement the method, there are several main parameter configuration steps which must be addressed:

(1)   Feature selection

(2)   Variable selection

(3)   Meta-model type

(4)   Design of experiments type

(5)   Definition of variable nominal values, perturbation levels, and bounds

(6)   Optimization cost-function metric

Most of these parameters require balancing capability and accuracy with computational expense. It is therefore useful to begin by estimating a computational budget—how long you can afford each correlation to take. Once a budget is set, the other pieces can be organized as follows.

E.3.1   Feature Selection

The model's intended use, and the features which will be required from the correlated model, should be examined first for the update feature set. Additionally, however, it can be desirable to maintain the model's physical correctness and thus features which may not be used once the model is correlated can still be included during update to help keep the model physically accurate and increase the confidence in which it can be used thereafter. From this pool, it is desirable to down-select to features which are sensitive to the input variables and relatively stable through the required finite element model runs as the variable values vary. If different feature forms are to be combined in one update—e.g., natural frequencies and mode shapes—there can be problems with low sensitivity features driving variable update, so maintaining relative equality between feature sensitivity can help with physically meaningful results. (See next section for notes on analysis of variance as a means of estimating feature-variable sensitivity.) Weighting can also potentially be applied to alleviate this problem; however, this is not explored further here.

E.3.2   Variable Selection and Analysis of Variance

Similarly, any type of variable which impacts the chosen physical model feature can theoretically be used for meta-model based test-analysis correlation, although, as with all model correlation techniques, judicious selection of specific variables should be applied in order to keep the model as physically reasonable as possible. Any number of variables is also theoretically possible; however, computational expense exponentially increases with extra variables, primarily because of the need to investigate variable interactions and the subsequent expansion of the design-of-experiments mandated physical model run count required to create the training database.

The *phenomenon influence and ranking table*, or *PIRT*, is an organizational tool which can be used to identify possible correlation variables and give a qualitative estimation of their importance. One way of proceeding is as follows. First, all possible variables which can be varied to affect the response of the model are listed. Next, each variable's assumed relative influence on the model response, and the total level of uncertainty—numerical uncertainty, influence uncertainty, etc.—are written in neighboring columns in the form of a rough qualitative scale (e.g., low, medium, high). Finally, a third column is added which reflects the product of the uncertainty with the influence, giving the qualitative importance of each variable and a qualitative basis for down-selecting. Table E-1 gives an example of what a PIRT could look like for a case considering several material properties.

Table E-1: Example of phenomenon and influence ranking table.

Variable	Uncertainty	Influence	Importance (Product)	Update Variable Set
E_{11}	high	High	High	E_{11}
E_{22}	high	High	High	E_{22}
v_{12}	high	low	medium	v_{12}
E_{12}	high	med high	high	G_{12}
E_{13}	medium	very low	low	-
E_{23}	medium	very low	low	-
ρ	medium	very high	high	ρ

Another tool for down-selecting variables is analysis of variance, or *ANOVA*—a statistical significance testing process which estimates the impact a variable has on the total variability. The influence is calculated using the R^2 statistic, which estimates the ratio of the variance of the response when that variable is fixed to the variance of response when the variable is free (also known as the correlation ratio η^2). The R^2 statistic is calculated for each feature with respect to each variable using data from design-of-experiment model runs via the equation

$$R^2 = 1 - \frac{\sum\limits_{k=1}^{N_L} \sum\limits_{j=1}^{N_R} \left(y_{k,j} - \bar{y}_k \right)^2}{\sum\limits_{j=1}^{N_P} \left(y_j - \bar{y} \right)^2}, \tag{E.8}$$

where y_j is the jth data point for the current feature, $\bar{y}$ is the mean feature value across all data points, $y_{k,j}$ is the jth data point for the current feature with the current variable fixed at its kth value, $\bar{y}_k$ is the mean feature value for all data points with the current

variable fixed at its kth value, N_P is the number of data points for the current feature, N_R is the number of data points for the current feature with the current variable fixed at its kth value, and N_L is the number of values for which the current variable is fixed across the available data. Once R^2 values have been calculated for all variables and all features of interest, they are compared. Variables showing high R^2 values can then be selected as those most likely to be influential on the model response (at least for the features of interest), and thus those that should be updated. If enough runs can be justified, parameters with estimated low importance (or even fabricated parameters with zero influence, initiated with producing random feature response levels) can be included as 'sanity checks', since the ANOVA should show that they do not correlate to the feature response.

The ANOVA can also potentially be used to estimate the sensitivity of features to variables, giving a basis for further down-selecting features or removing those with low sensitivity.

E.3.3   Meta-Model Order

Polynomial meta-models can potentially be created to any polynomial order, including variable interactions to any order, as discussed in Section E.2. Ideally, the polynomial order should be chosen to mimic expected physical model behavior across variable range (linear, quadratic, cubic, or higher). However, the number of design-of-experiment mandated training runs required to train the meta-models will increase

exponentially with meta-model order in addition to the exponential increase already required to add variables and interactions. This is because the maximum polynomial order that can be accurately fit to the training data is limited by the number of training points available in any particular variable direction, and increasing the polynomial order beyond this limit will increase fidelity to training data but at the cost of losing interpolation accuracy. In general, a polynomial of order S will require $S+1$ training points (for instance, a linear polynomial requires a minimum of two points for fitting, whereas a quadratic polynomial requires a minimum of three points). Fitting a higher-order polynomial with few than this minimum is still possible, but the polynomial behavior between the points is unpredictable and meaningless.

Because computational budget is the main constraint in determining how many training runs are available, there is a trade-off between the meta-model order and number of variables and interactions which can be investigated and updated. Increasing meta-model order increases computational cost; however, if too low an order meta-model is used variables updated on the basis of these models may not be meaningful when returned to the physical model. Ensuring a minimum acceptable meta-model order therefore should be given high priority, even if fewer variables can subsequently be used for update. On the other hand, if the cost can be afforded, using a higher order meta-model than is required for the physical model order should not harm results, assuming enough training runs are available, since meta-model training should eliminate the influence of the unnecessary higher-order terms. Meta-model order also factors into

feature selection, since some model features will demonstrate lower order behavior over the variable space than others and thus may lead to more meaningful update results overall.

For the remainder of this study, three main meta-model types are considered, of increasing order. *Linear* meta-models include only direct variable effects, with the form

$$Y_1 = c_{11} + c_{12}X_1 + c_{13}X_2,$$ (E.9)

for two variables and one feature. *Bilinear* meta-models include first-order variable interactions, as

$$Y_1 = c_{11} + c_{12}X_1 + c_{13}X_2 + c_{14}X_1X_2.$$ (E.10)

Finally, *quadratic* meta-models follow the bilinear form, additionally including the quadratic variable dependencies, giving the form

$$Y_1 = c_{11} + c_{12}X_1 + c_{13}X_2 + c_{14}X_1X_2 + c_{15}X_1^2 + c_{16}X_2^2.$$ (E.11)

E.3.4 Design-of-Experiments Type

The design-of-experiment should be constructed to give feature response data across the expected range of variable variation, with the complexity and number of combinations dictated by the order of meta-model to be used and the order of variable

interactions to be examined. If an ANOVA is to be conducted, the variables should additionally be run at a range of fixed values.

There are standard configurations which fulfill these needs in systematic ways. *Full factorial designs*, represented schematically for a generic three parameter system in Figure E-2, are the simplest, most complete, and most expensive options. A two-level full-factorial design designates a finite element model run for all possible combinations of nominal value plus and minus the specified perturbation for each variable, requiring 2^N runs for N variables. A three-level full factorial design adds the nominal value in addition to plus and minus the perturbation, requiring a total of 3^N runs. *Central composite designs*, represented schematically for a generic three parameter system in Figure E-3, call for a smaller number of runs with combined variable perturbations in order to only investigate select interactions between parameters and are therefore more efficient while retaining most of the required accuracy. A central composite design for nine parameters requires 147 model runs compared to 512 runs for a two-level full factorial design, and 19,683 runs for a three-level full factorial design. A three-level full factorial design will provide more information than the other two options, and hence more accurate meta-models and better final correlation; however, the central composite design can provide acceptable results and the computational savings becomes immense as the number of variables and interactions increases.
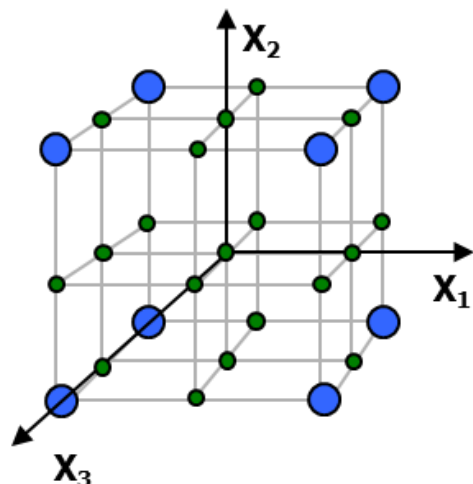
Figure E-2: Full factorial design for three parameters. 2-level with 8 runs is represented by blue circles; 3-level with 27 runs is represented by blue and green circles.
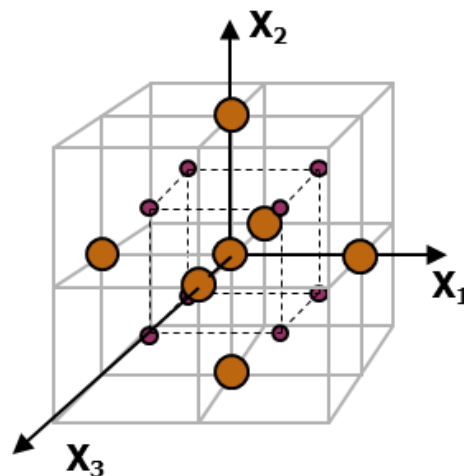
Figure E-3: Central composite design for three parameters, showing 15 runs.

The design-of-experiments available for a particular case are further limited by the minimum meta-model order required to accurately emulate physical model behavior. For example, linear polynomial meta-models, which only require two training points per variable dimension, can be trained with a two-level full factorial, whereas quadratic meta-models require at least a three-level full factorial design. Central composite designs allow training of linear and quadratic polynomial meta-models; however, with more training points being shared between meta-models and fewer overall training points there will still be some loss of overall fidelity to the physical model.

E.3.5   Variable Nominal Values, Perturbation Levels, and Bounds

The nominal values of variables should generally be taken as the current uncorrelated model properties, or otherwise estimated as best as possible. For the sake of

implementation, a scaled variable space—e.g., 1 for nominal, 1-Δ for minus the perturbation and 1+Δ for plus the perturbation, where Δ represents the scaled perturbation amount—can help avoid numerical error when variables have big differences in value.

The perturbation levels require a qualitative (or quantitative if available) estimation of variable uncertainty, and how much the variables are likely to vary during update. The perturbation levels will define the values at which design-of-experiment training runs are performed, and thus they define the space over which the meta-models are trained and likely to be meaningful. Meta-model accuracy will generally be at its highest close to the variable levels used for training—i.e., close to the nominal and plus and minus perturbation, depending on the specific design. On the other hand, physical models, and especially finite element models, will often demonstrate progressively higher order behavior as the variables are perturbed further from their nominal values, and thus a meta-model order which is appropriate for a low perturbation may generate increasing inaccuracy as variable perturbation grows. This effect can be seen in Figure E-4, which additionally shows how increasing meta-model order increases fidelity to the underlying physical model data (assuming the model is inherently of a higher order than can be exactly modeled with lower order meta-models). The perturbation levels should therefore be chosen such that correlated variables are within their bounds, and improved meta-model and correlation accuracy will most likely be achieved by shrinking the perturbation to be close to the variable update changes.

Meta-Model Fidelity to Training Data for Increasing Variable Perturbation
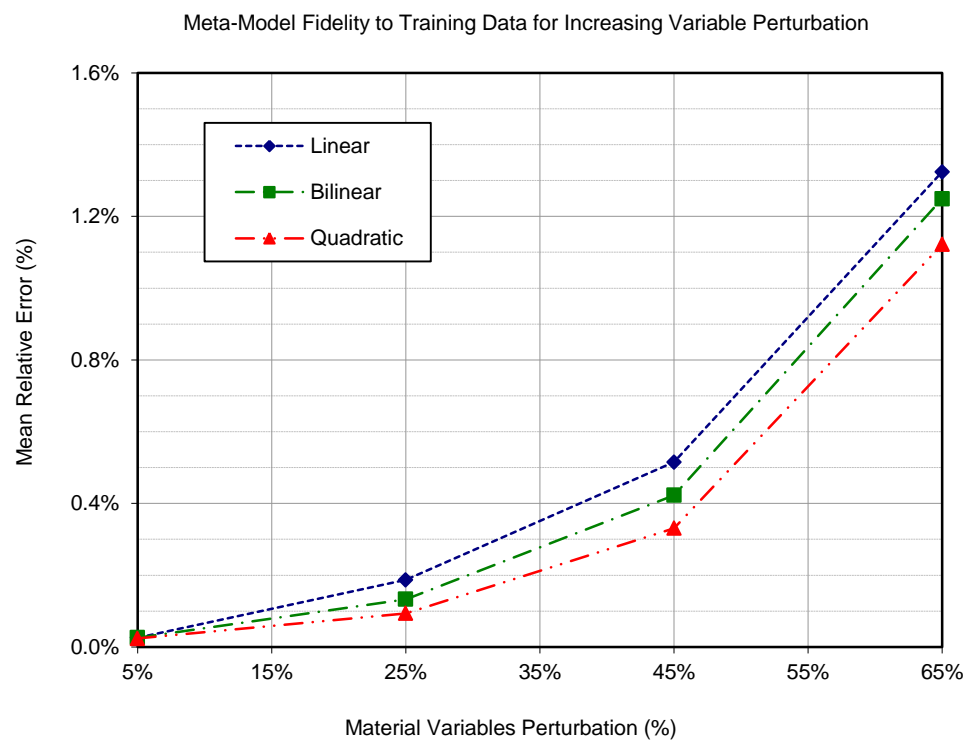
**Figure E-4: Example plot of meta-model fidelity to training data as
variable perturbation is increased.**

The bounds—values beyond which the variables cannot move—should be set to

keep the variables physically meaningful without restricting them to the point that good

correlation is hindered. As with the perturbation levels, bounds must be established on a

variable-by-variable basis, with consideration given to how much they can move for the

model to still run, how much they should move for the model to still be physically

meaningful, and how much it is desired they move relative to other variables.

E.3.6   Optimization Cost-Function Metric

Cost-functions to be minimized during meta-model training optimization and test-analysis optimization must also be specified for update to proceed. The most common cost-functions used in optimization are of the sum-of-squares error type, where the differences between predicted features $\{Y\}$ and reference features $\{\tilde{Y}\}$ are squared and summed, giving a scalar cost-function J as

$$J = \sum_{j=1}^{N_F} \left(\tilde{Y}_j - Y_j \right)^2 , \tag{E.12}$$

for N_F features being optimized. This general cost function form can also be generalized to the sum of higher or lower powers of feature difference, as

$$J_p = \sum_{j=1}^{N_F} \left| \tilde{Y}_j - Y_j \right|^p , \quad p > 0 . \tag{E.13}$$

There are many other cost function forms that can be used during the two optimization steps, as long as they work with the optimization scheme to bring the meta-models and training data, and correlation variables and reference data, into accordance, respectively.

E.4   Practical Implementation Issues and Algorithmic Additions

The meta-model based test-analysis correlation method was implemented for validation in the interest of updating a finite element model by minimizing natural

frequency differences. Three areas of implementation concern were identified—mode switching, local minima, and single iteration error—and algorithmic components were added to address each issue, as described below.

E.4.1   Mode Switching

In certain cases, when using modal data as features for correlation, there can be the tendency for modes to switch and blur between runs as variables are altered. Three steps can be taken to deal with this problem: (1) lower the perturbation, (2) only use modes that are stable across the variable space in spite of perturbations, and/or (3) include additional routines to track the modes and ensure correct frequencies are being compared.

For the implementation described herein, a mode tracking routine was written to automatically realign the physical model modes with the experimental reference modes by referencing the modal assurance criterion generated for each meta-model training run, using the equation

$$MAC_{ij} = \frac{\left(\{\tilde{\phi}_i\}^H \{\phi_j\}\right)\left(\{\tilde{\phi}_i\}^H \{\phi_j\}\right)}{\left(\{\tilde{\phi}_i\}^H \{\tilde{\phi}_j\}\right)\left(\{\phi_i\}^H \{\phi_j\}\right)}, \tag{E.14}$$

where $\{\tilde{\phi}_i\}$ is the reference mode shape vector for mode i, $\{\phi_j\}$ is the model mode shape vector for mode j, and $\{...\}^H$ refers to the Hermitian, or complex conjugate transpose, for the given vector. Since the reference modes don't change order, the physical model

modes are switched as necessary to give the highest modal assurance criterion values for each mode. It should be noted that this routine can only be used in cases where the mode shapes are available, such as during design-of-experiment training runs using a finite element model.

Another possible way of dealing with mode switching is to exclude closely spaced and unstable modes. Using the mode tracking routine along with careful feature selection means that the perturbation amount can be kept fairly high to cover the variable space without causing unmanageable mode switching.

E.4.2 Local Minima

The second major implementation issue involves the susceptibility of all sensitivity based line-search optimization methods to getting stuck at local minima points before reaching the global minimum. These locally minimum points in the variable space can easily occur in realistically sized finite element correlation problems when including a large number of update variables. For model correlation, it is desired to find a global minimum within the bounds imposed on the variables, and local minima will therefore give results which, although likely to be improved from the uncorrelated case, are not as good as possible or desired.

Figure E-5 illustrates the occurrence of local minima, showing the results of two analytical correlation cases where the design-of-experiment was used to provide multiple starting points for the test-analysis optimization step—one starting point from each
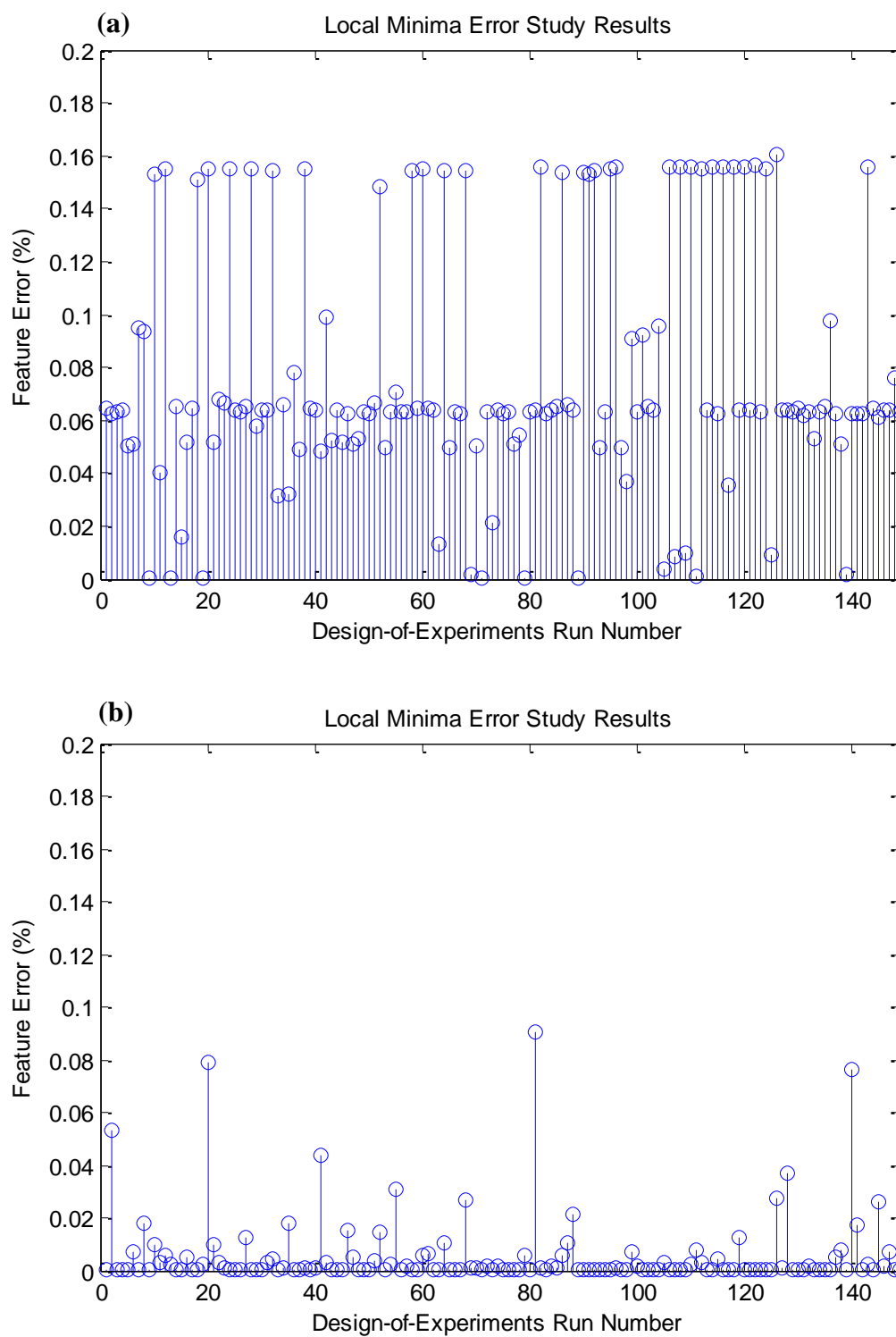
Figure E-5: Plots showing example results of multiple TAC runs, showing (a) local minima in the majority of runs, and (b) majority global minima.

design-of-experiment variable combination. Ideally, if the routine is finding the global minimum, every run will produce the same error (in this case equal to zero, since analytical data was used to provide an idealized test case) as can be seen for the majority of runs in Figure E-5(a). In a problem where there are bad local minima, however, the optimization converges to solutions that do not give the lowest possible error, sometimes only rarely achieving the global minimum, as is shown in Figure E-5(b). In this case, there are approximately five local minima that the update converges to, each one corresponding to a different overall error level, and it is only in a small number of the attempted runs that the zero error global minimum is reached.

To combat this problem in the meta-model based test-analysis correlation method, a routine was implemented to run the test-analysis optimization multiple times, once from each design-of-experiment variable combination—as was done to create Figure E-5—and keep the solution with lowest mean relative error. This is an ad-hoc solution, with no guarantee of producing the true global minimum; however, in practice the routine improves results markedly. It should be noted that the search for global minima in multi-variable optimization is a problem that has not been solved outside of particular applications, and may possibly not be solvable in a closed-form sense without brute-force sampling of every possible variable combination.

E.4.3   Iterative Capability

The third implementation issue involves iterating the entire meta-model based test-analysis correlation method to account for errors. Every stage of the meta-model based test-analysis correlation process involves some approximation, and the resulting errors compound into the final solution. Following the path of standard linear least-squares optimization for nonlinear problems, iterating the entire process allows a more accurate solution to be converged upon, since the errors in any given optimization run are usually proportional to the size of the required single-step variable update.

To include iterations with the meta-model based test-analysis correlation method, the correlated variables at each step are used as starting values for the next iteration, variable perturbations are updated to better match the expected variable change on the next step (usually smaller as the solution converges), a new design-of-experiment is generated accordingly, and the process continues. Iterating increases computational expense multiplicatively; however, if care is taken to set up the process parameters, and in particular to choose meta-models that emulate the training data well, desirable results can be achieved with a very few iterations. Iterating, however, also has the ability to generate instability. To counter this possible problem, physically realistic global parameter bounds should be implemented. (A demonstration of how iterative capability can improve final correlation is given in Section E.5.)

E.5   Code and Preliminary Validation

The meta-model based test-analysis correlation method was implemented in Matlab 7.0 [E-6] for use with MD. NASTRAN [E-7] finite element models. Code details and function are provided next, followed by results of initial validation studies using a sandwich plate.

E.5.1   Code Details

The code was designed to be free-running from program start to correlation end, including automated capability to write updates to NASTRAN input files (*.BDF), call NASTRAN to solve the normal modes problems, and read modal data from NASTRAN output files (*.F06). The built-in Matlab functions *ccdesign* and *fullfact* were used to generate central composite and full factorial design-of-experiments, respectively, and the constrained non-linear optimization function *fmincon* from the optimization tool-box was used for both meta-model training and test-analysis optimization. Once input parameters are specified—including feature sets, variable sets, nominal values, perturbations, bounds, meta-model order, design-of-experiment type, optimization cost-function type, convergence criteria, and number of iterations to run—the code would run the following sequence of operations:

(1)   Generate the design-of-experiments using the provided variable nominal values and perturbations;

(2)   Run the finite-element model according to the design-of-experiment

variable levels, saving the requested features for each variable level;

(3)   Run an analysis of variance, if requested;

(4)   Train the meta-models using unconstrained optimization;

(5)   Perform test-analysis optimization on the meta-models to get updated

variable values;

(6)   Return the updated variable values to the finite element model to get

updated feature values;

(7)   Assess correlation success and convergence;

(8)   Break from further correlation if results were converged, or loop back to

step (1) using the new variable values as nominal values.

E.5.2   Preliminary Validation Studies on a Composite Sandwich Plate

The meta-model based test-analysis correlation code was first applied to the

0.254×0.30 m rectangular composite sandwich plate and model discussed in Section 7.4.2

to demonstrate basic code functionality, investigate the performance of the iterations

routine, and provide additional information on meta-model type performance. The plate

was fabricated using the same 5-harness satin weave graphite-epoxy material system used

for the scaled wing sandwich material system with a layup of $[0/core/0]_T$.

Two reference data cases were considered using the first 10 natural frequencies as

correlation features in each case: (1) Analytically generated modal data, created using the

finite element model to produce an idealized zero-error case; and (2) experimentally

measured modal data, including irreducible error from modeling and experimental data

acquisition. Both cases used a basic variable set of E_{11}, E_{22}, v_{12}, and G_{12}, for the laminate,

plus G_{23} and G_{13} for the core. For the experimental reference data case, a second smaller

update variable case was additionally considered using only E_{11} and E_{22} for the laminate

plus G_{23} and G_{13} for the core. Perturbation was 8% and 6% for the first two iterations

with a further 0.8 reduction factor each iteration thereafter. A central composite design

was used to generate the design-of-experiment runs, and all three candidate meta-model

types were applied.

The code was shown to be functioning as expected. Figure E-6 shows results from

the respective cases—(a) analytical reference data, (b) experimental reference data using

6 variables, and (c) experimental reference data using 4 variables. All cases show that a

single iteration does not provide the best answer, but that correlation is reached by the

third iteration for the linear and bilinear meta-models, and by the second iteration with

quadratic meta-model. Additionally, quadratic meta-models were shown to produce the

best accuracy in every case. Although the experimental data reference case does not reach

zero error there is obvious convergence, which shows that the iterations can help in the

case of error from imperfect modeling and experimental reference data acquisition.

The relative efficiency of the different meta-model types was also investigated by

measuring how long each portion of the code would take to run. Results, summarized in

Figure E-7 in terms of normalized run time for each code module, showed that, although
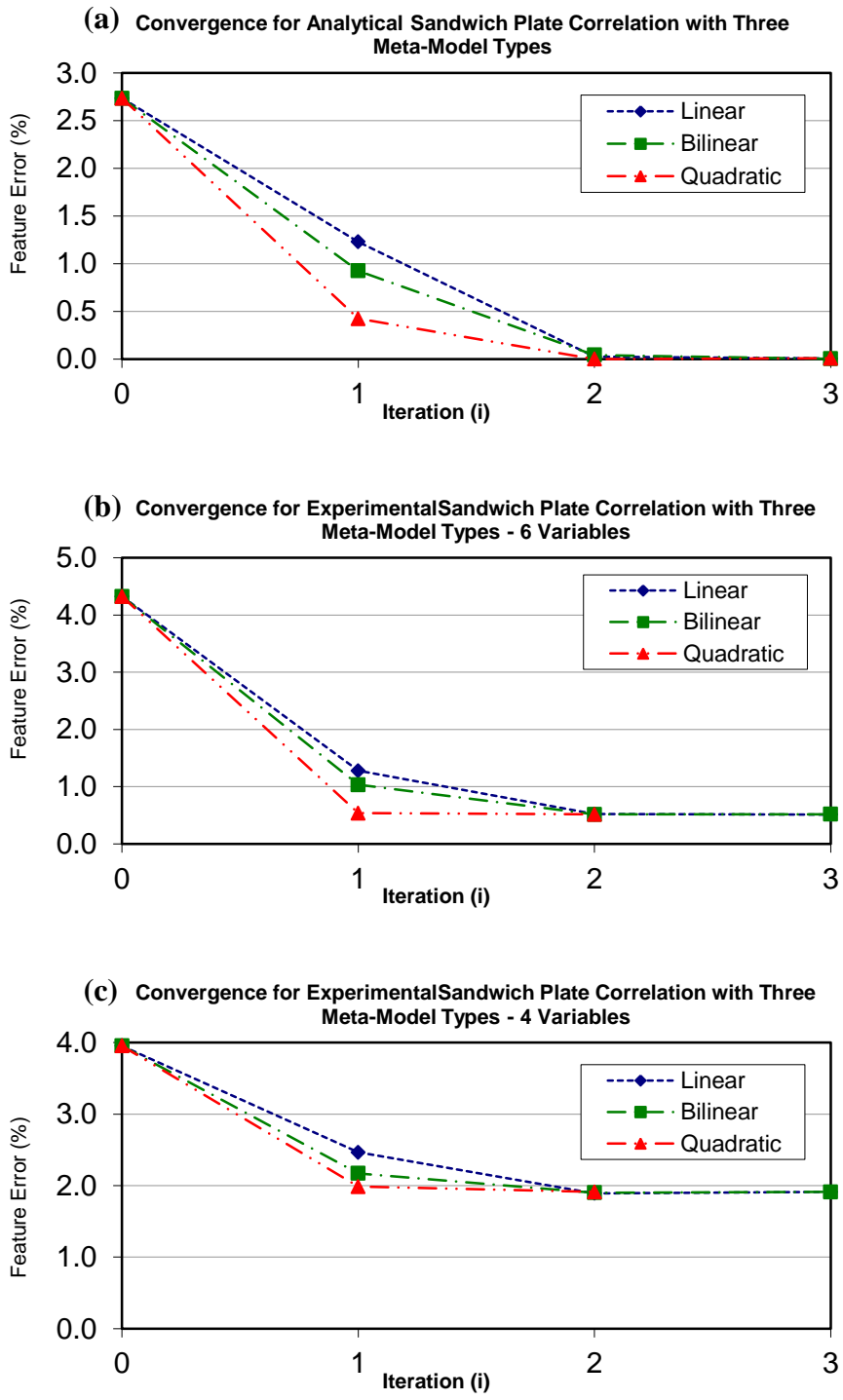
Figure E-6: Plots showing iteration-based convergence of the rectangular sandwich plate model to (a) finite element-generated analytical reference data using 6 variables, (b) experimentally measured vibration reference data using 6 variables, and (c) experimentally measured vibration reference data using 4 variables.
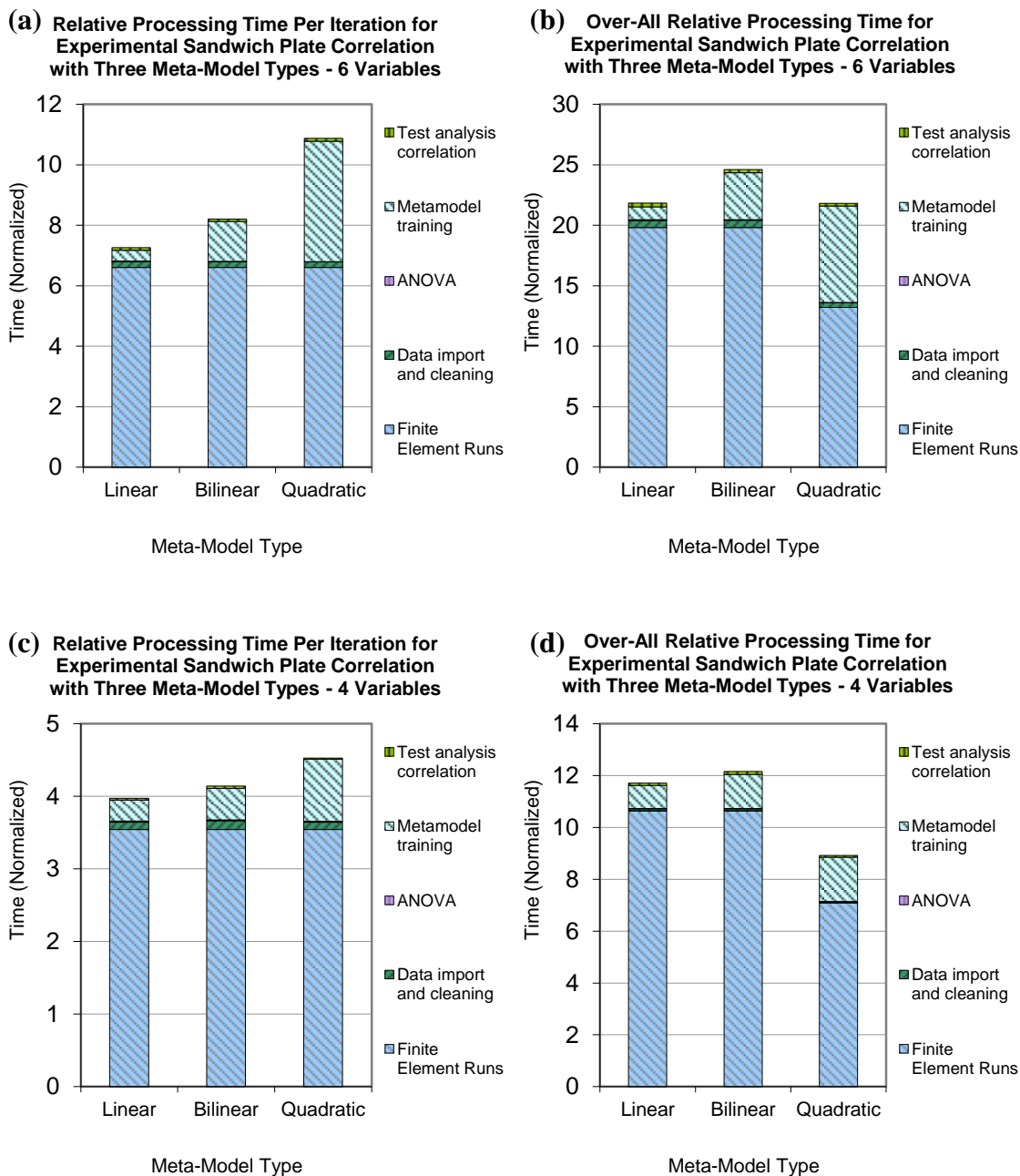
Figure E-7: Results of an investigation into the relative computational expense of the code modules for different meta-model types: (a) Per iteration computational expense using analytical reference data; (b) Total computational expense including iterations using analytical reference case; (c) Per iteration computational expense using experimental reference data; (d) Total computational expense including iterations using experimental reference data.

quadratic meta-models require longer per iteration, they can be faster overall by leading to faster convergence and therefore fewer iterations. It can also be seen in this figure that generating the original meta-model training data requires a large percentage of the overall correlation time.

E.6   Correlation of an Experimental Wing Structure

The meta-model test-analysis correlation technique was demonstrated using the lightweight composite wing structure, model, and vibration data presented in Chapter 7. Material stiffness and density properties were selected as correlation variables and modal frequencies selected as algorithm features. Polynomials up to the quadratic level were used to form the required meta-models, one for each feature, and central-composite design-of-experiments were used to create all meta-model training data.

E.6.1   Preliminary Correlation Variables Selection

As a first step to the correlation process, an initial pool of material properties—stiffnesses and densities—that could possibly be used for correlating the model was identified. It was decided for all pieces to treat properties in the material '1' and '2' directions independently (i.e., E_{11} independent from E_{22} and G_{13} independent from G_{23}). Furthermore, for the skins it was decided to treat the sandwich structure laminates separately from the plain laminate areas, allowing for the possibility of different

properties resulting from the co-cure process. This separation extended to the laminate density in this area relative to the density in the plain laminate areas. Equations were implemented in the code to modify the plain laminate density based on variations in the sandwich-laminate density, keeping the overall mass of the piece equal to the measured value. Finally, for the skins it was decided to include the possible influence of the honeycomb core properties.

For the spars, the caps were treated independently from the shear webs. There was more uncertainty in selecting parameters from these pieces because of the difference in natural modal response while in component form compared to their influence in the bonded wing for which they were designed. In other words, only E_{11} down the length of the caps and the in-plane shear properties through the shear web (and the density) significantly influence the assembled wing response; however, for free-free component pieces it was less obvious how the different material properties would affect response. The PIRT for the skins is shown in Table E-2 and the PIRT for the spars is shown in Table E-3.

Table E-2: Phenomenon influence and ranking tables for parameter identification and screening for top and bottom wing skins.

Region	Parameter	Uncertainty	Influence	Importance (Product)	Extended Parameter
Skin Plain Laminate (L)	E_{11}	high	High	high	$E_{11}(L)$
	E_{22}	high	High	high	$E_{22}(L)$
	v_{12}	high	low	medium	$v_{12}(L)$
	G_{12}	high	med high	high	$G_{12}(L)$
	G_{13}	medium	very low	low	**-**
	G_{23}	medium	very low	low	**-**
	ρ	medium	very high	high	***Dependent***
Skin Sandwich Laminate (S)	E_{11}	very high	high	very high	$E_{11}(S)$
	E_{22}	very high	high	very high	$E_{22}(S)$
	v_{12}	high	low	medium	$v_{12}(S)$
	G_{12}	very high	medium	high	$G_{12}(S)$
	G_{13}	medium	very low	low	**-**
	G_{23}	medium	very low	low	**-**
	ρ	high	very high	very high	$\rho(S)$
Skin Sandwich Core (C)	E_{33}	low	low	very low	**-**
	G_{23}	medium	medium	medium	$G_{23}(C)$
	G_{13}	medium	low	low	**-**

Table E-3: Phenomenon influence and ranking tables for parameter identification and screening for main and aft wing spars.

Region	Parameter	Uncertainty	Influence	Importance (product)	Extended parameter
Spar Laminate Cap (P)	E_{11}	medium	very high	high	$E_{11}(P)$
	E_{22}	medium	very low	med low	$E_{22}(P)$
	v_{12}	high	low	medium	$v_{12}(P)$
	G_{12}	high	medium	med high	$G_{12}(P)$
	G_{13}	high	medium	med high	$G_{13}(P)$
	G_{23}	med low	low	low	-
Spar Laminate Web (W)	ρ	medium	high	high	$E_{11}(W)$
	E_{11}	medium	high	high	$E_{22}(W)$
	E_{22}	very high	low	med high	$v_{12}(W)$
	v_{12}	high	low	medium	$G_{12}(W)$
	G_{12}	medium	low	med low	$G_{13}(W)$
	G_{13}	medium	low	med low	$G_{23}(W)$

It was decided that a 2-level full-factorial design-of-experiments with at most ten variables, which would require $2^{10} = 1024$ finite element runs, could be afforded for ANOVA based variable screening. The resulting ANOVA plot, shown in Figure E-8 for the top skin, shows the relative influence of each parameter on each of the 20 features (shown by the columns grouped above each parameter). This plot shows that $G_{12}(L)$ had the highest overall influence on the model response, with the highest influence of all being towards feature 1. The relative parameter influences shown in the ANOVA confirmed the PIRT influence estimates, with the exception of the $v_{12}(L)$ value, which showed higher influence than expected. Also, the $G_{23}(C)$ core shear stiffness coefficient

proved to have negligible influence as can be seen at the far right side of the plot. These

observations resulted in the decision to drop G_{23}(C) as an update variable for the wing

skins. Similar ANOVA based investigation of the spars produced the decision to carry the

initial correlation variables E_{11}(P), E_{22}(P), v_{12}(P), G_{12}(P), G_{13}(P), E_{11}(W), E_{22}(W), v_{12}(W),

and G_{12}(W) forward.
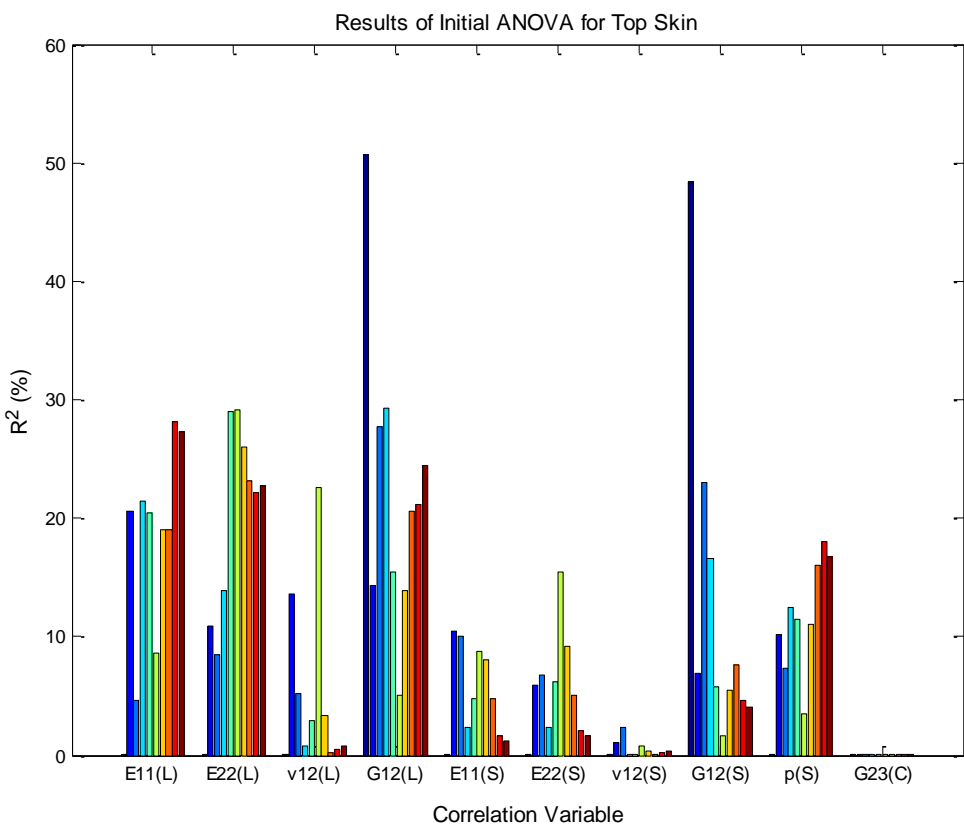
Figure E-8 – Initial analysis of variance plot for top skin using 2-level full-factorial design-of-experiment.

E.6.2   Preliminary Correlation Study on Top Wing Skin

With initial correlation variables selected, a study was performed on the top wing skin component in order to investigate the use of the local-minima reduction routine described in Section E.4.2, as well as to provide a basis for selecting a meta-model type and initial perturbation level for the full-correlation. Two cases were studied: (1) No local-minima reduction, where the test-analysis optimization was carried out once starting from the nominal starting variable values; and (2) Including local-minima reduction, where the test-analysis optimization was run many different starting points with lowest error run being kept as the final result. Each of these cases was run using all three meta-model types, over a range of perturbation amounts, for a single iteration each.

The results are summarized in Figure E-9. Some of the run parameter combinations lead to essentially the same result with and without the local-minima routine, suggesting that whether or not the global minimum was reached, the local-minima routine did not improve results. In most cases, however, a superior result was achieved by including the local-minima routine, meaning that previously the correlation had been caught at local minimum. Unfortunately there is still no guarantee that a global minimum will be reached using this routine; however, these results demonstrate that there is a better chance of achieving a superior final result by implementing the routine, and thus it was decided to include the routine for subsequent correlations.

(a) Single iteration meta-model correlation results for different amounts of initial perturbation - no local minima routine

(b) Single iteration meta-model correlation results for different amounts of initial perturbation - with local minima routine
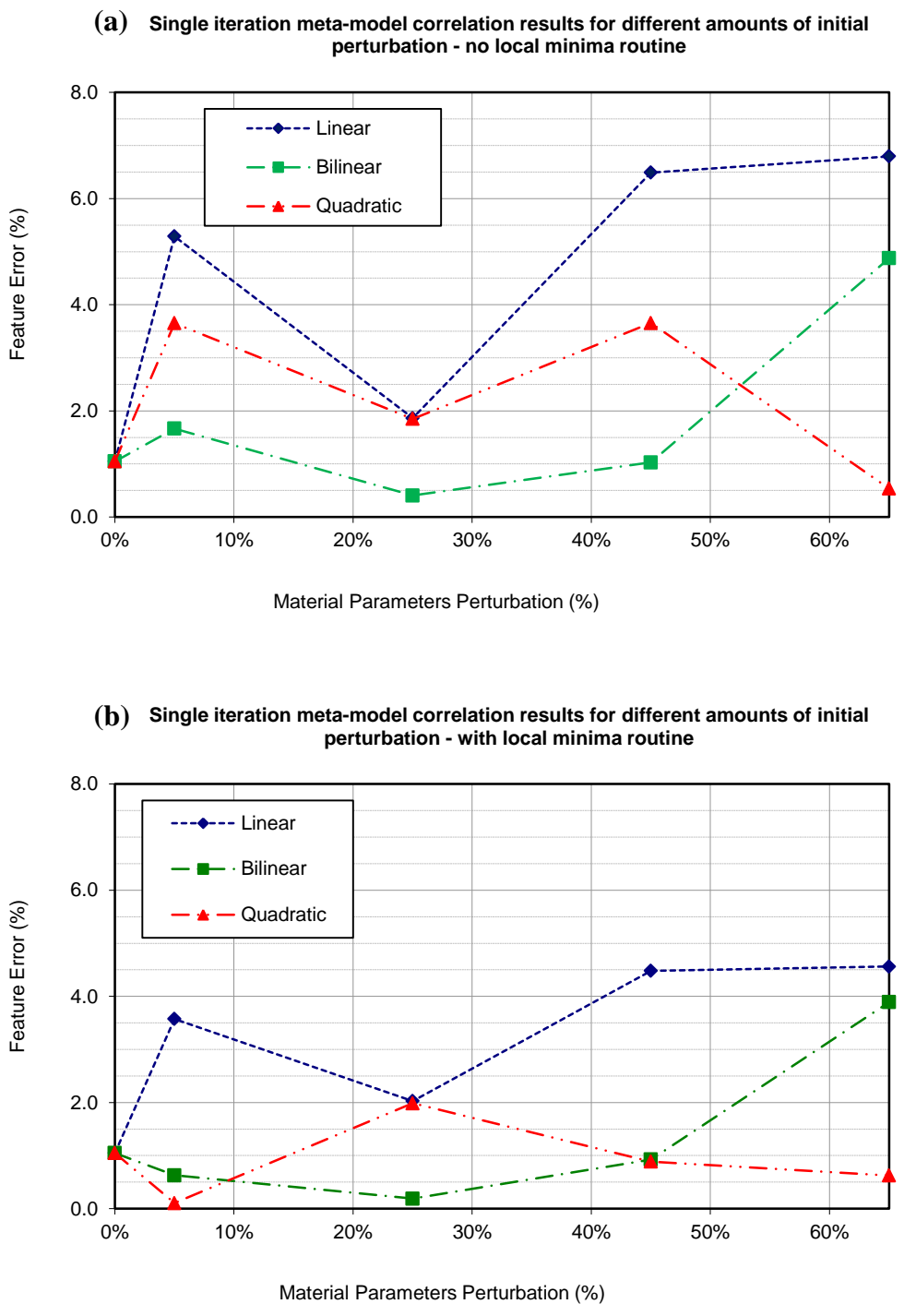
Figure E-9: Results showing net effect of the test-analysis optimization local minima routine on the top wing skin component with analytical reference data for a single iteration, over multiple perturbation amounts: (a) with no routine and (b) with the routine.

The study also showed that although the bilinear meta-model type often leads to good results and seems less susceptible to local minima, the best result can still be achieved using a quadratic meta-model, if only barely in this case.

E.6.3 Final Correlation Implementation

Based on the preliminary correlation study and initial correlation attempts, parameters for the final meta-model test analysis correlation were assigned as follows.

E.6.3.1 Variable Selection

Based on the desire to include only as many variables as would be useful, the expectation to use a central-composite design-of-experiment, and knowledge of the approximate run-time of each component model, it was decided that a maximum of ten parameters could be used for any one correlation, and fewer if possible. Density, which had been included on a relative basis between the plain laminate and sandwich laminate regions of the skins so that the total mass was consistent with measured values, was dropped after experimentation suggested that its inclusion was hurting the correlation overall, probably because of its disproportionately strong influence leading to low meta-model predictive capability. In the case of the spars, the main cap E_{11}(P) value was discarded for correlation because of fears that the experimental reference data, being from a C-section in free-free test configuration, was not reliable enough to correlate this property with accuracy commensurate to its major influence on the bending behavior of

the final assembled wing. Also, it was supposed that that particular property should be well represented by the available data from material coupon testing. Final correlation variables, eight variables for each skin and seven variables for each spar, are given in Table E-4.

Table E-4: Final correlation variable sets for each wing component.
(lam – laminate, SW – sandwich)

Top skin	plain lam	$E_{11}(L)$	$E_{22}(L)$	$v_{12}(L)$	$G_{12}(L)$
	SW lam	$E_{11}(S)$	$E_{22}(S)$	$v_{12}(S)$	$G_{12}(S)$
	core	(none)			
Bottom skin	plain lam	$E_{11}(L)$	$E_{22}(L)$	$v_{12}(L)$	$G_{12}(L)$
	SW lam	$E_{11}(S)$	$E_{22}(S)$	$v_{12}(S)$	$G_{12}(S)$
	core	(none)			
Main spar	cap lam	$E_{22}(P)$	$v_{12}(P)$	$G_{12}(P)$	
	web lam	$E_{11}(W)$	$E_{22}(W)$	$v_{12}(W)$	$G_{12}(W)$
Aft spar	cap lam	$E_{22}(P)$	$v_{12}(P)$	$G_{12}(P)$	
	web lam	$E_{11}(W)$	$E_{22}(W)$	$v_{12}(W)$	$G_{12}(W)$

E.6.3.2 Feature Selection

The remained some question about whether to use a large number of general frequencies or a few carefully selected frequencies. More frequencies would mean wider model response coverage, albeit at a higher computational expense since a separate meta-model must be trained for each; a small number would mean the influence of each is less

blurred by condensation into the optimization metric. It was also unclear whether to use lower-frequency modes, for their stability and tendency to be dominated by a single specific property or two at a time, or higher-frequency modes, which are more sensitive frequency-wise to property variation. Experimentation suggested that selecting a larger number of frequencies was preferred for these correlation cases. Modal-assurance criterion values between the experimental mode shapes and analytical finite element mode shapes of each component for different design-of-experiment variable combinations were referenced to avoid modes with low or unstable correlation behavior. The final mode feature selections are listed in Table E-5.

Table E-5: Final correlation feature sets for each wing component.

Component	Top skin	Bottom skin	Main spar	Aft spar
Feature set	1-12, 14-18	1-10, 14-20	2-9, 11, 12	2, 3-6, 8, 9, 11, 12, 14-17

E.6.3.3 Variable Nominal Values, Bounds, and Perturbation Amount

The exact initial variable values and bounds used for this study are presented along with the correlated results in Table E-6. Initial values for the sandwich region variables were approximated using results of the sandwich plate correlation discussed in Section E.4.2. Initial variable values for the plain non-sandwich laminate regions, in the skins and spars, were based on a mixture of results of material coupon testing, which

were available for E_{11} and E_{22}, and the results from the sandwich plate. In both cases, the low-influence transverse stiffness property values were filled in with generic values for similar materials. All honeycomb stiffness properties except for transverse shear (G_{13} and G_{23}) and transverse extensional (E_{33}) were set very small so as to have a negligible effect on the model response, to account for honeycomb's real physical structure. Bounds were set somewhat arbitrarily, loosely based on generous physical possibilities. It was supposed that manufacturing variation generally lowers stiffness constants, so bounds were set to allow more variation towards low values. Perturbation amount was chosen to be ±50%, although for the majority of runs (63/80) the effective perturbation was closer to ±18% because of the way central-composite design-of-experiment samples the requested space. Parametric studies on the wing-skins and sandwich plates suggested this to be a reasonable compromise between covering the variable space and remaining close to the expected values. In addition, the perturbation amount was set to decrease by a factor of two for every iteration starting with the third with the aim of helping convergence narrow in on the optimized values if necessary. Analysis of variance plots for the final variable and feature combinations are given in Figure E-10 and Figure E-11.
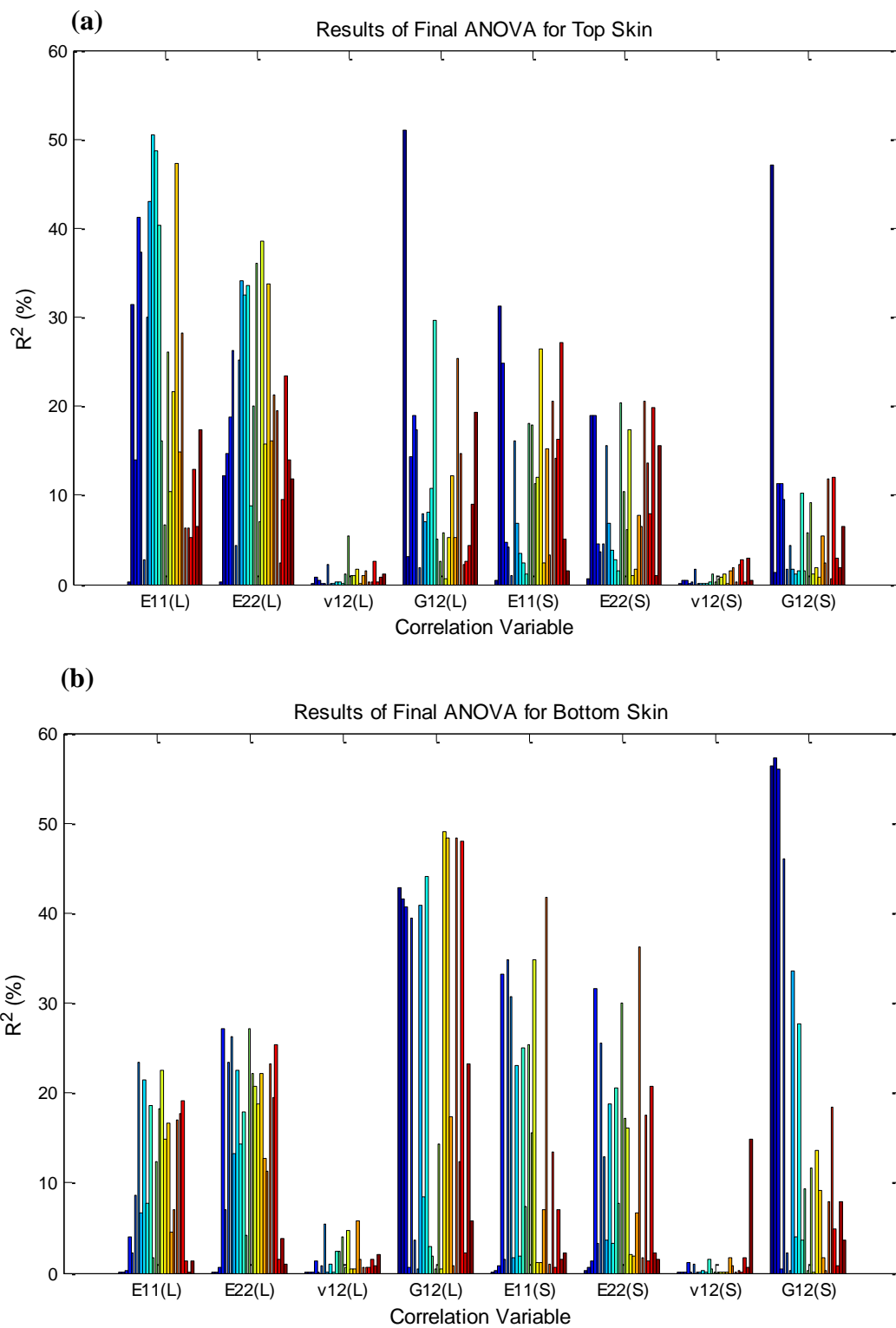
Figure E-10: Analysis of variance plots for wing skins with final variable and feature selections: (a) top skin and (b) bottom skin.

(a)

(b)
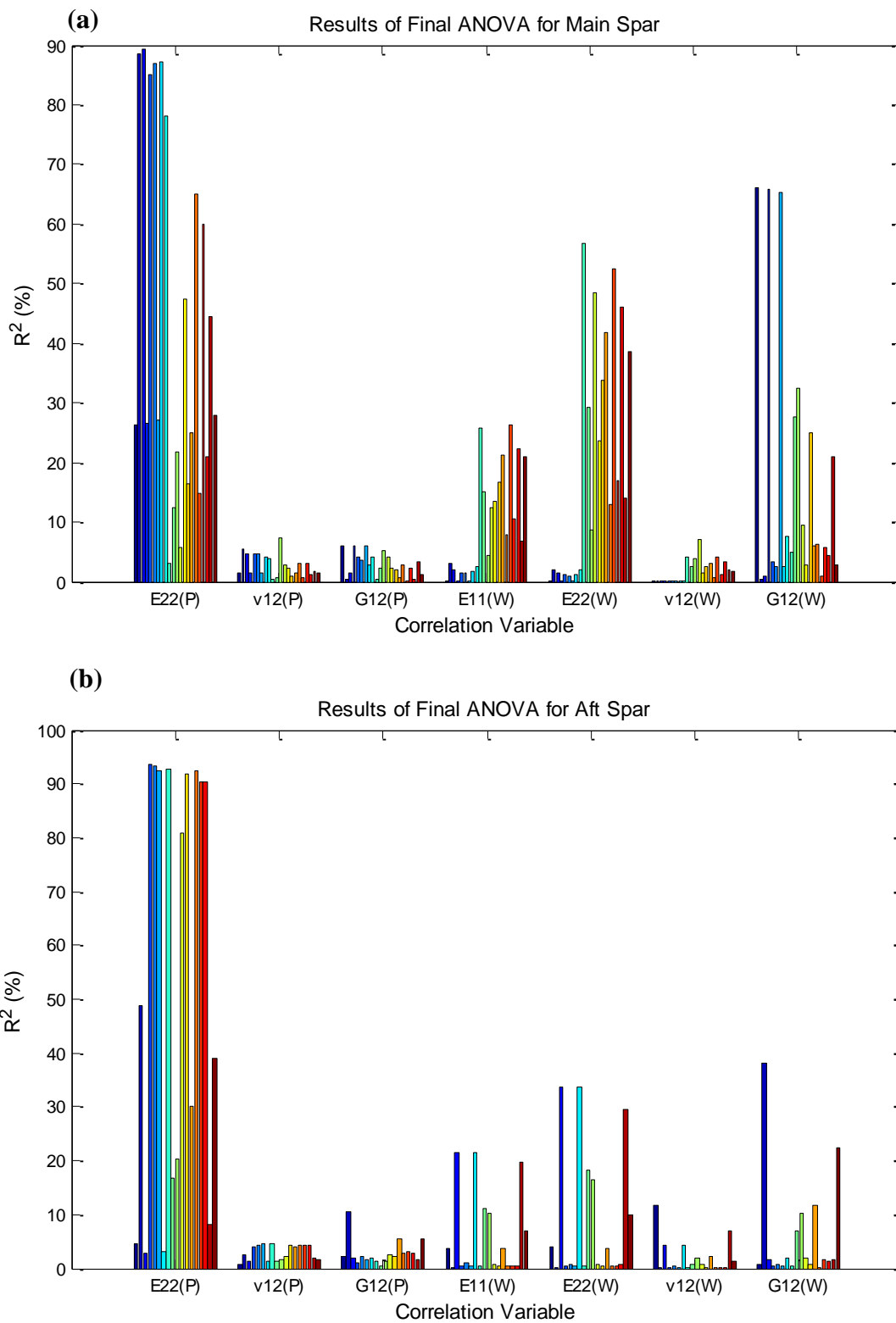
Figure E-11: Analysis of variance plots for wing spars with final variable and feature selections: (a) main spar and (b) aft spar.

E.6.3.4   Meta-model Type and Cost Function Metric

Quadratic polynomial meta-models were chosen for all correlations. For eight

variables this requires the training of 45 coefficients per feature (i.e., per meta-model).

Finally, the L^2 norm—sum of squared errors—between analytical and reference

frequencies was used as feature metric for all optimization cost functions. Correlation

success was evaluated using mean relative error between frequency sets.

E.6.4   Newton-Raphson Implementation

The pseudo Newton-Raphson iteration method used in this study is detailed in

Section 6.1.1. Implementation on the wing components proved the method to be very

unstable. As with the meta-model based test-analysis correlation method, initial

parameters—feature set, variable set, starting vales, perturbation amount—all affect the

outcome. In the Newton-Raphson case, the outcome was usually unviable (e.g., negative)

variable values which caused the finite element analysis to error and stop. There was a

question with how many features to include for this correlation, since results and stability

varied depending on the exact frequencies used. Experimentation in these cases suggested

that greater stability was allowed by using a large number of frequency features. In the

end, for the wing skins, convergence was only achieved with a maximum of 6

variables—E_{11}, E_{22}, and G_{12} for laminate and sandwich skin regions. The meta model

based test analysis correlation frequency sets for each piece were used in this analysis

along with the pseudo-inverse; initial variable values were set equal to those from the meta-model based analysis.

Results are given alongside meta-model based test-analysis correlation results in Table E-6. Pseudo Newton-Raphson correlation results did not converge for the spars, probably because of a lack of initial correlation between the model and the experimental data. In every attempt, the Newton-Raphson method diverged, producing unviable material properties and leading to crashing of the correlation routine.

E.6.5   Correlation Results and Comparison

The correlated material properties are given in Table E-6. It can be seen that the two methods approached different sets of material properties, suggesting that there was still non-uniqueness for at least one of the correlation techniques. Table E-7 and Table E-8 provide modal frequency correlation summaries for the wing skins and spars, respectively, giving values corresponding to the pertinent variable sets—nominal, Newton-Raphson correlated, meta-model based test-analysis correlation method correlated—in addition to the experimental reference values. These results are additionally summarized in plots of relative error vs. mode number in Figure E-12. Final statistics show that Newton-Raphson significantly improves correlation, resulting in mean relative errors across all optimization frequency sets of 0.81% and 5.33% for the top and bottom skins respectively, improved from 5.08% and 6.96% for the initial

Table E-6: Material property variables summary: initial values, bounds, and correlated values produced by Newton-Raphson and MMTAC methods for each wing component case ('lam' – laminate; 'SW' – sandwich; 'cap' – spar cap; 'web' – spar web).

			E_{11} (GPa)	E_{22} (GPa)	v_{12}	G_{12} (GPa)	G_{13} (GPa)	G_{23} (GPa)	ρ (g/cm^3)
Initial Values	general	plain/cap/web lam	128	123	0.150	5.68	4.14	4.14	n/a
		SW lam	93.8	84.8	0.150	5.68	4.14	4.14	n/a
		Core	6.89×10^{-6}	6.89×10^{-6}	0.001	6.89×10^{-6}	0.0288	0.0556	n/a
Bounds	Upper	plain/cap/web lam	138	138	0.400	8.27	n/a	n/a	n/a
		SW/web	138	138	0.400	8.27	n/a	n/a	n/a
		Core	6.89×10^{-6}	6.89×10^{-6}	0.001	6.89×10^{-6}	n/a	n/a	n/a
	Lower	plain/cap/web lam	68.9	68.9	0.001	1.38	n/a	n/a	n/a
		SW/web	48.3	48.3	0.001	0.69	n/a	n/a	n/a
		Core	6.89×10^{-6}	6.89×10^{-6}	0.001	6.89×10^{-6}	n/a	n/a	n/a
Newton Raphson	Top skin	plain lam	133	107	0.150	1.17	4.14	4.14	1.78
		SW lam	99.3	83.4	0.150	12.96	4.14	4.14	1.78
		Core	6.89×10^{-6}	6.89×10^{-6}	0.001	6.89×10^{-6}	0.0288	0.0556	0.14
	Bottom skin	plain lam	20.3	175	0.150	28.13	4.14	4.14	1.78
		SW lam	262	20.5	0.150	0.32	4.14	4.14	1.78
		Core	6.89×10^{-6}	6.89×10^{-6}	0.001	6.89×10^{-6}	0.0288	0.0556	0.14
	Main spar	cap lam	128	123	0.150	5.68	4.14	4.14	1.78
		web lam	93.8	84.8	0.150	5.68	4.14	4.14	1.78
	Aft spar	cap lam	128	123	0.150	5.68	4.14	4.14	1.62
		web lam	93.8	84.8	0.150	5.68	4.14	4.14	1.62
MMTAC	Top skin	plain lam	138	88.9	0.082	2.13	4.14	4.14	1.78
		SW lam	99.3	126	0.337	8.27	4.14	4.14	1.78
		Core	6.89×10^{-6}	6.89×10^{-6}	0.001	6.89×10^{-6}	0.0288	0.0556	0.14
	Bottom skin	plain lam	112	138	0.057	7.45	4.14	4.14	1.77
		SW lam	48.3	118	0.151	3.99	4.14	4.14	1.77
		Core	6.89×10^{-6}	6.89×10^{-6}	0.001	6.89×10^{-6}	0.0288	0.0556	0.14
	Main spar	cap lam	128	101	0.016	1.38	4.14	4.14	1.45
		web lam	138	79.3	0.034	1.85	4.14	4.14	1.45
	Aft spar	cap lam	128	113	0.153	1.38	4.14	4.14	1.62
		web lam	68.9	68.9	0.160	1.38	4.14	4.14	1.62

variable values, and that meta-model based test-analysis correlation improves correlation even more, with mean relative errors of 0.57% and 2.05% for the two skins. It should be noted that the added success of the meta-model based test-analysis correlation method was probably due at least in part to its ability to include more variables. As mentioned,

Newton-Raphson was not able to produce results for the spars; however, meta-model

based test-analysis correlation resulted in correlated mean relative errors of 4.17% and

7.04% for the main spar and aft spar, respectively, improved from initial values of

10.08% and 20.98%. It should be noted that these spar correlation values are approximate

because of mode blurring.

Table E-7: Correlation result frequencies—reference, initial finite element,
Newton-Raphson finite element, and meta-model based test-analysis
correlation finite element.

Mode	Top skin				Bottom skin			
	Ref (Hz)	FEM (Hz)			Ref (Hz)	FEM (Hz)		
		Nom	NR	MM		Nom	NR	MM
1	12.4	12.1	12.2	12.4	4.4	4.1	3.8	4.4
2	23.9	24.3	23.9	24.1	11.5	10.8	10.0	11.7
3	28.7	28.3	28.3	28.4	21.8	20.4	18.8	21.8
4	35.0	35.2	34.8	35.0	23.4	24.8	25.3	23.5
5	40.6	42.0	41.3	41.3	34.2	31.6	29.8	33.7
6	42.3	43.4	41.6	42.4	35.6	37.9	37.3	36.3
7	48.8	47.9	47.4	47.4	41.6	45.4	45.6	41.5
8	51.8	52.8	51.8	51.8	47.6	43.0	40.9	46.0
9	59.0	60.5	59.1	59.1	49.5	53.4	50.4	52.2
10	66.7	68.2	66.2	66.2	61.4	55.3	53.0	59.4
11	73.8	75.2	74.6	74.1	63.6	67.4	64.1	69.1
12	75.6	77.0	75.6	75.7	62.5	70.6	66.5	73.6
13	80.9	78.4	73.4	76.4	76.6	80.1	83.4	75.6
14	82.7	86.5	83.1	83.2	83.4	88.3	78.2	87.7
15	88.6	90.6	87.8	88.5	88.3	94.5	93.0	85.9
16	91.4	95.6	91.0	91.4	90.3	81.3	77.6	88.6
17	99.9	104.9	99.5	100.0	102.9	95.2	91.4	103.7
18	108.6	110.6	107.8	109.7	106.3	107.7	96.8	107.0
19	118.8	126.2	117.9	119.4	115.2	118.2	122.7	110.6
20	124.6	119.4	118.3	108.8	118.7	109.5	104.4	119.5

Table E-8: Correlation result frequencies—reference, initial finite element, Newton-Raphson finite element, and meta-model based test-analysis correlation finite element.

Mode	Main Spar				Aft Spar			
	Ref (Hz)	FEM (Hz)			Ref (Hz)	FEM (Hz)		
		Nom	NR	MM		Nom	NR	MM
1	22.2	24.7	n/a	22.5	24.4	26.0	n/a	24.0
2	33.8	31.5	n/a	31.0	48.3	70.2	n/a	64.0
3	46.1	48.6	n/a	47.4	62.3	67.4	n/a	65.9
4	59.0	64.8	n/a	59.1	75.2	78.0	n/a	74.6
5	70.2	75.2	n/a	72.8	103.5	116.1	n/a	111.0
6	101.9	109.4	n/a	106.1	133.5	137.1	n/a	126.6
7	116.4	126.8	n/a	115.6	137.4	164.1	n/a	156.8
8	131.7	139.9	n/a	135.6	151.0	218.5	n/a	162.2
9	154.4	183.1	n/a	176.1	187.7	225.7	n/a	210.7
10	175.3	199.0	n/a	172.0	239.8	273.7	n/a	261.4
11	186.8	206.9	n/a	188.0	267.0	168.3	n/a	308.8
12	222.4	266.4	n/a	232.2	314.6	314.7	n/a	302.5
13	240.0	241.5	n/a	237.4	308.8	344.6	n/a	328.5
14	251.7	271.9	n/a	262.0	357.8	412.2	n/a	392.3
15	261.0	301.2	n/a	271.9	333.9	470.6	n/a	355.2
16	271.0	320.1	n/a	291.8	385.4	466.0	n/a	429.9
17	282.3	329.9	n/a	314.3	*	*	*	*
18	308.9	365.5	n/a	331.8	*	*	*	*
19	343.6	394.6	n/a	370.6	*	*	*	*
20	359.5	406.8	n/a	373.7	*	*	*	*

A final comparison was made by assembling the component models into the full wing. Comparison to the measured experimental frequencies, as presented in Table E-8 and Figure E-13, produced a final mean relative error across structural modes of 6.9% for initial values, 9.4% for Newton-Raphson, and 10.0% for meta-model based test-analysis correlation. In this case, both correlation routines produce worse results. This is likely to be largely due to the difficulty in correlating the spars, which are open section and therefore behave differently when vibrating as an independent free-free structure

compared to when they are bonded in the full wing, but which to a large extent control

the structural modes of the assembled wing. An additional correlation would therefore

need to be performed on the assembled wing, with priority given to correlating the spar
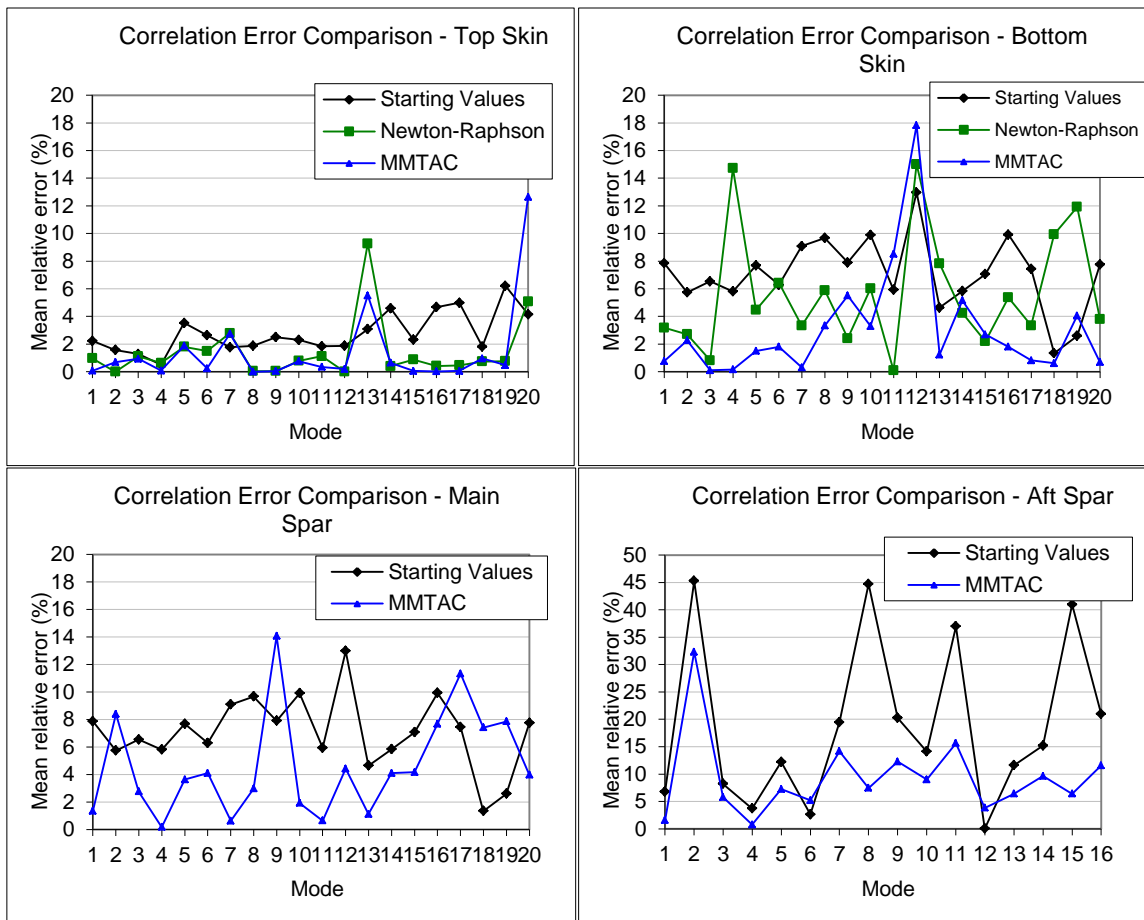
cap E_{11} material properties.

Figure E-12: Mean relative error of analytical frequencies to reference frequencies for the four wing components, showing relative correlation success: initial values vs. Newton-Raphson vs. meta-model based test-analysis correlation method.

A final observation about the correlation runs on the reasonably large wing component structures with all of the considered variables is that in most cases the results did not converge over the course of several iterations, and in some cases diverged after a certain point. This can be explained because of the lack of fit of meta-models to the finite element model, especially away from the training data. Since most of the training data is away from the point of initial values, as the iterations number grows and the perturbation amount shrinks, there is an ever greater region available away from the training data, and therefore greater risk of bad meta-model predictive capability. In this case, minimums can be created in the meta-model space that do not correspond to a finite element minimum, leading the variables to move away from the values they were approaching instead of converging.

Table E-9: Correlation results—experimental vs. finite element frequencies for assembled wing (structural modes only).

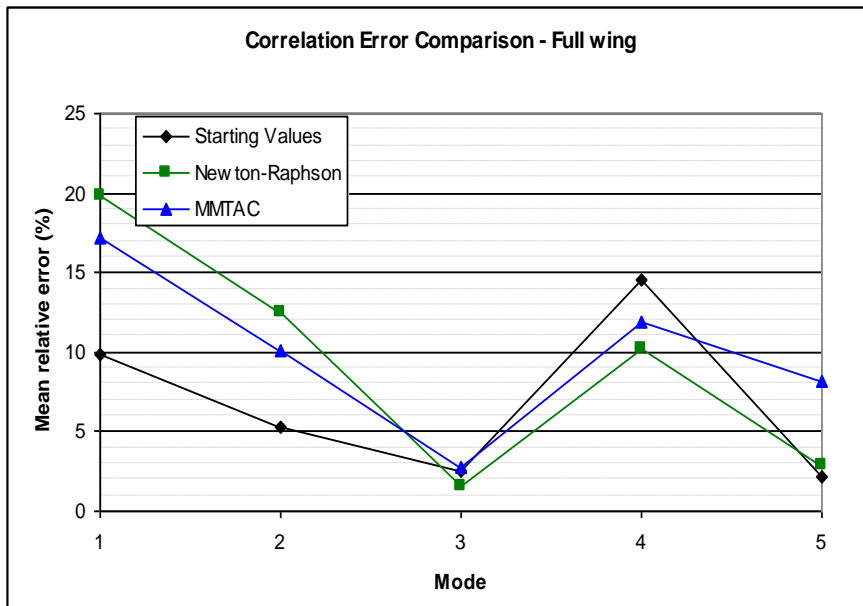| Mode	Ref (Hz)	Description	Finite Element (Hz)		
			Nom	NR	MM
1	7.5	1st bending	8.2	8.9	8.7
2	31.7	2nd bending	33.4	35.7	34.9
3	67.6	3rd bending	65.9	66.6	65.7
4	110.1	4th bending	94.1	98.9	97.1
5	262.5	torsion/bend	268.2	255.0	241.0

Figure E-13: Mean relative error of analytical frequencies to reference frequencies for the assembled wing for nominal values, Newton-Raphson correlated values, and meta-model test-analysis correlated values.

E.7   Meta-Model Based Test-Analysis Correlation Method Conclusions

The following conclusions can be drawn from the meta-model based finite

element model correlation work described in this chapter.

- Meta-model based test-analysis correlation and Newton-Raphson both

  improve results, with meta-model based test-analysis correlation providing

  better correlation than Newton-Raphson, at least partially by allowing stability

  and therefore a larger number of variables to be included.

- Both methods are sensitive to the various parameters that are required be specified, in particular the number and specific selection of update variables, and the number and specific selection of features.

- Modes can switch during variable variation, since finite element normal modes are always printed in order of ascending frequency, and so must be tracked to ensure that correct modes are being referenced; this can be accomplished algorithmically to allow automatic implementation.

- Local minima are produced in the current configuration, especially when a large number of variables is considered. This observation is linked to the fact that combinations of material properties appear to not be unique when all update features are boiled down into a single scalar cost-function metric. An algorithmic routine implemented to help counter local minima during optimization improved results.

- The form of the meta-models and their training—parameter selection, design-of-experiment type, perturbation, optimization—factor into their ability to emulate the finite element input-output behavior closely; this is helped to some extent by iterations, but iterations can hurt stability as well.

- The biggest single limiting factor in correlation accuracy, assuming all algorithm parameters are set intelligently, is getting meta-models which represent the finite element model well over a useful variable space.

- Meta-model based test-analysis correlation performance could be improved with more sophisticated components, such as better meta-models, more training data, and test-analysis optimization more robust to local minima.

The material contained in Appendix E was developed in collaboration with Prof. John B. Kosmatka, Prof. Charles Farrar, and Dr. Francois Hemez. The dissertation author was the primary investigator and author of this work.

E.8   Appendix E References

[E-1]   Oliver, J. A., Kosmatka, J. B., "Validating finite element models of composite aerospace structures for damage detection applications", *SPIE Smart Structures and Non-destructive Evaluation Conference*, San Diego, CA, February 26 - March 2, (2006)

[E-2]   Oliver, J. A., Kosmatka, J. B., "Finite element model correlation of a composite UAV wing using modal frequencies", *SPIE Smart Structures and Non-destructive Evaluation Conference*, San Diego, CA, March 19-22, (2007)

[E-3]   Hemez, F.M., *Uncertainty Quantification and the Verification and Validation of Computational Models*, Damage Prognosis for Aerospace, Civil and Mechanical Systems, Edited by D.J. Inman, C.R. Farrar, V. Lopes Jr., and V. Steffen Jr., John Wiley & Sons Ltd., London, United Kingdom, (2004). (LA-UR-03-8491)

[E-4]   Schultze, J. F., Hemez, F.M., Doebling, S. W., Sohn, H., "Statistical Based Non-Linear Model Updating Using Feature Extraction", *Proceedings of IMAC-XIX, the 19th International Modal Analysis Conference*, Kissimmee, Florida, February 5-8, (2001)

[E-5]   Hasselman, T. K., Wathugala, G. W., "A Hierarchical Approach for Model Validation and Uncertainty Quantification", *WCCM V Fifth World Congress on Computational Mechanics*, Vienna, Austria, July 7-12, (2002)

[E-6]   MATLAB version 7.8.0. Natick, Massachusetts: The MathWorks Inc., (2009)

[E-7]   MD. NASTRAN 2006 R1. Santa Ana, California: MSC Software., 2006